Functional Lanthanoid Cryptates – From Mononuclear Amino Acids to Luminescent Nanocodes

Dissertation

der Mathematisch-Naturwissenschaftlichen Fakultät
der Eberhard Karls Universität Tübingen
zur Erlangung des Grades eines
Doktors der Naturwissenschaften
(Dr. rer. nat.)

vorgelegt von
Elisabeth Kreidt, M. Sc.
aus Essen

Tübingen
2018

Gedruckt mit Genehmigung der Mathematisch-Naturwissenschaftlichen Fakultät der Eberhard Karls Universität Tübingen.

Tag der mündlichen Qualifikation:	30.11.2018
Dekan:	Prof. Dr. Wolfgang Rosenstiel
1. Berichterstatter:	Prof. Dr. Michael Seitz
2. Berichterstatter:	Prof. Dr. Hermann A. Mayer
3. Berichterstatter:	Prof. Dr. Peter Roesky

This work was carried out from December 2014 to October 2018 under the supervision of Prof. Dr. Michael Seitz at the Chair of Inorganic Chemistry I, Ruhr-University Bochum and at the Institute of Inorganic Chemistry, Eberhard Karls University Tübingen.

Publication List

E. Kreidt, L. Arrico, F. Zinna, L. Di Bari, M. Seitz
Circularly Polarised Luminescence in Enantiopure Samarium and Europium Cryptates
Chemistry - A European Journal **2018**, *24*, 13556-13564.

E. Kreidt, C. Kruck, M. Seitz
Nonradiative Deactivation of Lanthanoid Luminescence by Multiphonon Relaxation in Molecular Complexes
in *Handbook on the Physics and Chemistry of Rare Earths*, Elsevier: Amsterdam, **2018**, 35-79.

C. Wang, S. Otto, M. Dorn, E. Kreidt, J. Lebon, L. Sršan, P. Di Martino-Fumo, M. Gerhards, U. Resch-Genger, M. Seitz, K. Heinze
Deuterated Molecular Ruby With Record Luminescence Quantum Yield
Angew. Chem. Int. Ed. **2018**, *57*, 1112-1116.

E. Kreidt, C. Dee, M. Seitz
Chiral Resolution of Lanthanoid Cryptates with Extreme Configurational Stability
Inorganic Chemistry **2017**, *56*, 8752-8754.

E. Kreidt, C. Bischof, C. Platas-Iglesias, M. Seitz
Magnetic Anisotropy in Functionalized Bipyridyl Cryptates
Inorganic Chemistry **2016**, *55*, 5549-5557.

C.Doffek, J. Wahsner, E. Kreidt, M. Seitz
Breakdown of the energy gap law in molecular lanthanoid luminescence: the smallest energy gap is not universally relevant for nonradiative deactivation
Inorganic Chemistry **2014**, *53*, 3263-3265.

Danksagung

Ein besonderer Dank gilt meinem Doktorvater Prof. Dr. Michael Seitz für die Möglichkeit diese Arbeit anfertigen zu können, den stetigen wissenschaftlichen Austausch und die große Unterstützung.

Prof. Dr. Hermann A. Mayer danke ich für die Übernahme der Zweitbegutachtung.

Bei Prof. Dr. Bauke Albada (Wageningen University), Prof. Dr. Lorenzo Di Bari (Università di Pisa), Prof. Dr. Katja Heinze (Universität Mainz), Prof. Dr. Carlos Platas-Iglesias (Universidade da Coruña), Dr. Ute Resch-Genger (Bundesanstalt für Materialforschung und -prüfung Berlin), Dr. Andrey Turshatov (Karlsruher Institut für Technologie) und Dr. Francesco Zinna (Université de Genève) bedanke ich mich für spannende und produktive Kooperationen.

Bei Dr. Klaus Eichele und Kristina Strohmeier möchte ich mich für die Hilfe bei allen NMR-spezifischen Fragen und Problemen bedanken. Bei Dr. Dorothee Wistuba, Dr. Peter Haiss, Claudia Krause und Andrea Ewald für die ausdauernde Unterstützung durch die Anfertigung vieler MS-Messungen. Cornelia Halder danke ich für die große Hilfe bei der Anschaffung von Geräten und Materialien. Bei Dr. Eva Jürgens bedanke ich mich für das Messen, Lösen und Verfeinern von Kristallstrukturanalysen.

Bei Dr. Christine Doffek, Dr. Tuba Güden-Silber, Dr. Jessica Wahsner und bei Dr. Laura Büldt, Carolin Dee, Tobias Haas, Jens Kalmbach, Dr. Christian Kruck, Dr. Wolfgang Leis, Angelika Oswald, Markus Trautnitz bedanke ich mich für die gute Arbeitsatmosphäre und die tolle Zeit im Labor. Es war sehr schön mit Euch und ich werde Euch vermissen! Danke auch dem gesamten AK Kunz für große Hilfsbereitschaft insbesondere in der Anfangszeit in Tübingen.

Bei Dr. Kruck bedanke ich mich für eine lange und spezielle Freundschaft mit vielen besonderen Erlebnissen (zum Beispiel im Fachschaftsrat, nach letzten Klausuren, und beim Aussortieren von weißem Pulver).

Ein großer Dank gilt Dr. Wolfgang Leis für tatkräftige und moralische Unterstützung auf den letzten Metern, zum Beispiel Sonntags am NMR (und bei vielen guten Gesprächen über Chemie, Physik und anderes).

Für das Korrekturlesen dieser Arbeit danke ich Christian Baumhof, Dr. Michael Charlier, Carolin Dee, Tobias Haas, Jens Kalmbach, Dr. Annette Kreidt, Markus Trautnitz und Dr. Wolfgang Leis.

André, Bobo, David, Deike, Eva, Felix, Marlene, Therry und der ganzen Colle-Clique danke ich dafür, dass sie mir so schnell so wichtige Freunde geworden seid. Ihr habt meine Zeit in Tübingen wunderschön gemacht!

Karo und Tobi danke ich für Kochen am Mittwochabend und besonders treue Freundschaft.

Meinen Eltern danke ich dafür, dass sie immer, immer für mich da sind und mich immer unterstützen.

Bei Christian bedanke ich mich für Torte an den schwierigsten Labortagen (pars pro toto).

Zudem danke ich der Studienstiftung des deutschen Volkes für die finanzielle und ideelle Förderung.

Contents

Abbreviations and Definitions

APTE	“addition de photons par transferts d’énergie”
BCN	bicyclo[6.1.0]nonyne
CASSCF	complete active space self-consistent field
CD	circular dichroism
CET	cooperative energy transfer
COSY NMR	correlation spectroscopy nuclear magnetic resonance
CPL	circularly polarised luminescence
CS	contact shift
DCC	*N*,*N*’-dicyclohexylcarbodiimide
DCM	dichloromethane
DCTB	*trans*-2-[3-(4-*tert*-butylphenyl)-2-methyl-2-propenylidene]malononitrile
DDQ	2,3-dichloro-5,6-dicyano-1,4-benzoquinone
DFT	density functional theory
DIPEA	*N*,*N*-diisopropylethylamine
DMF	dimethylformamide
DMSO	dimethylsulfoxid
DNA	deoxyribonucleic acid
DOSY NMR	diffusion-ordered spectroscopy nuclear magnetic resonance
DOTA	1,4,7,10-tetraazacyclododecane-1,4,7,10-tetraacetic acid
DPA	dipicolinic acid
DS	downshifting
DTPA	diethylenetriaminepentaacetic acid
EDTA	ethylenediaminetetraacetic acid

eq.	equivalent(s)
ESA	excited state absorption
ESI-MS	electrospray ionisation mass spectrometry
FITC	fluorescein isothiocyanate
Fmoc	fluorenylmethyloxycarbonyl
HATU	2-(1H-7-azabenzotriazol-1-yl)-1,1,3,3-tetramethyluronoium hexafluorphosphate
hfa	1,1,1,5,5,5-hexafluoropentane-1,4-dione
HOBt	hydroxybenzotriazole
HPLC	high performance liquid chromatography
ICP-MS	inductively coupled plasma mass spectrometry
LDI-MS	laser desorption ionisation mass spectrometry
LIS	lanthanoid induced shift
Ln	lanthanoid
MALDI-MS	matrix-assisted laser desorption/ionisation mass spectrometry
mCPBA	*meta*-chloroperbenzoic acid
MOCA	metal-organic complex array
mRNA	messenger ribonucleic acid
NBS	*N*-bromosuccinimide
NHS	*N*-hydroxysuccinimide
NIR	near-infrared
NOE	nuclear Overhauser effect
OLED	organic light emitting diode
NMR	nuclear magnetic resonance
PA	photon avalanche
PCR	polymerase chain reaction
PCS	pseudocontact shift
PE	polyethylene
PEG	polyethylene glycol

PHB	polyhydroxybutyrate
ppm	parts per million
PRE	paramagnetic relaxation enhancement
QC	quantum cutting
RDC	residual dipolar coupling
RNA	ribonucleic acid
ROA	Raman optical activity
SA-ETU	sensitiser-activator energy transfer upconversion
SAP	square antiprism
SAS-ETU	sensitiser-activator-sensitiser energy transfer upconversion
SOI	spectral overlap integral
SMM	single-molecule magnet
SPPS	solid phase peptide synthesis
THF	tetrahydrofuran
TFA	trifluoroacetic acid
TLC	thin layer chromatography
TSAP	twisted square antiprism
UC	upconversion
UCNP	upconversion nanoparticle
UV	ultraviolet
VCD	vibrational circular dichroism

Some physical parameters have proven to be very useful for the quantification and the comparison of the photophysical properties of different lanthanoid complexes. However, the actual definitions of these parameters are not always consistent and in many studies not clarified, which obviously leads to inconsistencies. During this thesis, the following definitions and correlations will be applied:

- The **observable luminescence lifetime** τ_{obs} describes the experimentally determined time in which the luminescence of the luminophore can be detected after excitation under certain conditions.
- In contrast, the **radiative luminescence lifetime** τ_{rad} is usually not directly accessible. It describes the luminescence lifetime of the luminophore in the theoretical case of the absence of any quenching processes.

- Consequently, the **intrinsic quantum yield** $\Phi_{Ln}^{Ln} = \frac{\tau_{obs}}{\tau_{rad}}$ describes the amount of photons which, after successfully being transferred via the ligand to the lanthanoid, actually are emitted (and did not get lost due to nonradiative deactivation processes).

- The **absolute quantum yield** Φ_{Ln}^{L} refers to the ratio of photons emitted by the luminophore and the photons absorbed by the sample. This parameter is of utmost importance for most applications of lanthanoid luminophores. The absolute quantum yield can be derived experimentally via direct measurement with the aid of standard compounds with a known quantum yield.

- Finally the **sensitisation efficiency** $\eta_{sens} = \frac{\Phi_{Ln}^{L}}{\Phi_{Ln}^{Ln}}$ describes the efficiency of the indirect sensitisation via the antenna effect. Here, for example, the efficiencies of the internal transitions of the ligand and the energy gap ΔE between the triplet state of the ligand and the excited state of the lanthanoid play an important role.

For the sake of brevity, in this work it will not be explicitly discriminated between the terms “rare-earth element” and “lanthanoid”. Consequently, for example cryptates containing yttrium will also be termed as lanthanoid cryptates, though in the strict sense the correct denotation would be rare-earth cryptates.

1 Introduction

La	Ce	Pr	Nd	Pm	Sm	Eu	Gd	Tb	Dy	Ho	Er	Tm	Yb	Lu
Lanthanum	Cerium	Praseodymium	Neodymium	Promethium	Samarium	Europium	Gadolinium	Terbium	Dysprosium	Holmium	Erbium	Thulium	Ytterbium	Lutetium

Figure 1.1: Segment of the periodic table of elements showing the lanthanoids.

The term “lanthanoids” describes lanthanum and the following 14 elements of the periodic table (atomic numbers 57 to 71). These metals share very similar chemical properties and special photophysical and magnetic properties, which offer huge potential for a broad variety of applications and make these metals indispensable in modern technologies. The lanthanoids are most stable as trivalent cations Ln^{III}[1] with a completely filled xenon core [Xe] = $1s^2 2s^2 2p^6 3s^2 3p^6 3d^{10} 4s^2 4p^6 4d^{10} 5s^2 5p^6$ and electronic configurations $[Xe]f^x$ ($0 \leq x \leq 14$). Consequently all valence electrons are located in f-orbitals, which are gradually filled throughout the series.[2][3]

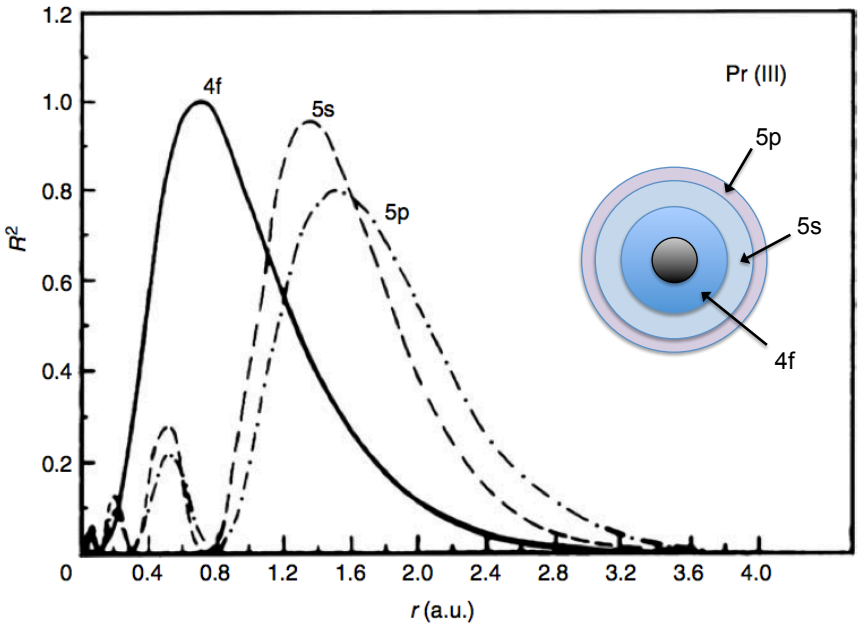

Figure 1.2: Radial charge density of some orbitals of Pr^{III}. Modified from reference [4].

The f-orbitals are spatially less extended than the energetically lower lying, filled 5s- and 5p-orbitals (see Figure 1.2), leading to the unique situation in which the valence shell is shielded by chemically inactive

electrons and hindered from interacting with the surrounding of the lanthanoid ion. This peculiarity results in the similar chemical properties and also some of the fascinating physical properties of the lanthanoids.[5] Depending on how the valence electrons of a lanthanoid ion are distributed on the different f-orbitals, the repulsion between the electrons can be higher or lower, resulting in electronic states of different energies. These states can be described with Russell-Saunders term symbols of the form

$$^{2S+1}L \tag{1}$$

where S corresponds to the total spin quantum number, 2S+1 is the spin multiplicity and L is the total orbital angular momentum quantum number, defined as the sum of all magnetic quantum numbers m_l of the involved electrons.[3][5] The resulting values for L are not given as numbers (0, 1, 2, 3, 4,...) but as capital letters (S, P, D, F, G,...). For a detailed understanding of the electronic states of the lanthanoids, also the spin-orbit coupling needs to be considered. This can be accounted for with an additional quantum number J, which refers to the total angular momentum and can be derived from the quantum numbers L and S as J = L+S, L+S-1..., |L-S|.

$$^{2S+1}L_J \tag{2}$$

Whenever the lanthanoid is surrounded with ligands, the ligand field effects result in further splitting into 2J+1 Stark levels.[2] Different from the situation found for transition metals, the ligand field splitting is small compared to the spin-orbit splitting and does not always need to be considered in detail. Further splitting of the Stark levels into two Zeeman levels m_j each, can be observed whenever a magnetic field is applied. With the aid of Hund's rules the term symbols $^{2S+1}L_J$ describing the electronic ground states of the free lanthanoid ions can easily be identified. The energetic order of the excited states is not that straightforward, but could be calculated for lanthanoids in crystalline matrices or in aqueous solution (see Figure 1.3).[6][7][8][9][10] Since the different relative energies of the electronic states of the various lanthanoids are largely independent from the actual coordination situation around the metal, the values found for lanthanoids in model environments are also suitable for describing the electronic situation in more complex lanthanoid compounds.

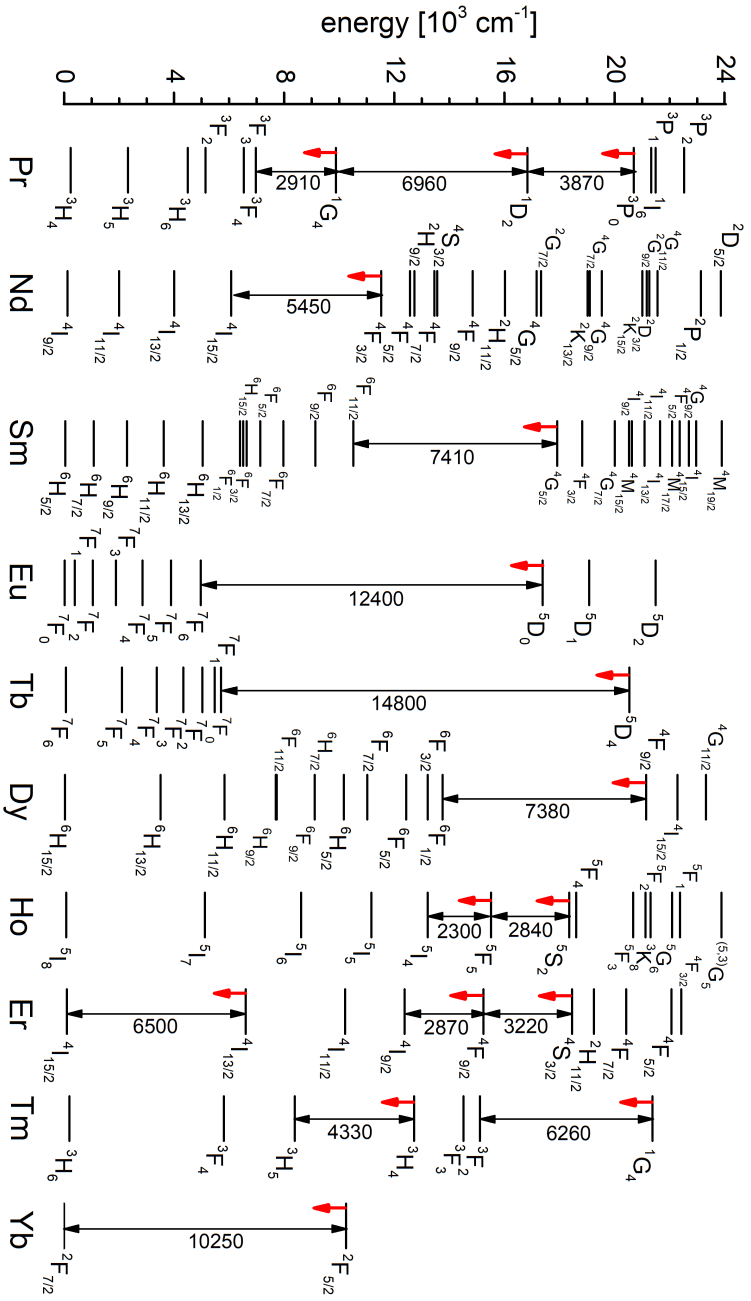

Figure 1.3: Partial energy level diagram for selected trivalent lanthanoid ions. Downward arrows: prominent emitting levels; double headed arrows: energy gap ΔE between emitting level and next lower level (in cm^{-1}). Term symbols $^{2S+1}L_J$ on the left of the lanthanoid manifolds are aligned in height with the quantum number J, the ones on the right with their multiplicities 2S+1. Figure adopted from reference [11].

1.1 Photophysical properties

After population of the excited states of the lanthanoids, the back-transition to the electronic ground state in many cases coincides with the emission of light. The lanthanoids' emission spectra can be recorded in the visible or near-infrared part of the electromagnetic spectrum (see Figure 1.4) and are substantially different from the spectra typically observed in the case of transition metal complexes. They are highly characteristic for the respective lanthanoid and largely independent from the actual chemical surrounding of the metal. Furthermore the transition bands are very narrow, exhibiting only a few nanometers width.[12][5]

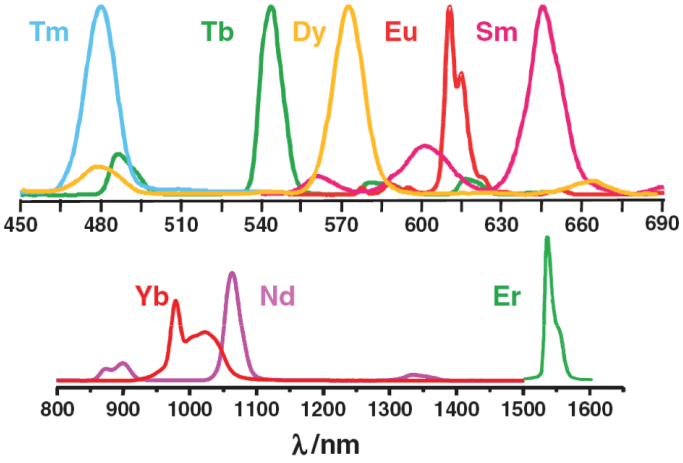

Figure 1.4: Typical emission spectra of some lanthanoids. Figure adopted from reference [13].

Both phenomena are a result of the shielding of the f-orbitals from the lanthanoids' surrounding. Neither are the excited or ground states of the lanthanoids significantly elevated or lowered in energy by interactions with the ligand nor are the emission bands broadened by vibronic couplings. Consequently, ligand-field effects are usually considered to be negligible for the emission spectra of the lanthanoids. In the strict sense this is not completely true, and indeed some recent studies treated the effects of controlled modifications in the coordinative situation on the lanthanoid's emission spectrum in detail.[14][15][16] Nevertheless, generally the emission spectra of the lanthanoids can be considered to be "fingerprint-like" and can be assigned to the respective metal unambiguously, offering optimal prerequisites for multiplexing applications. As the luminescence of the lanthanoids is also intrinsically insensitive to photobleaching, the lanthanoids offer versatile and robust possibilities for the labeling of molecular or nanoscaled structures, as they are e.g. needed for the construction of bioassays or for the quantification of functional groups via luminescence. Generally, the lanthanoids' photophysical properties are highly beneficial for bioimaging applications and related fields.[17][18]

All transitions which can be observed in the case of the trivalent lanthanoids are f-f-transitions and as such Laporte-forbidden, some transitions are also spin-forbidden.[5] This results in very low extinction coefficients (ε below 10 $M^{-1}cm^{-1}$) and consequently in many cases direct excitation of the lanthanoids is not sufficiently efficient.[5] After the lanthanoid has been excited, the Laporte-forbidden nature of the f-f-transitions also makes the back-transition to the ground state slow, resulting in remarkably long luminescence lifetimes.

For example in the case of molecular Eu^{III} or Tb^{III}-complexes, lifetimes in the range of milliseconds can be reached.[19][20] As these luminescence lifetimes significantly exceed the typical lifetimes of the autofluorescence of biological samples, lanthanoids are e.g. of outstanding suitability as luminophores for timegated bioimaging. A typical problem encountered in the field of lanthanoid luminescence is the lanthanoids' high susceptibility towards multiphonon quenching processes, which can drastically reduce the luminescence lifetime and quantum yields of lanthanoid compounds and materials.[20][11]

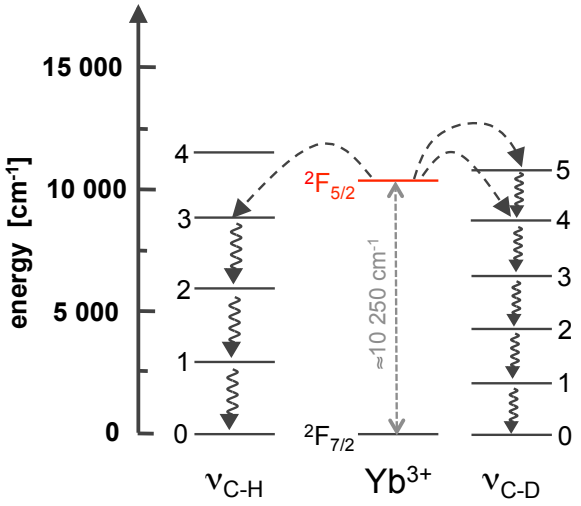

Figure 1.5: Nonradiative deactivation of an excited Yb^{III} ion via interaction with overtones of C-H or C-D oscillators in the close proximity. Figure adopted from reference [11].

Upon interaction with high-energy, anharmonic oscillators such as O-H, N-H or C-H bonds the energy of the excited lanthanoid ion can be transferred to the bond. The efficiency of such processes is directly linked to the spectral overlap of the lanthanoid's transitions and the overtones of the interfering oscillators[21], in other words: The energy transfer from the lanthanoid to an oscillator is the more likely the better the resonance between the two involved states is, and is the more likely the lower the involved overtone is.[11] The most obvious strategy to suppress these multiphonon quenching processes is of course the exclusion of high-energy oscillators from the close proximity of the lanthanoid, for example by designing the ligand in a way that allows for a complete encapsulation of the metal by the ligand, and excludes the very efficient O-H oscillators abundant in solvent molecules from the first coordination sphere around the lanthanoid. However, in most cases the exclusion of quenching oscillators is not completely possible, as for example most ligands used for the preparation of coordination compounds exhibit C-H bonds. In these cases another strategy can improve the photophysical properties of the compound considerably: Whenever the lighter atom of a quenching bond is replaced with an atom whose weight is more similar to the one of the heavier atom, this results in an increase of the reduced mass of the oscillator and consequently in a reduction of the vibrational frequency.[22][23][24] As shown in Figure 1.5 for C-H and C-D, this leads to a situation in which a higher overtone is needed to depopulate the excited state of the lanthanoid, which makes the process considerably less likely to occur. Furthermore, upon deuteration the anharmonicity of

the oscillator decreases significantly, which makes the oscillator more similar to a harmonic oscillator and consequently the selection rule for vibrational transitions in the harmonic model ($\Delta n = \pm 1$) more determinant for the situation. Consequently, the overtones necessary for the energy transfer to the quenching bond are more difficult to populate. Of course this strategy can also be applied to minimise the quenching effects of solvent molecules, typically lanthanoid complexes are more luminescent in deuterated solvents. This can also be employed to estimate the number of solvent molecules in the first coordination sphere q.[25][26][27] Multiphonon quenching is especially problematic for the lanthanoids with transitions in the near-infrared range of the spectrum. Until quite recently this limited strongly luminescent molecular lanthanoid compounds to the complexes of Eu^{III} or Tb^{III}, which are quite robust against these processes. But as a consequence of an improved understanding of the underlying processes, the availability of brightly luminescent molecular compounds of various lanthanoids has considerably improved in the past few years. This results also in an increased interest in more extraordinary luminescence phenomena exhibited by molecular lanthanoid complexes, such as energy transfer processes between lanthanoids[28] (or lanthanoids and d-block metals[29][30]), aiming for the development of molecular systems for upconversion applications.

1.2 Magnetic properties

The unusual electronic situation found for the lanthanoids does not only lead to special photophysical properties, but also results in unique magnetic properties, which differ substantially from the ones typically found for transition metals. In the case of the lanthanoids, where the crystal field effects are too small to lift the degeneracy of the valence orbitals significantly, the non-vanishing orbital angular momentum of the electrons results in a large spin-orbit coupling. It leads to the splitting into different J-states and is much stronger than the spin-orbit coupling usually observed for the transition metals. The ligand field effects do indeed lead to a crystal-field splitting, but the resulting energetic differences only amount to a few hundred wavenumbers. So in the case of a quantum mechanical analysis of the situation, the crystal field effects can be treated as a perturbation of the splitting resulting from the spin-orbit coupling, which is reverse to the strategy usually applied for a corresponding treatment of the transition metals.[31][3]

Differently to the case of the photophysical properties of the lanthanoids, where the influence of the crystal field splitting is so small that it usually can be neglected, in the case of the magnetic properties these effects are the ones which are decisive for the observed phenomena. Upon interaction with the ligand field, every J-state is splitting into 2J+1 sublevels m_J for even J, and (2J+1)/2 sublevels for uneven J.[34] This situation gives rise to considerable anisotropies of the magnetic susceptibility of the lanthanoids, which makes them highly suitable for different applications. By far the most widely established application is the use as contrast agents in bioimaging, most prominently for MRI.[35][36] But also in different fields such as the construction of single-molecule magnets (SMMs)[37][32][38] or the use as paramagnetic shifts reagents in NMR[39][40][41][42][43] lanthanoids have high potential. Since the effects responsible for the actual manifestation of the crystal field splitting and the resulting magnetic properties are complex, for an exact quantitative treatment of the situation found in a particular lanthanoid compound, elaborate “complete active space self-consistent

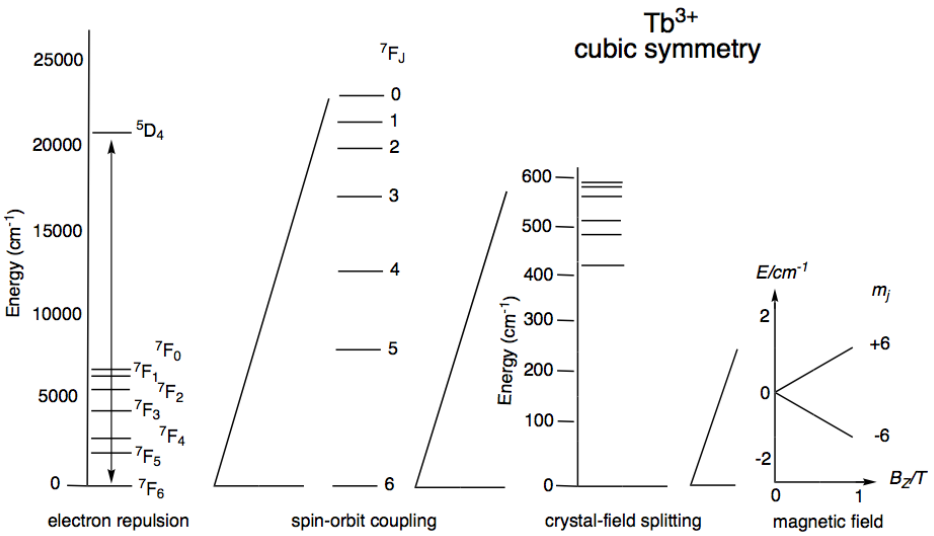

Figure 1.6: Different interactions and the resulting energy splittings in the case of a Tb^{III} in a cubic symmetrical coordination environment.[32] Figure adopted from reference [33].

field" (CASSCF) calculations are necessary.[44][45][46] Nevertheless, a qualitative approach based on purely electrostatic considerations has proven to be surprisingly successful in the rationalisation of the properties of various paramagnetic lanthanoid compounds.[47] In the simplest version of this model, the basic shapes of the electron densities of the lowest J states of the different lanthanoids are derived from the orbitals occupied in the respective situation, which can easily be deduced from Hund's rules. The resulting shapes of the f-electron density can be prolate (axially elongated, for example Yb^{III} or Er^{III}), oblate (equatorially expanded, for example Dy^{III} or Nd^{III}) or isotropic (spherical) (see Figure 1.7(a)). When in the next step the coordination symmetry of the ligand scaffold is considered, it is quite easy to estimate if the ligand will be suitable to stabilise the ground state via repulsive interactions between the electron distribution of the Ln^{III} and the coordinating ligand. This results in a highly anisotropic situation, as it is targeted for in the design of single-molecule magnets (see Figure 1.7). Based on these simple considerations it is for example possible to gain a qualitative understanding of the extraordinary suitability of axially-coordinating ligand environments to prepare Dy^{III}-based single-molecule magnets.[48][49]

Without losing the general simplicity of this model, it is also possible to explain more specific observations like the energetic order of the split J states of a lanthanoid compound, simply by considering the anisotropy of individual states m_J instead of the total electron density distribution.

In NMR experiments, the presence of an unpaired electron of paramagnetic substances leads to characteristic changes in the observed spectra. Some of the underlying effects are the paramagnetic relaxation enhancement (PRE)[50], residual dipolar couplings (RDC)[51], contact shifts (CS) and pseudocontact shifts (PCS)[50][52]. In the case of the contact shifts and the pseudocontact shifts, the interaction of the unpaired electron spin of the paramagnetic center with the probed nuclear spins leads to changes of their resonance frequency, and consequently to a shift of the corresponding signals.

Paramagnetic shift reagents are an example for a long known application based on these effects, where the

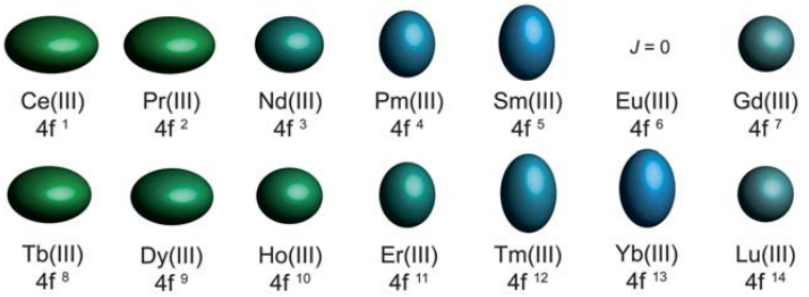

(a) Schematic representation of the 4f-orbital electron distribution for the Ln^{III}. Figure adopted from reference [47].

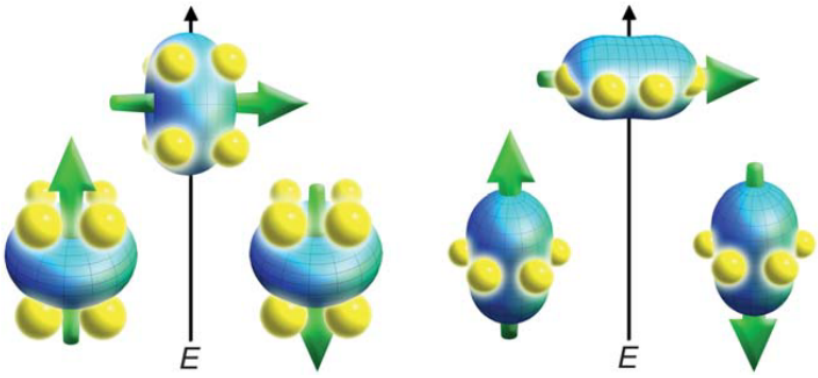

(b) Schematic representation of the interaction of an oblate (left) or a prolate (right) electron density distribution with crystal fields that typically leads to an energetic stabilisation of the m_J state. Figure adopted from reference [47].

Figure 1.7: Based on the shape of the electron densities of the f-orbitals occupied in the case of the lowest J states of the different lanthanoids, the corresponding electron distributions can be derived. In an easy but surprisingly successful model the magnetic properties can be rationalised based on consideration of the electrostatic interactions with different crystal field environments.[47]

distribution of the signals of complex organic molecules over a wider ppm range helps to interpret the spectra, or where chiral shift reagents help to determine the ratio of two enantiomeric forms of a compound.[53][54] For nuclei more than four bonds apart from the paramagnet, the contact shifts δ_C are usually assumed to be negligible, so that the observed shift $\Delta\delta_{obs}$ approximately equals the pseudocontact shifts δ_{PC}:

$$\Delta\delta_{obs} = \delta_C + \delta_{PC} \approx \delta_{PC} \tag{3}$$

δ_{PC} can be correlated with the position of the nucleus relative to the paramagnetic center. This is usually expressed in polar coordinates by the distance r and the angles Θ and Ω.

If the anisotropy of the magnetic susceptibility $\Delta_{\mathcal{X}}$ (which can be described as tensor consisting of axial and rhombic components $\Delta\mathcal{X}_{ax}$ and $\Delta\mathcal{X}_{rh}$) is known, the shift of the signals can be correlated with the position of the nucleus relative to the paramagnetic center. This is usually expressed in polar coordinates

with the distance r, and angles Θ and Ω relative to the principal axis of the $\Delta_{\mathcal{X}}$-tensor:[55][56]

$$\delta_{PC} = \frac{1}{12\pi r^3}\left[\Delta\mathcal{X}_{ax}\left(3cos^2\Theta - 1\right) + \frac{3}{2}\Delta\mathcal{X}_{rh}\left(sin^2\Theta cos\,2\Omega\right)\right] \quad (4)$$

Consequently, the paramagnetic shifts observed in NMR spectra can provide valuable structural information. A theory for the quantitative analysis of the paramagnetic shifts was introduced by Bleaney in 1972.[57] Based on some assumptions he concluded that the components $\Delta\mathcal{X}_{ax}$ and $\Delta\mathcal{X}_{rh}$ of the anisotropy of the magnetic susceptibility could be calculated from the second order ligand field parameters B_0^2 and B_2^2, respectively, and a tabulated parameter describing the lanthanoid under study, the so-called Bleaney constant C_J:

$$\Delta\mathcal{X}_{ax} = -\frac{\mu_0\mu_B^2 C_J B_0^2}{10\,(k_B T)^2} \quad (5)$$

$$\Delta\mathcal{X}_{rh} = -\frac{\mu_0\mu_B^2 C_J B_2^2}{30\,(k_B T)^2} \quad (6)$$

with the vacuum permeability μ_0, Bohr's magneton μ_B, the Boltzmann constant k_B and the temperature T. Though the second order ligand field parameters B_0^2 and B_2^2 are usually not easily accessible in the case of lanthanoid complexes, at least for isostructural complexes of different lanthanoids Bleaney's theory seemingly offers an appealing simplification and is still quite commonly used, though several studies already showed that drastic deviations from the predicted behaviour can be observed in many cases, as the assumptions made by Bleaney are often not appropriate.[58][59][60] For example, Bleaney's theory assumes the splitting of the crystal field to be small compared to kT (about 204 cm^{-1} at 293 K)[61], which at room temperature would lead to a comparable population of all states, completely neglects crystal field terms of orders higher than two[62] and assumes the ligand field to be independent of the coordinated lanthanoid ion. To obtain reliable results usually a more careful, analysis and also detailed information about the solution structure of the compound under study are needed. In many cases such an analysis of the paramagnetic properties was possible, and this also led to some studies in which lanthanoid tag molecules could e.g. be used for improving the understanding of biomolecules in solution.[63][64][65]

Since of course the underlying physical phenomena are generally the same for paramagnetic NMR and single-molecule magnets, the use of the extremely well established NMR spectroscopy could also be helpful for research towards improved SMMs. However, exchange between both communities seems to have been quite limited until now, and there are surprisingly few examples in which NMR data has been used for a rationalisation of the SMM-behaviour of a lanthanoid coordination compound.[66][67][68][69]

1.3 Coordination compounds of the lanthanoids - role of the ligand

The unusual electronic situation, in which the valence electrons are shielded by the filled 5s and 5p orbitals from potential interaction partners, is also dominating the coordination chemistry of the trivalent lanthanoids. Generally, the interaction between lanthanoids and their ligands is considered to be almost completely electrostatic, since at the encountered situation covalent contributions are almost completely prevented. As a consequence, the interactions between metal and ligand are non-directional and labile. Lanthanoid complexes in solution are typically of low stability and readily dissociate, the common strategy to circumvent or at least reduce this problem is the use of chelating ligands.[70] Even more challenging is the suppression of conformational rearrangement processes. In solution almost all lanthanoid complexes are present as a mixture of different interconverting isomers. This leads to severe difficulties in the context of various potential applications of lanthanoid coordination compounds, and of course also in the design of experiments for the improvement of the fundamental understanding of the physical properties of the lanthanoids. The aspects outlined above govern the ligand design for lanthanoid coordination compounds and make it substantially different to the strategies commonly applied for transition metal complexes.
When the photophysical properties of a lanthanoid coordination compound are to be studied, the ligand in most cases gains an additional and essential function. As already described in chapter 1.1, the Laporte-forbidden character of the f-f-transitions makes their extinction coefficients very small (ε below 10 $M^{-1}cm^{-1}$), and in most cases direct excitation is not feasible or at least not efficient.

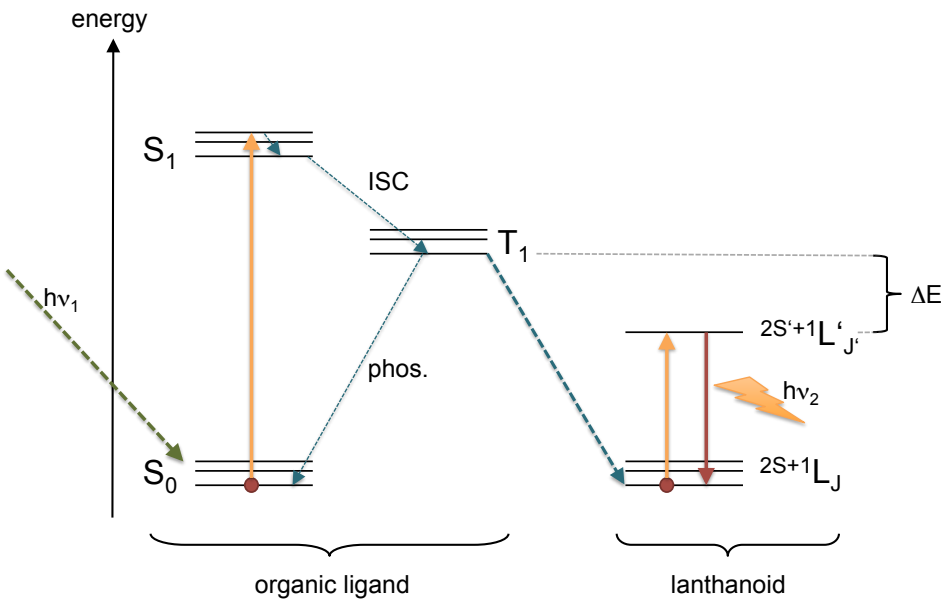

Figure 1.8: Indirect excitation of a lanthanoid ion via the so-called “antenna effect”. The organic ligand absorbs light, which results in the population of the excited singlet state S_1, and subsequently via an intersystem crossing (ISC) the energy is transferred to the excited triplet state T_1. The direct depopulation back to the electronic ground state, which would be attended by the emission of light (phosphorescence, phos.), is in principle possible, but as it is slow in a competing process a significant fraction of the energy can be transferred to the coordinated lanthanoid.

The so called “antenna effect” allows to bypass this problem in an elegant fashion:[71][5][20][72] To do so the lanthanoid is brought in close proximity to chromophoric (usually aromatic) groups of the ligand, which can easily and with a conventional light source be excited to a higher electronic level (usually a singlet state). After internal intersystem crossing (ISC) a triplet state of the ligand is populated. As the direct transition back to the singlet ground state is forbidden, the triplet state can be relatively long-lived, which makes an energy transfer to the coordinated lanthanoid feasible. Basically such an energy transfer can follow two possible mechanisms: the Dexter[73] or the Förster[74] mechanism. Since a Dexter-type energy transfer includes the exchange of electrons, it does require the overlap of orbitals of donor and acceptor. Consequently it is not likely to occur between a ligand and a lanthanoid with shielded valence electrons. The Förster-type energy transfer, in contrast, is a dipole-dipole interaction and as such does not need any covalent interaction between donor and acceptor. As a result this mechanism can usually be assumed to be at least the dominant contribution to the energy transfer from the ligand to the lanthanoid. In any case, as this indirect excitation does not involve f-f-transitions it can be much more efficient than the direct excitation. After the population of the excited state several scenarios are possible. Firstly, if the energy gap between the triplet state of the ligand and the excited state of the lanthanoid is too small, thermal activation can be sufficient to result in a back transfer of the energy to the ligand. As a rule of thumb this process is negligible whenever the energy gap ΔE exceeds 2000 cm^{-1}. Secondly, the excited state can be depopulated via nonradiative deactivation, as described in chapter 1.1, and last but not least the (in most cases) desired radiative deactivation under emission of light of the characteristic wavelengths can occur. The ligand does not only play a major role in the population of the excited state of the lanthanoid, it is also of utmost importance for the suppression of nonradiative deactivation processes and to ensure that a sufficient fraction of the excited lanthanoid ions relaxes under emission of light.[11] This can be accounted for in several aspects of ligand design. Whenever lanthanoid complexes in solution are studied, solvent molecules (more precisely: their high-energy, anharmonic oscillators, e.g. O-H bonds) in the first coordination spheres around the lanthanoid are especially efficient quenchers. An obvious consequence for ligand design is to exclude solvent molecules as effectively as possible from the close proximity of the lanthanoid. Unfortunately also the ligands usually possess bonds which can act as highly efficient quenchers, such as C-H bonds, which cannot be controlled that rigorously as they are an integral component of the ligand. As already described in chapter 1.1, the detrimental effect of these bonds can be reduced by exchanging the proton with a heavier atom. Chemically, this results in either halogenation or deuteration of the ligand scaffold. From a physical perspective (per)halogenation would be more efficient, but this usually cannot be realised synthetically.[75][76][20] In contrast, deuteration of the ligand does not influence its chemical properties and is consequently the much more feasible approach to improve the properties of a given ligand scaffold. Comparative studies of protiated ligands and their deuterated derivatives already proved the high impact of this strategy and also helped to improve the quantitative understanding of multiphonon quenching processes.[77][11]

Though the ligand of a lanthanoid coordination compound does not affect the shape of the emission spectrum of the lanthanoid strongly, for the reasons outlined above the right choice of the ligand is nevertheless extremely important for the preparation of highly luminescent lanthanoid complexes. Together with the general difficulty of the preparation of lanthanoid complexes which are stable in solution (vide supra), this

results in a situation where only a limited range of ligand scaffolds have proven to be of a broader applicability for the preparation of luminescent lanthanoid complexes. Some ligand scaffolds with typical coordination motifs are shown in Figure 1.9. As a consequence of the lanthanoids' character as hard Lewis

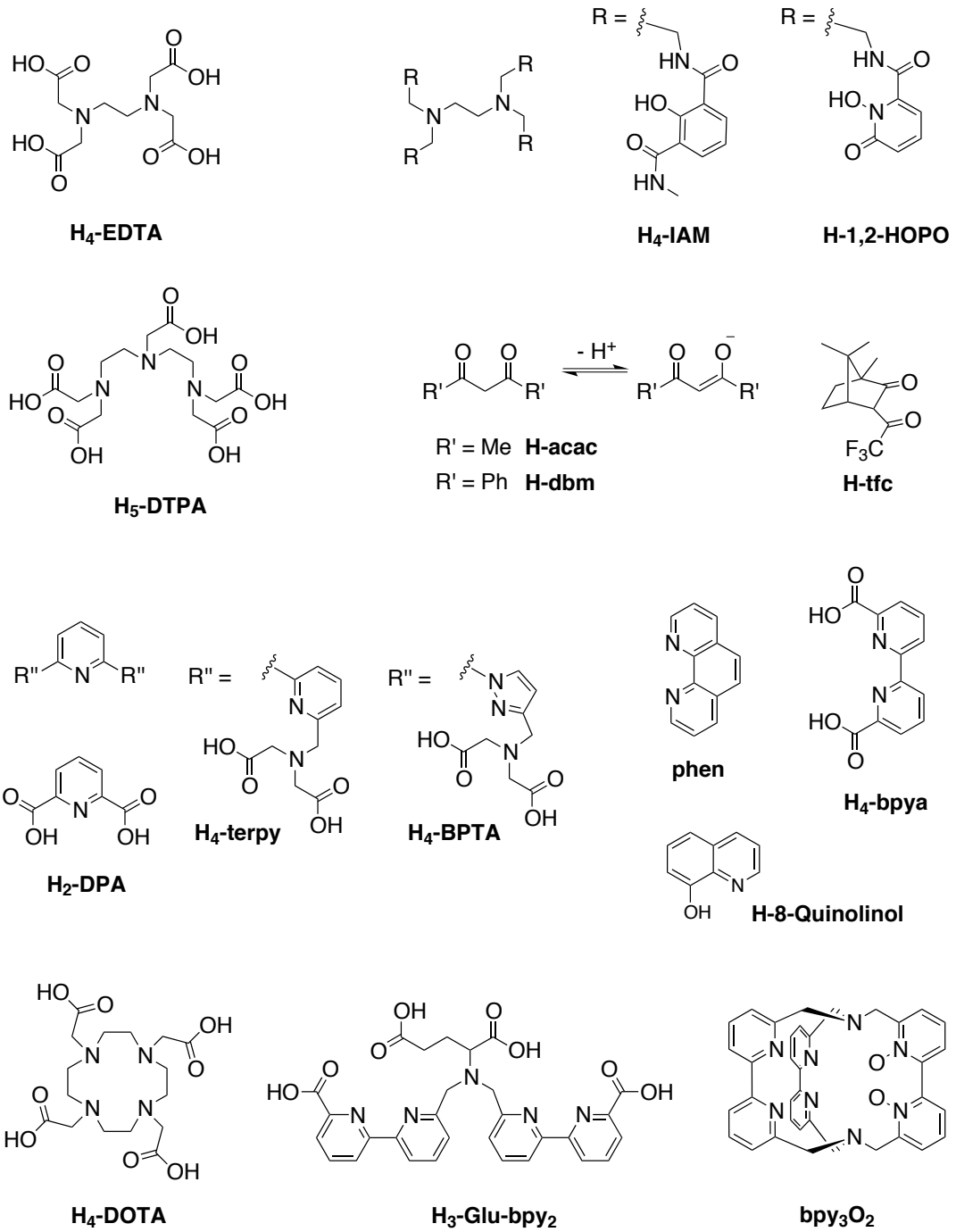

Figure 1.9: Representative examples of ligand architectures which have proven to be suitable for the preparation of lanthanoid coordination compounds. References are given in the text.

acids, nitrogen and oxygen are obvious choices as coordinating heteroatoms in ligands for lanthanoids.

For example this makes the chelating aminopolycarboxylic acids highly suitable coordination motifs for lanthanoids. **EDTA**[78][79][80] (ethylenediaminetetraacetic acid) and **DTPA**[81][35] (diethylenetriaminepentaacetic acid, pentetic acid) are two prominent examples of such compounds, which indeed allow for the preparation of stable lanthanoid compounds. Whereas Gd-DTPA is a very common contrast reagent for MRI, the lanthanoid complexes of EDTA are not so common. But similarly to EDTA, **IAM**[82][83][84] (chromophoric group: 2-hydroxyisophtalamide) and **1,2-HOPO**[85][83][84] (chromophoric group: 1-hydroxy-pyridin-2-one) can be considered derivatives of ethylene diamine. Compared to EDTA, the acetic acid groups have been replaced with more complex functionalities which allow for indirect excitation of the coordinated lanthanoid, an improved exclusion of solvent molecules from the first coordination sphere, and an overall improved control over the structure of the complex in solution. A vast group of lanthanoid ligands are the β-diketonates such as **acac**, **dbm** or **tfc**.[86][87] They are usually prepared as tris complexes, Lewis base adducts of the tris complexes, or tetrakis complexes and have proven to be of high potential for various applications. The synthesis of the ligands is relatively easy and a plethora of functionalisations and modifications have already been realised. Typically the lanthanoid complexes of β-diketonates are kinetically labile and readily undergo exchange processes in solution.[88] **DPA**[89][90][91][92] is the parent compound for another class of versatile ligands for lanthanoids, such as the **terpy**[93][94][95][96] or **BPTA**[97][98] scaffolds, which again can make use of aminopolycarboxylic acid groups for the stable coordination of the lanthanoid. Generally, aromatic nitrogen containing heterocycles[99] are a common ligand motif in lanthanoid coordination chemistry and have proven to be highly suitable chromophores for the indirect excitation via the antenna effect. An especially prevalent chromophoric group for lanthanoids are the 2-2'-bipyridines[100][101]. For example the corresponding dicarboxylic acid **bpya**[100][102][103] is a surprisingly efficient sensitiser for Tm^{III} luminescence, and also the 2-2'-bipyridine carrying two iminodiacetic acid groups in ortho position were found to be useful scaffolds for the preparation of luminescent compounds of Eu^{III}, Tb^{III} and even Sm^{III}, though Sm^{III} is a lanthanoid quite susceptible towards multiphonon quenching.[100][96] Often 2-2'-bipyridine units are incorporated into more complex ligand structures, such as the glutamic acid derivative **Glu-bpy$_2$**.[104] Due to the high structural similarity to 2,2'-bipyridine, it is not so surprising that phenanthroline **phen** can also be used as an efficient antenna ligand for the lanthanoids.[105][106] Compared to bpy-based ligands, the more extended chromophoric system allows for excitation at higher wavelengths. If no additional chelating ligands are used, the lanthanoid complexes of **phen** readily dissociate in solution[105], but for example in combination with additional β-diketonates the stability of the complexes can be significantly improved.[107] Analogously to the bpy unit, also the phenanthroline unit can be used for the coordination of lanthanoids as a dicarboxylic acid derivative[108] or as building block in more complex chelating ligands.[109] Complexes of **8-Quinolinol** and its derivatives are well known for their application as OLED emitters[110][111], but they are also another example for N-heterocyclic building blocks which serve as coordinating and sensitising units in lanthanoid coordination chemistry. Typically the energy of the triplet states of these chromophores amounts to around 19000 cm^{-1}, which is not enough energy for the sensitisation of lanthanoids emitting in the visible region of light, but sufficient in the case of the near-infrared emitting lanthanoids.[112][113][114][115]
An extremely well studied and established group of ligands for lanthanoids are based on the 1,4,7,10-tetraazacyclododecane-*N,N',N'',N'''*-tetraacetic acid (**DOTA**), which can be seen as a macrocyclic aminopolycarboxylic acid. The complexes of **DOTA** and the lanthanoids are extremely stable against decomplexa-

tion, and stability constants up to 10^{28} have been determined.[116][117][118] Since 1989 the corresponding Gd^{III} complex has been used as MRI contrast agent and is still one of the most prescribed substances for this purpose. The synthesis of the DOTA-type ligands from the cyclen ring and four pendant arms makes a wealth of derivatives easily accessible and for example allows for the introduction of different antenna moieties. A typical issue of lanthanoid coordination compounds which results from the absence of significant ligand field effects is the low configurational and conformational stability of these compounds in solution. The corresponding interconversion processes have been especially well studied in the case of

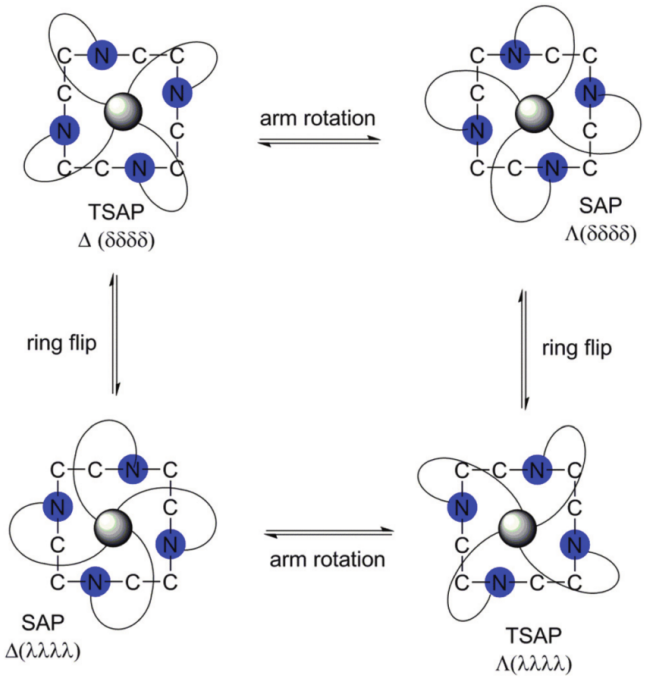

Figure 1.10: Schematic representation of the rearrangement processes relevant for DOTA-type complexes. The pendant arms can be arranged clockwise (Λ) or counterclockwise (Δ) and the ring can be arranged with a clockwise ($\lambda\lambda\lambda\lambda$) or counterclockwise ($\delta\delta\delta\delta$) helicity. This results in the presence of two diastereomers, each being present as an enantiomeric pair, and the presence of two isomers in solution, the monocapped Square Antiprism (SAP) and the monocapped Twisted Square Antiprism (TSAP). The ratio of the isomers is dependent on the coordinated lanthanoid ion and the modifications introduced to the DOTA-scaffold. Figure adopted from reference [119].

the DOTA-based ligands (see Figure 1.10).[120][121] Substantial effort has been invested to modify the ligand scaffold in order to suppress these processes, but this was not completely successful until now.[119] Consequently, whenever a sample of a DOTA-type complex is studied in solution it has to be considered as a mixture of interconverting isomers. Since the small structural variations resulting from these interconversion processes do not significantly affect the emission spectra of the complexes, they are usually not perceived as a substantial problem for the application as luminophores. But obviously the intrinsic flexibility of most lanthanoid complexes is a substantial problem for studies targeting an improvement of the basic understanding of the physics of the lanthanoids, and the strategical improvement of their coordination com-

pounds. Additionally, there are also some highly interesting applications for which lanthanoid coordination compounds have enormous potential, but which are drastically hindered by the typical interconversion processes outlined above. Important examples for such applications are the use of paramagnetic lanthanoid complexes for the structural elucidation of biomolecules (see chapter 1.2) or the phenomenon of circularly polarised luminescence (vide supra). Consequently, there is a general need for lanthanoid coordination compounds with a more well-defined structure in solution. A ligand scaffold which indeed allows for the preparation of extremely well-defined compounds in solution are cryptands consisting of three bipyridine units which are arranged around the coordinated lanthanoid in a macrobicyclic fashion.[122]

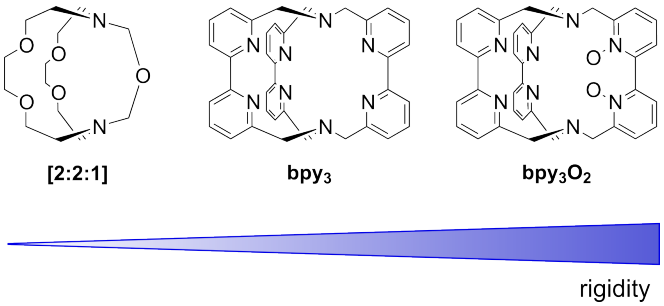

Figure 1.11: Evolution of cryptands used for the preparation of lanthanoid coordination complexes. From the macrobicyclic crown ether **[2.2.1]** over the tris-bipyridine **bpy$_3$** to the oxidised scaffold **bpy$_3$O$_2$** the rigidity of the corresponding complexes increases, allowing for an improved control over the exact coordination situation.

Originally, the cryptands were developed as macrobicyclic form of the crown ethers with improved stabilities and selectivities for the corresponding alkali metal complexes.[123][124] Soon these ligands were found to yield extraordinarily stable complexes with lanthanoids[125] and also the photophysical properties of **Eu-[2.2.1]** were studied.[126] But obviously the three-dimensional crown ether **[2.2.1]** is not a well-suited ligand for the preparation of luminescent lanthanoid complexes, since the scaffold does not contain any chromophoric groups which may serve as antenna. Furthermore it leaves the coordinated lanthanoid ion quite accessible for solvent molecules, which for example in water results in a quite efficient nonradiative deactivation and low luminescence efficiencies. A straightforward improvement was the partial or complete exchange of ether moieties with aromatic heterocycles, which for example resulted in the development of the bipyridine based cryptand **bpy$_3$**.[127] As expected, lanthanoid ions incorporated into this scaffold can be excited indirectly via the bipyridine moieties and the decent photophysical properties of these compounds have been studied in detail.[122][128][129]

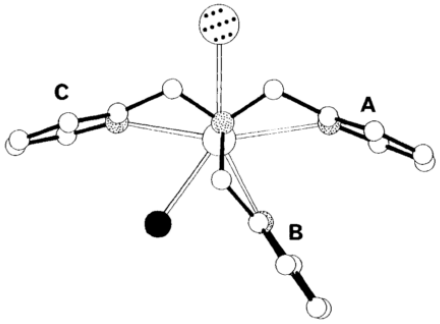

(a) Crystal structure of the terbium cryptate **Tb-bpy$_3$** with one chloride anion (large dotted circle) and one water molecule (oxygen atom: black circle) as additional ligands coordinated directly to the lanthanoid. Hydrogen atoms are omitted for clarity. Figure adopted from reference [130].

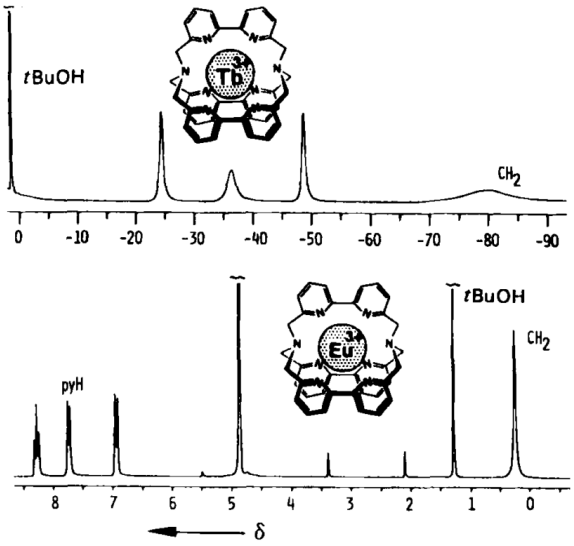

(b) ^{1}H NMR spectra (200 MHz, D_2O) of the lanthanoid cryptates **Tb-bpy$_3$** (top) and **Eu-bpy$_3$** (bottom). Figure adopted from reference [122].

Figure 1.12: Crystal structure (a) and ^{1}H NMR (b) of the lanthanoid cryptates **Ln-bpy$_3$** point towards the presence of several interconverting conformers in solution. In Figure (a) small white circles represent carbon atoms, small dotted circles represent nitrogen atoms and the big white circle represents the Tb^{III} cation.

Chemically the three bipyridine units of **bpy$_3$** are equivalent, but as the crystal structure of **Tb-bpy$_3$**[130] reveals they are not arranged around the coordinated lanthanoid in a symmetric fashion (see 1.12(a)). In the presence of chloride as additional anionic ligand, the angle between the adjacent bipyridine moieties is strongly widened up, with both bipyridine groups in positions A and C pointing away from the chloride. The third bipyridine is tilted towards the bipyridine in position A, resulting in an distorted T-shape arrangement. Whereas the bipyridines are clearly distinguishable in the crystal structure, the ^{1}H NMR spectra (see 1.12(b)) consist of only a few signals, which indicates that on the NMR time scale the bipyridines are seemingly equivalent, and gives evidence of the flexible nature of the ligand **bpy$_3$** in solution. Of course the bipyridine groups are by far more rigid than the ether moieties of the macrobicyclic crown ethers (e.g. **[2.2.1]**), but for the preparation of reliably rigid lanthanoid cryptates an additional modification is needed. A modification which has proven to be especially useful for this purpose is the introduction of N-oxides to one of the bipyridine units of **bpy$_3$**. The resulting ligand **bpy$_3$O$_2$** (see Figure 1.11)[131][132] allows for the synthesis of lanthanoid complexes of outstanding stability and rigidity, which have already proven to be highly suitable for basic research on the lanthanoids and have bright prospect for future applications. A closer look on the structural properties of the complexes **Ln-bpy$_3$O$_2$** reveals the reason for the outstanding rigidity of these complexes and their unprecedented conformational stability. As documented by structural data from crystallography and DFT calculations (see Figure 1.13), similarly to the cryptates **Ln-bpy$_3$**, the

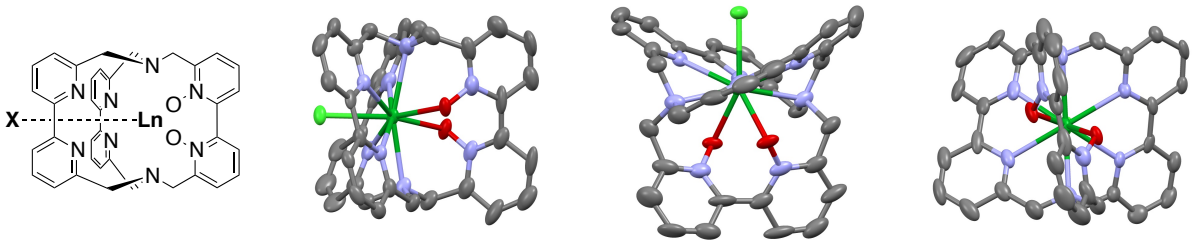

Figure 1.13: Crystal structure (thermal ellipsoid plots, 50% probability level) of **Lu-bpy$_3$O$_2$**. Grey: carbon, blue: nitrogen, red: oxygen, dark green: lanthanoid ion, light green: counter anion. Hydrogen atoms and external chloride ions are omitted for clarity.[133]

lanthanoid is placed virtually in the center of the cavity surrounded by the three bipyridines. But in this case the cavity enclosed by the three bipyridines also contains the two N-oxides, which are sterically pushed apart by the lanthanoid. This results in a distortion of the corresponding pyridines and induces a steric strain, which rigidifies the whole structure. Since the space in the cavity is limited, the N-oxides are locked in place, and cannot move to another position, which fixes the complexes in one conformational arrangement. Experimental evidence for the rigidity of the lanthanoid cryptates is given by their NMR spectra, which typically consist of sharp signals whose numbers reflect the C_2-symmetry of the complexes, and do not show any isomerisation or interconversion processes. The cage-like arrangement of the ligand around the lanthanoid, and its high rigidity result in an extremely high kinetic stability of these cryptates against decomposition processes, even under extreme conditions. For example, in earlier experiments a sample of the europium complex of **bpy$_3$O$_2$** in pure TFA did not show significant decomposition even after a month. This extraordinary stability does not only make the purification of the compounds via HPLC feasible, but also makes the cryptates lanthanoid coordination compounds of outstanding reliability.

Unlike the oxidised bipyridine, the non-oxidised bipyridines are not orientated perpendicular to the symmetry axis but slightly tilted, which makes the overall structure helical, gives rise to a stereogenic element and makes the lanthanoid cryptates chiral.

Typically, the cryptates are assembled as sodium cryptates which are obtained from a macrobicyclisation reaction of a nitrogen-fused macrocyclus of two bipyridines and the dibromide of the oxidised bipyridine in the presence of an excess of sodium carbonate (see Figure 1.14). The sodium cation serves as template

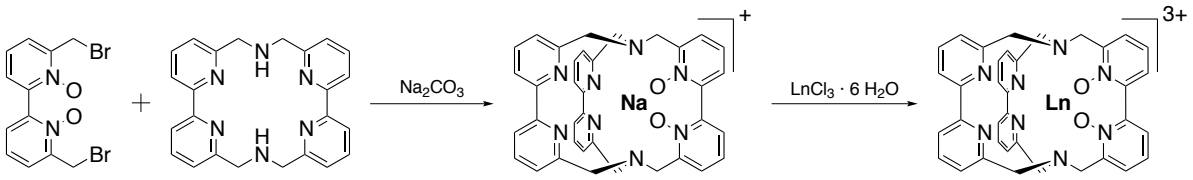

Figure 1.14: Preparation of the sodium cryptates from the corresponding bipyridine building blocks in the presence of sodium carbonate and subsequent conversion into the lanthanoid cryptates.

ion which makes the macrobicyclisation more favourable than the competing polymerisation reactions. Another strategy typically applied for this purpose is the high dilution of the reactants in a large amount of solvent. After purification, the sodium cryptates can be transformed into the complexes of the various

lanthanoids and can be purified via recrystallisation or via HPLC. Since the building blocks of the standard cryptates **bpy$_3$O$_2$** are achiral and neither during the macrobicyclisation nor the complexation reaction any chiral discrimination occurs (see Figure 1.14), the corresponding lanthanoid cryptates are obtained as racemic mixture. Almost all research on lanthanoid cryptates **Ln-bpy$_3$O$_2$** dealt with such racemic mixtures, except for one study which showed that a strategic modification of the bipyridine-N-oxide moiety subjected to macrobicyclisation makes the preparation of enantiopure lanthanoid cryptates possible.[134] This allows for an unprecedented degree of control over the total configuration around the lanthanoid and can become crucial for the use of cryptate-based molecules in the study of chiral systems e.g. most biomolecules, but also opens up new possibilities in fascinating fields of research such as circularly polarised luminescence (CPL).

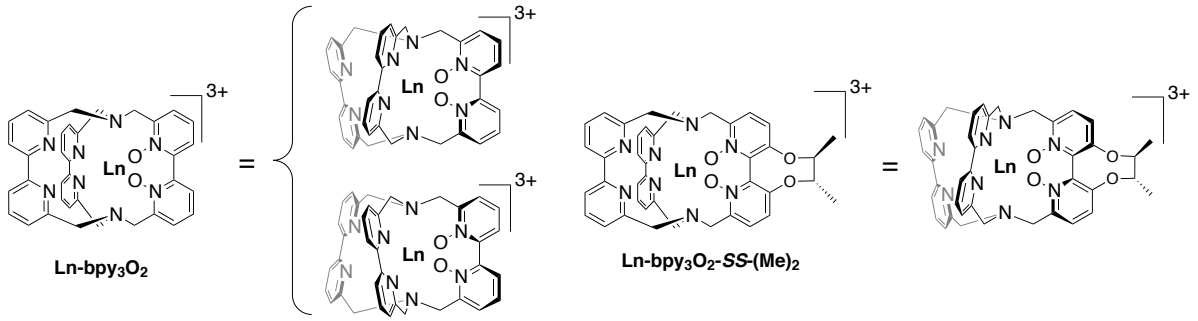

Figure 1.15: Typically cryptates **Ln-bpy$_3$O$_2$** are obtained from synthesis as racemic mixture, but a modification of one of the bipyridine units allows for the synthesis of enantiopure derivatives.

As expected for an assembly of bipyridines, the cryptates **bpy$_3$O$_2$** are well suited antenna chromophores for the indirect excitation of lanthanoids (see Figure 1.8). They absorb light of wavelengths between 300 and 320 nm, and after excitation internal conversion and intersystem crossing processes result in the population of a triplet state with an energy of about 20 500 cm^{-1}, which is sufficient for the sensitisation of many lanthanoids.

Compared to the parent compounds **Ln-bpy$_3$**, the accessibility of the coordinated lanthanoid for external ligands, like solvent molecules, is further reduced in the case of the complexes **Ln-bpy$_3$O$_2$**, which creates improved conditions for the preparation of highly luminescent complexes. As mentioned above, deuteration is a commonly applied strategy for the improvement of the luminescence properties of lanthanoids in organic ligand scaffolds (see Figure 1.5) and this has also proven to be very successful in the case of the lanthanoid cryptates. The stepwise assembly of the cryptates from bipyridine building blocks also allowed for the preparation of several partly deuterated derivatives, whose comparative characterisation gave important insights into the fundamental photophysical principles of molecular lanthanoid compounds. For example, a detailed analysis of the luminescence lifetimes of the complexes led to the calculation of the individual quenching contributions of different C-H oscillators,[135] and the photophysical data collected for the Sm^{III}-complexes also showed, that the so-called energy gap law[136][137][138] is not always applicable in the case of molecular lanthanoid complexes.[139] During these studies, especially in the case of the near-infrared emitting lanthanoids, luminophores with outstanding luminescence lifetimes and absolute

quantum yields could be realised.[133][140] Principally the use of these complexes is not limited to the fundamental research on lanthanoid photophysics but also offers a huge potential for different applications where stable and reliable luminophores are needed. Even more importantly, the extraordinary rigidity and the well defined structure of the lanthanoid cryptates are also of high potential for various fields of research and application, which typically suffer from the usually high structural flexibility of molecular lanthanoid compounds in solution. An important example is the use of paramagnetic lanthanoid complexes for the structural elucidation of biomolecules in solution (see chapter 1.2). An ideal tag molecule for such an application should allow for exactly one spatial arrangement of the paramagnetic center and the biomolecule under study, so that only one set of shifted signals is recorded and an unambiguous assignment is possible. Most molecules actually applied for this purpose are based on intrinsically flexible scaffolds which are modified aiming to control this flexibility, which results in obvious problems and ambiguities. Tag molecules based on oxidised cryptates **bpy$_3$O$_2$** would allow for a general preclusion of any interconversion processes, and would consequently provide improved conditions for studies as outlined above. But obviously an application for such a purpose (and generally most applications as luminophores e.g. in bioimaging) rely on a covalent attachment of the lanthanoid complex to other molecules or materials. For such a purpose some kind of initial functionalisation of the ligand scaffold is necessary. In the case of the more flexible scaffold **bpy$_3$**, such modifications have already been implemented successfully some time ago, and even led to the development of commercially available products based on lanthanoid cryptates. In the case of the ligand scaffold **bpy$_3$O$_2$** this could not be realised until now, which is the major obstacle for highly promising and interesting applications of the extremely stable and well-defined lanthanoid complexes of the type **Ln-bpy$_3$O$_2$**.

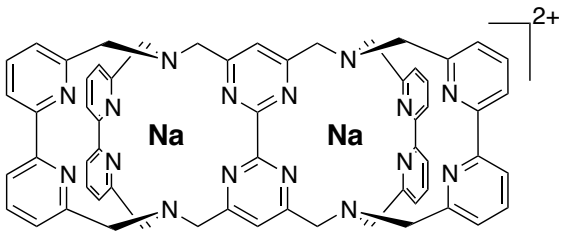

Na-Na-bpy$_2$-bpm-bpy$_2$

Figure 1.16: Scaffold consisting of two fused cryptates **bpy$_3$**, allowing for the controlled synthesis of homo- and heterobimetallic lanthanoid complexes.[141]

Until now the cryptates have been established mainly as scaffolds for the reliable and highly controlled complexation of one lanthanoid ion. But as another recent study showed, a cryptate scaffold can indeed be extended in a way that it accommodates two lanthanoids in separate but jointed cavities. Though the ligand scaffold employed for this purpose (see Figure 1.16) is based on the non-oxidised cryptate **bpy$_3$**, complexes of decent stability and improved rigidity could be realised and, most importantly, in many cases a purification via HPLC is possible. This allows for the highly controlled synthesis of heterobimetallic complexes, and consequently for the targeted combination of two lanthanoids and their respective special properties in one molecule. This is highly interesting e.g. in the context of bimodal imaging. Such compounds are also

very promising for the research on energy transfer processes between lanthanoids. In solid materials and nanoparticles containing lanthanoids there is a plethora of examples for such processes like upconversion, quantumcutting or downshifting. The realisation of these photophysical processes in molecular systems would open up new potentials and, even more importantly, could allow for an improved understanding of the underlying physics. Differently from e.g. nanoparticles or solid materials, a molecular system can be designed and realised in a highly controlled fashion, and can allow for the targeted modification of the parameters influencing the phenomenon under study. Consequently they should allow for a better understanding of these complex processes. The well-defined structure of the cryptates, and for example the fixed distance between both coordinated lanthanoid ions, offers best preconditions for such studies.

2 Objectives

Cryptates have already proven to be an excellent coordination scaffold for the lanthanoids. The efficient shielding of the coordinated metals, and the possibility of efficient suppression of nonradiative deactivation processes make these lanthanoid complexes outstanding luminophores. Due to their rigidity and the inertness of the complexes against decomposition, these complexes are highly reliable and offer best conditions for a wide range of applications. However, the realisation of such applications has been hampered due to the non-availability of reactive functionalisations at the periphery sphere of the ligand.

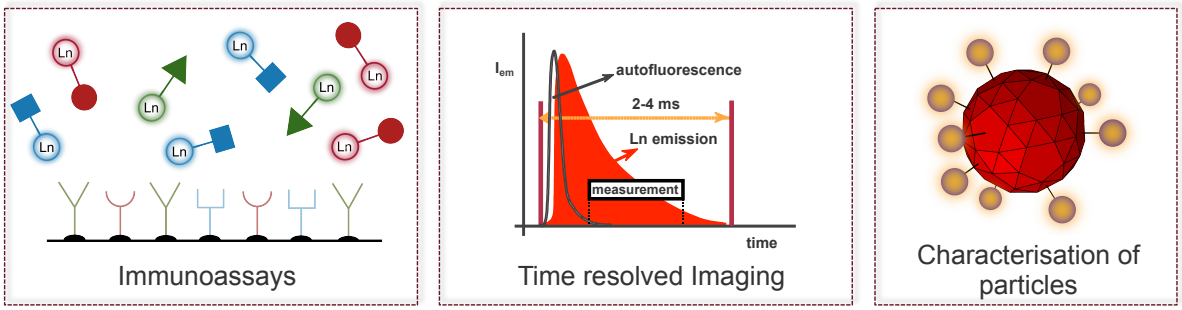

Figure 2.1: Examples for concrete applications based on the covalent attachment of luminophores, which can benefit from highly reliable lanthanoid complexes such as the cryptates **Ln-bpy$_3$O$_2$**.

One of the aims of this work is to overcome this limitation by developing a basis for the versatile functionalisation of lanthanoid cryptates for **various applications** which require a covalent and reliable attachment of the cryptate to another structure or molecule. The range of possible and high potential applications is vast, including e.g luminescent or paramagnetic **tag molecules** for biomolecules, or reagents for the quantification of functionalisations on materials. The following steps are necessary to establish a basis for such applications:

- Preparation of a derivative of the ligand **bpy$_3$O$_2$** with an initial functionalisation of versatile reactivity at the periphery of the scaffold, and preparation of the corresponding lanthanoid cryptates
- Examination of the influence of the initial functionalisation upon the photophysical, magnetic and general properties of the cryptate scaffold (e.g. as consequence of the influence of the functionalisation upon the symmetry of the molecule)
- Development of a general synthetic strategy of broad applicability for the attachment of various functional groups

- Preparation and characterisation of lanthanoid cryptates carrying different functionalities
- Utilisation of the functionalised cryptates for different applications e.g. as luminescent tag molecules

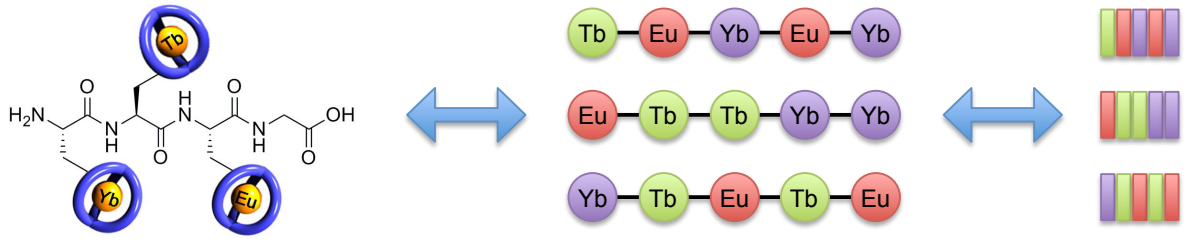

Figure 2.2: Concept of a molecular nanocode based on lanthanoid cryptates.

An especially fascinating application would be the development of a **molecular nanocode** assembled from highly reliable lanthanoid complexes, functionalised as amino acid. Such molecules would give unprecedented possibilities in the field of molecular encoding and the corresponding monomers themselves would be highly interesting for a variety of biological applications. Based on a successfully realised initial functionalisation (see above) the realisation of a molecular nanocode based on lanthanoid complexes shall be accomplished with the following steps:

- Preparation of lanthanoid cryptates functionalised with a protected amino acid, ready for SPPS
- Analysis of the potential influence of the functionalisation on the properties of the coordinated lanthanoid, e.g. the emissive properties
- Validation of the reactivity of the amino acid being unaffected by the attached lanthanoid cryptate
- Optimisation of the peptide coupling procedures for the new amino acids
- Preparation of a short nanocode
- Validation of the feasibility of the readout of the nanocode

The basic luminescence properties of the lanthanoid cryptates have already been studied thoroughly. The special properties of these complexes also offers optimal conditions for the fundamental study of more exotic, yet highly innovative and upcoming phenomena, such as circularly polarised luminescence (CPL) or energy transfer processes in molecular lanthanoid compounds. In the course of this work the knowledge about the lanthanoid cryptates shall be broadened into these aspects of photophysics and consequently pave the way for future applications.
The intrinsically low stability of lanthanoid complexes is a major obstacle in the preparation of **enantiopure lanthanoid complexes**. The rigid, well defined structure of the lanthanoid cryptates in solution offers best prerequisites for the preparation of enantiopure derivatives which, after the following steps, will allow for an improved understanding of the intrinsic properties of the lanthanoid cryptates **Ln-bpy$_3$O$_2$** and open up new possibilities for innovative applications:

- Initial study of the properties of luminescent lanthanoid complexes of a cryptate scaffold which is prepared in an enantiopure fashion
- Separation of lanthanoid cryptates prepared as racemic mixture into pure enantiomers
- Characterisation and study of the enantiopure samples with chiroptical techniques such as circular dichroism and circularly polarised luminescence

If a lanthanoid is “functionalised” with another lanthanoid in the close vicinity, **energy transfer processes** such as upconversion can become observable. While such processes can easily be observed e.g. in lanthanoid nanoparticles, there is only a very limited number of examples for molecular architectures in solution. Some time ago a lanthanoid cryptate “functionalised” with another lanthanoid cryptate was reported[141], such a dicryptate offers best prerequisites for the study of these phenomena. In order to provide a basis for a systematic study upon the feasibility of energy transfer processes in cryptate based ligand scaffolds, the following steps have to be accomplished:

- Improvement of the accessibility of the dicryptate ligand scaffold
- Preparation of dicryptates with promising combinations of lanthanoids
- Development of strategies for an efficient search for less obvious, yet promising combinations of lanthanoids
- Modification of the ligand towards new multimetallic cryptate derivatives

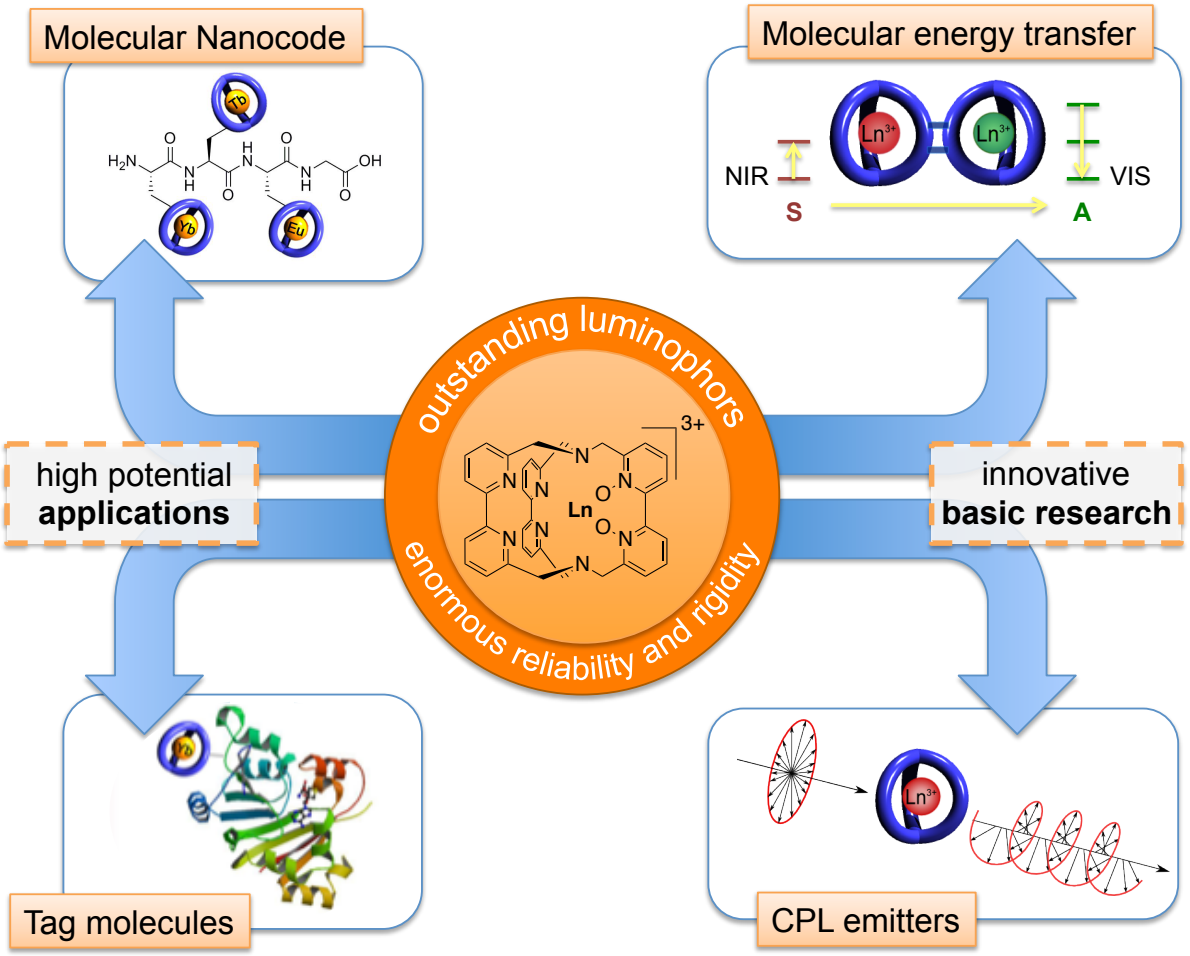
Molecular Nanocode
Molecular energy transfer
NIR
VIS
S
A
outstanding luminophors
enormous reliability and rigidity
high potential
applications
innovative
basic research
Tag molecules
CPL emitters

3 Lanthanoid Cryptates as Covalently Attached Tag-Molecules

3.1 Introduction

Many of the applications for which the lanthanoids and their special physical properties offer optimal prerequisites rely on a covalent attachment of the lanthanoid to additional functionalities or materials. Some examples where this is of obvious importance are fluorescence immunoassays, protein localisation or tracking studies, and the structural elucidation of biomolecules via paramagnetic NMR. A variety of reliable reactions has been well established for similar purposes, Figure 3.1 shows some examples.

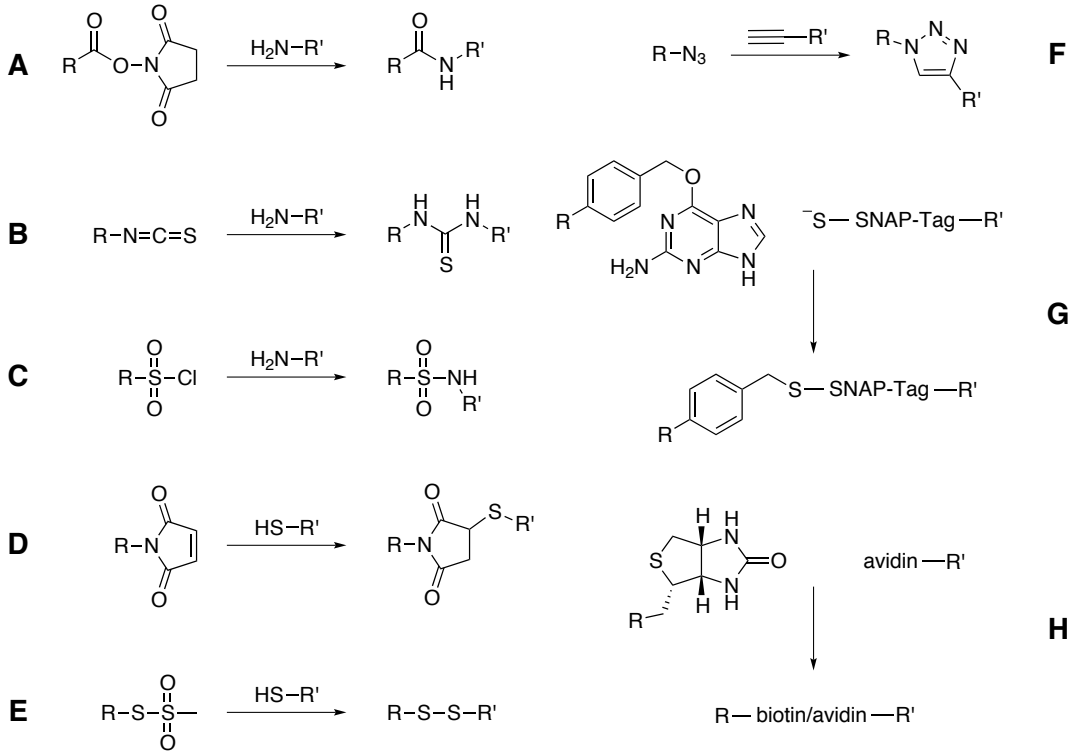

Figure 3.1: Well established conjugation reactions. Differently to the other examples depicted herein, the interaction of biotin and avidin is not covalent. Yet it is extremely strong, so that in many cases this interaction can be considered to be of comparable reliability.

Many of these reactions target functional groups which can be found in residues of amino-acids, for example the primary amine of lysine (reactions **A** to **C**) or the thiol of cysteine (reactions **D** and **E**). This makes the corresponding reactions highly suitable for the covalent modification of proteins. Another important example is the so-called click-reaction between azides and alkynes (reaction **F**). Apart from these relatively simple organic reactions, there are also many more biochemical strategies to obtain a reliable connection, like for example the SNAP-tagging[142] (reaction **G**), based on the special reactivity of an artificial derivative of the O^6-alkylguanine alkyltransferase, or the non-covalent but extremely stable attachment of biotin to avidin (reaction **H**).

Figure 3.2 shows examples of lanthanoid complexes modified with an attached application-specific functionalisation. The phenanthroline-derivative BCPDA[143] (tag **a**) combines an efficient antenna ligand with two chlorosulfonyl groups which readily react with primary amines of proteins. As such, Eu-BCPDA was the first example of a luminescent lanthanoid label for immunoassays and an important improvement compared to the DELFIA® system. The DELFIA® system employs non-luminescent lanthanoid labels, and after the immunoreaction the lanthanoids are cleaved from the tag-molecules and transformed into luminescent complexes which can then be quantified. This makes the procedure more tedious compared to the direct quantification, and the whole process more susceptible towards inaccuracies caused by contamination of Eu^{III}.[144] Cryptates have also been applied as luminescent tag molecules in immunoassays, for example as biotin functionalised complexes (tag **b**).[145] As a more specialised example, functionalised cryptates have also been commercialised as HTRF® kits for the study of protein/protein interactions. For this purpose individually functionalised Eu^{III} and Tb^{III} cryptates are combined and the Förster energy transfer between the tags, attached to different proteins, is monitored. In example **c**, modified EDTA complexes with lanthanoids were used to distinguish between two variations of the thiopurine S-methyltransferase gene, which differ in one nucleotide of the encoding DNA sequence ("single nucleotide polymorphism").[146] Via a phosphate ester a short oligodesoxyribonucleotide conjugate was attached to the EDTA moiety, which was either designed to complement the wild type (in the case of the Tb^{III}-complex) or the mutant (in the case of the Eu^{III}-complex) of the DNA sequence. Similarly a phenanthroline was attached to an oligodesoxyribonucleotide conjugate, which complements the next 15 bases of the gene. When all three labels are added to a sample of the gene under study, only the lanthanoid complex with the fitting oligodesoxyribonucleotide conjugate will be bound to the DNA, hence be in close proximity to the phenanthroline antenna (which in any case will be bound to the DNA), and consequently will be luminescent. Their special photophysical properties make the lanthanoids highly suitable for cellular imaging, example **d** shows one of the molecules developed for this purpose.[147][148] The complex is based on a macrotricyclic derivative of the **IAM** ligand[149] (see Figure 1.9), which is modified with a disulfide to carry two functional units.[150] Via a peptide bond a short PEG carrying a recognition structure, such as a benzyl guanine, is attached in a robust fashion. Additionally, via a disulfide a cell penetrating peptide (in this case nonaarginine) is bound, which delivers the complex into the cell and is then cleaved. In the cell the luminophore labels the proteins carrying the corresponding target structure, which can be confirmed via FRET measurements. Another lanthanoid complex used for cellular imaging is molecule **e**, which is an example for a zinc-sensitive luminescent chemosensor.[151] In the form shown in Figure 3.2, the DTPA-derivative is only moderately luminescent, with a quantum yield of below 1%. But if Zn^{II} is added, the coordination of Zn^{II} by the attached quinoline-containing second binding

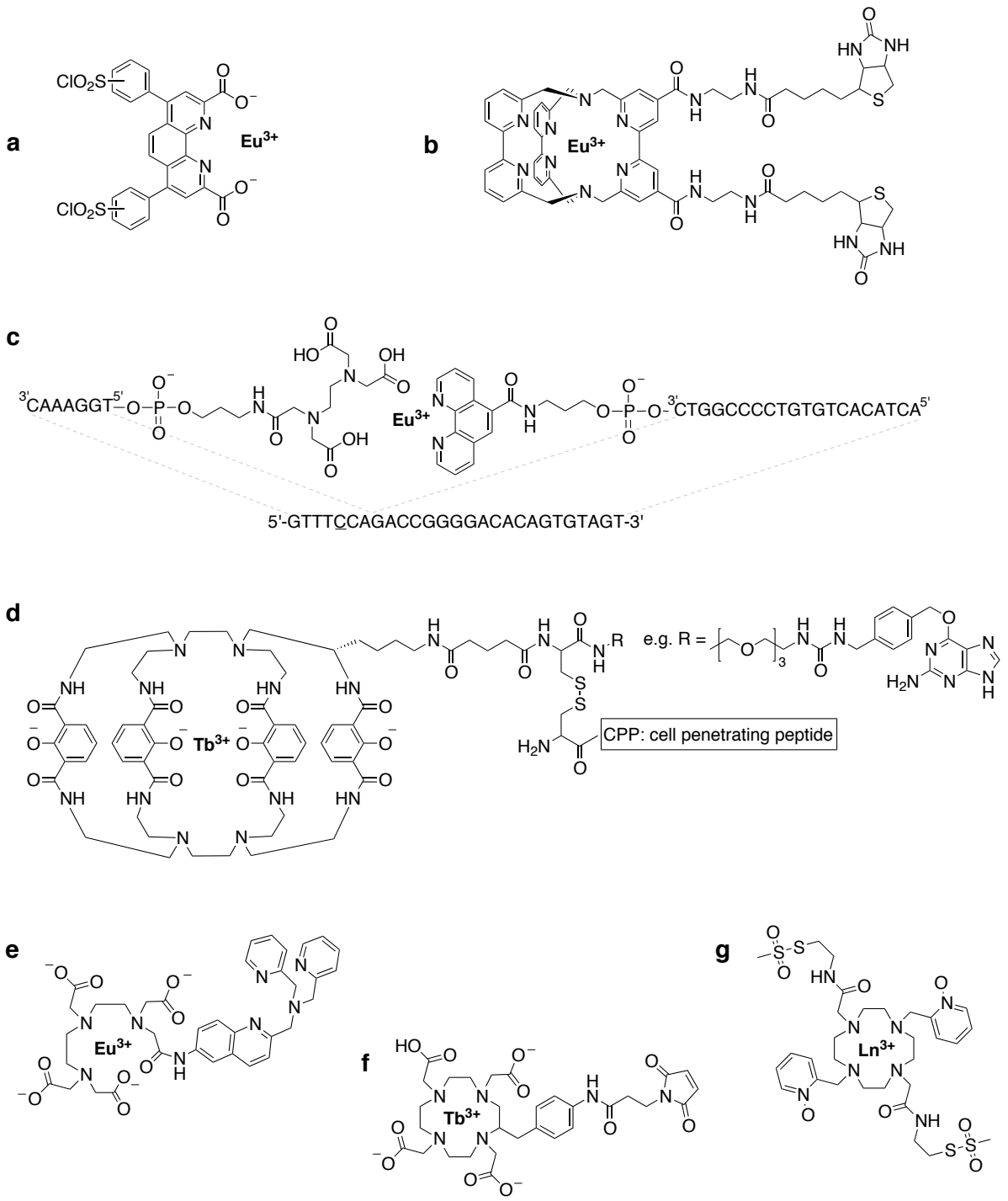

Figure 3.2: Examples for lanthanoid complexes with covalently attached functionalisations for various applications. References are given in the text. The protonation of the ligands is depicted as presented in the original publications. For the sake of clarity not all Ln-L bonds are shown.

pocket leads to an improvement of the antenna characteristics of the overall ligand, and consequently to a significant amplification of the luminescence and a resulting quantum yield of 7.4%. Apart from the in

general beneficial characteristics of lanthanoid complexes, the reversibility of the luminescence enhancement, the insensitivity of the complex to changes of the pH and the relatively high excitation wavelength of 340 nm offer best prerequisites for biological applications. Another field of applications which can greatly benefit from the special properties of the lanthanoids are mass spectrometry based quantifications of large biologically relevant molecules, such as proteins or specific DNA sequences in cellular samples. The high chemical similarity of the lanthanoids allows for the preparation of sets of mass spectrometry labels which show identical chemical behaviour and will only differ in their mass, therefore offering best prerequisites for the simultaneous quantification of different target molecules in one sample. For the actual quantification of the labeled molecules, ICP-MS (inductively coupled plasma mass spectrometry) is often the best choice, since it is a method which shows extremely high sensitivities for the lanthanoids. Molecule **f** was developed for such applications and was used for the quantification of DNA.[152][153] The maleimide group attached to the DOTA scaffold allows for a covalent attachment to thiol-modified oligonucleotides, complementing the DNA sequence under study. Together with an oligonucleotide carrying an avidin-group, which is designed for the hybridisation to another part of the sequence, the Tb-labeled DNA target can be quantified directly as a sandwich hybridisation assay or after an additional step of ligation mediated amplification. Example **g** is a tag molecule for the structural elucidation of proteins in solution.[154] Two of the pendant arms of the DOTA-type ligand carry disulfide groups which can react with thiol groups of the protein under study, as for example found in cysteine groups. For such studies typically amino acids in suitable areas of the protein are replaced with cysteines to bind the tag molecule. The twofold attachment improves the selectivity for the designed binding position over naturally occurring cysteines in the protein, and also makes the spatial arrangement of the tag molecule relative to the biomolecule more well-defined. The two remaining pendant arms of the ligand carry oxidised pyridines. Compared to the corresponding derivative with two carboxylic groups in this position, these groups suppress the tendency of the complex to undergo the isomerisation processes which are typical for DOTA compounds. Furthermore, the pyridine-N-oxides serve as antenna and allow for luminescence based localisation of the tag molecules.

Apart from examples **c** and **e**, where a change in the first coordination sphere around the lanthanoid leads to variations of the photophysical properties which are actually monitored, all of the applications outlined above could benefit from the enormous kinetic and coordinative stability of the oxidised lanthanoid cryptates $\mathbf{bpy_3O_2}$. Though the selection of the examples presented herein is somewhat arbitrary, it does indeed reflect the fact that the application of luminescent lanthanoids until now is still pretty much limited to the strongly luminescent lanthanoids Eu^{III} and Tb^{III}. Since the oxidised lanthanoid cryptates have already proven to be highly suitable scaffolds for the enhancement of the still underrepresented lanthanoids which are more susceptible towards multiphonon quenching, they are promising candidates for overcoming this limitation.

The only fundamental hindrance for the use of the highly beneficial properties of the oxidised bipyridine cryptates for various applications is the obvious lack of any reactive functionalisation at the outer sphere of the ligand, which is precondition for the introduction of further functional groups. The nature of the initial functionalisation is not critical, as long as the group is sufficiently reactive to attach linkers or different functionalities. In contrast, the position of the functionalisation can have a crucial impact onto the overall properties of the lanthanoid complexes, and consequently has to be chosen with care.

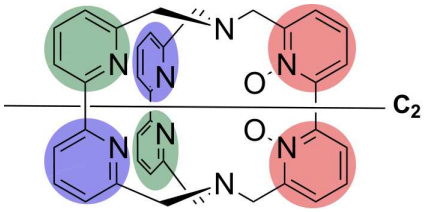

Figure 3.3: Symmetry of the cryptates **bpy$_3$O$_2$**: the C_2-symmetry axis converts pairs of equivalent pyridines into each other. The coordinated metal ion is omitted for clarity.

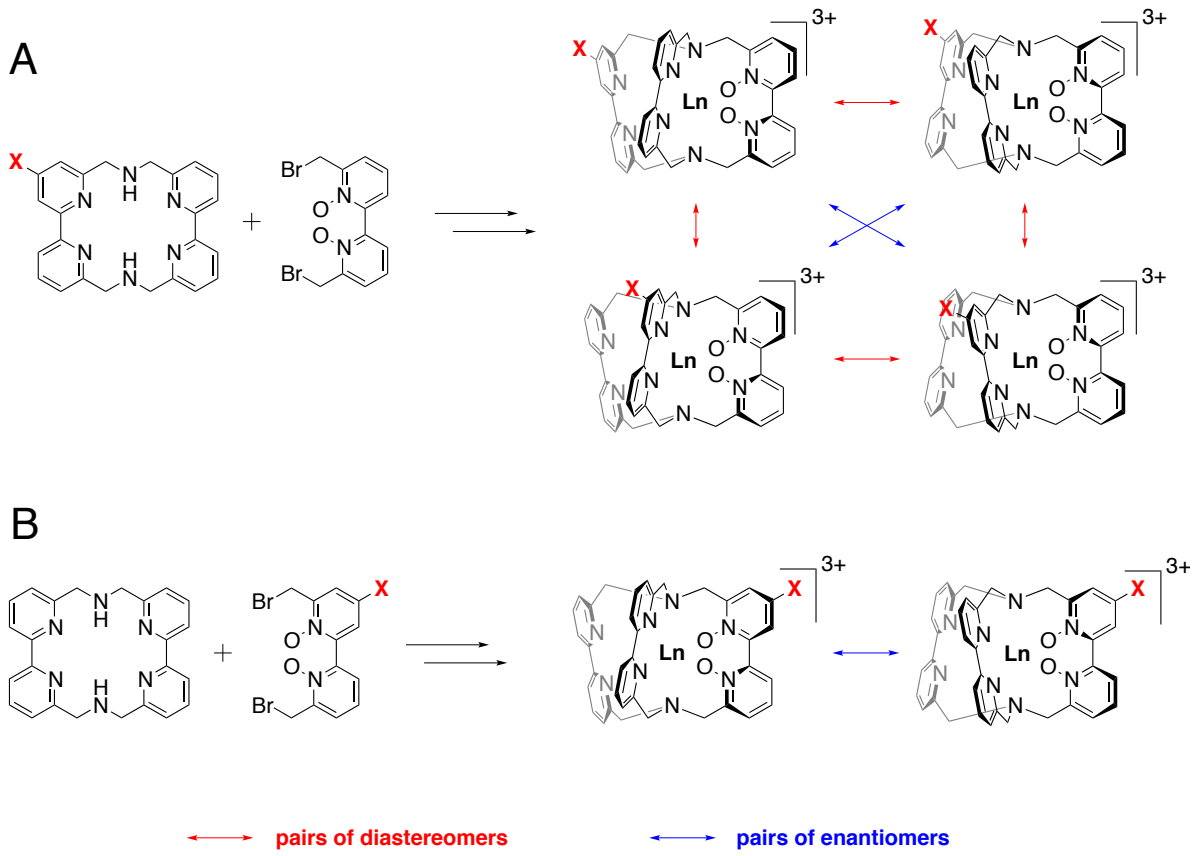

Figure 3.4: Resulting cryptates obtained from macrobicyclisation and complexation of the lanthanoid depending on the choice of the pyridine, to which the initial functionalisation is introduced. If the functionalisation is introduced to the macrocyclic building block (top, strategy **A**), several diastereomers will be obtained, whereas the functionalisation at the dibromide of the oxidised bipyridine (bottom, strategy **B**) will only yield one pair of enantiomers, which cannot be distinguished in the absence of additional chiral elements.

From a synthetic point of view, the introduction of an initial functionalisation in 4-position of one of the pyridines is most straightforward. As outlined in chapter 1.3, the cryptates **bpy$_3$O$_2$** are C_2-symmetric (see Figure 3.3) and exhibit axial chirality. Necessarily such a modification will lower the overall symmetry of the scaffold, but with regards to the chirality of the system, the choice of the pyridine which is modified will have a drastic impact upon the properties of the final product (see Figure 3.4). If the functionalisation is introduced to one of the four pyridines of the macrocyclic component (strategy **A**), upon macrobicyclisation

four distinguishable arrangements of the building blocks will result in the formation of an equal number of products. Importantly, there will be several diastereomers which can have distinctly different chemical properties and for example will have different NMR spectra. This would at least in part compensate the well-defined nature of the core scaffold **bpy$_3$O$_2$**, and make the corresponding compounds of only very limited interest for any application in the context of biological samples, where additional stereogenic elements will further complicate the situation. In contrast to that, if the functionalisation is introduced to the dibromide of the oxidised bipyridine (strategy **B**), only a pair of enantiomers will result and consequently this is the advantageous choice. The characterisation of the resulting cryptates will be by far more straightforward, and for example will offer better conditions for the study of the general influence of the functionalisation (e.g. the decrease of symmetry) on the properties of the lanthanoid cryptates. Many applications in the analysis of biomolecules or related fields would strongly benefit from the use of enantiopure tag molecules. In this case the whole potential of the well-defined structure of the cryptates **bpy$_3$O$_2$** can be utilised. Indeed, the preparation of enantiopure derivatives of these cryptates is possible, and fortunately the synthetic strategy applied for this purpose generally also allows for the modification of the methyl groups at the periphery of the scaffold.[134] In the resulting enantiopure tag molecules (see Figure 3.5) the C_2-symmetry of the core structure would be retained and the dual functionalisation would allow for a highly reliable and well-defined attachment to the target structure. The properties which can be expected for such a compound make it an ideal tag molecule e.g. for the structural elucidation of proteins via paramagnetic NMR. Despite the high potential of such a tag molecule no corresponding ligand could be realised until now.

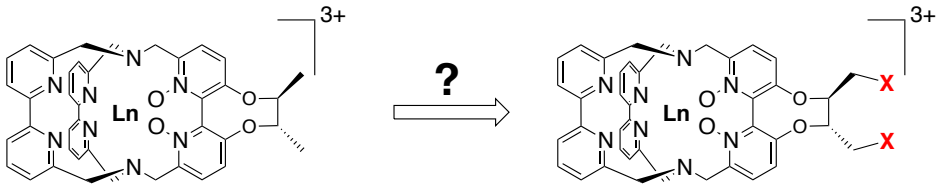

Figure 3.5: A twofold functionalised version of the already known enantiopure cryptates[134] would open up potential for especially interesting applications.

As outlined in section 1.2, the magnetic properties, such as the anisotropy of the magnetic susceptibility, of a lanthanoid coordination compound are by far more sensitive towards subtle changes in the exact spatial arrangement of the coordinating atoms around the lanthanoid center, than the photophysical properties are. Consequently, analytical methods which probe these properties are very valuable when the influence of modifications introduced to a ligand scaffold are to be studied. Especially accessible and well established are of course NMR experiments, which can give valuable information about the overall magnetic situation. Studying the magnetic properties of a lanthanoid coordination compound with these techniques has two additional benefits. Firstly, though the fundamental principles of magnetism are rather complicated, in the case of an NMR-based analysis they can be discussed in a framework which is familiar to most chemists. Secondly, and more importantly, a corresponding analysis is very similar to the process applied for the structural elucidation of biomolecules via paramagnetic NMR. Consequently, such an analysis can directly give valuable information on the applicability of a given lanthanoid complex as a tag molecule for such purposes. The information collected during the detailed analysis of the NMR spectra of the complex could

directly be used in the case of such an application.
From the different paramagnetic effects which can be observed in an NMR spectrum, the pseudocontact shifts (PCS, see chapter 1.2) can be considered to allow for the most straightforward analysis, at least in the case of lanthanoid coordination compounds.[155] Since they take effect through space, their impact upon the observed overall shift is dependent on the spatial arrangement between the paramagnetic center and the nucleus whose NMR signal is under study. Another effect, namely the contact shift, also has an influence upon the chemical shifts (see equation 3). The contact shift operates through bonds, which limits its operation range to nuclei quite close to the paramagnetic center. Similarly to the pseudocontact shifts, also the contact shifts contain structural information, but they are less often used to obtain structural constraint for the structure under study.[156] Usually the contact shift is assumed to be negligible for nuclei which are more than four bonds apart from the paramagnetic center and for some lanthanoids the contact contributions are known to be generally small. So indeed in many cases it is a reasonable approximation to neglect the contact shifts δ_C and to treat the observed change of the chemical shifts $\Delta\delta_{obs}$ as purely caused by the pseudocontact shift δ_{PC}:

$$\Delta\delta_{obs} = \delta_C + \delta_{PC} \approx \delta_{PC} \tag{3}$$

The pseudocontact shift δ_{PC} can generally be calculated from the atomic coordinates of the nuclei under study, and parameters describing the tensor of the anisotropy of the magnetic susceptibility. Depending on the choice of the form in which the coordinates are used and how the tensor is parameterised the used equation used can differ.[56] When the parameters describing the anisotropy of the magnetic susceptibility are known, with any of these equations for any point in space the corresponding pseudocontact shift can be calculated. A quite commonly used form, which is valid in the principal magnetic axis system, is shown in equation 4. Here the coordinates of the nuclei are given in polar coordinates r, Θ, Ω and the tensor is described with its axial and rhombic components $\Delta\mathcal{X}_{ax}$ and $\Delta\mathcal{X}_{rh}$, respectively:

$$\delta_{PC} = \frac{1}{12\pi r^3}\left[\Delta\mathcal{X}_{ax}\left(3cos^2\Theta - 1\right) + \frac{3}{2}\Delta\mathcal{X}_{rh}\left(sin^2\Theta cos\,2\Omega\right)\right] \tag{4}$$

Bleaney's theory offers one approach for the calculation of the tensor of the anisotropy of the magnetic susceptibility. But as stated in section 1.2, to do so some assumptions which are not universally applicable are necessary. If possible, a direct extraction of these values from experimental data is clearly preferential. Prerequisite to do so is a sufficiently accurate structural model of the molecule under study. In a first step the pseudocontact shifts, extracted with the aid of a diamagnetic reference compound, are assigned to the nuclei of the molecule, and for every nucleus an individual equation according to (4) is set up. Subsequently, in a global fit the parameters for the tensor can be extracted. Finally, a theoretic NMR spectrum can be calculated from the coordinates and the tensor parameters to verify that they are suitable to reproduce the experimental data, which means that they are describing the magnetic properties of the complex properly.
This strategy has already proven to be highly suitable for the analysis of lanthanoid cryptates **bpy$_3$O$_2$** and

very helpful for studies covering different aspects of their special properties.[135][134][157] Again, the well-defined structure of the compounds is highly beneficial and allows for a relatively straightforward assignment of the signals to the different nuclei and allows for the preparation of a suitable diamagnetic reference compound.

3.2 Conception of the Project

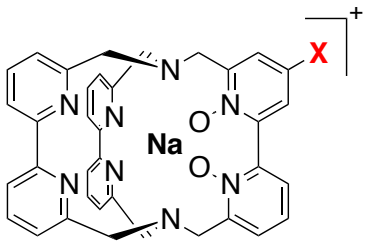

The necessary prerequisite for the utilisation of the cryptates **Ln-bpy$_3$O$_2$** as covalently attached tag molecules is the **realisation of a cryptate scaffold carrying a reactive functionality at the periphery of the ligand**. In order to maintain the beneficial properties of the parent system, the functionalisation should be introduced in a way that the symmetry related properties are affected as little as possible. Starting from this key intermediate the following steps will be:

- **Investigation of the influence of the initial modification at the periphery of the ligand on the photophysical and magnetic properties of the coordinated lanthanoid**

In order to study in how far the properties of the coordinated lanthanoid are affected by the peripheral functionalisation, several lanthanoid complexes of this new ligand will be prepared and investigated thoroughly. Apart from the luminescence properties a special focus will be laid on NMR studies of paramagnetic complexes, since these compounds allow for a deeper understanding of the solution structure of these compounds. Furthermore such results may pave the way for future applications in the structural elucidation of biomolecules.

- **Development of a general synthetic strategy of broad applicability for the attachment of various functional groups**

If the highly beneficial properties of the lanthanoid cryptates can be proven to be unaffected by the external functionalisation, the next step is to find a flexible and adaptable strategy to introduce diverse functionalisations to the scaffold, targeting for different applications.

- **Synthesis of a new difunctionalised and enantiopure lanthanoid cryptate**

As already mentioned, especially for application in the field of the structural elucidation of biomolecules via paramagnetic tag molecules, the use of difunctionalised and, even more importantly, enantiopure complexes would be highly beneficial. Another aim of this project is the realisation of a scaffold which meets these requirements.

3.3 Results and Discussion

3.3.1 Synthesis and characterisation of amino-functionalised lanthanoid cryptates

A significant proportion of the work presented herein will be concerned with the preparation of lanthanoid cryptates carrying various functionalities. As starting point for these studies a cryptate carrying some kind of initial functionalisation is needed. While the nature of the initial functionality is of secondary importance, the positioning is enormously important to maintain as many of the beneficial properties of the unfunctionalised cryptates **Ln-bpy$_2$O$_2$** (as already illustrated in Figure 3.4). To do so, the functionalisation should be introduced at the oxidised bipyridine moiety, which is used for assembly of the cryptate as dibromide of the *N,N*'-dioxide (see Figure 3.6).

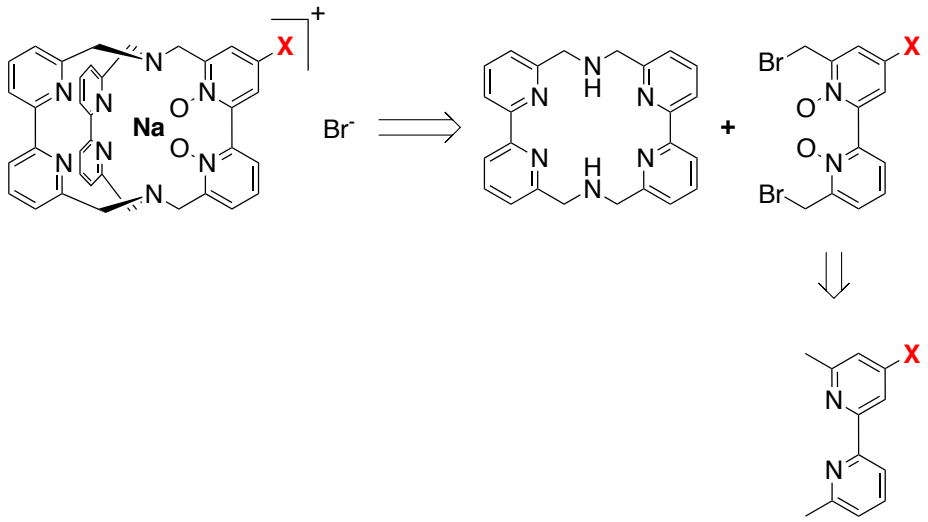

Figure 3.6: General retrosynthetic approach for the preparation of functionalised cryptates **bpy$_3$O$_2$**.

Upon macrobicyclisation and during preparation of the dibromide of the *N,N*'-dioxide, the functionalisation needs to be protected with a suitable group. In this case a methyl ester of a carboxylic acid was chosen as protected functionality. Methyl esters can be expected to tolerate the reaction conditions necessary for the preparation of the cryptate scaffold and the cleavage conditions typically applied for these groups (e.g. saponification with hydroxides in methanol) should be compatible with the assembled cryptate. The resulting key building block of the synthesis of a functionalised cryptate scaffold (see Figure 3.7), the methyl-ester of the 6,6'-dimethyl-2,2'-bipyridine-4-carboxylic acid can be prepared by a Stille coupling reaction.[158] Due to an improved purification procedure this could be done conveniently in large scale with 70% yield. Using mCPBA the bipyridine can be oxidised to give the corresponding *N,N*'-dioxide in 84% yield, and can then be transformed into the dibromide using a modified Boekelheide rearrangement (66% yield). The last step towards the dibromide of the *N,N*'-dioxide is another oxidation, which was performed in analogy to a method developed for the oxidation of electron deficient pyridines by Caron *et al.*[159] (78% yield). Sub-

sequently the macrobicyclisation with the macrocyclus consisting of two bipyridines could be performed to yield the methyl ester-functionalised sodium cryptate. A cleavage of the methyl ester using NaOH in CH_3OH is indeed possible, yet initial studies showed that the resulting carboxy-functionalised cryptate is a very sluggish reactant.[160] At the same time some kind of linker between the cryptate core scaffold and the reactive functionality might become beneficial for further uses. After a number of unsuccessful trials the methyl ester-functionalised cryptate was found to undergo a substitution reaction in the presence of an excess of neat ethylene diamine, and after subsequent column-chromatography the amino-functionalised derivative **Na-1** could be obtained.

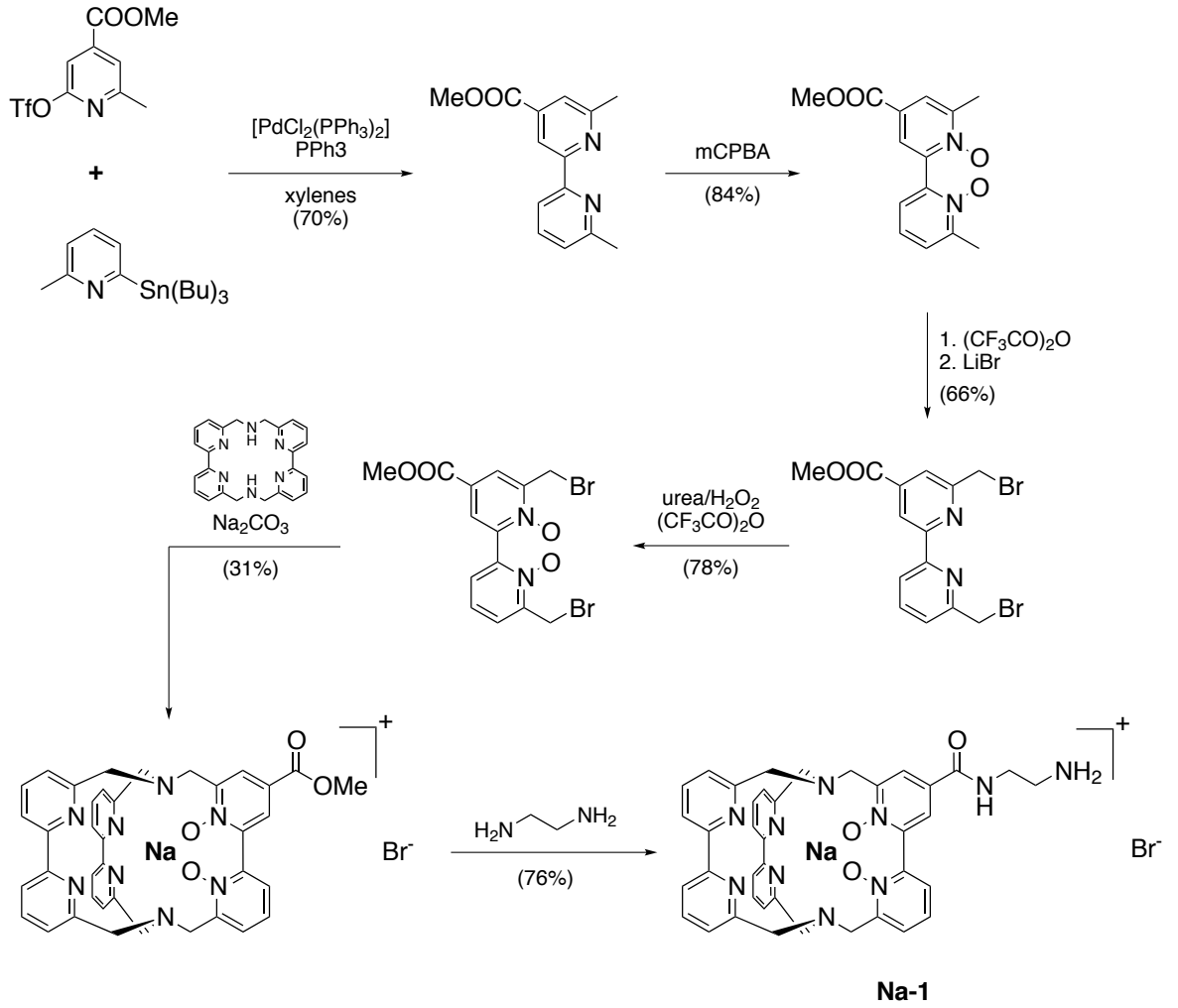

Na-1

Figure 3.7: Schematic representation of the synthesis of the amino-functionalised sodium cryptate **Na-bpy$_3$O$_2$-en (Na-1)**.[161]

The amino-functionalised sodium cryptate **Na-bpy$_3$O$_2$-en (Na-1)** is a highly suitable starting point for opening up possibilities in various fields which could benefit from covalently attached lanthanoid cryptates. The initial functionalisation as a primary amine allows for various and versatile transformations which are well-

established in organic synthesis and biochemistry and is often used in conjugation chemistry. Of practical interest is of course also the relatively good availability of **Na-1**. Apart from the macrobicyclisation reaction, which is inherently problematic, all steps proceed with yields above 65% and preparation of **Na-1** on a multigram scale is possible. This makes **Na-1** a solid basis for the development of functionalised lanthanoid cryptates for various applications. As the functionalisation is placed at the oxidised bipyridine unit, the effect of the functionalisation upon the general geometric properties of the scaffold is minimised and no diastereomers are formed during synthesis (see Figure 3.4). Nevertheless, the lowering of the symmetry from C_2 to C_1 can of course have an impact on the overall properties of the ligand and its lanthanoid complexes. A comparative study of the lanthanoid complexes **Ln-1** and the parent compounds **Ln-bpy$_3$O$_2$** is the most direct and easiest way to access whether the peripheral functionalisation and the loss of symmetry have an impact on the properties of the lanthanoid complexes.

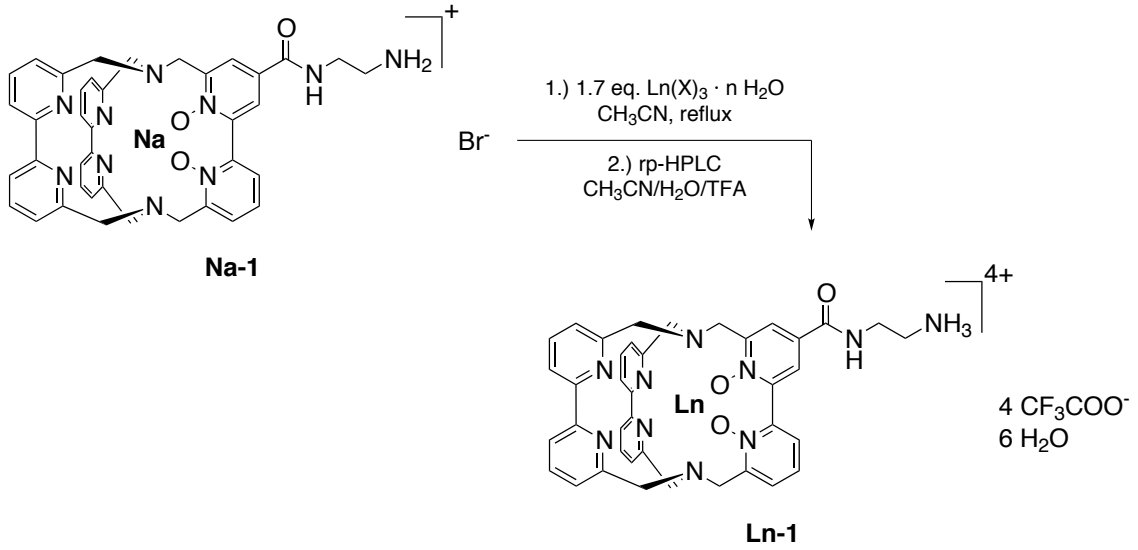

Na-1 **Ln-1**

Figure 3.8: Schematic representation of the preparation of the amino-functionalised lanthanoid cryptates **Ln-bpy$_3$O$_2$-en (Ln-1)**.

In preliminary studies during my master thesis[162] I could show that the lanthanoid complexes **Ln-1** can be prepared in close analogy to the unfunctionalised complexes (Figure 3.8). In principle, these reactions can be performed in CH_3OH or CH_3CN, whereby the solubility of the starting compounds is typically lower in CH_3CN, so that under the conditions commonly applied the reaction mixture is not a clear solution. This might be considered detrimental, but as the lanthanoid complexes obtained from the reaction are typically even less soluble in this solvent and precipitate from the reaction mixture, this does not have a negative impact on the reaction. At the same time CH_3CN itself is a less suitable ligand for Ln^{III} than CH_3OH, so the solvation shell formed by CH_3CN around a Ln^{III} will be easier to remove, which makes the complexation reaction faster and CH_3CN the better choice for the solvent. Compared to the formation of the unfunctionalised cryptates **Ln-bpy$_3$O$_2$**, slightly higher equivalents of the lanthanoid salt were used herein to compensate for the fact that also the amino-group might coordinate Ln^{III} and thereby hinder the exchange of the lanthanoid for Na^+. For purification lanthanoid cryptates can be recrystallised from CH_3OH.

To do so the crude product is dissolved in a minimum of the solvent, filtered over cotton and overlayered with Et_2O. Typically the material isolated from this procedure has three chloride anions as counter ions, but also the coordination of complex anions of the type $[Ln(Cl)_5(H_2O)_x]$ could be observed.[135] An alternative purification, which allows for better control over the coordinating ions, is reversed phase HPLC, during which the initially bound anions are reliably replaced with TFA^-. This allows for a better control over the exact composition of the isolated material and is favourable if different compounds are to be compared, as it is the case in this study. Following these considerations complexes of five different lanthanoids and the amino-functionalised ligand scaffold were prepared, purified and studied. Fortunately the HPLC method already established for the purification of complexes **Ln-bpy$_3$O$_2$** was found to be suitable also for the complexes **Ln-1**. The different lanthanoids were chosen in a way that different important aspects of the overall properties of the complexes **Ln-1** can be studied. Eu^{III} and Tb^{III} are lanthanoids typically employed for luminescence applications. As a lanthanoid which emits in the visible and in the near-infrared part of the electromagnetic spectrum, also the luminescence of Sm^{III} is highly interesting. It is studied less frequently, as Sm^{III} complexes are prone to undergo nonradiative deactivation processes and are typically only weakly or not luminescent. However, cryptates have already proven to allow to circumvent this problem.[139] Yb^{III} can be considered to be the best established near-infrared emitting lanthanoid. Apart from that, due to their specific paramagnetic character, Yb^{III} complexes are also of special potential for the structural elucidation via NMR spectroscopy. The Lu^{III} complex was chosen as reference compound for both, the photophysical and the paramagnetic properties. In Table 3.1 representative experiments performed for the synthesis of the different complexes **Ln-1** are summarised.

Table 3.1: Representative experiments performed for the synthesis of **Ln-1**. All analytical HPLC runs were performed with program **A**. In the course of this project subsequently two different HPLC setups **A** and **B** were available.

	$Ln(X)_3$	n(**Na-1**) [μmol]	V(MeCN) [mL]	reaction time [h]	yield [%]	R_f, analytical HPLC	
						setup **A**[1]	setup **B**[1]
Sm-1	$SmCl_3 \cdot 6\,H_2O$	13.0	15	65	42	11.8 min	-
Eu-1	$EuCl_3 \cdot 6\,H_2O$	44.0	17	70	23	11.7 min	-
Tb-1	$TbCl_3 \cdot 6\,H_2O$	37.7	17	40	27	11.4 min	-
Yb-1	$YbCl_3 \cdot 6\,H_2O$	37.7	15	186	26	11.4 min	12.7 min
Lu-1	$Lu(OTf)_3$	25.0	15	168	51	-	12.6 min

[1] see page 208 for details.

The yields were found to be fluctuating between 8% to 42% from experiment to experiment. In tendency they are lower than for the parent system **Ln-bpy$_3$O$_2$**, where typically yields between 60 and 70% can be realised after HPLC purification. The preparative HPLC runs indicate that in many cases the crude reaction mixture contained a relatively big fraction of unreacted **Na-1**, even after elongated reaction times.

Attempts were made to monitor the progress of the reaction by taking samples from one reaction mixture after different periods of time, but due to the inhomogeneity of the reaction mixture it was not possible to obtain representative samples. Noteworthy the highest yields were obtained in the case of the experiment in which the sodium cryptate was reacted with $Lu(OTf)_3$. Perhaps trifluoromethanesulfonates of the lanthanoids generally allow for better yields from this reaction, this could be a starting point for a more systematic improvement. Until now this was not necessary due to the relatively good availability of **Na-1**.
The retention times of the complexes **Ln-1** during analytic HPLC do not show a systematic shift compared to the unfunctionalised analogues. The complexes **Ln-1** were subsequently analysed via NMR spectroscopy and mass spectrometry (MALDI-MS and high resolution ESI-MS, see page 232 and the following). The ^{1}H NMR spectra of **Lu-1**, **Sm-1**, **Eu-1** and **Tb-1** are shown in Figure 3.9 to Figure 3.12. The ^{1}H NMR spectrum of **Yb-1** will be discussed in chapter 3.3.4. Though Lu^{III} is diamagnetic the spectrum of the corresponding amino-functionalised cryptate is rather complicated to interpret. Since many of the protons of the molecule are very similar in terms of their chemical and magnetic properties, many signals are grouped in three extended multiplets. In the two multiplets between 4.2 to 3.9 ppm and 3.9 to 3.6 ppm doublets with coupling constants characteristic for the benzylic protons of lanthanoid cryptates can be identified. The signals of the CH_2-groups of the linker can be identified quite easily. One of the signals is observed as a triplet at 3.23 ppm, the other one can be observed at about 3.75 ppm as part of one of the multiplets.

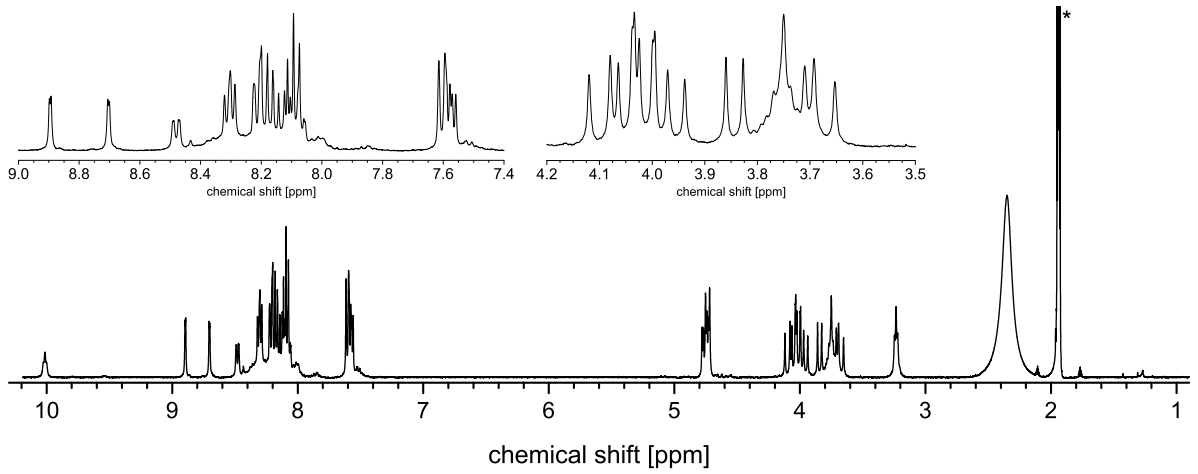

Figure 3.9: ^{1}H NMR spectrum (400 MHz, CD_3CN) of the amino-functionalised lutetium cryptate **Lu-1**. Unambiguously identified solvent signals are marked with an asterisk.

Sm^{III} is only slightly paramagnetic, yet the effects upon the ^{1}H NMR spectrum are significant. Since they are closer to the paramagnetic center, the signals of the benzylic protons experience a stronger shift than the ones of the aromatic protons and can here be found shifted more downfield. Compared to the spectrum of **Lu-1** the signals are better separated from each other, and despite the paramagnetism of Sm^{III} they are very sharp, so that an integration of the signals is more straightforward in this case. The C_1-symmetry is nicely reflected in the signals of the benzylic protons now typically being observable as pairs of two similar doublets (corresponding to one proton each), which are close by or even overlapping. Again the signals of

the ethylene linker can easily be identified. As expected they do not experience a strong shift compared to the diamagnetic analogue and can be observed at 3.66 and 3.15 ppm, respectively.

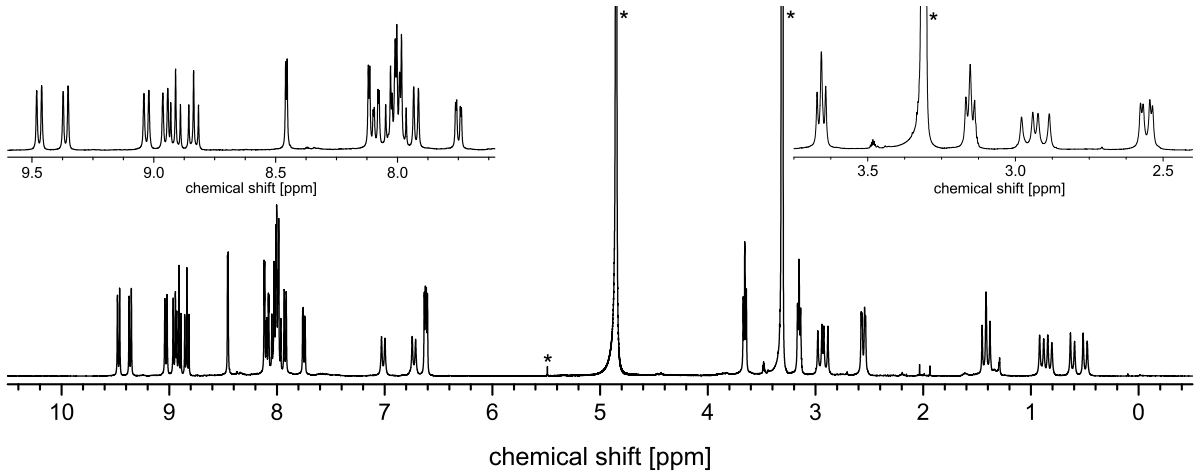

Figure 3.10: ^{1}H NMR spectrum (400 MHz, CD_3OD) of the amino-functionalised samarium cryptate **Sm-1**. Unambiguously identified solvent signals are marked with an asterisk.

In the ^{1}H NMR spectrum of **Eu-1** the signals of the benzylic protons are now even more separated from the middle region of the spectrum and experience a considerable broadening. In the case of the very paramagnetic **Tb-1** the signals of the ^{1}H NMR spectrum are distributed between 230 and -330 ppm and the signals at extreme shifts are so broad that a reliable integration is no longer possible.

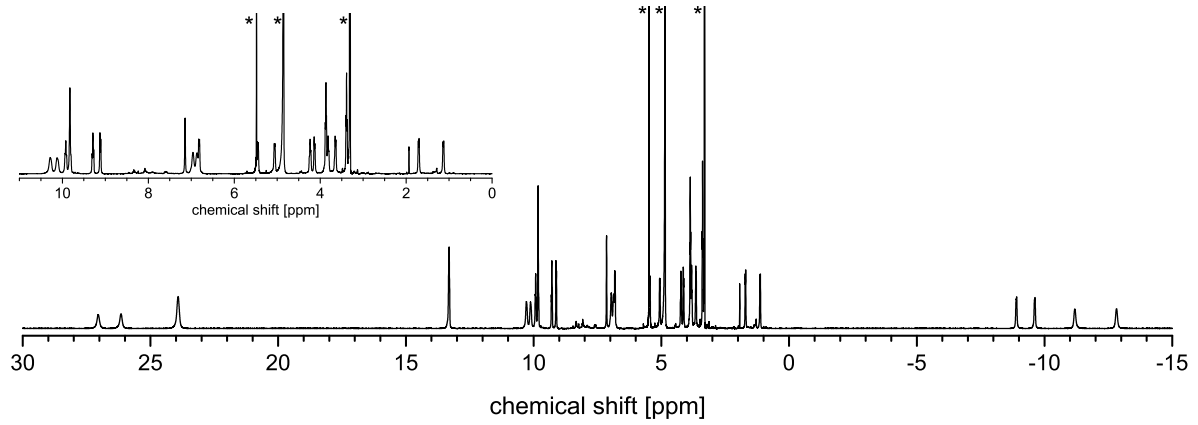

Figure 3.11: ^{1}H NMR spectrum (400 MHz, CD_3OD) of the amino-functionalised europium cryptate **Eu-1**. Unambiguously identified solvent signals are marked with an asterisk.

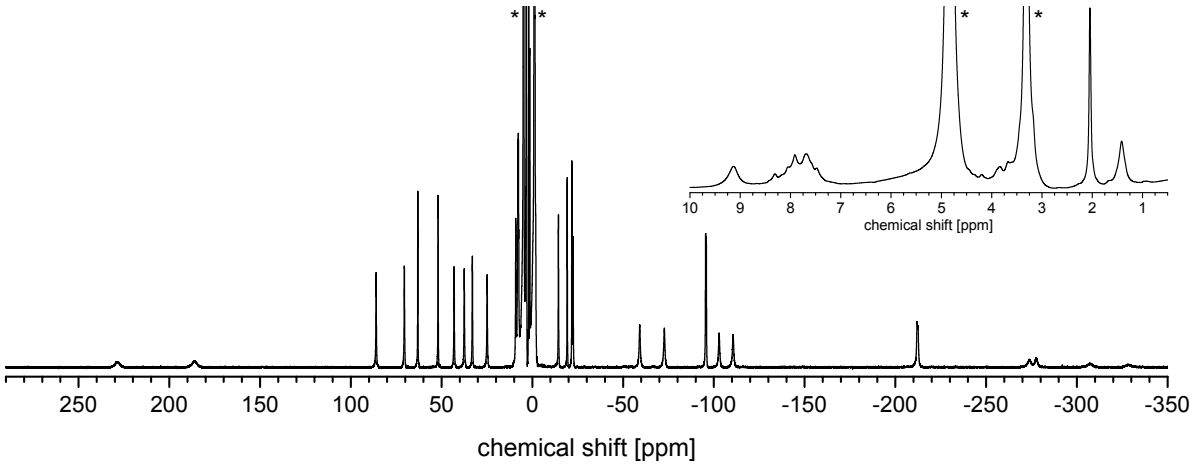

Figure 3.12: ^{1}H NMR spectrum (500 MHz, CD_3OD) of the amino-functionalised terbium cryptate **Tb-1**. Unambiguously identified solvent signals are marked with an asterisk.

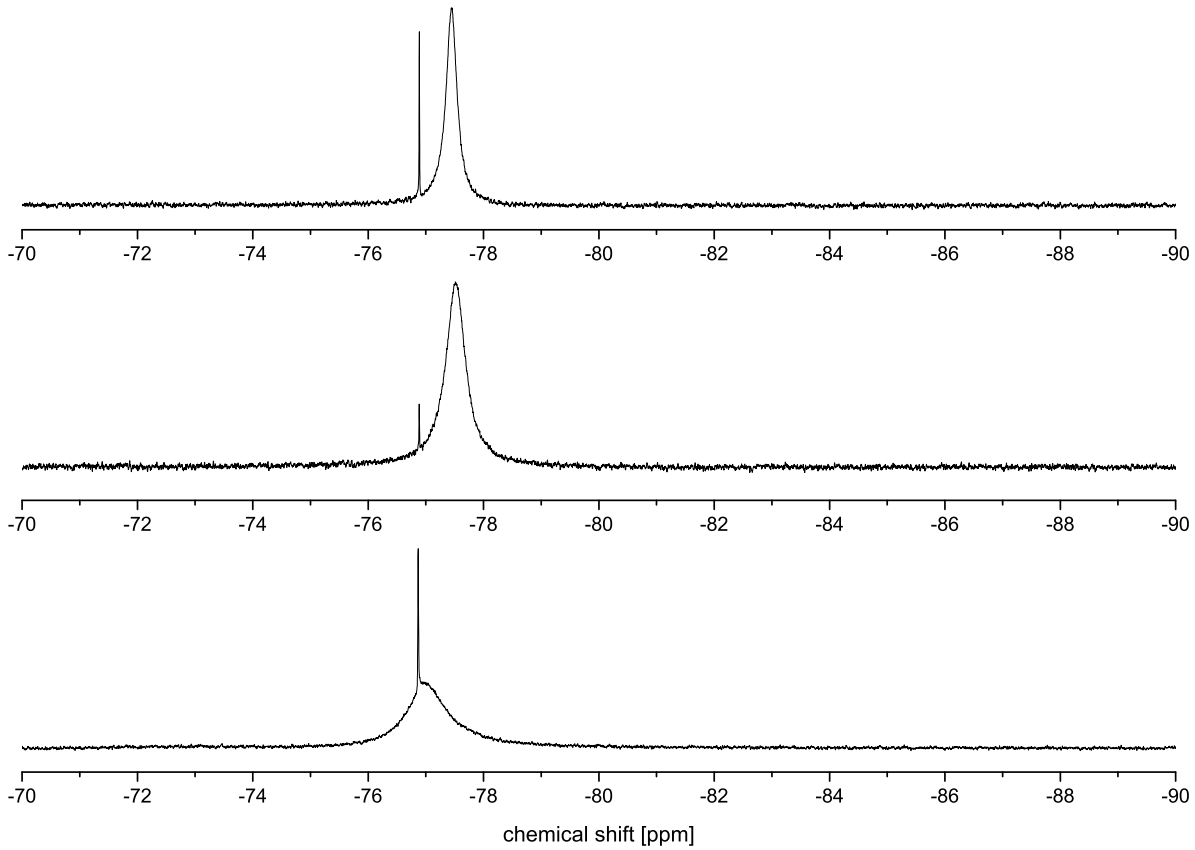

Figure 3.13: ^{19}F NMR spectra (376 MHz, CD_3OD) of amino-functionalised lanthanoid cryptates **Ln-1**: **Sm-1** (top), **Eu-1** (middle) and **Tb-1** (bottom).

The ^{19}F NMR spectra of the complexes **Sm-1**, **Eu-1** and **Tb-1** are shown in Figure 3.13. They all show broadened signals, which strongly points towards the coordination of TFA^- anions directly to the Ln^{III}. The

broadening of the signal correlates to the paramagnetism of the lanthanoid. Upon standing, an additional sharp signal was emerging which might be caused by the presence of an ester formed from TFA and the solvent (CD_3OD).

3.3.2 Photophysical properties

As outlined in chapter 1.3, the ligand around the coordinated lanthanoid is of critical importance for the preparation of luminescent molecular lanthanoid compounds. The most important aspect is the utilisation of the ligand as antenna for the indirect sensitisation of the lanthanoid. Two characteristics of the ligand are especially important in this context: The spectral absorption of the ligand and the energy of the excited triplet state from which the energy can be transferred onto the lanthanoid. The spectral absorption behaviour of the ligand can easily be studied by a simple UV/Vis experiment. Since the absorption coefficients of the lanthanoids are so very small, the UV/Vis spectra are effectively independent from the coordinated lanthanoid. In principle any lanthanoid complex of the ligand under study can be used for such an experiment. In contrast to that, for the study of the triplet state a complex of a lanthanoid which cannot accept the energy from the triplet state should be used, commonly a good choice (as reference for small lanthanoids) is the photoinactive Lu^{III}.

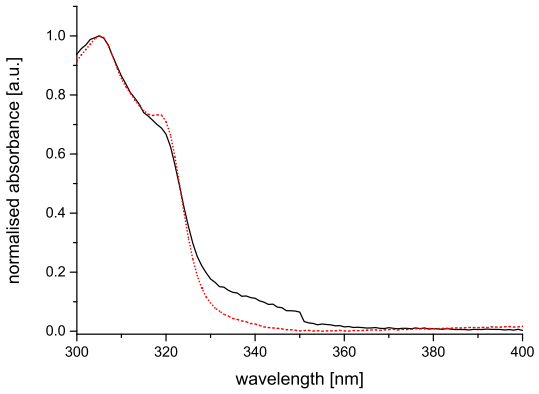

(a) Normalised UV/Vis spectra of **Eu-1** (black, solid line) and **Eu-bpy$_3$O$_2$** (red, dotted line) in CD_3OD.

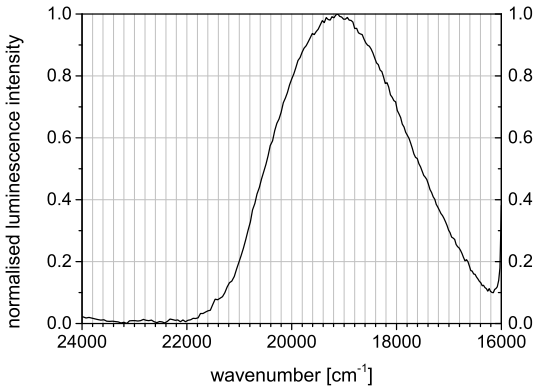

(b) Normalised low-temperature steady state emission spectrum (λ_{exc} = 315 nm, T = 77 K) of **Lu-1** in a glassy CH_3OH/EtOH matrix (1:1, v/v). Figure modified from reference [160].

Figure 3.14: Ligand-centered photophysical properties of the amino-functionalised cryptates **Ln-1**.

Figure 3.14(a) shows the UV/Vis spectrum of the europium complex of the amino-functionalised ligand under study together with the UV/Vis spectrum of the unfunctionalised analogue, further UV/Vis spectra of studied complexes **Ln-1** can be found in the appendix (see Figure 9.1, page 259). Comparison of the spectra reveals the virtually identical absorption behaviour of both complexes. For both complexes the maximum of the absorption can be observed at 305 nm and a shoulder can be observed at around 319 nm. Based on these results, just as it is the case for the complexes **Ln-bpy$_3$O$_2$**, the amino-functionalised derivatives can be expected to be efficiently sensitised at wavelengths between 305 and 320 nm.

From the low-temperature steady state emission spectrum of **Lu-1** (Figure 3.14(b)) an estimate for the zero-phonon $T_1 \rightarrow S_0$-transition $E(T_1)$ of around 20400 cm^{-1} could be obtained, which coincides with the respective value obtained for **Lu-bpy$_3$O$_2$**. Consequently, the amino-functionalised antenna can be expected to be able to indirectly excite all Ln^{III} for which the unfunctionalised analogue has been found suitable. In

conclusion, the analysis of the ligand-centered photophysical properties of the complexes **Ln-1** reveals no significant influence of the introduced peripheral functionalisation.

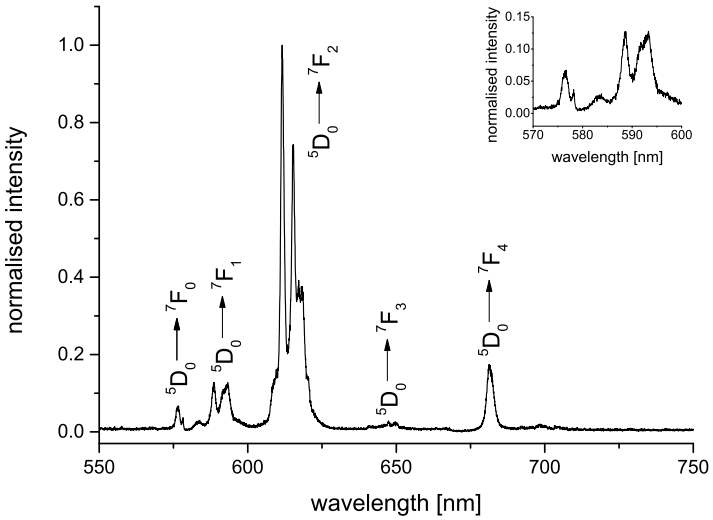

Figure 3.15: Normalised high resolution steady state emission spectrum of **Eu-1** (CD_3OD, $\lambda_{exc} = 320$ nm). Insert: Magnification of the range between 570 and 600 nm.

In the next step the lanthanoid-centered emissive properties of the complexes were studied. The spectrum of the Eu^{III} complex is especially interesting, as the special electronic structure of this lanthanoid allows for a more detailed interpretation than it is the case for other lanthanoids.[163] The $^5D_0 \rightarrow {}^7F_0$-transition is parity and spin forbidden and can only be detected for Eu^{III} compounds of low symmetry. As it can typically be observed for C_2-symmetric cryptates, it could be expected that it can also be observed for C_1-symmetric derivatives, which indeed is the case. Since neither the $^5D_0$- nor the $^7F_0$-level are degenerate, for any europium species a maximum of one $^5D_0 \rightarrow {}^7F_0$-transition is possible. Consequently the existence of two of these transitions, as it was found for **Eu-1** (see Figure 3.15), strongly points to the presence of two at least slightly different Eu^{III} complexes in the sample. This can be explained e.g. by different possible hydration states or different anions coordinating to the lanthanoid as external ligand. Analogously for the $^5D_0 \rightarrow {}^7F_1$-transition a maximum of three subtransitions is expected (resulting from a maximum of three sublevels of $^7F_1$ in the absence of any crystal field degeneracies). In this case four subtransitions are perceptible, which is in line with the interpretation of the $^5D_0 \rightarrow {}^7F_0$-transition. Figure 3.16 (page 44) shows the emission spectra of **Sm-1**, **Yb-1** and **Tb-1**. All of them show the characteristic transitions expected for the respective lanthanoids.

Apart from the indirect sensitisation, another important role of the ligand around the lanthanoid is to protect the excited ion against nonradiative deactivation processes, which will shorten the luminescence lifetime. Consequently, the observable luminescence lifetime τ_{obs} is a valuable measure for the ability of the ligand to shield the lanthanoid from solvent molecules in the first coordination sphere. In Table 3.2 the luminescence lifetimes for the luminescent complexes **Ln-1** in CD_3OD are summarised. Unfortunately due to technical problems for **Eu-1** no luminescence lifetime could be determined. For **Sm-1** and **Tb-1** a biexponential de-

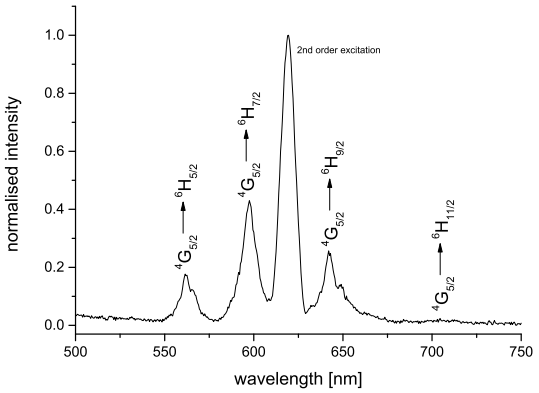

(a) Normalised steady state emission spectrum of **Sm-1** (CD_3OD, $\lambda_{exc} = 310$ nm).

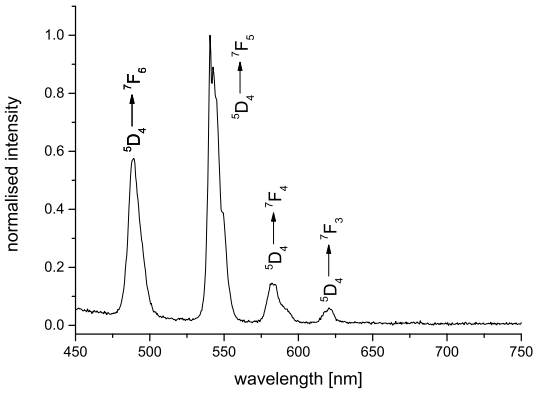

(b) Normalised steady state emission spectrum of **Tb-1** (CD_3OD, $\lambda_{exc} = 305$ nm, excitation path: long pass filter LP399).

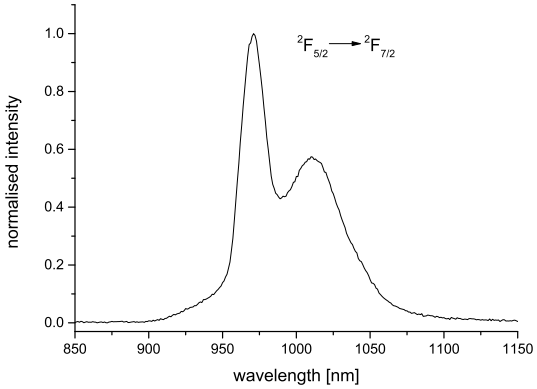

(c) Normalised steady state emission spectrum of **Yb-1** (CD_3OD, $\lambda_{exc} = 305$ nm, emission path: long pass filter RG780. Modified from Reference [160]).

Figure 3.16: Steady state emission spectra of **Ln-1**.

Table 3.2: Luminescence lifetimes τ_{obs} determined for cryptates **Ln-1** in CD_3OD.

	observed transition	τ_{obs} **in** CD_3OD
Sm-1	$^4G_{5/2} \rightarrow {}^6H_{9/2}$ [b]	43.1 μs (47.8%) + 12.0 μs (52.2%)
Tb-1	$^5D_4 \rightarrow {}^7F_5$ [c]	1.43 ms (81.7%) + 0.30 ms (18.3%)
Yb-1	$^2F_{5/2} \rightarrow {}^2F_{7/2}$ [d]	10.8 μs [160]

[b] $\lambda_{em} = 597$ nm, $\lambda_{exc} = 320$ nm. [c] $\lambda_{em} = 540$ nm, $\lambda_{exc} = 305$ nm. [d] $\lambda_{em} = 970$ nm, $\lambda_{exc} = 305$ nm.

cay was found. This is in congruence with the interpretation of the steady state emission spectrum of **Eu-1** and points towards the presence of two species which are equivalent on the NMR time scale but differ on the luminescence time scale. Most probably for the two species different external ligands are bound to the additional coordination site of the Ln^{III}, which is not saturated by the cryptate. The longer component of the lifetime determined for **Sm-1** is quite similar to the value determined for the unfunctionalised parent compound **Sm-bpy$_2$O$_3$** in CD_3CN (30 μs[139]). The longer component of the lifetimes detected for **Tb-1** (1.43 ms) is surprisingly long. Due to the mismatch between the energies of the excited state of Tb^{III} and the triplet state of the **bpy$_3$O$_2$** scaffold, these ligands are typically considered to be inefficient sensitisers for Tb^{II} and only few values determined for comparable systems can be found in literature. For the unoxidised terbium cryptate **Tb-bpy$_3$** in D_2O a monoexponential decay with a lifetime of 0.43 ms was reported.[164] For **Yb-1** a monoexponential decay was found, in the range of experimental error the value determined herein is identical to the one found for the unfunctionalised analogue **Yb-bpy$_2$O$_3$** (12.3 μs[165]). Indeed, if the lanthanoids less susceptible towards nonradiative deactivation by quenching oscillators show a biexponential decay, a monoexponential decay for the NIR-emitting Yb^{III} complex is counterintuitive. The reasons for this behaviour are unclear until now.
A possible reason for the observation of biexponential decays might be the presence of several N-H oscillators in close vicinity of the lanthanoid. A first step towards the closer study of this phenomenon would be the repetition of the measurements in CH_3OH.[25] Since the main components of the determined lifetimes are not critically shorter than the ones of unfunctionalised cryptates, the biexponential decay will not be problematic for further applications of the complexes studied.

In summary the results from the study of the photophysical properties of the amino-functionalised lanthanoid cryptates show, that the peripheral functionalisation does not have a negative impact on the highly useful photophysical properties of the oxidised lanthanoid cryptate scaffolds **bpy$_3$O$_2$**. Hence it is a very useful starting point for the introduction of further functionalities, which will allow for concrete applications.

3.3.3 Preparation and characterisation of luminescent lanthanoid tags for different applications

Various fields of research and technology can benefit from highly reliable, covalently attached lanthanoid luminophores. As it was shown in the previous chapter, the amino-functionalised lanthanoid cryptates **Ln-1** combine the highly beneficial properties of the oxidised bipyridine cryptates with a peripheral functionalisation and therefore offer an ideal starting point for the development of such tag molecules. The aim of this chapter is to develop a general strategy for the simple preparation of such molecules for various applications. The approach followed for this purpose is shown schematically in Figure 3.17.

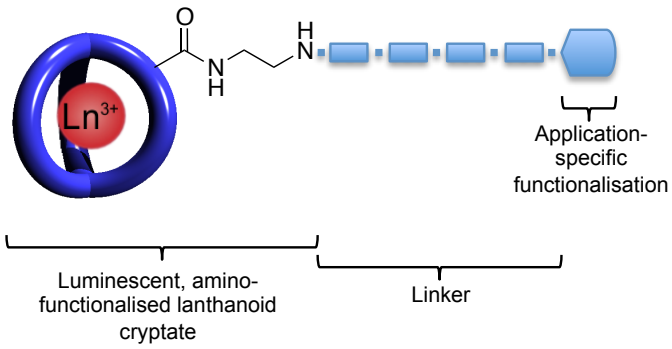

Figure 3.17: Concept for the preparation of tailor-made luminescent cryptates based on **Ln-1**.

Depending on the desired conjugation reaction, luminescent tags with different functionalisations have to be prepared. Another characteristic of the tag molecule which can become critical is the rigidity of the overall tag, it can be modulated with the length of the linker between the lanthanoid cryptate and the functional group. For this exemplary study PEG-linkers were chosen. They are available in different lengths and can be supposed to have a beneficial effect upon the overall solubility of the complete molecule. Furthermore, PEGs with various symmetric and unsymmetric terminal functionalisations are commercially available.
In principle two different synthetic strategies can be followed for the preparation of such tag molecules (see Figure 3.18). To ensure high purity of the material reversed phase HPLC should be performed at some step of the synthesis after the complexation reaction. When the functional group introduced for the targeted application is sufficiently stable, it is of course beneficial to perform the purification as the very last step of the synthesis (early stage functionalisation, strategy **A**). However, many functionalisations will not be compatible with the harsh conditions applied herein, in this case the functionalisation has to be introduced after the purification of the lanthanoid cryptate (late stage functionalisation, strategy **B**).
As the cryptates of Eu^{III} are typically the most luminescent, this lanthanoid was chosen for the preparation of the tag molecules which will be described in the following. Due to the extreme chemical similarity of the lanthanoids and the nature of the core scaffold **bpy$_3$O$_2$**, the respective tag molecules of different lanthanoids can be expected to be accessible completely analogously.

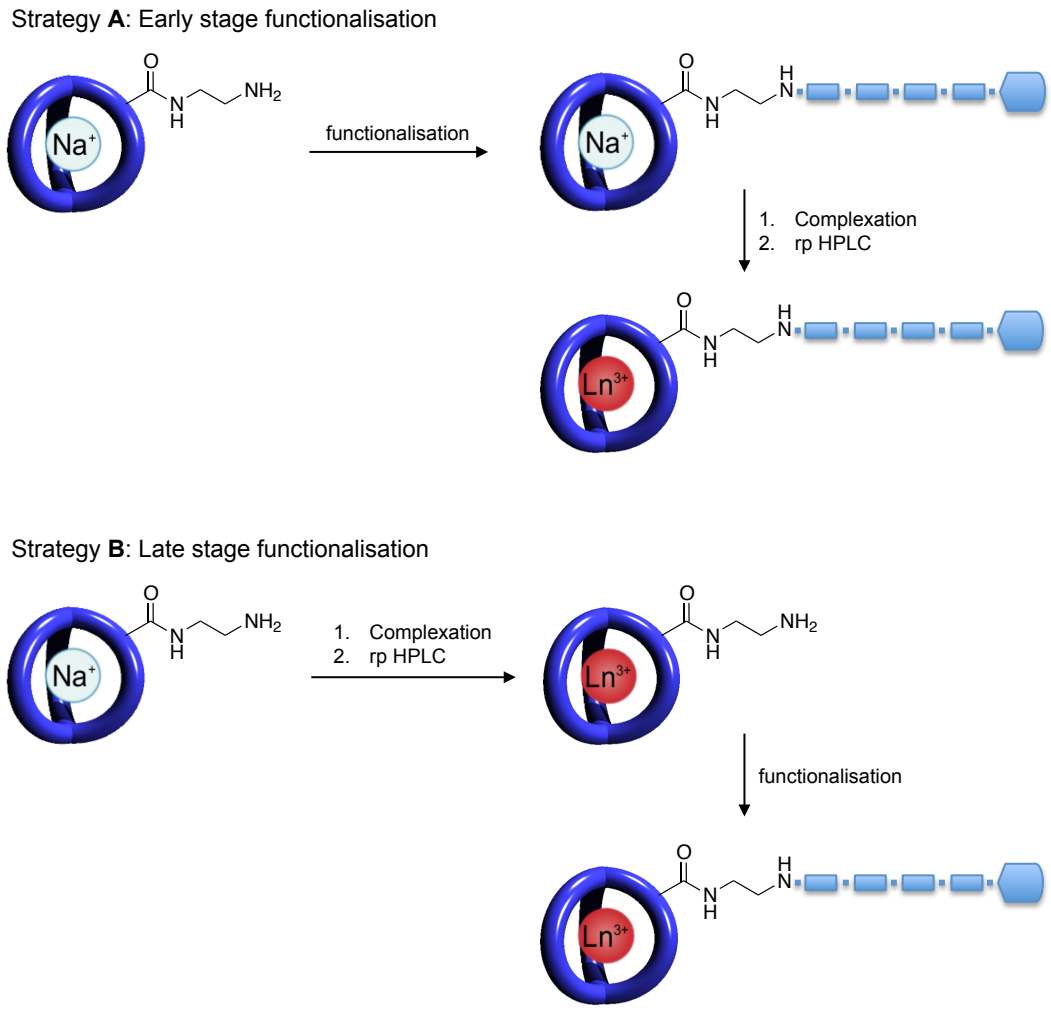

Figure 3.18: Depending on the stability of the functional group which is to be introduced, an early stage or a late stage functionalisation should be applied.

3.3.3.1 Synthesis and characterisation of an azide-functionalised europium tag

The azide-alkyne Huisgen cycloaddition is maybe the best established representative of the highly reliable and typically biocompatible so-called “click reactions”. With an azide-functionalised europium tag this chemistry can be used to e.g. prepare luminescent bioconjugates, or to quantify the alkyne functionalisation upon some kind of material or particles which shall be used for bioconjugation.

Since organic azides are relatively stable in acidic aqueous media, purification of the functionalised cryptate via HPLC appears feasible and synthesis strategy **A** was applied. Accordingly, in a first step the azide-functionalised sodium cryptate **Na-2** was prepared from the amino-functionalised sodium cryptate **Na-1** and a commercially available NHS ester of an azide-functionalised PEG in the presence of slight excess of a sterically hindered base. The reaction was performed in a mixture of DMF and CH_3CN to ensure that all components of the reaction stay in solution, and due to the thermal instability of the azide it was performed at room temperature. After column-chromatography the azide-functionalised sodium cryptate could be ob-

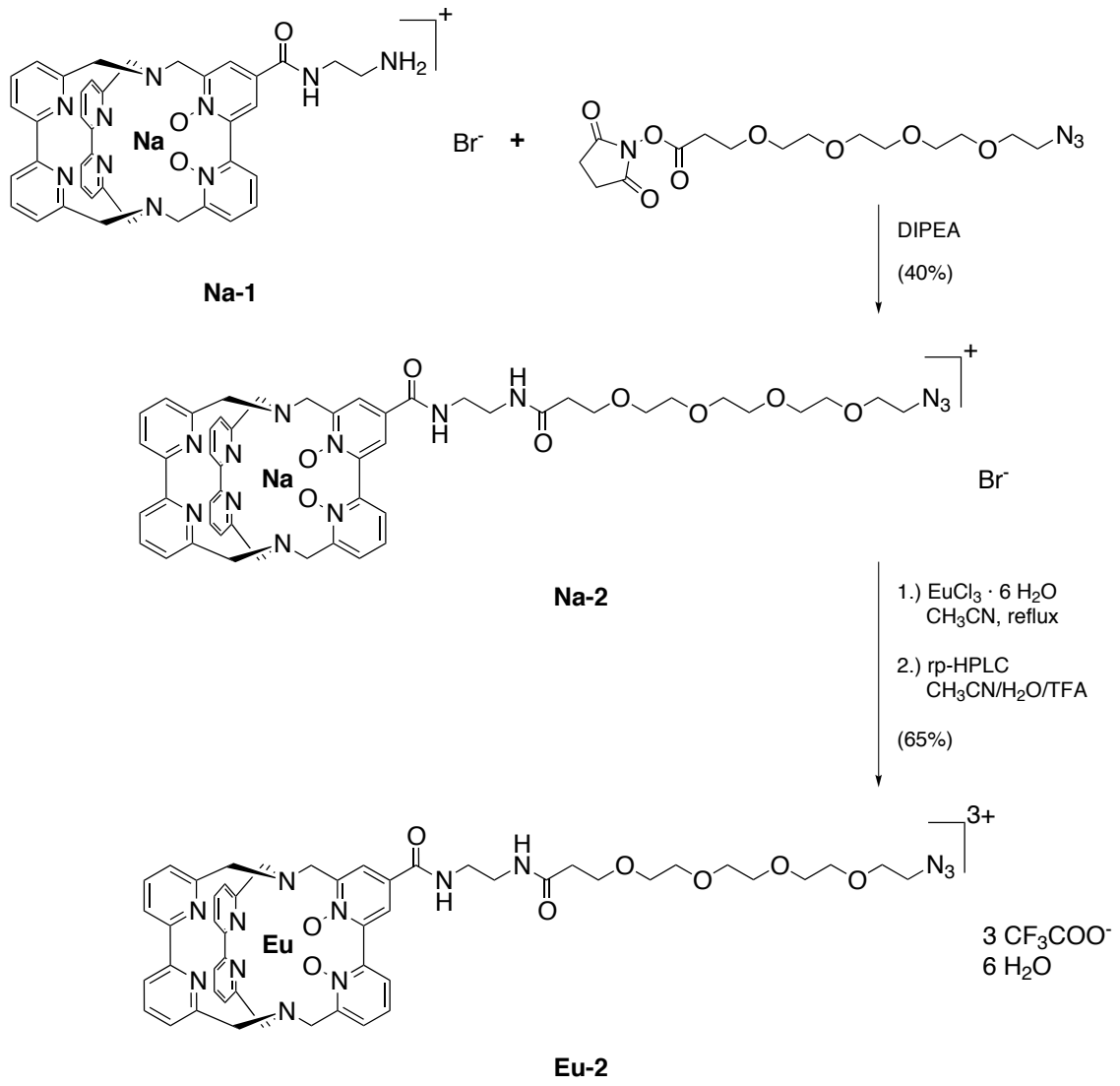

Figure 3.19: Synthesis of the azide-functionalised europium cryptate **Eu-2** from the amino-functionalised sodium cryptate **Na-1** in two steps.

tained in moderate yield (40%) and be characterised via ESI-MS, ^{1}H NMR and ^{13}C NMR spectroscopy (see page 227 for details). Subsequently the sodium cryptate could be transferred into the corresponding europium cryptate. Compared to the standard conditions for the preparation of lanthanoid cryptates from sodium cryptates only slight modifications were necessary. Since the PEG-linker itself can function as ligand for lanthanoids the amount of $EuCl_3 \cdot 6\,H_2O$ was increased to 2.5 equivalents. For this reaction heating to reflux temperature is necessary. Because of the potentially explosive nature of the organic azide the reaction was placed behind a blast shield. The HPLC protocol established for the purification of unfunctionalised lanthanoid cryptates **Ln-bpy$_2$O$_3$** was found to be also suitable for the azide-functionalised compound **Eu-2** and yielded the product **Eu-2** in 65% yield. Under analytical HPLC conditions **Eu-2** (R_f = 13.9 min) was found to have a slightly longer retention time than **Eu-1**. After purification the complex could be char-

acterised with MALDI-MS, ^{1}H NMR and ^{19}F NMR spectroscopy.

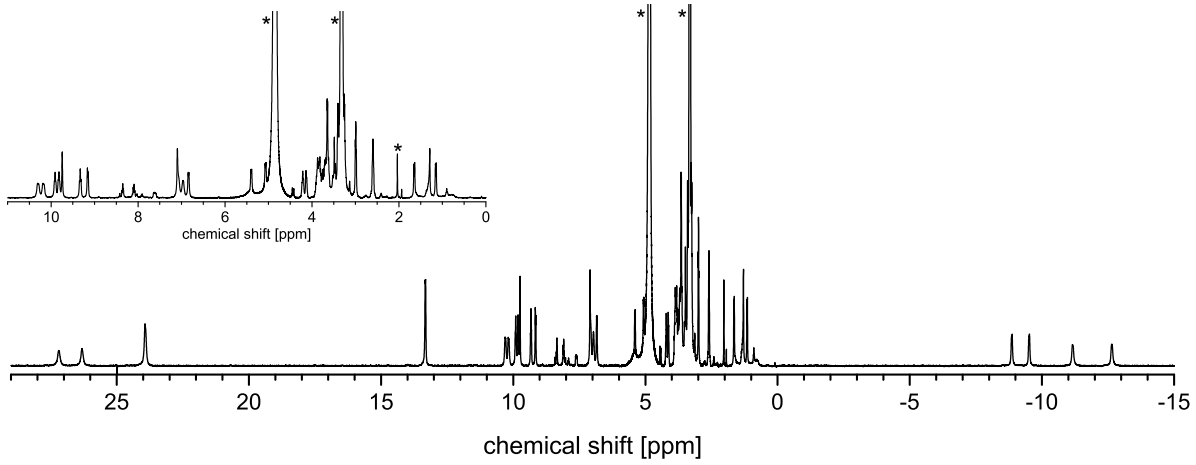

Figure 3.20: ^{1}H NMR spectrum (400 MHz, CD_3OD) of the azide-functionalised europium cryptate **Eu-2**. Unambiguously identified solvent signals are marked with an asterisk.

As expected, the ^{1}H NMR spectrum (see Figure 3.20) is very similar to the one of the amino-functionalised europium cryptate **Eu-1**. The strongly shifted signals of the ligand core remain virtually unaffected by the attachment of the PEG-derivative, and the only significant change is the appearance of the signals representing the protons of the PEG-linker. They can be found between 4.0 and 2.3 ppm. In the case of the only slightly paramagnetic Eu^{III} no strong paramagnetic shifts are expected for protons at this distance from the paramagnetic center. Again the presence of coordinating TFA^- could be revealed via ^{19}F NMR, whereby the resonance frequencies are almost identical for **Eu-2** and **Eu-1**. The photophysical properties of the azide-functionalised cryptate **Eu-2** are currently under study in cooperation with Dr. Ute Resch-Genger (Bundesanstalt für Materialforschung und -prüfung (BAM)) where also the conjugation of the tag molecules to alkyne-functionalised nanoparticles is studied.

3.3.3.2 Synthesis and characterisation of an NHS-functionalised europium tag

Another functionalisation of versatile applicability is the NHS ester group. As deprotonated *N*-hydroxysuccinimide is a very good leaving group such esters can be considered to be activated carboxylic acids, which are highly reactive. In principle any nucleophile can react with an NHS ester, typical reaction partners are carboxylic acids or amines. Despite their high reactivity, NHS esters are more stable than for example acid chlorides. A storage of these compounds at low temperature in the absence of water is usually possible for reasonable periods of time, which makes the use of NHS-functionalised reagents quite convenient and a lanthanoid tag with a respective functionalisation a highly interesting target compound.
Under the strongly acidic conditions typically applied for the HPLC-purification of lanthanoid cryptates NHS esters will readily undergo hydrolysis. Consequently the synthesis of the NHS-functionalised europium tag **Eu-3** has to be done following strategy **B** (Figure 3.18). For the preparation of the azide-functionalised derivative **Eu-2** the reaction of the amino-functionalised cryptate and the NHS-functionalised terminus

of the PEG successfully yielded the conjugated product. In analogy for the preparation of the NHS-functionalised tag molecule a doubly NHS-functionalised PEG was chosen. To suppress the formation of double cryptate-substituted PEGs the synthesis has to be designed with care. For the solution of such a problem one might consider adding the amino-functionalised cryptate slowly to an excess of the PEG-reagent. But because it is unlikely that a separation of the excess of reagent from the product would be possible, and since a contamination with unreacted PEG-linker would be strongly detrimental for any application of the substance, this is not a good choice in this case. In some cases it is also possible to perform such reactions in a solvent from which the mono-substituted, desired product precipitates. Due to the nature of the PEG-linker this is no promising approach for this concrete problem either. Instead the reaction was performed under high dilution conditions: equimolar amounts of the amino-functionalised europium cryptate **Eu-1** and the NHS-functionalised PEG were dissolved in high amounts of solvents. A slight excess of a sterically hindered base was added to the solution of the cryptate, which was then added dropwise via a Teflon tube to the solution of the PEG (for experimental details see page 238). If the tube is thin enough the dropping rate can be controlled precisely by the relative heights of the ends of the tube, so that a very slow addition over several weeks is possible. At the beginning of the reaction these conditions are similar to the use of a high excess of the PEG linker described above, at the end of the reaction the high dilution prevents the formation of local maxima of the concentration of the cryptate.

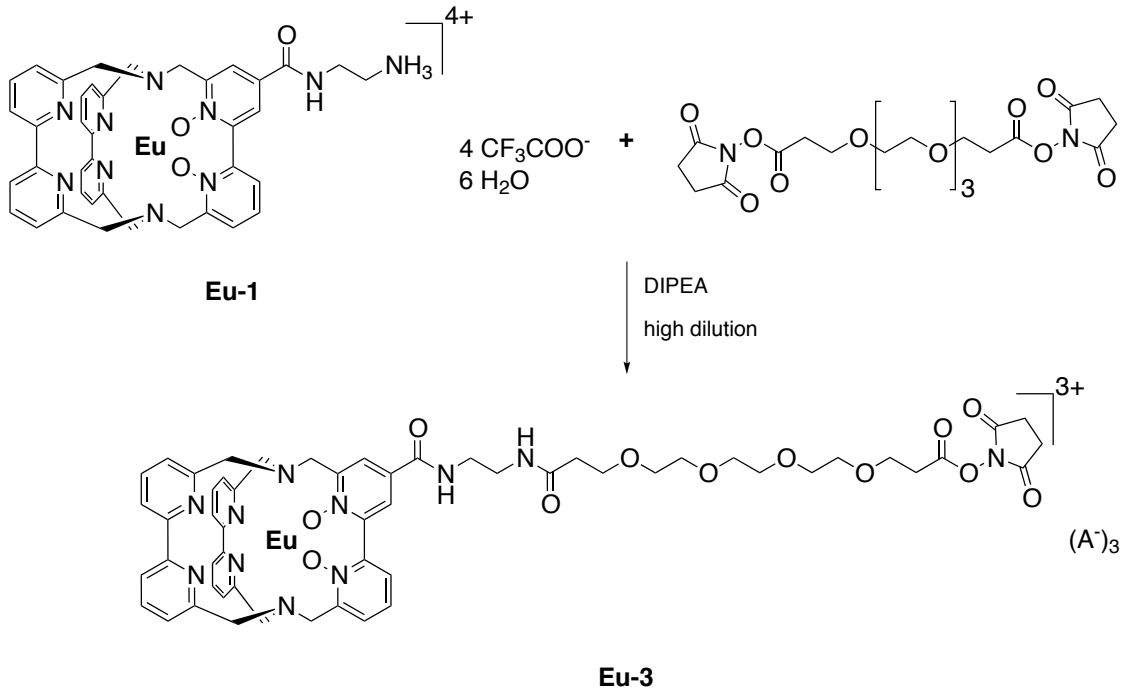

Figure 3.21: Synthesis of the NHS-functionalised europium cryptate **Eu-3** from the amino-functionalised europium cryptate **Eu-1**.

After completion of the reaction the solvent was removed *in vacuo* and the resulting solid was dried thoroughly to remove residues of the added base. Due to the high reactivity of the NHS ester it was re-

frained from undertaking attempts to purify the material isolated. The substance was analysed via ESI-MS whereby all detected signals point towards the successful formation of the desired 1:1 conjugation product (see appendix, page 276). A small amount of the material was analysed via analytical HPLC. To prevent the material from undergoing decomposition during the process (which would make the chromatogram difficult to interpret) the sample was left standing in a solution similar to the mobile phase used for the HPLC method, to ensure a completion of the decomposition prior to the analysis. At the retention time typically observed for the starting material **Eu-1** only small intensities were observed. The main component (most likely the hydrolysed **Eu-3**) is eluted at a retention time of 12.4 min, followed by three minor species.

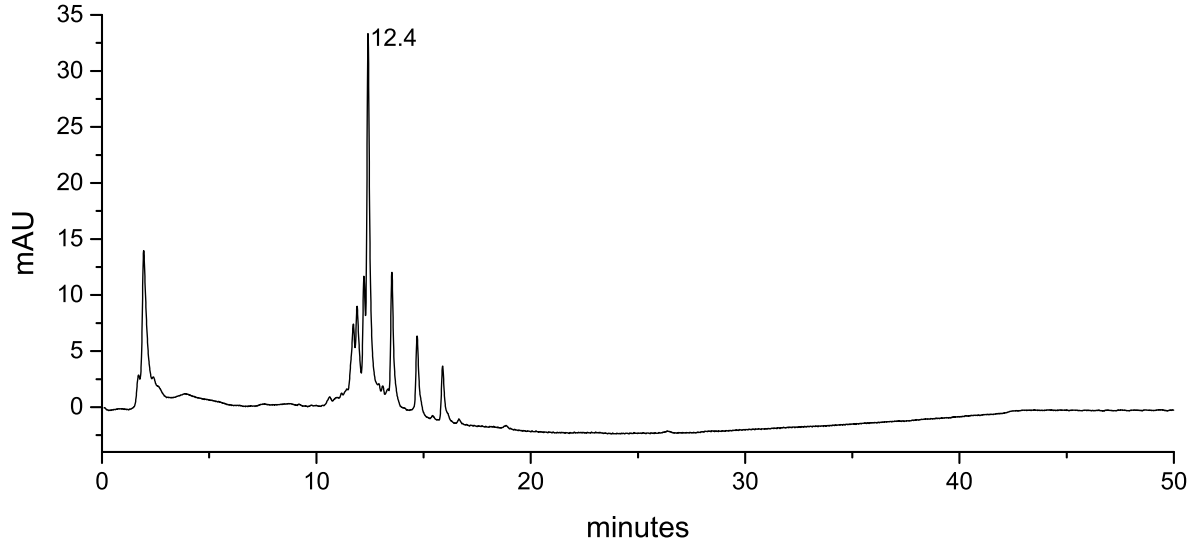

Figure 3.22: Chromatogram from the analytical HPLC (program **A**, setup **A**) of the crude product obtained from synthesis of **Eu-3**.

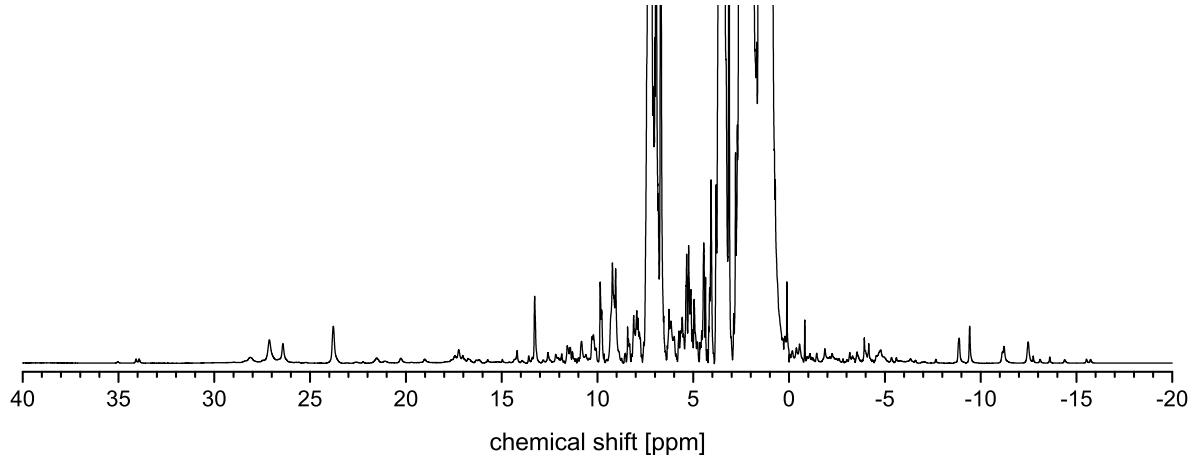

Figure 3.23: ^{1}H NMR spectrum (500 MHz, CD_3CN) of material isolated from the synthesis of the NHS-functionalised europium cryptate **Eu-3**.

Since for the ^{1}H NMR measurement (see Figure 3.23) the complete amount obtained from synthesis was

used, to minimise the risk of hydrolysis in this case CD_3CN was used as solvent. This limits the comparability of the spectrum to the ones obtained for the related europium cryptates. Due to the crude nature of the substance studied, the spectrum is generally difficult to interpret, but some typical signals of europium cryptates can be identified unambiguously between 27 and 24 ppm. Interestingly, at even higher chemical shifts some signals with small integrals can be observed. These might originate from some kind of small organic molecule bound as external anion to the Eu^{III}, for example deprotonated *N*-hydroxysuccinimide. However, based on the ^{19}F NMR spectrum of the sample also a TFA^- anion could be bound. Unfortunately the ^{19}F NMR spectra of these samples in CD_3CN are hardly comparable to the ones in CD_3OD.
As it is the case for **Eu-2**, also **Eu-3** is currently studied with respect to its photophysical properties and its conjugation chemistry in cooperation with Dr. Ute Resch-Genger (Bundesanstalt für Materialforschung und -prüfung (BAM)).

3.3.3.3 Synthesis and characterisation of a BCN-functionalised europium tag

The azide-alkyne Huisgen cycloaddition, for which the azide-functionalised tag **Eu-2** was developed, is typically copper catalysed. This is not always compatible with applications in biological systems, in these cases the copper-free variation of this reaction is a valuable alternative. Here instead of a terminal alkyne a cyclooctyne derivative is used, whose ring strain is the driving force of the reaction with the organic azide.[166][167] As third example of a functionalised europium cryptate such a tag molecule **Eu-4** carrying a bicyclononyne (BCN) was prepared.

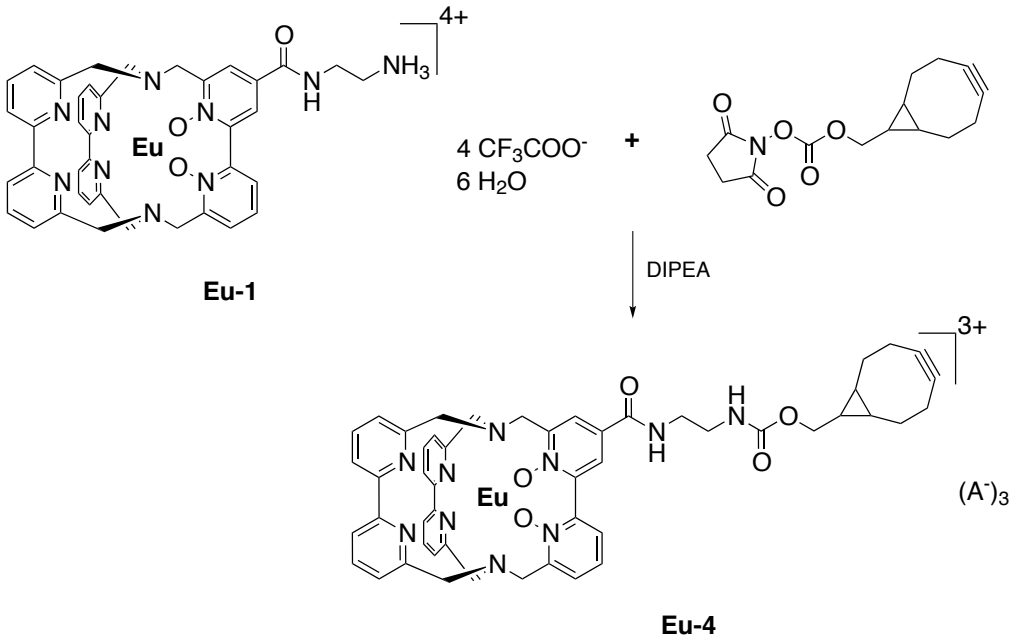

Figure 3.24: Synthesis of the BCN-functionalised europium cryptate **Eu-4** from the amino-functionalised europium cryptate **Eu-1**.

Bicyclononynes can be expected to be less susceptible to hydrolysis than NHS esters, but nevertheless a

HPLC purification of the completely assembled tag molecule did not seem feasible. Consequently synthesis strategy **B** (Figure 3.18) was chosen. In contrast to the synthesis of the NHS-functionalised derivative, in this case purification via recrystallisation from CH_3OH, as established for lanthanoid cryptates, seemed to be a potential alternative. To improve chances for such a purification in this case no PEG linker was used. This also gives the possibility of probing if a direct attachment of a functional group without a flexible linker is possible. The reaction between the amino-functionalised europium cryptate **Eu-1** and the bicyclononyne NHS ester was performed in CH_3CN at room temperature. To ensure complete conversion of the cryptate 1.5 equivalents of the bicyclononyne reagent were used, and an equimolar amount of a sterically hindered base was added. Unfortunately, the crude product obtained after removal of the solvents and excess base *in vacuo* could not be purified by recrystallisation. The crude product was taken up in a minimum amount of CH_3OH and overlayered with Et_2O, but even after elongated storage at 4 °C no solid precipitated. Consequently in the following the crude material was studied.
Upon analytical HPLC no unreacted starting material **Eu-1** could be detected (see Figure 3.25), instead two main components of the substance with retention times of 14.3 and 16.0 minutes were observed.

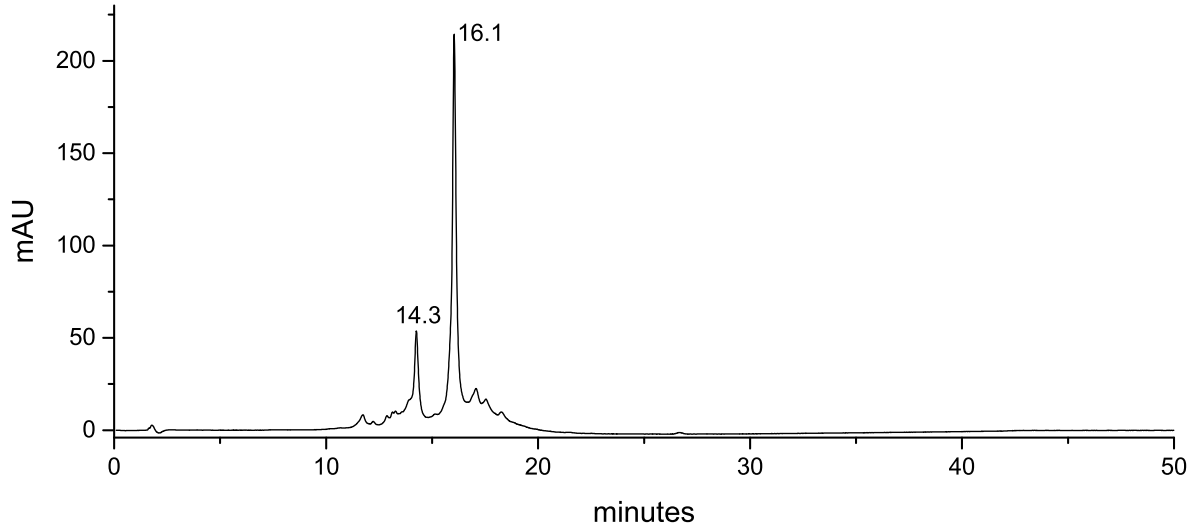

Figure 3.25: Chromatogram from the analytical HPLC (program **A**, setup **A**) of the crude product obtained upon synthesis of **Eu-4**.

The signals detected in the MALDI-MS spectrum strongly point towards the formation of the desired product, with one of the signals indicating that a DIPEA molecule is attached to the detected species. The ^1H NMR spectrum of the isolated compound is shown in Figure 3.26. The characteristic signals of the cryptate scaffold can be identified unambiguously. In this spectrum very clearly the presence of additional paramagnetically shifted signals can be observed, due to the crude nature of the sample it is difficult to assign these signals. They might originate from anions bound to the lanthanoid, from the bound BCN group (bended towards the lanthanoid) or from external, unreacted BCN-NHS. A more detailed study should be performed with a pure sample of **Eu-4**, which might be accessible by reacting the starting materials in a 1:1 ratio. Maybe also purification via HPLC is feasible, since the analytical HPLC did not show any decomposition processes. Further attempts in this regard will be undertaken after initial studies upon the conjugation of

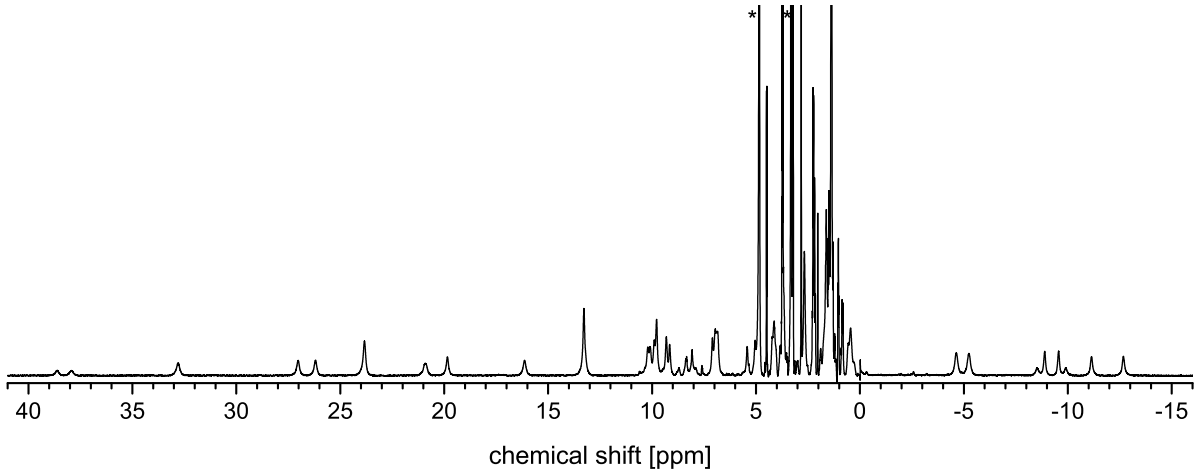

Figure 3.26: ^{1}H NMR spectrum (400 MHz, CD_3OD) of the material isolated from the synthesis of the BCN-functionalised europium cryptate **Eu-4**. Unambiguously identified solvent signals are marked with an asterisk.

Eu-4 to DNA conjugates, which are currently underway in cooperation with the group of Prof. Dr. Bauke Albada (Wageningen University). An initial study of the photophysical properties of **Eu-4** did not reveal any significant variations compared to the amino-functionalised parent compound. The steady state emission spectrum points towards the presence of two species in solution (see Figure 3.27(a)) and so does also the determined biexponential decay of the lifetime (1.11 ms (52.3%) + 0.72 ms (47.7%)). The UV/Vis spectrum of the compound is virtually identical to the one measured for **Eu-1** (see Figure 3.27(b)).

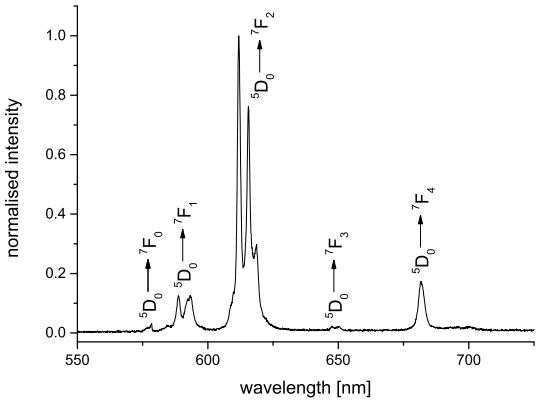

(a) Normalised steady state emission spectrum of **Eu-4** (CD_3OD, λ_{exc} = 320 nm).

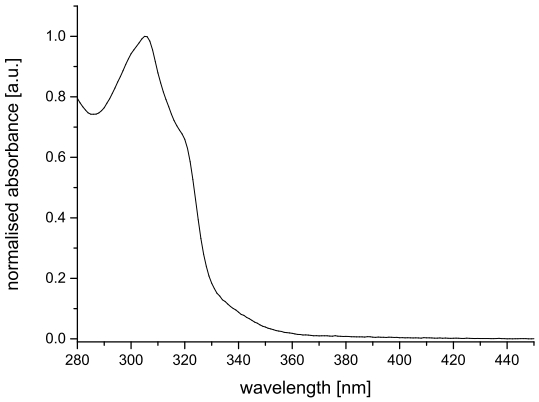

(b) Normalised UV/Vis spectrum of **Eu-4** in CD_3OD.

Figure 3.27: Photophysical properties of the BCN-functionalised europium cryptate **Eu-4**.

3.3.4 Structure in solution and magnetic anisotropy

Due to the typically low conformational stability of lanthanoid complexes in solution, the understanding of their structures is often limited to crystallographic data. Necessarily this leads to at least inaccuracies when properties of the complexes in solution are correlated with the resulting structural models. The high stability and the high rigidity of the cryptates **bpy$_3$O$_2$** are two of their most outstanding properties. They indeed allow for an elucidation of the exact structure of these complexes in solution, and consequently for a more in-depth interpretation of their e.g. photophysical properties in solution. For the cryptate **Yb-bpy$_3$O$_2$** the structure in solution could already be resolved in a combined NMR/DFT study some time ago.[135] The strategy employed herein is based on the lanthanoid-induced paramagnetic shifts which can be observed in the ^{1}H NMR spectrum of the complex. As already outlined before, the paramagnetic shift δ_{para} a nucleus experiences is highly specific for its point in space relative to the paramagnetic center (see page 30 and following). It can be derived from the experimentally accessible shift δ_{obs} with the aid of a diamagnetic reference compound:

$$\Delta\delta_{obs} = \delta_{para} = \delta_{obs} - \delta_{dia} \tag{7}$$

Generally higher shifts and broader signals can be expected for nuclei closer to the paramagnetic center, which allows for an initial assignment of groups of signals to groups of protons. Based on an initial structural model (for example a DFT-optimised structure) now in a global fit the assignment of the protons can be optimised.[168][169] Therefore the paramagnetic shift δ_{para} is assumed to be purely caused by the pseudocontact shift δ_{PC} (see equation 3, page 8) which is a reasonable assumption in the case of Yb^{III}.[170]
δ_{para} can be expressed as linear combination of five components of the magnetic susceptibility tensor χ:[171]

$$\delta_{para} = \left(\chi_{zz} - \frac{1}{3}Tr\chi\right)\left(\frac{3z^2 - r^2}{r^5}\right) + \left(\chi_{xx} - \chi_{yy}\right)\left(\frac{x^2 - y^2}{r^5}\right) + \chi_{xy}\left(\frac{4xy}{r^5}\right) + \chi_{xz}\left(\frac{4xz}{r^5}\right) + \chi_{yz}\left(\frac{4yz}{r^5}\right) \tag{8}$$

with

$$r = \sqrt{x^2 + y^2 + z^2} \tag{9}$$

and x, y, z being the Cartesian coordinates of the observed nuclei relative to the paramagnetic ion (which is placed at the origin). In the principal magnetic axis system χ is diagonalised, so that $\chi_{xy} = \chi_{xz} = \chi_{yz} = 0$, which reduces the problem to a five-parameter least-square search. Thereby (χ_{zz} - (1/3)Trχ), (χ_{zz} - χ_{yy}) and a set of Euler angles that relate the principal magnetic axis system to the molecular coordinate system are varied, to minimise the difference between the experimental paramagnetic shifts δ_{para} and the calculated paramagnetic shifts which result from χ and x, y, z of the respective nucleus.
Such analysis, which proved to be successful for the unfunctionalised ytterbium cryptate, is especially interesting for the amino-functionalised cryptates **Ln-1**. It will allow for a detailed comparison of the solution structure of the complexes of both ligands and reveal in how far the loss of symmetry upon functionalisation

affects the geometry of the core scaffold. An analysis as outlined above is in principle based on the very specific magnetic properties of the lanthanoid ion in the complex under study. The magnetic properties (which result in the specific manifestation of the magnetic susceptibility tensor χ) of a lanthanoid complex are by far more sensitive for subtle changes in the coordination geometry (see chapter 1.2). Consequently, this will also allow for a more in-depth comparison of the electronic situation of the Yb^{III} ion as it is possible by photophysical methods. Last but not least such a study will provide valuable information for a potential application of the functionalised lanthanoid cryptates in the field of the structural elucidation of biomolecules in solution.

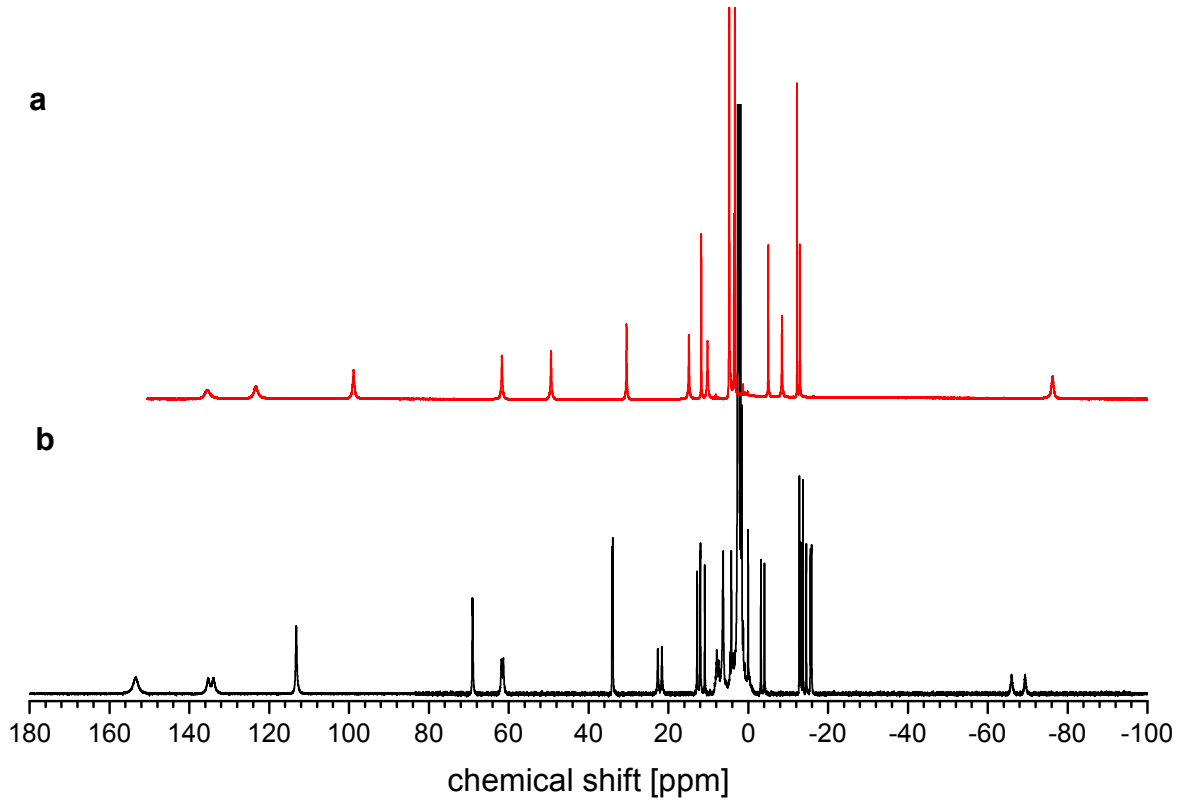

Figure 3.28: ^{1}H NMR spectra of a) unfunctionalised **Yb-bpy$_3$O$_2$** with chloride in the inner coordination sphere (CD_3OD, 400 MHz) and b) amino-functionalised **Yb-1** with TFA^- bound to the lanthanoid (CD_3CN, 500 MHz). Due to the overlap with the intense signals of the solvent molecules the protons of the ethylene diamine group could not be identified unambiguously. Adopted from reference [160].

A simple comparison of the ^{1}H NMR spectra of **Yb-bpy$_3$O$_2$** and **Yb-1** (see Figure 3.28) already reveals some important information. In principle upon functionalisation the symmetry changes drastically and the formerly pairwise symmetry related protons could now in principle be observed at different shifts. But in the case of **Yb-1** the resulting difference of chemical shifts (which can be seen as a measure for the deviation from the C_2-symmetry of the parent system) is surprisingly small. In two cases the signals could not even be resolved from each other, for the other signals signals they are only separated by less than 3.5 ppm and

can unambiguously be assigned to the respective signal of **Yb-bpy$_2$O$_2$**.
Again, the experimental findings show only a very small effect of the introduced peripheral functionalisation on the properties of the core ligand scaffold. This is not only a promising first result of the analysis of the NMR data obtained for **Yb-bpy$_2$O$_2$**, but also makes the next step of the analysis of the magnetic anisotropy straight forward, which is the initial assignment of the signals to the different protons of the complex under study. The subsequent analysis was performed in cooperation with Carlos Platas-Iglesias, Universidade da Coruña. In a first step, independently from the NMR data, DFT calculations (TPSSh/LCRECP(6-31G(d,p)) level) were used to optimise the structure in CH_3CN. The anions were omitted to reduce the computational costs of this in any case demanding calculation, instead a water molecule was bound to the lanthanoid. As expected the structure is very similar to the one of the unfunctionalised **Yb-bpy$_3$O$_2$**. In line with the NMR data obtained for **Yb-1**, the direct coordination environment around the metal ion has a virtually undistorted C_2-symmetry.

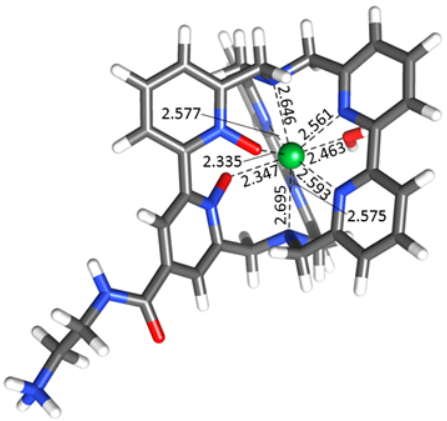

Figure 3.29: DFT optimised structure of **Yb-1** in CH_3CN (TPSSh/LCRECP/6-31g(d,p)) with the bond distances of the direct coordination environment. Grey: carbon, blue: nitrogen, red: oxygen, green: Yb^{III}, white: hydrogen. The coordinates of the atoms can be found in the appendix (see page 308).

In analogy to the analysis performed on **Yb-bpy$_3$O$_2$** now signals and protons were assigned. Since the actual geometry of the complex is so close to C_2-symmetry, pairs of symmetry related protons were assigned to average shifts of pairs of signals. The paramagnetic shifts were extracted from the experimentally observed shifts according to equation 7, whereby **Lu-bpy$_2$O$_3$** was used as diamagnetic reference. Subsequently they were analysed as described above with a five-parameter least-squares search using equation 8, minimising the difference between the experimental and calculated pseudocontact shifts.
The experimental and calculated ^{1}H NMR shifts are summarised in Table 3.3. Using the agreement factor AF a very good agreement of the experimental and calculated shifts could be found (AF = 0.0321):

$$AF = \sqrt{\frac{\sum_i \left(\delta_{obs,i} - \delta_{calc,i}\right)^2}{\sum_i \left(\delta_{obs,i}\right)^2}} \tag{10}$$

Table 3.3: Comparison of experimental (δ_{obs}), averaged experimental (δ^{avg}_{obs}) and calculated (δ^{avg}_{calc}) ^{1}H NMR shifts of **Yb-1** in CD_3CN. See Figure 3.30 for the numbering scheme of the protons.

proton	δ_{obs}	δ^{avg}_{obs}	δ^{avg}_{calc}
H1o	-69.35 / -65.97	-67.66	-68.4
H2o	21.63 / 22.55	22.09	25.89
H3o	12.79 / 10.88	11.84	12.73
H4o	0.02	0.02	2.11
H5o	-13.19 / 14.55	13.87	-13.96
H1b	153.49	153.49	148.05
H2b	61.82 / 61.35	61.59	63.50
H3b	-3.18 / -4.07	-3.63	-2.65
H4b	-12.82 / -13.72	-13.27	-11.88
H5b	-15.59 / -15.85	-15.72	-15.06
H6b	12.04 / 11.97	12.01	10.63
H7b	34.09 / 33.97	34.01	33.32
H8b	69.10 / 68.99	69.05	68.81
H9b	113.22	113.22	114.63
H10b	135.27 / 133.96	134.62	137.96

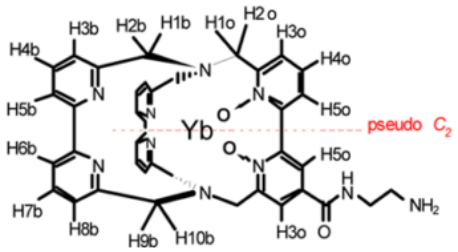

Figure 3.30: Numbering scheme applied for the lanthanoid induced shift analysis of **Yb-1**. Figure adopted from reference [160].

This becomes more graphic in Figure 3.31(b), where the experimentally found chemical shifts are plotted together with the calculated ones. As indicated by the green line there is an excellent agreement between them. Consequently, the description of the tensor of the magnetic susceptibility χ developed in the least-square fit can reproduce the experimental NMR shifts accurately and successfully describes the

magnetic anisotropy of **Yb-1**. This also suggests that the bound TFA-anion, which was exchanged for a water molecule for the purpose of this study, is not critical for the magnetic anisotropy of the system.

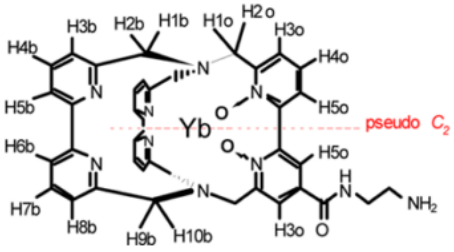

(a) Numbering scheme applied for the lanthanoid induced shift analysis of **Yb-1**.

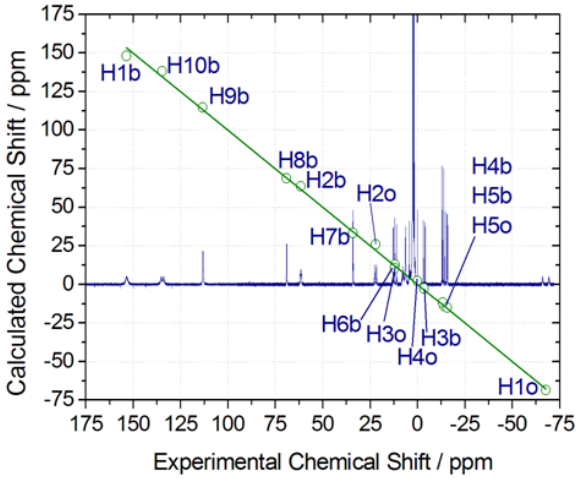

(b) Experimental ^{1}H NMR spectrum (CD_3CN, 500 MHz) of **Yb-1** with plot of the calculated shifts of the compound.

Figure 3.31: Comparison of the experimentally found and calculated ^{1}H NMR shifts of **Yb-1**. Figures adopted from reference [160].

From the fit the parameters describing χ are obtained as $(\chi_{zz} - (1/3)\mathrm{Tr}\chi) = 2740 \pm 62$ ppm Å^3 and $(\chi_{zz} - \chi_{yy}) = -8601 \pm 138$ ppm Å^3. Together with equation 8 these values were used to calculate and plot pseudocontact shift surfaces of the tensor. For this purpose a mayavi2[172]/python script was coded whose source code can be found in the appendix (see page 278). Such a representation allows for a much more vivid understanding of χ of a given paramagnetic compound. In Figure 3.32(a) compound **Yb-1** is shown schematically together with two pseudocontact shift surfaces (for +12 ppm and -12 ppm, respectively). The green line represents the effective C_2-symmetry axis of the molecule, which is perpendicular to the symmetry axis of the surfaces. Such representations are also extremely helpful for a comparison of the magnetic anisotropies of different paramagnetic complexes. In Figure 3.32(b) pseudocontact shift surfaces of **Yb-1** and **Yb-bpy$_3$O$_2$** are shown. Both complexes are closely related but differ in terms of two characteristics which in principle can have an immense influence on the magnetic properties: the symmetry and the species bound at the additional coordination site of the lanthanoid (water in the model used for **Yb-1**, Cl^- in the case of **Yb-bpy$_3$O$_2$**). Yet the pseudocontact shift isosurfaces which directly result from the underlying tensors are almost indistinguishable and show only very small differences in size and virtually none in terms of orientation. Obviously χ of these complexes under study are remarkably tolerant for changes in the inner coordination sphere and at the periphery of the ligand. From these results it can be extrapolated that the attachment of further groups to the primary amine, or changes in the media in which the NMR experiment is performed, also will not critically affect the susceptibility of the magnetic anisotropy. This is a precondition for the use of paramagnetic complexes for the structural elucidation of biomolecules via paramagnetic NMR.

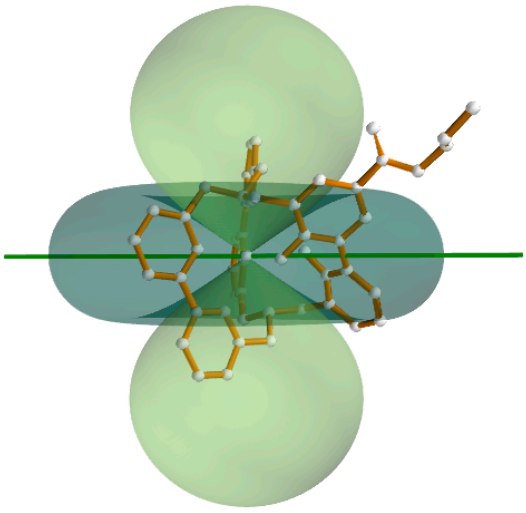

(a) Representation of **Yb-1** (without the bound water molecule) and two pseudocontact shift surfaces (light green: +12 ppm and dark green: -12 ppm) derived from the susceptibility of the magnetic anisotropy tensor χ. The green line illustrates the effective C_2-symmetry axis of the complex.

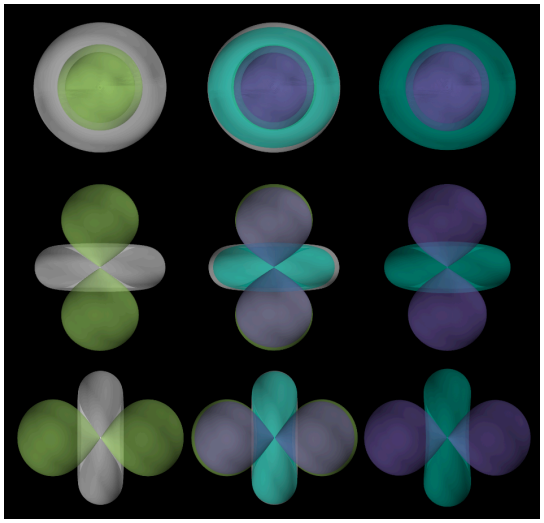

(b) Size and orientations of the pseudocontact shift isosurfaces of the functionalised (**Yb-1**, left) and unfunctionalised (**Yb-bpy$_3$O$_2$**, right) cryptate along the three different Cartesian coordinate axes. In the middle the isosurfaces of both compounds are overlayed.

Figure 3.32: Representations of the susceptibility of the magnetic anisotropy tensor χ of **Yb-1** and **Yb-bpy$_3$O$_2$**. Figures adopted from reference [160].

3.3.5 Towards an enantiopure, twofold functionalised tag molecule for the structural elucidation of biomolecules

The classical method for the structural characterisation of large biomolecules is X-ray crystallography. Such studies have allowed for a substantial understanding of many important principles of biochemistry, but severe limitations arise from the fact that typically biomolecules are active in solution, where their structure can largely differ from the one in the solid state. NMR techniques are obviously an excellent choice to circumvent this problem and many different ones have been employed for this purpose. Maybe the most established and best known example is the utilisation of the nuclear Overhauser effect (NOE), but indeed a variety of complementary techniques is used. The attachment of paramagnetic tag molecules and the interpretation of resulting pseudocontact shifts of the biomolecule is one of them. In principle such analysis is quite similar to the one describe for the complex **Yb-1** in the previous chapter, but due to the enormously higher complexity of most biomolecules, for these molecules such studies are of course more complicated. In order to obtain analysable data special care has to be taken for the design of the paramagnetic tag molecule. Generally paramagnetic lanthanoid complexes are considered to be a very good choice for this purpose, e.g due to the availability of diamagnetic but chemically virtually identical reference compounds. But since the paramagnetic shift of the signals of the biomolecule under study depend on the very exact geometric arrangement of the nuclei and the paramagnetic center, again the low coordinative stability of most lanthanoid complexes becomes a major problem. In light of this, a tag molecule based on a rigid and well-defined cryptate **Ln-bpy$_3$O$_2$** is a target structure of enormous potential. The analysis of the magnetic anisotropy of **Yb-1** can be seen as a promising first result towards this. However, for several reasons the cryptates **Ln-1** do not have ideal properties for such an application and fundamental modifications of the ligand design are reasonable. In order to provide a stable alignment of tag molecule and biomolecule a dual, rigid attachment is preferential. Even more importantly the used tag molecules should be achiral or enantiopure, since otherwise the attachment to chiral biomolecules will lead to the formation of diastereomers and consequently to the observation of a doubled set of signals. Furthermore the placement of the ethylene diamine group of **Yb-1** relative to the pseudocontact shift surfaces, as they can be seen in Figure 3.32(a), is not optimal. In this area of space relative to the paramagnetic center only small shifts are expected, which would at least complicate the study of smaller biomolecules (like they would be chosen for initial experiments).

A variation of the oxidised cryptates, whose core structure allows to meet all these requirements, had already been published some time ago: The attachment of an enantiopure tether to one of the bipyridine building blocks leads to a prearrangement of its pyridine rings and upon macrobicyclisation the formation of only one enantiomer (see page 18 and Figure 3.33).[134] Conceptually the transformation of **Ln-bpy$_3$O$_2$-*SS*-(Me)$_2$** into a dually functionalised tag molecule is straightforward, the methyl-groups need to be substituted for some kind of group carrying a reactive functionalisation. An enlargement of the peripheral groups at the eightmembered ring should rather have a positive than a negative impact upon the prearrangement of the rings. An adverse effect upon e.g. the macrobicyclisation reaction is not likely, either. The nature of the initial reactive function at the desired tag molecule is also not critical, since in any case some kind of linker would be used for the attachment to the biomolecule. But what is indeed critical is the choice of the

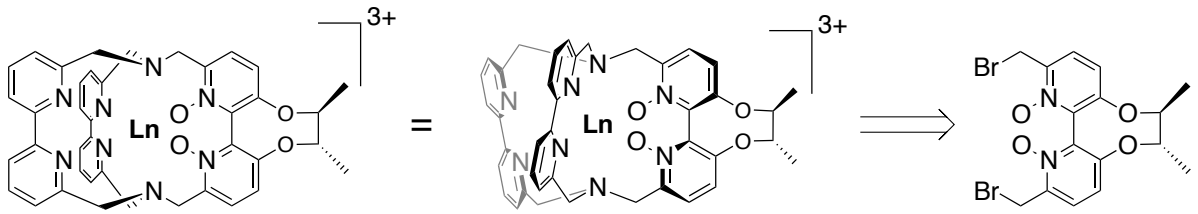

Ln-bpy$_3$O$_2$-*SS*-(Me)$_2$

Figure 3.33: Enantiopure cryptates can be synthesised when the relative arrangement of the pyridines of the oxidised bipyridine building block is fixed in one of the atropisomeric forms.[134]

protecting group which is attached to the functional groups during assembly of the cryptate. The protecting group has to be stable under a variety of conditions, especially the conditions in the two oxidation steps are challenging. At the same time there should be a reliable and clean, yet mild cleavage reaction for the removal of the protecting groups. Of course this is always desirable, but in this case it is especially important since the multistep synthesis of cryptates limits the accessibility of these compounds and the options for the purification of cryptates are also limited. A group for which all these requirements can be expected to be fulfilled are benzyl ethers protected hydroxy-groups. Benzyl ethers are considered to be one of the most robust protecting groups. They are invariant to many challenging reaction conditions, e.g. a wide range of basic and acidic conditions, most metal hydrides and (mild) oxidising agents.[173] Deprotection is typically achieved via Pd-catalysed hydrogenation at relatively mild conditions and with good to excellent yields, and many variations or alternative deprotection strategies have been published.[173][174]

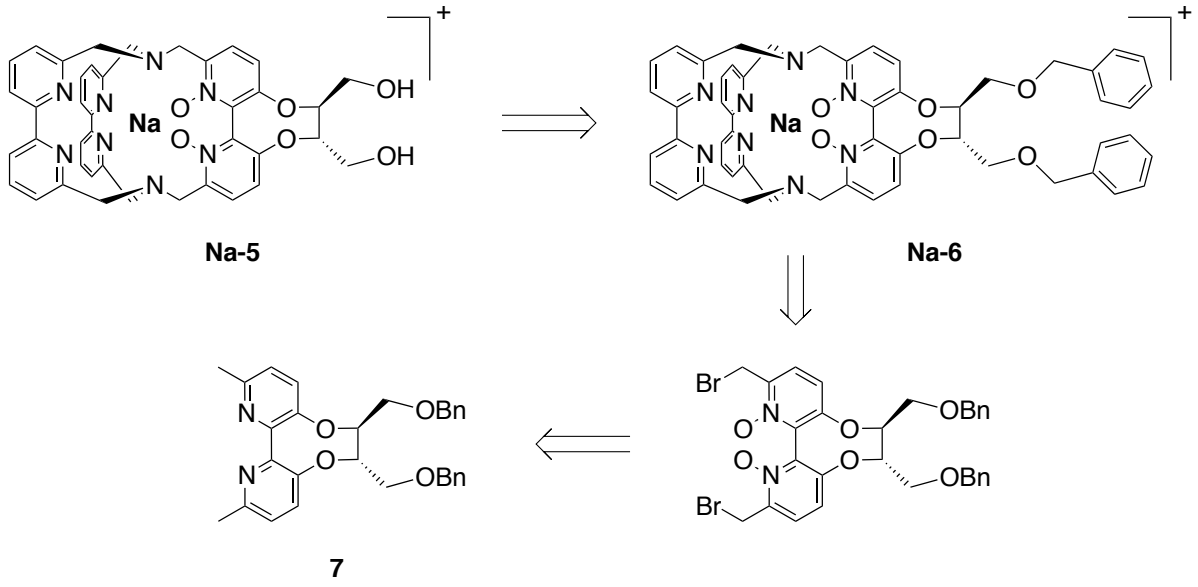

Figure 3.34: Retrosynthetic approach for the preparation of a diol-functionalised, enantiopure cryptate **Na-5**.

Based on these considerations, and in analogy to the synthesis of **Ln-bpy$_3$O$_2$-*SS*-(Me)$_2$**[134], for the synthesis of the diol-functionalised enantiopure cryptate **Na-5** the retrosynthetic plan shown in Figure 3.34 was developed. The hydroxy-groups can disturb most reaction steps necessary for the construction of the

cryptate scaffold, including the macrobicyclisation itself. Consequently the protecting groups should be maintained until completion of the very last step of ligand synthesis, in which the protected cryptate **Na-6** is assembled. In the course of my master thesis (where also the experimental details can be found[162]) I could already establish the synthesis of **Na-6**.

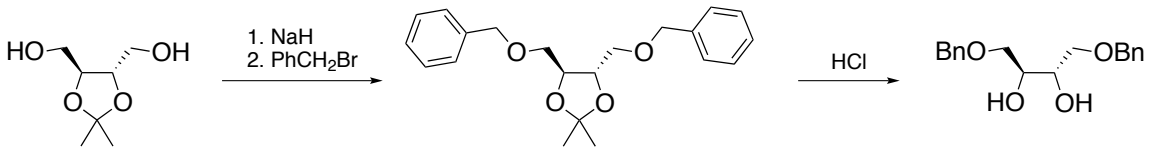

Figure 3.35: Synthesis of (2*S*,3*S*)-1,4-bis(benzyloxy)butane-2,3-diol from an enantiopure, acetonid-protected threitol-derivative as published by Mash *et al.*[175]

Starting point for the synthesis of **Ln-bpy$_3$O$_2$-*SS*-(Me)$_2$** was the commercially available (*R*,*R*)-2,3-butanediol. Fortunately, the synthesis of an equivalent building block for the preparation of **Na-6** was already published by Mash *et al.* (see Figure 3.35).[175] For the preparation of the bipyridine key building block **7** initially the hydroxy-groups are activated as sulfonic acid esters. Since triflate is a very good leaving group, in the subsequent step the introduction of the pyridines can easily be archived by a nucleophilic substitution. For this reaction, in which an inversion of the stereocenters occurs, 3-hydroxy-2-iodo-6-methylpyridine is deprotonated with sodium hydride and subsequently added to the sulfonic acid esters (see Figure 3.36).[176]

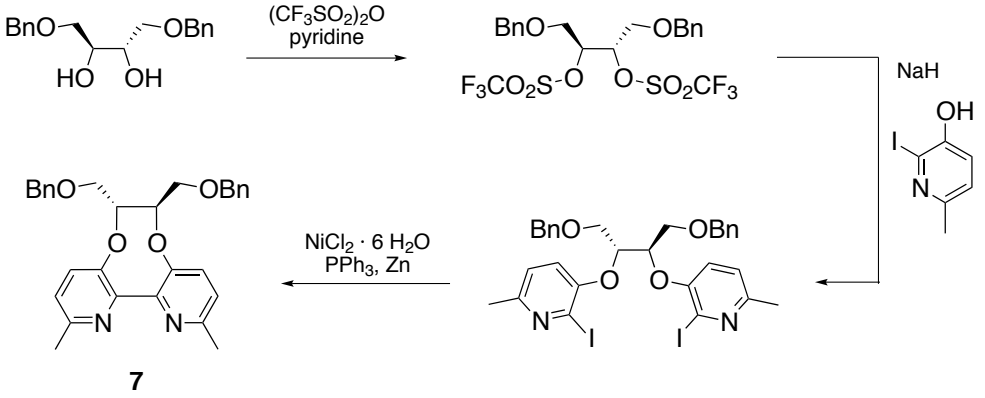

Figure 3.36: Preparation of bipyridine **7** from (2*S*,3*S*)-1,4-bis(benzyloxy)butane-2,3-diol.

The subsequent steps for the preparation of the benzyl-protected sodium cryptate **Na-6** could be realised with reactions typically used for the preparation of cryptates (see Figure 3.37). Initially bipyridine **7** is oxidised with mCPBA, which in this case could be realised with 80% yield. The N-oxide is cleaved in the subsequent modified Boekelheide rearrangement which was used to brominate the methyl groups. Hereby addition of trifluoroacetic anhydride is followed by lithium bromide, which reacts in a nucleophilic substitution with the trifluoroacetylated intermediate. The relatively low yield of 55% can be explained by the relative thermal instability of the bromide. Higher yields might be possible when additional care is taken

concerning this. For the following oxidation step for the preparation of different cryptates the use of an adduct of urea and hydrogen peroxide had already been found beneficial to the oxidation with mCPBA. In line with these findings the corresponding reaction was found to proceed with very high yield (98%) in this case. Unfortunately, yet not surprisingly, the following macrobicyclisation reaction could only be realised with a low yield of 17%.

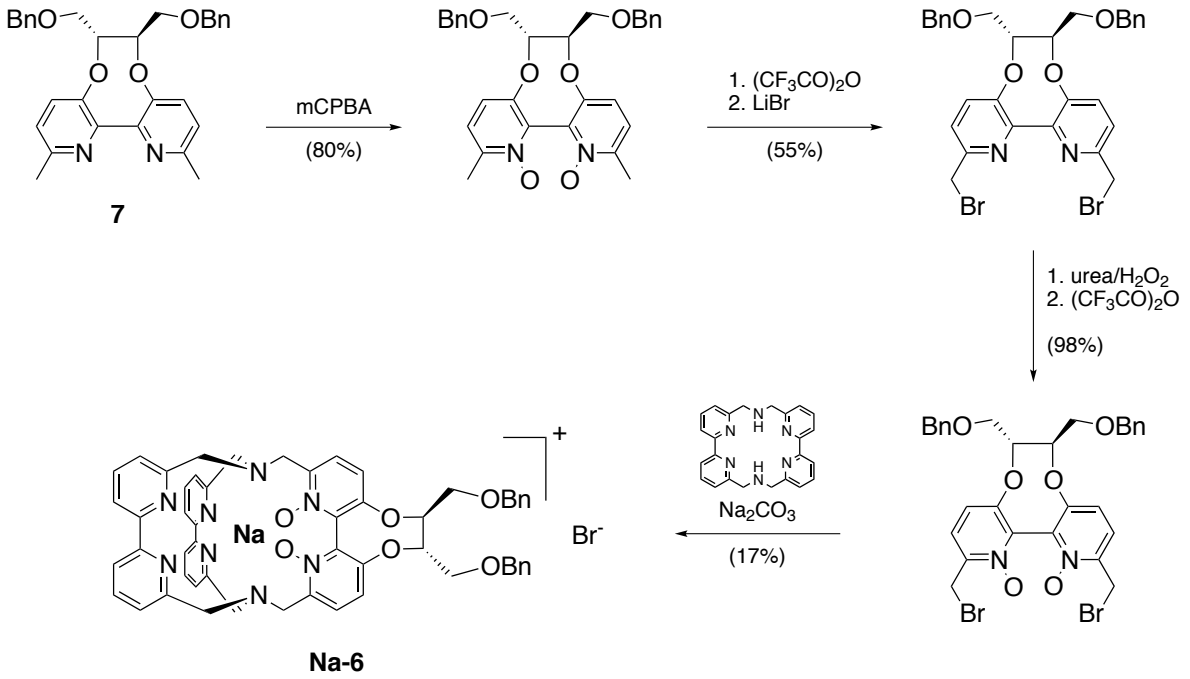

Figure 3.37: Preparation of the protected diol-functionalised sodium cryptate **Na-6** from bipyridine **7**.

Due to the limited availability of **Na-6**, prior to deprotection of the cryptate to yield **Na-5**, the deprotection reaction should be optimised with the bipyridine **7**. This compound is by far more accessible and with the oxygen-containing eightmembered ring already possesses the structural motif which is the most likely to lead to problems during deprotection. Unfortunately it turned out to be surprisingly difficult to remove the protecting groups at all, and a variety of reaction conditions had to be tested until a successful one could be identified. The reactions known from literature whose conditions were tried to be applied onto this deprotection problem are shown in Figure 3.38 and Figure 3.39.

Pd-catalysed hydrogenolysis is the typical and most established method to remove benzyl protecting groups. Indeed, Stavrakov *et al.* published a successful hydrogenolytic cleavage of the benzyl protecting groups of a highly related system (see Figure 3.38).[177] The reaction was performed in EtOAc with $Pd(OH)_2$ (10% on carbon) at atmospheric pressure of H_2 to yield the diol in 79% yield after 2 hours. Surprisingly, in the case of the bipyridine **7** even after 24 hours at these reaction conditions no reaction could be detected. After filtration the isolated substance could be identified as the starting material via ^{1}H NMR spectroscopy. The same result was found after the reaction was repeated with 4 bar H_2 pressure. The most relevant difference between the molecule studied by Stavrakov *et al.* and bipyridine **7** is the presence

Method A: **Pd-catalysed hydrogenolysis**

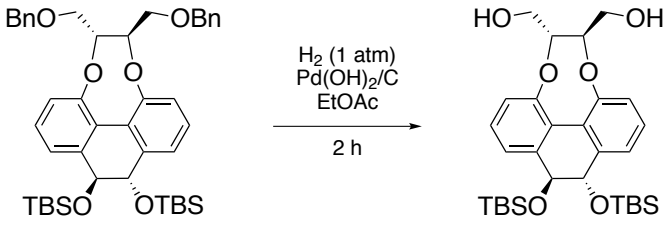

Method B: **Substitution with subsequent hydrolysis**

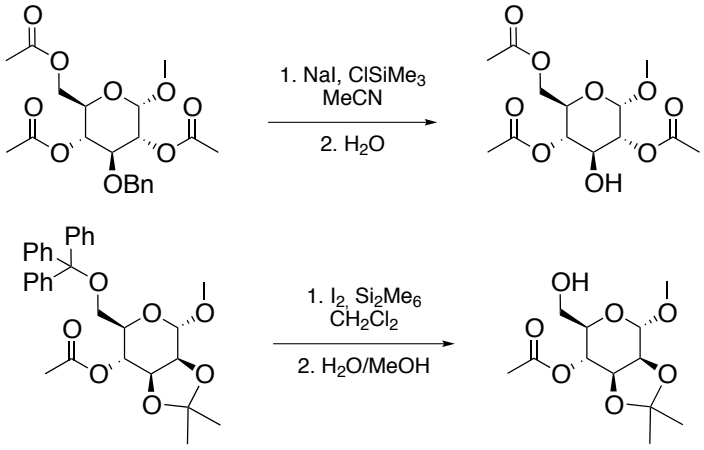

Method C: **Photochemical reaction with *N*-bromosuccinimide with subsequent hydrolysis**

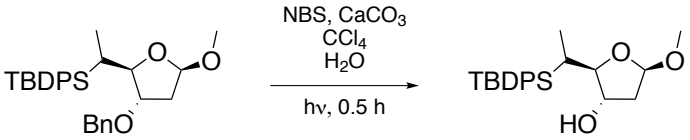

Figure 3.38: OBn-deprotection reactions successfully applied to molecules with structural similarity to **7**. References are given in the text.

of the nitrogen atoms of the pyridine rings, which might indeed hinder the reaction by complexation of Pd^{II}. To prevent the bipyridine from deactivating the metal ion, the reaction was also repeated in the presence of 2.4 equivalents of acetic acid. Under these conditions the nitrogen atoms should be protonated and consequently complexation of Pd^{II} is not possible any longer, still no reaction could be observed. Afterwards some more experiments were performed, varying solvents and reaction conditions. In neither of these experiments, not even partial deprotection of **7** could be observed. Consequently, different synthetic approaches which could already successfully be realised on molecules with related structural motifs were searched. For example Klemer *et al.* presented two related methods for the cleavage of benzyl ethers from sugar molecules.[178] General principle is to substitute the benzyl ether with an in situ prepared trimethylsilyl iodide, which is subsequently hydrolysed. Both methods basically only differ in the in situ preparation of

the trimethylsilyl iodide, both were applied to **7**. In the case of the first variation, where trimethylsilyl iodide is prepared from NaI and $ClSiMe_3$, the precipitation of a colourless solid indicated that the formation of the trimethylsilyl iodide was successful. For this experiment, the reaction time was prolonged compared to the example from literature. Unfortunately the changes observed in the ^{1}H NMR spectrum of the reaction mixture after aqueous work up point towards decomposition of **7**. In the case of the second variation of the reaction, where trimethylsilyl iodide is prepared from I_2 and Si_2Me_6, two experiments with **7** were conducted. The first with only a few minutes reaction time (as described in literature), the second with two hours of reaction time. In both cases the characteristic dark violet mixture of reagents discoloured upon addition to the protected starting material, but no further changes could be observed until the reaction mixture was subjected to an aqueous work up. The ^{1}H NMR spectra of both isolated crude products indicate that some kind of reaction had taken place, but the desired deprotection could not be observed.

As another promising strategy the photolytic reaction of *N*-bromosuccinimide with the CH_2-groups of the benzyl ether followed by basic hydrolysis was identified. This is another example for a strategy used in sugar chemistry[179] and was described by Giuliano *et al.* for the molecule shown in Figure 3.38.[180] For this molecule deprotection could be achieved in 70% yield by irradiating a degassed mixture of the protected starting material, 1.4 equivalents NBS, 4.4 equivalents $CaCO_3$ and H_2O in CCl_4 for 30 minutes, followed by stirring the crude product obtained after filtration and complete evaporation of the organic phase for 18 hours in a methanolic solution of potassium hydroxide. In an initial experiment the same reaction conditions with a slightly elongated radiation time (40 minutes) were applied to the protected bipyridine **7**. The ^{1}H NMR spectrum of the isolated crude product after this experiment again showed some interesting changes compared to the starting material, and an intense smell of benzaldehyde also indicated that the benzyl ether groups might have been cleaved during the reaction. But after column-chromatography no clear evidence for the isolation of the deprotected compound could be given via NMR spectroscopy, only the study via mass spectrometry indicated that the desired compounds might at least be component of some of the fractions isolated. After these quite promising results the reaction was repeated with different reaction times and conditions for the hydrolysis step (details are given in reference [162]), but unfortunately in neither of the experiments it was possible to isolate the partly or completely deprotected bipyridine. From the analytical data collected during these experiments it is quite likely that under these condition the benzyl ether is indeed cleaved, but also a decomposition of **7** occurs.

Another typical method for the cleavage of benzyl ethers is the use of Lewis acids such as ferric chloride. For example Park *et al.* successfully performed such reactions on monosaccharides by addition of 2.0 equivalents of anhydrous $FeCl_3$ in dry CH_2Cl_2, with reaction times of only a few minutes and subsequent quenching with H_2O (see Figure 3.39).[181] Initial attempts to use these conditions showed no promising outcome and the paramagnetic nature of the iron species involved complicated the analysis of the obtained crude products. Before a final decision concerning the feasibility of such a reaction in the case of **7** was made, another reaction brought positive results. In the light of the predominance of hydrogenolysis as cleavage method for benzyl ethers it seems counterintuitive, but also oxidative methods can be employed for this purpose. A reagent which can be used for such reactions is 2,3-dichloro-5,6-dicyano-1,4-benzoquinone (DDQ), which is typically used as dehydrogenation or oxidation reagent.[182] As deprotection reagent it is used more often in the case of the more electron-rich *p*-methoxybenzyl ethers,[183] but e.g. in

Method D: **With anhydrous $FeCl_3$**

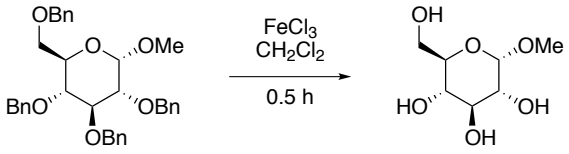

Method E: **Oxidation with DDQ in the presence of H_2O**

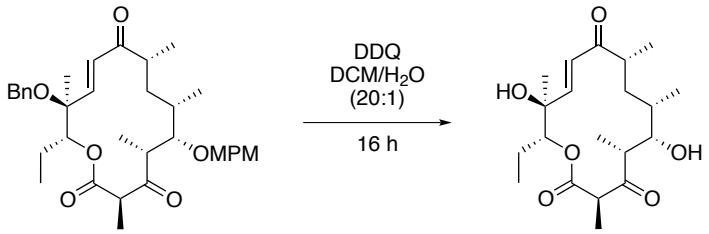

Figure 3.39: Continuation: OBn-deprotection reactions successfully applied to molecules with structural similarity to **7**. OBn = OCH_2Ph. References are given in the text.

an example by Nakajima *et al.* DDQ was used to cleave the *p*-methoxybenzyl ether *and* the benzyl ether in the last step of a total synthesis of pikronolide (see Figure 3.39).[184] They used 10.0 equivalents of DDQ in a 20:1 (v/v) mixture of CH_2Cl_2 and H_2O at room temperature and could isolate the complex product after 16 hours with 81% yield. For an initial attempt to use these reaction conditions for the cleavage of the protecting groups of **7**, the used amount of DDQ was increased to 20.0 equivalents and the reaction time to 24 hours (at room temperature). In the course of the reaction a large amount of solids precipitated with different colours ranging from yellow, orange to almost black. The crude mixture obtained after filtration smelled intensively of benzaldehyde and in a ^{1}H NMR spectrum of the crude mixture in CD_2Cl_2 characteristic signals of benzaldehyde could be observed. The ^{1}H NMR of the components of the mixture soluble in CD_3CN showed a set of signals pointing towards the formation of the desired completely deprotected **8**, and some large signals which most likely correspond to species which result from the reduction of DDQ. Also ESI-MS indicated the successful formation of the product. Separation of the byproducts from **8** turned out to be quite difficult. In this initial experiment after work up with a diluted aqueous solution of $NaHCO_3$ (pH 9) and subsequent column-chromatography with basic Al_2O_3 as solid phase only 17% of **8** could be isolated. With elevated temperatures (37 °C), only 9.0 equivalents of DDQ (added in portions), and two consecutive column-chromatographies (first SiO_2, than basic Al_2O_3 as solid phase, see page 215 for details) higher yields (48%) could be realised. In analogy to a report by Rahim *et al.* it was also tried to perform the reaction under photoirradiation at room temperature with 3.0 equivalents of DDQ.[185] After aqueous work up (with saturated aqueous $NaHCO_3$) and column-chromatography (SiO_2) the product could be isolated with only 11% yield, and consequently this strategy was not pursued further.

Comparison of the ^{1}H NMR spectra of **7** and **8** (see Figure 3.41) reveals characteristic changes as they would be expected for the deprotection of **7**. The less structured component of the multiplet observed between 7.5 and 7.0 ppm in the spectrum of **7** has disappeared, as it is also the case for the multiplet ob-

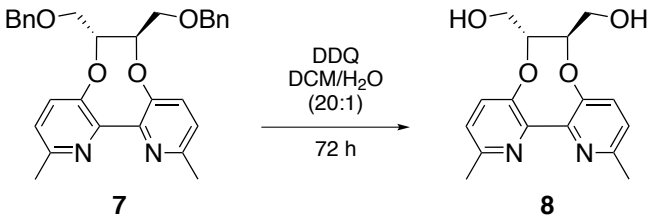

7 **8**

Figure 3.40: Successful cleavage of the benzyl ether protecting groups of **7** using DDQ and 20:1 (v/v) DCM/H_2O as solvent yielded the deprotected bipyridine **8**.

served at around 4.5 ppm. Both signals correspond to the aromatic and benzylic protons of the protecting groups, respectively. Upon deprotection the complex multiplet of the two CH-groups of the tether attached to the bipyridine experiences an upfield shift of about 0.2 ppm, while the multiplet representing the four neighbouring CH_2-protons remains virtually unshifted. The signal of the protons of the methyl groups also experiences a slight upfield shift.

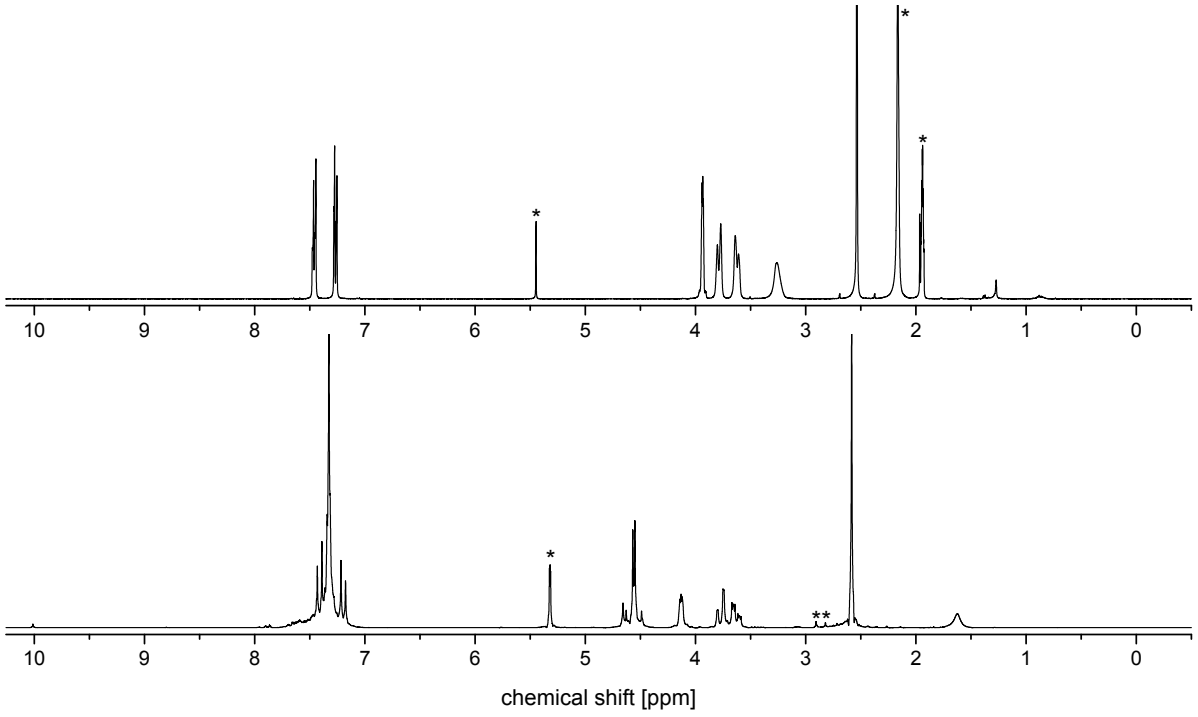

Figure 3.41: ^{1}H NMR spectra of the deprotected bipyridine **8** (top, 400 MHz, CD_3CN) and the protected **7** (top, 200 MHz, CD_2Cl_2). Unambiguously identified solvent signals are marked with an asterisk.

Fortunately, the conditions found suitable for the deprotection of **7** could be transferred to the deprotection of **Na-6**, so that finally the difunctionalised enantiopure sodium cryptate **Na-5** could be prepared. At first the reaction was carried out on a small scale with 12.8 mg of the starting material **Na-6** in a total of 10.5 mL solvent. Again, a total of nine equivalents of DDQ was added in portions and subsequently heated to 37 °C bath temperature. The reaction was monitored via TLC and stopped when after 22 hours

no starting material could be detected any longer. Due to the low R_f observed during TLC (0.12 upon SiO_2 with CH_2Cl_2/CH_3OH 1:1) and the general problem that column-chromatography of sodium cryptates can result in significant loss of product, in this case no dual column-chromatography was performed. Instead the crude material was purified with a work up with saturated, aqueous $NaHCO_3$ and afterwards subjected to column-chromatography with a relatively short column of basic Al_2O_3. In the previous experiments the column-chromatography with basic Al_2O_3 was typically found to be the more efficient step for the removal of DDQ-related byproducts. A complete removal of these impurities from the isolated **Na-5** (45% yield) was not possible using this approach (see NMR in Figure 3.43), but since these contaminations are not likely to affect the subsequent reaction steps and most likely will be easily removable in the following purification procedures, this can be rated as less problematic.

Upscaling of the reaction turned out to be not completely straightforward. Due to the limited solubility of DDQ in CH_2Cl_2 the amount of solvent used was scaled with the amount of starting material. For bigger volumes of the solvent mixture it is more difficult to obtain a thorough mixing of the organic and the aqueous phase. After 22 hours under the reaction conditions described above no turnover could be detected. In the following the amount of water in the solvent mixture was doubled and CH_3CN was added to provide a component in which CH_2Cl_2 and H_2O are soluble. Furthermore 20.0 equivalents of DDQ were used. After 24 hours of reaction time and after 48 hours of reaction time further 5.0 equivalents of DDQ were added, and the reaction was stopped after a total of 66 hours. After purification (analogous to the procedure described above) the compound could be isolated with a lower yield of 30% compared to the reaction performed on a smaller scale. If a larger amount of **Na-5** shall be prepared, some further modifications of the reaction conditions (e.g. use of a KPG stirrer) or the simultaneous performance of several small scale reactions and combination of the crude products for a single work up procedure will be reasonable.

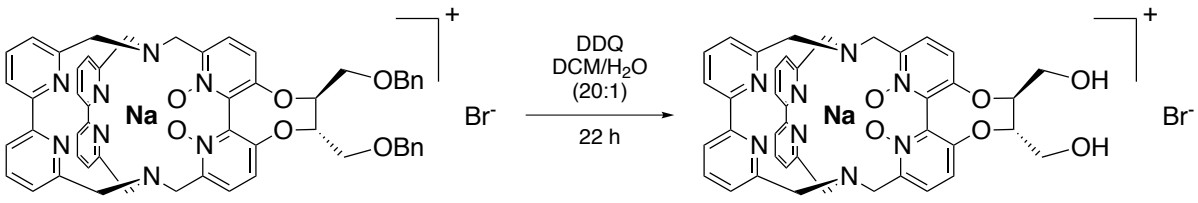

Na-6 **Na-5**

Figure 3.42: Successful cleavage of the benzyl ether protecting groups of **Na-6** using DDQ and 20:1 (v/v) DCM/H_2O as solvent yielded the deprotected cryptate **Na-5**.

Comparison of the ^1H NMR spectra of **Na-6** and **Na-5** (see Figure 3.43) reveals characteristic changes very similar to the ones observed upon deprotection of the bipyridine **7**. The characteristic signal of the aromatic protons of the benzyl ethers disappears and so does also the signal corresponding to the benzylic protons of the protecting groups, which could be observed at about 4.5 ppm in the case of the ^1H NMR spectrum of **Na-6**. The remaining signals experience more pronounced changes as it was the case for the deprotection of **7**, which is not surprising in the light of the higher complexity of the molecule.

A partial assignment of the signals corresponding to the benzylic protons of the cryptate and the protons of

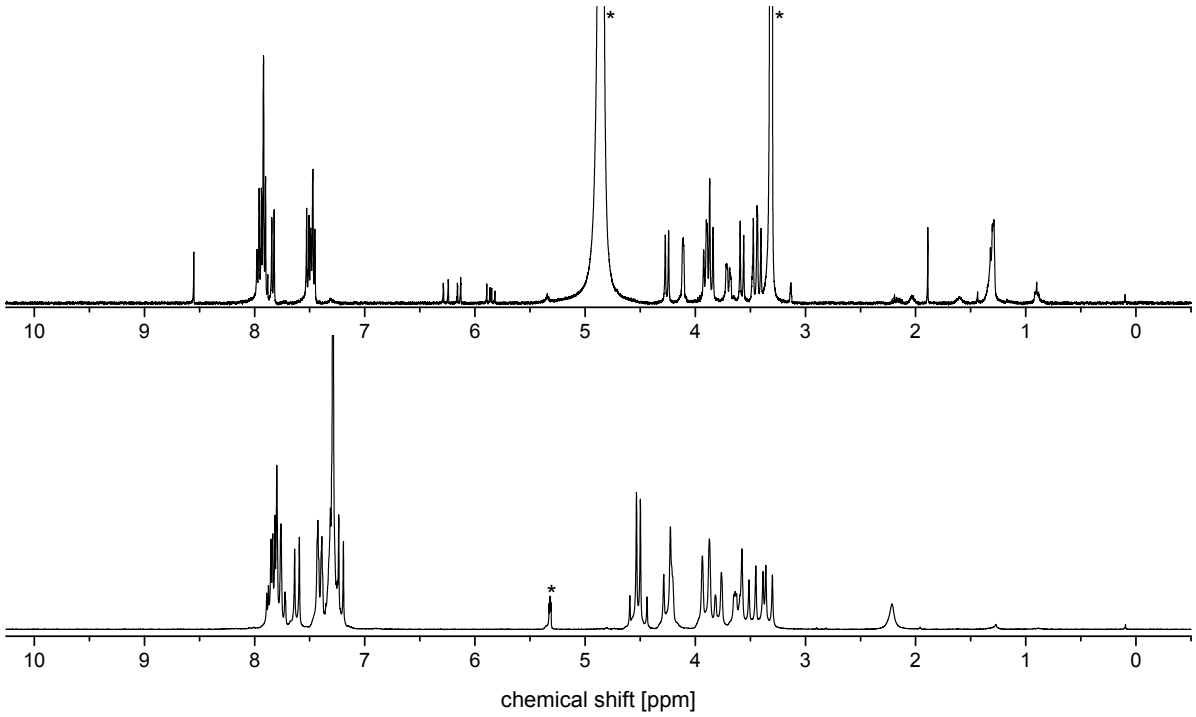

Figure 3.43: ^{1}H NMR spectra of the deprotected enantiopure sodium cryptate **Na-5** (top, 400 MHz, CD_3OH) and the protected enantiopure sodium cryptate **Na-6** (bottom, 200 MHz, CD_2Cl_2). Unambiguously identified solvent signals are marked with an asterisk.

the tether observed between 4.3 and 3.3 ppm was possible with the aid of a ^{1}H-^{1}H COSY NMR spectrum (see Figure 3.44). The shape of the multiplets found between 3.95-3.82 ppm (integral equivalent to six protons) and 3.50-3.39 ppm (integral equivalent to four protons) indicates that different signals are overlayered in this area, the coupling scheme revealed by the ^{1}H-^{1}H COSY supports this interpretation. The doublet observed at 4.26 ppm and the doublet observed at 3.58 ppm, with integrals equivalent to two protons each, resemble the typical shape of signals of benzylic protons of sodium cryptates. The signal at 4.26 ppm exhibits a coupling to the multiplet observed at 3.50-3.39 ppm, while the signal at 3.58 ppm couples to the multiplet at 3.95-3.82 ppm. Additionally, a coupling between both multiplets can be observed. Also the multiplets show some similarity to the shape observed for the signals of the benzylic protons. Considering the symmetry of the molecule and the fact that a coupling of the benzylic protons to the protons of the tether is unlikely to be observed in a ^{1}H-^{1}H COSY experiment, an assignment of four benzylic protons to both of the multiplets is reasonable. Due to the complex shape of the multiplet, and in analogy to the ^{1}H NMR spectrum of **8**, the signal observed between 4.15 and 4.08 ppm is very likely to represent the protons of the two neighbouring CH-groups of the tether. The signal shows a weak coupling to the multiplet observed between 3.75 and 3.66 ppm and an even weaker coupling to the multiplet at 3.95-3.82 ppm. In contrast there is a strong coupling between the two later multiplets, which leads to the interpretation that the signal between 3.75 and 3.66 ppm (with an integral equivalent to two protons) and a component of the signal at 3.95-3.82 ppm (equivalent to the two remaining protons represented by this signal, which had not been

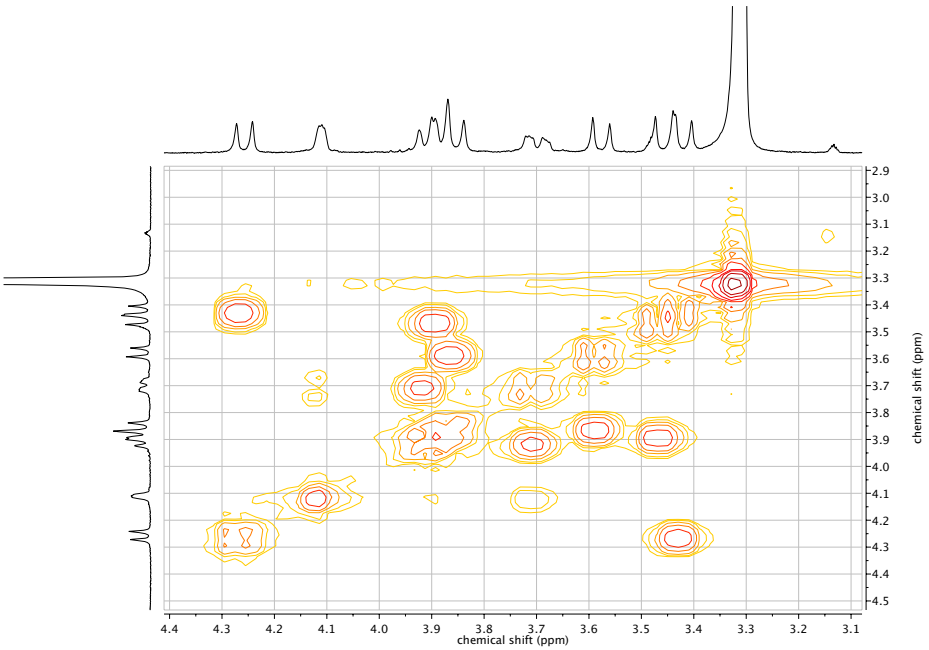

Figure 3.44: Detail of the ^{1}H-^{1}H COSY NMR spectrum (400 MHz, CD_3OD) of the deprotected enantiopure sodium cryptate **Na-5**. The complete spectrum is shown on page 266.

assigned until now) correspond to the two CH_2-groups of the tether.

The sodium cryptate **Na-5** can be seen as the enantiopure, difunctionalised analogue of **Na-1**, which overcomes two limitations of this ligand which would be especially problematic for a potential application in the structural elucidation of biomolecules via paramagnetic NMR. For such an application the right choice of the final functionalisation will be crucial. In the case of proteins, a commonly applied strategy for the attachment of such tag molecules to specific sites of the molecule under study is the use of disulfide bonds, which connect the tag molecule to cysteines introduced using site-directed mutagenesis. For this purpose the tag molecules are typically functionalised as methanesulfonothioates.[186][154][50][187] The reactive group has to be attached with some kind of linker, whose length and flexibility should ideally be adapted to the very specific biomolecule under study, and which is reliably connected to the actual paramagnetic unit of the tag molecule. For the proof-of-principle study in which the general feasibility of the preparation of such molecules based on **Na-5** should be shown, as final functionalisation a carbamate-attached ethylmethanesulfonothioate was chosen (see Figure 3.45).

Isocyanates like reagent **10**, which is needed for the realisation of the approach shown in Figure 3.45, typically can be prepared from the corresponding primary amines or their hydrobromides. A suitable precursor for the preparation of **10** is commercially available but quite expensive, and can easily be prepared from very affordable compounds.

A nucleophilic substitution of the chloride of methanesulfonyl chloride with sodium sulfide in H_2O yields

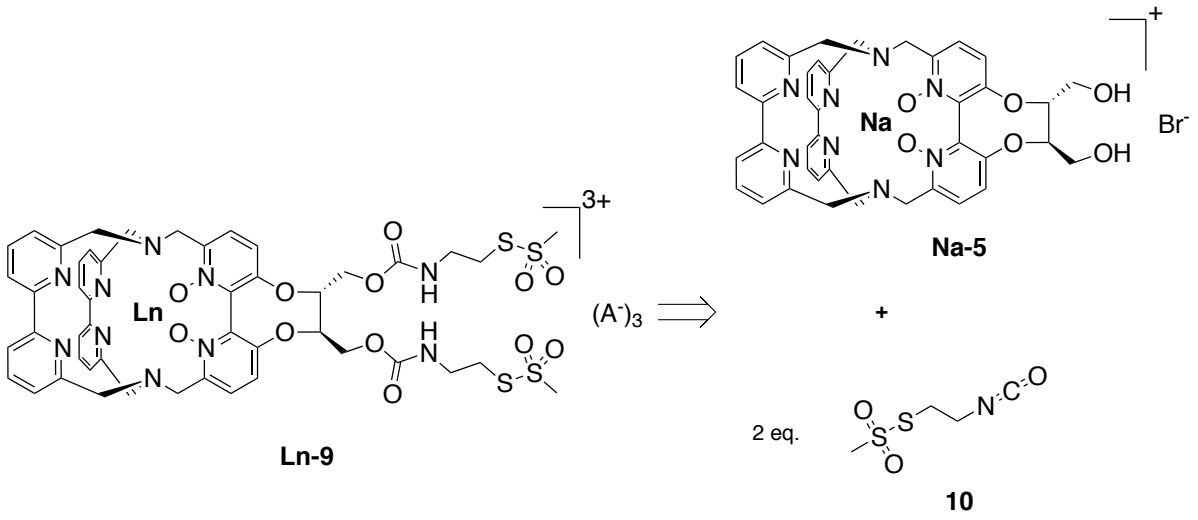

Figure 3.45: Retrosynthetic approach for the preparation of the paramagnetic tag molecule **Ln-9** from the diol-functionalised enantiopure cryptate **Na-5**.

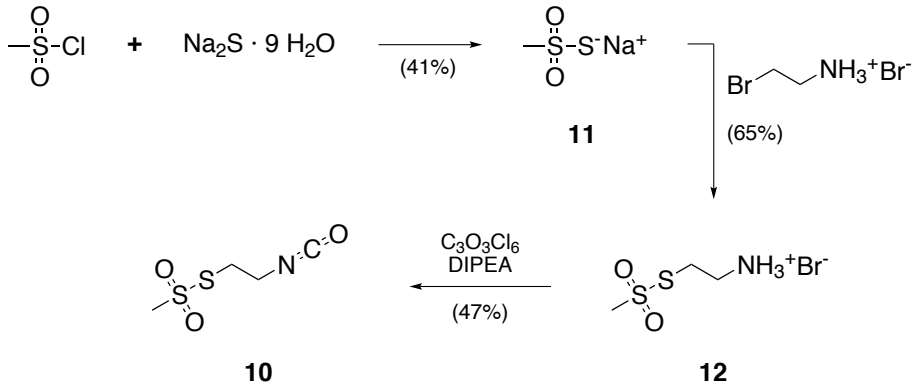

Figure 3.46: Preparation of **10** from affordable precursors.[188][189]

sodium methane-thiosulfonate **(11)** in moderate yields after recrystallisation.[188] The next step is another nucleophilic substitution in which the thiosulfonate reacts with 2-bromoethylamine hydrobromide to give the disulfide-functionalised ethylamine derivative **12**.[189] After recrystallisation a yield of 65% was determined, but presumably higher yields are possible when the mother liquor is recrystallised another time. In the last step the hydrobromide is activated for the attachment to hydroxy groups. In the presence of 2.42 equivalents of DIPEA the starting material was initially deprotonated and then reacted with triphosgene to give the isocyanate **10** with 47% yield. The reactive compound can be purified with an aqueous work up and be stored for a limited period of time. Though in most cases it will be beneficial to prepare the compound fresh shortly before use.

The ^{1}H NMR spectrum of compound **10** (obtained after aqueous work up) shows two triplets corresponding to the two CH_2-groups, of which the one observed more upfield is overlapping with the signal corresponding to the protons of the methyl groups. In the ^{13}C NMR spectrum the resonance of the carbon atom of the isocyanate-group can be observed at 123.7 ppm.

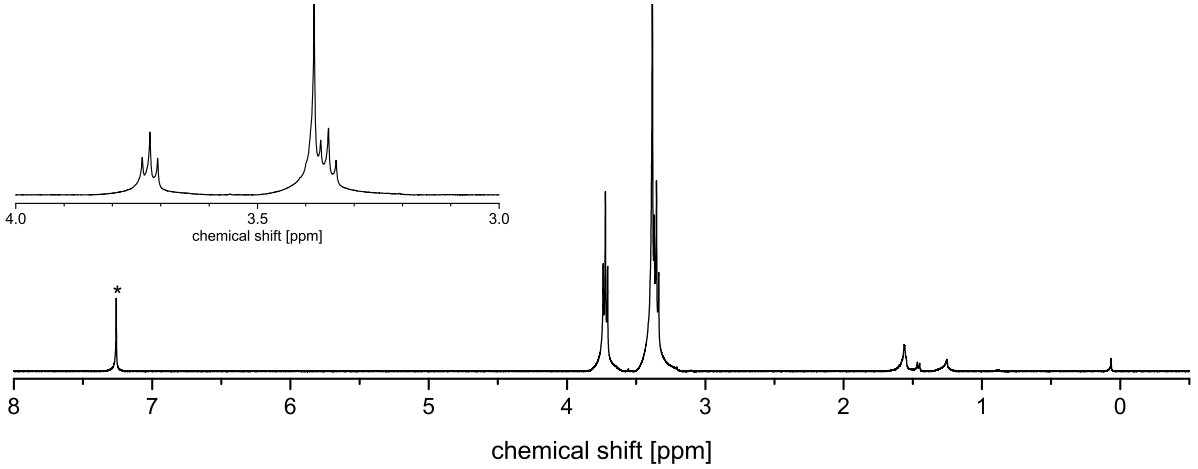

Figure 3.47: ^{1}H NMR spectrum (400 MHz, $CDCl_3$) of the isocyanate-activated linker **10**. Unambiguously identified solvent signals are marked with an asterisk.

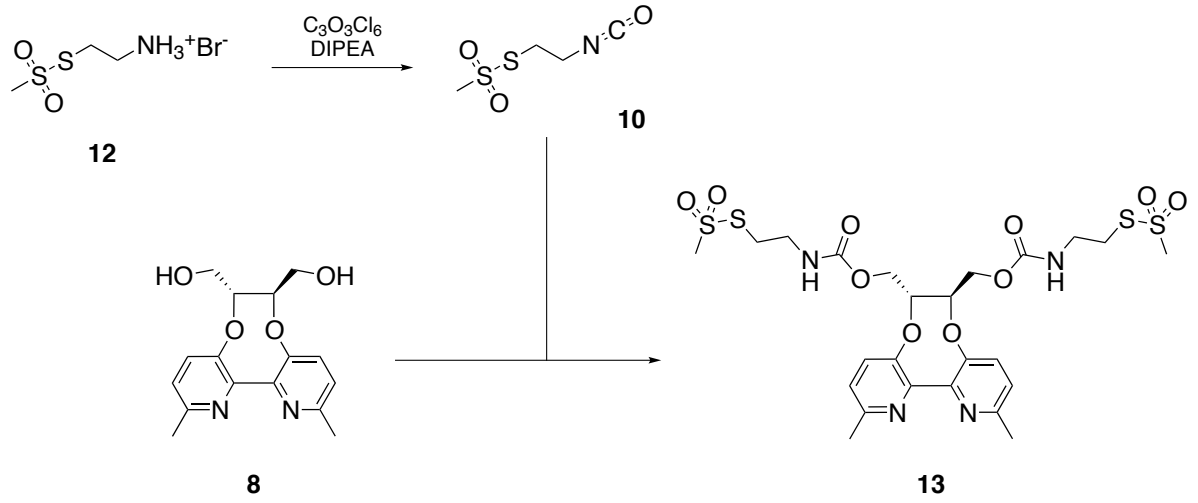

Figure 3.48: Preparation of the disulfide-functionalised bipyridine **13** from the deprotected bipyridine **8** and isocyanate **10**.

As preliminary test isocyanate **10** was reacted with the deprotected bipyridine **8**. For this experiment the isocyanate **10** was prepared directly prior to the reaction, subjected to fast aqueous work up and briefly analysed via ^{1}H NMR spectroscopy. Since the preparation of the isocyanate will not proceed quantitatively and losses due to the work up can be expected, a 2.5 fold excess of **12** with respect to **8** was used. In order to allow for reaction control via ^{1}H NMR spectroscopy, the subsequent reaction of **8** and **10** was performed in $CDCl_3$. 19 hours after mixing of the reactants, a portion of the reaction mixture was analysed with this technique, the resulting spectrum pointed towards the presence of mainly one C_2-symmetric species with signals of the bipyridine being slightly shifted compared to the starting compound. After complete evaporation of the solvents further ^{1}H NMR experiments were performed in $CDCl_3$ and CD_2Cl_2, but the resulting

spectra were less clear and pointed towards the presence of several species. The crude product could be purified via column-chromatography using SiO_2 as solid phase. In the ^{1}H NMR spectrum of the product (see Figure 3.49), the signals of the attached disulfide experience a shift to the upfield compared to the starting material. The signal found between 3.59 and 3.51 ppm is no longer observed as a triplet but has a structure which resembles of a quartet. This might be due to a coupling to the proton of the neighbouring secondary amine. Compared to the deprotected bipyridine **8** the signals of the aromatic protons remain virtually unshifted for the purified **13**, while the signal of the protons of the CH_2-groups of the tether experience a significant downfield shift. The signals of the neighbouring CH-groups can now be observed at 4.12 ppm, which corresponds to a downfield shift compared to **8** and is almost identical to the resonance frequency of these protons observed for the protected bipyridine **7**. The successful preparation of **13** was also supported by ^{13}C NMR spectroscopy and ESI-MS.

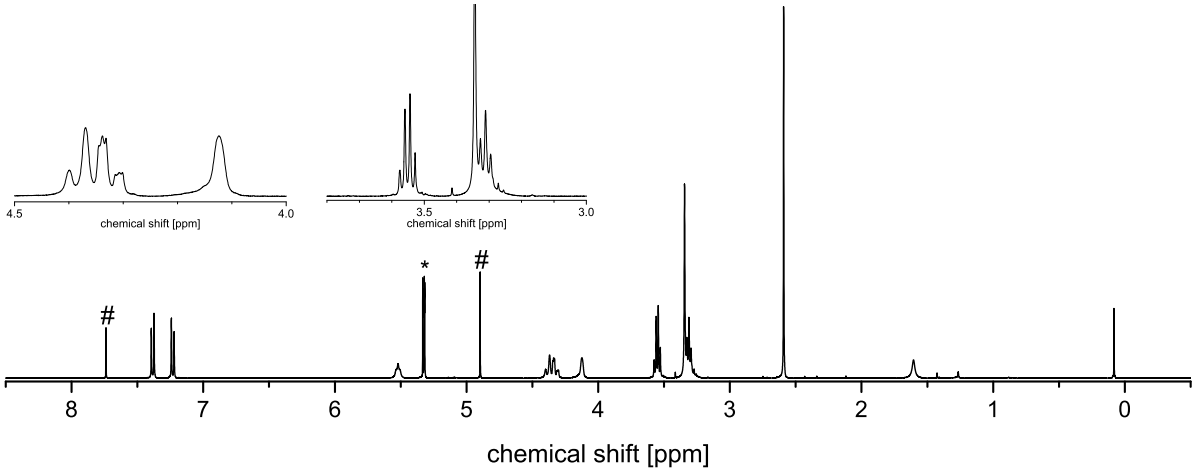

Figure 3.49: ^{1}H NMR spectrum (400 MHz, CD_2Cl_2) of the disulfide-functionalised bipyridine **13**. Unambiguously identified solvent signals are marked with an asterisk, signals corresponding to a contamination with 3,6-bis(chloromethyl)pyridazine are marked with an hash.

After these promising results the attachment of the isocyanate linker as successfully executed for the model compound **8** was transferred upon the diol-functionalised, enantiopure sodium cryptate **Na-5** to yield the completely assembled sodium precursor **Na-9**.

The reaction was conducted on a small scale in analogy to the preparation of the disulfide-functionalised bipyridine **13**. The isocyanate was prepared a few hours before use. Again the crude product could be purified via column-chromatography. In short succession after another the desired difunctionalised sodium cryptate **Na-9** and the monofunctionalised derivative were eluted. Unfortunately the amounts isolated were too small to determine reliable yields, and the solutions studied via ^{1}H NMR spectroscopy were not concentrated enough to obtain spectra which can reliably be discussed in detail (the spectra are shown on page 267). The identity of the compounds isolated could be established via ESI-MS and the ^{1}H NMR spectra are in line with the assignment.

Due to the limited availability of **Na-5**, and as the used isocyanate-functionalised linker **10** not necessarily has the optimal length and rigidity for a potential application, no further experiments for the preparation of

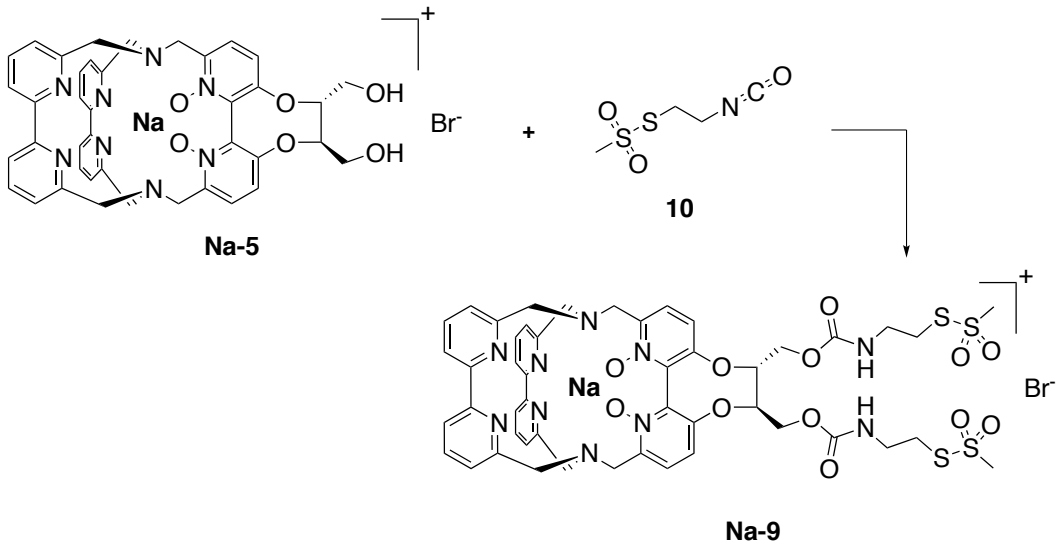

Figure 3.50: Preparation of the twofold disulfide-functionalised sodium cryptate **Na-9** from the deprotected sodium cryptate **Na-5** and isocyanate **10**.

Na-9 were performed after it could be demonstrated that the reaction is in principle feasible. Preliminary experiments towards the preparation of the corresponding lanthanoid cryptates **Ln-9** had promising results. The preparation of **Na-9** (see Figure 3.50) corresponds to an early stage functionalisation (see Figure 3.18, page 47). But for the preparation of a paramagnetic tag molecule based on lanthanoid cryptates a late stage functionalisation, which includes the preparation of the diol-functionalised lanthanoid cryptate and a subsequent attachment of the linker might be preferential. Unlike it is the case for the completely assembled tag molecule **Ln-9**, for the diol-functionalised lanthanoid cryptates decomposition processes during HPLC purification are not to be expected. This approach would also allow for the preparation of differently functionalised tag molecules without individual HPLC purifications.

For first experiments following a late stage functionalisation strategy Tb^{III} was chosen as lanthanoid. Compared to Yb^{III} it leads to stronger paramagnetic shifts of the nuclei in the vicinity, which can be beneficial in the study of large biomolecules. Furthermore terbium cryptates are luminescent, which can be helpful in the preparation of bioconjugates. Again, the replacement of the sodium cation with the lanthanoid cation could be realised using standard conditions. For recrystallisation the crude material was dissolved in a minimum amount of CH_3OH, filtered over cotton and overlayered with Et_2O. After storage at 4 °C overnight the terbium cryptate could be isolated in 99% yield. Evidence of the identity of the complex isolated could be given via high resolution ESI-MS.

A characteristic part of the ^1H NMR spectrum of the complex is shown in Figure 3.52. The signals are distributed over a wide ppm-range, and further signals can be expected at shifts even more apart from the center of the spectrum. Since the signals typically are getting broader when they experience a strong paramagnetic shift, unambiguous identification is difficult and needs special care during measurement and processing of the data. Unfortunately in this case not enough material of the complex was available to do so. Between 115 and -400 ppm fifteen signals of roughly identical integrals can be observed which strongly

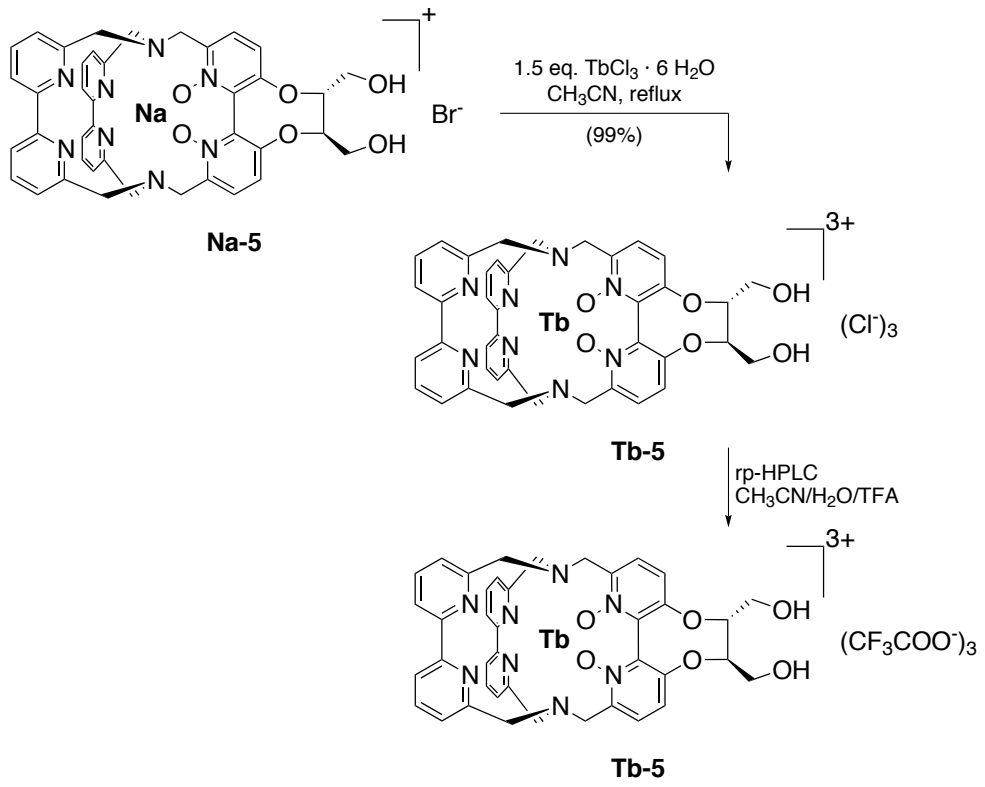

Figure 3.51: Preparation of the diol-functionalised terbium cryptate **Tb-5** from the respective sodium cryptate **Na-5** and subsequent HPLC purification.

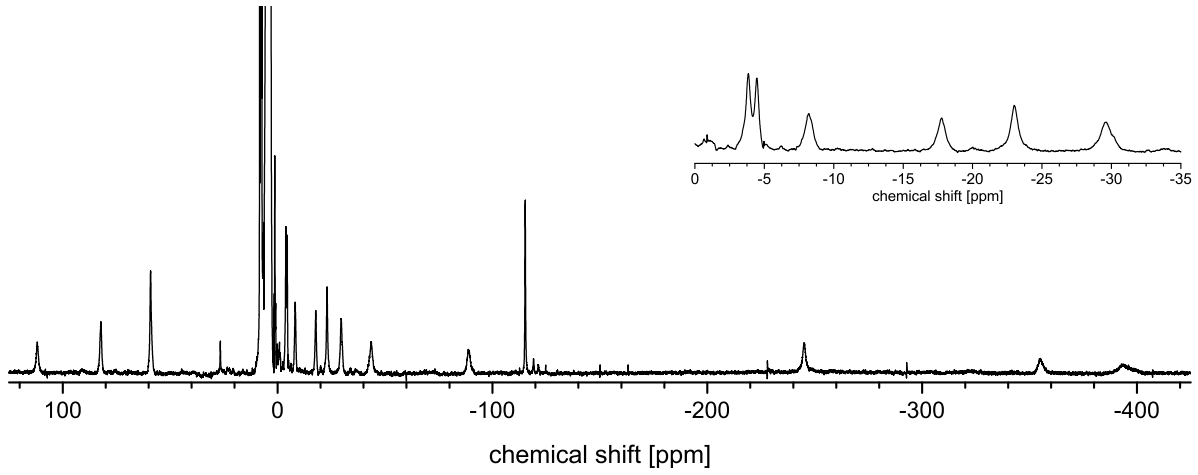

Figure 3.52: Part of the ^{1}H NMR spectrum (500 MHz, CD_3OD) of the diol-functionalised terbium cryptate **Tb-5** obtained after recrystallisation.

indicates the presence of one Tb^{III} complex in the sample. The complex was found to show surprisingly strong luminescence. Different from what is typically observed for terbium cryptates, already relatively dilute samples show the characteristic green emission visible to the naked eye under excitation with 302 nm. The normalised steady state emission spectrum is shown in Figure 3.53.

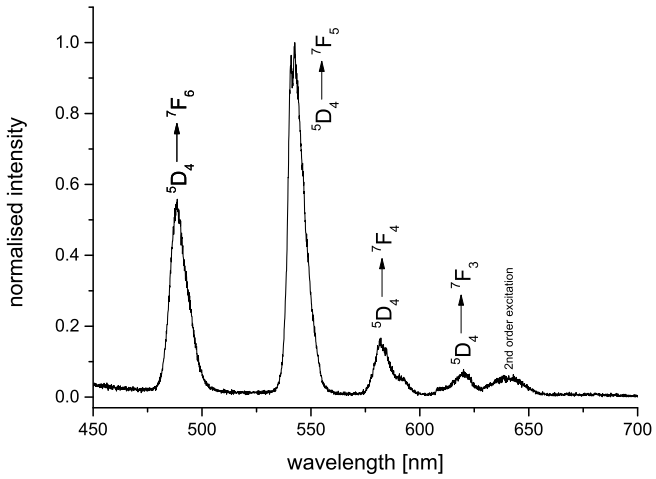

Figure 3.53: Normalised steady state emission spectrum of **Tb-5** (CD_3OD, λ_{exc} = 320 nm).

Figure 3.54 shows an analytical HPLC chromatogram of the material isolated after recrystallisation. The main component was eluted after 11.4 minutes, which is very similar to the value observed for the amino-functionalised lanthanoid cryptates **Ln-1**.

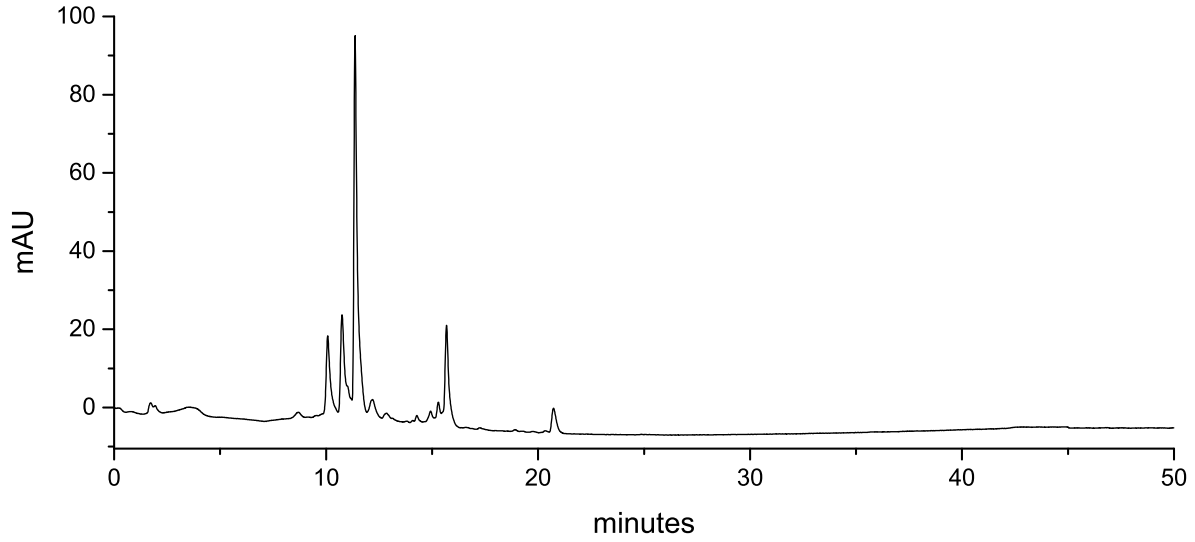

Figure 3.54: Chromatogram from the analytical HPLC (program **A**, setup **A**) of the terbium cryptate **Tb-5** as obtained after recrystallisation.

A portion of the diol-functionalised terbium cryptate **Tb-5** was subjected to semi-preparative reversed-phase HPLC under the conditions established for lanthanoid cryptates. The compound isolated afterwards (R_f = 11.4 minutes) was again studied via NMR spectroscopy. The ^{19}F NMR spectrum shows a signal at -77.1 ppm, which most likely corresponds to the TFA^- bound after HPLC purification. The material was also studied via ^1H NMR spectroscopy, but due to the even smaller amount of material available the measurement was further complicated compared to the case of the material obtained from recrystallisation.

Figure 3.55 shows the middle region of the spectrum, for which a processing of the raw data was reasonable. Interestingly the spectrum shows some characteristic changes compared to the one from the complex obtained after recrystallisation. Several aspects could be responsible for that phenomenon, for example there might be some kind of concentration-dependency, or the exchange of the counter anion (Cl^- for TFA^-) could affect the structural arrangement of the ligand around the metal or the exact nature of the tensor of susceptibility of the magnetic anisotropy χ.

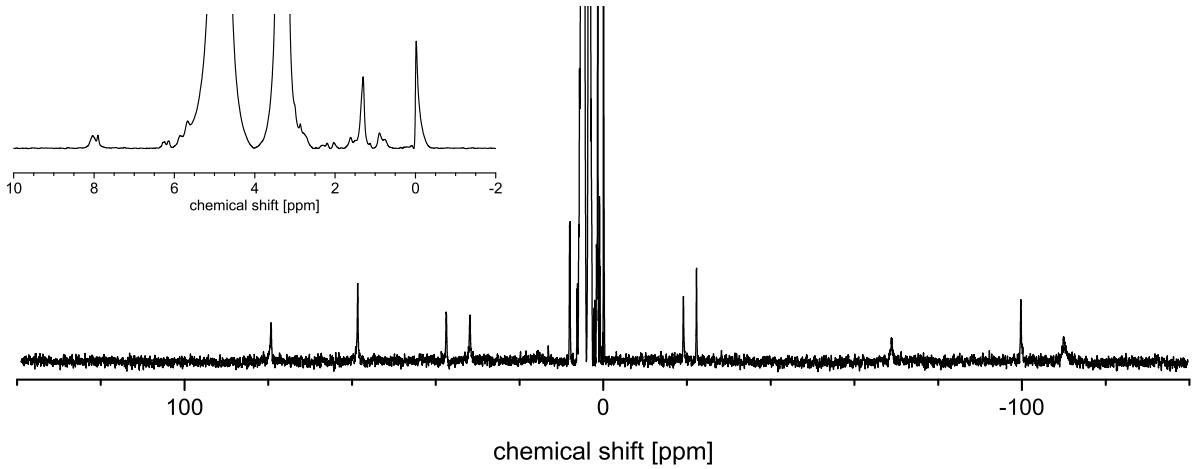

Figure 3.55: Middle region of the ^{1}H NMR spectrum (400 MHz, CD_3OD) of the diol-functionalised terbium cryptate **Tb-5** obtained after reversed-phase HPLC.

While this may be objective of further studies, until now it could be shown that the preparation of the diol-functionalised enantiopure lanthanoid cryptates **Ln-5** and their purification via reversed-phase HPLC analogously to established methods is possible and can become starting point for the actual application of this scaffold for the preparation of paramagnetic tag molecules.

3.4 Conclusion

The aim of this project was to provide a basis for the utilisation of rigidified lanthanoid cryptates **Ln-bpy$_3$O$_2$** for any kind of application based on a covalent attachment of lanthanoid complexes. The prerequisite for such applications is a reactive functionalisation at the periphery of the core scaffold. With the amino-functionalised cryptates **Ln-1** the first examples of such cryptates could be prepared.

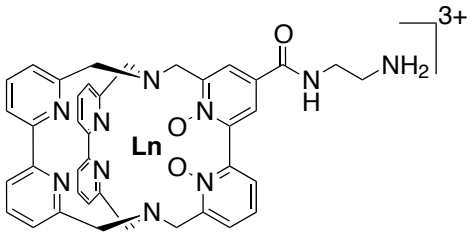

Ln-1

Figure 3.56: Structure of the amino-functionalised lanthanoid cryptates **Ln-1** which combine the rigidified lanthanoid cryptates **Ln-bpy$_3$O$_2$** with a peripheral functionalisation.

The study of the ligand-centered and lanthanoid-centered photophysical properties of these complexes revealed that the beneficial emissive properties are not significantly affected and that the amino-functionalised cryptates **Ln-1** will allow the use of the photophysical properties of the well-studied cryptates **Ln-bpy$_3$O$_2$** in new contexts.

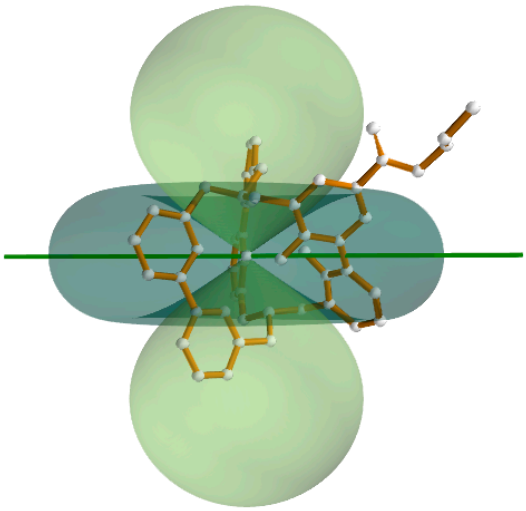

(a) Representation of **Yb-1** and two pseudocontact shift surfaces derived from the susceptibility of the magnetic anisotropy tensor χ. The green line illustrates the effective C_2-symmetry axis of the complex.

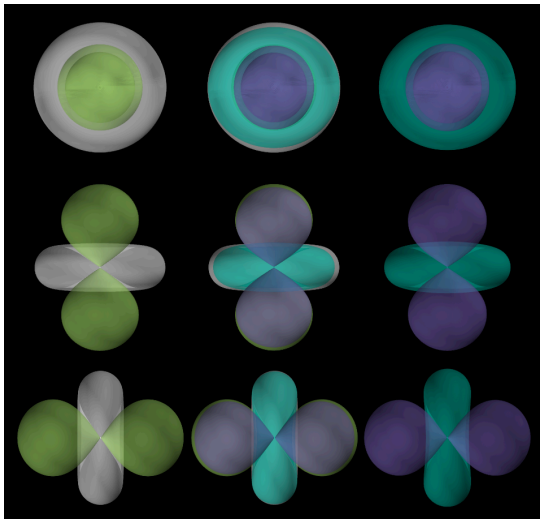

(b) Size and orientations of the pseudocontact shift isosurfaces of the functionalised (**Yb-1**, left) and unfunctionalised (**Yb-bpy$_3$O$_2$**, right).

Figure 3.57: Representations of the susceptibility of the magnetic anisotropy tensor χ of **Yb-1** and **Yb-bpy$_3$O$_2$**. Figures adopted from reference [160].

For a deeper understanding of the effect of the functionalisation on the effective coordination geometry around the lanthanoid and on the crystal field, a detailed analysis of the lanthanoid induced shifts was performed. In line with the results from the analysis of the photophysical properties, it could be shown that the influence of the functionalisation (and the resulting decrease of the overall symmetry) on the arrangement of the coordinating atoms around the lanthanoid is minimal.

Following two different functionalisation strategies, three derivatives of **Eu-1** with final functionalisations targeting specific applications were prepared and characterised. Depending on the chemical stability of the target functionalisation the sequence of reaction and purification steps was adapted, and the reaction with NHS ester-functionalised PEGs was found to be a versatile and quick strategy to introduce a variety of different functionalisations. All three prepared europium tags are now in use for different applications by cooperation partners.

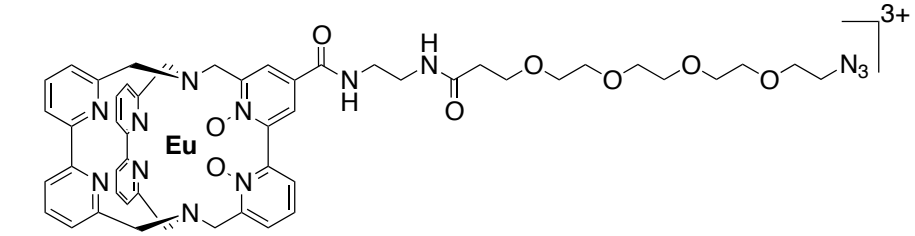

Eu-2

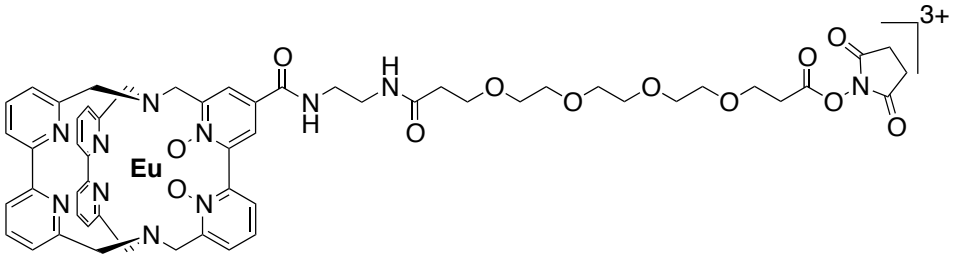

Eu-3

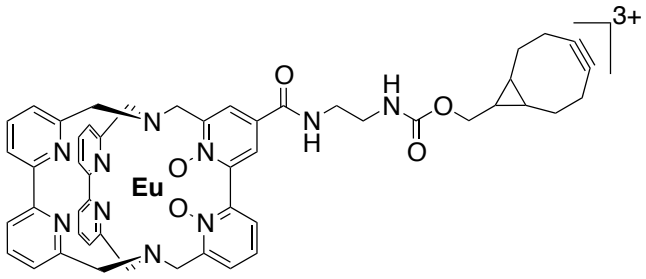

Eu-4

Figure 3.58: Structures of the prepared europium tags with different functionalisations targeting for versatile applications.

To extend the toolbox of cryptates carrying a reactive functionalisation at the periphery, the enantiopure

diol-functionalised cryptate **Na-5** was developed. The enantiopurity of these compounds can be critical for different applications e.g. applications based on NMR techniques. Together with the possibility of a dual, especially rigid attachment this ligand scaffold offers best prerequisites for the development of innovative paramagnetic tags for the structural elucidation of biomolecules.

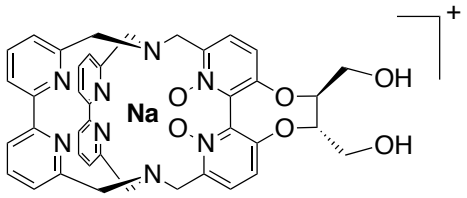

Na-5

Figure 3.59: Structure of the enantiopure diol-functionalised cryptate **Na-5**.

Inspired by tag molecules which are already used for such applications, the enantiopure diol-functionalised cryptate **Na-5** was decorated with linkers carrying a disulfide, targeting for cysteine groups of the protein under study and providing a reliable attachment of the tag.

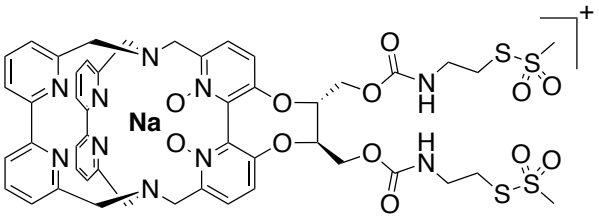

Na-9

Figure 3.60: Structure of the enantiopure disulfide-functionalised cryptate **Na-9**.

In the case of both scaffolds **Na-1** and **Na-5**, the initial introduction of a reactive peripheral group was synthetically challenging. In contrast, the transformation into further derivatives was found to be very straight forward and a variety of lanthanoid cryptate derivatives will be accessible now, making the outstanding properties of the lanthanoid cryptates **Ln-bpy$_3$O$_2$** accessible for various fields of research.

4 Construction of a Molecular Nanocode

4.1 Introduction

Since the digital revolution led to the transformation of the industrial age to the information age, the need for computational resources and data storage steadily increases. With Moore's law reaching its limitations, the need for new strategies and approaches to these problems becomes obvious. Apart from efforts to further miniaturise the conventional architectures which are the basis of current computing, genuinely new ideas turn towards molecules as the smallest units of innovative data storage and processing. Concerning the processing of information, concepts such as the quantum computer[190], "molecular information processing"[191][192] or "molecular electronics"[193] and research towards their realisation already led to some highly interesting molecular systems, but are still far away from the actual construction of a universally applicable computer from such building blocks. In the case of the storage of information the situation is different. Indeed the oldest known methods for the storage of any information are based on molecules, namely the RNA and the DNA. At the same time the DNA is superior to any man made data storage device with respect to important parameters such as the density of information and the durability of information.[194] The fact that the basis of the complete physical existence of any living being on earth is encoded in its DNA gives remarkable evidence of the enormous reliability, the small error-proneness, and the fascinating self-healing abilities of this molecular data storage system. Nature has developed an elegant and highly sophisticated biochemical apparatus to prepare the proteins whose building plans are encoded in the DNA (see Figure 4.1), but in principle any kind of information can be encoded in DNA molecules and later on be decoded with the aid of the polymerase chain reaction (PCR) and sequencing.

In the last few years different strategies for the use of DNA for this purpose were developed and impressive examples could be reported.[196][197][198][199] A clever design of the encoding and decoding processes allows for a combination of the extremely high information density and a good reliability, also in an artificial system. Generally, for the decoding a replication of the DNA strands is necessary, which makes the readout process several orders of magnitudes slower than the readout of information from magnetic or digital data storage devices. But for many interesting potential applications of a molecular nanocode a fast and easy access of the encoded information is necessary. Examples are the anti-counterfeiting labeling of drugs, the homogeneous labeling of medical samples, multiplexing assays[200] or applications in the field of combinatorial chemistry.

Strategy of the combinatorial chemistry is the simultaneous synthesis of many related but different molecules, for example in search of a new pharmaceutical ingredient. An example for a synthetic strategy used for this purpose is the so-called "Split & Mix"-technique, where the separate synthesis processes take place

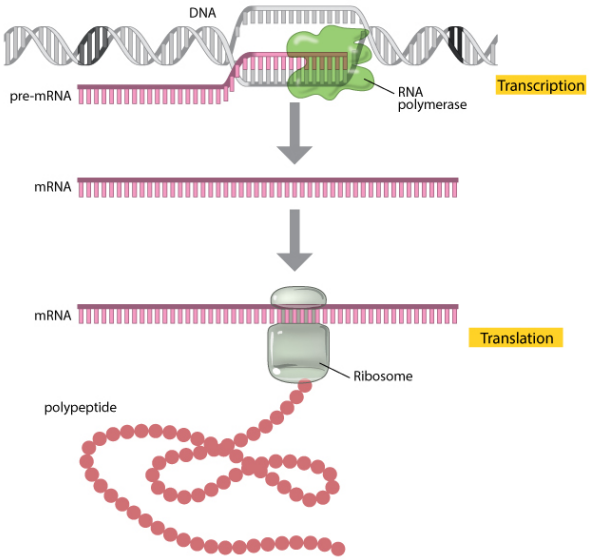

(a) Protein biosynthesis generally consists of two main steps. During the first step (transcription), the DNA is used to prepare the messenger RNA (mRNA). In the subsequent step (translation) the ribosomes assemble amino acids in the sequence given by the mRNA.

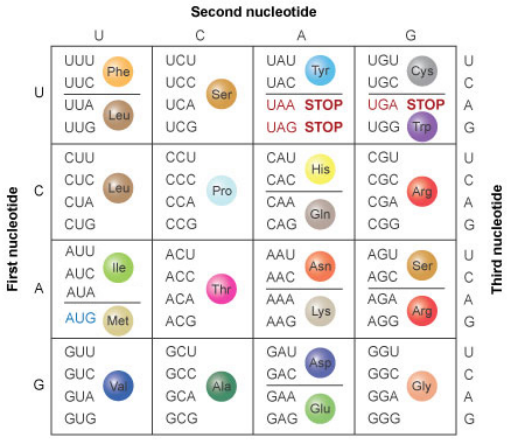

(b) Groups of three subsequent monomers of the mRNA form a codon which is encoding a specific amino acid or the command to stop the translation.

Figure 4.1: The natural process in which the information encoded in the DNA is used to prepare the corresponding proteins is highly complex and relies on a machinery of aiding biomolecules, such as the RNA polymerases or the ribosomes. Figures adopted from reference [195].

in shared reaction vessels but immobilised on an individual particle (“Bead”). After every reaction step the particles are mixed and redistributed among the reaction vessels with individual reaction conditions. This leads to the fast preparation of a library of different molecules, which is then tested for the desired reactivity or medical activity. Only for promising candidates the exact chemical structure is determined subsequently. Often this is done in an indirect fashion via the reconstruction of the synthesis path the particle has run through. To track the individual particles during synthesis they can be tagged with some kind of code, which can either be done by a stepwise construction of the code during synthesis, or by giving every particle a unique code prior to synthesis and monitoring the course of every single particle for every step. Since reliable coding and identification are critical for these approaches, in the context of the combinatorial chemistry a variety of different nanocodes has been developed and applied. Several reviews give an overview of the concrete techniques used.[201][202]

As already implied earlier, the critical point in the design of a nanocode is the readout or decoding process, which should be fast and reliable. A variety of well established spectroscopic methods is in principle applicable for the identification or decoding of a nanocode, particularly suitable are mass spectrometric methods.[203] They belong to the most sensitive analytical methods known and very small amounts of the nanocode substance are sufficient for a reliable analysis. Also an evaluation based on optical properties of a nanocode offers a very promising approach. The corresponding methods have moderate apparative

costs, are relatively simple and non-invasive. In this case, in order to allow for the preparation a sufficiently large amount of possible codes, several chromophores have to be combined so that the information can be encoded in the ratio of the chromophores in the nanocode, and measured as the ratio of the respective luminescence intensities.

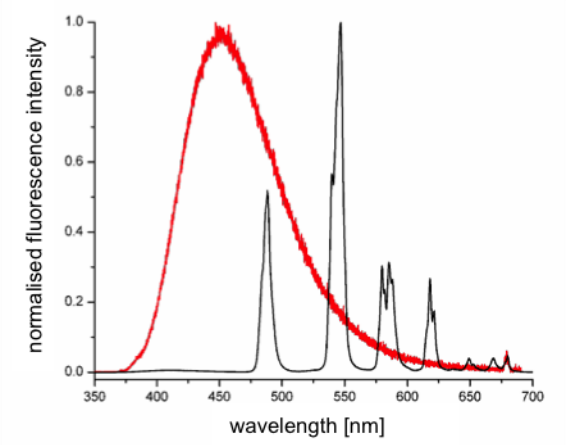

Figure 4.2: Comparison of a typical emission spectrum of an organic chromophore (quinine) and a lanthanoid complex (Ln = Tb^{III}). Since the transition bands of the lanthanoids are much more narrow than the ones found for organic chromophores, they offer by far better possibilities for multiplexing and related applications, e.g. in the construction of luminescent nanocodes.

Based on organic chromophores only quite a small number of such codes would be realisable, since the emission spectra of such dyes are typically broad and tend to overlap, which drastically hinders an unambiguous quantification. Furthermore organic fluorophores are prone to undergo photobleaching, and in many cases several excitation wavelengths would be necessary for the excitation of the combined fluorophores. This would make the read-out process considerably more complex. By the use of lanthanoid-based chromophores all these problems can be circumvented in an elegant fashion. Typically lanthanoid luminophores do not undergo photobleaching and due to the use of an antenna chromophore typically all luminescent lanthanoid complexes of one ligand can be excited at the same wavelength. Most importantly, as outlined in chapter 1.1 and visualised in Figure 1.4 and Figure 4.2, lanthanoid complexes exhibit highly characteristic and sharp emission bands. At the same time the lanthanoids are also well suited for an evaluation based on ICP-MS (inductively coupled plasma mass spectrometry), which is a mass spectrometric method of especially high accuracy and in principle even allows for an absolute quantification of some elements.[204][205]

In fact there have already been some examples for nanoparticles with some kind of coding functionality based on lanthanoids.[206][207] For the development of such nanoparticle-based nanocodes it could be made use of the extensive body of work already published about lanthanoid nanoparticles in general. But a problem which is typical in the field of the preparation of nanoparticles becomes critical in the context of nanocoding: The exact composition of a nanoparticle can neither be controlled during synthesis nor be reproduced reliably. Consequently such approaches do not allow for the targeted preparation of a specific code, and a relational coding is not realisable based on usual nanoparticles.

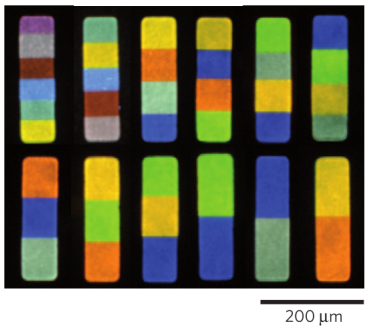

(a) Nanocode-plates prepared from different lanthanoid-nanocrystals embedded in a carrier substance. Figure adopted from reference [208].

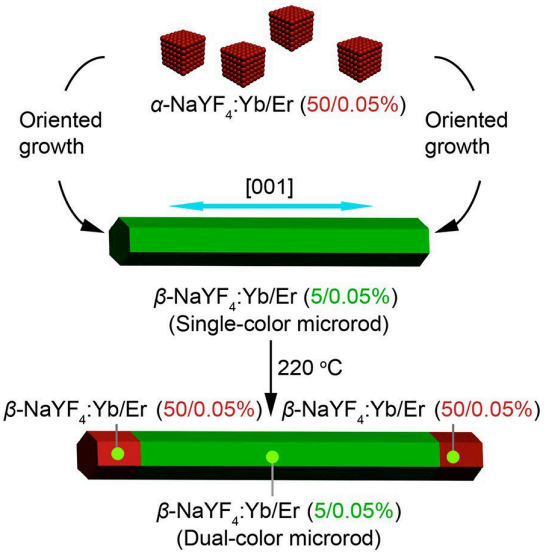

(b) Preparation of two-coloured hexagonal-phase $NaYF_4$-nanorods via epitaxial end-on growth. Figure adopted from reference [209].

Figure 4.3: Examples of nanoparticles prepared for nanocoding following the approach of controlled spatial separation of different emissive properties.

Some examples in literature (mainly based on different luminophores than lanthanoids) aim to circumvent this problem by giving the particles some kind of substructure which allows for the combination of regions of different properties and subsequently facilitates the somewhat targeted preparation of distinguishable particles.[200] For example, Lee *et al.* presented a lithographic method which was used to prepare photopolymerized 200 μm short barcode-like plates from laminar streams of lanthanoid nanocrystals in a carrier substance (see Figure 4.3(a)).[208] With a related approach Zhang *et al.* prepared nanorods of hexagonal-phase $NaYF_4$ with different dopants in the tips and central regions, which results in different emissive properties (see Figure 4.3(b)).[209] Such techniques indeed allow for the preparation of versatile and tailor-made nano- or microcodes applicable for many purposes, but at the same time the preparation becomes quite tedious and needs specialised equipment. Furthermore, the general problem of the low reproducibility of the used nanomaterials is in principle not solved.

Further problems which are inherently connected with the use of nanoparticles can only be circumvented by the use of molecular compounds. Only molecular codes allow for the preparation of monodisperse samples and only for molecular codes full control over the exact composition of the nanocode is possible. A purely organic nanocode is quite complicated to decode when limited to generally available tools and without a sophisticated and highly specialised system as nature's strategy for the synthesis of proteins from the DNA. Nevertheless some efforts towards the development of such codes, often referred to as "digital polymers" were reported.[210][211]

Conceptually it is by far more straightforward to combine the desirable properties of molecular compounds outlined above with the highly characteristic and readily identifiable properties of metals which allow for a

decoding based on mass spectrometric or optical techniques.

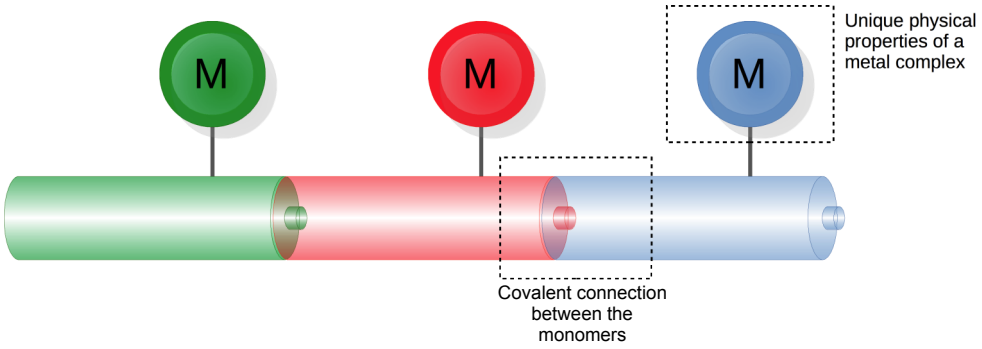

Figure 4.4: Schematic representation of a molecular nanocode based on covalently connected metal complexes.

As visualised in Figure 4.4 such a nanocode could be designed as a polymer of reliably attached building blocks, whereby the information is encoded in the ratio or the sequence of the used monomers. In order to make them identifiable with an optical or mass spectrometric method, each monomer should carry some kind of reporter unit. For this purpose metal ions incorporated into a coordination compound are generally highly suitable, and for the reasons outlined above the lanthanoids offer especially good prospects. Another necessary condition for the preparation of such a nanocode is a highly reliable connection between the different monomers, as it is only possible with a covalent (organic) bond. With the amino acids nature offers a class of building blocks which offer best prerequisites for this purpose.

The twofold reactive functionalisation of the amino acids allows for the connection via amide bonds yielding a very stable backbone of the resulting polymer. Since the development of solid phase peptide synthesis[212] (see Figure 4.5), the synthesis of peptides in the laboratory became an easy, fast and well-established technique which can even be automated. Furthermore the process is compatible with a variety of different residues attached to the amino acid, and is not limited to naturally occurring amino acids. This makes the covalent attachment of additional groups with special chemical or physical properties easily feasible, e.g. via the well established click-chemistry.[213] Obviously this offers enormous potential in various fields of research connected with biological systems, for example in the targeted molecular imaging[214] or for the development of innovative drugs.[215][216] Apart from that also completely innovative materials based on peptides are accessible.[217]

Examples for such peptide-based materials which do indeed include covalently connected metal complexes were presented by Tashiro *et al.*[218][219][220][221] They fused different metal complexes to amino acids and used up to six of these monomers in a modified solid phase peptide synthesis for the preparation of “metal-organic complex arrays” (MOCAs) (see Figure 4.6), and subsequently the short polymers could also be assembled to bigger linear or branched structures. The ^{1}H NMR and mass spectrometric properties of the resulting compounds were studied and also the self-assembly behaviour, but unfortunately the optical properties of the monomers or polymers were not described. Molecular compounds with (different) covalently attached lanthanoids which could generally be applicable as nanocodes are not known until now, neither based on amino acids nor on any other toolkit of modular organic synthesis. Despite the highly beneficial physical properties of the lanthanoids this is not really surprising, because their chemical

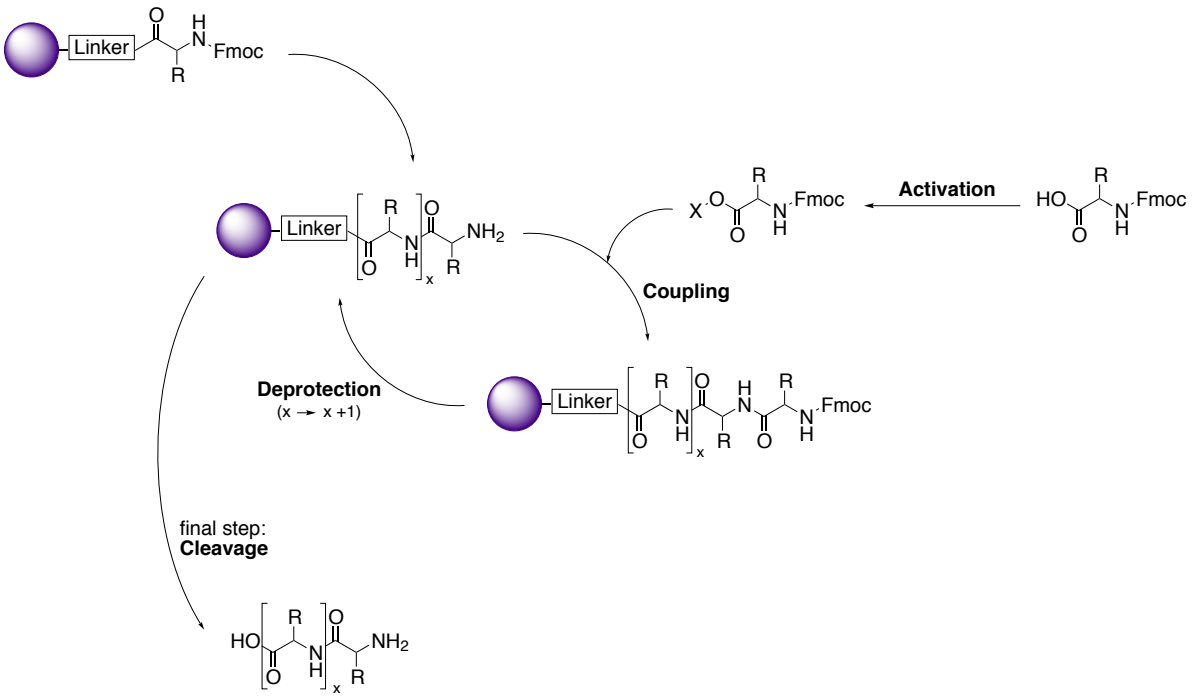

Figure 4.5: General principle of solid phase peptide synthesis (SPPS), following the Fmoc-strategy. In most cases a suitable peptide synthesis resin is commercially available with the first, Fmoc-protected amino acid of the desired sequence already attached via a linker. After an initial deprotection step the next amino acid is activated in situ and added to the resin, whereby an amide bond is formed between the first and the second amino acid. Subsequent deprotection and coupling steps lead to the formation of the desired peptide, covalently attached to the peptide resin until the linker is cleaved and the peptide is released into the solution.

properties are indeed problematic for the realisation of a molecular nanocode. An obvious condition for the preparation of a molecular nanocode with a general structure as shown in Figure 4.4 is the accessibility of stable and reliable complexes of the used metals. For the lanthanoids the preparation of such complexes is by far more complicated as for e.g. transition metals. For example DOTA-type complexes (which are usually considered to be very stable) would readily undergo decomplexation under the conditions typically applied during peptide synthesis, and consequently are definitely not suitable for the construction of such codes. In contrast the cage like structure of the cryptates **bpy$_3$O$_2$** allows for the preparation of complexes which even under extreme conditions, such as the storage in pure TFA, do not undergo decomposition. Such complexes are very likely to withstand the conditions applied during peptide synthesis and also a huge variety of conditions the prepared nanocode may be exposed to. The results from chapter 3 showed that it is indeed possible to prepare cryptates carrying a reactive functionalisation without diminishing the outstanding overall properties as a coordination scaffold. Consequently, a ligand structure which is suitable for the preparation of amino acids carrying a stable lanthanoid complex as a residue finally became available, and subsequently the preparation of a peptide-based lanthanoid nanocode comes into reach. Such a compound (see Figure 4.7) would allow for unprecedented possibilities in the field of nanocoding which result from the absolute control over the sequence and ratio of monomers connected during solid

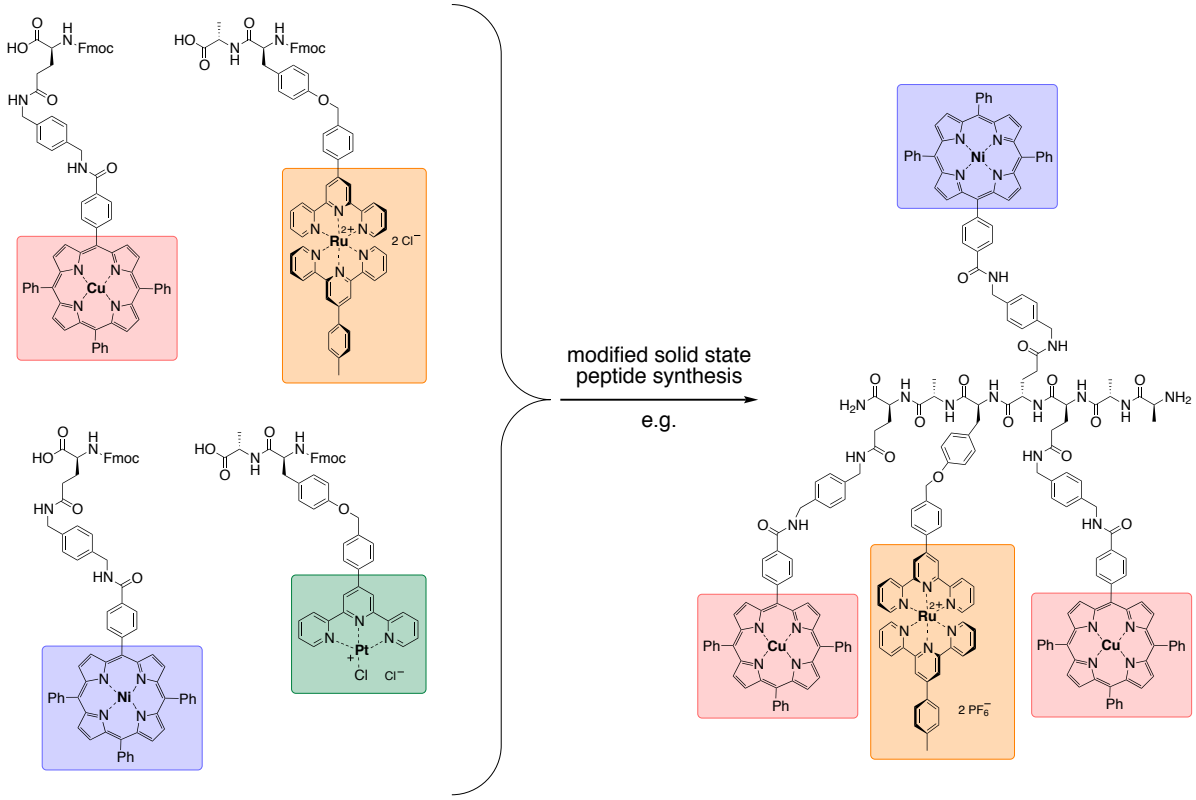

Figure 4.6: Example of a "metal-organic complex array" (MOCA) prepared from amino acids containing a metal complex.[218]

phase peptide synthesis, the exquisite suitability of lanthanoids as reporter units in a nanocode, and the molecular nature of the code which will allow for the preparation of homogeneous samples.

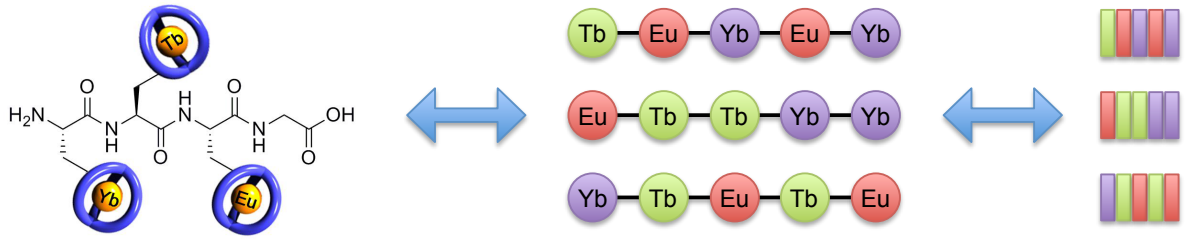

Figure 4.7: A peptide-based conjugate of highly reliable lanthanoid cryptates, assembled in a fully controlled fashion, allows for the preparation of barcode-like molecular nanocodes. These structures would allow for the encoding of information in the sequence and/or ratio of different lanthanoids, which can be decoded with well-established and highly reliable methods such as luminescence spectroscopy or mass spectrometry.

4.2 Conception of the Project

After it could be established that the general properties of the cryptates **Ln-bpy$_3$O$_2$** are not affected by an initial peripheral functionalisation, the amino-functionalised building block **Na-bpy$_3$O$_2$-en** shall be used for the construction of a molecular nanocode based on lanthanoid cryptates connected as a peptide. In order to do so the following steps are to be carried out:

- **Preparation and characterisation of lanthanoid cryptates functionalised with an Fmoc-protected amino acid**

Initially the monomers of the nanocode have to be prepared by introducing an amino acid functionality to the cryptate. Ideally the functionality should be introduced to the sodium cryptate which can afterwards be transformed into the various lanthanoid complexes. An efficient route for the purification of these compounds has to be found and the photophysical properties of the monomers shall be characterised.

- **Validation of the amino acids' characteristic reactivity**

Peptide synthesis is known to be robust and to tolerate various side chains carried by the amino acid. Yet such bulky and highly charged residuals are uncommon and the reactivity of both functional groups, the carboxylic acid and the (deprotected) amine, should be tested.

- **Connection of several lanthanoid-functionalised amino acids to short peptides and first experiments towards the readout of the nanocodes**

In the last step, as a proof of concept the amino acid-functionalised cryptates shall be connected to short nanocodes via solid phase peptide synthesis. The subsequent characterisation of the compounds should focus on techniques which will also be of use for the readout of the nanocodes, and consequently will give evidence of their applicability to do so.

4.3 Results and Discussion

4.3.1 Development of a cryptate-based amino acid-functionalised ligand for lanthanoids

Peptide synthesis is an extremely well established technique. Furthermore, the general properties e.g. the high stability of lanthanoid cryptates **Ln-bpy$_3$O$_2$** can be expected to be compatible with the conditions applied during solid phase peptide synthesis. Consequently the most critical part of this project is to provide a ligand scaffold which allows to connect both aspects necessary for the construction of a peptide-based nanocode from lanthanoid cryptates. The essential property of such a ligand scaffold is of course a functionalisation as amino acid. The amino-functionalised cryptates **1** provide an excellent starting point for the preparation of such a molecule. As it could be shown in the previous chapter, the initial peripheral functionalisation does not affect the beneficial properties of the core ligand **bpy$_3$O$_2$**. A variety of further functionalisations could already be attached to the amino-group of **Na-1** or **Eu-1** which also had no negative influence. The good availability of **Na-1** is also relevant, since it provides a reliable starting point for further developments.

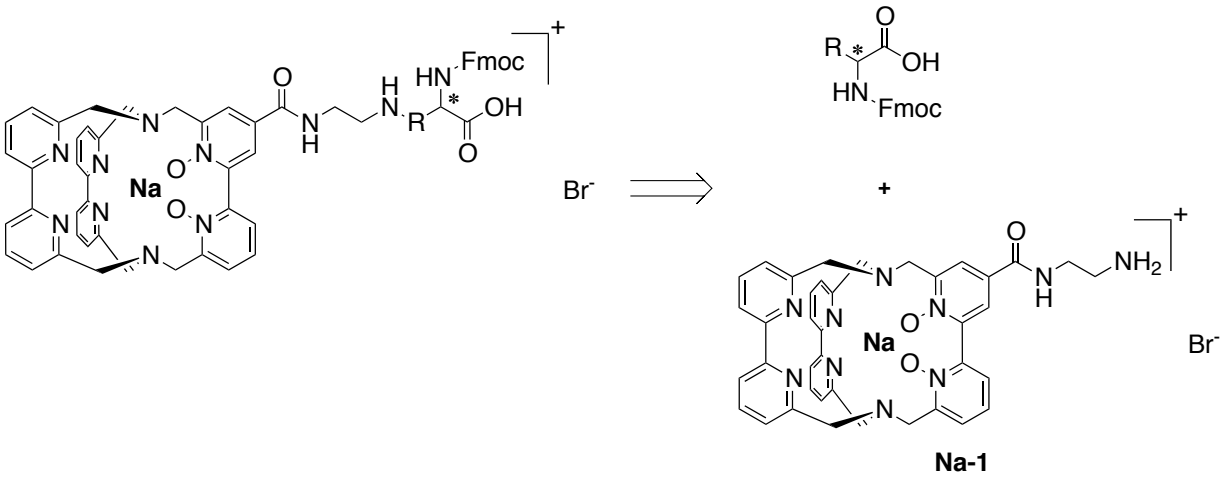

Figure 4.8: General retrosynthetic approach for the preparation of an amino acid-functionalised cryptate starting from the amino-functionalised cryptate **Na-1**. Fmoc = fluorenylmethyloxycarbonyl.

An obvious strategy for the preparation of an amino acid-functionalised cryptate from the amino-functionalised cryptate **Na-1** is the attachment of a complete amino acid to the amino group. In principle any amino acid carrying a reactive group in its side chain is potentially suitable to do so. As these compounds are building blocks of any peptide synthesis, they are often commercially available in different variations and with different protecting groups, depending on which peptide synthesis approach is to be followed (Fmoc or Boc stategy). For this project the Fmoc-strategy was chosen since the conditions applied herein are typically considered to be milder and, more importantly, this strategy has developed to be the better established one.[222]

Ideally the reaction outlined in Figure 4.8 would be carried out with enantiopure lanthanoid cryptates to prevent the formation of diastereomers. However, this would make the preparation of the starting material more tedious. At the same time it is unlikely that the use of diastereomeric mixtures of the amino acid-functionalised lanthanoid cryptates will have a significant negative impact upon the targeted application in solid phase peptide synthesis. Consequently for this proof of concept study the better available racemic lanthanoid cryptates were used.

Importantly, and as already indicated by Figure 4.8, for the preparation of amino acid-functionalised lanthanoid cryptates an early stage functionalisation (see Figure 3.18, page 47) is preferred, so that a larger amount of the amino acid-functionalised sodium cryptate is prepared as precursor and then transformed into the complexes of the different lanthanoids. This also minimises necessary HPLC purifications and at the same times allows for high purity of the amino acid-functionalised lanthanoid cryptates.

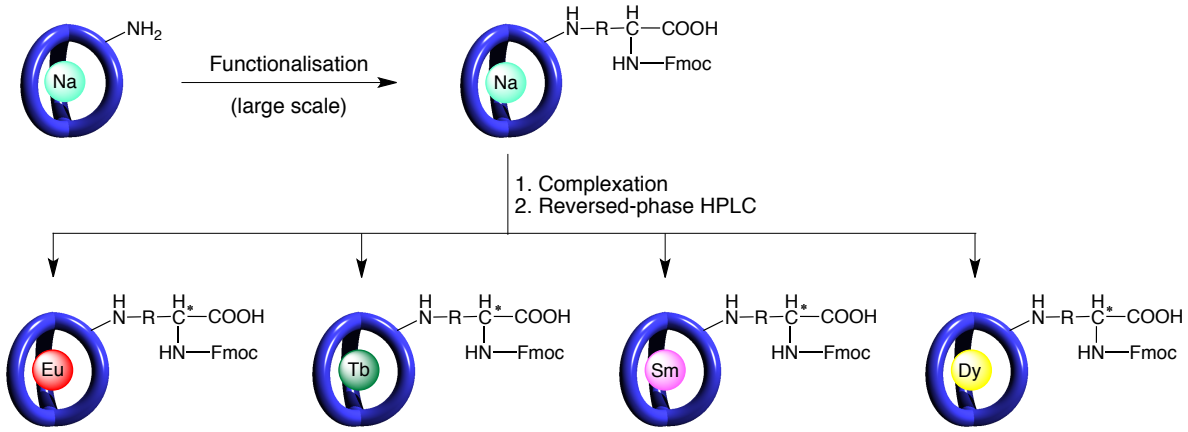

Figure 4.9: Early stage functionalisation approach for the preparation of amino acid-functionalised lanthanoid cryptates. Charges of the metal ions and counter anions are omitted for clarity.

From the many different amino acids which come into question for the realisation of the retrosynthetic approach shown in Figure 4.8, glutamic acid is especially promising. With the side chain carrying a terminal carboxylic acid, attachment to **Na-1** via an amide bond is possible, and the C_2H_4-unit of the side chain would give some flexibility to the assembled cryptate. For the formation of the amide bond, the toolbox of peptide chemistry offers many useful possibilities. Indeed with reaction conditions typically applied in peptide synthesis I was already able to prepare a glutamic acid-functionalised sodium cryptate during preliminary studies (see Figure 4.10).[162]

Typically coupling reagents are used for the formation of peptide bonds between amino acids and oligopeptides. A variety of these reagents have been developed with slightly different properties, and different capabilities to circumvent characteristic problems which can occur during peptide bond formation.[222][223] Of course short reaction times and high efficiencies are needed, and e.g. in most cases a coupling reagent which helps to suppress racemisation of the amino acids is chosen. For most coupling reagents, the experimental procedure is quite similar. Typically the coupling reagents are added to the carboxylic acid directly prior to the coupling step, since the high reactivity of the active esters precludes purification or isolation.

The glutamic acid-functionalised sodium cryptate could be prepared with two different coupling reagents. HATU (hexafluorophosphate azabenzotriazole tetramethyl uronium) is typically considered to be the best coupling reagent for difficult coupling reactions. It provides fast and efficient amide bond formation and efficiently suppresses racemisation. Its potentially explosive nature and its high price are disadvantageous, but typically not problematic for reactions on a rather small scale. An alternative coupling reagent is DCC (dicyclohexylcarbodiimide), which is typically used together with additives such as HOBt (1-hydroxybenzotriazole). When DCC is used, racemisation processes can become problematic but since the adjacent carbon atom of the carboxylic acid group which is to be activated in this case is non-stereogenic this should not lead to problems. Both coupling reagents were found to be in principle suitable for the preparation of the glutamic acid-functionalised sodium cryptate. Yet the yields were low (in all experiments below 25%) and could not reliably be reproduced. Furthermore the work up procedures developed to purify the crude product were quite tedious and these reactions did not provide a suitable basis for further developments.

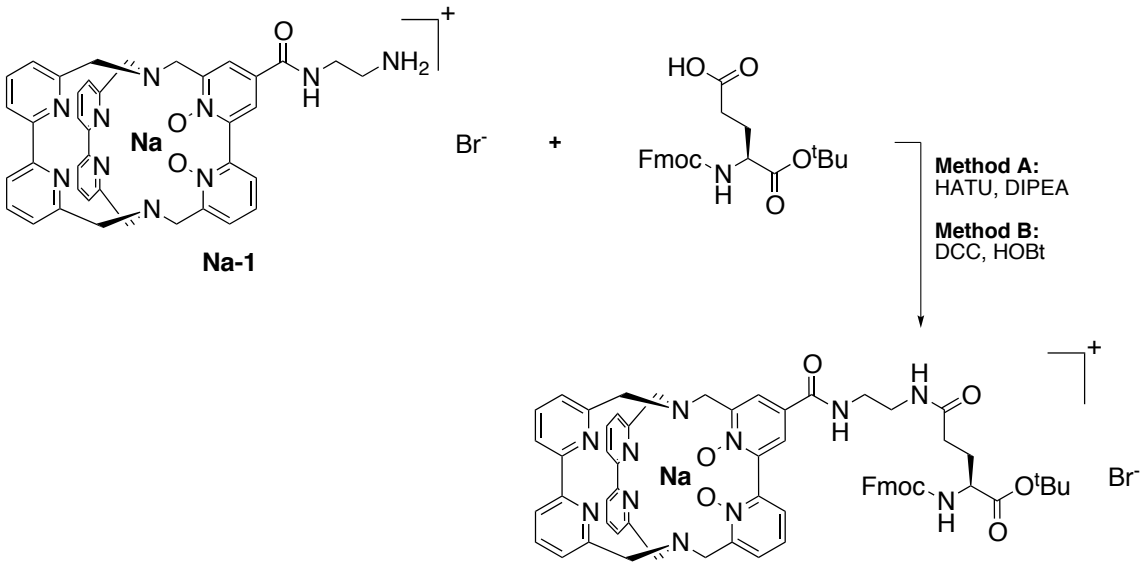

Figure 4.10: Preparation of a glutamic acid-functionalised sodium cryptate from the amino-functionalised sodium cryptate **Na-1** under different conditions.[162]

While the in situ preparation of the activated carboxylic acid is of course convenient in many cases, it becomes rather problematic when the reaction is not proceeding as desired, as it hinders attempts to strategically optimise the reaction. Furthermore in the light of the limited availability of **Na-1** it would be beneficial to utilise this building block in a subsequent reaction step under more controlled conditions. Indeed there are reagents which allow for the preparation of activated carboxylic acids which are highly reactive, yet stable enough to be purified, analysed and stored. Examples are *N*-hydroxysuccinimide or 2-mercaptothiazoline which can be added to a freshly prepared mixture of a carboxylic acids and a peptide coupling reagent, like the ones mentioned above, and thereby transform the active ester into an isolable reagent. Compared to *N*-hydroxysuccinimide, 2-mercaptothiazoline has a special characteristic which allows for a detailed monitoring of the reaction and purification of the intermediate. Since its amides forms

with carboxylic acids are brightly yellow (like the active esters HATU forms), the successful formation of the amide and its substitution with the primary amine in the subsequent reaction step can easily be observed.

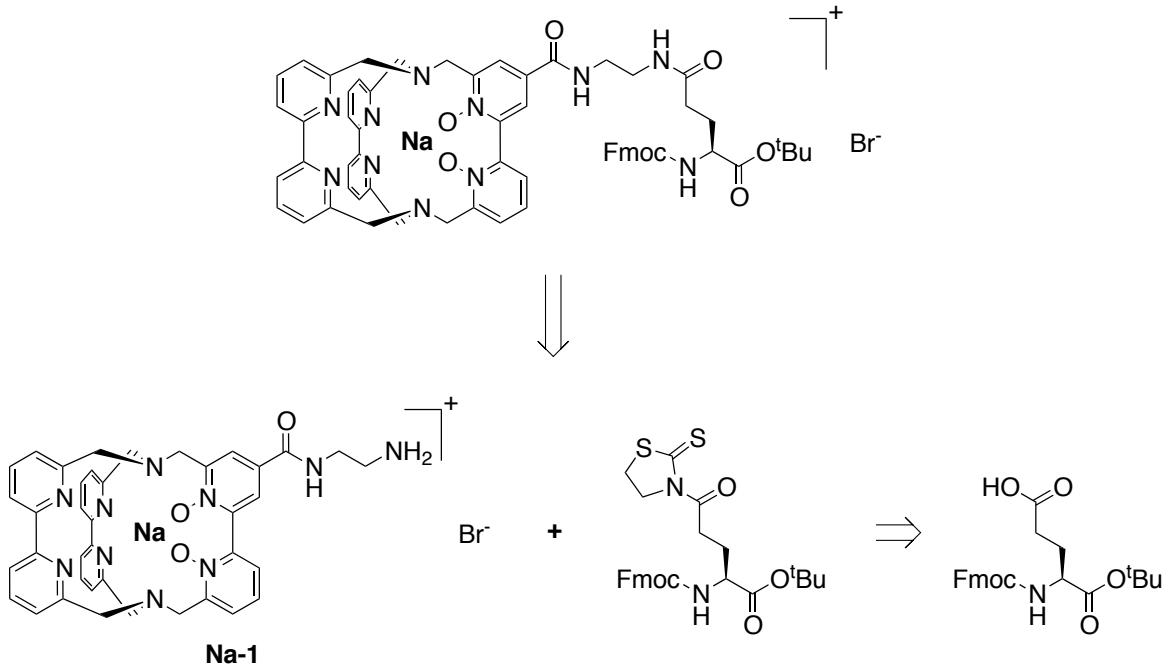

Figure 4.11: Retrosynthetic approach for the preparation of the glutamic acid-functionalised cryptate starting from the amino-functionalised cryptate **Na-1** and using a 2-mercaptothiazoline-activated glutamic acid.

In an initial experiment for the preparation of the 2-mercaptothiazoline-activated glutamic acid, the protected glutamic acid was dissolved in dry DMF and 1.2 equivalents HATU together with 2.5 equivalents DIPEA were added. After a few seconds the mixture turned yellow, which indicates the formation of the active ester of the carboxylic acid and HATU. After the mixture had been stirred for a few minutes, 1.1 equivalents of 2-mercaptothiazoline (dissolved in dry DMF) were added, upon which no further changes of the colour could be observed. The solution was stirred for 18 hours at room temperature before the solvent was removed *in vacuo* whereby the solution was warmed to 40 °C. The resulting pale yellow to slightly brownish residue was subjected to column-chromatography (SiO_2, CH_2Cl_2/CH_3OH 100:1), the fractions which were eluted as a yellow solution were collected. TLC of these fractions indicated that they contained two components. The ^1H NMR spectrum of the material isolated shows signals which are characteristic for the glutamic acid, and signals characteristic for derivatives of 2-mercaptothiazoline, yet the ratio of the integrals indicates that the structural motifs are not present in the desired 1:1 ratio. Furthermore a closer look at the signals of 2-mercaptothiazoline revealed that indeed two closely related molecules were in the sample. To test the reactivity of the isolated material a small portion of it was dissolved in $CHCl_3$. Upon addition of ethylamine the solution rapidly decoloured, as it is expected for 2-mercaptothiazoline-activated carboxylic acids. Based on these results it was concluded that the isolated material is a mixture of the desired product and unreacted 2-mercaptothiazoline.

Attempts to separate both components with another column-chromatography (SiO_2, Hexanes/EtOAc 5:1) were not successful. Afterwards no substance whose ^1H NMR spectrum was promising could be isolate, the analysis was complicated by the small amounts of substance left and an unfavourable separation during column-chromatography. In two subsequent experiments with decreased equivalents of 2-mercaptothiazoline and prolonged reaction times (0.9 equivalents and 23 hours or 1.0 equivalents and 72 hours at 40 °C bath temperature) the moderately promising results after the first column-chromatography of the first experiment could not be reproduced, and consequently this approach was not pursued any further.

After the attempts to prepare the amino acid-functionalised sodium cryptates with techniques established from peptide synthesis did not lead to the desired results, a different approach was developed. The fundamental synthetic problem which had to be resolved is the covalent and reliable attachment of the side chain of any amino acid to the amino-functionalised sodium cryptate **Na-1**. While the exact nature of the covalent bond is almost arbitrary, the efficiency of the reaction with respect to the cryptate starting material is crucial. Similar problem sets are e.g. relevant in the labeling of biomolecules, where small amounts of biomolecules have to be labeled with high efficiencies, whereby a high excess of the used labeling reagent (and a higher price or tedious preparation of it) is tolerable. Such a labeling reagent which allows for an efficient labeling of amino-groups with a fluorescent dye is fluorescein isothiocyanate (FITC).[224] Upon reaction with a primary amine a thiourea-derivative is formed, which reliably connects the biomolecule and the fluorescent dye. In order to transfer this successful strategy to the preparation of an amino acid-functionalised sodium cryptate, an amino acid functionalised with an isothiocyanate is needed. Such a compound can be prepared from an amino acid whose side chain is carrying an additional amino-group, like it is the case for lysine. A typical method for the preparation of isothiocyanates from primary amines is the reaction with a small excess of thiophosgene in the presence of a base, typically $CaCO_3$.[225] Under elimination of one equivalent HCl in a first step a thiocarbamide acid chloride is formed which subsequently undergoes decomposition, whereby another equivalent of HCl is eliminated and the isothiocyanate is formed. Isothiocyanates are significantly more stable against hydrolysis than the corresponding isocyanates so that the reaction can be performed in aqueous solution. When an aliphatic primary amine is to be transformed into the corresponding isothiocyanate, the amine can initially be dissolved in diluted hydrochloric acid which is then added to a solution of the thiophosgene with a base in a suitable solvent.[226] Since the Fmoc-protected lysine-derivative **14**, which is the best choice as starting material in this case, is barely soluble in organic solvents or water, at first this strategy was pursued. With 1.1 equivalents of HCl the lysine derivative dissolves quickly in water and a clear solution is obtained which was added dropwise to a warmed suspension of 1.0 equivalents thiophosgene and 2.2 equivalents $CaCO_3$ in CH_3CN. Initially due to the toxicity of thiophosgene it was refrained from the use of an excess of the reagent, and instead the reaction was performed in high dilution to prevent the reaction of the formed isothiocyanate with another equivalent of the lysine derivative to give the symmetric thiourea-derivative. After 3 hours another 1.1 equivalents of HCl were added to the reaction mixture and the solution was extracted with CH_2Cl_2 to separate the product from residual starting material and $CaCO_3$. With this method the isocyanate-functionalised lysine derivative **15** could be isolated in moderate yields (32% to 44%). Due to the high dilution an upscaling of this reaction was not practicable, furthermore the procedure was relatively tedious. In order to make the preparation of

a large amount of **15** feasible another strategy for the preparation of the important reagent was developed.

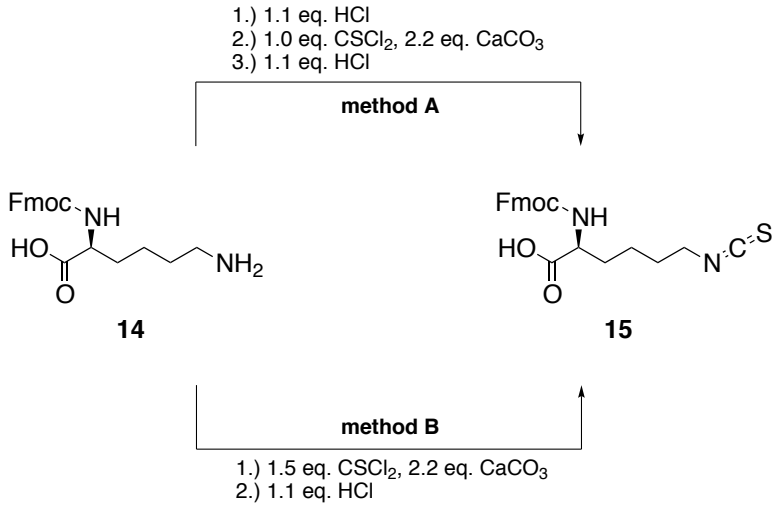

Figure 4.12: Synthesis of the isothiocyanate-functionalised lysine-derivative **15** from the Fmoc-protected lysine-derivative **14** following two different methods.

From the experiments following method A (see Figure 4.12) it was known that the product of the reaction **15** in contrast to the starting material **14** is highly soluble in CH_2Cl_2, and it was observed that the residual thiophosgene can easily be removed *in vacuo* from the crude product, so that handling of the material becomes unproblematic. Based on these observations, as alternative synthesis strategy the Fmoc-protected lysine-derivative **14** was added directly as solid to a mixture of 1.5 equivalents thiophosgene and 1.1 equivalents $CaCO_3$ in CH_2Cl_2. To provide a partial solution of the base in the organic solvent, the suspension of both was stirred for 30 minutes before thiophosgene was added, directly followed by **14**. Over the course of the reaction the Fmoc-protected lysine-derivative is dissolved and transformed into the well-soluble product **15**. After 24 hours a slightly turbid reaction mixture is obtained and upon addition of 1.1 equivalents of diluted HCl, the insoluble components of the mixture accumulate in the aqueous phase, and the crude product can be obtained from the organic phase in good purity according to ^{1}H NMR spectroscopy. Unfortunately *in vacuo* residual thiophosgene cannot be removed completely from the material obtained. This is indeed critical, since in subsequent reaction steps with primary amines the residual thiophosgene can transform them into isothiocyanates, so that an attachment of the activated amino acid is no longer possible. To solve this problem the crude isothiocyanate **15** was purified via column-chromatography. No decomposition of the reagent was observed during this and the fractions containing the thiophosgene can easily be identified via TLC. A complete separation of both compounds could not be achieved, typically some fractions containing both are obtained. Yet following this strategy a yield of up to 47% could be realised. Since the yields for the experiments performed following method A were determined without purification via column-chromatography, method B can be concluded to be more efficient. In any case method B is less tedious and can easily be scaled up as long as the necessary precautions considering the toxicity of thiophosgene are taken. Figure 4.13 shows the ^{1}H NMR spectrum of the substance isolated after column-

chromatography. In the range between 7.8 and 7.2 ppm three multiplets which are characteristic for the eight aromatic protons of the Fmoc-group can be observed. Another signal characteristic for this group is the triplet observed at 4.2 ppm (corresponding to one proton) and the doublet at 4.4 ppm (equivalent to two protons) which in this case is overlapping with the signal of the α-proton of the amino acid and consequently cannot be integrated separately. The multiplet between 3.59 and 3.47 ppm which resembles a triplet corresponds to the two protons of the CH_2-groups next to the isothiocyanate-group, and the signals of the other six protons of the aliphatic chain of the lysine are observed as three multiplets between 2.0 and 1.3 ppm.

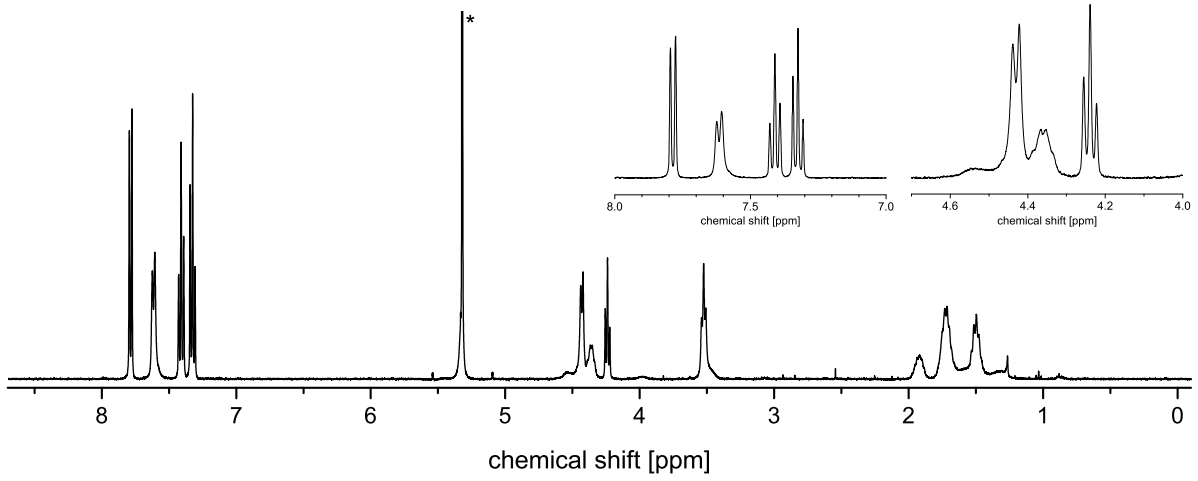

Figure 4.13: ^{1}H NMR spectrum (400 MHz, CD_2Cl_2) of the isothiocyanate-activated lysine derivative **15**.

Evidence for the successful preparation of **15** could also be given via ^{13}C NMR spectroscopy and ESI-MS. Via ^{1}H NMR spectroscopy neither after storage in CD_2Cl_2 at room temperature nor after storage over several weeks in the solid state at -30 °C any decomposition of the isothiocyanate **15** could be observed. Still there are indices that subsequent reaction steps proceed cleaner and with higher yields when **15** had not been stored for an prolonged period of time prior to use. Furthermore the lysine derivative **15** shows a high affinity towards solvents. To remove traces of the solvent and to obtain the reagent as glossy solid, which can be scraped from the glass vessel, the material isolated after column-chromatography was dried *in vacuo* overnight, otherwise it remains a sticky oil which is rather difficult to handle.

The reactivity of the isothiocyanate **15** was tested directly with the amino-functionalised sodium cryptate **Na-1**. In a first preliminary experiment equimolar amounts of both compounds were stirred at room temperature in dry DMF. In an ESI-MS of the crude product obtained after evaporation of the volatiles already a signal which points towards a partly formation of the desired lysine-functionalised sodium cryptate **Na-16** could be detected. In order to improve the efficiency of the reaction with respect to the amino-functionalised sodium cryptate **Na-1**, the employed equivalents of the isothiocyanate-functionalised lysine-derivative **15** were increased and the reaction was performed in basic solution. Importantly the pH should not be too high since otherwise the base-labile Fmoc protecting group might be cleaved. The best results obtained so far were realised with 3.0 equivalents of the lysine-derivative **15** at 40 °C in dry DMF in the presence of 1.5 equivalents $NaHCO_3$ and a reaction time of 17.5 hours. Purification of the lysine-functionalised sodium

cryptate **Na-16** via column-chromatography is possible, yet relatively tedious and significantly decreases the yield of the reaction (51% after column-chromatography). The mass spectrometric characterisation of the crude product points towards a rather clean progression of the reaction, so the more promising strategy to make larger amounts of **Na-16** accessible might be an optimisation of the reaction conditions until no further purification is needed. Since the isothiocyanate **15** can conveniently be prepared on a large scale, a possible approach could be to gradually add a large excess of **15** to the reaction mixture until a complete conversion of **Na-1** is reached. Removal of the residual isocyanate from the dried crude product should be easily realisable by washing the material with CH_2Cl_2, since in contrast to the product **Na-16** the reagent is highly soluble in this solvent.

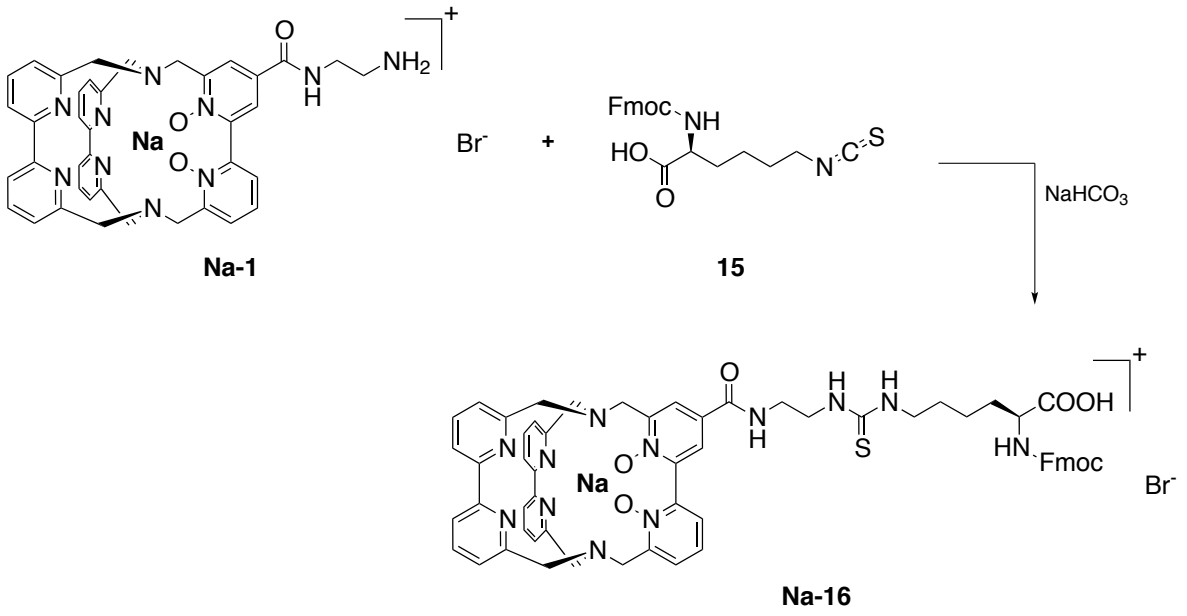

Figure 4.14: Synthesis of the lysine-functionalised sodium cryptate **Na-16** from the amino-functionalised sodium cryptate **Na-1** and the isothiocyanate-functionalised lysine **15**.

Generally the lysine-functionalised sodium cryptate **Na-16** is only slightly soluble in (nonpolar) organic solvents. This is not uncommon for sodium cryptates and in this case the Fmoc-group can be expected to diminish the solubility in solvents like methanol, which are typically relatively good choices for the NMR spectroscopic characterisation of sodium cryptates. The low solubility of **Na-16** hinders the NMR spectroscopic characterisation of the compound. Best result were obtained after the sample was initially suspended in CD_3OD followed by the dropwise addition of CD_2Cl_2 until the solid was partially dissolved. Interestingly, also after evaporation of CD_2Cl_2 under air the compound remained dissolved. The ^{1}H NMR spectrum obtained after preparation of the sample in such a mixture of solvents is shown in Figure 4.15 together with the ^{1}H NMR spectrum of the starting materials **Na-1** and **15**. Due to the overlapping and the low intensity of the signals no reliable integration was possible. Yet the presence of characteristic motifs of both starting compounds together with some slight changes strongly points towards the successful preparation of the lysine-functionalised sodium cryptate **Na-16**, and overall the spectrum is in compliance with expectations.

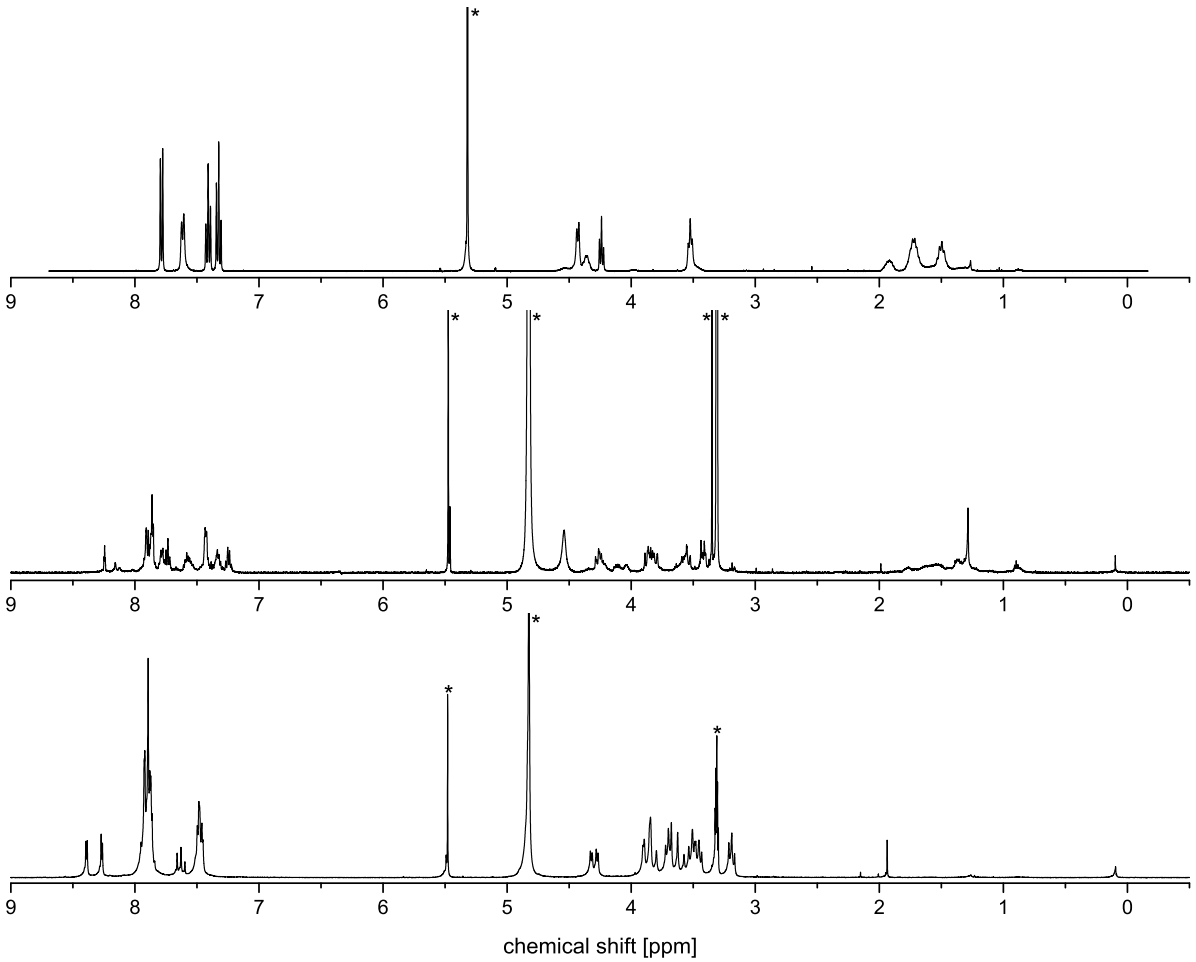

Figure 4.15: ^{1}H NMR spectra of the isothiocyanate-activated lysine derivative **15** (top, 400 MHz, CD_2Cl_2), the lysine-functionalised sodium cryptate **Na-16** (middle, 500 MHz, CD_3OD + CD_2Cl_2), and the amino-functionalised sodium cryptate **Na-1** (bottom, 250 MHz, CD_3OD). Unambiguously identified solvent signals are marked with an asterisk.

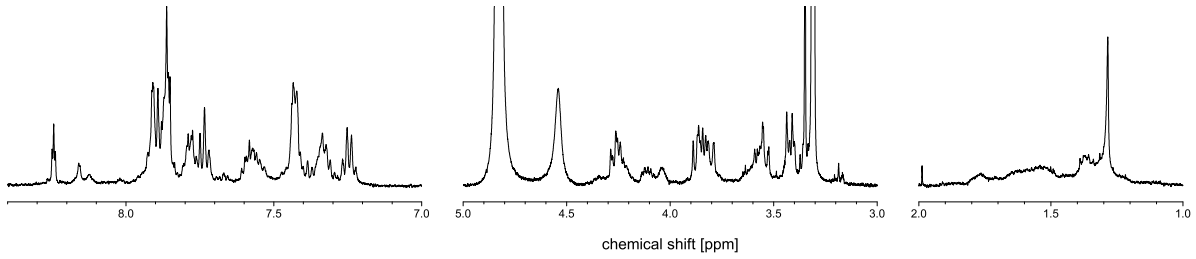

Figure 4.16: Magnifications of parts of the ^{1}H NMR spectrum (500 MHz, CD_3OD + CD_2Cl_2) of the lysine-functionalised sodium cryptate **Na-16**.

Unfortunately, also the ^{1}H-^{1}H COSY NMR spectrum recorded from the sample could only partially resolve this problem (see Figure 4.17 and page 270 of the appendix). Two crosspeaks at (4.04, 1.65) ppm and (3.57, 1.72) ppm allowed for the identification of the signals corresponding to the α-proton of the amino

acid and the signals of the two protons of the CH_2-groups next to the isothiocyanate. This facilitated a rough integration of the signals, which again was in line with the structure of **Na-16**.

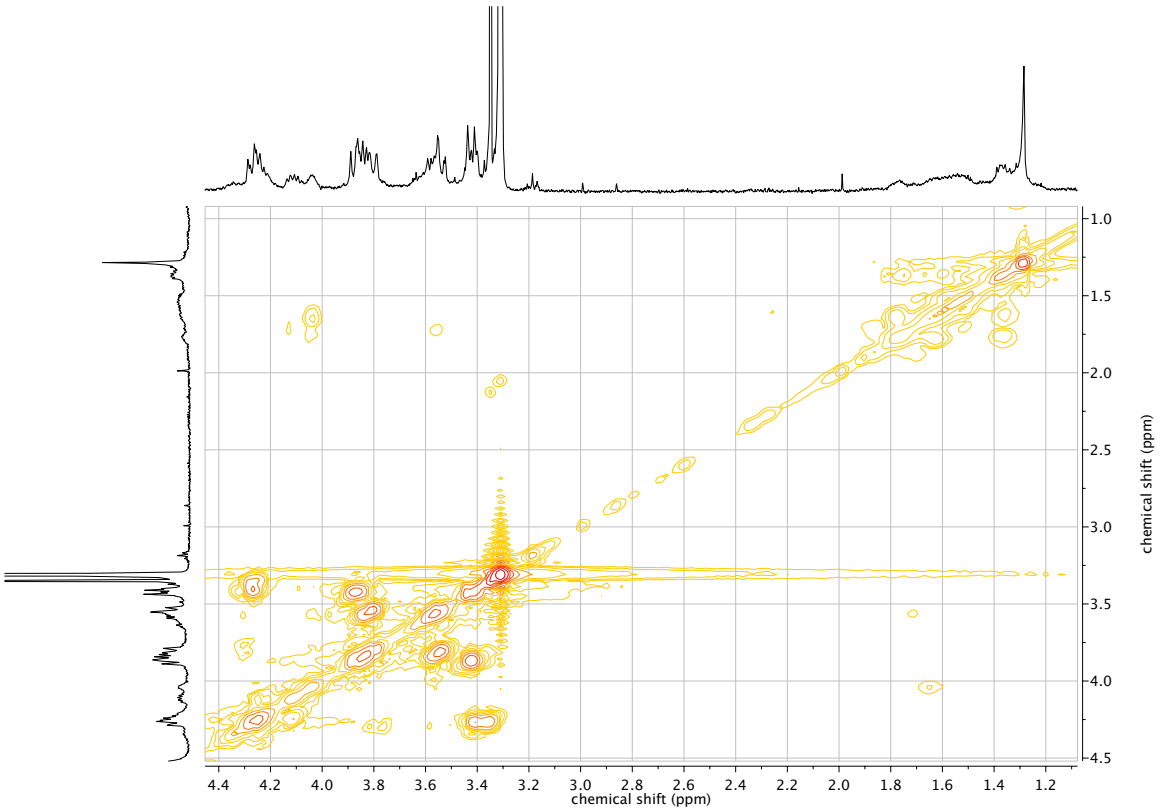

Figure 4.17: Part of the ^{1}H-^{1}H COSY NMR spectrum (500 MHz, CD_3OD + CD_2Cl_2) of the lysine-functionalised sodium cryptate **Na-16**. The complete spectrum can be found in the appendix (page 270).

ESI-MS was found to be the more straightforward technique for the unambiguous identification of the lysine-functionalised sodium cryptate **Na-16** (m/z = 1125.2). Typically also ESI mass spectra of the crude product show only signals corresponding to the product and the amino-functionalised sodium cryptate **Na-1**. Since sodium cryptates generally can be detected easily with this method this points to a clean progression of the reaction without the formation of sodium cryptate byproducts.

4.3.2 Preparation and characterisation of the monomers

Since the trivalent lanthanoid cryptates are typically much more soluble in polar solvents such as CH_3OH or CH_3CN than the corresponding sodium cryptates are, the low solubility of **Na-16** in these solvents which are typically used for the complexation reactions is not necessarily problematic. Consequently despite the low solubility of **Na-16** attempts for the preparation of the corresponding lanthanoid cryptates from this complex were undertaken.

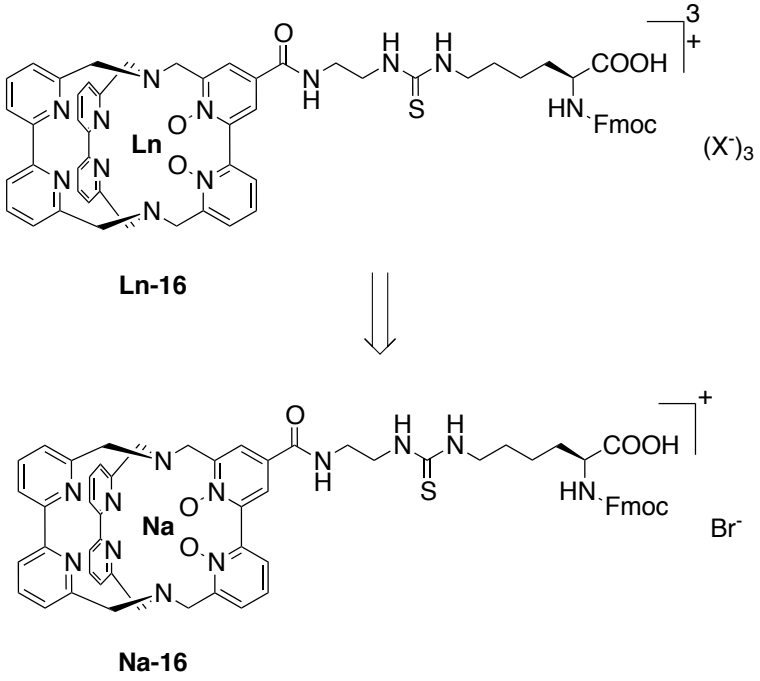

Figure 4.18: Retrosynthetic approach for the preparation of the lysine-functionalised lanthanoid cryptates **Ln-16** from the corresponding sodium cryptates **Na-16**.

For these experiments Yb^{III} was chosen as lanthanoid. Due to the distinct paramagnetic nature of Yb^{III} and the resulting shifts in NMR spectra it is easy to distinguish the signals of a Yb^{III} cryptate from the signals of the corresponding sodium cryptate. Consequently and because the ^1H NMR spectrum of **Yb-1** was already analysed and described thoroughly (see section 3.3.4), reaction control via ^1H NMR spectroscopy should be straightforward in this case.

As already described above (see page 36), in most cases for these reactions CH_3CN is the better choice compared to CH_3OH and allows for shorter reaction times. Consequently in a first experiment the sodium cryptate **Na-16** and 1.5 equivalents $YbCl_3 \cdot 6\ H_2O$ were heated to reflux temperature in CH_3CN for 64 hours. After evaporation of the solvents a mixture of different solvents (CD_3CN, CD_3OD and CD_2Cl_2) was necessary to prepare a sample for ^1H NMR spectroscopy of the crude material. The resulting spectrum is difficult to interpret, which might be due to the inhomogeneity of the sample, and the use of a (different) mixture of solvents further complicated the comparison to the spectra of the sodium cryptates **Na-1** and **Na-16**. Still the absence of paramagnetically shifted signals of the cryptate strongly points towards the ab-

sence of the expected Yb^{III} cryptate in the sample. The material isolated after evaporation of the solvents was suspended in a mixture of CH_3CN with 10 vol.-% CH_3OH, but after 120 hours of stirring the mixture at reflux temperature again no paramagnetically shifted signals of a cryptate could be observed via ^1H NMR spectroscopy. Subsequently the content of CH_3OH in the solvent mixture was gradually increased, also with addition of small amounts of CH_2Cl_2, but at neither of these conditions the starting material dissolved. Finally it was heated to reflux temperature in pure CH_3OH for 72 hours and subsequently a sample of the material was analysed via MALDI-MS and via ESI-MS, trying to detect traces of the lanthanoid cryptate which might have been formed. In the MALDI-MS spectrum only signals which arise from the matrix material used (DHB) were detected, in the ESI-MS spectrum a signal with m/z = 338.4 could be observed, but the isotope pattern of the signal is not in line with the presence of Yb^{III} in the observed species. During the attempts to perform the complexation reaction several samples for analysis via reversed-phase HPLC were taken. To do so the solid was suspended in CH_3CN/H_2O 1:1 (v/v) and filtered over a nylon filter. Some of the samples prepared were slightly yellow which pointed towards a partial dissolvation of the solid, but with the HPLC program established for the HPLC analysis of cryptates no substance could be detected. The retention time of the amino-functionalised Yb^{III} cryptate under these conditions is known, and in order to estimate if the target compound would be eluted from the column under the used conditions also an analytical HPLC run of the Fmoc-protected lysine derivative **14** was performed. The compound was detected as a sharp signal after 15.3 minutes. Since both compounds have rather similar retention times it is quite likely that also the lysine-functionalised ytterbium complex **Yb-16** assembled from both molecules should be detectable under these conditions.

In conclusion, the observations made during the experiments for the preparation of a lysin-functionalised lanthanoid cryptate **Ln-1** following the strategy outlined in Figure 4.18 strongly point towards the interpretation that these compounds are not accessible with this approach, probably because the solubility of the lysine-functionalised sodium cryptate in solvents which can be used for the metal exchange reaction is just too low.

Retrospectively, the poor solubility of **Na-16** is not very surprising. The introduction of Fmoc-protecting groups is known to have a potentially large impact upon the solubility of a molecule. Fmoc-groups tend to undergo π-stacking and can drastically hinder solvation in polar solvents. The observation that the additions of small portions of halogenated solvents improved the solubility of **Na-16** is in line with that, since these solvents are known to be helpful to break up these interaction. In case of the covalent attachment of an Fmoc-protected amino acid to a sodium cryptate it comes to an unfortunate interplay of the limited solubilities of both components, which results in the product being insoluble in solvents which could be used for the subsequent complexation reaction. The same behaviour can be expected for any reaction product of the amino-functionalised sodium cryptate **Na-1** and an Fmoc-protected amino acid as long as no special modifications for an improvement of the solubility are included, such as for example the use of a PEG linker. Also the earlier attempts to prepare an amino acid-functionalised sodium cryptate might have been hindered due to similar solubility problems. Nonetheless there is strong evidence that the amino group of the correspondingly functionalised cryptates shows a strong reactivity towards the isothiocyanate functionalised lysine **15**. Since also the availability of this reagent is quite good it was reasonable to maintain it - and to change the functionalisation strategy to a late stage functionalisation instead (see Figure 4.19).

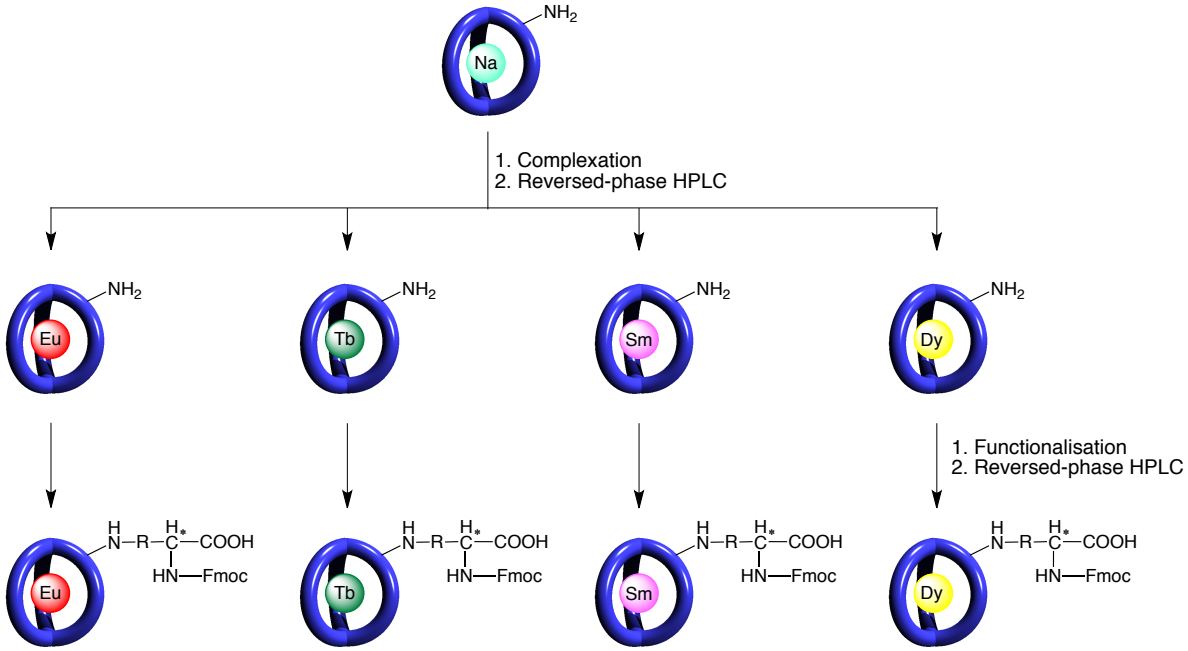

Figure 4.19: Late stage functionalisation approach for the preparation of amino acid-functionalised lanthanoid cryptates. Charges of the metal ions and counter anions are omitted for clarity.

Following this approach the amino-functionalised sodium cryptate **Na-1** is at first transformed into the lanthanoid cryptates **Ln-1**. After purification the complexes are individually reacted with the isothiocyanate **15** to give the amino acid-functionalised derivatives **Ln-16**. For these compounds improved solubility in polar solvents such as CH_3OH can be expected due to their higher charge. Apart from that, the reaction steps which have to be performed with the amino acid-functionalised derivatives **Ln-16** to prepare a molecular nanocode should be performed in DMF, in which **Na-16** is soluble and for which no problems concerning the solubility of the corresponding lanthanoid complexes have to be expected.

The reaction between **Ln-1** and **15** was found to be feasible quite easily in a mixture of CH_3OH and CH_2Cl_2 in the presence of DIPEA. Under optimised conditions the lanthanoid cryptate was initially dissolved in a small amount of CH_3OH. Since the complexes **Ln-1** are obtained from HPLC as TFA salts (see Figure 4.20) initially 1.5 equivalents of DIPEA were added to deprotonate the primary amine. Due to the small amount of substance typically handled in these experiments for this purpose a 0.1 M solution of DIPEA in CH_3OH was prepared. Prior to the addition of a first portion of isothiocyanate **15** (under optimised conditions 1.5 equivalents) an equimolar amount of DIPEA was added to ensure neutralisation of the protons which are released during the reaction of the primary amine and the isothiocyanate. The isothiocyanate itself was added to the starting material dissolved in a 1:1 (v/v) mixture of CH_3OH and CH_2Cl_2. After 30 minutes of reaction time another 1.5 equivalents of DIPEA and **15** were added analogously. Afterwards the reaction mixture was stirred for at least 14 more hours before the solvents were removed and the residual solid was dried to remove excess DIPEA. Reduction of the equivalents of **15** (under adjustment of the added amount of DIPEA) to two portions of 1.0 equivalents was not found to have a drastic influence on the yields of the

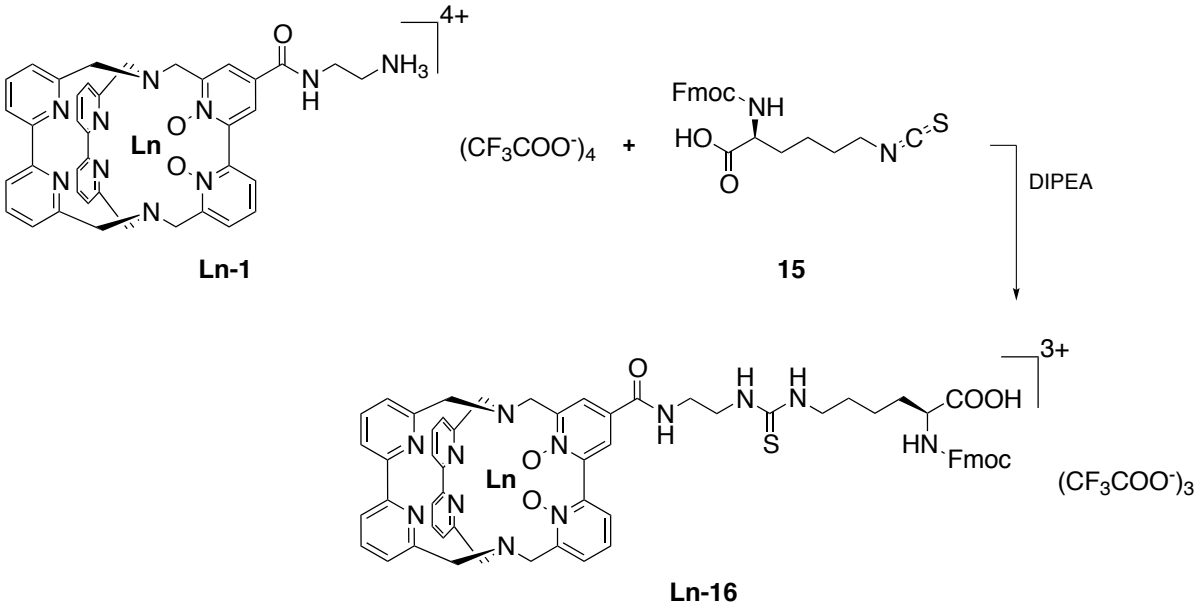

Figure 4.20: Synthesis of the amino acid-functionalised lanthanoid cryptates **Ln-16** from the amino-functionalised lanthanoid cryptates **Ln-1** and the isothiocyanate **15**.

reaction, but since the availability of isothiocyanate **15** is so much better than the one of the complexes **Ln-1**, also slightly improved yields justify the use of significantly higher equivalents. Surprisingly in an experiment with addition of a single portion of 2.1 equivalents of **15** no product formation could be observed, while a continuous addition of a relatively dilute solution of **15** was found to be a possible variation, yet not beneficial. For the purification of the crude complexes **Ln-16** via HPLC a modified strategy was necessary. In the 1:1 (v/v) mixture of CH_3CN and H_2O typically used for preparation of the solution which is subjected to HPLC, the material isolated was usually not sufficiently soluble. Best results were obtained when instead a 1:1 (v/v) mixture of CH_3CN and 1 vol.-% TFA in H_2O was used and the mixture was treated in a ultrasonic bath before filtration. Also the HPLC method utilised had to be modified. When the usually applied method was used any product fraction isolated after the first run was contaminated with a species with significantly longer retention times. After these HPLC procedures, during the end runs performed to bring the column to storage conditions, quite large amounts of unidentified species were eluted. This points to the presence of a species in the crude mixture which is not eluted from the column during a single run and will instead contaminate the subsequent runs. The HPLC method was consequently varied in a way that during every single run the storage conditions are reached and the remaining impurities are washed from the column, which was indeed suitable to solve the problem. Starting from the HPLC purified complexes **Ln-1** the amino acid-functionalised cryptates **Ln-16** could be obtained in yields from 20% to 54%. Typically also unreacted amino-functionalised lanthanoid complex **Ln-1** could be isolated from HPLC. While the initial amino-functionalisation of the cryptates did not affect the retention time observed during HPLC significantly, the functionalisation as Fmoc-protected lysine lead to considerably longer retention times (see Table 4.1) and consequently the cryptates **Ln-1** and **Ln-16** can easily be separated from each other.
The need for two HPLC purifications during the preparation of **Ln-16** from **Na-1** in two individual steps

was soon identified to be quite problematic for the preparation of larger amounts of **Ln-16**. Consequently an alternative synthesis strategy was developed, which circumvents this problem by simply omitting the HPLC purification after the complexation reaction and instead using the crude material obtained from the synthesis of **Ln-1** for the reaction with isothiocyanate **15** (see Figure 4.20).

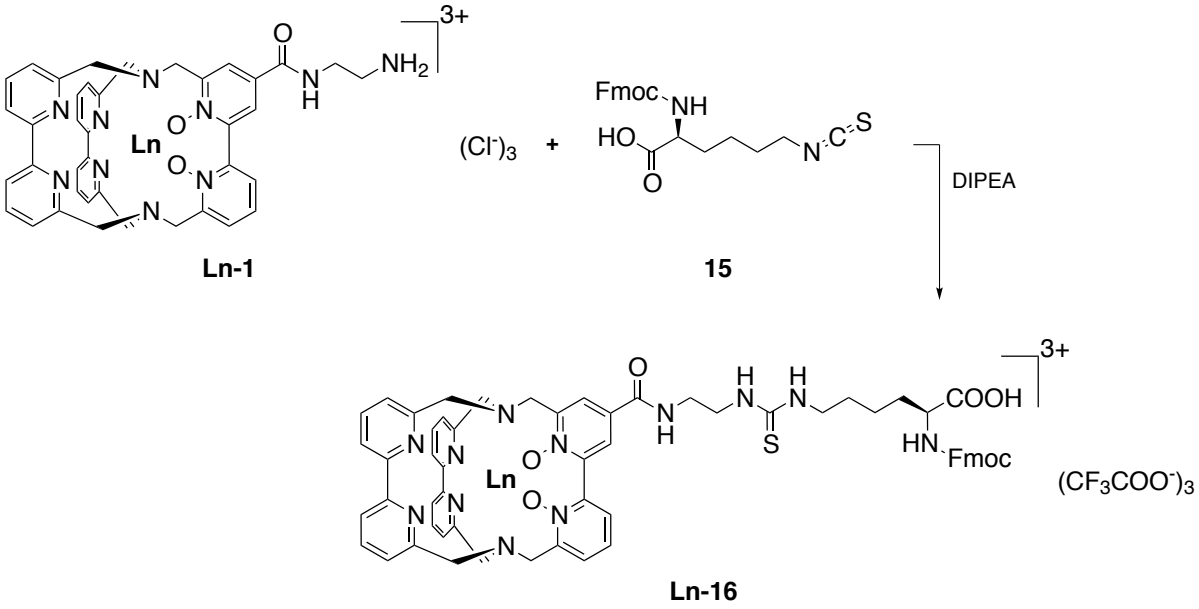

Figure 4.21: Synthesis of the amino acid-functionalised lanthanoid cryptates **Ln-16** from the crude amino-functionalised lanthanoid cryptates **Ln-1** and the isothiocyanate **15**.

Since the complexation reaction transforming **Na-1** into **Ln-1** does not proceed completely, the resulting crude mixtures can be assumed to contain a maximum of 30-50% of **Ln-1**. Furthermore the composition of **Ln-1** prior to the reaction with **15** will be slightly different. The amino group will not be protonated and instead of the TFA^- anions most likely Cl^- will be bound. For the reactions performed with the crude **Ln-1** the initial addition of DIPEA for deprotonation of the starting material was omitted, despite from that the reaction was performed analogously to the procedure described above. In some cases also an excess of DIPEA was used (the first portion of **15** was dissolved in the 0.1 M solution of DIPEA in CH_3OH instead of the mixture of CH_3OH and CH_2Cl_2), but this was not found to have significant effect on the reaction. When the reaction was performed with the crude **Ln-1** shortly after addition of the first portion of **15** the precipitation of a solid could be observed. Most likely this correlates to the formation of insoluble **Na-16** from the remaining **Na-1** in the starting material.

Since the exact composition of the starting material is not known, for these reactions no yield was determined. Interestingly, the HPLC traces recorded during purification of the product did not show the presence of any **Ln-1**, which could point towards the reaction being more efficient if performed with unprotonated **Ln-1**. In any case this is the more convenient route when large amounts of **Ln-16** have to be prepared.

The amino acid-functionalised lanthanoid cryptates of Sm^{III}, Eu^{III}, Tb^{III} and Yb^{III} were prepared and studied via MALDI-MS, high resolution ESI-MS and with ^1H and ^{19}F NMR spectroscopy.

Table 4.1: Representative yields of experiments performed for the synthesis of **Ln-16** and retention times of the complexes. All analytical HPLC runs were performed with program **A**.

	yield [%]	R_f, analytical HPLC setup **A**
Sm-1	24	17.1 min
Eu-1	20	17.1 min
Tb-1	40	17.1 min
Yb-1	58	16.9 min

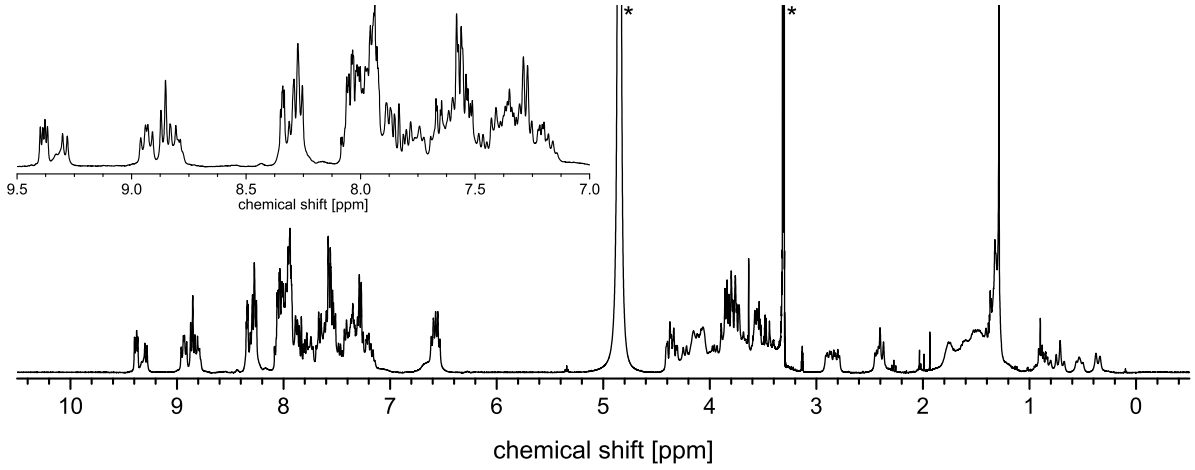

Figure 4.22: ^{1}H NMR spectrum (400 MHz, CD_3OD) of the amino acid-functionalised samarium cryptate **Sm-16**. Unambiguously identified solvent signals are marked with an asterisk.

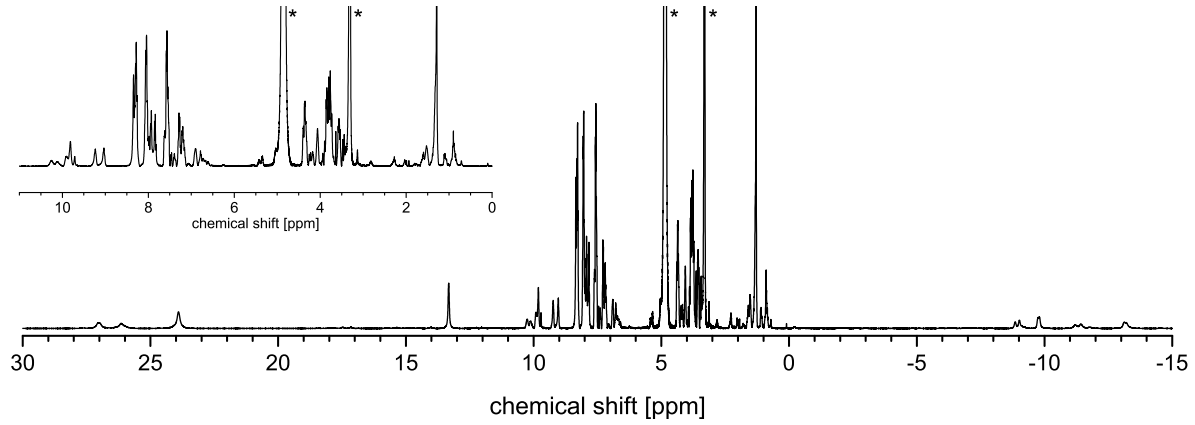

Figure 4.23: ^{1}H NMR spectrum (400 MHz, CD_3OD) of the amino acid-functionalised europium cryptate **Eu-16**. Unambiguously identified solvent signals are marked with an asterisk.

The ^{1}H NMR spectra of **Sm-16**, **Eu-16**, **Tb-16** and **Yb-16** are shown in Figure 4.22 to Figure 4.25. A com-

parison to the ^{1}H NMR spectra of the amino-functionalised cryptates **Ln-1** is most straightforward for the slightly paramagnetic Sm^{III} complexes. The signals of the attached lysine are not significantly shifted compared to the isothiocyanate **15** and can easily be identified as additional signals in the ^{1}H NMR spectrum of **Sm-16**. As discussed above, since the cryptates **bpy$_3$O$_2$** are used as racemic mixture, upon reaction with the chiral isothiocyanate **15** a pair of diastereomers is formed. The presence of two diastereomers becomes especially perceptible in the spectrum of the Sm^{III} complex, where several signals which were well defined in the case of the amino-functionalised cryptate now can be observed as multiplets consisting of two overlapping signals (e.g. between 9.5 and 9.0 ppm or between 3.0 and 2.9 ppm). Also in the range between 90 and 30 ppm of the spectrum of the Tb^{III} complex overlapping signals of the diastereomers can clearly be identified.

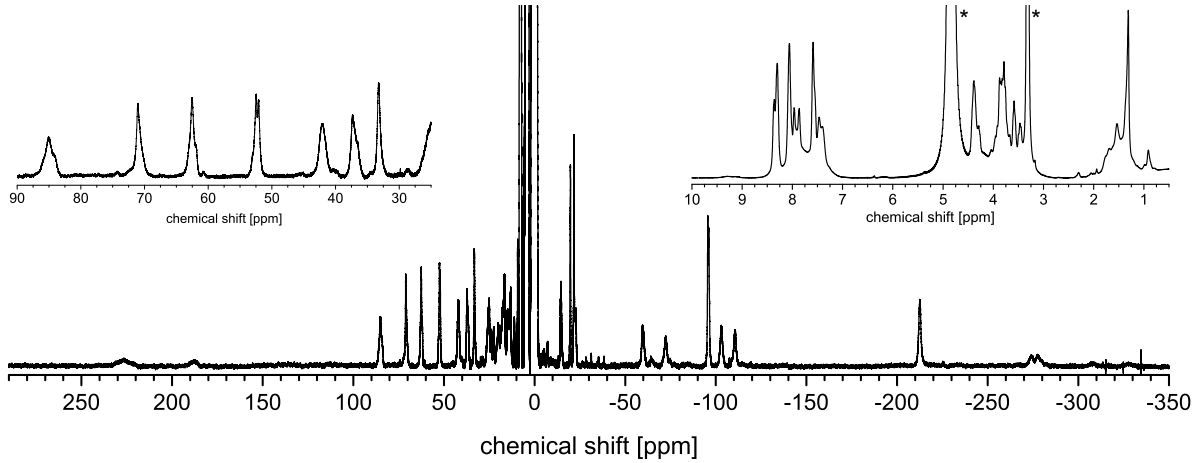

Figure 4.24: ^{1}H NMR spectrum (500 MHz, CD_3OD) of the amino acid-functionalised terbium cryptate **Tb-16**. Unambiguously identified solvent signals are marked with an asterisk.

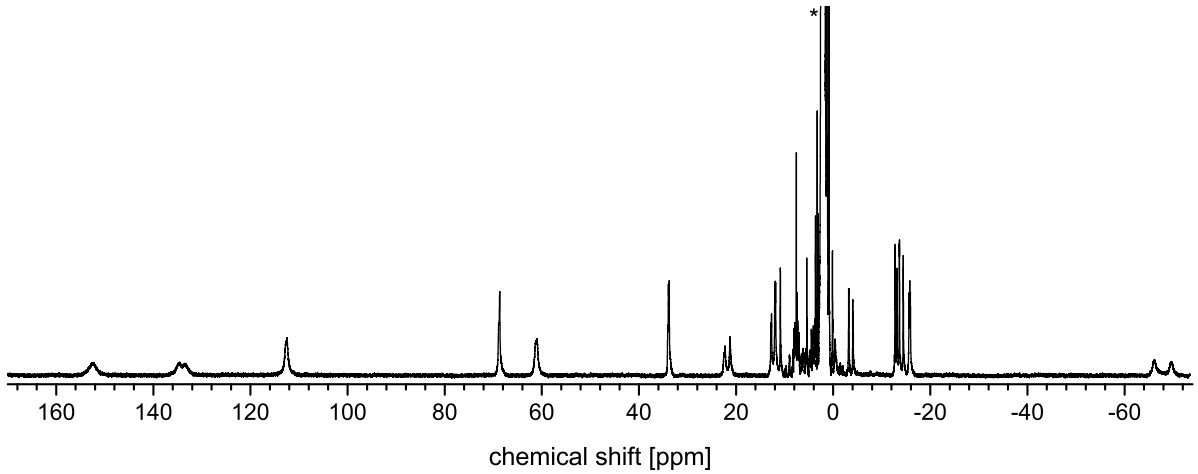

Figure 4.25: ^{1}H NMR spectrum (500 MHz, CD_3CN) of the amino acid-functionalised ytterbium cryptate **Yb-16**. Unambiguously identified solvent signals are marked with an asterisk.

Yet for all lanthanoids studied the general appearance and structure of the ^{1}H NMR spectrum is not significantly affected by the attachment of the amino acid, so there is no evidence that the solution structure or the tensor of the susceptibility of the magnetic anisotropy change. This interpretation is supported by the ^{19}F NMR spectra of the complexes (see Figure 4.26 for representative examples), which are virtually identical to the ones of the amino-functionalised analogues. Again, shift and width of the signals correlate with the paramagnetism of the lanthanoid.

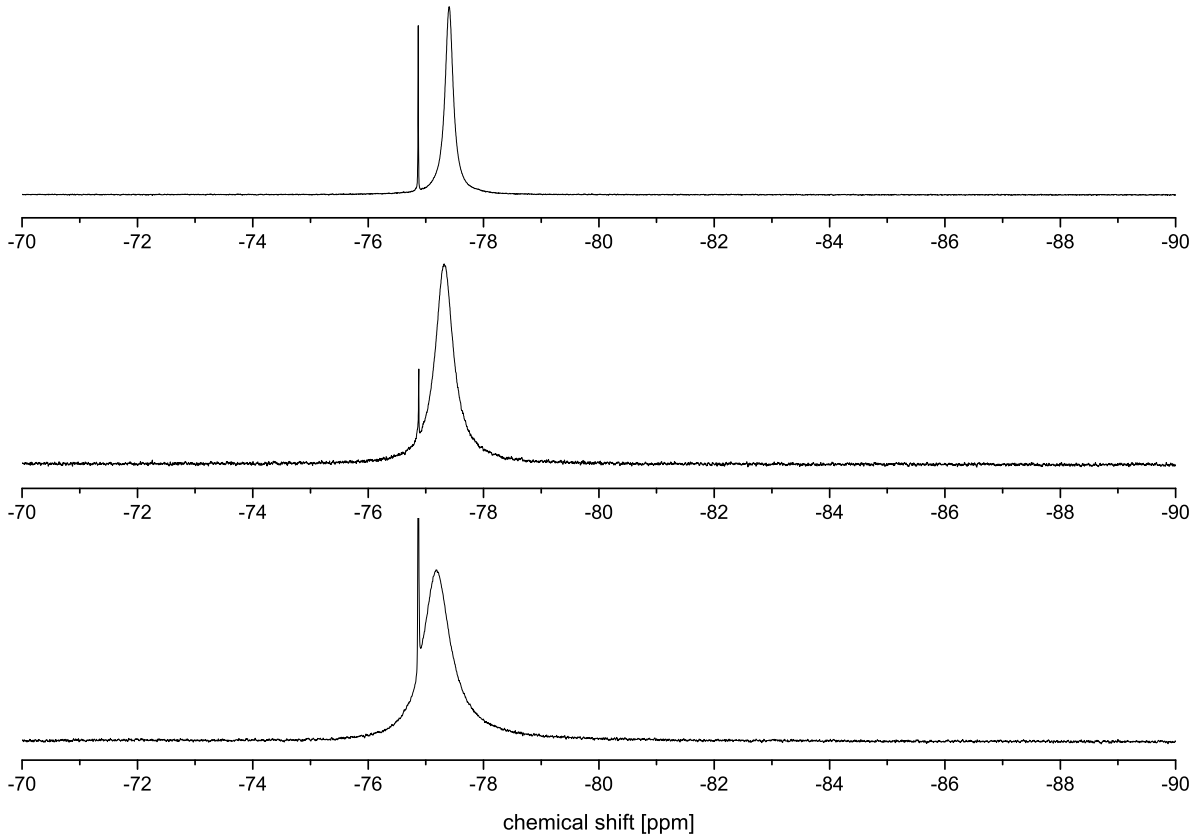

Figure 4.26: ^{19}F NMR spectra (376 MHz, CD_3OD) of the amino-functionalised lanthanoid cryptates **Ln-16**: **Sm-16** (top), **Eu-16** (middle) and **Tb-16** (bottom).

However, for the ligand-centered photophysical properties of the complexes some interesting changes compared to **Ln-1** were found. Figure 4.27(a) shows the UV/Vis spectrum of **Sm-16**, together with the one of the amino-functionalised parent compound. For the amino acid-derivative the absorption maximum is shifted to slightly shorter wavelengths and can be observed at 301 nm. At lower wavelengths the shape of the spectrum is different to the ones typically observed for cryptates **Ln-bpy$_3$O$_2$**. Most likely the additional features observed herein corresponds to Fmoc-centered absorbance, and the observed shift of the maximum of the absorbance is not a genuine shift of the cryptate-centered absorbance. To further study this phenomenon the Yb^{III}-complex was excited with light of wavelengths of 265 nm and 300 nm, the resulting emission spectra are shown in Figure 4.27(b). Since ytterbium is only emitting in the near-infrared part of the electromagnetic spectrum any emission of a Yb^{III} complex observed in the visible part of the elec-

tromagnetic spectrum has to be ligand-centered. Indeed the broad signals which were detected are very similar to the characteristic emission spectrum of Fmoc-groups.

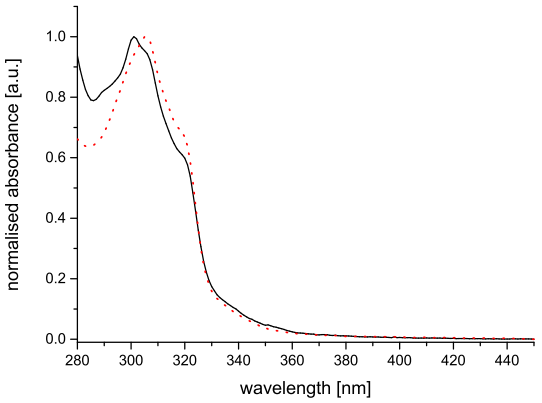

(a) Normalised UV/Vis spectra of **Sm-16** (black, solid line) and **Sm-1** (red, dotted line) in CD_3OD.

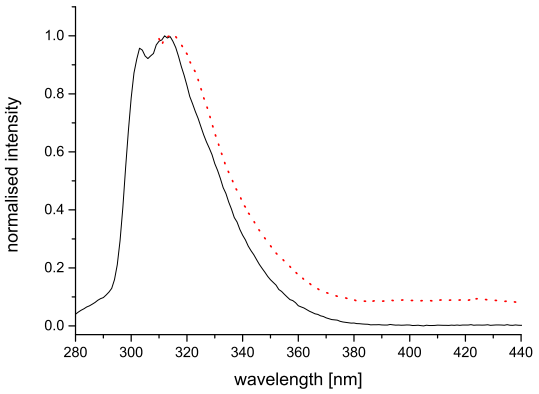

(b) Normalised steady state emission spectrum of **Yb-16** under excitation with λ_{exc} = 265 nm (black, solid line) and λ_{exc} = 300 nm (red, dotted line).

Figure 4.27: Ligand-centered photophysical properties of the amino acid-functionalised cryptates **Ln-16**.

Finally also the lanthanoid-centered emission of the complexes was studied. As expected, the steady state emission spectra of the complexes (see Figure 4.28) do not significantly differ to the ones obtained for the amino-functionalised complexes. Again the spectrum recorded for **Eu-16** points towards the presence of two Eu^{III} species as it was already discussed for **Eu-1** (see Figure 3.15, page 43). The luminescence lifetimes τ_{obs} are summarised in Table 4.2, for all complexes studied biexponential decays were found. In tendency the values are a bit lower than the ones found for the corresponding amino-functionalised cryptates, but since the expected errors for these measurements are quite high they should rather be interpreted in terms of orders of magnitudes, which again meet the expectations.

Table 4.2: Luminescence lifetimes τ_{obs} determined for cryptates **Ln-16** in CD_3OD.

	observed transition	τ_{obs} **in** CD_3OD
Eu-16	$^5D_0 \rightarrow {}^7F_2$	1.19 ms (67.0%) + 0.71 ms (33.0%)[a]
Sm-16	$^4G_{5/2} \rightarrow {}^6H_{9/2}$[b]	35.1 μs (40.9%) + 11.8 μs (59.1%)
Tb-16	$^5D_4 \rightarrow {}^7F_5$[c]	1.35 ms (83.6%) + 0.21 ms (16.4%)

[a] preliminary result. A repetition of the measurement was not possible until now due to technical problems. [b] λ_{em} = 597 nm, λ_{exc} = 310 nm. [c] λ_{em} = 541 nm, λ_{exc} = 305 nm.

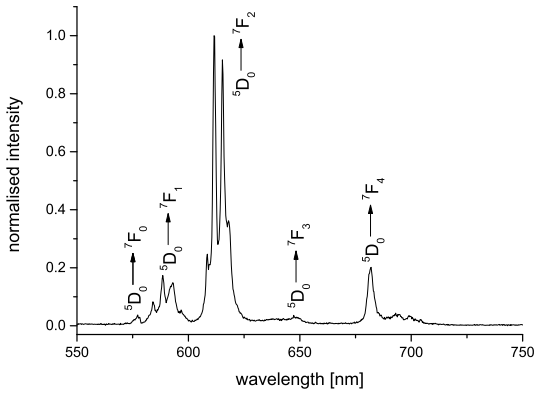

(a) Normalised steady state emission spectrum of **Eu-16** (CD_3OD, $\lambda_{exc} = 320$ nm).

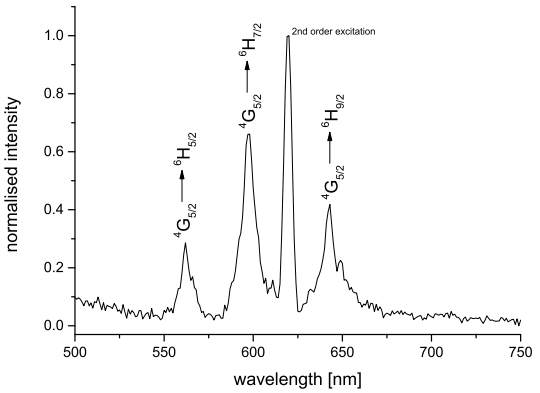

(b) Normalised steady state emission spectrum of **Sm-16** (CD_3OD, $\lambda_{exc} = 310$ nm).

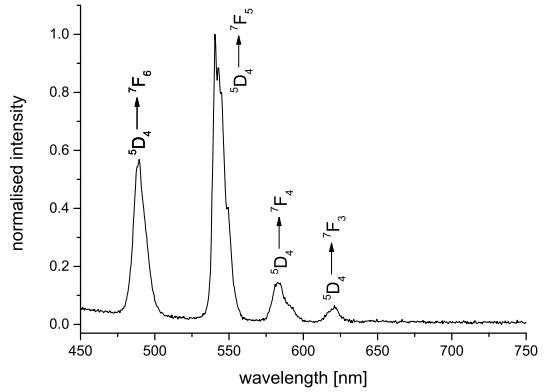

(c) Normalised steady state emission spectrum of **Tb-16** (CD_3OD, $\lambda_{exc} = 305$ nm, excitation path: long pass filter LP399).

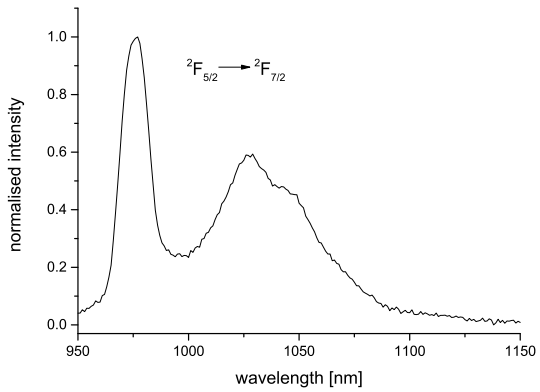

(d) Normalised steady state emission spectrum of **Yb-16** (CD_3OD, $\lambda_{exc} = 300$ nm, emission path: long pass filter RG780).

Figure 4.28: Steady state emission spectra of **Ln-16**.

4.3.3 Preliminary tests for peptide synthesis

As it was shown in the last chapter, the lanthanoid specific properties of the cryptates remain largely unaffected by the attachment of the amino acid. For the success of this project it is equally crucial that also the specific properties of the amino acid remain unaffected by the rather exceptional side chain and retain their specific reactivity. To probe this, and to simultaneously develop a synthesis protocol for the preparation of a molecular nanocode, a series of solid phase peptide synthesis experiments of increasing complexity were performed, each targeting a specific aspect of the reactivity of Fmoc-protected amino acids. Primary aim of these experiments was not a complete characterisation of the products or an unambiguous proof for the feasibility of the single steps. Due to the small amounts of the amino acid-functionalised lanthanoid cryptates which were available for these test reactions, and due to the complicated analysis of the resulting products this would have been too time consuming. Instead when the analytical results pointed towards the success of the experiment being sufficiently likely, it was proceeded with the next, more complex experiment. As the amino-acid functionalised lanthanoid cryptates were prepared (and used) as mixture of diastereomers, the products of the peptide coupling experiments with these amino acids will be obtained as a mixture of different species. Drastic differences in terms of reactivity of the diastereomers are not to be expected.

As solid support for all peptide coupling experiments an Fmoc-Gly-Tentagel® PHB resin with an increased swelling volume and a relatively low loading of 0.15-0.20 mmol/g was used. This is generally useful for the synthesis of peptide sequences which are considered to be difficult and will also be helpful to minimise problems resulting from steric overcrowding or charge agglomeration. Tentagel® PHB resins are Wang type resins which are typically cleaved with TFA. Between the matrix of the beads and the acid labile group a PEG linker (molecular weight in the range of 3000 Da) provides the necessary flexibility and dominates the physico-chemical properties of the material.

For all coupling steps HATU was used as coupling reagent as it is considered to be the first choice for difficult coupling reactions. In a typical solid phase peptide synthesis with HATU for any coupling step 5.0 equivalents of the Fmoc-protected amino acid and 4.9 equivalents of HATU are used with a rather short reaction time of 30 minutes. For commercially available amino acids and longer sequences this is obviously reasonable und usually no attempts to reduce the equivalents are undertaken. But due to the limited availability of the amino acid-functionalised lanthanoid cryptates, for development of a molecular nanocode based on these compounds the use of smaller equivalents would be highly desirable. At the same time longer reaction times are less problematic because of the rather short sequences which will be synthesised. In order to test the applicability of fewer equivalents of the amino acids with longer reaction times under the conditions which will be used herein a short peptide was prepared from commercially available amino acids, in a first experiment with the established equivalents and in a second experiment with drastically decreased equivalents (1.1 equivalents of the amino acid, 1.05 equivalents of HATU) and reaction times increased to 24 hours for every coupling step.

Both reactions were performed on identical scales and in plastic syringes equipped with a PE frit. After synthesis the peptides were cleaved from the resin with TFA (+ 5 vol.-% H_2O) and the isolated material was analysed without further purification. The ESI mass spectra of both substances are virtually identical. For

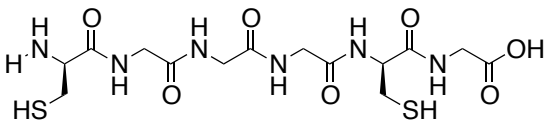

17

Figure 4.29: Structure of the peptide synthesised to test the use of fewer equivalents of amino acids.

both spectra the dominant main species is the Na^+ adduct of peptide **17** and no signals corresponding to a shorter peptide which might result from an incomplete synthesis sequence were detected. In the analytical HPLC experiments performed with the crude materials the component which most likely relates to the product was eluted after 25.9 minutes (see Figure 9.22, page 275). Both chromatograms revealed an individual contamination of the HPLC run, due to the small amount of material this might originate from sample preparation. If the coupling would be incomplete in the case of the synthesis with lower equivalents, a series of species with more or less gradually varying retention times would have been expected upon HPLC analysis. Mainly based on the results of mass spectrometry it was concluded that the use of lower equivalents of amino acids and longer reaction times is a reasonable modification to be made for the following experiments.

4.3.3.1 Reactivity of the carboxylic acid: Attachment to the resin

To be of use for peptide synthesis the carboxylic acid of the Fmoc-protected amino acid must be transformable into an active ester with some kind of coupling reagent, and the resulting active ester must be cleavable with a primary amine. An easy and also the most suitable experiment to test if these reactions can be performed under the conditions of peptide synthesis, is the attachment of **Ln-16** to the deprotected primary amine of the glycine which is already attached to the peptide synthesis resin (see Figure 4.30). In a plastic syringe equipped with a PE frit the resin was prepared for synthesis by swelling it in CH_2Cl_2, washing it with DMF and then cleaving the Fmoc protecting group with 20% piperidine in DMF. For the very first coupling experiment with an amino acid-functionalised lanthanoid cryptate the europium amino acid was chosen. As mentioned before the strong luminescence of Eu^{III} cryptates is often helpful for monitoring the progress of a reaction and facilitates the identification of the product. 1.1 equivalents of the europium amino acid were dissolved in a few drops of DMF and 1.05 equivalents of HATU and 2.2 equivalents of DIPEA were added. After a few moments the dilute mixture turned slightly yellow, which indicates that the active ester was successfully formed, subsequently the mixture was transferred to the resin in the syringe. Under excitation with 302 nm light the solution was found to show the characteristic emission of Eu^{III}. The syringe was mounted onto a vibrating plate and gently shaken for 24 hours. Afterwards under excitation with light of 302 nm a very promising observation could be made: Now the red emission was localised on the particles, which strongly indicates that the europium cryptate was no longer homogeneously dissolved in the solution but had been attached to the particles. Considering the nature of the peptide resin this is most likely to be consequence of the formation of the desired covalent bond between the amino acid and the primary amines at the surface of the beads.

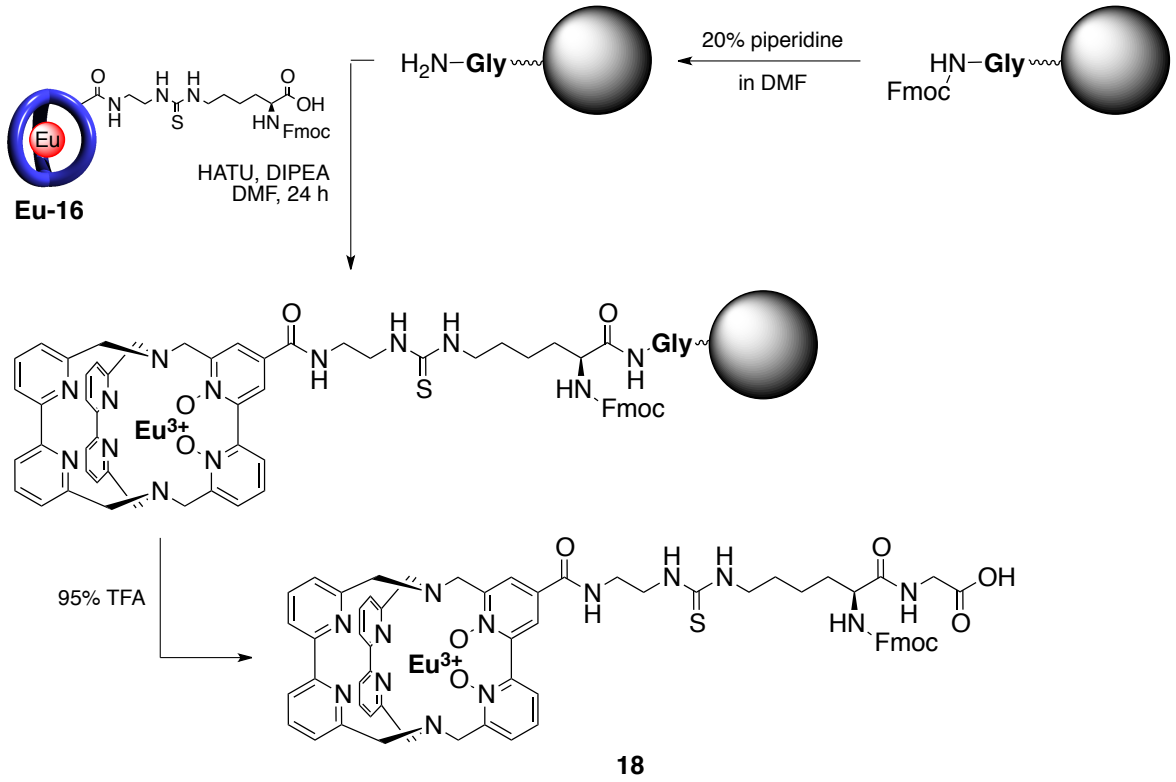

Figure 4.30: Synthesis performed to test the reactivity of the carboxylic acid moiety of the amino acid-functionalised cryptates **Ln-16**.

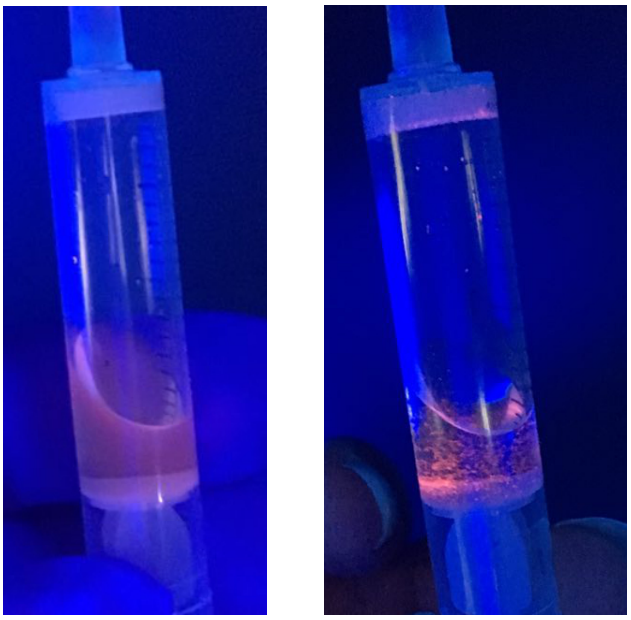

(a) Shortly after addition. (b) After 24 hours.

Figure 4.31: Photographs of the syringe with the deprotected peptide synthesis resin with the solution of **Eu-16**, HATU and DIPEA in DMF under a 302 nm lamp.

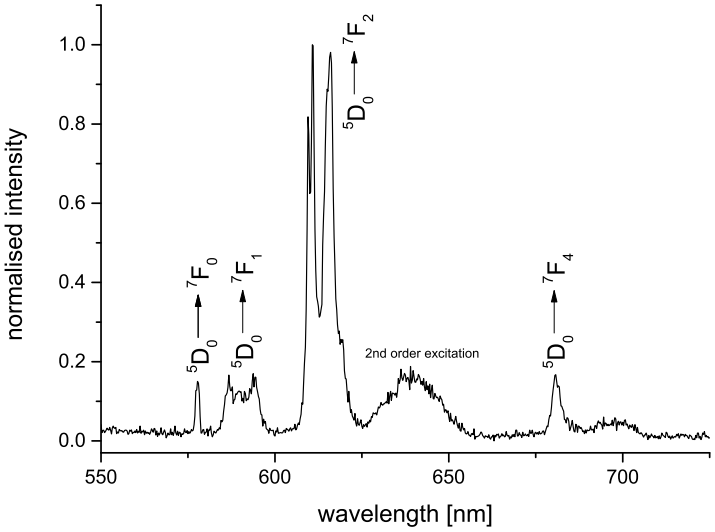

Figure 4.32: Normalised high resolution steady state emission spectrum of **18** (CD_3OD, λ_{exc} = 320 nm).

After the solution was drained from the syringe the resin was washed thoroughly with DMF and then shrinked before TFA with 5 vol.-% H_2O was added for cleavage of the dipeptide from the resin. The obtained solution was drained into a flask and the volatiles were removed. Due to the small scale of the experiment no attempts to purify the material were undertaken and instead the crude material was studied. The red emission of the substance observed before could unambiguously be identified as the characteristic emission of Eu^{III} via luminescence spectroscopy (see Figure 4.32). Interestingly, the shape of the signals is slightly changed compared to the functionalised cryptates **Eu-1** and **Eu-16**. For **18** no longer two $^5D_0 \rightarrow {}^7F_0$-transitions are observed, so that there is no evidence for different photophysical properties of the different species resulting from the use of diastereomeric **Ln-16**. Also the shape of the other signals is slightly changed.

Subsequently the material should be studied via MALDI-MS. Though MALDI-MS is in principle a very suitable method for the study of such molecules, the practical utilisation of this method was found to be hindered by some fundamental problems. In contrast to the sodium cryptates which can very easily be detected in any mass spectrometric method, the trivalent lanthanoid cryptates are generally significantly more problematic. The use of a suitable matrix material in MALDI-MS was found to be helpful to circumvent this problem by aiding the transfer of the analyte into the gaseous phase, but no general strategy for the MALDI-MS characterisation of lanthanoid cryptates has been established until now. The individual optimisation for any of the compounds studied in this chapter was not possible due to the very small amounts of substance obtained. Often the spectra were dominated by signals originating from the matrix material and the relevant signals could only be observed with very small intensities and under exposure to high laser intensities (so that fragmentation is quite likely to occur). For example during MALDI-MS of dipeptide **18** with DCTB as matrix material two weak signals at m/z = 966.064 and m/z = 1137.470 were observed.

Due to the low intensity no isotope patterns could be resolved. Figure 4.33 shows two species which are potential derivatives of **18** and have the exact masses which can be considered to be equivalent to the observed signals under the conditions of the measurement. The loss of N-oxides during MALDI-MS is quite

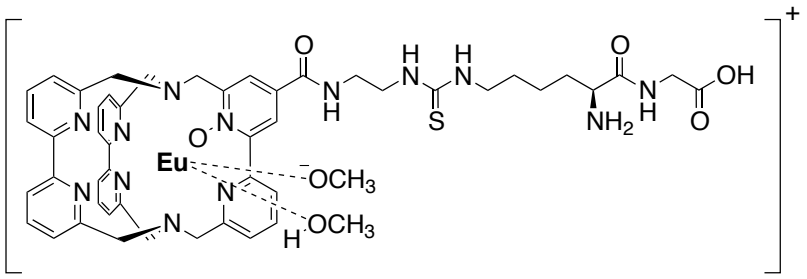

Chemical Formula: $C_{52}H_{61}EuN_{14}O_7S^+$
Exact Mass: 1137.35

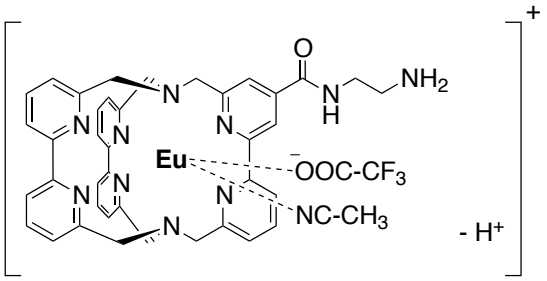

Chemical Formula: $C_{43}H_{38}EuF_3N_{11}O_3^+$
Exact Mass: 966.23

Figure 4.33: Species with suitable exact masses to cause the signals observed during MALDI-MS of **18** with DCTB as matrix material.

commonly observed and also the reduction of the rather redoxactive Eu^{III} to Eu^{II} is plausible under these conditions. In addition to the MALDI-MS experiments also an LDI-MS experiment was performed. Herein no signals corresponding to **18** could be detected, yet rather strong signals corresponding to polypropylene glycoles and polysiloxanes. Since this contamination presumably originates from the plastic syringe used as reaction vessel, the following experiments were performed in a custom-build glass vessel (see page 210). Mainly based on the observations made during synthesis and the interpretation of the emission spectrum from the substance isolated, it can be concluded that the carboxylic acid of the amino acid-functionalised cryptates **Ln-16** indeed shows the expected characteristic reactivity which is prerequisite for the attachment of the cryptate to the primary amine of another amino acid.

4.3.3.2 Reactivity of the protected amine: Cleavage of Fmoc and attachment of another amino acid

The aim of the next experiment was to study the reactivity of the Fmoc-protected amino-group of the complexes **Ln-16**. To probe if the protecting group can be cleaved under standard conditions applied in solid phase peptide synthesis and to test if subsequently another amino acid can be attached to the primary amine, again a peptide synthesis experiment was performed (see Figure 4.34). Apart from the change of the reaction vessel to a custom-build glass vessel the experiment was performed analogously to the one described before (until the amino acid **Eu-16** was attached to the resin).

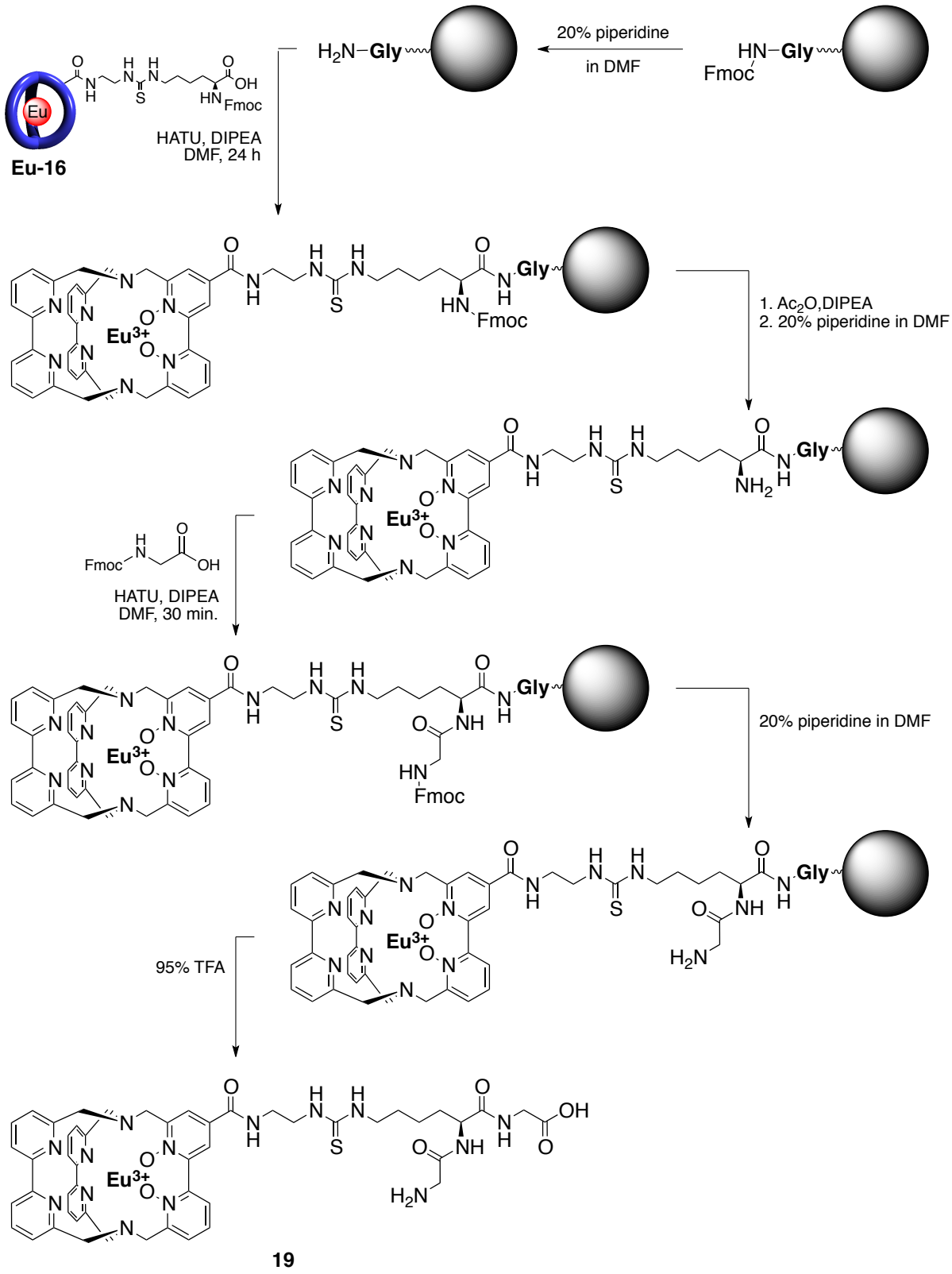

Figure 4.34: Synthesis performed to test the reactivity of the protected primary amine of the amino acid-functionalised cryptates **Ln-16**.

Differently to the previous experiment now the dipeptide bound to the resin was not cleaved but the resin was treated with Ac_2O to cap the unreacted primary amines at the beads. Afterwards an Fmoc deprotection step was performed to yield the primary amine of the dipeptide. In the subsequent step 5.0 equivalents of Fmoc-protected glycine together with 4.9 equivalents of HATU and 10.0 equivalents of DIPEA were mixed in a small amount of DMF and added to the vessel. Analogously to the standard procedure for peptide coupling reactions the mixture was shaken for 30 minutes before the solution was drained and the resin washed with DMF. After another Fmoc deprotection step to yield the primary amine, the tripeptide was cleaved from the resin with TFA as described for the previous experiment. During this experiment the typical red emission of Eu^{III} was only weakly detectable as soon as the slightly yellow solution with the active ester was transferred into the glass vessel, accordingly also the red colouring of the beads was only faintly perceptible. In contrast to that, upon addition of the TFA the colouring of the resulting solution was apparently much stronger than in the previous experiment. Most likely these phenomena result from the optical properties of the vessels used.

The capping steps after the attachment of an amino acid are typically performed to ensure that a peptide strand for which a coupling step was not successful is permanently "deactivated" for the subsequent steps. Though this is not necessary for the testing of the reactivity of the amino group of **Ln-16** this step was performed in this experiment to test the compatibility of the lanthanoid containing amino acid with the conditions applied during this procedure. As another modification towards the previous experiment the assembled tripeptide was deprotected prior to cleavage from the resin so that it can be isolated as primary amine. The reason for this variation was the finding that the amino-functionalised cryptates **Ln-1** can be detected more easily during MALDI-MS with DCTB as matrix material, since reaction of the primary amine and DCTB leads to formation of a species which presumably is more likely to undergo co-crystallisation with the matrix.[227]

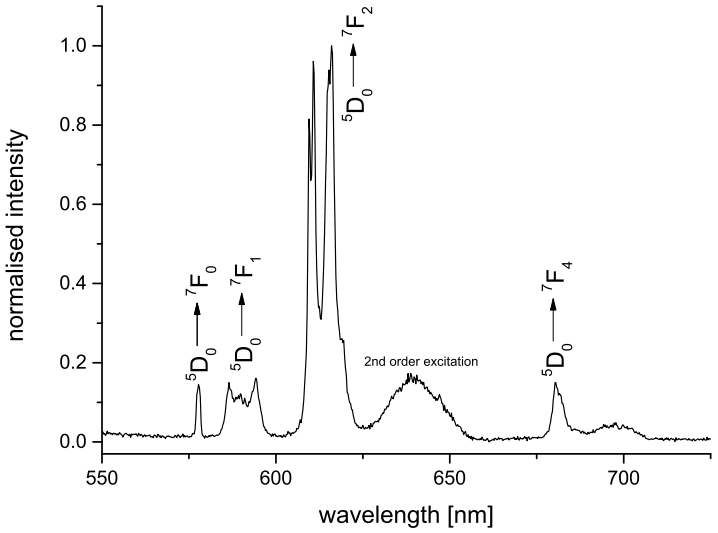

Figure 4.35: Normalised high resolution steady state emission spectrum of **19** (CD_3OD, λ_{exc} = 320 nm).

Again the high resolution steady state emission spectrum (see Figure 4.35) of the substance isolated un-

ambiguously proves the presence of Eu^{III} in the material. The spectrum is very similar to the one of the previously prepared **18** and again the $^5D_0 \rightarrow {}^7F_0$-transition does not allow for the distinction of several species.

Because in this case the luminescence of the material is indeed not suitable to give evidence of reactivity which was to be studied in this experiment, in this case the mass spectrometric characterisation is especially important. Fortunately the strategy followed by deprotecting the assembled tripeptide was successful and the spectrum obtained from MALDI-MS in this case is more meaningful than the one discussed before.

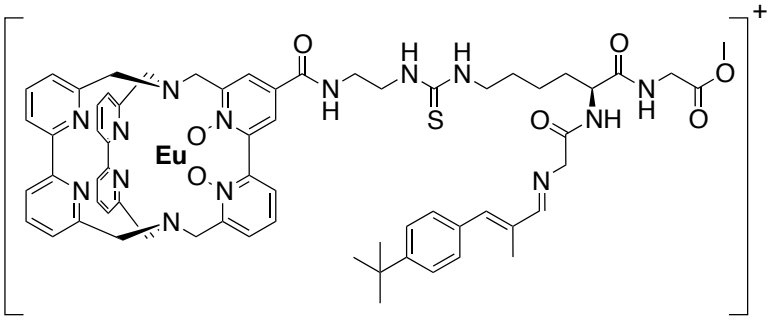

Chemical Formula: $C_{65}H_{72}EuN_{14}O_7S^+$
Exact Mass: 1345.46

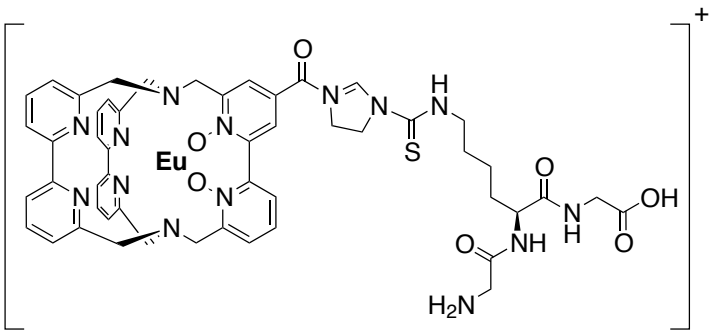

Chemical Formula: $C_{51}H_{53}EuN_{14}O_7S^+$
Exact Mass: 1158.32

Figure 4.36: Species with suitable exact masses to cause the signals observed during MALDI-MS of **19** with DCTB as matrix material.

The signal observed at m/z = 1345.351 nicely correlates to a twofold reduced DCTB adduct (see Figure 4.36). The second species shown in Figure 4.36 might evoke the signal at m/z = 1158.12. The modification of the ethylene-amine linker of this species results from a reaction of 1,2-ethylenediamines and formaldehyde, which usually is a trace contamination even in methanol of high purities.[228]

After this experiment in which the reactivity of the amino group of the lysine-functionalised **Ln-16** was probed, and after the previous one in which the feasibility of the attachment to amino groups was tested, the given evidence of the desired reactivity and the compatibility of **Ln-16** with the conditions applied was evaluated as sufficient to use the amino acid-functionalised lanthanoid cryptates in more sophisticated experiments.

4.3.3.3 Feasibility of the connection of several lanthanoid amino acids

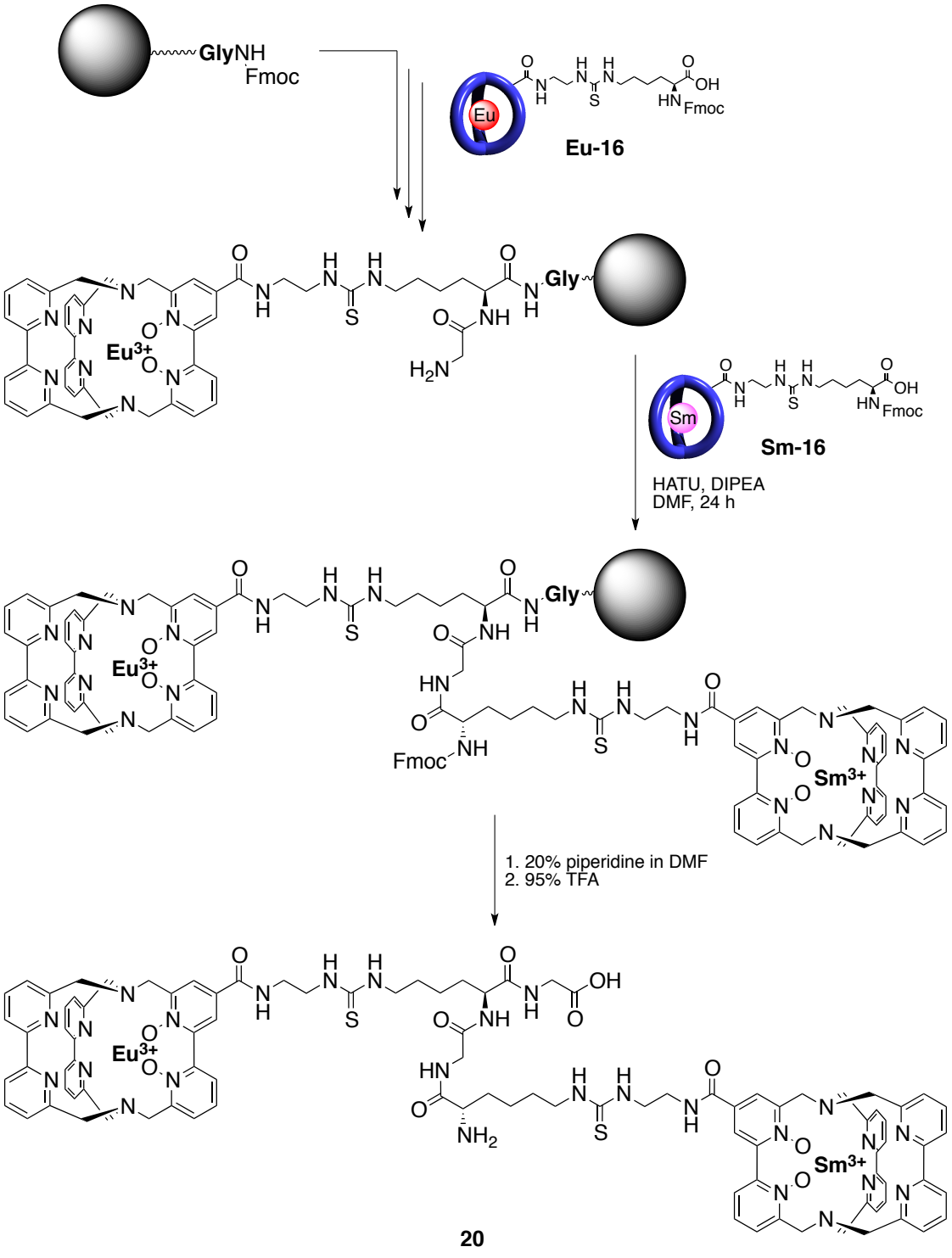

Figure 4.37: Synthesis performed to test the feasibility of the connection of several cryptates **Ln-16** via solid phase peptide synthesis.

For the construction of a molecular nanocode based on the amino acids **Ln-16** it is of critical importance that the monomers containing the different lanthanoids can be connected to each other, not just to any amino acid. Compared to natural amino acids the cryptates **Ln-16** have a special property which might indeed become problematic, which is the relatively high charge of the individual amino acids. During synthesis the resulting repulsion between the cryptates might indeed inhibit the active esters from approaching the peptide strain on the beads to an extend which prevents the formation of a covalent bond. Of course this problem can be circumvented or at least reduced by the use of spacers from natural amino acids between the lanthanoid-containing ones. In principle also possible, but associated with a fundamental redesign of the lanthanoid containing amino acids, would be the introduction of negatively charged groups to the scaffold, like for example carboxylates or sulfonates, which is not pursued here.
In a first experiment to test the feasibility of the connection of several **Ln-16** a short glycine spacer was chosen to be placed between the lanthanoid containing amino acids. While the preparative effort for the introduction of one separating amino acid is very low, the resulting increase of flexibility might already be sufficient. The resulting synthesis which was performed is shown schematically in Figure 4.37. In principle the experiment started with the sequence already performed for the previous experiment (see Figure 4.34), but after assembly and deprotection of the tripeptide consisting of the initially bound glycine, the lysine-functionalised europium cryptate and another glycine, in this case **Sm-16** (1.1 equivalents) together with HATU (1.05 equivalents) and DIPEA (2.2 equivalents) was added to the resin. As already done for the attachment of **Eu-16** this reaction mixture was shaken for 24 hours. After completion of the coupling procedure again a deprotection step was performed prior to cleavage. It should be noted that after the attachment of the spacer glycine between **Eu-16** and **Sm-16** no capping step was performed. The feasibility of a direct attachment without any spacer would be a valuable result, too.
The observations made during synthesis did show no deviations from the ones made during the previous experiments. Upon addition of the lysine functionalised samarium cryptate no variation of the emissive properties of the resin under 302 nm excitation was monitored, but as samarium cryptates are typically by far less luminescent than the corresponding europium compounds this would also not have been expected. Importantly, despite the big number of washing steps performed during this synthesis, also no decrease of the characteristic red emission was noticeable. This is only likely to be the case when the luminophore is indeed covalently attached to the beads.
After isolation of the substance the luminescence properties of the isolated material **20** were studied. The normalised high resolution steady state emission spectrum recorded between 530 and 750 nm is at first sight very similar to the one recorded for **19** (see Figure 4.38), the shape of all Eu^{III} centered transitions is virtually unchanged. But indeed there is a small feature which could not be observed before, which is a flat structure centered around 562 nm. Indeed, upon recording the region between 540 and 600 nm another time with an increased number of single measurements the shape of the signal becomes clearer (see Figure 4.39), so that it could unambiguously be identified as the $^4G_{5/2} \rightarrow {}^6H_{5/2}$-transition of Sm^{III}. This proves that the material under study contains both lanthanoids. Considering the process applied during the preparation of the material, this effectively also gives evidence of the reaction taking place as shown in Figure 4.37.
Subsequently the substance was also studied via MALDI-MS with DCTB as matrix material. Despite of sig-

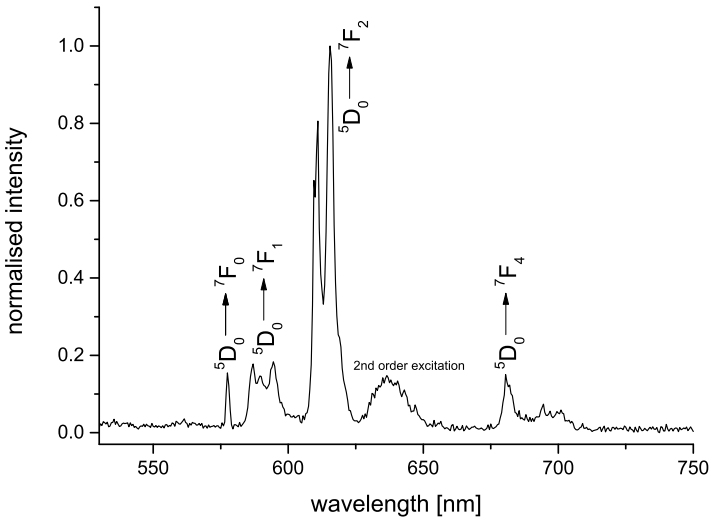

Figure 4.38: Normalised high resolution steady state emission spectrum of **20** (CD_3OD, λ_{exc} = 320 nm).

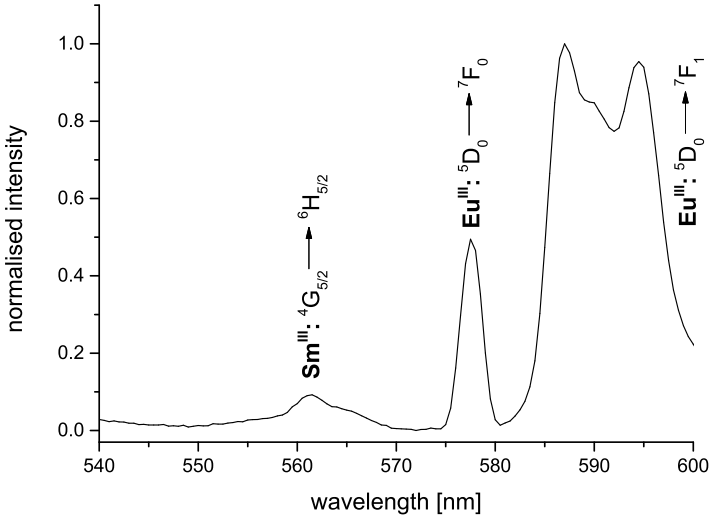

Figure 4.39: Normalised high resolution steady state emission spectrum of **20** (CD_3OD, λ_{exc} = 320 nm).

nals which can be assigned to matrix adducts, a single weak signal could be detected at m/z = 2239.011. A species which could possibly evoke this signal is shown in Figure 4.40.

Again the results obtained from MALDI-MS are difficult to interpret. In contrast to that the study of the luminescence properties is giving strong evidence for the successful preparation of the target compound. The obtained results show that the connection of several cryptates **Ln-16** is indeed possible with the aid of solid phase peptide synthesis. So the preparation of **20** is a successful proof-of-principle for the applicability of these complexes for the preparation of a molecular lanthanoid nanocode and in principle already the first example of such a nanocode.

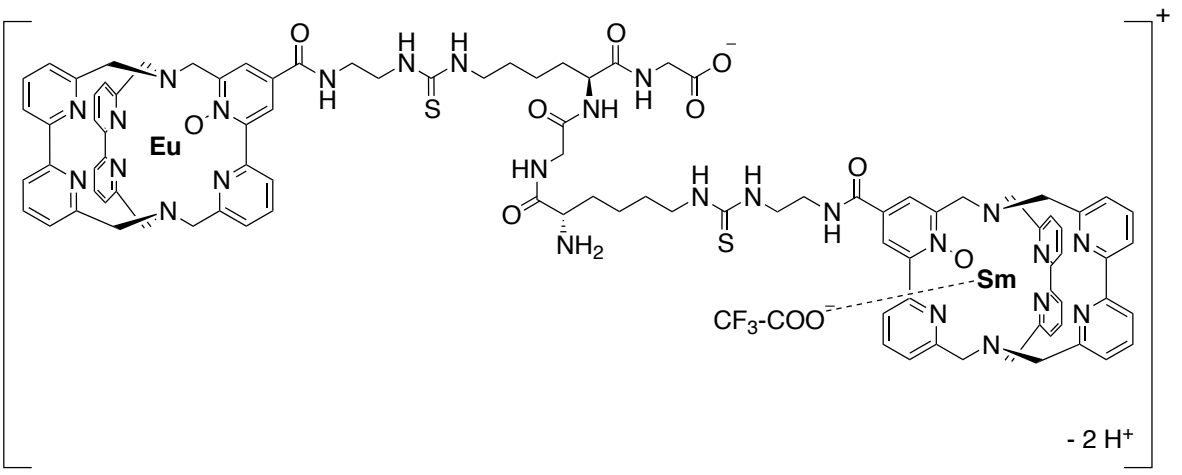

Chemical Formula: $C_{98}H_{97}EuF_3N_{26}O_{11}S_2Sm^-$
Exact Mass: 2239.56

Figure 4.40: Species with might cause the signal observed during MALDI-MS of **20** with DCTB as matrix material.

4.3.4 Preparation of a molecular nanocode based on lanthanoids

In principle the tetrapeptide **20** in which an europium and a samarium cryptate are covalently attached can already be considered a short nanocode. Based on analysis of the codes of two cryptates using luminescence or ICP-MS, and using the four lanthanoid cryptates **Ln-16** already prepared, ten different codes would be accessible (which relates to a “k-combination with repetitions”). Considering the results of the previous chapter also the combination of at least three lanthanoid cryptates in one nanocode seems feasible, which would allow for the preparation of twenty codes distinguishable for luminescence spectroscopy or ICP-MS. When the sequence can be resolved with use of MS-MS methods even 64 distinguishable codes are possible (which relates to a “permutation with repetition”).

While realisation of the reactions described in the preliminary studies was found to be quite straightforward with only slightly modified standard procedures, the analysis was found to be very difficult. The preparation of the nanocode on a slightly bigger scale might help to reduce the problem, but upon design of the nanocode and the synthesis additional measures were taken to provide best prerequisites for an unambiguous analysis.

The most important modification compared to the previous experiments is the use of ^{13}C and ^{15}N enriched glycines as spacer between the lanthanoid-containing amino acids. These provide additional probes for NMR spectroscopy and might help to document the experimental realisation of the synthesis sequence. Based on the process of solid phase peptide synthesis the detection of the signal of the heteronucleus of the correspondingly labeled amino acid will strongly indicate that the previous synthesis steps were successful. In order to make this argument valid after any coupling step a capping step has to be performed. Due to its higher relative sensitivity chances for the detection of the labeled ^{13}C are better than for the labeled ^{15}N. Consequently the ^{13}C-labeled glycine was placed between the second and the third lanthanoid cryptate where the detection of the heteronucleus can provide evidence for the completion of more steps. For similar reasons it was decided to introduce the europium cryptate in the very last step

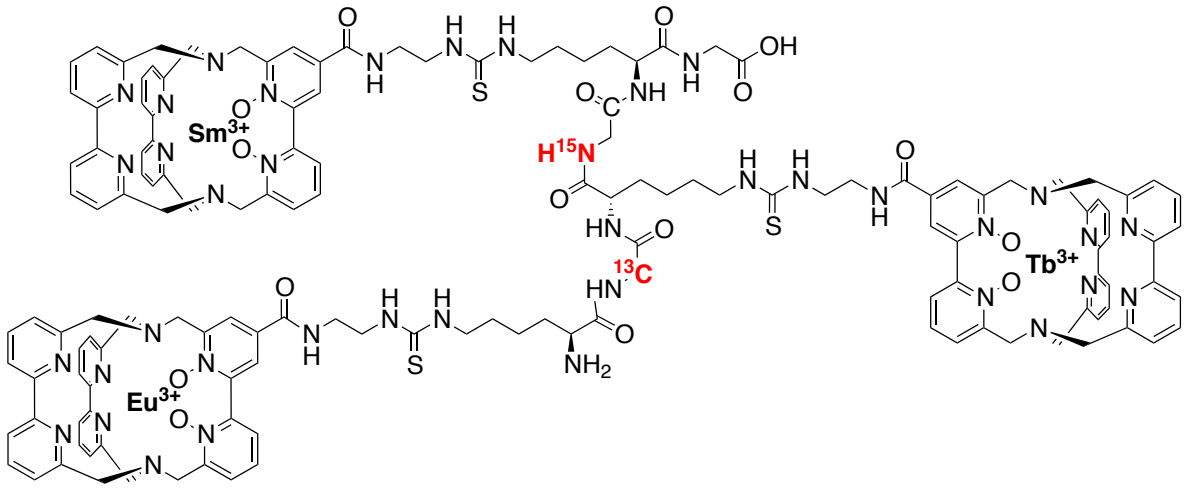

21

Figure 4.41: Structure of the molecular nanocode **21** in which Sm^{III}, Tb^{III} and Eu^{III} cryptates are covalently attached to each other via a peptide backbone.

of the synthesis. Since the attachment of **Eu-16** can be monitored with the naked eye, this will potentially allow for a very easy, yet quite meaningful observation. For this experiment the equivalents of the amino acid-functionalised cryptates were increased to 1.5 equivalents for every coupling step and the equivalents of HATU and DIPEA were adapted to 1.45 and 3.0 equivalents, respectively. Due to the small porosity of the frit the individual washing steps are quite time consuming, consequently the reaction times for the coupling steps with **Ln-16** were reduced to a minimum of 12 hours. For the coupling steps with isotope enriched glycines two identical subsequential coupling procedures were performed, respectively: After reacting the resin with the solution of reagents for at least nine hours, the solution was drained, and after washing of the resin a freshly prepared identical reaction mixture was added and reacted with the resin for further 30 minutes. If sufficient amounts of the amino acid are available this is a very easy, yet effective strategy to improve the yield of the respective coupling step.

Despite the modifications mentioned, the synthesis was performed in analogy to the ones described above. As expected upon attachment of **Eu-16** the red emission was localised on the beads and under cleavage conditions again released into the solution. After the cleavage with several portions of TFA (with 5 vol.-% H_2O) the reactor was also washed with CH_3OH, and the resulting solution was combined with the substance isolated from the TFA solutions, evaporated to dryness and dried thoroughly.

In this case already the steady state emission spectrum recorded over the range from 450 to 750 nm (see Figure 4.42) strongly points towards the successful preparation of **21**, as the spectrum clearly shows characteristic transitions of Eu^{III} and Tb^{III}. The detection of the characteristic luminescence of Eu^{III} is in a way the more important observation. As after every coupling step a capping step was performed, the attachment of the europium cryptate is in principle only possible when the samarium and terbium cryptates had been successfully attached to the peptide strain. In a separate measurement focusing on the range between 530 and 600 nm also the $^4G_{5/2} \rightarrow {}^6H_{5/2}$-transition of Sm^{III} could be observed. The uncommon shoulder of the $^5D_0 \rightarrow {}^7F_2$-transition of Eu^{III} is most likely relates to the $^5D_4 \rightarrow {}^7F_4$-transition of Tb^{III}.

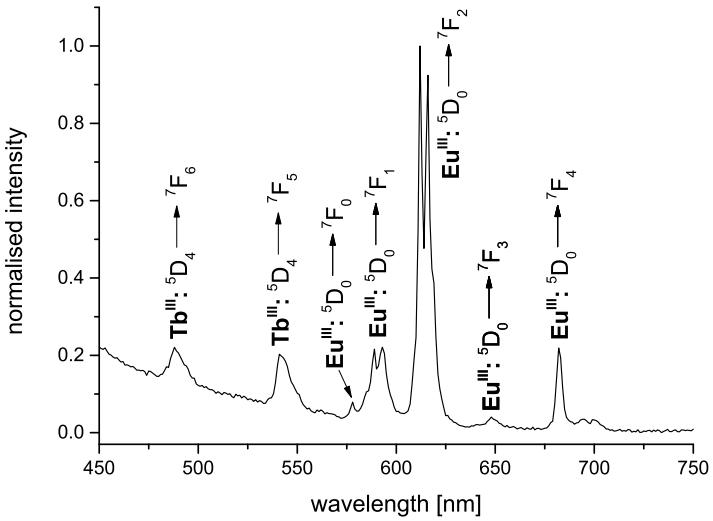

Figure 4.42: Normalised high resolution steady state emission spectrum of **21** (CD_3OD, $\lambda_{exc} = 320$ nm, excitation path: long pass filter LP399).

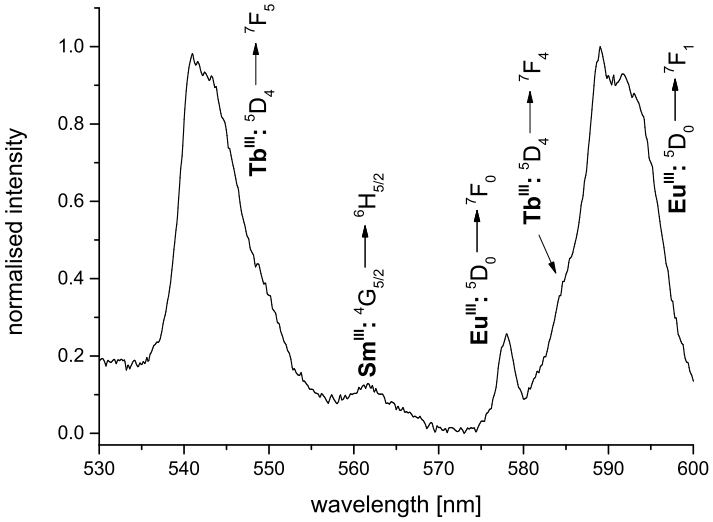

Figure 4.43: Normalised high resolution steady state emission spectrum of **21** (CD_3OD, $\lambda_{exc} = 320$ nm, excitation path: long pass filter LP399).

After the initial study of the luminescence properties of **21** different NMR techniques were used to study the material. Unfortunately neither the ^{13}C NMR spectrum nor the ^{15}N NMR spectrum revealed signals which can be assigned to the isotope enriched glycines. Also in the ^1H NMR spectrum the signals with distinct and characteristic shifts typical for the oxidised cryptates of Eu^{III} and Tb^{III} could not be identified, most likely due to the low concentration of the sample. In the middle region of the ^1H NMR spectrum, apart from some signals which can be assigned to a contamination from the PEG linker of the resin or the ester of TFA and CH_3OH, also some rather weak signals between 8.5 and 7.5 ppm can be identified. Most likely these correspond to protons of the peptide backbone or the linkers between the backbone and the individual cryptates. Focussing on these signals a ^1H DOSY NMR[229][230][231] experiment was performed

(see Figure 4.44, all ^{1}H NMR DOSY experiments were performed together with Dr. Wolfgang Leis).

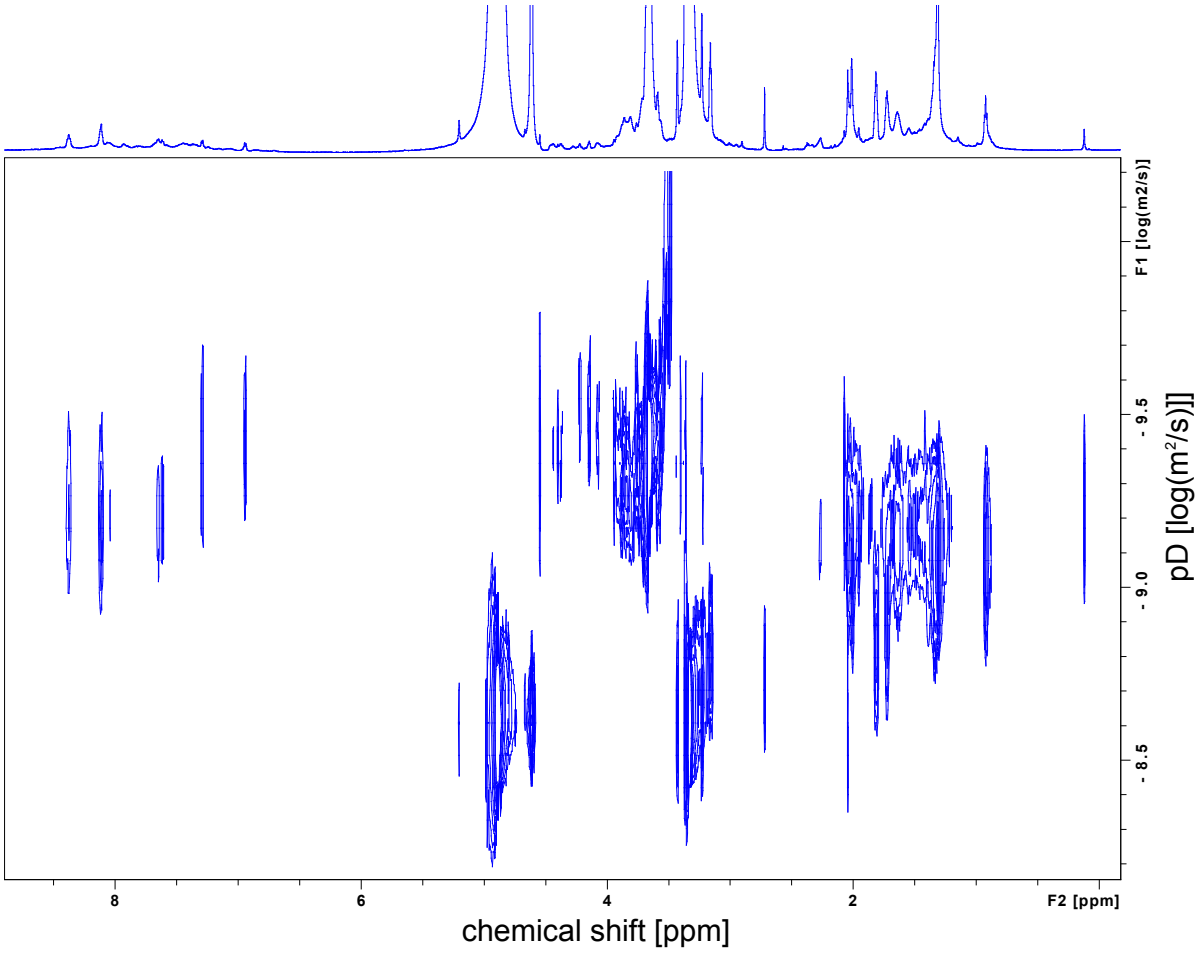

Figure 4.44: ^{1}H DOSY NMR spectrum (CD_3OD, 700 MHz) of the nanocode **21**.

A ^{1}H DOSY NMR allows to extract the diffusion coefficients of the species to which the protons under study belong. According to the Einstein-Stokes equation the diffusion coefficient D is dependent on the Boltzmann's constant k_B, the temperature T, the mobility of the particles η (which relates to the viscosity of the medium) and the hydrodynamic radius r of the object under study, which is assumed to be spherical:

$$D = \frac{k_B\, T}{6\, \pi\, \eta\, r} \tag{11}$$

For the signals assigned to the nanocode **21** a diffusion coefficient of $4.2 \cdot 10^{-10}$ m^2/s was determined. This is in line with an estimation of the solvent accessible volume of **21**, which was obtained from a MOPAC calculation (calculations performed by Dr. Wolfgang Leis, see experimental section for details). This already points towards the presence of a species in the sample which has a size comparable to the one expected for **21**. For a more systematic study a series of five related compounds was studied in ^{1}H DOSY experiments. Due to the uncommon combination of structural features of the nanocode the reference com-

pounds were chosen in a way that they either reflect the peptide-character or the cryptate-character of **21**. Three commercially available short peptides were studied (their sequences and structures are shown on page 283), the amino acid-functionalised samarium cryptate **Sm-16** and the partially deuterated lutetium cryptate **Lu-bpy$_3$O$_2$-D$_4$**[135]. Selected parameters obtained from the ^{1}H DOSY experiments and the molar masses of the compounds are summarised in Table 4.3. For the cryptates the molar masses were calculated assuming that under the conditions of the experiment one anion is bound rather tight to the cryptate and will hence diffuse together with the cation. The mobility of the particles η was approximated as the viscosity of the solvents which can be calculated from the diffusion coefficients of the solvent molecules.

Table 4.3: Diffusion coefficients and further data for the compounds studied in ^{1}H DOSY NMR experiments.

	nanocode **21**	**Sm-16**	**Lu-bpy$_3$O$_2$-D$_4$**	magainin I	angiotensin II	kemptide
-pD [log(m^2/s)]	9.38	9.32	9.20	9.57	9.63	9.58
D [10^{-10} m^2/s]	4.17	4.82	6.37	2.68	2.35	2.66
η_{solv} [mPa s]	0.59	0.61	0.59	0.68	1.10	1.09
M [g/mol]	3579.01	1366.63	646.20	2409.85	1046.18	771.92
$D \cdot \eta_{solv}$ [10^{-10} mPa m^2]	2.46	2.93	3.78	1.81	2.58	2.89
$1/M$ [10^{-3} mol/g]	0.28	0.73	1.55	0.41	0.96	1.30

According to equation 11 the product of D and η will be indirectly proportional to the radius r. Furthermore for closely related molecules with similar shapes and densities r should in some way correlate with the mass of the molecules under study. In principle this is equivalent to the intuitive expectation that heavier species will diffuse slower than lighter ones. While this approach indeed neglects many important properties and differences of the compounds under study, it has the clear advantage that the molar mass can easier be quantified than the exact density of a molecule or its shape during a ^{1}H DOSY experiment. Based on these consideration the results obtained from the performed ^{1}H DOSY experiments were interpreted assuming the following correlation to be valid:

$$D \cdot \eta \propto \frac{1}{M} \tag{12}$$

for:

$$T = const. \tag{13}$$

The corresponding plot of the results from the ^{1}H DOSY experiments as summarised in Table 4.3 is shown in Figure 4.45. If the data points obtained for peptides and cryptates are considered independently from each other for both groups a linear correlation can be found. The fact that no single correlation for all studied

compounds was found reflects the limitations of the assumptions made above. But for closely related molecules with a similar shape and density, like the studied small peptides, this simple approximations gives surprisingly good results. Also for the studied cryptates the properties relevant for the diffusion coefficients can be assumed to be comparable. All three molecules should have comparable densities and polarities. Assuming that correlation 12 is as valid for the comparison of the cryptates studied herein, as it was found to be for the peptides studied, the diffusion coefficient determined for **21** is completely in line with expectations for a cryptate compound of this molar mass, which strongly points towards the successful preparation of the nanocode. However, to prove this unambiguously some further studies are in progress, for example the analysis of the material with high resolution ESI-MS and via ICP-MS.

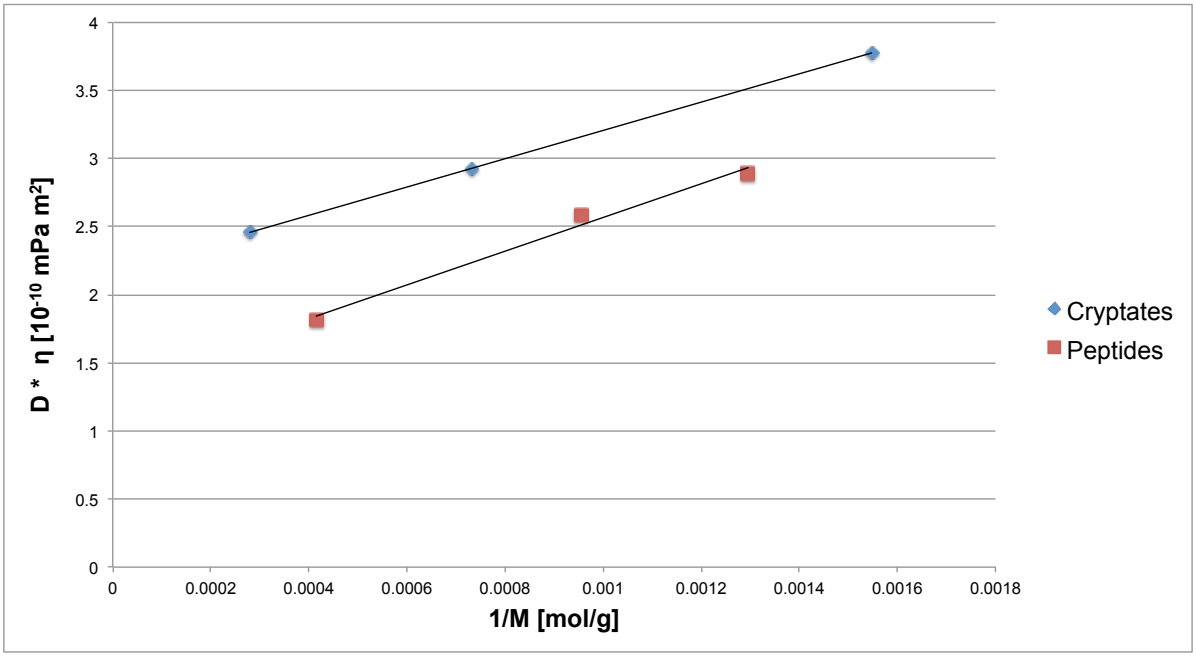

Figure 4.45: Plot of the products of the determined diffusion coefficients and the viscosity of the solvents versus the reciprocal molar mass of the compounds studied via ^{1}H DOSY NMR experiments, see Table 4.3.

In conclusion, the results from luminescence spectroscopy and the ^{1}H DOSY NMR experiments performed so far strongly point towards the successful preparation of the nanocode **21**. Considering the experimental procedure performed for synthesis, the detection of all three lanthanoids in the steady state emission spectrum makes a successful realisation of the shown synthesis sequence very plausible. The findings from ^{1}H DOSY NMR, pointing to the presence of a molecule of the expected size, give additional evidence.

4.4 Conclusion

One of the most innovative applications which came into reach with the preparation of lanthanoid cryptates carrying a peripheral functionalisation is the construction of a molecular nanocode based on lanthanoid cryptates, which was the aim of this project. As building blocks the amino acid-functionalised lanthanoid cryptates **Ln-16** were developed and characterised. The beneficial photophysical properties of the lanthanoids were found to be invariant towards the extended functionalisation at the periphery.

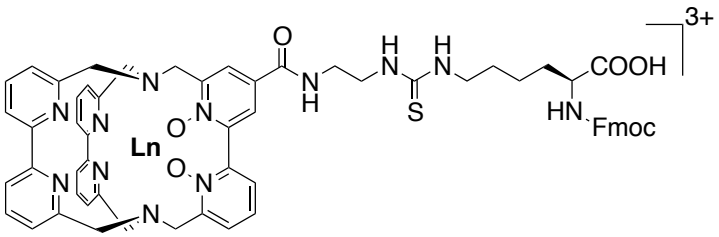

Ln-16

Figure 4.46: Structure of the amino acid-functionalised lanthanoid cryptates **Ln-16**.

Subsequently in solid phase peptide synthesis experiments of increasing complexity the reactivity of the amino acid attached to the cryptate was studied. The cryptates **Ln-16** were found to be completely compatible with standard procedure of this well established technique. This opens up interesting possibilities for different aspects of research, as it will now be possible to introduce a lanthanoid cryptate into the sequence of a peptide during SPPS.

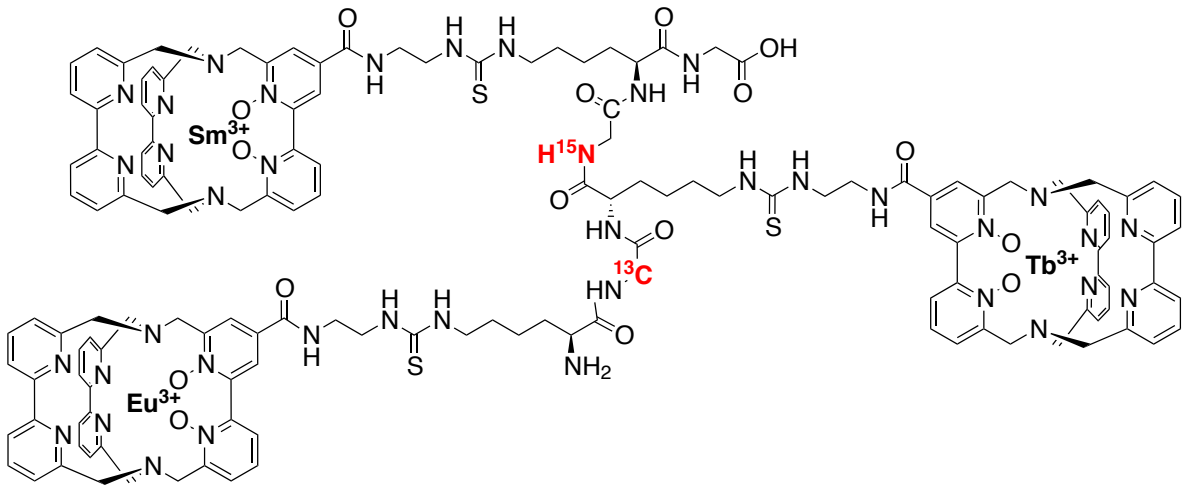

21

Figure 4.47: Structure of the molecular nanocode **21** in which Sm^{III}, Tb^{III} and Eu^{III} cryptates are covalently attached to each other via a peptide backbone.

After the preliminary experiments testing the reactivity of the complexes **Ln-16**, finally the first molecular nanocode could be prepared as a peptide consisting of three different lanthanoid cryptates. Luminescence spectroscopy could unambiguously prove the presence of Sm^{III}, Tb^{III} and Eu^{III} in the material isolated, which already gives strong evidence of the synthesis being successful. The results from ^{1}H DOSY NMR also give evidence of the successful preparation of the molecular nanocode **21**.

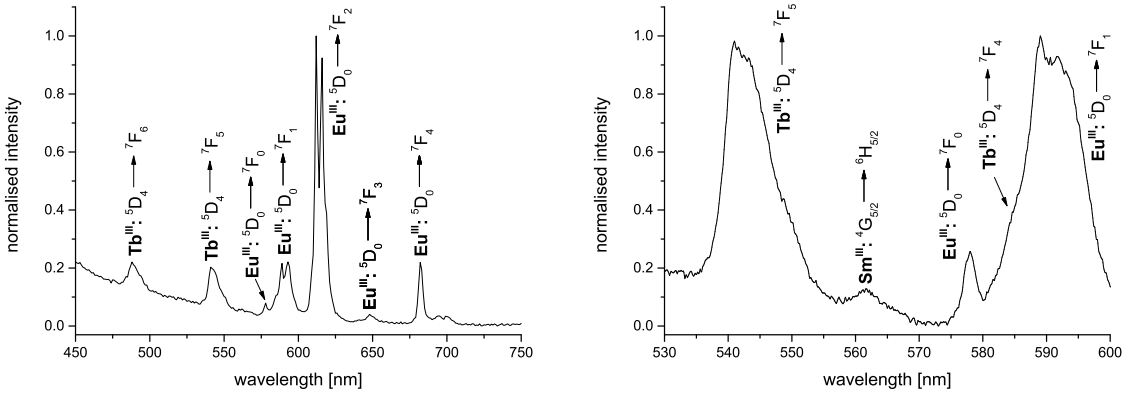

(a) CD_3OD, $\lambda_{exc} = 320$ nm, excitation path: long pass filter LP399.

(b) CD_3OD, $\lambda_{exc} = 320$ nm, excitation path: long pass filter LP399.

Figure 4.48: Normalised steady state emission spectra of **21** giving evidence of the successful preparation of the first molecular nanocode consisting of three different lanthanoids.

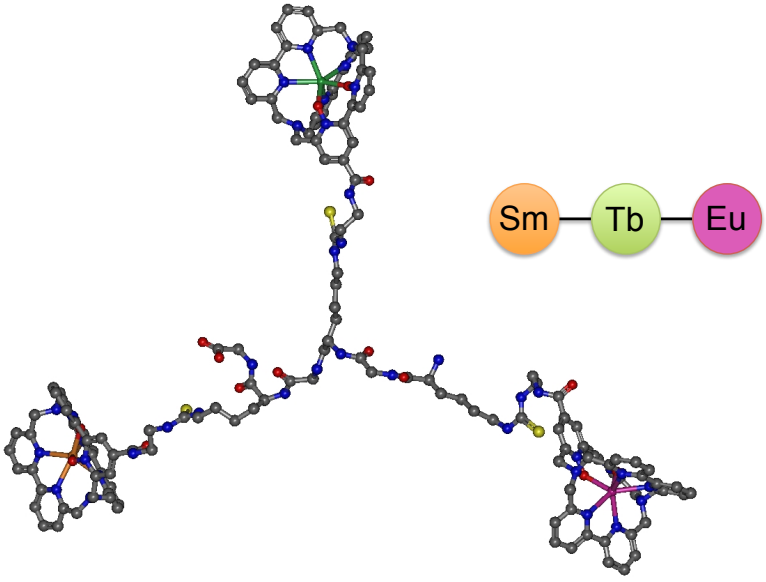

Figure 4.49: Molecular structure of the realised nanocode, obtained from geometry optimisation with MOPAC (charges and hydrogen atoms omitted for clarity).

The preparation of discrete molecules with more than two lanthanoids attached to another in a very con-

trolled process is highly innovative and can only be realised when a highly reliable ligand core scaffold like the cryptates **bpy$_3$O$_2$** is combined with well established building blocks like the amino acids, as it was realised with the cryptates **Ln-16**.

5 Enantiopure Lanthanoid Cryptates

5.1 Introduction

Chirality is a fundamental concept which can be found in the macroscopic everyday life and on the molecular level, as such it is omnipresent in diverse fields of science and technology. Any object which cannot be superimposed with its mirror image is chiral, and as indicated by this relatively general definition, chirality can be manifested in different ways, also on the molecular level.[232][233]

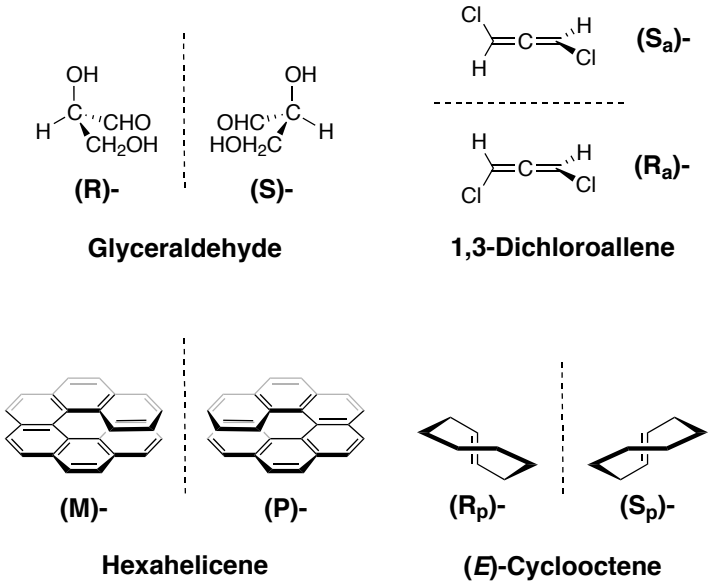

Figure 5.1: Chiral molecules which are archetypical for different forms of molecular chirality.

Figure 5.1 shows enantiomeric pairs of some molecules which can be considered archetypical for the type of chirality they exhibit. The central carbon atom of **glyceraldehyde** is bound to four substituents which are arranged in a tetrahedral fashion. As they all are different this makes the central carbon atom an asymmetric carbon atom and the stereogenic center of glyceraldehyde, which exhibits point chirality. In contrast to that, the stereogenic element of for example **1,3-dichloroallene** is an axis of chirality, and accordingly the substance is referred to as axially chiral. A special case of the axial chirality is the helical chirality, as it is exhibited by **hexahelicane**. In this case the molecule is winding around the axis of chirality in a helical fashion, as it can be found for many big biomolecules, such as DNA, amylose or some proteins. Another manifestation of molecular chirality is planar chirality, as it can be found in the case of (*E*)-cyclooctene.
When the properties of a molecule which emerge from its chirality are to be exploited for some kind of

application or study, typically enantiopure samples are desired. For organic molecules or coordination compounds of transition metals, in many cases an excellent control over their stereogenic elements is possible, so that the compounds can either be prepared in an enantiopure fashion or the racemic mixture can be separated into pure enantiomers. Again the situation is by far more difficult in the case of lanthanoid coordination compounds. Indeed most lanthanoid coordination compounds exhibit at least one stereogenic element, but their intrinsically high coordinative flexibility and their proneness to undergo decomplexation paves the way for various isomerisation processes, of course also including racemisation. At the same time enantiopure lanthanoid complexes are highly interesting target compounds. As already outlined in chapter 3.3.5 they have high potential for the structural elucidation of biomolecules in solution. Here the need for enantiopure compounds emerges from the fact that the biomolecules under study are chiral and so the use of racemic lanthanoid compounds would lead to the formation of diastereomers and a significant complication of the analysis. Another reason for the high interest in enantiopure lanthanoid coordination compounds is the unparalleled suitability of these compounds for the observation of circularly polarised luminescence.

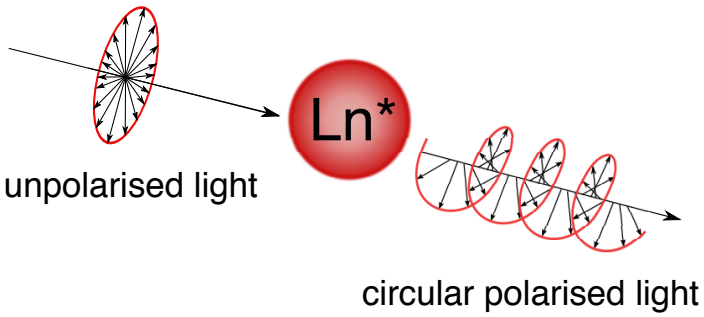

Figure 5.2: Under excitation with unpolarised light, a CPL emitter (like for example a nonracemic chiral lanthanoid complex) preferentially emits left or right polarised light.

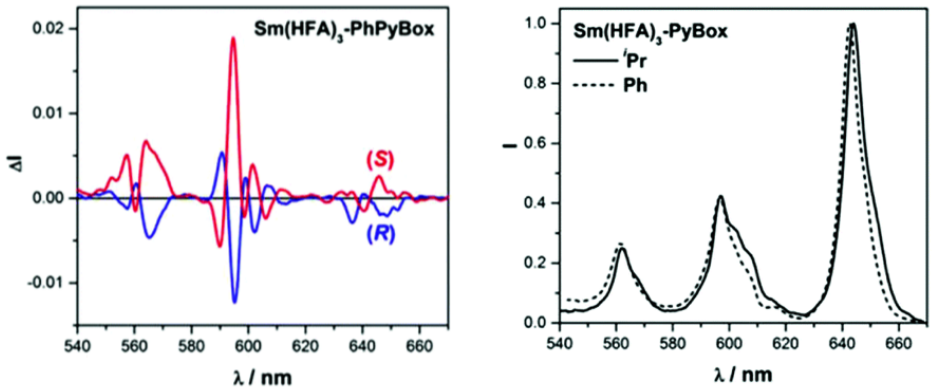

Figure 5.3: Circularly polarised (left) and total luminescence (right) of Sm^{III} complexes with a diketonate (HFA) and a PyBox-derivative (see below).[234] Comparison of both spectra reveals that from the CPL spectrum information about the fine structure of the transition and the crystal field parameters is by far more accessible.

Circularly polarised luminescence (CPL)[235][236][237][238][239][240] can be seen as the emission analogue to circular dichroism (CD). Under excitation with unpolarised light, a compound which exhibits CPL preferentially emits left or right polarised light, whereby the observable direction of rotation is typically wavelength specific. As it is the case for any kind of optical activity, in a racemic mixture the effects cancel out, but when an enantiopure sample is available the substance specific CPL properties can be quantified by comparison of the CPL spectrum and the total luminescence spectrum. Usually for this purpose the luminescence dissymmetry factor g_{lum} is calculated as the quotient of the difference of the intensities of left and right polarised light (I_L - I_R) and the half of the total intensity (I_L + I_R):

$$g_{lum} = \frac{I_L - I_R}{\frac{1}{2}(I_L + I_R)} = \frac{\Delta I}{I} \tag{14}$$

For a given transition a$\rightarrow$b, g_{lum} is dependent on both, the transitions rotary strength R_{ab} and its oscillator strength D_{ab}. The rotary strength of a transition is determined by the magnitudes and the relative orientations of the magnetic and electric dipole moments ($R_{ab} = |M_{ba}||P_{ab}| \cdot cos\ \tau_{ab}$) and its oscillator strength can be approximated with the square of the electric dipole moment ($D_{ab} = |P_{ab}|^2$), and so g_{lum} can also be calculated as:

$$g_{lum} = \frac{4R_{ab}}{|D_{ab}|} = \frac{4|M_{ba}| \cdot cos\ \tau_{ab}}{|P_{ab}|} \tag{15}$$

Differently to the total luminescence of the lanthanoids, as reflected by equation (15) and the factor $cos\ \tau_{ab}$, the circularly polarised luminescence is strongly dependent on the exact spatial arrangement of the ligands around the lanthanoid. This could already be used for the study of biomolecules,[241][242][243] but the main potential of CPL can be found in different fields of research. The polarised nature of the light emitted by CPL offers innovative possibilities for the construction of organic light emitting diodes (OLEDs)[244][245] and since the background emission of biological samples will typically be unpolarised, the use of CPL-emitters for bioimaging promises significantly improved signal to noise ratios.[246] Furthermore in CPL spectra it is often significantly easier to differentiate between the different components of a transition, so they can be helpful for the extraction of crystal field parameters (see Figure 5.3).

CPL used to be quite an exotic technique requiring custom-built devices, but as commercial spectrometers became available the technique gained more attention and first applications are coming into reach. In principle any chiral luminescent compound can exhibit CPL, but whereas purely organic molecules typically exhibit g_{lum} values between 10^{-4} and 10^{-2},[239] lanthanoid complexes can outperform this by orders of magnitude as their g_{lum} values usually lay between 0.1 and 1.[235][238] Indeed the suitability of the different lanthanoids for the observation of CPL differs largely. Generally (as is reflected by equation (15)) transitions which are magnetic dipole allowed and electric dipole forbidden (ΔJ = 0, ±1; except J' = J" = 0) offer optimal preconditions for the observation of CPL as long as any process is active which leads to the electric dipole moment P_{ab} being nonvanishing. The two limiting cases which can be operating in this sense are the static and the dynamic coupling mechanism. Conceptually they can be distinguished from whether the

coordination polyeder itself is chiral or not, and experimentally the operating mechanism can be studied for example by recording circular dichroism spectra of the Yb^{III} derivative of the complex of interest.[238][247] Already in 1980 Richardson deduced the general suitability of the lanthanoids' transitions for the observation of CPL and sorted them into corresponding classes (see Table 5.1).

Table 5.1: Lanthanoid ions and their luminescence transitions which typically exhibit sizeable CPL signals, with the corresponding wavelengths and their classification following Richardson.[248][238]

ion	transition	wavelength [nm]	class following Richardson[248]
Sm^{III}	$^4G_{5/2}\rightarrow{}^6H_{5/2}$	565	*DII*
	$^4G_{5/2}\rightarrow{}^6H_{7/2}$	595	*DIII*
Eu^{III}	$^5D_0\rightarrow{}^7F_1$	595	*DI*
Tb^{III}	$^5D_4\rightarrow{}^7F_5$	545	*DII*
Dy^{III}	$^4F_{9/2}\rightarrow{}^6H_{11/2}$	670	*DIII*

As a consequence of the purely magnetic dipole character of the $^5D_0\rightarrow{}^7F_1$-transition of Eu^{III}, according to Richardson for this transition the largest g_{lum} values can be expected, this transition is the single example representing the class *DI* easily accessible to CPL measurements. Indeed Eu^{III} is the lanthanoid of which the most examples of CPL active compounds were reported and typically the first choice when the CPL properties of a new ligand are to be studied. Both, the $^4G_{5/2}\rightarrow{}^6H_{5/2}$ transition of Sm^{III} and the $^5D_4\rightarrow{}^7F_5$ of Tb^{III} are categorised as class *DII*, and consequently according to Richardson for both transitions decent g_{lum} values can be expected. But while CPL of Tb^{III} complexes is quite commonly reported,[249][250][251][252][253] examples for enantiopure Sm^{III} complexes which exhibit CPL are scarce.[254][255][256][257][258][259][234][260] Importantly, this is not in contradiction with Richardson's classification. Tb^{III}, which is largely insusceptible towards nonradiative deactivation via multiphonon quenching, is typically strongly luminescent, which of course facilitates the measurement of CPL. In contrast to that, Sm^{III} is only relatively weakly luminescent under most conditions, so a good signal to noise ratio in a CPL measurement will be much more difficult to realise in the case of a Sm^{III} complex.

Generally, Richardson's classification of the transitions has proven to be reliable and successful. In contrast to that, the influence of the crystal field on the CPL properties of a given complex has been only poorly understood until now. A detailed understanding of the way the arrangement of the coordinating atoms has an impact upon the CPL emission of the coordinated lanthanoid ion would pave the way for a tailored design of CPL luminophores. The intrinsically low conformational stability of lanthanoid complexes can be considered to be the main obstacle for a development of the necessary understanding. For example a sample of a DOTA-type complex in solution should be considered to be a mixture of different interconverting species. If this sample is CPL-active, in most cases it will not be possible to determine which species contributes to this optical activity to what extent and how their exact spatial structure in solution is. At least the second problem will be encountered for most lanthanoid complexes, and consequently until now it was not possi-

ble to establish reliable structure-property correlations for CPL-active lanthanoid coordination compounds. Nevertheless there have been some efforts, in most cases based on crystallographic data. For example in 2002, Bruce *et al.* presented a comparative study in which the structural and CPL properties of several DOTA-type Eu^{III} complexes with twisted square antiprismatic or capped twisted square antiprismatic coordination geometries were analysed.[261] The authors related the local helicity around the lanthanoid ion to the angle between the magnetic and electric dipole transition moment vectors and concluded, that the angle of twist about the principal axis Θ will define the CPL activity of these compounds. They predicted 22.5° to be the optimum value for Θ, and as the average coordination geometry of the emission timescale is determinative, they noted that the rigidity of the complex will also be of influence. Indeed in this study the complexes with a higher rigidity were found to be also the ones with higher g_{lum} values. Furthermore the authors stated that a highly polarisable axial ligand will result in a more intense total luminescence intensity of the $\Delta J = 2$ transition, but will minimise the luminescence dissymmetry factor for this transition.

The highest luminescence dissymmetry factor reported until now was found for the complex Cs[Eu((+)-hfbc)$_4$] with g_{lum} values of 1.38 in solution[262] and 1.45 in the solid state[263]. In this complex the lanthanoid is surrounded by four (+)-3-heptafluorobutyryl camphorate ligands whose perfluorinated chains also enclose a caesium ion (see Figure 5.4 for the structure of the ligand). The choice of the alkali metal ion incorporated in the complex was shown to have a significant impact onto its CPL properties[262][264] and it was concluded that increased rigidity of the overall structure leads to higher g_{lum} values. In the case of Cs[Eu((+)-hfbc)$_4$] analysis of the paramagnetic ^{1}H and ^{13}C NMR shifts of the ytterbium analogue allowed for a detailed understanding of the structure of the complex in solution.[265] The diketonates are arranged in a twisted square antiprismatic geometry around the lanthanoid, with a twist around the principal axis Θ of -41.4°. This value is quite similar to the ones typically found for DOTA-derivates (Θ ~40°) and differs substantially from the optimum of 22.5° estimated by Bruce *et al.* Consequently, the twist angle (which is associated with a static coupling mechanism[238]) alone cannot account for the exceptional CPL properties. The situation becomes a bit clearer when also the dynamic coupling mechanism[238] is taken into account. If the lanthanoid and a chromophoric ligand are spatially close, the (excited) electric multipole of the lanthanoid and the ligand-centered electric multipoles can interact and give rise to a rotary strength of the transition. For this mechanism the angle between the C_4-axis and the diketonate planes is determinative, for Cs[Eu((+)-hfbc)$_4$] this angle was determined to be -27.5°, for which an efficient dynamic coupling can be expected.

Generally, rationalisation of the processes leading to CPL seems feasible, but to improve the understanding of the mechanisms underlying CPL and to establish structure-spectra correlations, clearly more examples of CPL active complexes with a stable and well-defined structure in solution are needed. Another aspect which has been largely underdeveloped until now is broadening of CPL to lanthanoid ions different than Eu^{III} and Tb^{III}. This is especially regrettable in the case of Sm^{III}. As listed in Table 5.1, the $^4G_{5/2} \rightarrow {}^6H_{5/2}$-transition of this lanthanoid ion belongs into Richardson's class *DII*, and accordingly should be of similar suitability for the observation of CPL than the $^5D_4 \rightarrow {}^7F_5$ transition of Tb^{III}. Sm^{III} also has another transition for which sizeable g_{lum} values can be expected and also exhibits transitions in the near-infrared, which might become an additional benefit: Near-infrared CPL should allow for unprecedented signal to noise ratios in studies upon biological samples. Indeed there were some initial studies[249][266] on Yb^{III}- and Nd^{III}-

centered CPL around 1999, but the publication of results stopped quickly and at the moment no instrument capable for the measurement of CPL in this part of the spectrum is available. More recently there are efforts to revive this field of study.

Most likely the lack of known CPL active Sm^{III} complexes is simply due to this lanthanoid's high susceptibility to multiphonon quenching and the resulting relatively low total luminescence which complicates the measurement of CPL. The few reported examples of Sm^{III} CPL (see Figure 5.4) do indeed reflect Richardson's classification and point towards a high potential of these compounds.

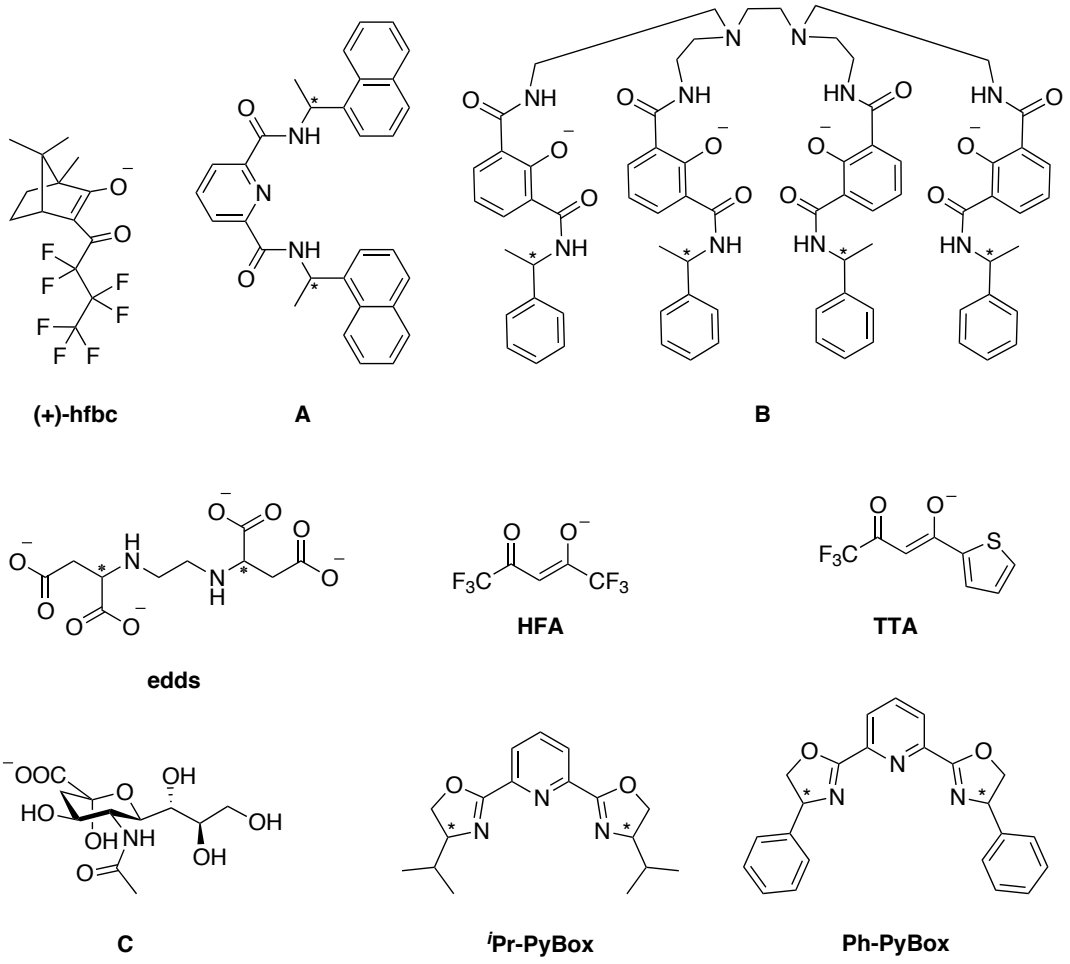

Figure 5.4: Ligands used for the preparation of CPL-active Sm^{III} complexes. (+)-hfbc = (+)-3-heptafluorobutyryl camphorate[264], A = pyridine-2,6-dicarboxylic acid bis-[(1-naphthalen-1-yl-ethyl)-amide][258], B = 1-phenylethyleneamine substituted 2-hydroxyisophtalamide[257], edds = ethylenediamine-*N,N'*-disuccinate[259], HFA = hexafluoroacetylacetonate[234], TTA = 2-thenoyltrifluoroacetonate[234], C = β-anomer of *N*-acetylneuraminic acid anion,[260], ^{i}Pr-PyBox = 2,6-Bis(4-iropropyl-2-oxazolin-2-yl)[234], Ph-PyBox = 2,6-Bis(4-phenyl-2-oxazolin-2-yl)[234]. Modified from Reference [267].

The highest g_{lum} value reported for a Sm^{III} complex was found for the respective analogue of the CPL record holder $Cs[Eu((+)\text{-hfbc})_4]$.[264] In the case of the $^4G_{5/2} \rightarrow {}^6H_{5/2}$-transition a luminescence dissymmetry factor of -1.15 was determined, for the $^4G_{5/2} \rightarrow {}^6H_{7/2}$-transition a value of +1.15 was reported. This points

towards an exceptional general suitability of this alkali metal-rigidified ligand system for the observation of CPL, and since the values reported for the Eu^{III} and the Sm^{III} complex are both in the same order of magnitude also points to the high potential of Sm^{III}-CPL. Also for the complexes of Sm^{III} and the pyridyldiamide **A** (see Figure 5.4) remarkably high g_{lum} values of 0.50 for the $^4G_{5/2}\rightarrow{}^6H_{5/2}$-transition and 0.28 for the $^4G_{5/2}\rightarrow{}^6H_{7/2}$-transition were reported.[258] Also ligand **B**, a chiral derivate of the IAM-ligand, is suitable to generate CPL-active Sm^{III} complexes, with g_{lum} values of -0.027 ($^4G_{5/2}\rightarrow{}^6H_{5/2}$) and -0.028 ($^4G_{5/2}\rightarrow{}^6H_{7/2}$), respectively.[257] In the case of ligand **edds** only for the typically more luminescent transition $^4G_{5/2}\rightarrow{}^6H_{7/2}$ a g_{lum} value could be reported (+0.066).[259] Using the Raman optical activity (ROA) technique CPL activity of samples consisting of the *N*-acetylneuraminic acid anion **C** and Sm^{III} could be detected. The authors reported circular intensity differences (CID) in the range of 10^{-2} to 10^{-3}. In a recent publication diketonates and PyBox derivatives were combined to prepare four different but related Sm^{III}complexes **Sm(diketonate)$_3$-PyBox** which all do show CPL emission.[234] While the three diketonates provide a relatively high stability, the additional PyBox ligands introduce chirality to the overall complex. $Sm(HFA)_3$-$_i$PrPyBox turned out to show the most intense CPL transition ($|g_{lum}| = 0.18$ for $^4G_{5/2}\rightarrow{}^6H_{7/2}$ and $|g_{lum}| = 0.013$ for $^4G_{5/2}\rightarrow{}^6H_{9/2}$), for the $^4G_{5/2}\rightarrow{}^6H_{7/2}$-transition the strongest CPL was reported for $Sm(TTA)_3$-^{i}PrPyBox ($|g_{lum}| = 0.08$). The authors characterised the compounds with several techniques such as circular dichroism (CD) and vibrational circular dichroism (VCD) and their approach could become valuable for the development of a more quantitative understanding of CPL. Yet it should be kept in mind that the compounds dealt with in this study are present as a mixture of different conformers. Interestingly, for many of the Sm^{III} complexes for which CPL was reported, for the $^4G_{5/2}\rightarrow{}^6H_{5/2}$-transition and the $^4G_{5/2}\rightarrow{}^6H_{7/2}$-transition similar g_{lum} values were reported, though according to Richardson's classification g_{lum} would be expected to be considerably higher in the case of the former transition.

For a simplified overview, the presented examples for Sm^{III}-centered CPL and additional photophysical data (if available) of several complexes discussed above are summarised in a table which can be found in the appendix (see page 334). However, upon direct comparison of the complexes it should be kept in mind that the values were obtained from samples in different solvents and that for example a well-defined structure of the complexes is not always given.

As already addressed in chapters 1.3 and 3, lanthanoid cryptates **Ln-bpy$_3$O$_2$** are chiral. They exhibit axial or helical chirality with their axis of chirality being perpendicular to the C_2-symmetry axis and going through the two tertiary amines which connect the three bipyridines. Both building blocks which are assembled for synthesis of the unfunctionalised ligand **bpy$_3$O$_2$** are achiral, yet in the case of the oxidised dibromide **bpyO$_2$Br$_2$** the steric demand of the two oxygen atoms will lead to the presence of two interconverting structures of identical energy, which can be considered comparable to atropisomers (see Figure 5.5).[233] However, both organic building blocks can be considered to be relatively flexible. This is not the case in the assembled macrobicyclic structure. For steric reasons, the coordinated metal ion will be placed at least partly between the oxygen atoms, which will raise the energetic barrier between the possible arrangements of the oxidised pyridines and induce a corresponding overall rigidity of the scaffold. This is for example reflected in the ^{1}H NMR spectra of the cryptates, which do not give any evidence of interconversion processes. Until now all experimental findings indicate that even under challenging condition no interconversion of the two enantiomeric forms of **Ln-bpy$_3$O$_2$** can take place. As both arrangements of the

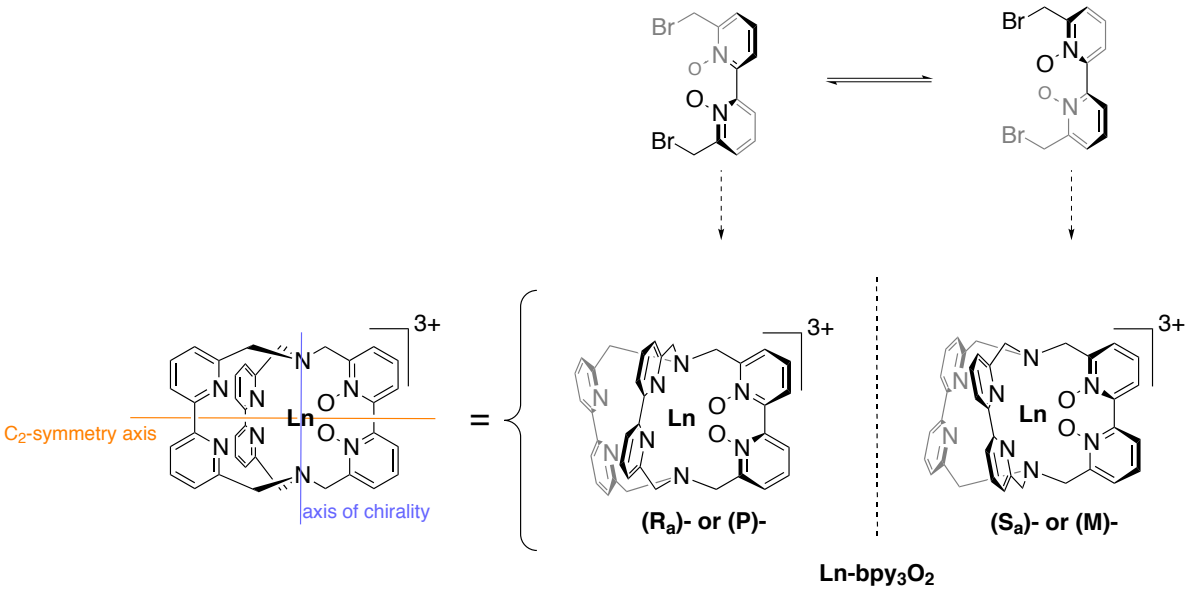

Figure 5.5: Lanthanoid cryptates exhibit axial/helical chirality. Both building blocks employed in the synthesis of the ligand are achiral, yet the atropisomer character of the oxidised bipyridine relates to the chirality found in the assembled scaffold.

oxidised bipyridine are of identical energy and no chiral discrimination occurs during the macrobicyclisation step, these compounds are always obtained as racemic mixture from synthesis. The non-availability of enantiopure samples hampered a more detailed study of a possible racemisation of **Ln-bpy$_3$O$_2$** or the corresponding energetic barrier until now.

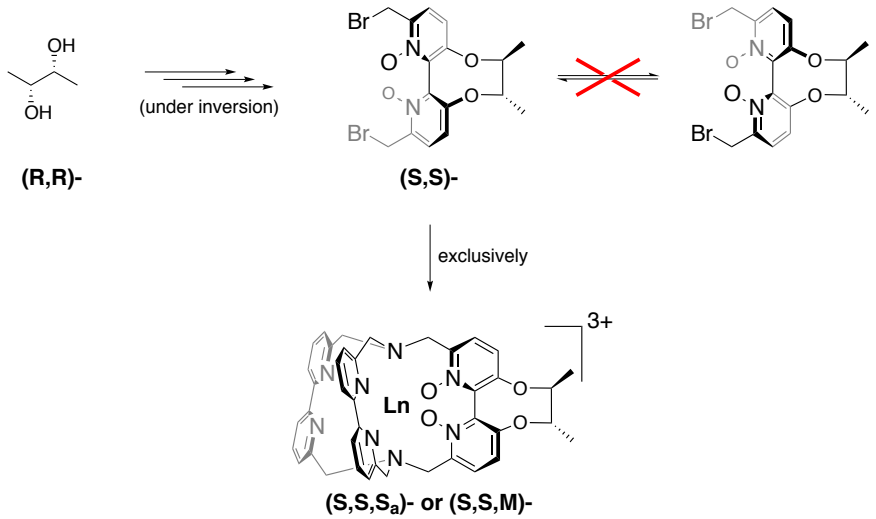

Figure 5.6: The principle of the synthesis of an enantiopure lanthanoid cryptate starting from enantiopure (R,R)-2,3-butanediol as initial chiral building block.

Yet it is possible to prepare enantiopure derivatives of the core structure **Ln-bpy$_3$O$_2$**.[134] Similarly to the preparation of the derivatives carrying a reactive functionalisation discussed in chapter 3, the key building

block to do so is a modified dibromide of the oxidised bipyridine. By introduction of an enantiopure tether derived from 2,3-butanediol, the relative orientation of the pyridines of this unit can be controlled (see Figure 5.6). The steric strain induced by the methyl groups at the eight-membered ring directs them into equatorial positions and presets the overall orientation of the ring and the attached pyridines. The presumed impact on the macrobicyclisation reaction could be proven by combined NMR and DFT studies. For the theoretically possible diastereomers **Yb-(S,S,S_a)-bpy$_3$O$_2$** and **Yb-(S,S,R_a)-bpy$_3$O$_2$** full geometry optimisations using DFT calculations were performed and resulted in an optimised structure for **Yb-(S,S,S_a)-bpy$_3$O$_2$** (see Figure 5.7(a)) which is by 23.7 kJ mol^{-1} more stable than the one found for **Yb-(S,S,R_a)-bpy$_3$O$_2$**. The ^{1}H NMR spectrum was found to be consistent with the presence of a single C_2-symmetric species and an analysis of the "lanthanoid induced shifts" (LIS) found a better agreement with the (S,S,S_a), than with the (S,S,R_a) enantiomer. The enantiopurity of the sample was proven by ^{1}H NMR experiments in chiral solvents (see Figure 5.7(b)).

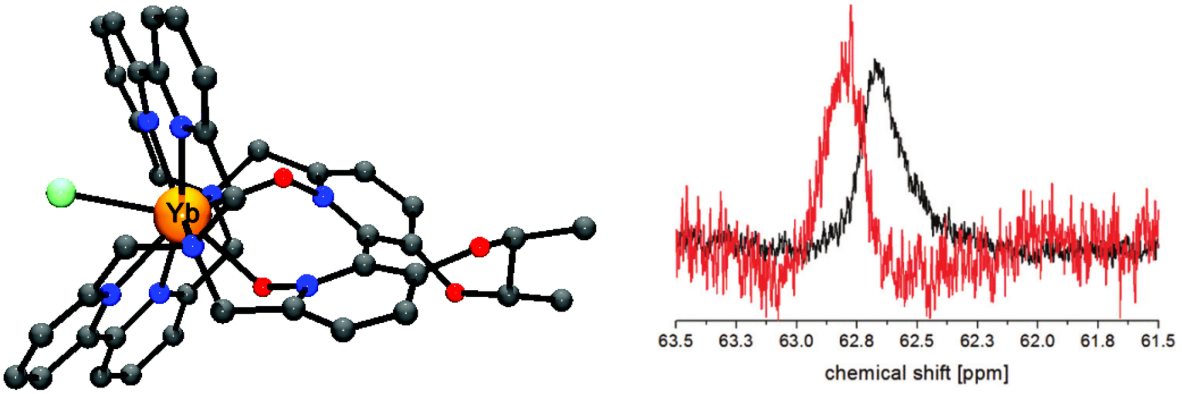

(a) DFT optimised structure of the energetically strongly preferred diastereomer **Yb-(S,S,S_a)-bpy$_3$O$_2$**. Grey: carbon, blue: nitrogen, red: oxygen, turquoise: chloride, orange: Yb^{III}. Hydrogen atoms are omitted for clarity.

(b) Single signal from the ^{1}H NMR (250 MHz, methyl lactates/CD_2Cl_2, 11:1 v/v, TMS) of the cryptate **Yb-(S,S,S_a)-bpy$_3$O$_2$** in enantiopure solvents (red: methyl D-lactate, black: methyl L-lactate).

Figure 5.7: Optimised DFT structure calculated for the enantiopure lanthanoid cryptate and ^{1}H NMR data of the compound in enantiopure solvents. Figures adopted from reference [134].

In the course of the study, no loss of configurational information could be observed, yet the stability against such processes had not been tested directly. With respect to the unfunctionalised cryptate **Ln-bpy$_3$O$_2$** this would also provide only very limited information since the tether introduced for the enantiopure synthesis is very likely to make the overall complex more stable against any isomerisation process than the parent compound. Independently from that, the general accessibility of enantiopure lanthanoid cryptates offers exciting new possibilities, most importantly in the study of their CPL properties. Due to their fundamental properties the rigid lanthanoid cryptates have high potential to be efficient CPL emitters and importantly could also pave the way to an improved understanding of CPL. Unlike most chiral lanthanoid complexes they exhibit an extremely well-defined structure in solution and analysis of the lanthanoid induced shifts together with DFT calculations has proven to be extremely successful for the determination of the exact

structure of cryptates in solution. Earlier studies indicated that the rigidity itself might also be beneficial for the observation of CPL. Finally the suitability of (deuterated) cryptates to efficiently sensitise and protect the lanthanoids which are especially prone to undergo nonradiative deactivation processes, such as e.g. Sm^{III} or Yb^{III}, points towards a high suitability of these compounds for the preparation of CPL-active complexes of these lanthanoids.

The extraordinary stability of the cryptates of the type **bpy$_3$O$_2$** against decomplexation processes might also allow for a fundamentally different approach for the preparation of enantiopure lanthanoid cryptates, which is the separation of racemic mixtures as obtained from the regular synthesis (see Figure 5.5) via chiral HPLC. Generally it is of course favourable and more efficient to prepare both enantiomers simultaneously and separate them in a subsequent step. Unfortunately, most lanthanoid complexes cannot be purified via HPLC at all, since the typically applied conditions (e.g. low pHs) lead to decomposition. Even in cases where the overall stability might be sufficient, under such conditions rapid interconversion processes are highly favoured and would lead to the loss of any chiral information. Until now only for a group of closely related complexes based on trispyridylphosphinate substituted 1,4,7-triazacyclononanes separation into enantiopure samples via chiral HPLC was reported. Lanthanoid cryptates **Ln-bpy$_3$O$_2$** can easily be purified via reversed phase HPLC and typically the stability of the complexes against decomplexation is not an issue in this context. In the light of the high rigidity of these compounds a separation into both enantiomers via chiral HPLC might also be possible.

5.2 Conception of the Project

The intrinsically low stability of lanthanoid complexes is a major obstacle in the preparation of enantiopure lanthanoid complexes and the detailed study of their structure in solution. In contrast to that, the high rigidity of the lanthanoid cryptates gives the best prerequisite for a closer study of their chirality and related phenomena, such as CPL.
This will be conducted with two independent approaches:

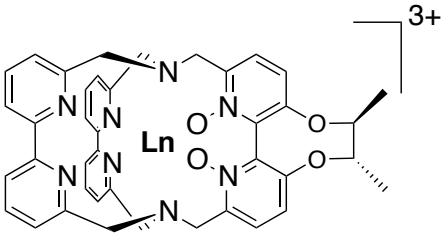

Ln-bpy$_3$O$_2$-*SS*-(Me)$_2$

- **Initial study of the chiroptical properties of luminescent lanthanoid complexes with an enantiopure cryptand scaffold**

The cryptates obtained from enantiopure synthesis have mainly been structurally characterised until now. No complexes of this ligand which are emissive in the visible part of the electromagnetic spectrum have been prepared so far. During this study the preparation of corresponding complexes will allow for an in-depth comparison of the properties of the complexes obtained from enantiopure synthesis to the one from racemic synthesis. More importantly these complexes will allow for the first studies of the CPL properties of lanthanoid cryptates.

- **Separation of lanthanoid cryptates prepared as racemic mixture into pure enantiomers**

The preparation of enantiopure samples of the unmodified, racemic lanthanoid cryptates **bpy$_3$O$_2$** (for example via chiral HPLC) would allow for detailed studies of the stability against configurational rearrangements or decomplexation processes. Furthermore, the comparison of the CPL properties of these compounds to the ones of the samples from enantiopure synthesis might give interesting insights in how far subtle changes of the coordination geometry affect them.

5.3 Results and Discussion

5.3.1 Chiroptical studies on enantiopure lanthanoid cryptates

Circularly polarised luminescence is one of the emerging topics in lanthanoid coordination chemistry. Until now the fundamental understanding of this highly interesting phenomenon (and consequently also the realisation of concrete applications) was hindered by a lack of CPL-active systems which allow for an in-depth study of how their structure and crystal field influence the CPL properties. The outstanding potential of the lanthanoid cryptates to illuminate these relations is obvious and one of the aims of this chapter is to provide first results towards this. At the same time the cryptates' outstanding ability to protect the coordinated lanthanoid against nonradiative deactivation processes shall be used to help establish the CPL of the lanthanoids more sensitive towards multiphonon quenching. The most important example being Sm^{III}. Though its high potential for the preparation of highly CPL active compounds is predicted by theory and there is also experimental evidence, CPL of Sm^{III} has been underdeveloped so far.
With the enantiopure cryptates which could already be realised by the aid of an enantiopure tether attached to one of the bipyridines, a highly suitable system for the aim of this study was already available.[134] To improve prospects for the observation of intense luminescence of the lanthanoids more susceptible to nonradiative deactivation, the partially deuterated derivative **22** (see Figure 5.8) was chosen for this study. Generally deuteration of the benzylic positions of the cryptates **bpy_3O_2** was already found to be especially effective to enhance the luminescence of these compounds.[133][135][139][268] An efficient trade-off between efficient ligand synthesis and optimisation of the photophysical properties offers the deuteration of only the benzylic positions of the non-oxidised bipyridines. Herein the deuterated and the enantiopure building blocks of the synthesis are connected in the very last step of ligand assembly, and the synthesis of the enantiopure bipyridine derivative is not further complicated by deuteration.

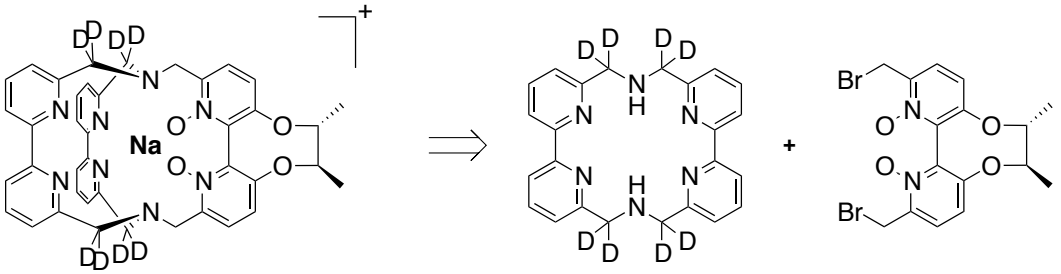

Figure 5.8: The partially deuteration of the cryptate **Na-22** can be realised with an efficient synthesis in which the deuterated and the enantiopure building blocks are assembled in the last step of ligand assembly.[134]

For this study the corresponding Eu^{III} and Sm^{III} cryptates were prepared analogously to a procedure known for the Yb^{III} complex before[134] and purified via recrystallisation to yield both complexes in 61% yield (see Figure 5.9). The identity of the complexes could be confirmed via ^1H NMR spectroscopy and high resolution ESI-MS, via analytical HPLC the absence of any residual sodium cryptate in the material isolated could be established (see page 331 in the appendix).

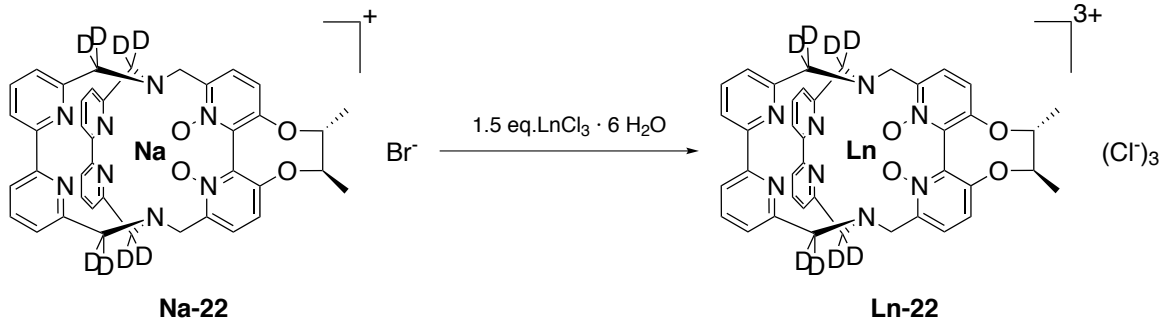

Na-22 **Ln-22**

Figure 5.9: Preparation of the lanthanoid cryptates **Ln-22** from the corresponding sodium cryptate **Na-22**.[134]

The ^{1}H NMR spectra of the complexes in CD_3OD (see Figure 5.10 and Figure 5.11) reflect the C_2-symmetry of the compounds, their well-defined structure and the absence of any interconversion processes between different isomers. In the case of **Eu-22** the signals of the protons which experience the most pronounced paramagnetic shift in the case of **Eu-1** can no longer be observed as a result of the deuteration. Most signals are well separated from each other, only for signals in the range between 3.0 to 2.5 ppm and 1.0 to 0.7 ppm signals are overlapping which prevents integration. In line with the C_2-symmetry of the compound a total of seven signals with an integral of two protons, one multiplet with an integral equivalent to six protons and one multiplet representing eight protons can be identified. In analogy to the previously discussed NMR spectra the signals which experience the strongest paramagnetic shift can be assigned to the benzylic protons and the signal of the six CH_3-protons can be identified at 0.85 ppm.

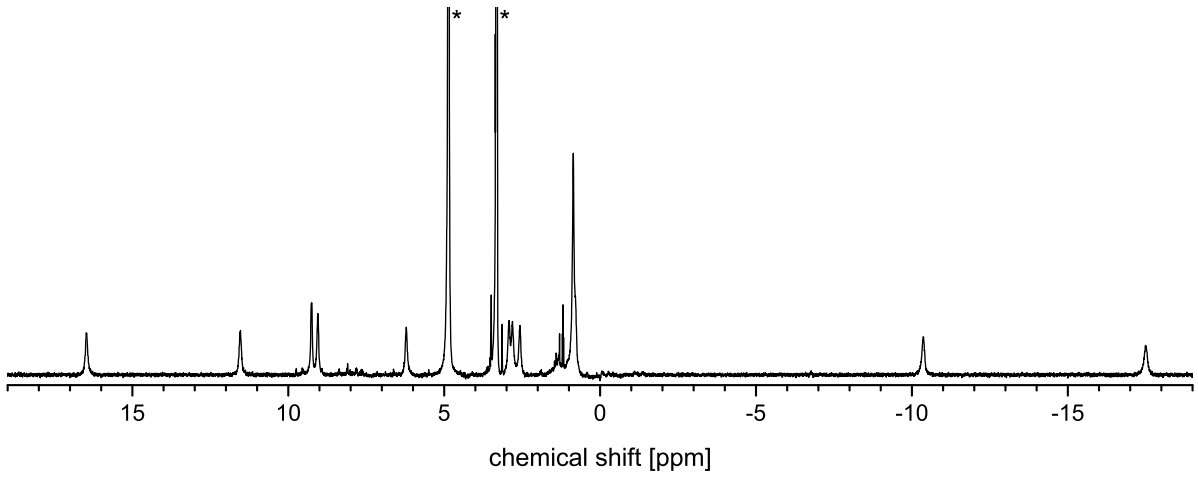

Figure 5.10: ^{1}H NMR spectrum (400 MHz, CD_3OD) of the enantiopure europium cryptate **Eu-22**. Unambiguously identified solvent signals are marked with an asterisk. Modified from reference [267].

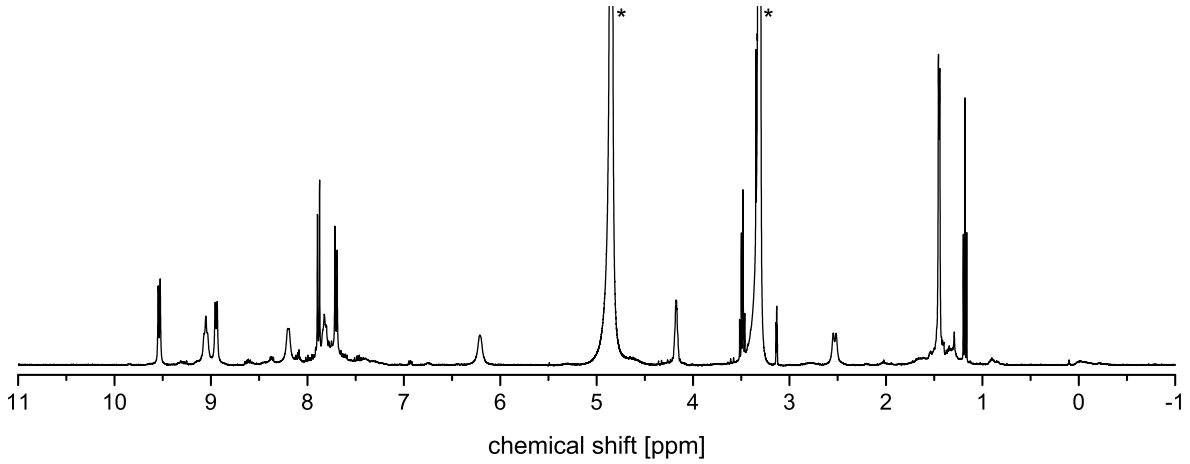

Figure 5.11: ^{1}H NMR spectrum (400 MHz, CD_3OD) of the enantiopure samarium cryptate **Sm-22**. Unambiguously identified solvent signals are marked with an asterisk. Modified from reference [267].

Due to the weak paramagnetism of Sm^{III} and the relatively long distance between the aromatic protons and the paramagnetic center, for **Sm-22** the aromatic protons can be expected to be virtually unshifted and correlate to 14 of the 16 protons of the partially overlapping signals observed between 9.8 and 7.5 ppm. Also the signals of the CH_3-groups will not experience a considerable shift and can be assigned to the signal at 1.45 ppm with an integral of six protons.

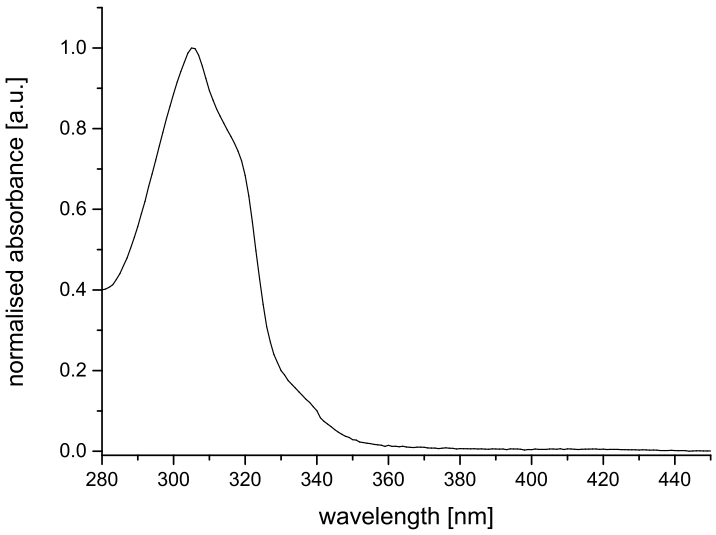

Figure 5.12: Normalised UV/Vis spectrum of **Eu-22** in CD_3OD.

Until now the general luminescence properties of cryptates **Ln-22** emitting in the visible part of the electromagnetic spectrum had not been studied. To provide a basis for a comparison to the unfunctionalised lanthanoid cryptates **Ln-bpy$_3$O$_2$**, prior to the investigation of the CPL properties a thorough photophysical characterisation of the corresponding europium and samarium complexes was performed. As expected, the shape of the normalised UV/Vis spectrum of both complexes (see Figure 5.12 for the one of **Eu-22**)

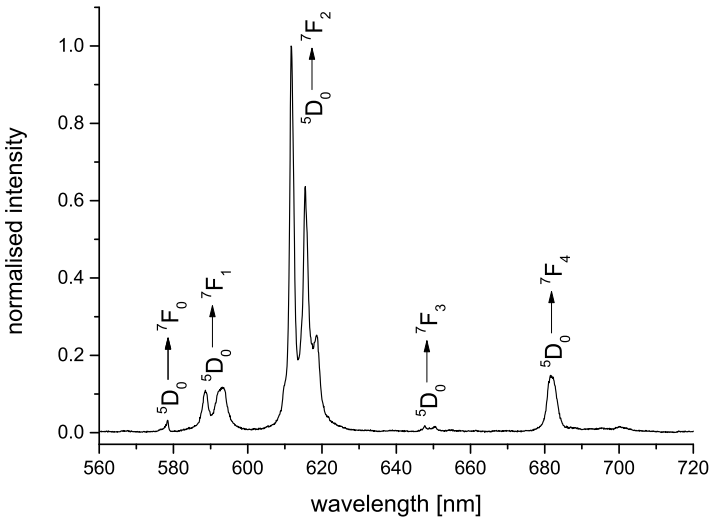

Figure 5.13: Normalised high resolution steady state emission spectrum of **Eu-22** (CD_3OD, λ_{exc} = 305 nm). Modified from reference [267].

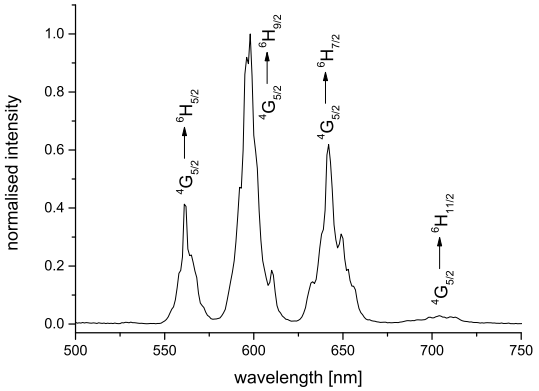

(a) Normalised high resolution steady state emission spectrum of the emission in the visible part of the electromagnetic spectrum.

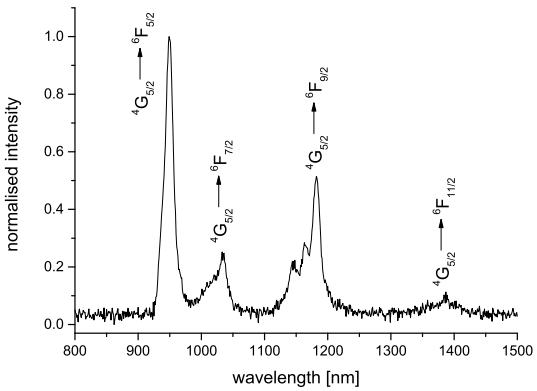

(b) Normalised steady state emission spectrum of the emission in the near-infrared part of the electromagnetic spectrum.

Figure 5.14: Normalised steady state emission spectra of **Sm-22** (CD_3OD, λ_{exc} = 320 nm). Modified from reference [267].

does not show any deviations to the ones of the unfunctionalised cryptates **Ln-bpy$_3$O$_2$**.

The high resolution steady state emission spectrum of **Eu-22** (see Figure 5.13) is completely in line with the presence of exactly one C_2-symmetric Eu^{III} species. The samarium complex was found to be indeed highly luminescent, so that partial resolution of the fine structure of the transitions in the visible part of the electromagnetic spectrum was possible. Furthermore also the transitions in the near-infrared could be detected (see Figure 5.14). In Table 5.2 further photophysical parameters determined for **Eu-22** and **Sm-22** are summarised. For both compounds the luminescence lifetimes τ_{obs} and the overall quantum yields Φ_{Ln}^{L} were determined. Both compounds exhibit monoexponential luminescence decays. This is again in line with the presence of exactly one luminescent species and of enormous importance for the subsequent

analysis of the CPL properties. The lifetimes are higher than the ones which were discussed earlier in this work, which can be accounted for by the deuteration of the scaffold.

Table 5.2: Luminescence lifetimes τ_{obs}, radiative lifetimes τ_{rad}, overall quantum yields Φ_{Ln}^{L}, intrinsic quantum yields Φ_{Ln}^{Ln} and sensitisation efficiencies η_{sens} of **Eu-22** and **Sm-22** in CD_3OD.

Compound	τ_{obs}	τ_{rad}	Φ_{Ln}^{L} [a]	Φ_{Ln}^{Ln}[b]	η_{sens}[c]
Eu-22	1.6 ms[d]	4.2 ms	5.9%	38%	15%
Sm-22	90 μs[e]	-	0.26%	-	-

[a] Determined using quinine in 0.5 M H_2SO_4 as reference compound, see experimental section and reference [269], [b] $\Phi_{Ln}^{Ln} = \tau_{obs}/\tau_{rad}$, [c] $\eta_{sens} = \Phi_{Ln}^{L}/\Phi_{Ln}^{Ln}$, [d] $\lambda_{exc} = 320$ nm, $\lambda_{em} = 610$ nm ($^5D_0 \rightarrow {}^7F_2$), [e] $\lambda_{exc} = 320$ nm, $\lambda_{em} = 597$ nm ($^4G_{5/2} \rightarrow {}^6H_{7/2}$).

Of course also the solvent in which the measurement is performed will have an impact on the determined lifetime. In a rough approximation, due to the absence of C-H- and O-H-oscillators, CD_3OD, CD_3CN and D_2O can be assumed to be solvents which do not cause nonradiative deactivation of the excited lanthanoid. But indeed at least the O-D-oscillators will cause nonradiative deactivation and shorten the luminescence lifetime. Analogously to general experience shorter lifetimes will be expected for measurements in D_2O and longer lifetimes can be expected in CD_3CN.[11] A rough comparison of lifetime data measured in these solvents is possible, when this is kept in mind.

While the lifetime determined for **Eu-22** is about one third higher than the corresponding value determined for the parent compounds **Eu-bpy$_3$O$_2$** in D_2O ($\tau_{obs} = 1.15$ ms),[132] the overall quantum yield Φ_{Ln}^{L} of **Eu-22** is about one order of magnitude smaller than the one reported for **Eu-bpy$_3$O$_2$** in D_2O ($\Phi_{Ln}^{L} = 30\%$)[132], which is counterintuitive. Due to the special electronic structure of Eu^{III} for the complexes of this lanthanoid some photophysical parameters can be extracted quite easily from the results of standard experiments. For example, the purely magnetic dipole character of the $^5D_0 \rightarrow {}^7F_1$-transition allows for the direct determination of the radiative lifetimes τ_{rad} from a corrected emission spectrum.[270][271] τ_{rad} can be calculated from the ratio of the integrated total emission intensity I_{tot} and the intensity of the $^5D_0 \rightarrow {}^7F_1$-transition ($I_{MD}$):

$$\frac{1}{\tau_{rad}} = A_{MD,0} \cdot n^3 \left(\frac{I_{tot}}{I_{MD}} \right) \tag{16}$$

with $A_{MD,0}$ being the probability of the spontaneous emission of the $^5D_o \rightarrow {}^7F_1$-transition in vacuo (14.65 s^{-1}) and n being the refractive index of the surrounding medium (1.326 for CD_3OD). The radiative lifetime is a measure for the theoretical lifetime of the excited lanthanoid in the absence of any nonradiative deactivation processes, and allows for the calculation of the intrinsic quantum yield Φ_{Ln}^{Ln} as the ratio of the observed luminescence lifetimes τ_{obs} and the radiative lifetimes τ_{rad}.

From the overall quantum yields Φ_{Ln}^{L} and the intrinsic quantum yields Φ_{Ln}^{Ln} finally the sensitisation efficiency η_{sens} could be determined. η_{sens} describes the efficiency of the indirect sensitisation via the antenna effect.

In the case of **Eu-22** the sensitisation efficiency was found to be lower than expected. This points towards some kind of energetic mismatch between the triplet state of the ligand and the excited state of the lanthanoid, which could explain the relatively low overall quantum yield. Indeed the introduction of the tether at the oxidised bipyridine unit is quite likely to affect the electronic structure of the overall ligand.
The lifetime determined for the samarium cryptate **Sm-22** can be compared to the values determined for the undeuterated and the perdeuterated **Sm-bpy$_3$O$_2$** in CD_3CN (31 and 394 μs, respectively). As expected it lies between them, the threefold increase compared to the undeuterated compound points towards the high impact of the oscillators in the benzylic positions.
In conclusion the study of the photophysical properties of the complexes **Eu-22** and **Sm-22** gave evidence of their high suitability for the aim of this project. All experimental results point towards the presence of exactly one well-defined species in solution and the deuteration of the ligand was found to have the desired effect upon the luminescence properties.

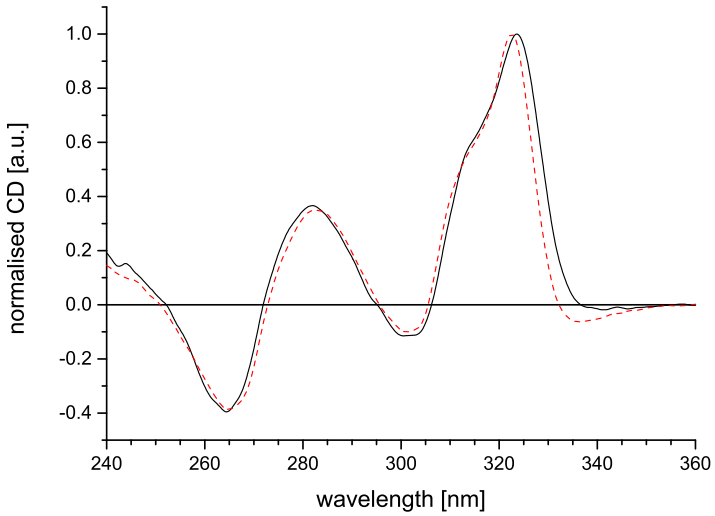

Figure 5.15: CD spectra of **Eu-22** (black, solid line) and **Sm-22** (red, dashed line) in CD_3OD (3mM) at room temperature. Both spectra were independently normalised on a scale of 0 to 1. Modified from reference [267].

In the next step in cooperation with Prof. Dr. Lorenzo Di Bari (Università di Pisa) and Dr. Francesco Zinna (Université de Genève) the chiroptical properties of the compounds were studied. As expected the circular dichroism spectra of both compounds are identical, as it was found to be also the case for the UV/Vis spectra before. Finally the CPL spectra were recorded. For technical reasons both complexes were excited with light of 254 nm, which is not optimal for cryptates. Yet for both compounds circularly polarised luminescence could be detected. The normalised CPL spectra and the corresponding total luminescence spectra are shown in Figure 5.16. In the CPL spectrum of **Eu-22** the $^5D_0 \rightarrow {}^7F_2$-transition is split into two components of opposite sign, whereby the one with the positive sign ($g_{lum} = +0.02$) dominates the CPL signal of the transition. The CPL signal of the $^5D_0 \rightarrow {}^7F_1$-transition has an opposite sign compared to the main component of the transition mentioned before and a quite similar rotary strength, which gives the

spectrum a shape which can be observed quite often in CPL spectra of Eu^{III} complexes. Due to the lower total luminescence intensity and in agreement with Richardson's classification the luminescence dissymmetry factor of the $^5D_0 \rightarrow ^7F_1$-transition is about one order of magnitude higher (g_{lum} = -0.19) than the one determined for the $^5D_0 \rightarrow ^7F_2$-transition. While CPL of europium compounds has already been described quite often, the CPL activity of the samarium cryptate **Sm-22** is one of only few examples known until now. Both, the $^4G_{5/2} \rightarrow ^6H_{5/2}$-transition and the $^4G_{5/2} \rightarrow ^6H_{7/2}$-transition, have distinct rotary strengths resulting in luminescence dissymmetry factors of up to +0.13 for the less intense $^4G_{5/2} \rightarrow ^6H_{5/2}$-transition. For the $^4G_{5/2} \rightarrow ^6H_{7/2}$-transition again splitting in components with opposite signs (g_{lum} = -0.03 and g_{lum} = +0.03) can be observed, which gives additional information of the fine structure of this transition. An important result from the study of the CPL properties of these complexes is that the maximum g_{lum} values measured for the europium and the samarium complexes are in the same order of magnitude. Such a finding has already been reported for the europium and samarium complexes of the CPL record holder Cs[Ln((+)-hfbc)$_4$].[264] This gives evidence of the high potential of samarium-centered CPL when the processes diminishing the luminescence of these complexes can be controlled, as it was done in this case by deuteration. The luminescence dissymmetry factors reported herein are not exceptionally high, but the distinct rotary strengths which were detected together with the well-defined structure of the cryptates have a high potential for a rationalisation of the basic principles of CPL.

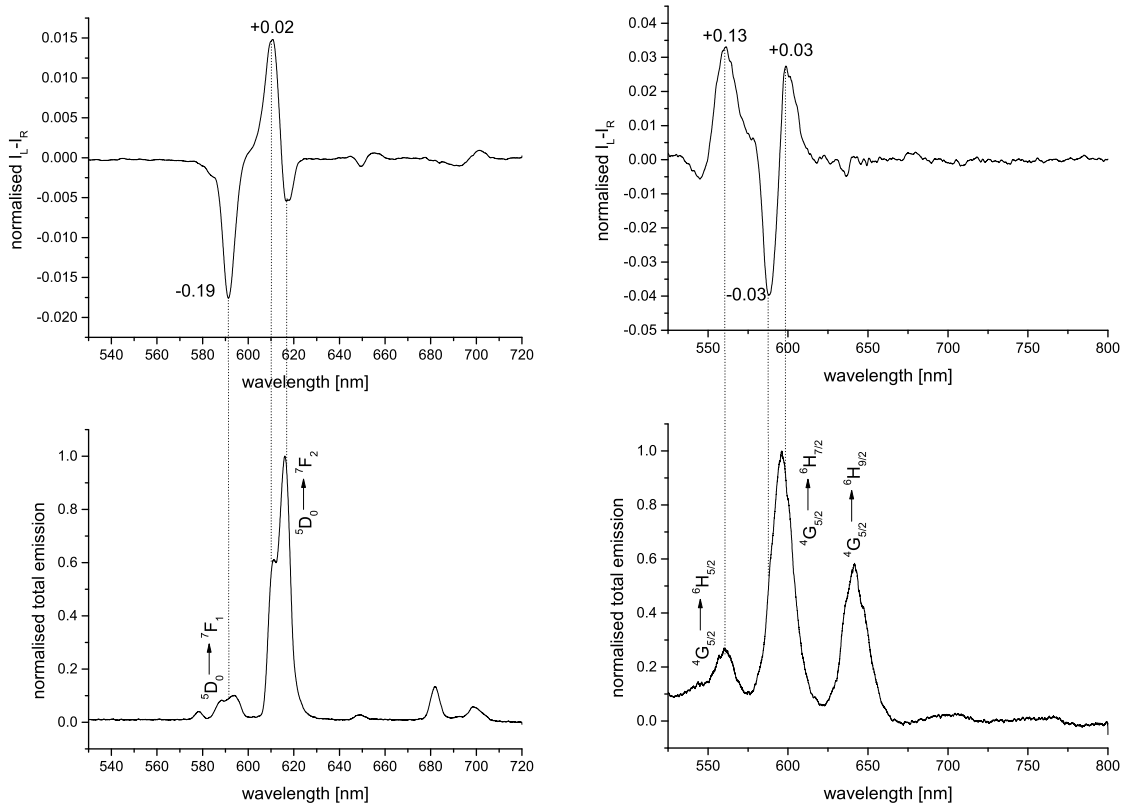

(a) **Eu-22** (CD_3OD (3 mM), λ_{exc} = 254 nm). (b) **Sm-22** (CD_3OD (3 mM), λ_{exc} = 254 nm).

Figure 5.16: Normalised CPL spectra (top) with the luminescence dissymmetry factors g_{lum} and total emission spectra (bottom). Modified from reference [267].

5.3.2 Separation of racemic Ln-bpy$_3$O$_2$ into enantiopure samples and their stability against racemisation

All studies upon the structure of cryptates **bpy$_3$O$_2$** performed until now pointed towards the structure being very rigid and the absence of any interconversion processes. While these processes are very difficult to be studied with racemic samples, it is quite straightforward when enantioenriched or even enantiopure samples are available. The method of choice for the separation of enantiomers of complex molecules is typically HPLC with a chiral solid phase. Indeed, using a CHIRLPAK IE column and CH_3OH with 0.5 vol.-%TFA as mobile phase, for all cryptates **Ln-bpy$_3$O$_2$** tested separation into two components of identical integrals could be observed (see Figure 5.17).

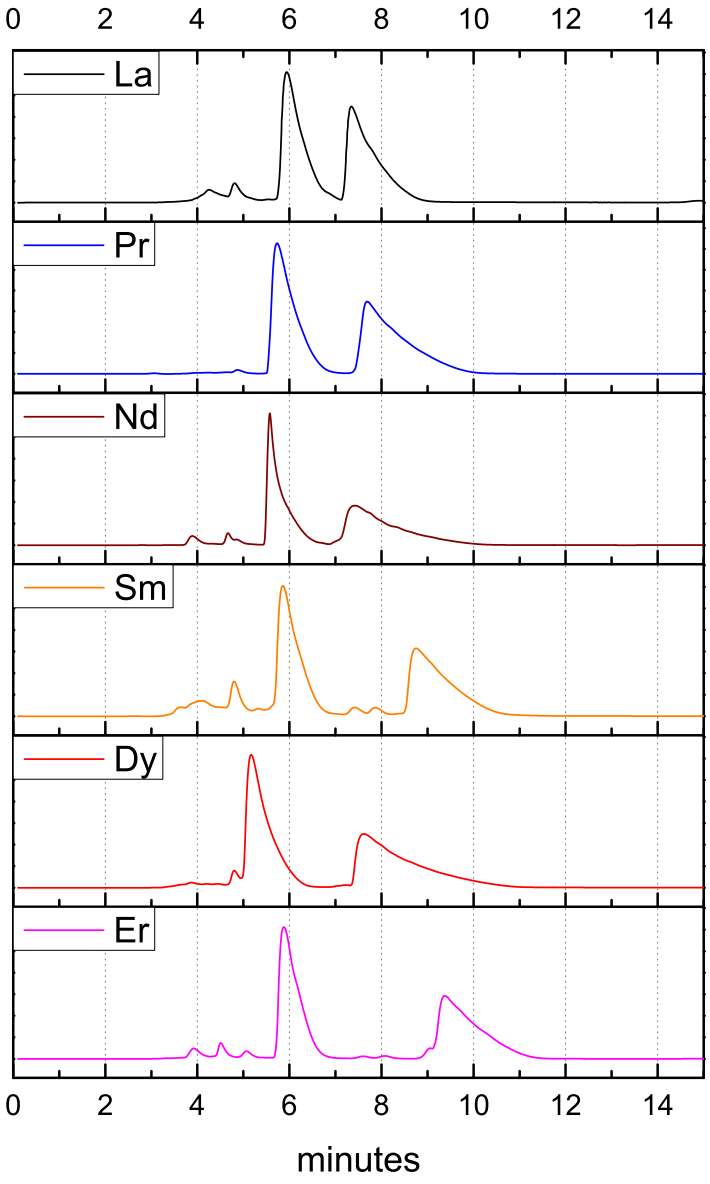

Figure 5.17: Normalised chiral HPLC traces of racemic **Ln-bpy$_3$O$_2$**. Modified from reference [272].

The total retention times were found to be varying (later experiments indicate that there is quite a strong dependence on the concentration of the sample), and the same is the case for the relative retention times of both components. Yet there is a tendency for larger separations for the later lanthanoids. It could be observed that for all **Ln-bpy$_3$O$_2$** tested, the component eluting earlier can be detected as a relatively sharp peak. In contrast, the peak of the second component has a significantly lower maximum intensity and a strong tailing. The relatively high content of TFA in the mobile phase was found to be critical for the separation. The mobile phase has to be prepared directly prior to use, because upon standing TFA and CH_3OH form the corresponding ester F_3C-CO-OMe. The resulting loss of free TFA is sufficient to lead to a significant decrease of the separation. According to experience a portion of the mobile phase should not be used longer than about one hour after preparation.
In order to prove that the two components observable in chiral HPLC indeed relate to the two enantiomers of the lanthanoid cryptates, several milligrams of **Lu-bpy$_3$O$_2$**[135] as obtained after recrystallisation were subjected to chiral HPLC in subsequent runs, whereby the fractions of both components were collected (see appendix page 318 for details). The samples of the substances isolated from these fractions were again subjected to analytical chiral HPLC (see Figure 5.18). As it can easily be seen in the respective HPLC traces the isolated samples contain no contamination with the other component, which offers best prerequisites for further studies towards an unambiguous identification of the isolated compounds.

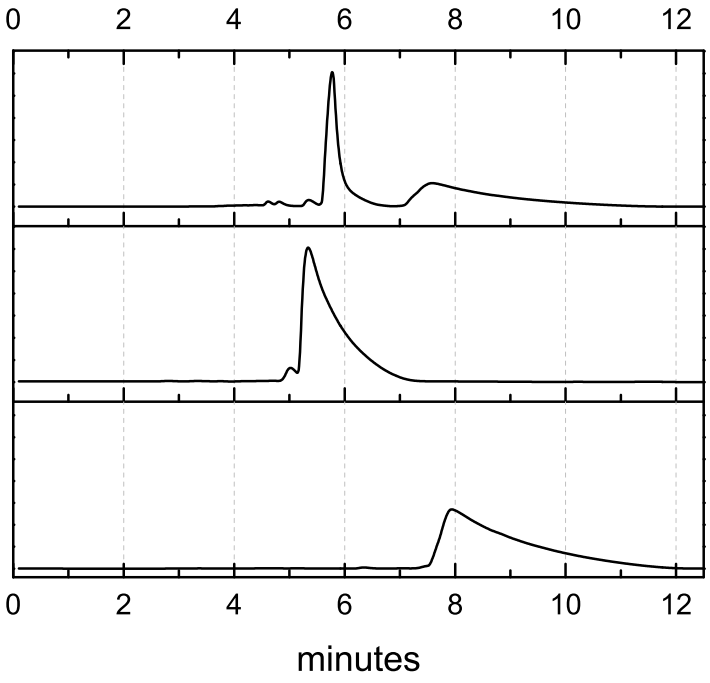

Figure 5.18: Normalised chiral HPLC traces of racemic **Lu-bpy$_3$O$_2$** (top) and the samples isolated from the first component (middle) and second component (bottom). Modified from reference [272].

The easiest experiment which can be performed for this purpose is a simple ^{1}H NMR experiment. As it can be seen in Figure 5.19, the ^{1}H NMR spectra of both components are indistinguishable from each other and the spectrum of a sample prepared from the racemic starting material with a few drops of TFA. Together

with the traces obtained from chiral HPLC of the isolated compounds this already gives very strong evidence for the components being the two enantiomers of **Lu-bpy$_3$O$_2$**.

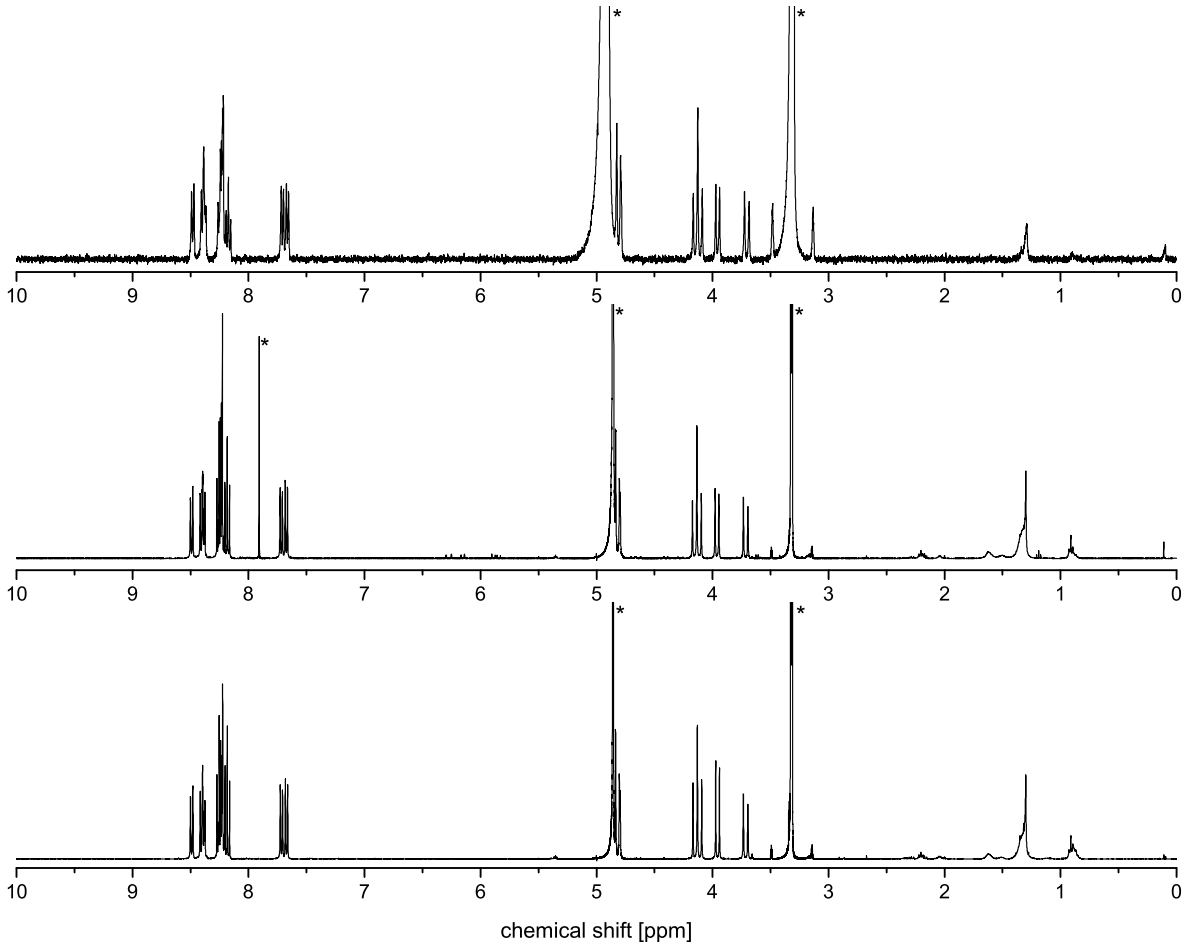

Figure 5.19: ^{1}H NMR spectra of the racemic **Lu-bpy$_3$O$_2$** (top, 400 MHz, CD_3OD + TFA), the first component eluted from chiral HPLC (middle, 400 MHz, CD_3OD) and the second component eluted from chiral HPLC (bottom, 400 MHz, CD_3OD). Unambiguously identified solvent signals are marked with an asterisk.

To unambiguously proof this, CD spectra of both substances were recorded (see Figure 5.20) and indeed they are perfect mirror images. Furthermore the shape of the CD spectrum of the first component (shown in black) is very similar to the ones of the complexes obtained from enantiopure synthesis (see Figure 5.15). Consequently in this case the enantiomer which was eluted from the HPLC as first component can preliminary be assigned to be the R_a enantiomer.

The fact that the enantiomers can be separated via chiral HPLC and even after elongated standing in solution no racemisation was observed already gives evidence for a high stability of the oxidised lanthanoid cryptates against configurational rearrangement processes. Based on these results it can be concluded that enantiopure samples of **Ln-bpy$_3$O$_2$** will indeed be suitable for e.g. the study of their CPL properties and potentially arising applications. Apart from that the enantiopure samples already prepared to give evidence of the feasibility of the separation, can also be used to study the stability of these compounds

against racemisation and related processes even in more detail.

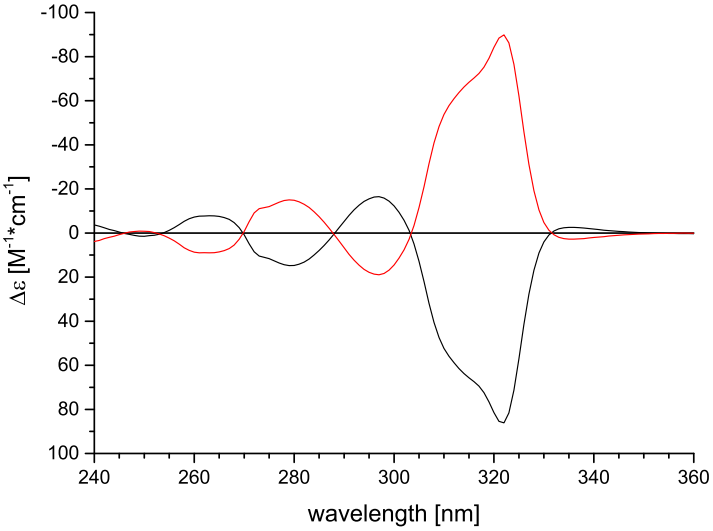

Figure 5.20: CD spectra of the first (black) and second component (red) obtained from chiral HPLC of **Lu-bpy$_3$O$_2$** in CH_3OH ($c \approx 0.4$ mM) at room temperature. Modified from reference [272].

To do so in two separate experiments samples of the S_a enantiomer of **Lu-bpy$_3$O$_2$** were subjected to challenging conditions under which racemisation is very likely to occur. In the first experiment the compound was stirred in pure TFA at room temperature. Most lanthanoid complexes would undergo rapid decomplexation under such conditions and any of the many lanthanoid complexes which are based on carboxylates (such as DOTA complexes) would at least loose any configurational information. In the second experiment the complex and 10.0 equivalents of $LuCl_3 \cdot 6\,H_2O$ were stirred in CH_3CN at reflux temperature. This experiment targets the mechanism which seems to be the most likely to result in a racemisation of the oxidised bipyridine cryptates. Upon exchange of the inner lanthanoid for an external one the ligand would necessarily have to undergo some kind of rearrangement process which would inevitably lead to racemisation. From both experiments in time steps of about one day samples were taken and subsequently analysed via chiral HPLC (see Figure 5.21). Even after five days in neither of the experiments any racemisation or decomposition of the cryptate under study could be observed which gives evidence of the remarkable stability of the cryptates **Ln-bpy$_3$O$_2$**.

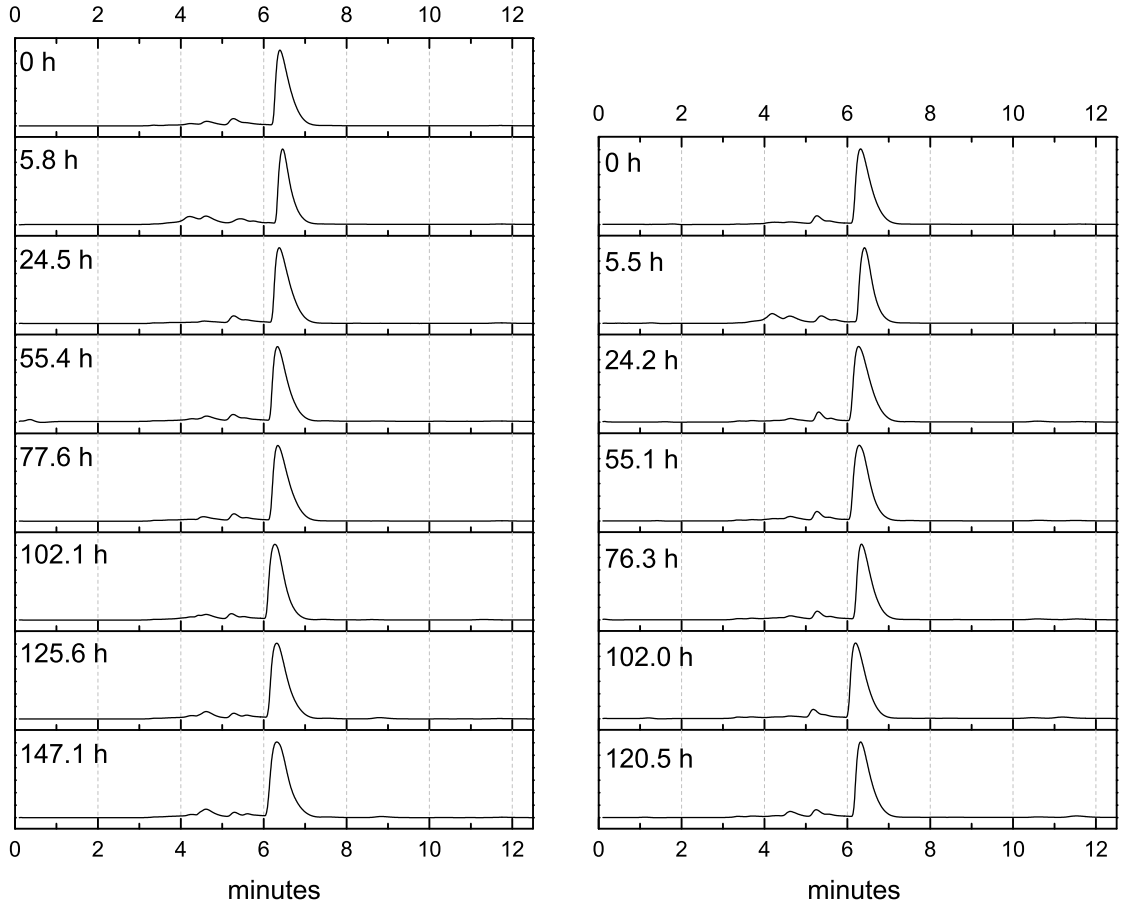

(a) neat TFA, room temperature.

(b) Ten equivalents of $LuCl_3 \cdot 6\,H_2O$, Ch_3CN, reflux temperature.

Figure 5.21: Configurational stability tests by chiral HPLC of the S_a enantiomer of **Lu-bpy$_3$O$_2$**. Modified from reference [272].

5.4 Conclusion

The aim of this study was to improve the understanding of the properties of the cryptates which correlate with their chirality and make first steps towards their utilisation. In the first part of the project the first enantiopure lanthanoid cryptates which are luminescent in the visible part of the electromagnetic spectrum (**Eu-22** and **Sm-22**) were prepared and their photophysical properties were studied thoroughly. This included the study of their circularly polarised luminescence, both compounds exhibit distinct rotary strengths. **Sm-22** is one of only few examples for a samarium complex exhibiting CPL. The results presented herein at the same time give evidence of the high potential of samarium centered CPL (the g_{lum} values of the Sm^{III} and the Eu^{III} complex are in the same order of magnitude) and point towards the control of nonradiative deactivation being key for the observation of CPL of these compounds, as it was done here by a partial deuteration of the ligand scaffold.

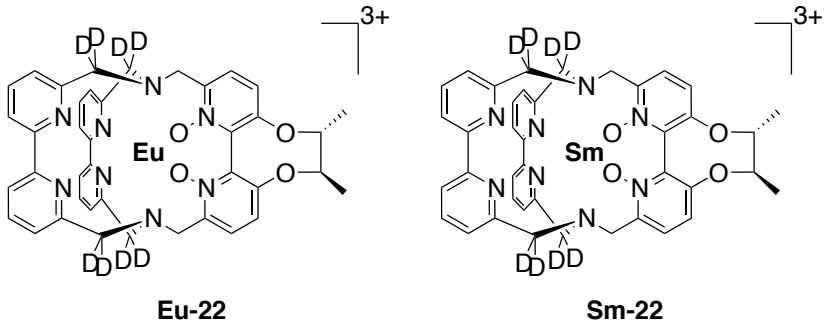

Eu-22 **Sm-22**

Figure 5.22: Enantiopure complexes **Eu-22** and **Sm-22** prepared for the initial study of the CPL properties of cryptates.

In the second part of the project a method for the separation of the racemic lanthanoid cryptates **Ln-bpy$_3$O$_2$** into samples of pure enantiomers via chiral HPLC was successfully established. With the aid of the separated samples of **Lu-bpy$_3$O$_2$** It was proven unambiguously that the fractions isolated from this process correspond to the individual enantiomers of the complex.

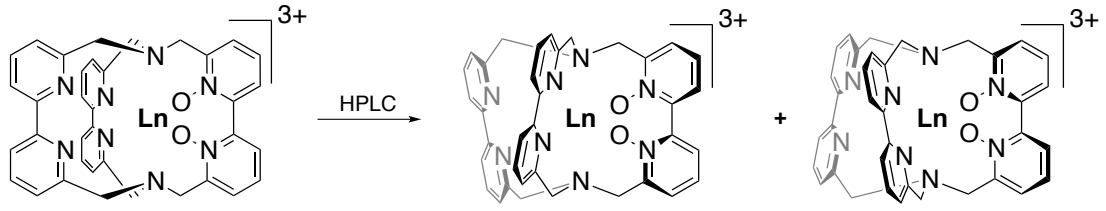

racemic **(R_a)- or (P)-** **(S_a)- or (M)-**

Figure 5.23: Racemic samples of **Ln-bpy$_3$O$_2$**, as obtained from synthesis, can be separated into samples of the pure enantiomers via chiral HPLC.

The accessibility of enantiopure samples of **Lu-bpy$_3$O$_2$** allowed for an in-depth study of the configurational

stability of the oxidised lanthanoid cryptates. Even after 5 days at extreme conditions no traces of racemisation or decomposition could be detected, which gives remarkable evidence of the outstanding stability of these compounds. This is also an important finding for the application of the results from the earlier chapters.

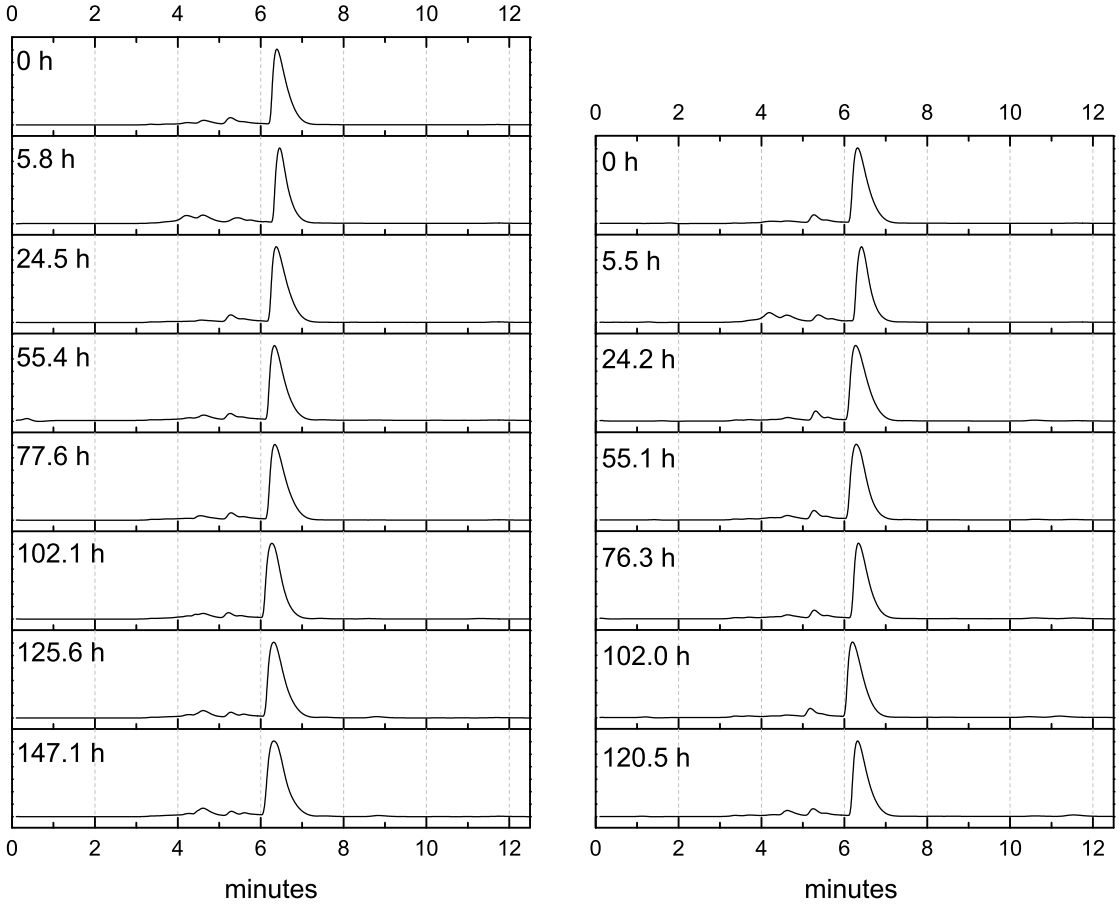

(a) Neat TFA, room temperature.

(b) Ten equivalents of $LuCl_3 \cdot 6\,H_2O$, Ch_3CN, reflux temperature.

Figure 5.24: Configurational stability tests by chiral HPLC of the S_a enantiomer of **Lu-bpy$_3$O$_2$**. Modified from reference [272].

In latest experiments now both parts of the project are combined and chiral HPLC was used to prepare enantiopure lanthanoid cryptates for the study of their CPL properties, which is currently underway and might open up perspectives for the rationalisation of correlations of the coordination geometry and the CPL properties of lanthanoid complexes.

In conclusion, in this chapter the chirality of the cryptates was proven to be one of their useful features which opens up possibilities for innovative applications. Apart from that in this chapter a contribution to a better understanding of one of their most important properties, namely their outstanding stability, could be made.

6 Cryptates for the Controlled Synthesis of Homo- and Heteropolymetallic Complexes

6.1 Introduction

Apart from the possibilities which arise from the general covalent connection of several lanthanoids in a molecular structure (see chapter 4), intrinsically new phenomena become observable when the lanthanoids are combined in a way that allows for a direct interaction between the metals. As described earlier, the Laporte-forbidden nature of the f-f transitions results in a long-lived population of the excited states of the lanthanoids. In most cases upon relaxation the energy of the excited states can be released in the form of a photon, be transferred onto quenching oscillators or be back-transferred onto the antenna ligand. But if another lanthanoid ion is close enough to the initially excited lanthanoid ion, this neighbouring ion can also function as an acceptor of energy, which results in a transfer of energy between both ions and subsequently to emission of light of the second lanthanoid ion. In principle, such energy transfer processes between the initially excited lanthanoid ion Ln_A and the energy accepting lanthanoid ion Ln_B can be divided into three groups which are shown schematically in Figure 6.1.

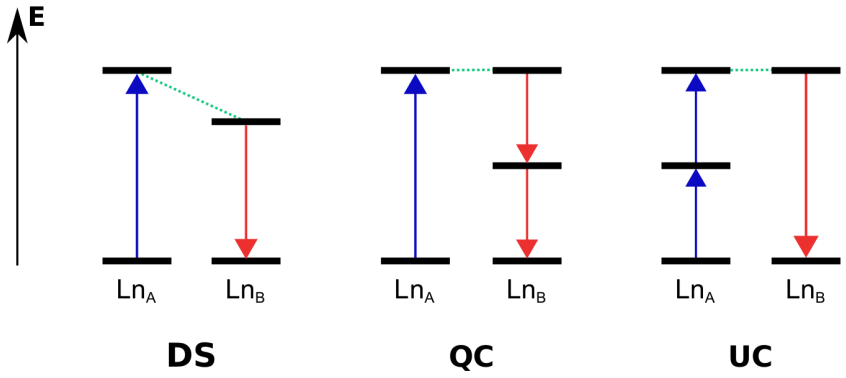

Figure 6.1: Different energy transfer processes between two lanthanoid ions Ln_A and Ln_B: Downshifting (DS), quantum cutting (QC) and upconversion (UC). Energy uptake leading to an excitation of lanthanoid ions is represented with blue arrows, the emission of photons is represented with red arrows. Green, dotted lines represent radiationless transitions.

During a downshifting (DS) process only a part of the energy of the initially excited lanthanoid ion Ln_A is transferred onto the adjacent lanthanoid Ln_B, the indirectly excited transition of Ln_B has a smaller energetic difference than the transition between the involved states of Ln_A. Consequently in a subsequent step Ln_B

can emit a photon with a higher wavelength. The excess energy of the excited Ln_A is released into the surrounding area, this process is similar to the antenna effect. Other processes which can occur when two lanthanoids interact are quantum cutting (QC) processes. In this case, the energy of Ln_A is split and transferred to two neighbouring Ln_B. Ideally the energy of the excited Ln_A should equal twice the amount of energy necessary to excite Ln_B, and after the energy transfer double the intensity of light of a higher wavelength will be emitted. The third group of processes shown in Figure 6.1 are upconversion (UC) processes, which are significantly different to the previously described. Here, Ln_A is excited stepwise with at least two photons before the energy is transferred onto Ln_B and subsequently emitted as a photon of higher energy. If Ln_A is excited with a pump laser, the efficiency of the process will be proportional to the square of the pump intensity. In this regard upconversion processes resemble non-linear optical processes (like for example “second harmonic generation” or “two photon absorption”) but in fact the processes are significantly different.[273]

Upconversion processes are relevant for a variety of applications, e.g. for photovoltaic cells or for biological or medicinal applications. Upconversion contrast agents can be excited with low energetic NIR-radiation for which biological tissues are transparent and which is less phototoxic. After the upconversion process such contrast agents emit light in the NIR, visible or UV part of the spectrum. To some extent related target compounds are nanocarriers containing drugs which are released upon NIR-irradiation.[274] In principle many different upconversion mechanisms are possible, some of the most relevant are shown in Figure 6.2.[275] The conceptually most straightforward mechanism is the “excited-state absorption” (ESA). Here, in the initial step the absorption of a photon brings a lanthanoid into a first excited state. If a second photon is absorbed before a radiative or nonradiative deactivation takes place, a second excited state can be reached from which a photon is emitted whose energy equals the sum of the two in the forehand absorbed photons. Typically, in this case no energy transfer from another lanthanoid or a ligand is responsible for the population of the excited states but instead the lanthanoid is directly excited with a pump laser. As the three involved energy levels often are not equidistant, sometimes the use of pump lasers with two different wavelengths is beneficial or necessary. Different from that, the other mechanisms shown in Figure 6.2 require two elements, a sensitiser S and an activator A between which the energy is transferred. In the simplest case this results in a SA-“energy transfer upconversion” mechanism (which also used to be called “addition de photons par transferts d’énergie”, APTE). Thereby one sensitiser and activator each form an upconversion pair. Firstly the sensitiser S is excited (directly or indirectly) and transfers its energy onto the activator A. Activator A remains in the excited state until the sensitiser has been excited another time and again transfers the energy onto activator A, which results in the population of a higher excited state of A. From this excited state finally a photon of the corresponding energy can be emitted. The SAS-“energy transfer upconversion” mechanism is closely related with the only difference that here the activator is in contact with two sensitisers. Another variation is the “cooperative energy transfer upconversion”. Here the activator does not have an intermediate energy level, so that a stepwise energy transfer from the sensitisers is not possible and the transfer from both sensitisers has to take place simultaneously. In literature also further upconversion mechanisms are discussed, for example the “photon avalanche”-mechanism (PA)[276] or mechanisms for more specialised cases like for example upconversion-nanoparticles[275] for which surface effects or coatings are relevant.

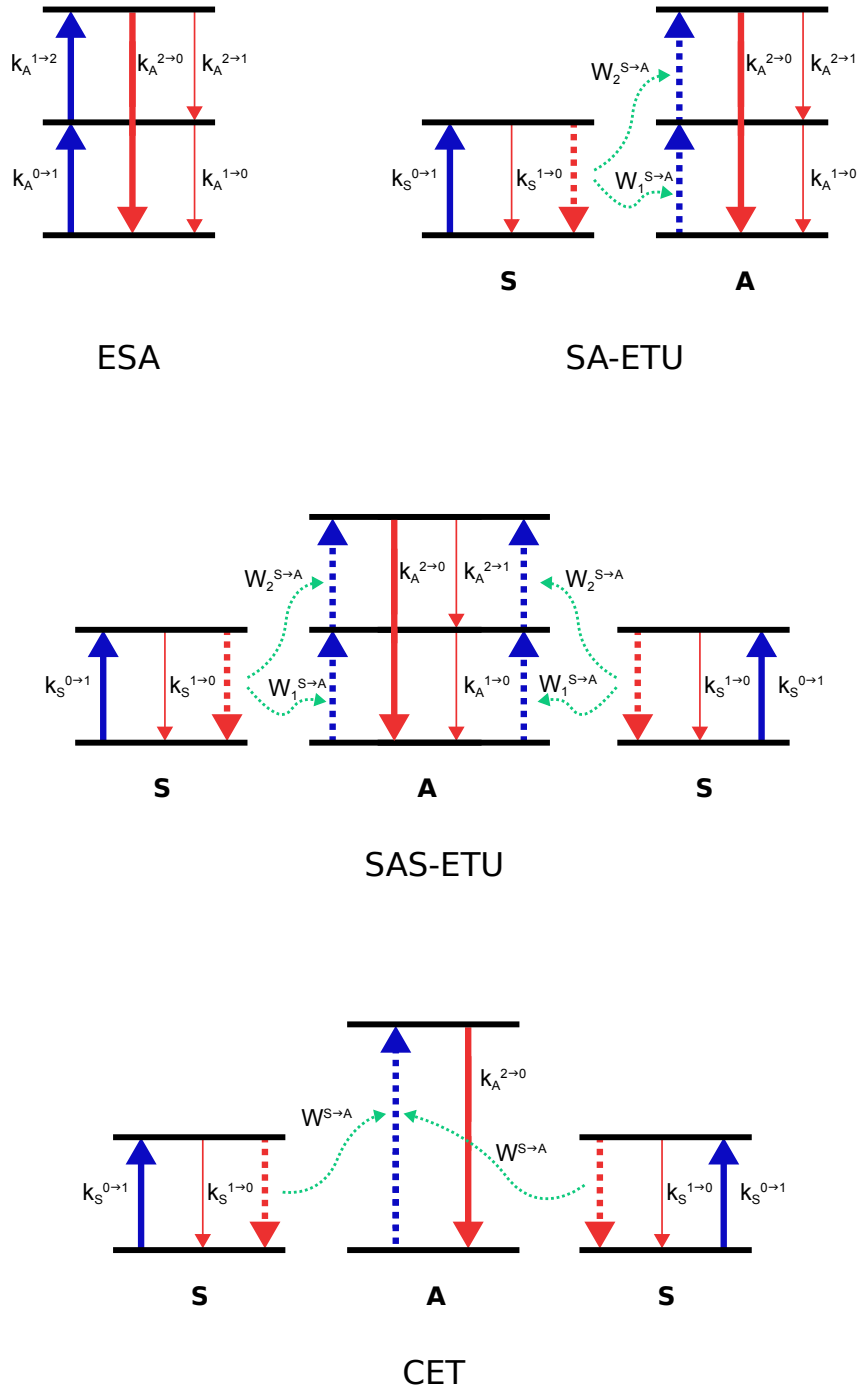

Figure 6.2: Schematic representation of some upconversion mechanisms: ESA (excited state absorption), ETU (energy transfer upconversion), CET (cooperative energy transfer). Excitation processes are represented with blue arrows, deactivation processes are represented with red arrows and transfer processes are represented with dotted, green arrows.

Prerequisite for the observation of upconversion is the population of the second excited state of the activa-

tor. Consequently in a first approximation the normalised population density of the activator in the second excited state $N_A^{|2\rangle}$ can be treated as a measure for the intensity of the emitted upconverted radiation. Under steady state conditions ($dN_A^{|2\rangle}/dt = 0$) and when the sensitiser is directly excited with a pump laser ($k_A^{exc(i\rightarrow j)} = \left(\lambda_p/hc\right) \cdot p \cdot \sigma_A^{i\rightarrow j}$), the following applies to an ESA-process:[30]

$$N_A^{|2\rangle}(ESA) = \left(\frac{\lambda_p}{hc}\right)^2 p^2 \times \frac{\sigma_A^{0\rightarrow 1}\sigma_A^{1\rightarrow 2}}{\left(k_A^{2\rightarrow 1} + k_A^{2\rightarrow 0}\right)\left[k_A^{1\rightarrow 0} + \left(\lambda_p/hc\right) \cdot p \cdot \sigma_A^{1\rightarrow 2}\right]} \times N_A^{|0\rangle} \tag{17}$$

Analogously a SA-ETU process can be described as:[30]

$$N_A^{|2\rangle}(SA\text{-}ETU) = \left(\frac{\lambda_p}{hc}\right)^2 p^2 \times \frac{\left(\sigma_S^{0\rightarrow 1}\right)^2 W_1^{S\rightarrow A} W_2^{S\rightarrow A}\left(N_S^{|0\rangle}\right)^2}{\left(k_A^{2\rightarrow 1} + k_A^{2\rightarrow 0}\right) k_{S,obs}^{1\rightarrow 0}\left[k_A^{1\rightarrow 0} k_{S,obs}^{1\rightarrow 0} + \left(\lambda_p/hc\right) \cdot p \cdot \sigma_S^{0\rightarrow 1} W_2^{S\rightarrow A} N_S^{|0\rangle}\right]} \times N_A^{|0\rangle} \tag{18}$$

Whereby λ_p is the pump wavelength, h is the Planck constant, c is the speed of light *in vacuo*, p is the incident pump intensity, σ are absorption cross sections, k are the relaxation rate constants and W are the second order rate constants for energy transfer processes (see Figure 6.2). The total deactivation of the first excited state of the sensitiser ($k_{S,obs}^{1\rightarrow 0}$) includes radiative and nonradiative processes and also the energy transfer onto the activator:

$$k_{S,obs}^{1\rightarrow 0} = k_S^{1\rightarrow 0} + W_1^{S\rightarrow A} \cdot N_A^{|0\rangle} \tag{19}$$

Generally the ESA-mechanism is considered to be less efficient than ETU-mechanisms, very high absorption cross sections σ_A and pump intensities are necessary. In some cases the resulting luminescence could only be observed at pump intensities at which also two-photon absorption processes would be possible, which cannot be easily distinguished from upconversion processes.[30][277] Also, the SAS-ETU-mechanism is significantly more efficient than the SA-ETU-mechanism, which can be explained by the fact that in the case of an SAS-ETU-mechanism the doubled amount of activators is available for every sensitiser (see equation 18).

The ladder like arrangement of the energy levels of many lanthanoids and the long lifetimes of their excited states generally offer good conditions for upconversion processes.[278] Evidence for this general and intrinsic suitability of the lanthanoids for the observation of upconversion was given by Xiao *et al.*[279] As they reported, complexes of DPA or EDTA with Er^{III}, Tm^{III} or Nd^{III} prepared in H_2O or D_2O emit upconverted light when irradiated with two lasers of different wavelengths which were chosen to be in resonance with specific transitions of the respective lanthanoid. Using peak laser powers as high as 100 kW they were able to pump enough energy into the lanthanoids that following an ESA-mechanism upconverted light of detectable intensities was emitted. Three years earlier, Reinhard *et al.* had not observed any upconverted emission from DPA complexes of Er^{III}, Tm^{III} or Yb^{III} after excitation with only one wavelength.[280]

Upconversion materials based on lanthanoids and also the corresponding nanoparticles (upconversion nanoparticles, UCNPs) can be prepared quite easily and a huge variety of examples can be found in liter-

ature. UCNPs consist of a photophysically inactive host material in which a certain amount of the cations has been replaced with photophysically active guest-ions during synthesis (e.g. via coprecipitation, thermal decomposition or solvothermal synthesis).[281] Since most materials target an upconversion process following the efficient ETU-mechanism both components, a sensitiser and an activator are needed. Yb^{III} is usually considered to be the best choice for the sensitiser since it has an absorption cross section which is quite high for a lanthanoid ion (9.11 x 10^{-21} cm^{-2} for $^2F_{7/2} \rightarrow {}^2F_{5/2}$), and has only one excited state, so that the amount of energy which can be delivered from a Yb^{III} ion is well defined. In the case of the activator the lanthanoid should have excited states with sufficiently high and preferentially equidistant energy levels. Er^{III}, Tm^{III} and also Ho^{III} ideally comply with these requirements and provide transitions which are in resonance with the one of Yb^{III}. Under these three Er^{III} is regarded as the activator which allows for the highest ETU-efficiencies (see Figure 6.3).[275]

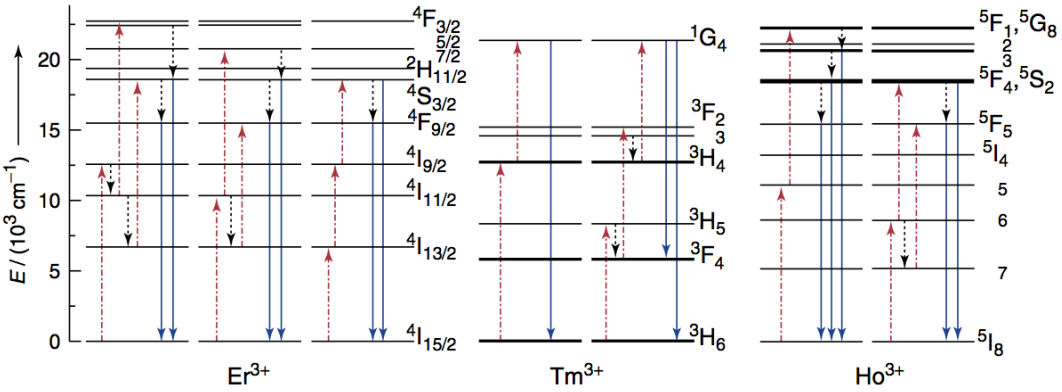

Figure 6.3: Different energy transfer paths between the energy levels of Er^{III}, Tm^{III} and Ho^{III}. Excitation processes are represented with red arrows, nonradiative deactivation processes are represented with black arrows and the emission of photons is represented with blue arrows. Figure adopted from reference [281].

Nevertheless also all other trivalent lanthanoid ions except for La^{III}, Ce^{III} and Lu^{III} could already be combined with Yb^{III} to form an upconversion pair (see section 9.8, page 284 in the appendix). Since for the activators several energy levels can be populated, not only different excitation paths (see Figure 6.3) are possible, but also light of different wavelengths can be emitted. As the probabilities for the corresponding excitation paths show different dependencies on the distance between sensitiser and activator, a change of the relative concentration of the guest ions can allow for a manipulation of the emission colour of the corresponding material. Also the addition of a third lanthanoid can have an impact onto the emitted light.[282] But unfortunately this does not allow for a targeted design. Though the growing experience in this field is indeed helpful, in principle the optimisation of any new UCNP is some kind of a trial and error process and the underlying concurring processes which result in the observation of lanthanoid-centered upconversion are not completely understood until now.

Whenever nanoparticles are prepared, the product is obtained as a statistical mixture of different particles and an exact reproducibility cannot be given. Furthermore in a single nanoparticle different pairs of sensitisers and activators with slightly different distances can be found, which can also influence each other and

further complicate the situation. Consequently, neither the exact characterisation of a single S/A-pair nor a targeted design of such a pair in a nanoparticle is possible.

In stark contrast to that, molecular coordination compounds generally provide by far better possibilities for the preparation of metal-consisting compounds with designed properties, such as a well-defined distance between two metal centers. Particularly, these compounds allow for the preparation and characterisation of uniform samples of exactly one species. Consequently molecular lanthanoid compounds are more suitable for understanding the underlying principles which are responsible for energy transfer processes between lanthanoids. Unfortunately such molecular compounds which exhibit these energy transfer processes are more difficult to create than the corresponding nanoparticles. In nanoparticles, interactions with the lattice vibrations of the material can deactivate the excited states of lanthanoids and diminish the upconversion efficiency. Unfortunately the high-energy oscillators omnipresent in coordination compounds, such as C-H- or N-H-bonds, are even more effective quenchers. Consequently, the critical step of the upconversion process after the initial energy transfer to the activator, and during which it has to stay in this state until it receives another energy transfer, is more difficult to realise in a molecular compound. Generally also the organic ligand as a whole (or more specifically: its triplet state) can act as acceptor of the energy accumulated on a lanthanoid and lead to a nonradiative deactivation which competes with the emission of upconverted light.[277][283]

The typically low kinetic stability of lanthanoid complexes represents another important challenge for the design of molecular lanthanoid upconversion compounds. The limited availability of ligand scaffolds which allow for the preparation of stable lanthanoid compounds narrows the design possibilities for potential molecular lanthanoid upconverters. Whenever coordination compounds in which several lanthanoids are combined in a controlled fashion are to be prepared, of course also the high chemical similarity of the lanthanoids becomes an important challenge.

In principle every nonradiative energy transfer between two lanthanoids can follow a Förster or a Dexter mechanism. Förster energy transfers are dipole-dipole (or multipole-multipole) interactions whereby the initially excited donor induces an oscillation of the acceptor and thus transfers its energy. Both, the spin of the donor and of the acceptor remain unaffected. The efficiency E of the energy transfer is strongly dependent on the distance r between donor and acceptor. k_D is the rate of the nonradiative deactivation of the donor in absence of an acceptor, τ_D is the corresponding lifetime. k_{ET} is the rate of the energy transfer and k_i are the rates of any other processes which lead to a deactivation of the donor.

$$E = \frac{k_{ET}}{k_D + k_{ET} + \sum k_i} = \frac{1}{1 + (r/R_0)^6} \tag{20}$$

$$k_{ET} = k_D \frac{R_0^6}{r^6} = \frac{1}{\tau_D} \frac{R_0^6}{r^6} \tag{21}$$

The Förster radius R_0 is the distance between donor and acceptor at which the energy transfer has an efficiency of 50%:

$$R_0^6 = \frac{9 \cdot \ln(10)}{128\pi^5 \cdot N_A} \cdot \frac{\kappa^2 Q_D}{n^4} \cdot J \tag{22}$$

Here κ describes the relative orientation of donor and acceptor, which for isotropic systems usually is

assumed to be 2/3. Q_D is the quantum yield of the donor in absence of an acceptor, n is the refractive index of the medium and J represents the spectral overlap integral (SOI). Typically, energy transfer processes which follow this mechanism can be observed at distances up to about 100 Å. In contrast to that, the Dexter energy transfer, which shows an exponential dependence from the distance r and the sum of the Van der Waals radii of the donor and the acceptor (L), can only operate in a significantly shorter range and is limited to distances of about 10 Å:

$$k_{ET} \propto J \cdot \exp\left(\frac{-2r}{L}\right) \tag{23}$$

Differently to the Förster energy transfer, in the case of the Dexter energy transfer donor and acceptor exchange electrons (whereby the total spin of the system remains unaffected). Both mechanisms require sufficient overlap between the emission spectrum of the donor and the absorption spectrum of the acceptor.[284] In the case of the typically narrow band widths of the lanthanoids this is more difficult to realise than for e.g. organic chromophores. Another characteristic feature of the lanthanoids, namely the low spatial expansion of the f-orbitals, makes energy transfers between lanthanoids following Förster mechanisms appear more likely than the ones following Dexter mechanisms.

A few molecular systems already allowed for the study of energy transfer processes between lanthanoids. For example Faulkner *et al.* in 2003 described a complex of two Tb^{III}-ions and one Yb^{III}-ion which does show the characteristic emission of Yb^{III} centered at around 980 nm not only after excitation of the ligand, but also after direct excitation of the neighbouring Tb^{III}-ions. In both cases a lifetime of 4.2 μs could be determined in D_2O.[285] The ligand consists of two DOTA-type Tb^{III}-complexes which are connected by two aminobenzyl units and a DTPA-type binding pocket by which the Yb^{III} is coordinated. As the Tb^{III}-complexes are prepared prior to the attachment to the third binding pocket, and since the DOTA complexes are sufficiently stable, a uniform compound could be realised and studied.

Also between Eu^{III} and Tb^{III}[284][286] or between Eu^{III} and Nd^{III}[287] already energy transfer processes in molecular systems could be observed. In principle any pair which allows for the observation of energy transfer processes in UCNPs is potentially of interest for such studies. Interestingly there are also examples for energy transfer processes between the uranyl ion UO_2^{2+} and lanthanoids, where the uranyl ion sensitises the characteristic luminescence of the respective lanthanoid. This phenomenon was observed in the solid state[288] as well as in solution[289] and the presented results indicate that they can proceed with high efficiencies. In this context it should be noted that the generally higher tendency of the (early) actinides to show interactions with significant covalent character would facilitate a Dexter-type energy transfer.

Some especially interesting possibilities for the study of energy transfer processes between several lanthanoids are provided by homopolynuclear complexes of Eu^{III}. The special electronic structure of Eu^{III} makes detailed information about the coordination sphere around the lanthanoid ion accessible.[163] Both, the $^5D_0$ and the $^7F_0$ state of Eu^{III} are non-degenerate, consequently exactly one transition between both states is possible and no splitting can be observed in the corresponding emission spectra. The very exact energetic position of this transition is dependent on a variety of parameters, for example the nature and number of coordinating solvent molecules. For the evaluation of these “nephelauxetic effects” some empirical formulas were developed which can allow to draw some conclusions about the chemical surrounding of the Eu^{III} under study from the exact position of this transition.[290][291][292] Whenever two Eu($^5D_0 \rightarrow {}^7F_0$)-

transitions can be observed in an emission spectrum of a compound with several Eu^{III}-ions this indicates that the ions are at least slightly different in terms of their coordination environment, which is a prerequisite for the observation of an energy transfer process between two ions of the same element. In such a complex it is possible to excite the Eu^{III}-ions independently from each other by direct excitation of their respective Eu($^7F_0 \rightarrow ^5D_0$)-absorption bands. If afterwards the emission of the other lanthanoid or of both lanthanoid ions can be observed, this would strongly indicate that an energy transfer between both metals is taking place.[284] Also the kinetics of the deactivation of the excited states in such a compound can make interesting information accessible and point towards an energy transfer.[284][293] If it is possible to assign single transitions reliably to one of the Eu^{III}-ions (which can for example be done by luminescence experiments in different solvents) this can in principle also be done when both Eu^{III}-ions are conjointly excited via the ligand.

As it is the case for any f-f-transition, also the Eu($^5D_0 \rightarrow ^7F_0$)-transition is Laporte-forbidden. As it is also spin-forbidden it is especially difficult to excite this transition directly. Also the so-called hypersensitive Eu($^5D_0 \rightarrow ^7F_2$)-transition, which is usually dominating the emission spectrum of Eu^{III}, is sensitive towards small variations in the environment of the lanthanoid. Often the intensity of this transition is treated as a measure for the symmetry of the coordination environment of the Eu^{III}, as corresponding to the Judd-Oddfelt theory this transition must be forbidden for a coordination symmetry with an inversion center. In contrast to that, the Eu($^5D_0 \rightarrow ^7F_1$)-transition is considered to be especially insensitive towards changes in the coordination sphere and its intensity is often assumed to be constant to compare different spectra quantitatively.[163]

Until now only two examples for molecular compounds which exhibit upconversion in solution as consequence of an energy transfer between two lanthanoid ions are known.

The first of these examples is a fluoride bridged dimeric assembly of two indazolyl-functionalised DOTA complexes coordinating an Er^{III}-ion.[28] The typically high affinity between lanthanoid ions and fluoride leads to a short distance between the Er^{III}-ions of only 4.484 Å (DFT calculation), hydrogen bonds and π-π-stacking interactions further stabilise the dimer. In the DFT optimised structure both lanthanoid ions and the fluoride ion are arranged in a linear fashion. After excitation at 980 nm (Er($^4I_{15/2} \rightarrow ^4I_{11/2}$)), a solution of the dimer in D_2O (obtained by addition of 0.5 equivalents of NaF to a solution of the monomeric form, see Figure 6.4(a)) exhibits emission bands centered at around 525, 550 and 650 nm which can be assigned to the $^2H_{11/2} \rightarrow ^4I_{15/2}$-, $^4S_{3/2} \rightarrow ^4I_{15/2}$- and $^4I_{9/2} \rightarrow ^4I_{15/2}$-transitions of Er^{III} (see Figure 6.4(b)). Also without the addition of NaF a weak signal of upconverted emission could be detected, and also when Er^{III} was indirectly excited via the ligand ($\lambda_{exc} = 294$ nm) a characteristic emission could be detected, even in the absence of NaF but not in H_2O. The dominating mechanism of the upconversion process is assumed to be an ETU-mechanism. This interpretation is supported by the relatively long rise time of the upconverted luminescence (5 μs) and the significantly lower upconversion efficiency found for the solution of the monomer without NaF (an ESA-mechanism can also operate without a second monomer in the close vicinity). Presumably the fluoride ion has another important role in this system apart from connecting the monomers, since it will also shield the lanthanoid ions from surrounding solvent molecules and consequently protect the excited Er^{III}-ions from nonradiative deactivation processes.

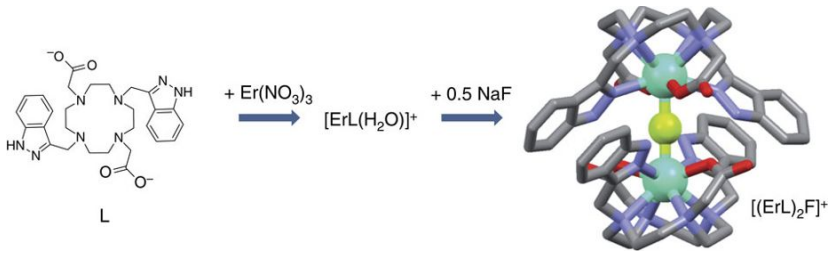

(a) Formation of the monomeric Er^{III} complex from the ligand and assembly of the fluoride bridged dimeric compound.

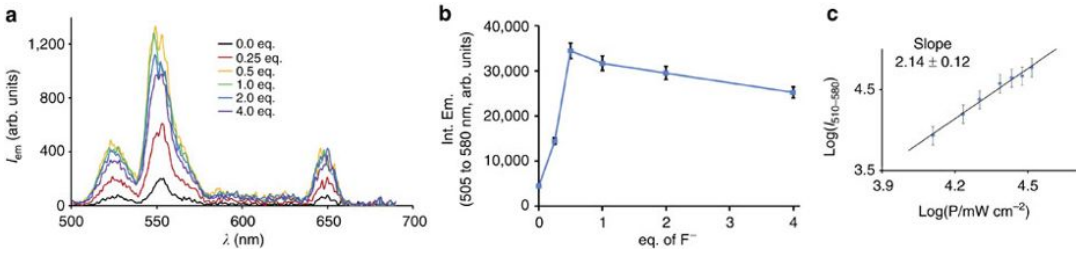

(b) Photophysical data revealing the Er^{III}-centered upconversion. The sample in D_2O was excited at 980 nm, which corresponds to the $^4I_{15/2} \rightarrow {}^4I_{11/2}$-transition. Figure a): Emission of the sample between 500 and 700 nm at excitation at 980 nm after addition of different equivalents of fluoride. Figure b): Integrated intensity (505 to 580nm) as a function of added equivalents of fluoride. Figure c): log-log plot of the UC emitted intensity (integrated from 505 to 580 nm) as function of the incident pump intensity. The slope of approximately two corresponds to a two photon process.

Figure 6.4: Formation of a dimeric Er^{III} complex and selected photophysical data revealing the observed upconversion process in D_2O.[28] Figures adopted from reference [28].

The second molecular system which allows for the observation of lanthanoid-centered upconversion in solution is based on a partially deuterated phosphonated bipyridyl ligand (see Figure 6.5(a)). Upon reaction with slightly less than one equivalent of $LnCl_3 \cdot 6\,H_2O$ in aqueous solution (at neutral pH) and subsequent recrystallisation the corresponding mononuclear complexes are accessible.[295] In these complexes the lanthanoid is coordinated in an octadentate fashion and well protected against surrounding solvent molecules ($q = 0$). The complexes show high kinetic stability. If a buffered aqueous solution of the corresponding Yb^{III} complex is titrated with a buffered solution of $TbCl_3 \cdot 6\,H_2O$, upon direct excitation of the Yb^{III} ion the characteristic emission of the Tb^{III} ions can be observed (see Figure 6.5(b)). If instead Tb^{III} is added to the corresponding Lu^{III} complex, excitation at 980 nm does not lead to Tb^{III}-centered emission, which allowed to rule out nonlinear processes as responsible for the excitation of the Tb^{III}-ions. From the analysis of the photophysical data collected during the titration the authors of the study conclude that in the sample under study three different species $[(YbL)_2Tb_x]$ with $x = 1,2$ or 3 are in equilibrium. The DFT structures of the compounds indicate that the YbL-units coordinate the first Tb^{III}-ion in a more or less linear fashion via their phosphonate groups. The coordination of the second and the third Tb^{III}-ion, respectively, is realised relatively similar. In all three calculated structures the Yb-Tb distances are very short (between 3.85 and 4.56 Å) and the Tb-Tb distances tend to be even shorter. If all three species exhibit upconversion activity cannot be concluded on the basis of the data presented in the study.

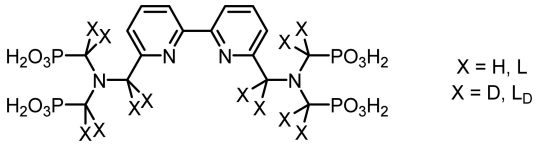

(a) Structure of the ligand L and its partially deuterated analogue L_D which was used for the preparation of the samples.

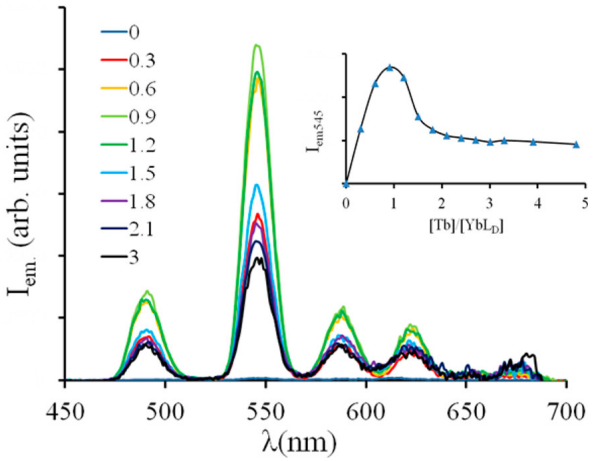

(b) Emission spectra recorded upon titration of a solution of YbL_D in D_2O with $TbCl_3 \cdot 6\,H_2O$

Figure 6.5: With the aid of the ligand L_D it was possible to observe $Yb^{III} \rightarrow Tb^{III}$ upconversion in D_2O. Figures adopted from reference [294].

It is important to note that both systems which are known to exhibit lanthanoid centered upconversion (as a consequence of an energy transfer mechanism) in solution were prepared in situ and most likely cannot be isolated in the studied form. Both systems resemble more a supramolecular assembly than a discrete molecule which results in severe limitations for the unambiguous characterisation of the actually upconverting species and, even more importantly, for any application e.g. in a biological sample.

In the light of the very limited examples for lanthanoid upconversion in molecular systems it is reasonable also to consider compounds which do exhibit upconversion in the solid state to improve the general understanding of the underlying processes. A group of compounds which are interesting in this context are 2D coordination polymers made from 4,4'-bipyridine-*N*,*N*'-dioxide and Yb^{III} and Er^{III} in variable proportions.[296] Though the lanthanoid ions in these compounds are in close vicinity to deactivating C-H-bonds and even H_2O molecules, upon excitation at $\lambda_{exc} = 980$ nm upconverted emission at 548 nm and 525 nm ($Er(^4S_{3/2} \rightarrow {}^4I_{15/2})$ and $Er(^2H_{11/2} \rightarrow {}^4I_{15/2})$, respectively) could be observed, even at relatively low pump intensities of about 10 mW. At higher pump intensities an additional emission band centered at 409 nm could be observed, which corresponds to the $^2H_{9/2} \rightarrow {}^4I_{15/2}$ transition of Er^{III}. The authors describe a dependence of the operating upconversion mechanism from the pump intensity and the amount of Er^{III} doped into the material: Upon increase of Er^{III} the previously dominating ESA-mechanism is progressively replaced by an ETU-mechanism. Furthermore the authors consider that low energy phonon modes might facilitate the nonradiative energy transfers which are basis of the upconversion process. This is quite an important note, since in these materials quenching oscillators such as C-H or O-H bonds are omnipresent and this points towards a special importance of the low energy phonon modes, since they seem to overcompensate these detrimental effects.

In order to observe upconversion following an ETU-mechanism with a lanthanoid as activator, not nec-

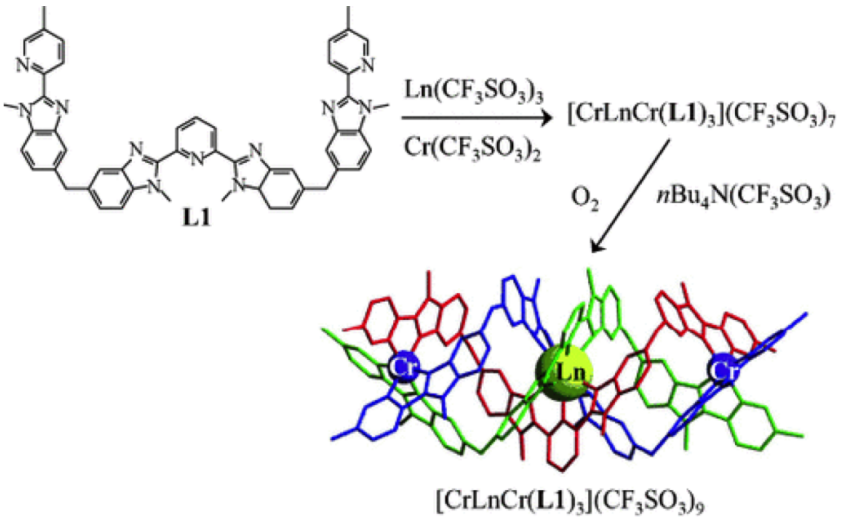

(a) General preparation of the heterometallic complex containing two Cr^{III} ions and one lanthanoid ion.

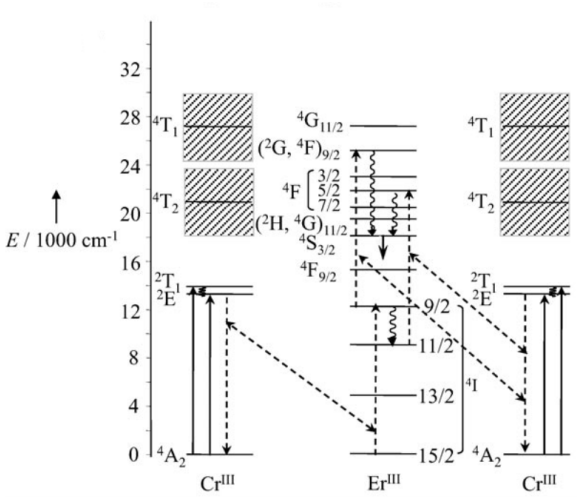

(b) Jablonski diagram of the energy transfer processes in the helical Cr-Er-Cr complex. Excitation processes are represented with upward solid arrows, ETU-processes are represented with dotted arrows, nonradiative deactivation processes are represented with curled arrows and emission processes are represented with downward solid arrows.

Figure 6.6: Preparation of the helical heterometallic complexes in which a lanthanoid ion can be combined with two adjacent Cr^{III}-ions and the Jablonski diagram formulated for the rationalisation of the underlying processes resulting in the observed upconversion. Figures adopted from reference [29].

essarily a lanthanoid has to be employed as sensitiser. In fact the use of different sensitisers seems to facilitate the construction of molecular lanthanoid upconverters. An interesting example is the first compound which was reported to exhibit NIR $\rightarrow$ VIS upconversion in an isolated molecular system. The complex is a supramolecular assembly of three identical ligands which jointly coordinate two terminal Cr^{III}-

and one central Er^{III}-ion and as such allows for a SAS-ETU-mechanism (see Figure 6.6(a)).[29] For the Eu^{III} and Yb^{III} derivatives of the compound X-ray diffraction studies allowed for the determination of the Cr-Ln-distances which are 8.8(1) Å and 8.9(1) Å, respectively. Figure 6.6(b) shows a Jablonski diagram of the energy transfer processes which are responsible for the observed upconversion process: Initially at 450 nm the $^4A_2 \rightarrow {}^4T_2$-transition of Cr^{III} is excited. An intersystem crossing results in the population of the $Cr(^2E)$-state and luminescence of the transition $Cr(^2E \rightarrow {}^4A_2)$ (747 nm) can be observed. An alternative energy path transfers the energy to the central Er^{III}-ion, which is consequently excited to the $Er(^4I_{9/2})$-state. After an additional energy transfer from Cr^{III} the $Er(^4S_{3/2})$-state can be populated and subsequently a photon with a wavelength of 543 nm can be emitted ($Er(^4S_{3/2} \rightarrow {}^4I_{15/2})$). After an initial study in the solid state at 4K, these results could also be reproduced in a frozen acetonitrile solution at 30.6 K. Systems like this, where d- and f-metals are combined, have the advantage that the significantly different coordination behaviour of the d-metals facilitates the control over the spatial arrangement of the different metals in such a heterometallic complex. Furthermore, in the case of the d-metals a manipulation of the exact energetic position of the excited states is possible via a modification of the ligand, and generally their emission bands are broader which leads to an increase of the spectral overlap integral compared to systems in which the energy has to be transferred between two lanthanoids.

In another example also an antenna ligand could be employed as sensitiser to generate upconverted lanthanoid-luminescence: An adduct of $Er(TTA)_4$ (TTA = 2-thenoyltrifluoroacetone) and the organic dye IR-806 exhibits upconverted Er^{III} emission ($Er(^2H_{11/2} \rightarrow {}^4I_{15/2})$ and $Er(^2S_{3/2} \rightarrow {}^4I_{15/2})$) in $CDCl_3$ at room temperature and after excitation with a 808 nm laser diode. Neither the pure potassium salt of $Er(TTA)_4$ nor the pure iodide of IR-806 showed any emission in the range of the upconverted Er^{III}-emission after excitation at 808 nm, so the process which is observed in the sample containing both components is likely to be consequence of an energy transfer process. Furthermore the emission intensity depends on the square of the excitation intensity, which gives evidence of the observed process being an upconversion process. Unfortunately the efficiency of the process is very low, at a laser intensity of 9.5 W/cm^2 it was estimated to be 0.1%.[297]

Considering the diverse examples described above, it can be concluded that the fascinating field of energy transfer processes between lanthanoids in molecular systems is still in its infancy but has yet shown a glimpse of its potential. As next step towards an utilisation of these phenomena there is definitely a need for well-defined and controllable systems which allow for a systematic study and understanding of the relevant processes. Again this is a task where the cryptates have an outstanding potential. As already outlined in earlier chapters, these complexes show outstanding kinetic stabilities and can protect the lanthanoids efficiently from nonradiative deactivation processes caused by high-energy oscillators in the close vicinity. This has proven to be especially effective in the case of the NIR-emissive lanthanoids such as Yb^{III}, which are particularly important in the context of upconversion processes.[133][140]

In order to expand the beneficial impact of this ligand scaffold onto two lanthanoids in a single molecule, it is conceptually straight forward to attach two cryptate cavities to each other in a rigid fashion by exchanging one of the bipyridines of each cryptate with a shared bipyrimidine unit (see Figure 6.7). After considerable preparative efforts it was indeed possible to prepare such a dicryptate scaffold and also the corresponding complexes **Eu-Eu-bpy$_2$-bpm-bpy$_2$** and **Eu-Y-bpy$_2$-bpm-bpy$_2$**.[141]

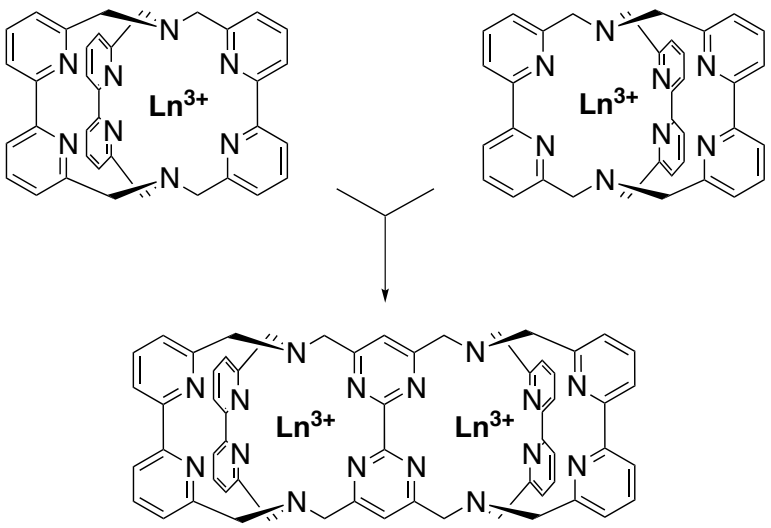

Ln-Ln-bpy$_2$-bpm-bpy$_2$

Figure 6.7: In order to extend the concept of the tris-bipyridine cryptates to a ligand scaffold for the controlled coordination of two lanthanoids, two cryptates were fused by exchange of two bipyridines for a shared bipyrimidine.[141]

It could be shown that this ligand scaffold offers unprecedented possibilities for the highly controlled synthesis of heterodinuclear lanthanoid complexes. In a first step, the sodium cryptate **Na-Na-bpy$_2$-bpm-bpy$_2$** obtained after the synthesis of the ligand can be transformed into a mono-substituted lanthanoid complex **Ln-Na-bpy$_2$-bpm-bpy$_2$** which can be purified via reversed phase HPLC. Most importantly this removes any remains of unreacted lanthanoid salt. In a subsequent reaction step the second cavity of the scaffold can be filled with a (different) lanthanoid. For a first study upon this ligand and the properties of its complexes, the homobimetallic compound **Eu-Eu-bpy$_2$-bpm-bpy$_2$** was prepared. Interestingly, the emission spectrum of the compound shows two clearly distinguishable bands for the Eu($^5D_0 \rightarrow {}^7F_0$)-transition (at 572 and 575 nm, respectively) which is a strong evidence for differences in the exact coordinative situation of the two binding pockets. In line with that, the luminescence lifetime of the compound exhibits a biexponential decay whereby both components contribute equally to the determined total luminescence lifetime. Comparison of the lifetimes determined in CH_3OH and CD_3OD indicates that the coordinated Eu^{III}-ions differ significantly in terms of the number of solvent molecules coordinated in the first coordination sphere around the lanthanoid. Furthermore some of the results point towards a strong mechanical coupling between both binding pockets. The unprecedented synthetic possibilities which result from the stepwise metal exchange of **Na-Na-bpy$_2$-bpm-bpy$_2$** and the interesting photophysical properties reported for the homobimetallic Eu^{III}-derivative (e.g. the differences of the coordinative situations found for both cavities) make this ligand scaffold particularly attractive for the search of molecular lanthanoid upconverters.

6.2 Conception of the Project

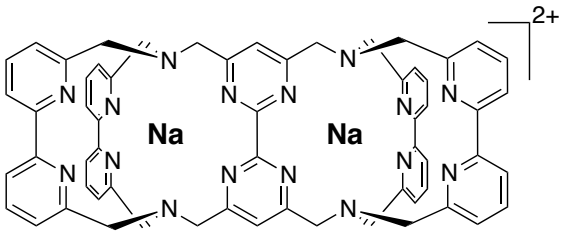

Na-Na-bpy$_2$-bpm-bpy$_2$

After the preparation of the dicryptates **Na-Na-bpy$_2$-bpm-bpy$_2$** and initial studies on corresponding lanthanoid complexes, now the study of cryptate-based molecular systems for the observation of energy transfer processes between lanthanoids shall be broadened.

- **Improvement of the accessibility of the ligand**

Until now the synthesis of **Na-Na-bpy$_2$-bpm-bpy$_2$** could only be performed with low overall yields. This obviously hampered the preparation and study of complexes of different combinations of lanthanoids in this scaffold. To solve this problem and to provide a better basis for extended studies of these compounds the yield of the synthesis has to be improved. Also a facilitation of the work up procedures would be desirable.

- **Synthesis and characterisation of new complexes Ln-Ln-bpy$_2$-bpm-bpy$_2$**

After the improvement of the accessibility of the ligand several new complexes shall be prepared, in which combinations of lanthanoids are realised which are promising for the observation of energy transfer processes, especially for upconversion processes. To improve the general understanding of these compounds and facilitate the identification of interesting pairs of lanthanoids to be combined also the structural properties of these compounds shall be studied.

- **Development of new ligands for multimetallic cryptate-derivatives**

Ligands for the controlled synthesis of heteropolymetallic complexes of lanthanoids are still extremely underrepresented in literature, though they offer many interesting properties which can be of potential for different applications. Furthermore, for an improvement of the understanding of energy transfer processes between lanthanoids, reference systems with slightly different coordinative situations might be extremely helpful. Last but not least, the dicryptates **Ln-Ln-bpy$_2$-bpm-bpy$_2$** can obviously only allow for upconversion processes following a SA-ETU mechanism. In a complex of three lanthanoids the more effective SAS-ETU mechanism could operate, which would improve chances for the observation of upconversion.

6.3 Results and Discussion

6.3.1 Optimisation of ligand synthesis

Energy transfer processes (most prominently upconversion) between lanthanoids are well-known for nanoparticles and a plethora of systems exhibiting such phenomena has been described. Recently more and more effort is invested in realising related molecular systems which will allow for innovative applications and an improved understanding. Unfortunately this is significantly more difficult than for the particle-based systems and only very few examples have been published until now. A promising scaffold for the preparation of molecular compounds with several lanthanoids between which energy transfer processes can be observed are dicryptates **Ln-Ln-26** (see Figure 6.8).[141]

In analogy to the preparation of the sodium cryptates **Na-bpy$_3$** and **Na-bpy$_3$O$_2$** and their derivatives, the sodium dicryptates **Na-Na-26** are assembled from the macrocyclus consisting of two bipyridines and a building block of two nitrogen heterocycles with bromides in benzylic positions. To offer nitrogen chelators for the lanthanoids in both binding pockets, in this case a bipyrimidine instead of a bipyridine is necessary, and of course it needs to be a tetrabromide instead of a dibromide. The resulting tetrabromide 4,4',6,6'-tetrakis(bromomethyl)-2,2'-bipyrimidine **25** is the key building block of the synthesis (see Figure 6.8).

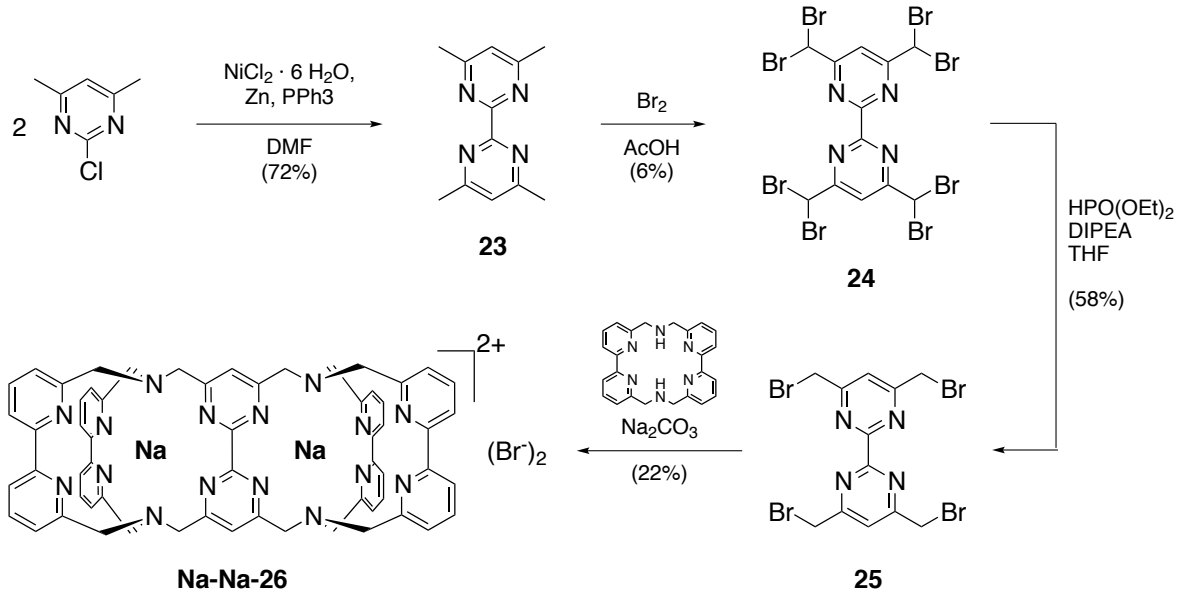

Figure 6.8: Preparation of the sodium dicryptate **Na-Na-26** starting from 4,6-dimethyl-2-chloropyrimidine as established until now.[141]

Starting from 4,6-dimethyl-2-chloropyrimidine[298] the initial step is a Ni^0-promoted coupling reaction.[299][300] The reaction has a rather high yield of 72% of the bipyrimidine **23**, but the work up procedure tends to be cumbersome and the removal of excess PPh_3 and the corresponding oxide often requires two subsequent column-chromatographies. The next reaction turned out to be the bottle-neck of the synthesis of **Na-Na-26** until now: The bromination reaction using elemental bromine in glacial acetic acid at 80 °C yields only 6%

of the desired octabromide **24** after column-chromatography. In the final step of the synthesis of the tetrabromide **25** four of the bromines are reduced by addition of diethyl phosphite in the presence of DIPEA. This reaction proceeds with a moderate yield of 55% after column-chromatography and the subsequent double macrobicyclisation turned out to proceed with a surprisingly good yield of 22%. But since the previous three steps did only proceed with an overall yield of 3.5% the sodium dicryptate **Na-Na-26** has been available in only very limited quantities until now. This of course hinders the synthesis and characterisation of the corresponding lanthanoid dicryptates and the systematic search for pairs of lanthanoids which exhibit interesting energy transfer processes in this scaffold. In order to solve this problem and provide a better basis for efforts towards this aim, the steps for the synthesis of tetrabromide **25** from 4,6-dimethyl-2-chloropyrimidine were optimised in terms of yields and time efficiency.

In the case of the Ni^0-promoted coupling reaction towards the bipyrimidine **23** the yield of the reaction was already satisfactorily good, but the work up procedure should be improved. The reaction is performed in DMF and after 24 hours reaction time the crude mixture is poured into 4 M ammonia which leads to precipitation of a dark solid. The solid is separated from the solution via filtration, the filtrate is extracted with CH_2Cl_2, dried and evaporated to dryness. Main components of the material obtained are the bipyrimidine **23**, PPh_3 and triphenylphosphine oxide. In principle separation of these compounds via column-chromatography is possible, but often the product isolated afterwards is still contaminated so that the column-chromatography has to be repeated and the overall procedure becomes quite tedious. As a very time saving modification a two step aqueous work up was developed for the crude material obtained after filtration. To do so the concentrated organic phases are taken up in 1 M HCl and subsequently extracted with Et_2O. Under these conditions the product of the reaction is protonated and stays in the aqueous phase while the phosphines are transferred into the organic phase. Subsequently the aqueous phase is brought to pH 8-9 with saturated aqueous Na_2CO_3, so that the product is deprotonated and can be extracted from the aqueous phase with $CHCl_3$. The same procedure can be repeated with the solid obtained from filtration. Usually the material isolated herein is less pure than the first fraction, and often a repetition of the work up procedure is reasonable. Still the purification following this strategy is significantly faster and even a slight increase of the yield could be found (74%).

The next step of the synthesis has been the most problematic so far but could be drastically improved with a very simple modification. Until now the bromination reaction was performed at a bath temperature of 80 °C. By increasing the bath temperature for the initial 30 minutes of the reaction, so that the internal temperature of the reaction mixture actually reaches 80 °C, a much more vivid reaction could be observed. In the subsequent 17 hours at 80 °C bath temperature the continuous precipitation of a white solid could be observed, which had not been mentioned in the previous description of the experiment. In line with that also the work up procedure had to be adapted. The crude material isolated after evaporation of the volatiles could not be dissolved in saturated aqueous $NaHCO_3$ as it had been described before. Instead the material showed hydrophobic behaviour and only slowly dissolved under stirring after addition of $CHCl_3$. This already pointed towards a higher content of polybrominated species in the mixture. Indeed after extraction and purification a higher yield of the octabromide **24** (15%) could be isolated, but also the previously unknown heptabromide **27** (which was characterised via ^1H NMR and ^{13}C NMR spectroscopy and via ESI-MS) in a surprisingly high yield of 53% (see Figure 6.11, page 174). Figure 6.9 shows the ^1H

NMR spectra of both polybrominated bipyrimidines **24** (top) and **27** (bottom). The spectrum of the highly symmetric octabromide **24** has only two signals with integrals in a ratio of 2:4, the signal of the aromatic protons at 8.51 ppm and the signal corresponding to the four protons of the $CHBr_2$-groups at 6.72 ppm. In the ^1H NMT spectrum of the heptabromide **27** two signals with only slightly different shifts compared to the spectrum of **24** can be found, at 8.49 and 6.73 ppm the signals of the protons of the fourfold brominated pyrimidine unit can be found. The signal of the aromatic proton of the opposite pyrimidine can be observed at 8.17 ppm and the signal of the proton of the corresponding $CHBr_2$-group can be observed closely to the one of the other $CHBr_2$-groups (6.69 ppm). The signal at 4.67 ppm corresponds to the protons of the CH_2Br-group of **27**.

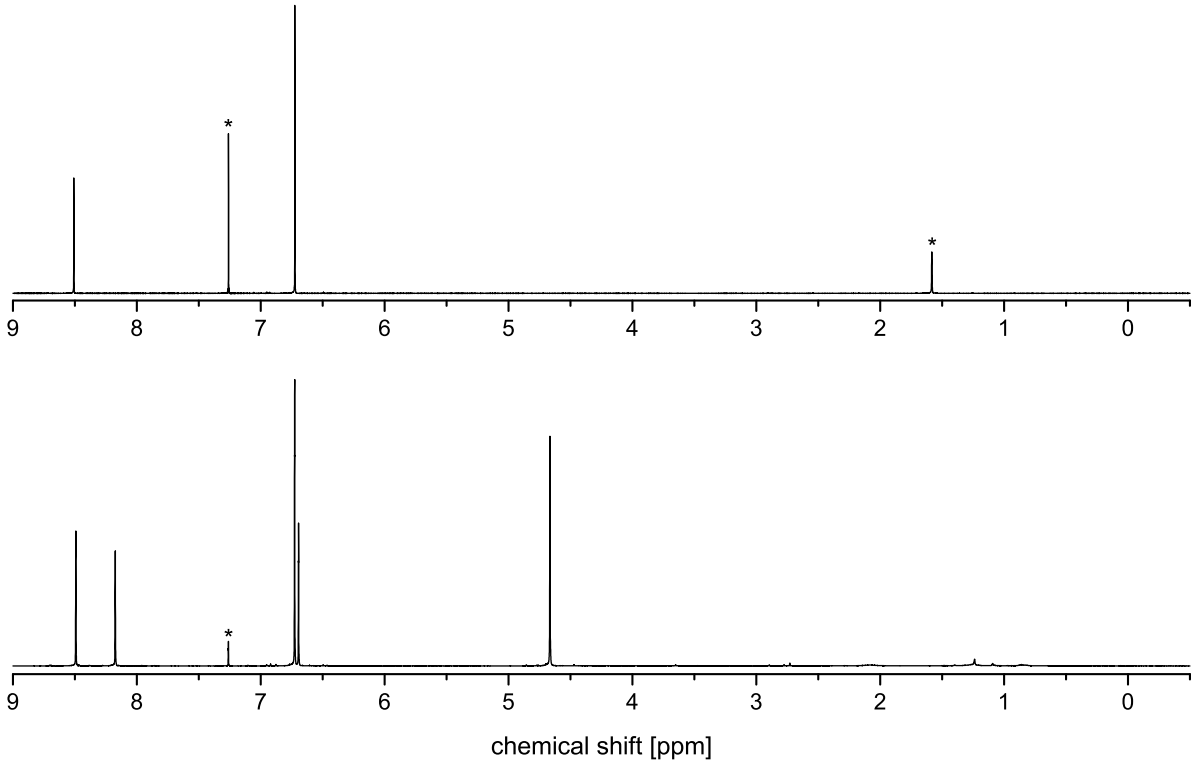

Figure 6.9: ^1H NMR spectra of the octabromide of the bipyrimidine **24** (top, 400 MHz, $CDCl_3$) and the heptabromide of the bipyrimidine **27** (bottom, 400 MHz, $CDCl_3$). Unambiguously identified solvent signals are marked with an asterisk.

Initially the octabromide **24** was isolated from column-chromatography with a significant contamination of heptabromide **27**. Due to the low solubility of **24** in $CHCl_3$ the compound could easily be purified via re-crystallisation. Most likely it is also possible to separate **24** from the crude mixture via recrystallisation so that the already quite convenient column-chromatography to isolate the heptabromide **27** will be further facilitated.

For **24** it was possible to obtain a crystal suitable for single-crystal X-ray crystallography. The structure (see Figure 6.10) was solved in the monoclinic space group $P2_1/c$ upon which a R-factor of 4.06% was

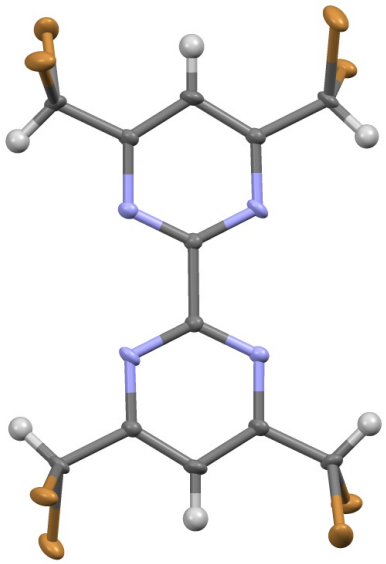

Figure 6.10: X-ray structure of **24**, thermal ellipsoid plot (Mercury, 50% probability level). Free CH_3Cl in the unit cell is omitted for clarity. Colour scheme: C, grey; N, light blue; H, white; Br, brown.

obtained. The structure is completely in line with expectations and the results from NMR spectroscopy.
The isolation of heptabromide **27** is so important since it is in principle as suitable for the subsequent reaction step as the octabromide **24**. Indeed a simple adaption of the equivalents of diethyl phosphite and DIPEA from 8.0 to 7.0 equivalents was found to be sufficient to modify the reaction towards tetrabromide **25** for the new starting material. For this reaction also a purification without column-chromatography could be developed. After extraction the crude material isolated was dried for several hours in vacuo to remove excess DIPEA. Subsequently CH_3OH was added to the solid and the resulting suspension was stirred to remove impurities from the product (which itself is not soluble in this solvent). After filtration the solid was dissolved in $CHCl_3$, evaporated to dryness and extracted another time with CH_3OH. The extraction performed directly after quenching the reaction by pouring the mixture onto ice was previously performed with Et_2O. $CHCl_3$ and CH_2Cl_2 were found to be the more efficient solvents for this step and actually Et_2O seems to preferentially remove some byproducts from the crude mixture. In an early attempt to perform the reaction, the aqueous phase was initially extracted with Et_2O but as the subsequent column-chromatography yielded only a small amount of the product the aqueous phase was extracted another time with CH_2Cl_2. The material obtained from this extraction was treated as described above and the product isolated afterwards was pure enough for elemental analysis. For the reaction transforming heptabromide **27** into the tetrabromide **25** a yield of 69% could be determined. Eventually a slight improvement of the yield of the originally reported reaction starting from **24** is possible when the column-chromatography is substituted with the procedure described herein.
Figure 6.11 shows the modified synthesis strategy for the preparation of the sodium dicryptate **Na-Na-26** together with the yields of the individual steps. For the total sequence starting from 4,6-dimethyl-2-chloropyrimidine now a total yield of 33.5% can be realised which is an improvement of about one order

of magnitude. Furthermore the purification procedures are now significantly less time consuming and as a result the sodium dicryptate **Na-Na-26** is now by far more accessible.

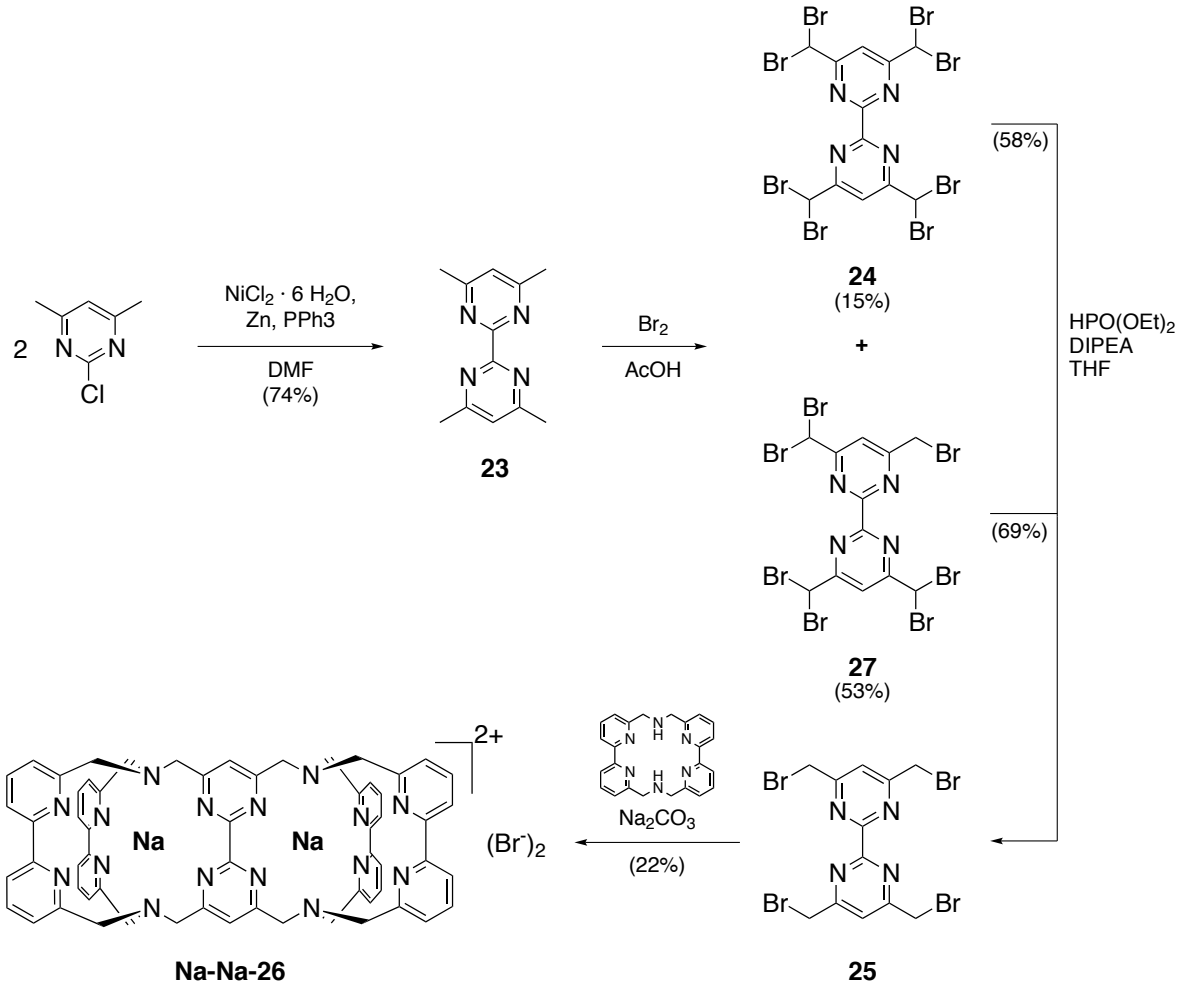

Figure 6.11: Modified preparation of the sodium dicryptate **Na-Na-26** starting from 4,6-dimethyl-2-chloropyrimidine with improved yields and facilitated purification procedures.

6.3.2 Preparation and study of sodium and lanthanoid dicryptates

6.3.2.1 Characterisation of the homobimetallic dicryptate

The results obtained from the previous studies on the dicryptates prepared so far point towards some very interesting structural features (see page 167 and following). For example there is strong evidence that upon coordination of two Eu^{III} ions the cavities provide a significantly different coordination environment and that there is some kind of mechanical coupling between both binding pockets. Though the binding pockets do not carry N-oxides the overall structure seems to be significantly more rigid than the corresponding cryptates **Ln-bpy$_3$O**.

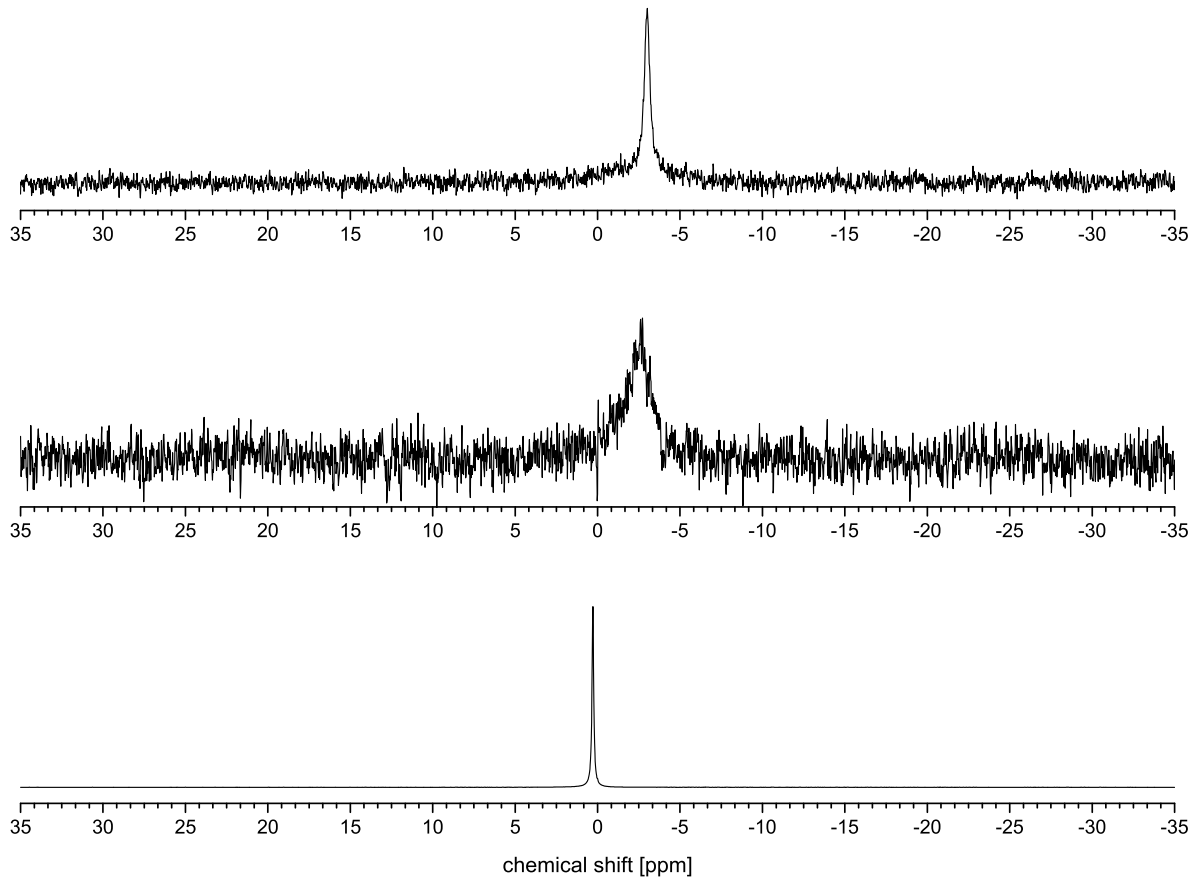

Figure 6.12: ^{23}Na NMR spectra of the sodium dicryptate **Na-Na-26** (top, 66.2 MHz, CD_3OD), the sodium cryptate **Na-bpy$_3$** (middle, 66.2 MHz, CD_3OD) and NaCl (bottom, 66.2 MHz, D_2O).

For an improvement of the general understanding of the overall properties of the ligand scaffold the sodium dicryptate **Na-Na-26** can provide some valuable information. As a spin 3/2 nucleus ^{23}Na is quadrupolar and therefore the width of the observed signals will be the smaller the higher the symmetry around the observed nucleus is. In Figure 6.12 the ^{23}Na NMR spectrum of **Na-Na-26** (top), the sodium cryptate **Na-bpy$_3$** (middle) and NaCl in D_2O (bottom) as reference are shown. The spectra were recorded in direct

succession without locking or shimming so that the signal of NaCl could be used for referencing the signals of the cryptates. In line with the results from ^{1}H NMR spectroscopy the ^{23}Na NMR spectrum of **Na-Na-26** gives evidence of both binding pockets being equivalent on the NMR time scale.

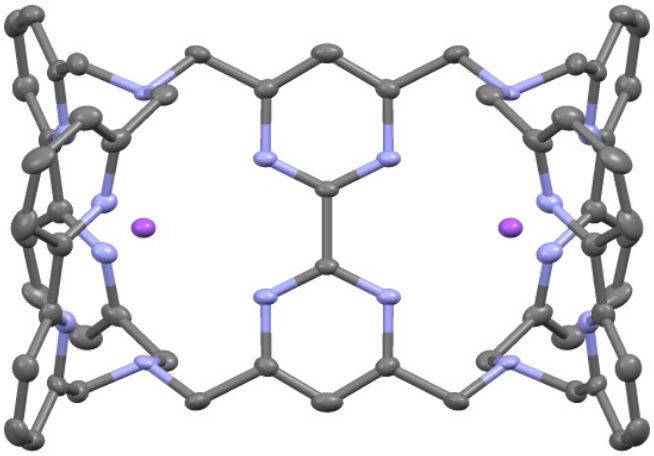

Figure 6.13: X-ray structure of **Na-Na-26**, thermal ellipsoid plot (Mercury, 50% probability level). Hydrogen atoms and external Br^- are omitted for clarity. Colour scheme: C, grey; N, light blue; Na, purple.

From a solution of **Na-Na-26** in CD_3OD a crystal suitable for single-crystal x-ray crystallography could be obtained. The structure (see Figure 6.13) was solved in the monoclinic space group C2/m upon which a R-factor of 10.38% was obtained. It is C_2-symmetric and in line with the previous results from the characterisation of the compound.
In the crystal structure the sodium cations have a distance of about 7 Å. It is reasonable to assume that the distance between the metal centers in solution or in lanthanoid complexes will be very similar. Consequently the distance between the lanthanoid centers in a complex **Ln-Ln-26** would be in the range of experimentally observable Förster radii for f-f transfer processes (5 Å $\leq R_0 \leq$ 15 Å).[284] Also the distances between the sodium cations of the complexes in different layers of the crystal lie in this range, but for the lanthanoid dicryptates (which would also be expected to have different counter anions) a different packaging can be expected.

6.3.2.2 Preparation of dicryptates of small lanthanoids: Example of the homobimetallic erbium dicryptate

As discussed above Er^{III} is one of the best suited activators for lanthanoid centered upconversion (see page 160) and based on a supramolecular assembly of two erbium complexes it was already possible to observe molecular upconversion in deuterated water.[28] Consequently the corresponding dicryptate **Er-Er-26** is a highly interesting target structure. It could be prepared analogously to the procedure already published for the synthesis of homodinuclear europium dicryptates.[141]

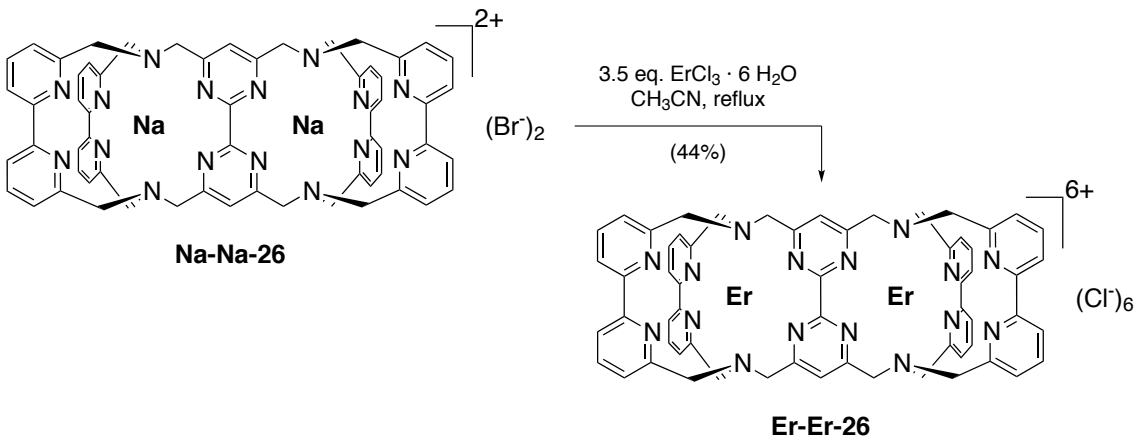

Figure 6.14: Synthesis of the erbium dicryptate **Er-Er-26** from the corresponding sodium dicryptate **Na-Na-26**.

While for the corresponding homodinuclear europium complex a purification via reversed-phase HPLC is possible,[141] the feasibility of an analogous purification of the erbium dicryptate **Er-Er-26** is questionable. While for the rigidified lanthanoid cryptates **Ln-bpy$_3$O$_2$** HPLC purification for all lanthanoids is possible, in the case of the cryptates **Ln-bpy$_3$** the stability of the compounds is not sufficiently high for the smaller lanthanoids, and for example preparative HPLC of **Er-bpy$_3$** is not feasible.

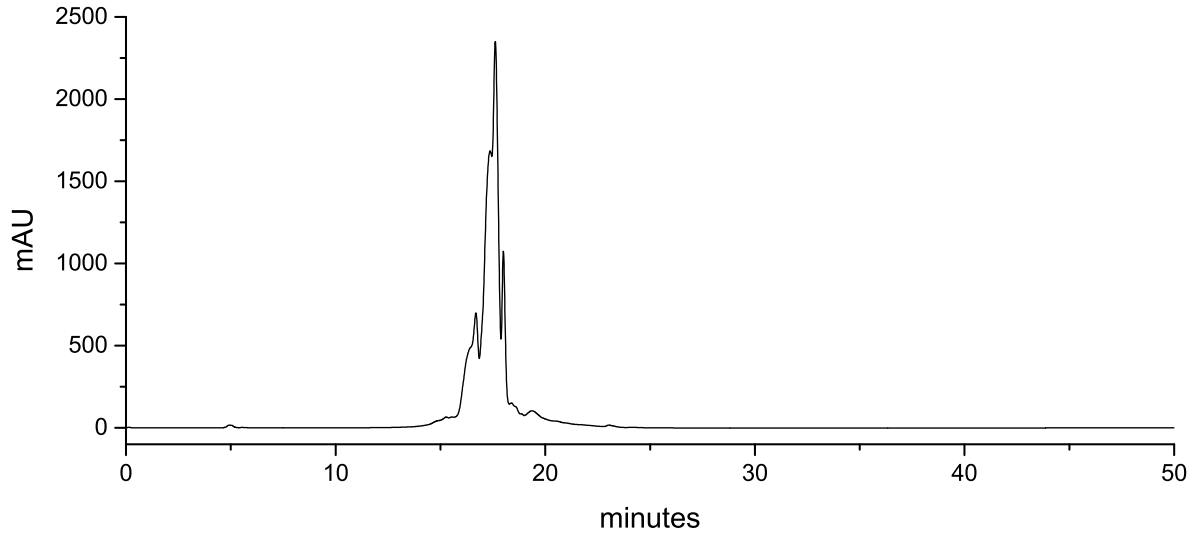

Figure 6.15: Chromatogram from the preparative HPLC (program **A**, setup **A**) performed for the purification of **Er-Er-26**.

Yet, based on the previous analysis of the dicryptates, the rigidity and stability of these complexes can be expected to be at least a bit higher than the ones of the directly related mononuclear cryptates **Ln-bpy$_3$** and consequently the feasibility of a HPLC purification was tested. To do so a portion of the crude material obtained from synthesis was subjected to a preparative HPLC with program **A** (see Figure 6.15). Two fractions (from 15.6 to 16.9 minutes and from 16.9 to 17.9 minutes) were collected and the volatiles were removed as quickly as possibly to reduce the exposure of the complex to the strongly acidic conditions.

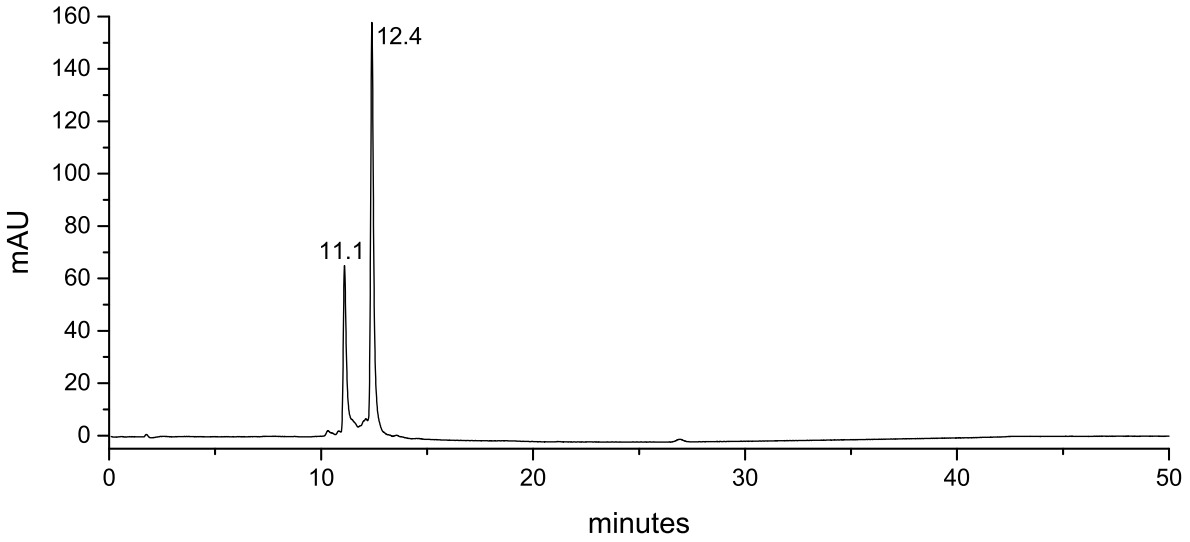

Figure 6.16: Chromatogram from the analytical HPLC (program **A**, setup **A**) of the first fraction (15.6 to 16.9 minutes) obtained from preparative HPLC of **Er-Er-26**.

The resulting material was subjected to analytical HPLC and for both fractions the presence of several peaks strongly points towards a decomposition into several species (see Figure 6.16 for the chromatogram obtained for the first fraction), consequently HPLC purification of **Er-Er-26** is not feasible with the methods available at the moment. As a result also the mono-substituted complex **Er-Na-26** will not be accessible with the HPLC-based strategy reported earlier.[141] The same will be the case for the analogous complexes of the even smaller Yb^{III} and Tm^{III}, and most likely also for the slightly bigger Ho^{III}. Consequently controlled synthesis of the high potential target compounds in which two of these lanthanoids are combined in a dicryptate will not be possible with the methods available until now.

Further studies on **Er-Er-26** were performed with the material obtained from recrystallisation. Unfortunately an interpretable ^{1}H NMR spectrum could not be obtained due to the strong paramagnetism of Er^{III} so that no structural characterisation of the complex was possible. During the initial study of the photophysical properties in solution (CD_3OD) and in a frozen matrix of CD_3OD/CD_3CD_2OD (1:1, v/v) after ligand excitation characteristic transitions of this lanthanoid in the visible and near-infrared part of the electromagnetic spectrum could be detected (see Figure 6.17). Since Er^{III} is quite susceptible towards nonradiative deactivation by e.g. C-H oscillators, the emission of this lanthanoid is not necessarily detectable in undeuterated complexes and in solution. In the next step the photophysical properties of the complex under direct excitation of the $^4I_{15/2} \rightarrow {}^4I_{15/2}$)-transition are to be studied, which is currently under way in cooperation with Dr. Andrey Turshatov from Karlsruhe Institute of Technology.

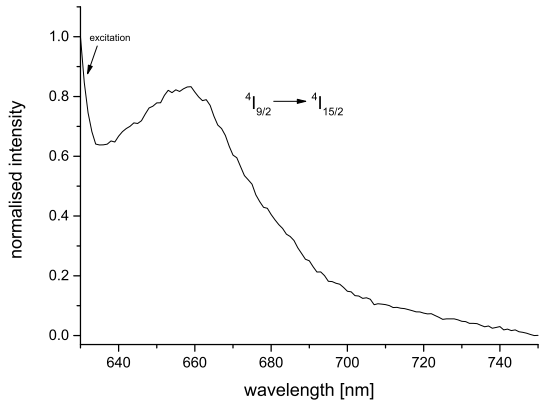

(a) Normalised steady state emission spectrum of the $^4I_{9/2} \rightarrow {}^4I_{15/2}$-transition of the erbium dicryptate **Er-Er-26** (CD_3OD, room temperature, $\lambda_{exc} = 307$ nm).

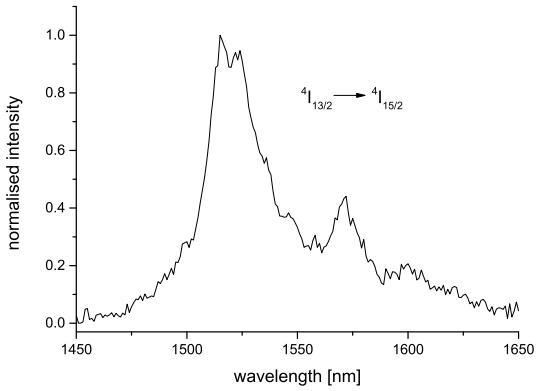

(b) Normalised steady state emission spectrum of the $^4I_{13/2} \rightarrow {}^4I_{15/2}$-transition of the erbium dicryptate **Er-Er-26** (frozen matrix of CD_3OD/CD_3D_2OD (1:1, v/v), 77K, $\lambda_{exc} = 307$ nm).

Figure 6.17: Normalised steady state emission spectra of **Er-Er-26**.

6.3.2.3 Modification of the strategy: Preparation of statistical mixtures

The outstanding characteristic of the dicryptates is the possibility of purifying them via HPLC. This allows for high control over the actual composition of the samples under study and even for the controlled preparation of heterobimetallic compounds. Consequently the resulting relatively time consuming procedure for the preparation is justified. At the same time the number of interesting pairs of lanthanoids between which an energy transfer process could potentially be observable is high and it is difficult to identify the ones which are most promising in a dicryptate scaffold. It should also be kept in mind that there is evidence for the binding pockets being not equivalent when they are filled with lanthanoids. The geometries of the binding pockets might in solution be interconverting into each other, but it might also be that upon exchange of the first sodium cation with a lanthanoid the geometry of the overall scaffold is defined so that the sequence in which the lanthanoids are introduced might indeed have an influence on the local geometry the lanthanoids experience. In principle this doubles the number of heterobimetallic dicryptates which could potentially be prepared and studied. In order to make a systematic search for lanthanoid dicryptates in which energy transfer processes can be observed feasible the preparation of the complexes had to be made more time efficient. This can be done by giving up the stepwise and controlled synthesis and instead preparing statistical mixtures of several complexes simultaneously. If the sodium dicryptate is reacted with two lanthanoid salts simultaneously up to four bimetallic complexes can be prepared with a single reaction (see Figure 6.18). The resulting mixture will contain both homobimetallic cryptates and the heterobimetallic cryptates. As outlined above, depending on which lanthanoid is reacting at first with the sodium dicryptate these can potentially be two different compounds, or both compounds are identical due to some kind of interconversion process. Initially the mixture will also contain intermediates for which only one of the sodium cations has been replaced with a lanthanoid. These compounds might indeed also be interesting, but they also can be separated from the mixture quite easily via HPLC (when the used lanthanoids are big enough

to make the corresponding dicryptates sufficiently stable).

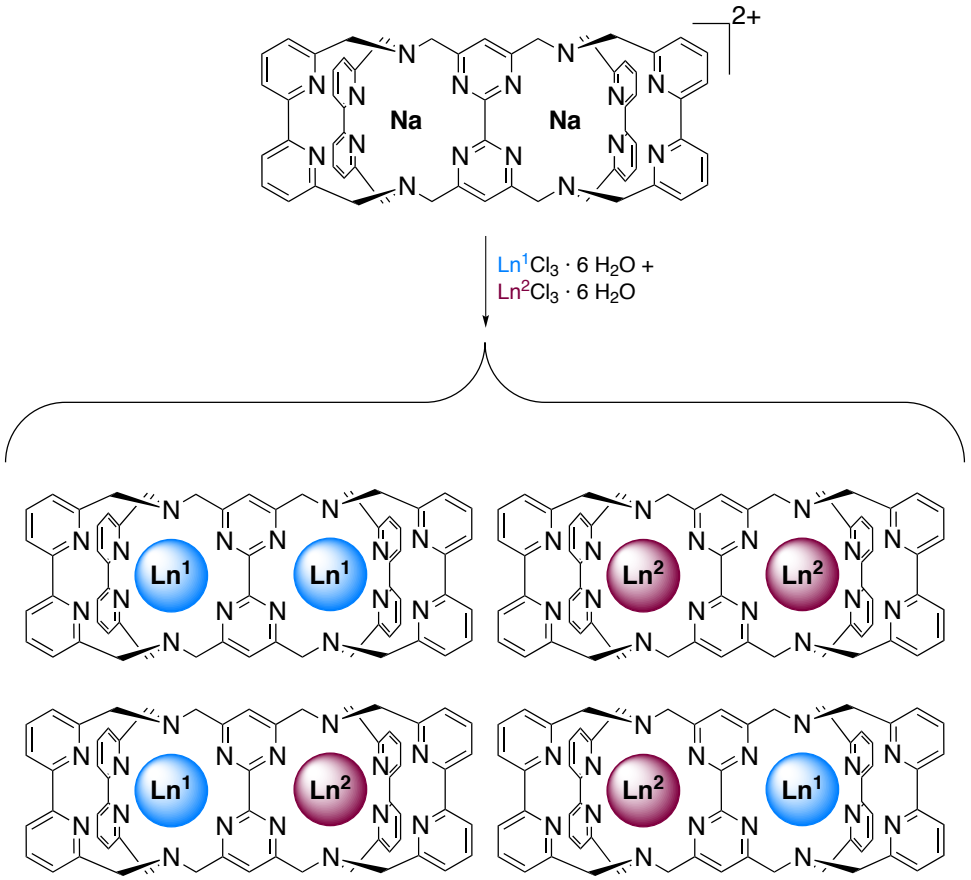

Figure 6.18: By simultaneous reaction with two lanthanoid salts the sodium dicryptate **Na-Na-26** can be transferred into up to four related lanthanoid dicryptates in a single reaction. Charges of the metal ions and counter anions are omitted for clarity.

After preparation of these mixtures a study of the photophysical properties will reveal if for one of the species an energy transfer process can be observed. In most cases it will not be possible to identify the species unambiguously, but an individual synthesis of the compounds of the mixture will allow to do so in the next step. When the lanthanoid ions are sufficiently big this can be done with the established, controlled approach using HPLC. For the smaller lanthanoids the homobimetallic dicryptates will be the most important reference compounds.

For an initial experiment following this approach europium and yttrium were chosen since the corresponding heterobimetallic complex has already been described in literature.[141] To optimise comparability, after reaction the isolated material was purified via reversed-phase HPLC following the standard procedure. The HPLC trace of one of the preparative runs is shown in Figure 6.20. The material eluting between around 17.7 and 19.6 minutes was collected, the analytical HPLC runs performed upon the isolated fractions clearly show that the material consists of three different species (and some additional impurities).

Figure 6.22 shows the normalised steady state emission spectrum obtained for the substance. Interestingly the shape of the spectrum is quite different to the ones reported earlier for **Eu-Y-26** and **Eu-Eu-26**,[141]

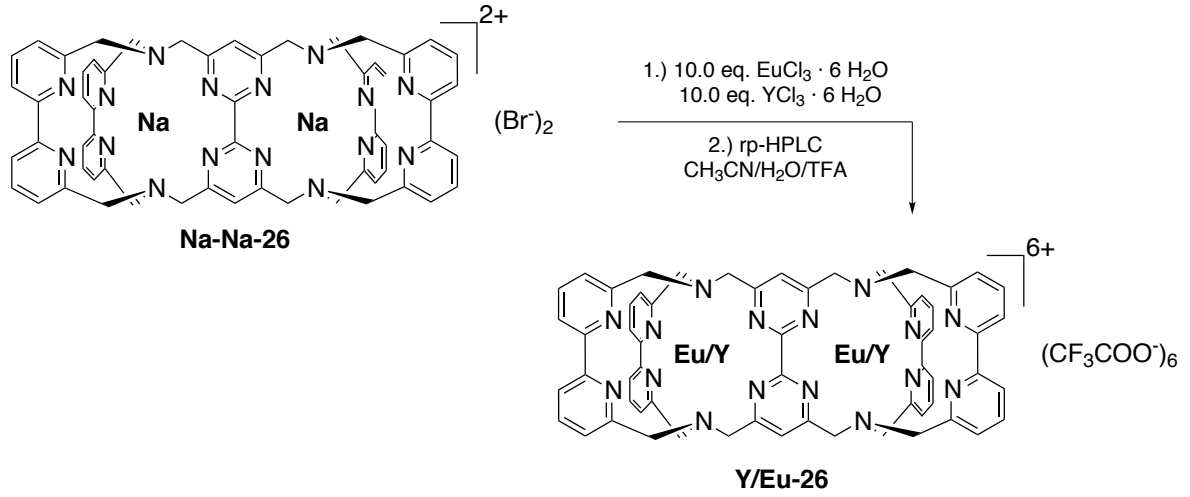

Figure 6.19: Synthesis of a mixture of several europium and yttrium containing dicryptates from the corresponding sodium dicryptate **Na-Na-26**.

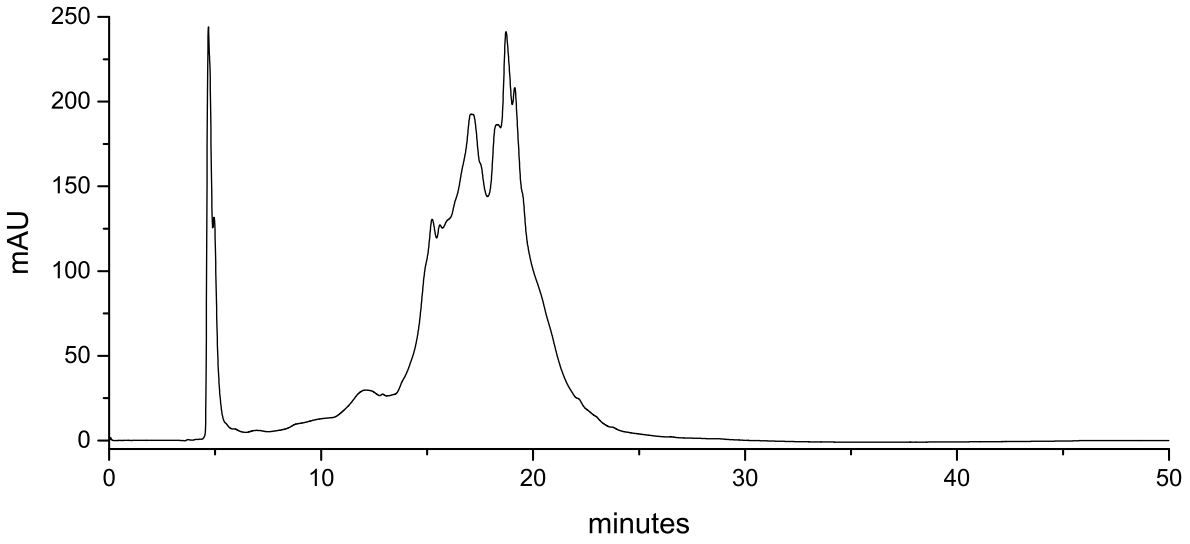

Figure 6.20: Chromatogram from the preparative HPLC (program **A**, setup **A**) performed for the purification of the statistical mixture of dicryptates containing europium and yttrium.

what would not have been expected. Apart from that the spectrum is well in line with expectations, as the shape of the $^5D_0 \rightarrow {}^7F_1$- and $^5D_0 \rightarrow {}^7F_1$-transitions point towards the presence of at least two Eu^{III} species. More detailed studies are under way in cooperation with Dr. Andrey Turshatov from Karlsruhe Institute of Technology.

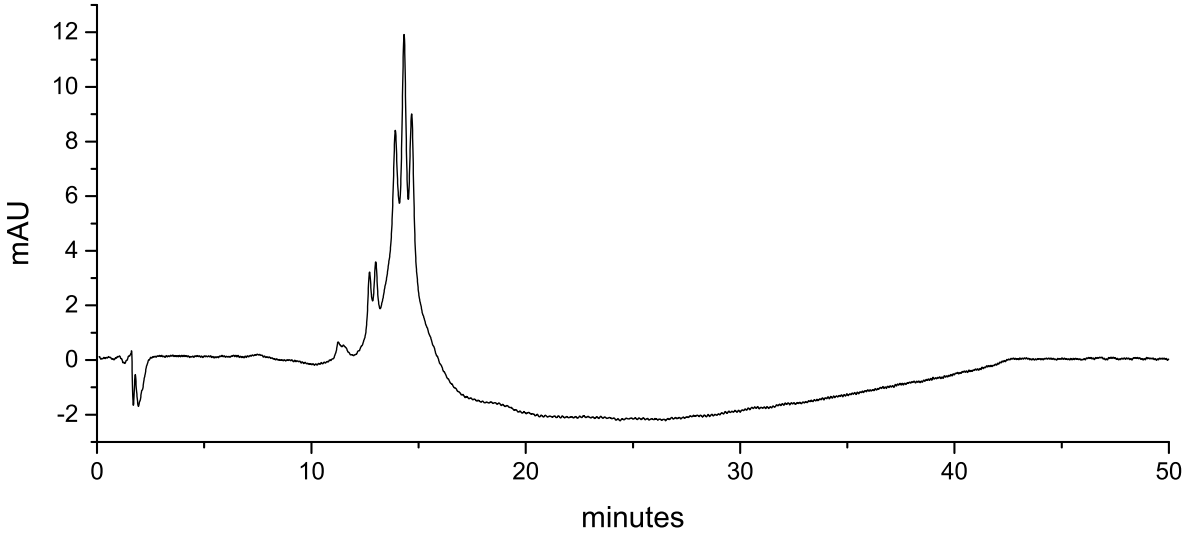

Figure 6.21: Chromatogram from the analytical HPLC (program **A**, setup **A**) of the material obtained from preparative HPLC of dicryptates containing europium and yttrium.

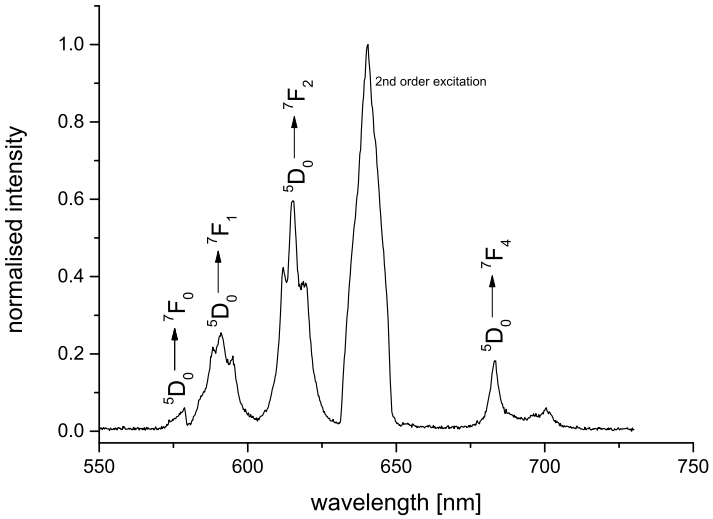

Figure 6.22: Normalised high resolution steady state emission spectrum of **Y**/**Eu-26** (CD_3OD, $\lambda_{exc} = 320$ nm).

For a second experiment following the approach shown in Figure 6.18 europium and terbium were chosen (see Figure 6.23). From the energetic position of the respective emitting levels it can be concluded that after initial direct excitation of Tb^{III} an energy transfer to Eu^{III} should be feasible. Since both lanthanoids are very luminescent, also in the presence of quenching oscillators, for this pair the chances that a potential energy transfer will actually be detectable are good and can further be improved by performing experiments in the solid state. Corresponding experiments are also done in cooperation with Dr. Andrey Turshatov from Karlsruhe Institute of Technology.

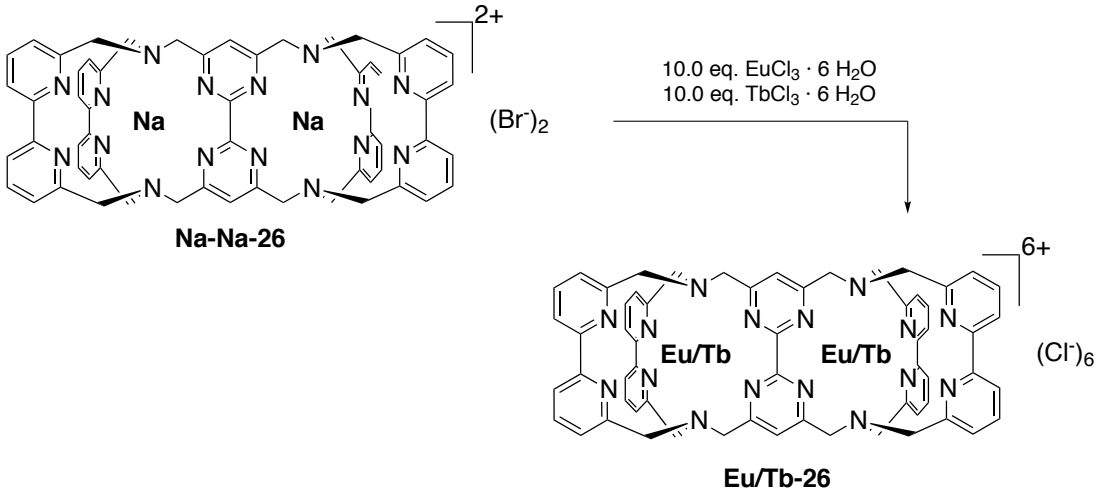

Na-Na-26 **Eu/Tb-26**

Figure 6.23: Synthesis of a mixture of several europium and terbium containing dicryptates from the corresponding sodium dicryptate **Na-Na-26**.

6.3.3 Towards new ligands for polymetallic lanthanoid complexes

Already in the first experiment performed to prepare **Na-Na-26** for this study a byproduct could be isolated which quickly turned out to be highly interesting. As the ^{1}H NMR spectrum of the compound (see Figure 6.25) is very similar to the one of the sodium dicryptate **Na-Na-26** it could easily be identified as a closely related substance. From the ratio of integrals it could finally be identified as the product of the macrobicyclisation of one tetrabipyrimidine **25** and one macrobicyclus which corresponds to a bromide-functionalised sodium cryptate.

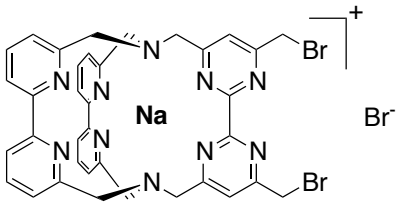

Na-28

Figure 6.24: The bromide-functionalised sodium cryptate **Na-28**.

Compared to the ^{1}H NMR spectrum of sodium dicryptate **Na-Na-26**, the signals of the aromatic bipyridine protons of **Na-28** have a very similar shape and are just slightly shifted downfield. At 7.74 ppm the aromatic protons of the bipyrimidine can be observed. The multiplet which can be observed at 4.70-4.66 ppm corresponds to the protons of the CH_2Br-groups. Finally also the signal of the 12 benzylic protons of the cryptate scaffold experiences a slight downfield shift to 3.96-3.82 ppm. The compound could also be characterised via ^{13}C NMR spectroscopy and ESI-MS.

By simple adaption of the equivalents used the bromide-functionalised sodium cryptate **Na-28** can be made the main product of the reaction. To improve chances for the formation of the desired 1:1 product the macrocyclus was added in portions over 3.5 hours to a mixture of tetrabromide **25** and ten equivalents of Na_2CO_3

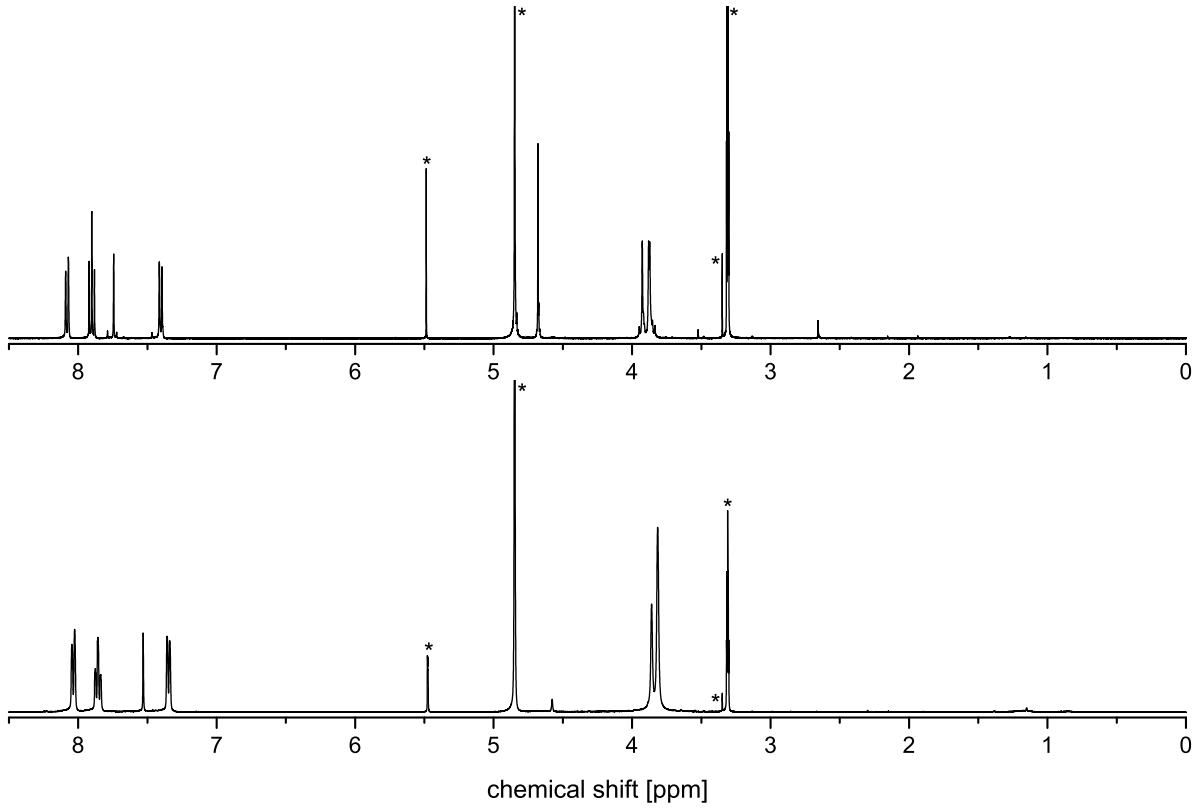

Figure 6.25: ^{1}H NMR spectra (400 MHz, CD_3OD) of the bromide-functionalised sodium cryptate **Na-28** (top) and the sodium dicryptate **Na-Na-26** (bottom). Unambiguously identified solvent signals are marked with an asterisk.

in CH_3CN (about 1 mL per 1 mg of tetrabromide **25**), which was already brought to reflux temperature beforehand. After complete addition of the macrocyclus the mixture was heated for another 14.5 hours before the crude product was isolated by complete evaporation of the volatiles. After column-chromatography the bromide-functionalised sodium cryptate **Na-28** could be obtained in 51% yield together with 7% of the dicryptate **Na-Na-26** and 31% of the starting material. Considering the high amount of starting material which could be isolated this reaction is surprisingly efficient.

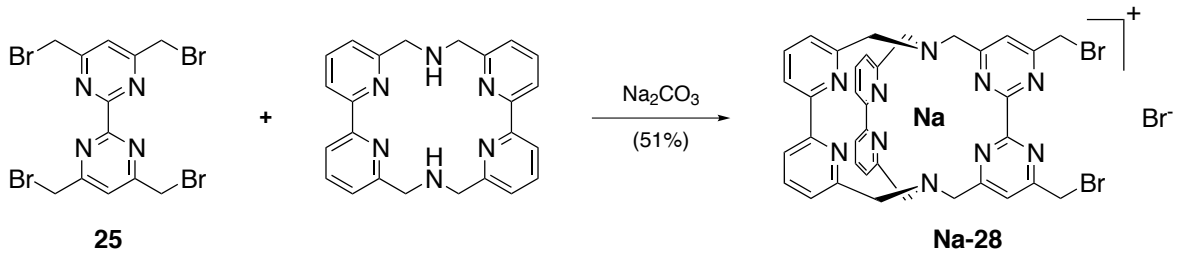

Figure 6.26: Synthesis of the bromide-functionalised sodium cryptate **Na-28**.

With the bromide-functionalised sodium cryptate **Na-28** it was surprisingly easy to make an intermediate for the development of new ligand systems for polymetallic lanthanoid complexes accessible. The design

of such new ligands and attempts towards their preparation and study will be described in the subsequent sections.

6.3.3.1 New ligands for the coordination of two lanthanoids

Though the emission spectra of the lanthanoids are typically considered to be unaffected by the coordinative situation around the lanthanoid this is not universally true. Of course the changes are very small compared to the transition metals, but e.g. for europium it is even possible to extract some structural information from the relative intensities and shapes of the individual transitions.[163] Slight shifts of the position of the maxima and the fine structure of the transitions can also be expected for the other lanthanoids. For the search for energy transfer processes between lanthanoids such small variations can indeed become crucial. Firstly, between two completely identical lanthanoid ions principally no energy transfer process can be observed. This is e.g. the case when the two binding pockets of a lanthanoid dicryptate are completely identical. Until now it is not completely resolved whether or when this is the case, but a general decrease of symmetry of the ligand would circumvent this problem. Secondly, a variation of the coordination sphere around one or both of the coordinated lanthanoids and the resulting small variations of the energetic position of their transitions might be useful for improving the spectral overlap integral of the coordinated lanthanoids. Of course this is not a strategy which can be used in a designed fashion but still the availability of different binding pockets will generally enhance changes for the observation of energy transfer processes. A highly suitable group for the construction of the new binding pocket are imminodiacetates. These groups are known to reliably coordinate lanthanoids and can typically be prepared quite easily.

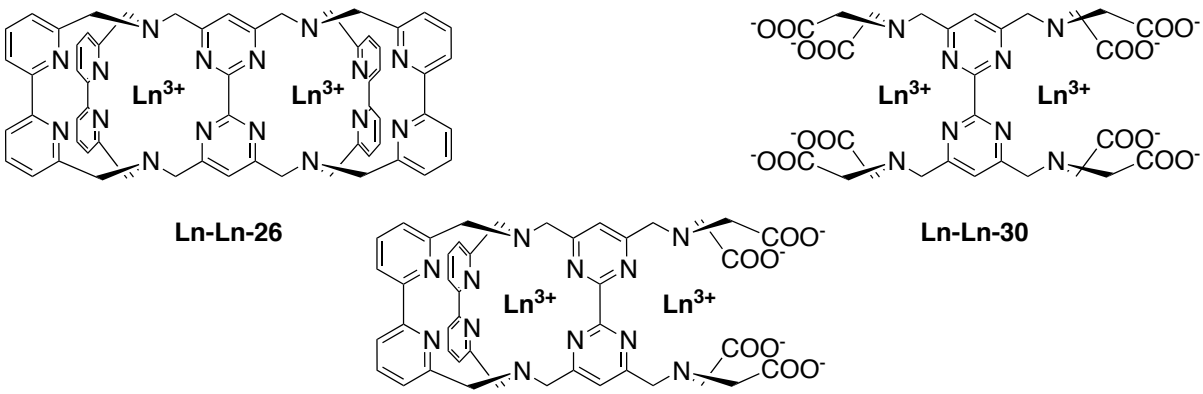

Figure 6.27: The lanthanoid dicryptate **Ln-Ln-26** and the targeted new ligand for two lanthanoids **Ln-Ln-29** and **Ln-Ln-30**

Following this approach and starting from the bromide-functionalised sodium cryptate the ligand for the preparation of **Ln-Ln-29** (see Figure 6.27) should be prepared. Analogously the ligand for the preparation of **Ln-Ln-30** should be prepared from the tetrabromide **25**. This can be expected to be feasible quite analogously to the preparation of the compound mentioned before, enlarge the library of available ligands for

two lanthanoids and be suitable for the preparation of reference compounds in comparative studies of complexes **Ln-Ln-26** and **Ln-Ln-29**. Subject of such a comparative study could for example be the influence of the number and nature of the different chromophoric groups in these compounds or the mechanism of the energy transfer between the lanthanoids. In line with that the complex **Y-Y-30** would allow for a detailed study upon the photophysical properties of the bipyrimidine between the lanthanoids in the dicryptates **Ln-Ln-26**.

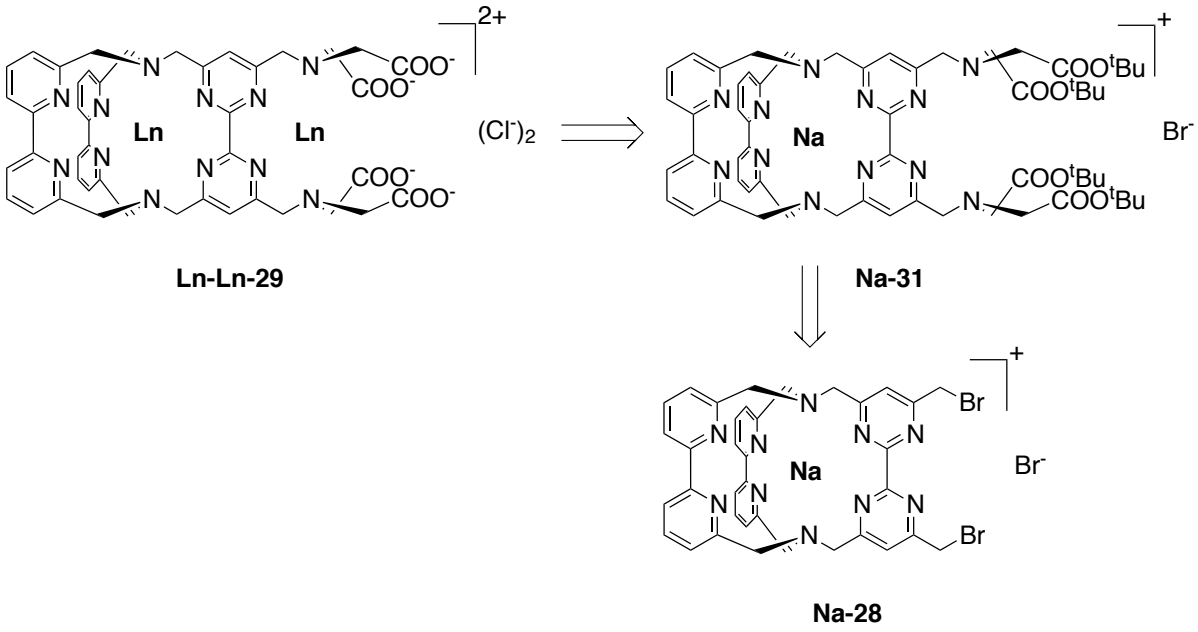

Figure 6.28: Retrosynthetic approach for the preparation of the iminodiacetate-functionalised cryptates **Ln-Ln-29** starting from the bromide-functionalised cryptate **Na-28**.

For the heterobimetallic complexes **Ln-Ln-29** (see Figure 6.28) even partial purification via reversed-phase HPLC seems feasible. After the protected diiminodiacetate-functionalised sodium cryptate **Na-31** has been reacted with a lanthanoid salt to exchange the sodium cation, for sufficiently large lanthanoids the *tert*-butyl groups can be cleaved and the resulting material be subjected to HPLC. This will help to ensure that no remaining cations of this lanthanoid are bound in the second binding pocket when the second lanthanoid is added to the intermediate. After addition of the second lanthanoid recrystallisation is the most promising technique for purification. If a small lanthanoid like Ho^{III}, Er^{III} or Yb^{III} is to be introduced into the cryptate it will be the more promising strategy to leave the protecting groups attached until the intermediate has been purified e.g. by recrystallisation and to cleave them in a separate step. For the homobimetallic complexes of this ligand it will most likely be the most efficient strategy to cleave the protecting groups initially and then insert the lanthanoid into both binding pockets simultaneously. In the case of the complexes **Ln-Ln-30** (see Figure 6.29) presumably only the homobimetallic compounds will be accessible. After cleavage of the protecting groups from **32** both binding pockets are filled with a lanthanoid simultaneously. The resulting complexes will not be stable in strongly acidic media and will not be purificable via HPLC. Again recrystallisation is the most promising technique for purification of the resulting complexes.

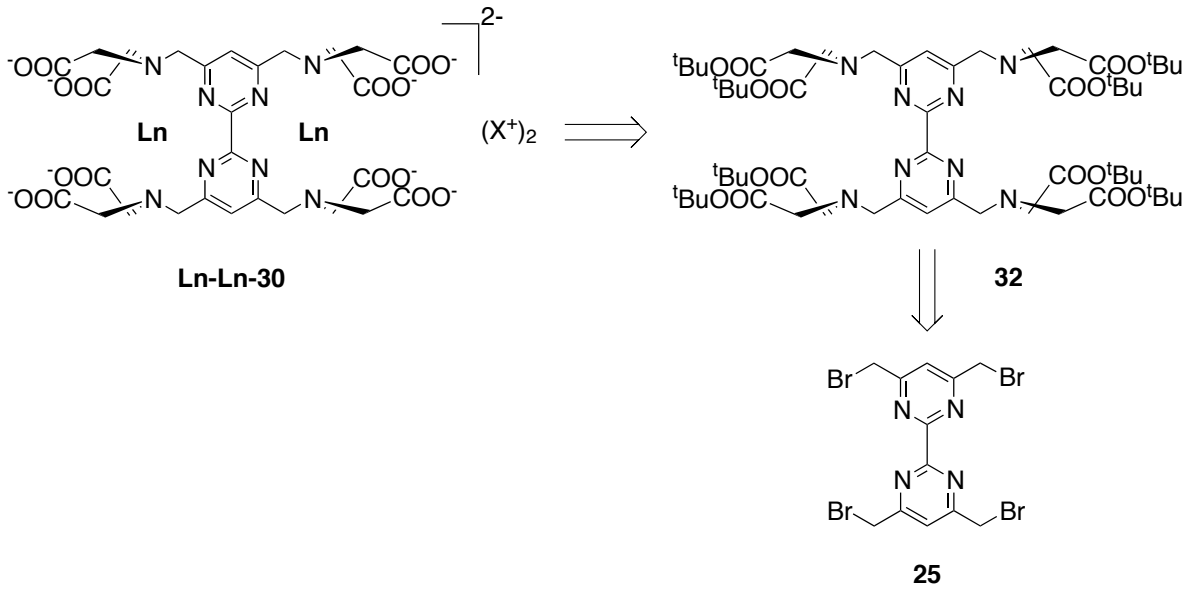

Figure 6.29: Retrosynthetic approach for the preparation of the iminodiacetate-functionalised complexes **Ln-Ln-30** starting from the tetrabromide **25**.

Since the availability of the tetrabromide **25** is better than the one of the bromide-functionalised sodium cryptate **Na-28**, first reactions to test the general feasibility of the attachment of the iminodiacetates to the bipyrimidine building block were performed with this starting material and towards the protected compound **32**.

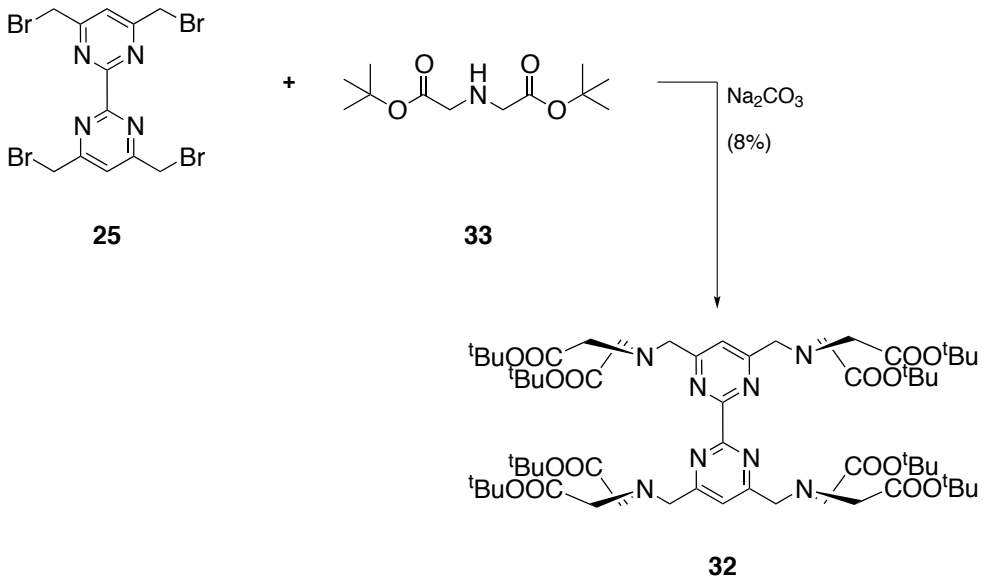

Figure 6.30: Preparation of the protected ligand **32** from the tetrabromide **25**.

To do so the tetrabromide **25** together with 10.0 equivalents of Na_2CO_3 and 4.4 equivalents of di-(*tert*-butyl)iminoacetate **33** was brought to reflux temperature in CH_3CN. After 14 hours the mixture was al-

lowed to come to room temperature and purified in several steps. Though only a slight excess of di-(*tert*-butyl)iminoacetate **33** had been used it was found to be quite difficult to remove remainders of the compound from the product. In this case several purification steps had to be performed (see experimental section, page 224), this presumably lead to the loss of a significant amount of product so that only 8% of **32** could be isolated, still with small impurities of reagent **33**. The compound was characterised via ^{1}H NMR spectroscopy, ^{13}C NMR spectroscopy and ESI-MS.

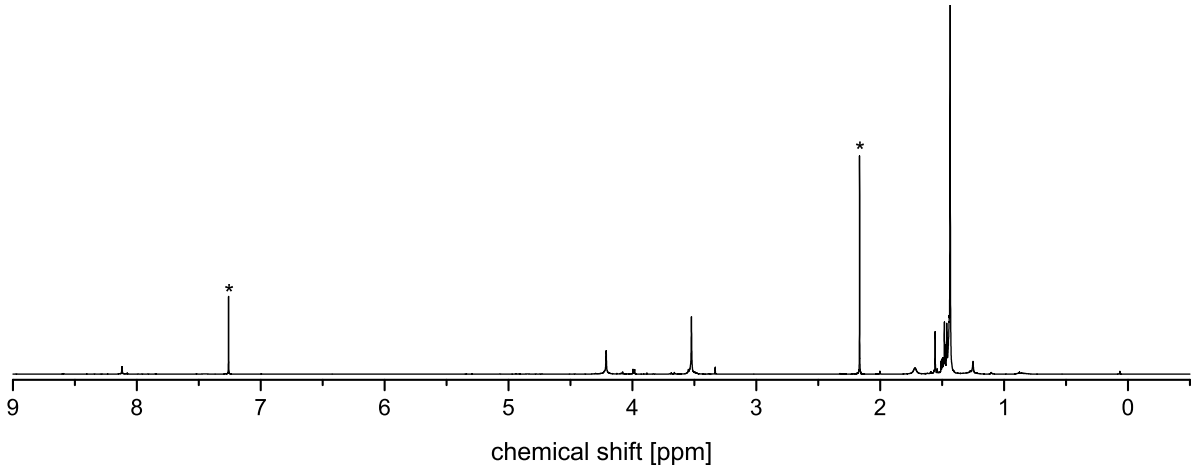

Figure 6.31: ^{1}H NMR spectrum of the protected ligand **32** (400 MHz, $CDCl_3$). Unambiguously identified solvent signals are marked with an asterisk.

The ^{1}H NMR spectrum of the isolated compound is shown in Figure 6.31. The spectrum is dominated by the signal corresponding to the 72 protons of the *tert*-butyl groups at 1.44 ppm. The signal of the only two aromatic protons at 8.12 ppm is shifted downfield compared to the starting material **25**, where the signal of these protons can be observed at 7.86 ppm. In contrast the signal of the eight benzylic protons of the bipyrimidine building block experience a highfield shift from 4.64 to 4.21 ppm. The 16 protons of the CH_2-groups of the iminodiacetates can be observed at 3.52 ppm.

In a first experiment towards the deprotected ligand **30** the protected precursor **32** was stirred for two hours in TFA with 10 vol.-% H_2O to cleave the acid labile *tert*-butyl groups. TFA was chosen since it is quite volatile and can easily be removed from the reaction mixture, together with the *tert*-butanol into which the protecting groups are transformed. H_2O was added as scavenger to trap reactive intermediates. Unfortunately the ^{1}H NMR spectrum of the crude product obtained after removal of the volatiles *in vacuo* did not point towards a clean progress of the reaction. The signals of the CH_2-groups could no longer be identified unambiguously and at the same time signals between 1.4 and 1.1 ppm pointed towards the cleaving processes being not complete or residual *tert*-butanol being left in the substance. The latter is less likely since the material had been dried *in vacuo* for several hours. In an attempt to recrystallise the substance it was taken up in a minimum amount of CH_3OH, overlayered with Et_2O until a solid started to precipitate and stored at 4 °C overnight. Unfortunately the ^{1}H NMR spectrum of the collected solid and the solid isolated from the filtrate after evaporation were almost identical and no improvement could be realised. For more systematic studies towards the realisation of this reaction, conditions should be chosen which allow for a

higher degree of control over the reaction. Suitable conditions might for example be stirring in 6 N HCl at 90 °C for several hours or days. In the case of a related, bipyridine-based system Havas *et al.* found a quantitative deprotection with these conditions within 72 hours.[301] When the reaction is initially performed at lower temperatures and with control via TLC, chances are good that conditions for the successful deprotection of **32** can be identified with this approach.

The conditions identified as suitable for the preparation of the protected ligand based on the bipyrimidine could be transferred on the preparation of the protected diiminodiacetate-functionalised sodium cryptate **Na-31**. The used equivalents of di-(*tert*-butyl)iminoacetate **33** were adapted to 2.2, and analogously the amount of added Na_2CO_3 was reduced to 5.0 equivalents. In this case after isolation of the crude product two of the three purification steps used for the preparation of **32** were omitted, and instead the compound was subjected to a single column-chromatography using basic Al_2O_3 as solid phase. Indeed in this case a slightly higher yield of 16% could be realised. After isolation the compound was characterised via ^{1}H NMR spectroscopy and ESI-MS. The ^{1}H NMR spectrum is depicted in Figure 6.33.

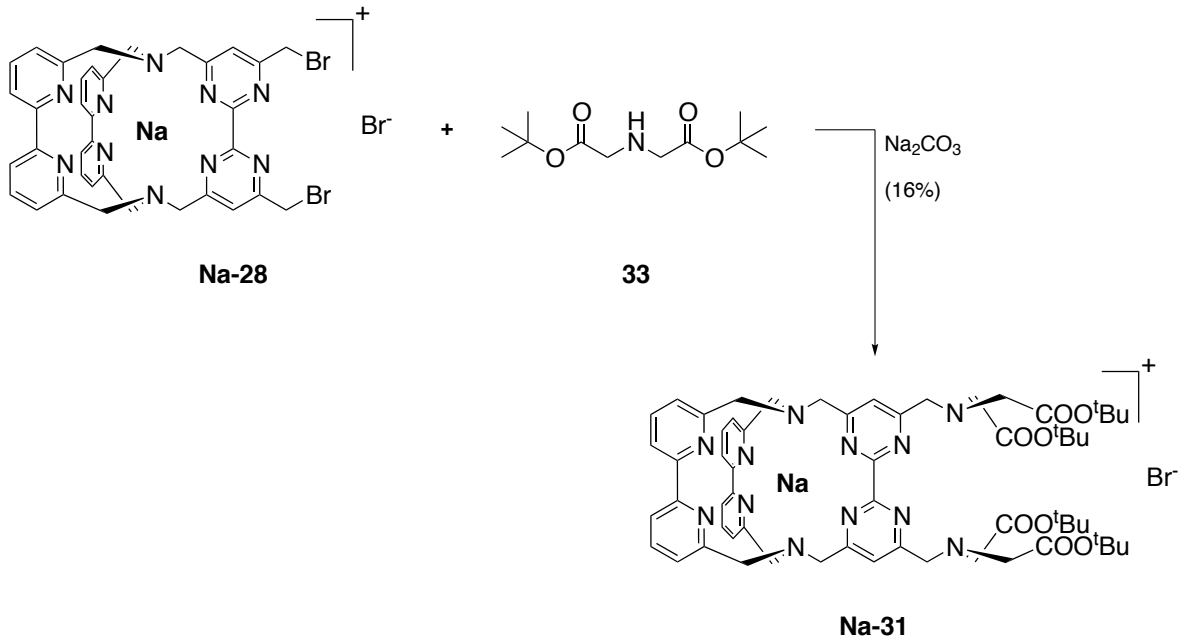

Figure 6.32: Preparation of the protected diiminodiacetate-functionalised sodium cryptate **Na-31** from the bromide-functionalised sodium cryptate **Na-28**.

The signals of the 14 aromatic protons are distributed over three multiplets found between 8.11 and 7.38 ppm. The signal of the aromatic protons of the bipyrimidine is part of the multiplet between 7.93-7.78 ppm and can be identified at 7.90 ppm. This is a significant shift compared to the bromide-functionalised starting material where the signal of these protons can be observed at 7.74 ppm. As expected also the signal of the four protons of the CH_2NR_2-groups experiences an upfield shift compared to the CH_2Br-groups and can be found at 4.16 ppm. The shifts of the signals of the 12 benzylic protons of the cryptate scaffold are virtually unaffected (3.95-3.81 ppm). Finally at 3.52 and 1.38 ppm the signals of the attached iminodiacetate-moieties can be found.

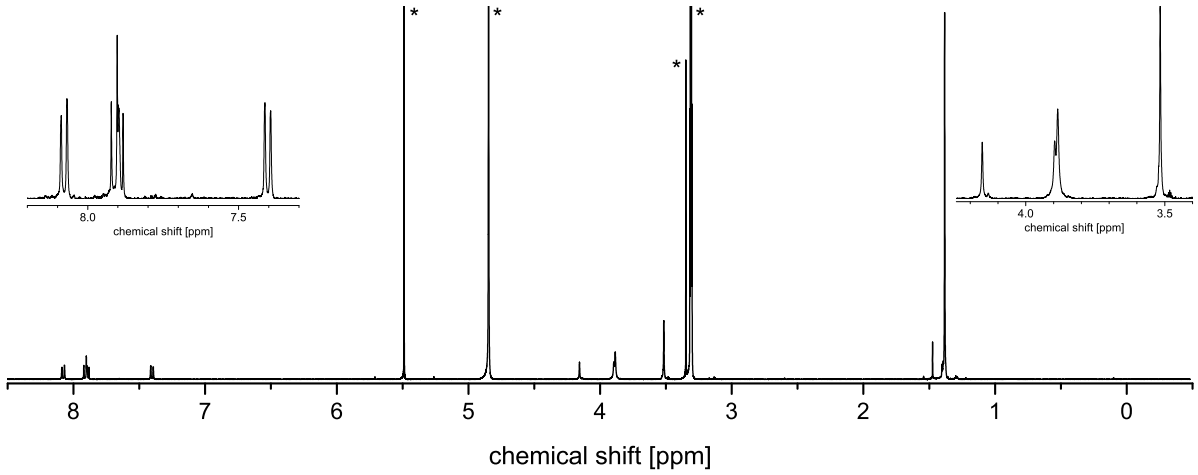

Figure 6.33: ^{1}H NMR spectrum of the protected diiminodiacetate-functionalised sodium cryptate **Na-31** (400 MHz, CD_3OD). Unambiguously identified solvent signals are marked with an asterisk.

Presumably when a method for the deprotection of the bipyrimidine based system **32** is found, it will be transferrable to the deprotection of the protected diiminodiacetate-functionalised sodium cryptate **Na-31**. Since the success of this project is dependent on the identification of a method suitable for the cleavage of the protecting groups until now no further studies (e.g. the preparation of lanthanoid cryptates) on these compounds have been made.

6.3.3.2 New ligands for the coordination of three lanthanoids

The dicryptates and the iminodiacetate-functionalised ligands described in the previous chapter are ligands for the coordination of two lanthanoids. Upconversion processes would be limited to ESA or SA-ETU processes in these scaffolds (see Figure 6.2, page 158). Most importantly the more effective SAS-ETU process is only accessible when two sensitising centers transfer their energy onto the activator localised between them. Since in such a process the two individual energy transfer processes may be performed simultaneously or very shortly after each other (differently to the CET-mechanism), it is much more likely that the activator actually reaches the energy level necessary for the emission of upconverted light before some kind of quenching process carries away the energy from the first transfer. Consequently upconversion based on a SAS-ETU process is more likely to be detectable. By combining a cryptate with a 2,2'-bipyridine-6,6'-dicarboxylate in a single molecule (see Figure 6.34) a cryptate based ligand for the preparation of supramolecular assemblies consisting of three lanthanoids, for which a SAS-ETU process is in principle feasible, can be realised.

Again the bromide-funcionalised sodium cryptate **Na-28** is a suitable precursor for the preparation of the necessary ligand. Typically to prepare a carboxylic acid from a bromide, the bromide is initially transformed into a hydroxide under basic conditions. The hydroxide is afterwards oxidised. However, the hydrolysis step turned out to be surprisingly difficult to accomplish in this case. In an initial experiment the starting material **Na-28** was dissolved in a mixture of CH_2Cl_2 and CH_3CN before 0.1 M aqueous NaOH was added and the mixture was stirred vigorously for 3 hours. After complete evaporation of the volatiles a ^{1}H

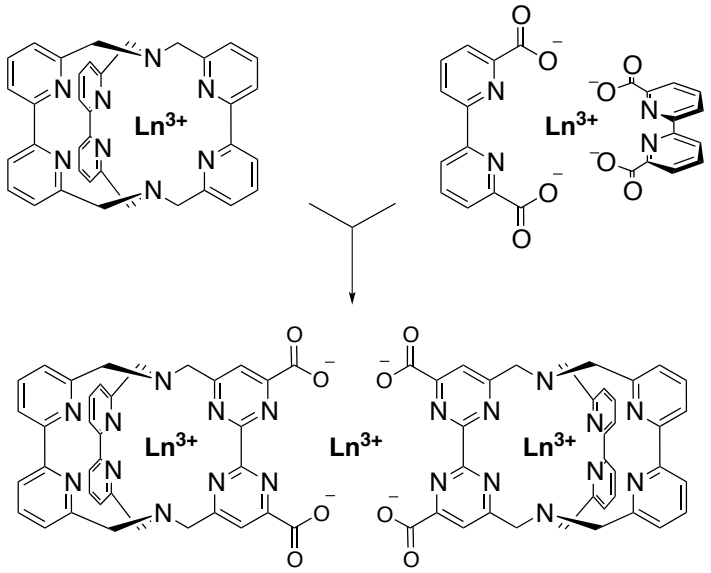

Figure 6.34: By combining the cryptate scaffold with the ligand motif of a 2,2'-bipyridine-6,6'-dicarboxylate a supramolecular assembly of three lanthanoid can be realised.

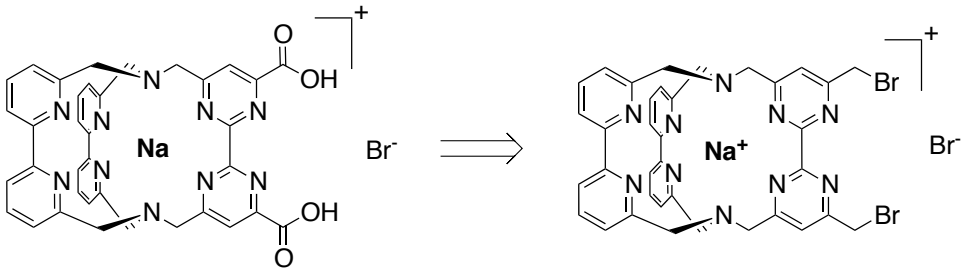

Na-28

Figure 6.35: Retrosynthetic approach for the preparation of a carboxylic acid-functionalised cryptate from the bromide-funcionalised sodium cryptate **Na-28**.

NMR spectrum of the isolated material only showed signals of the starting material. The most plausible reasoning therefore is that under the conditions applied no sufficient mixing of the phases containing the bromide and the hydroxide could be realised. Consequently in the next experiment the basic phase transfer reagent tetraethylammonium hydroxide was used and added to a solution of **Na-28** in CH_3CN. Somewhat unexpectedly, the ^1H NMR spectrum from the crude product strongly points towards decomposition of the cryptate. Indeed, in the presence of tetraethylammonium hydroxide decomplexation of the sodium ion from a **bpy$_3$** scaffold might be possible. Since these simple approaches were not successful, it was searched for related reactions in literature and two interesting examples were identified. As reported by Vögtle *et al.* 2,2'-bipyridine-6,6'-dibromide could be transformed into the corresponding aldehyde by heating the starting material in DMSO for several hours (see Figure 6.36).[302] Since it is usually very easy to transform aldehydes into carboxylic acids this seemed to be a promising and very simple approach.

For the experiments following this strategy a small amount of **Na-28** was dissolved in d_6-DMSO and the

Figure 6.36: Preparation of 2,2'-bipyridine-6,6'-dicarbaldehyde from 2,2'-bipyridine-6,6'-dibromide by heating in DMSO as reported by Vögtle *et al.*[302]

reaction was performed in a NMR tube to monitor its progress via ^{1}H NMR spectroscopy. In order to diminish the probability of decomplexation of Na^+, 10.0 equivalents of NaBr were added to the mixture. Indeed already after a few minutes at room temperature, the first ^{1}H NMR spectrum recorded showed a signal at a shift characteristic for aldehydes. Also some interesting changes in the aromatic region could be observed, but soon it turned out that this is due to decomposition of the starting material to 2,2'-bipyridine-6,6'-dicarbaldehyde.

The other example found in literature was reported by Zhong *et al.* In a single step they prepared 4,7-diphenyl-1,10-phenanthroline-2,9-dicarboxylic acid from the corresponding dibromide with (diacetoxyiodo)-benzene as oxidant and different Fe^{III} porphyrins as catalyst.[303] The presence of H_2O was found to accelerate the reaction which was performed in CH_3OH (see Figure 6.37).

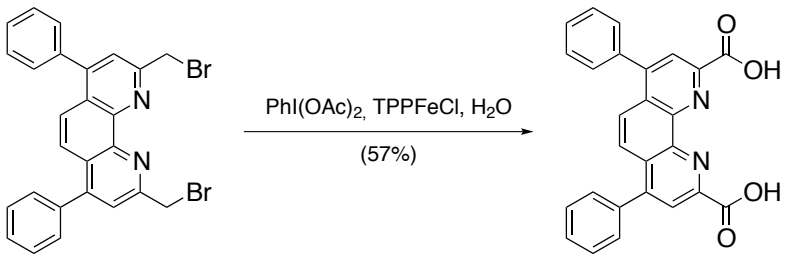

Figure 6.37: Preparation of 4,7-diphenyl-1,10-phenanthroline-2,9-dicarboxylic acid from 2,9-bis(bromomethyl)-4,7-diphenyl-1,10-phenanthroline in a single step with (diacetoxyiodo)benzene as oxidant and 5,10,15,20-tetraphenyl-21*H*,23*H*-porphyrin iron(III) chloride as catalyst.[303]

First experiments following this strategy were quite promising but further experiments have to be performed to unambiguously prove the feasibility of this approach for the transformation of **Na-28** into the carboxylic acid-functionalised derivative.

Since the preparation of the target ligand for the formation of complexes as shown in Figure 6.34 turned out to be surprisingly difficult, a model system which is easier to synthesise was designed to provide a basis for the search of suitable combinations of lanthanoids. Similar to carboxylic acids also ether functionalities can coordinate to a lanthanoid, though the interaction will be weaker. Consequently the supramolecular assembly based on ether-functionalised cryptates as shown in Figure 6.38 will be less stable and presumably being only one of several structures in the equilibrium. For an initial search of potentially interesting pairs of lanthanoids this is not problematic.

The synthesis of the methoxy-functionalised sodium cryptate **Na-34** could be accomplished in a single step from the tetrabromide **25** and the macrocyclus. Initially the bromide-functionalised sodium cryptate

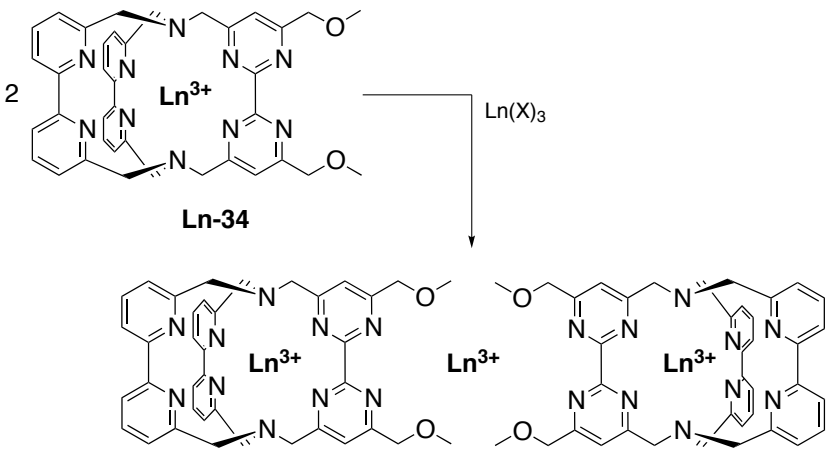

Figure 6.38: Model system for the preparation of supramolecular assemblies of three lanthanoids.

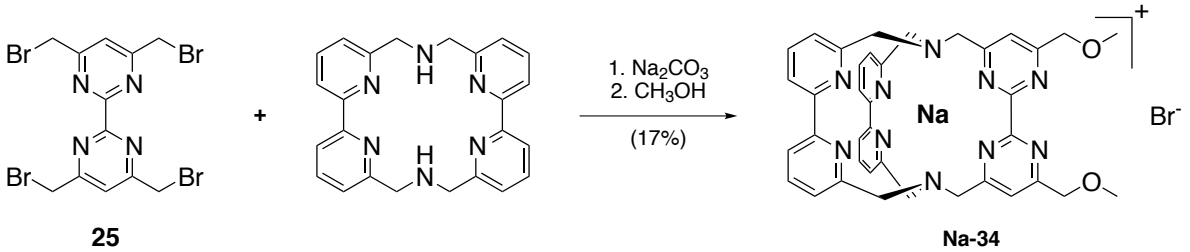

Figure 6.39: Synthesis of the methoxy-functionalised sodium cryptate **Na-34**.

was prepared. After evaporation of the solvent and without previous isolation of the material from the crude mixture it was transformed into the methoxy-derivative by heating the crude material for a few minutes in CH_3OH. The methoxy-functionalised sodium cryptate **Na-34** could be purified via column-chromatography and was characterised via ^{1}H NMR spectroscopy, ^{13}C NMR spectroscopy and via ESI-MS.

In Figure 6.40 the ^{1}H NMR spectrum of the methoxy-functionalised sodium cryptate **Na-34** is shown together with the ^{1}H NMR spectrum of the bromide-functionalised derivative **Na-28**. Apart from the signal of the aromatic protons of the bipyrimidine, which can be observed at 7.65 ppm in the case of the methoxy-functionalised sodium cryptate **Na-34**, not any signal experiences a considerable shift compared to the bromide-functionalised derivative. Interestingly the signals of the benzylic protons between the bipyrimidine and the methoxy ether (4.70-4.66 ppm) and also the signals of the protons of the CH_3-groups (3.56-3.49 ppm) are not observed as singlets but more as multiplets of two related but slightly shifted signals. At a closer look also the signals of the aromatic protons reveal an unusual shape. Most likely this is due to the presence of different isomers of the molecule in solution which correspond to different arrangements of the CH_3-groups.

For the preparation of the first lanthanoid cryptates of the new ligand scaffold ytterbium was chosen because of its outstanding suitability as sensitiser for upconversion processes. Because HPLC purification will not be possible for the complexes **Ln-34** of the smaller lanthanoids, yet it is very important for subsequent experiments that no free lanthanoid salt contaminates the sample, in this case a shortage of $YbCl_3 \cdot 6\,H_2O$ was used (see Figure 6.41).

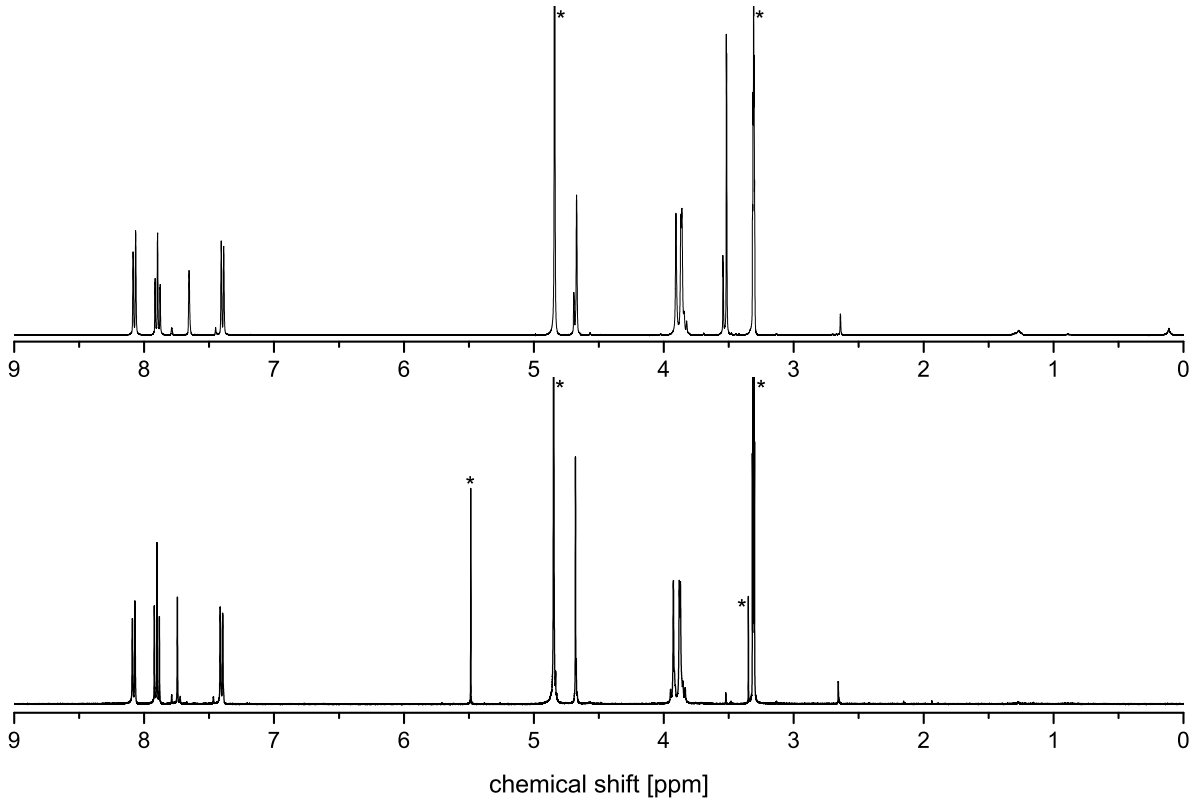

Figure 6.40: ^{1}H NMR spectra (400 MHz, CD_3OD) of the methoxy-functionalised sodium cryptate **Na-34** (top) and the bromide-functionalised sodium cryptate **Na-28** (bottom). Unambiguously identified solvent signals are marked with an asterisk.

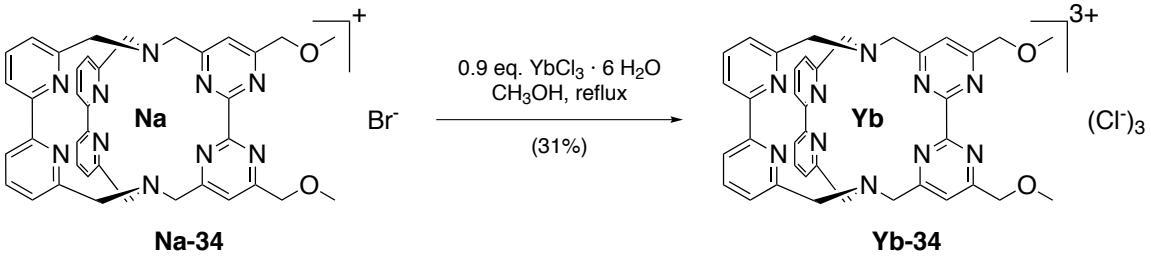

Figure 6.41: Synthesis of the methoxy-functionalised ytterbium cryptate **Yb-34**.

Since this is usually the better choice for these reactions, initially it was tried to perform this reaction in CH_3CN. The cryptate **Na-34** and the lanthanoid salt were well soluble in this solvent, but already after two hours at reflux temperature a large amount of an orange to red solid precipitated. After a total of 47 hours of reaction time the volatiles were removed and a ^{1}H NMR spectrum of the crude mixture in CD_3OD was recorded. Surprisingly, no paramagnetically shifted signals could be observed. Probably in CH_3CN the complex resulting from the coordination of the lanthanoid to the methoxy-groups is not sufficiently soluble, the complex precipitates and the reaction cannot progress further, but upon preparation of the sample in CD_3OD the complex dissolves and dissociates. Subsequently the reaction was repeated in CH_3OH. After

60 hours at reflux temperature the reaction mixture was still a clear solution. Again the volatiles were removed and a ^{1}H NMR spectrum in CD_3OD was recorded. This time signals with a distinct paramagnetic shift could be detected. The crude product was taken up in a minimum amount of CH_3OH and overlayered with Et_2O. While stored at 4°C overnight an orange solid precipitated which was collected on a filter. As it could be identified as the sodium cryptate **Na-34**, subsequently the filtrate was evaporated to dryness, dried and suspended in CH_2Cl_2. After the mixture had been stirred for a few minutes it was again filtered and this time the collected solid could be identified as the desired ytterbium cryptate.

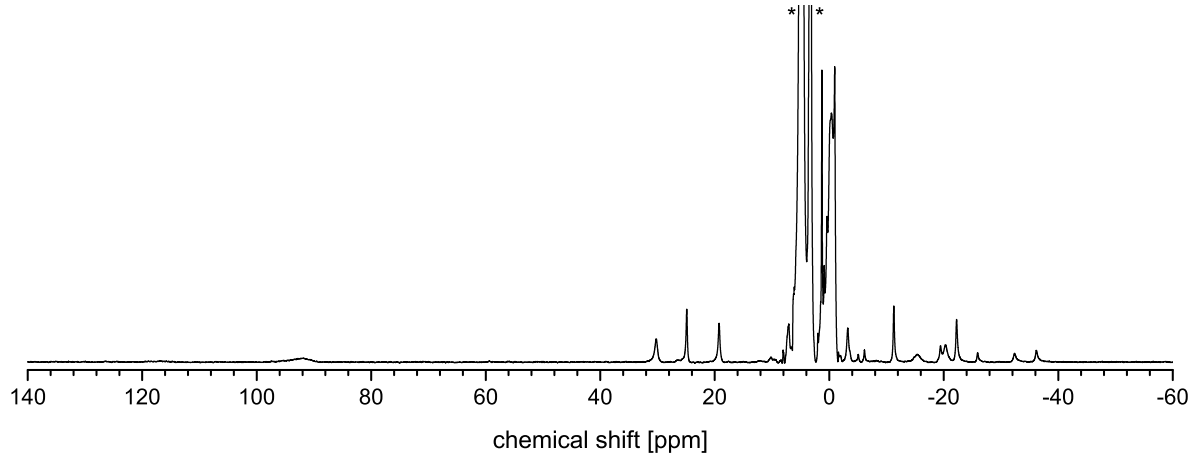

Figure 6.42: ^{1}H NMR spectrum (500 MHz, CD_3OD) of the methoxy-functionalised ytterbium cryptate **Yb-34**. Unambiguously identified solvent signals are marked with an asterisk.

Figure 6.42 shows the ^{1}H NMR spectrum of the methoxy-functionalised ytterbium cryptate **Yb-34**. The shifts the identified signals are experiencing are in a range similar to the ones observed for the amino-functionalised ytterbium cryptate **Yb-1** (see chapter 3.3.4). However, in this case the interpretation of the spectrum is less straightforward. In the case of the cryptates of the type **Ln-bpy$_3$** less reference data is available and the flexibility of the scaffold makes the assignment of the signals more difficult. Additional data, e.g. from 2D NMR experiments will be needed before a detailed discussion of the spectrum is reasonable.

6.4 Conclusion

Some time ago a cryptate based ligand scaffold for the controlled preparation of homo- and heterobimetallic lanthanoid complexes could be realised, which has an enormous potential for the study of energy transfer processes between lanthanoids. However, until now the accessibility of the dicryptates had not been sufficient for extended studies on these compounds. To provide a basis for such studies, in this project the synthesis of the ligand scaffold was optimised. Now the key precursor for the synthesis of the dicryptates can be prepared with an efficiency increased by one order of magnitude and significantly facilitated purification procedures. In the subsequent studies on the sodium dicryptate new data for an improved structural understanding of these compounds could be collected, like for example by X-ray crystallography.

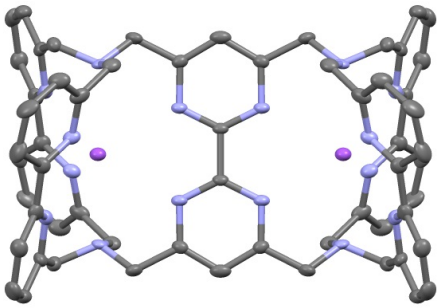

Figure 6.43: X-ray structure of **Na-Na-26**, thermal ellipsoid plot (Mercury, 50% probability level). Hydrogen atoms and external Br^- are omitted for clarity. Colour scheme: C, grey; N, light blue; Na, purple.

Since some of the smaller lanthanoids can be considered to be the most promising in terms of energy transfer processes, in the next step studies towards the preparation of the corresponding dicryptates were undertaken. Unfortunately these compounds were found to be not purificable via HPLC. Initial studies on the homobimetallic dicryptate **Er-Er-26** revealed that this compound is indeed luminescent in the visible and near-infrared part of the electromagnetic spectrum, which is not necessarily the case for undeuterated ligand scaffolds.

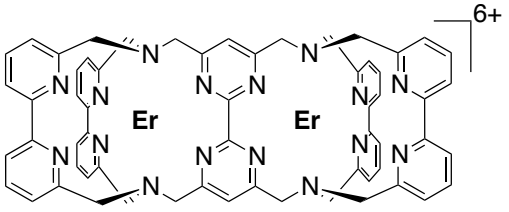

Er-Er-26

Figure 6.44: Structure of the homobimetallic erbium dicryptate **Er-Er-26**.

For a detailed understanding of energy transfer processes between lanthanoids, related but slightly different ligand systems for two lanthanoids will be useful. Apart from that the preparation of controlled assemblies

of three lanthanoids is desirable, since based on the physical principles of upconversion such processes will be more likely to be observable in such architectures. During this project a new intermediate for the preparation of such compounds could be isolated. The dibromide-functionalised sodium cryptate **Na-28** is another example for a cryptate carrying a peripheral functionality realised during this work.

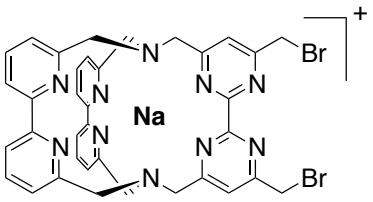

Na-28

Figure 6.45: Structure of the dibromide-functionalised sodium cryptate **Na-28**.

7 Summary

In the course of this work, a number of important scientific milestones could be achieved:

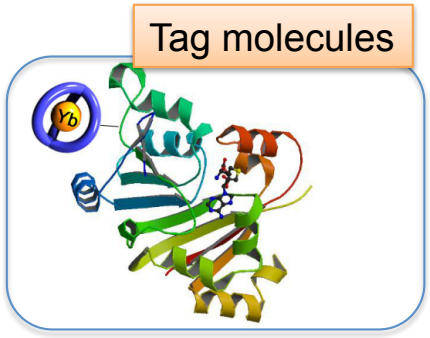

"Lanthanoid Cryptates as Covalently Attached Tag-Molecules":

- Realisation of two new cryptates for the preparation of rigid and stable lanthanoid complexes of the type **Ln-bpy$_3$O$_2$** carrying a peripheral functionalisation
- Validation of the photophysical and paramagnetic properties of the cryptates **Ln-bpy$_3$O$_2$** being invariant towards the introduction of a peripheral amino-functionalisation
- Development and implementation of a general strategy for the preparation of cryptate based tag-molecules
- Realisation and attachment of a functionalised linker moiety, transforming the enantiopure diol-functionalised cryptate into a tag-molecule for the structural elucidation of proteins in solution

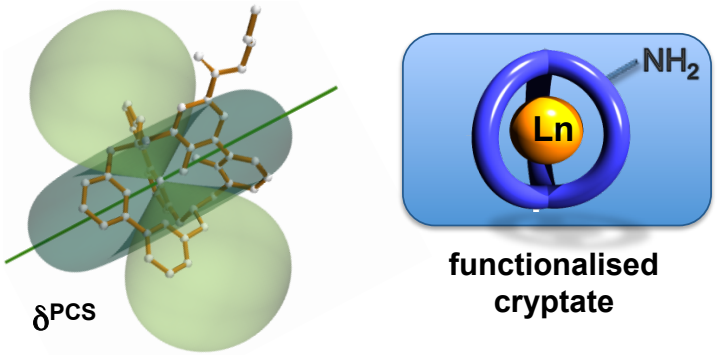

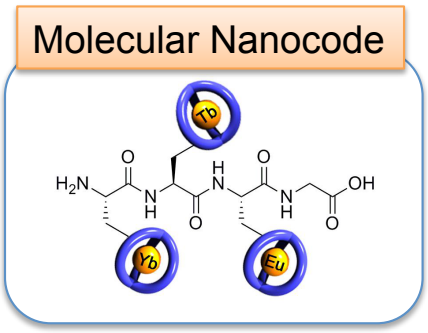

"Construction of a Molecular Nanocode":

- Realisation of an amino acid carrying a covalently attached lanthanoid cryptate which is suitable for standard Fmoc peptide synthesis
- Validation of the properties of the lanthanoid cryptate being unaffected by the attachment of the amino acid-functionalisation
- Verification of the amino acids reactivity and suitability for the use in solid phase peptide synthesis
- Synthesis of a nanocode with the sequence **Sm-Tb-Eu** which is the first example of a heterotrimetallic, covalently linked lanthanoid coordination compound prepared by solid phase peptide synthesis
- Read-out of the nanocode via luminescence spectroscopy

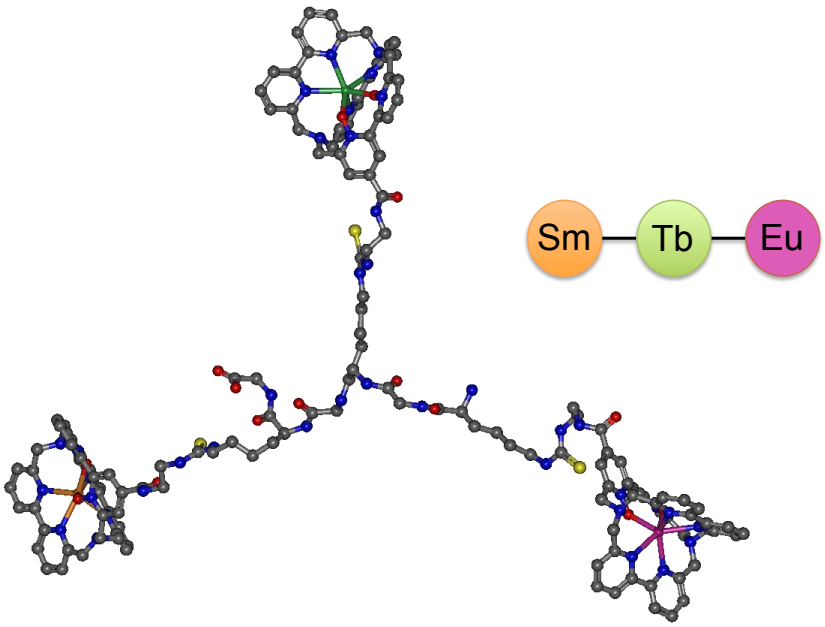

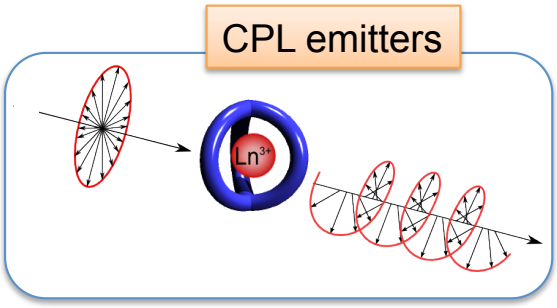

"Enantiopure Lanthanoid Cryptates":

- Realisation of the first cryptate-based emitters for circularly polarised luminescence
- Transfer of the deuteration strategy to the problem of enhancing CPL of lanthanoids more susceptible towards multiphonon quenching
- Preparation of the first enantiopure samples of **Ln-bpy$_3$O$_2$** via chiral HPLC
- Demonstration of the unprecedented stability of the lanthanoid cryptates **Ln-bpy$_3$O$_2$** by an in-depth study of their configurational stability

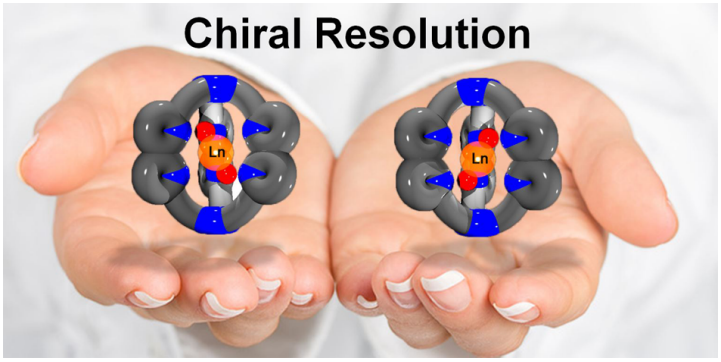

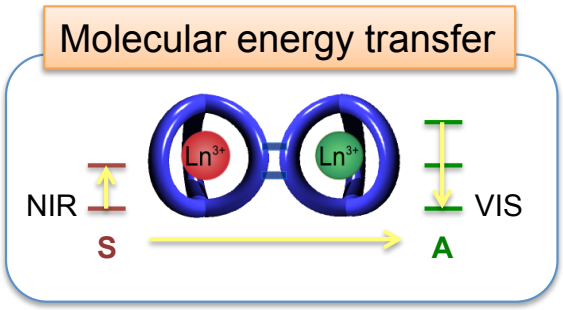

"Cryptates for the Controlled Synthesis of Homo- and Heteropolymetallic Complexes":

- Significant improvement of the synthetic availability of the dicryptates **Ln-Ln-26** by stepwise optimisation of synthesis
- Preparation and study of lanthanoid dicryptates with new combinations of lanthanoids
- Development of a modified synthetic strategy for a more efficient search for pairs of lanthanoids exhibiting energy transfer processes
- Preparation of a new bromide-functionalised cryptate scaffold which opens up possibilities for the realisation of new cryptate-based architectures of several lanthanoids

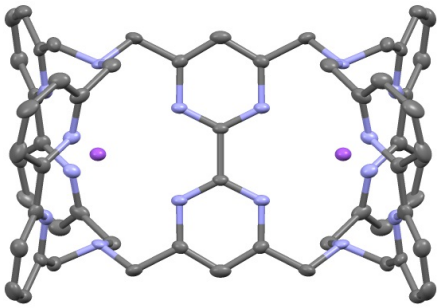

In conclusion, during this thesis several aspects of new functionalities could be added to the lanthanoid cryptates. The contributions of the broadest impact are the ones presented in the chapter *"Lanthanoid Cryptates as Covalently Attached Tag-Molecules"*, as they provide a solid basis for the evolution of the cryptates **Ln-bpy$_3$O$_2$** from a well-defined and highly reliable test system for hypotheses about specific aspects of lanthanoid photophysics into well-defined and highly reliable tag-molecules for concrete applications. In the chapter *"Construction of a Molecular Nanocode"* an outstanding example for such an application could be given. At the same time it gives remarkable evidence of the high potential of the lanthanoid cryptates for concrete problem sets and is enormously innovative. Here it was possible to realise an architecture which normally would be considered to be impossible, namely a molecular coordination compound combining three different lanthanoids in a highly controlled, covalent fashion. The chapter *"Enantiopure Lanthanoid Cryptates"* extends the functionalities of the lanthanoid cryptates to a further aspect, namely the circularly polarised luminescence. This phenomenon is gaining more and more attention at the moment and as it could be shown herein, enantiopure lanthanoid cryptates can contribute to both, concrete applications and an improved understanding of CPL. Finally the chapter *"Cryptates for the Controlled Synthesis of Homo- and Heteropolymetallic Complexes"* can be considered as dealing with the functionalisation of a lanthanoid cryptate with further lanthanoids, aiming for the observation of energy transfer processes such as upconversion, which is another current focus of interest in lanthanoid coordination chemistry.

Based on the results presented in this dissertation further studies can lead to broader applications and further highly interesting systems and results:

- Use of the enantiopure diol-functionalised lanthanoid cryptate as **paramagnetic tag-molecule** for the structural elucidation of peptides or proteins

After all necessary building blocks have been developed, use of the lanthanoid cryptates as tag-molecule for such a purpose is only a few steps away. For a proof-of-principle a short peptide with a suitable sequence would be attached to the tag-molecule, and subsequently be studied via ^{1}H NMR spectroscopy and analysis of the paramagnetic shifts.

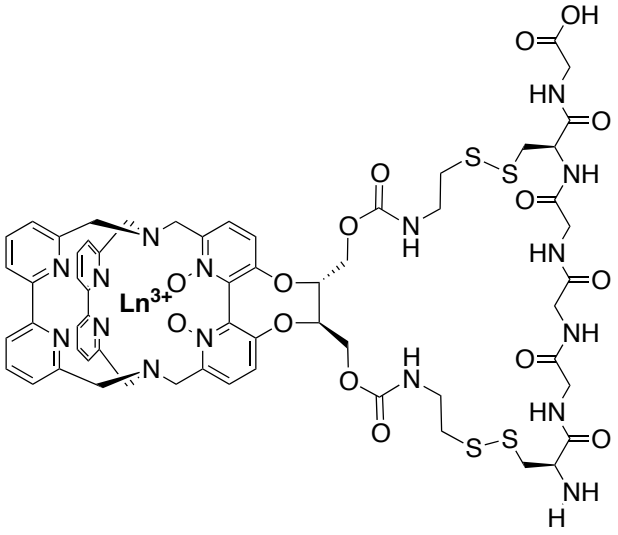

- **Incorporation of amino acid-functionalised lanthanoid cryptates into various peptides** via solid phase peptide synthesis

Since the amino acid-functionalised lanthanoid cryptates are compatible with solid phase peptide synthesis they can easily be introduce into any peptide sequence. This allows for the introduction of e.g. a luminescent tag to a given structure without any additional techniques.

- Preparation of **enantiopure samples of emissive cryptates Ln-bpy$_3$O$_2$** and study of their CPL properties

Since the separation of racemic **Ln-bpy$_3$O$_2$** into pure enantiomers is now possible, the preparation of samples for CPL studies is now far easier. This will allow for a more systematic study of the CPL properties of cryptates. Together with their well-defined structure a correlation of the CPL properties and the very specific structure of the complexes under study might become possible, allowing for an unprecedented understanding of CPL.

- Preparation of new **"multicryptates"**

The cryptates **Ln-bpy$_3$** are accessible by assembly of three bipyridine dibromides. The dibromide functionalised cryptate **Na-28** is highly related to these building blocks and their use in reactions related to the ones described above could lead to extended "multicryptates" for the study of e.g. energy transfer processes between lanthanoids (see Figure 7.1, page 204).

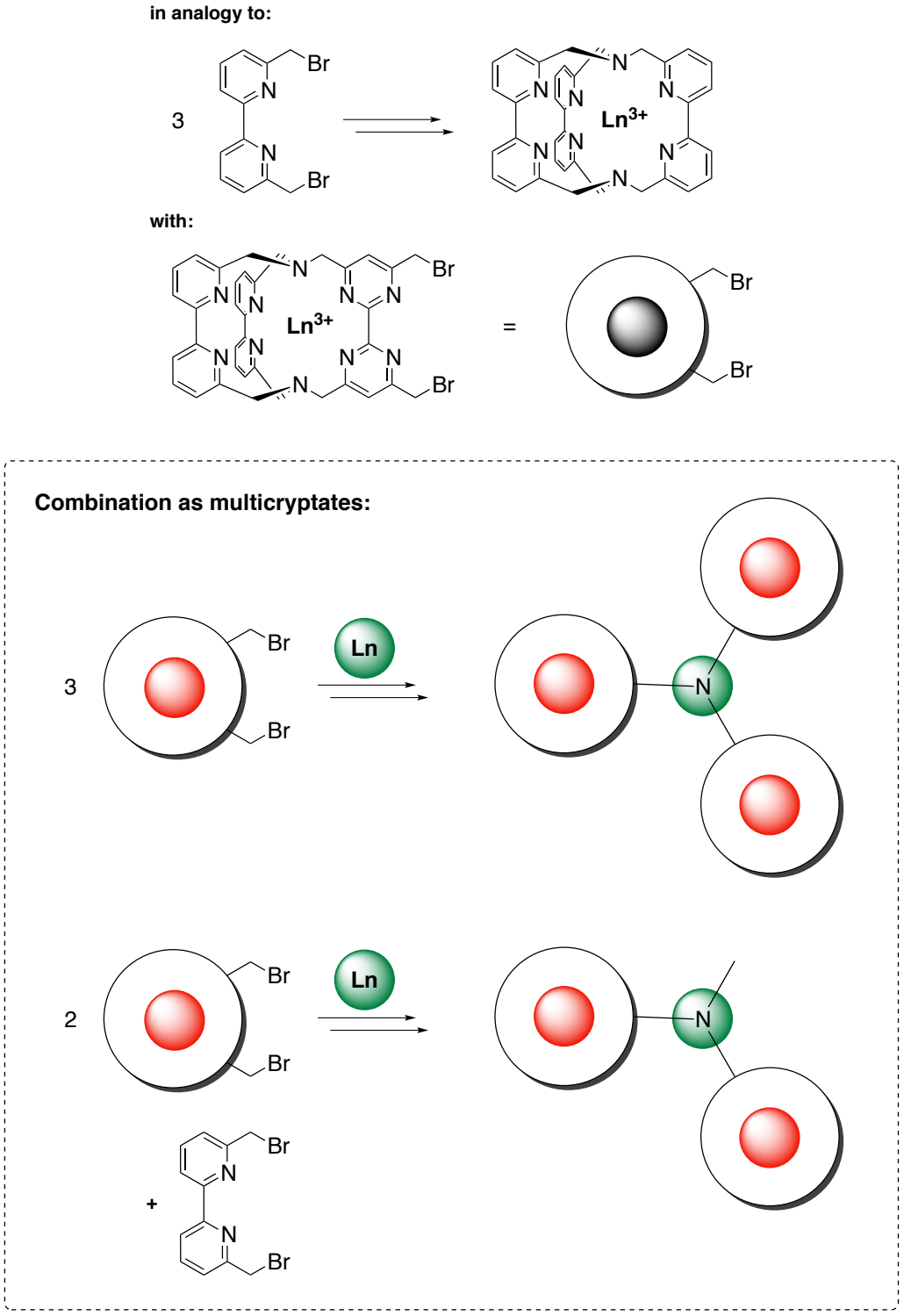

Figure 7.1: Concept of new “multicryptates”.

8 Experimental Section

8.1 General

Chemicals were purchased from commercial suppliers and used as received unless stated otherwise. Deuterated solvents/reagents had deuterium contents > 99.5%. For the preparation of the lanthanoid cryptates used for the experiments towards molecular nanocodes, lanthanoid salts with 99.99% purity (REO, in regards to contaminations with different lanthanoids) were used. CH_3CN used for the synthesis of the cryptates was HPLC-grade. TFA was HPLC-grade. Dry THF and dry CH_3CN were dried using a MBraun SPS-800 solvent purification system. Dry DMF (Acros Organics) was used as purchased. Air-sensitive reactions were carried out under a dry, dioxygen-free atmosphere of N_2 or Ar using Schlenk technique. Column-chromatography was performed with silica gel 60 (Merck, 0.063 - 0.200 mm) or basic Al_2O_3 90 (Sigma-Aldrich, 0.063 - 0.200 mm). Analytical thin layer chromatography (TLC) was done on silica gel 60 F_{254} plates (Merck, coated on aluminium sheets), silica gel RP-18 W/UV_{254} plates (Macherey-Nagel, coated on aluminium sheets) or Al_2O_3 N/UV_{254} (Macherey-Nagel, coated on polyester sheets). Elemental analysis was performed using elementar vario Micro cube.

NMR

NMR spectra were measured at 26°C on Bruker DPX-200 (^{1}H: 200 MHz, ^{13}C: 50.3 MHz), DPX-250 (^{1}H: 250 MHz, ^{13}C: 62.9 MHz, ^{23}Na: 66.2 MHz), AVII+400 (^{1}H: 400 MHz, ^{13}C: 100.6 MHz, ^{19}F: 376 MHz), AVII+500 (^{1}H: 500 MHz) or Avance III HDX 700 (^{1}H: 700 MHz) spectrometers. All chemical shifts δ are reported in parts per million (ppm). For ^{1}H and ^{13}C NMR spectra they are reported relative to TMS and the residual solvent signals have been used as internal reference. For ^{1}H DOSY NMR experiments the z-gradient strength was determined using a sample of 1 wt-% H_2O and 0.1 wt-% $CuSO_4$ in D_2O. All NMR spectra were analysed using MestReNova (Mestrelab Research) and/or Origin (OriginLab) and/or TopSpin (Bruker). Observed multiplicities are specified as: singlet (s), doublet (d), triplet (t), quartet (q), and multiplet (m). Further abbreviations: br = broad.

Mass spectrometry

ESI mass spectrometry was measured using Bruker Daltonics Esquire6000 and Bruker Daltonics Esquire 3000plus. MALDI mass spectrometry was performed using Bruker Autoflex and 2,5-dihydroxybenzoic acid

(DHB), *trans*-2-[3-(4-*tert*-butylphenyl)-2-methyl-2-propenylidene]malononitrile (DCTB), 6-aza-2-thiothymine (ATT) or sinapinic acid (SA) as matrix material. Isotopic patterns were only reported when the overall intensity of the signal was sufficiently high. The following abbreviations were used for the description of the results obtained from MALDI-MS: $[DHB\text{-}H]^-$: deprotonated DHB, $C_7H_5O_4$, [ox. DHB]: oxidised DHB, $C_7H_4O_4$, $[SA\text{-}H]^-$: deprotonated SA, $C_{11}H_{11}O_5$. In high resolution ESI-MS the species were typically observed as formiate adducts. The formiate originates from the formic acid added to the mobile phase.

MOPAC geometry optimisations

Geometry optimisations were performed using MOPAC2016[304] with the semi-empirical method PM7[305]. The lanthanoid centers are calculated within the sparkle model[306], each is represented as a pure 3+ ion without basis functions.

X-ray Analysis

For analysis the crystals were mounted on a glass fiber using perflouropolyether oil. The measurements were carried out on a Bruker Apex 2 Duo using Mo Kα radiation. Data were collected at a temperature of 100(2) K. Frames corresponding to an arbitrary hemisphere of data were collected using ω scans. The structure was solved within the Wingx[307] package using direct methods (SIR92[308]) and expanded using Fourier techniques (SHELXL-97[309]) on F^2. Hydrogen atoms were included but not refined. All non-hydrogen atoms were refined anisotropically. Further information is summarised in Table 8.1.

Table 8.1: Crystallographic data for **24** and **Na-Na-26**.

compound	**24**	**Na-Na-26**
formula	$C_7H_4Br_4N_2Cl_3$	$C_{30}H_{25}BrN_8Na$
mol. wt.	542.11	600.48
cryst appearance	colourless block	colourless block
cryst syst	monoclinic	monoclinic
space group	$P2_1/c$	C2/m
a [Å]	12.741(3)	16.91(6)
b [Å]	7.1842(18)	15.19(6)
c a [Å]	16.601(4)	10.62(4)
α [deg]	90.00	90.00
β [deg]	112.238(3)	97.14(13)
γ [deg]	90.00	90.00
vol [Å^3]	1406.5(6)	2707(19)
Z	4	4
ρ [g cm^{-1}]	2.560	1.473
Θ max [deg]	28.48	23.81
measd reflns	15938	19931
independent reflns	3552	2161
reflns in ref	2493 ($I \geq 2\sigma(I)$)	1641 ($I \geq 2\sigma(I)$)
params	145	186
R[a]	0.0406	0.1038
wR[b]	0.0904	0.2925
R[a] (all data)	0.0720	0.1304
wR (all data)	0.1014	0.3169
GOF	0.991	1.127

HPLC

Most HPLC runs were performed on a Knauer Azura HPLC system (setup **A**). Resulting from a different void volume, the runs performed on a Knauer Smartline HPLC system (setup **B**) typically show longer retention times.

Reversed-phase HPLC

For the purification and analysis of lanthanoid cryptates via reversed-phase HPLC the following columns and conditions were used:

- Analytical reversed-phase HPLC: Lichrospher RP-18e (Merck), 125x4 mm - 5 μm, flow rate: 1 mL min^{-1}
- Semi-preparative reversed-phase: HPLC Lichrospher RP-18e (Merck), 250x10 mm - 10 μm, flow rate: 3 mL min^{-1}

In both cases, UV detection (300 nm) was used for the detection of eluted substances. Using mobile phases A (degassed HPLC-grade H_2O + 1 vol.-% HPLC-grade CF_3COOH, v/v) and B (degassed HPLC-grade CH_3CN) the following programs were applied:

Program A		
min	%A	%B
0	85	15
5	85	15
19	45	55
25	45	55
40	85	15
50	85	15

Program B		
min	%A	%B
0	85	15
5	85	15
19	45	55
41	0	100
48	0	100
78	85	15
90	85	15

If not stated differently, the samples for semi-preparative reversed-phase HPLC runs were dissolved in CH_3CN/H_2O (HPLC-grade, 1:1, v/v). All samples were filtered with a 0.45 μm nylon membrane filter (GE Healthcare Life Sciences) before injection.

Separation of enantiomers via HPLC

For the preparation of enantiopure lanthanoid cryptates from racemic samples and the study of the racemisation of these compounds the following columns and conditions were used:

- Analytical chiral phase HPLC: CHIRALPAK IE (Daicel Corporation), 250x4.6 mm - 5 μm, flow rate: 1 mL min^{-1}
- Semi-preparative chiral phase HPLC: CHIRALPAK IE (Daicel Corporation), 250x10 mm - 10 μm, flow rate: 4 mL min^{-1}

In both cases, UV detection (300 nm) was used for the detection of eluted substances. As mobile phase freshly prepared solution of CH_3OH (degassed, HPLC-grade) with 1 vol.-% CF_3COOH (HPLC-grade) was used. All samples were prepared using HPLC-grade CH_3OH and were filtered with a 0.45 μm nylon membrane filter (GE Healthcare Life Sciences) before injection.

Photophysical measurements

UV/VIS spectra were measured on a Jasco V-770 spectrophotometer using quartz cuvettes (Suprasil, 1 cm pathlength) at room temperature.

Steady state emission spectra were acquired on a Horiba Fluorolog-3 DF spectrofluorimeter using quartz cuvettes (Suprasil, 1 cm pathlength) at room temperature or in a solid matrix of CD_3OD/CD_3CD_2OD (1:1, v/v) in an NMR tube at 77 K. The excitation light source was a 450 W xenon lamp. Emission was monitored at 90° using a Hamamatsu R2658P PMT (UV/vis/NIR, 200 nm < λ_{em} < 1010 nm) or a Hamamatsu H10330-75 PMT (NIR, 950 nm < λ_{em} < 1700 nm). Spectral selection was achieved by double grating monochromators (excitation: 1200 grooves/nm, blazed at 300 nm, visible emission: 1200 grooves/nm, blazed at 500 nm, NIR emission: 600 grooves/nm, blazed at 1000 nm).
Luminescence decay profiles were determined with the same instrumental setup as described above for the steady state experiments. The light source for the recording of the decay profiles was a 70 W xenon lamp (pulse width ca. 2 μs FWHM). Lifetime data analysis (deconvolution, statistical parameters, etc.) was performed using the software package DAS from Horiba. Lifetimes τ_{obs} were determined by fitting the middle and tail portions of the decays. Estimated uncertainties in τ_{obs} are ±10%. Absolute quantum yields Φ_{Ln}^{L} were determined with at least two independent sets of samples, using quinine sulfate in 0.5 M H_2SO_4 as quantum yield standard (Φ = 54.6%[269]). For analysis the optically dilute method was employed:

$$\Phi_x = \Phi_s \cdot \left(\frac{Grad_x}{Grad_s}\right) \cdot \left(\frac{n_x}{n_s}\right)^2 \tag{24}$$

where Φ_x/Φ_s are the quantum yields of the sample (x) or the standard (s), $Grad_x/Grad_s$ are the linearly fitted sloped from the plot of the integrated luminescence intensity of the sample (x) or the standard (s) versus the absorbance at the excitation wavelength and n_x/n_s are the refractive indices of the medium or the sample. Estimated uncertainties in Φ_{Ln}^{L} are ±15%.

Circular dichroism (CD) spectra were collected on a Jasco J-720 spectropolarimeter, using rectangular quartz cuvettes (Suprasil, d = 1 mm path length), or in cooperation with Prof. Dr. Lorenzo Di Bari (Università di Pisa) and Dr. Francesco Zinna (Université de Genève)) on a Jasco J-715 spectropolarimeter using a 0.1 mm optical path cell.

Circular polarised luminescence (CPL) was measured in cooperation with Prof. Dr. Lorenzo Di Bari (Uni-

versità di Pisa) and Dr. Francesco Zinna (Université de Genève) on a home-built spectrofluoropolarimeter described in reference [310]. The samples were irradiated in a 90° geometry with an UVC high pressure mercury lamp ($\lambda_{exc} = 254$ nm).

Peptide synthesis

All peptides were prepared via Solid Phase Peptide Synthesis (SPPS) following the Fmoc approach and using standard techniques.[222] DMF (Acros Organics, 99.8%, for peptide synthesis) and piperidine (Roth, $\geq$99.5%, for peptide synthesis) were used as purchased. As solid support Fmoc-Gly-Tentagel® PHB resin (particle size 90 μm, capacity 0.15-0.20 mmol/g) was used. Standard Fmoc-protected amino acids were used as purchased (purity $\geq$ 95%), isotopically enriched Fmoc-protected glycines (Cambridge Isotope Laboratories, Inc.) had chemical purities $\geq$ 98% and were 99% (2-13C) or 98% (15N) enriched. As coupling reagent HATU was used, as base *N*,*N*-diisopropylethylamine (DIPEA) was added. All reactions were performed in plastic syringes (BD Discardit™ II) equipped with PE frits (average pore diameter of 0.35 μm) or in a custom-build glass-vessel (see Figure 8.1). To minimise adhesion of the resin to the glass surface of the vessel it was silanised with trimethylsilyl chloride.

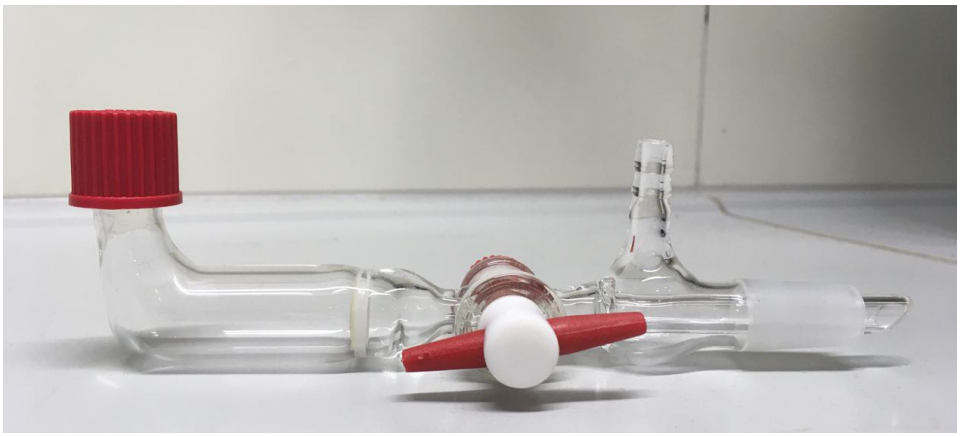

Figure 8.1: Custom-build glass-vessel used for the synthesis of peptides.

The following standard procedures were carried out:

Washing: About three bed volumes (at least 1 mL) of the solvent were added to the reaction vessel, the suspension was shaken for about one minute, afterwards the solvent was drained. The procedure was performed a total of five times.

Swelling of the resin: Prior to the first coupling step, the dry resin was placed in the reaction vessel and at least a three bed volumes of CH_2Cl_2 were added. The suspension was shaken carefully and left standing for about 30 minutes before the suspension was shaken for about 20 minutes. The CH_2Cl_2 was drained, afterwards the resin was washed with DMF (see above).

Coupling: If not stated otherwise, in the case of commercially available amino acids the Fmoc-protected

amino acid (5 eq.) and HATU (4.9 eq.) were dissolved in a minimum amount of DMF. After addition of DIPEA (10 eq.) the mixture was added to the deprotected, washed resin immediately. The suspension was shaken for at least 30 minutes before the solution was drained and the resin was washed with DMF (see above). In the case of the lanthanoid-containing amino acids the equivalents were reduced and the reaction times were elongated (see main text and below).

Capping: A 50-fold excess of acetic anhydride together with DIPEA and DMF (1:1:20 v/v/v, freshly prepared) was added to the washed resin and shaken for 30 minutes. The solution was drained and the resin was washed with DMF (see above).

Deprotection: About three bed volumes (at least 1 mL) of 20% piperidine in DMF (v/v) were added to the washed resin. The suspension was gently shaken for about 2 minutes before the solution was drained and the process was repeated two more times. Afterwards the resin was washed with DMF (see above).

Shrinkage of the resin: The DMF-washed resin was washed with CH_2Cl_2 and subsequently with Et_2O (see above). To remove remaining solvent the resin was dried *in vacuo* for several hours and subsequently dried in air overnight.

Cleavage of the peptide from the resin: About three bed volumes (at least 1 mL) of trifluoroacetic acid (TFA, HPLC-grade) with 5 vol.-% H_2O were added to the shrinked resin and the suspension was shaken for 10-60 minutes. The solution was drained into a round-bottomed flask equipped with a magnetic stirrer. Typically this step was repeated 1-3 times. Under these conditions also additional protecting groups like the trityl-group attached to cysteines are cleaved.

8.2 Organic building blocks

Sodium methane-thiosulfonate (11)

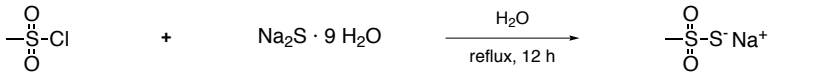

CH_3ClO_2S	$Na_2SH_{18}O_9$	$CH_3NaO_2S_2$
Exact Mass: 113.95	Exact Mass: 240.05	Exact Mass: 133.95
Molecular Weight: 114.55	Molecular Weight: 240.18	Molecular Weight: 134.15
d: 1.48 g cm^{-3}		
1.0 eq.	1.0 eq.	
36	**35**	**11**

The synthesis of sodium methane-thiosulfonate **(11)** was performed slightly modified to a procedure reported earlier.[188]

Under stirring $Na_2S \cdot 9\,H_2O$ **(35)** (25 g, 104 mmol, 1.0 eq.) was dissolved in 40 mL H_2O to give a yellow solution. Methanesulfonyl chloride **(36)** (11.9 g, 104 mmol, 8.05 mL, 1.0 eq.) was added dropwise via a dropping funnel. The resulting mixture was slowly heated and then refluxed for 12 h, which yielded a dark orange solution. The volatiles were evaporated and the resulting yellow solid was pestled to give a colourless powder which was dried overnight *in vacuo*. The crude product was taken up in 200 mL EtOH, brought to reflux temperature and the resulting suspension was filtered hot when it started to turn green. The solid residue was washed with 40 mL hot EtOH. The combined filtrates were concentrated and redissolved in a minimum amount of boiling EtOH. After the solution was allowed to slowly come to room temperature it was cooled with an ice bath and colourless crystals started to precipitate. After 12 h at room temperature the crystals were collected (1.7 g) and the filtrate was concentrated and recrystallised as described above to give another portion (4.0 g) of the product which was dried thoroughly and stored under Ar.

Yield: 5.7 g, 42.5 mmol, 41%.
^{1}H NMR (400 MHz, D_2O): δ = 3.37 (s, 3 H) ppm.
m.p.: 269.5-270.5 °C.

S-(2-Aminoethyl)-methanethiosulfonate hydrobromide (12)

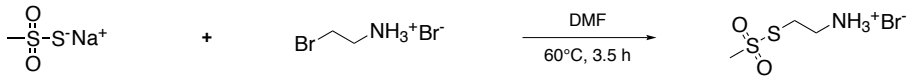

$CH_3NaO_2S_2$	$C_2H_7Br_2N$	$C_3H_{10}BrNO_2S_2$
Exact Mass: 133.95	Exact Mass: 202.89	Exact Mass: 234.93
Molecular Weight: 134.15	Molecular Weight: 204.89	Molecular Weight: 236.15
1.0 eq.	0.94 eq.	
11	**37**	**12**

The synthesis of *S*-(2-aminoethyl)-methanethiosulfonate hydrobromide **12** was performed slightly modified to a procedure reported earlier.[189]

Sodium methane-thiosulfonate **(11)** (1.43 g, 10.6 mmol, 1.0 eq.) and 2-bromoethyl amine hydrobromide **(37)** (2.04 g, 9.96 mmol, 0.94 eq.) were dissolved in 18 mL dry DMF to give a clear, slightly yellow solution. The mixture was stirred at 60 °C bath temperature for 3.5 h before the solvent was removed *in vacuo*. The remaining viscous red to orange oil was dried thoroughly before 50 mL CH_2Cl_2 were added and the resulting suspension was stirred vigorously for 2 h. The mixture was left to settle, the liquid phase was decanted and the remaining light orange residue was taken up in 175 mL boiling CH_3CN (HPLC-grade). While hot, a colourless fine solid was filtered off. Upon coming to room temperature a colourless solid started to precipitate from the filtrate, which was overlayered with Et_2O and stored at 4 ° overnight. After filtration and washing with CH_2Cl_2 a colourless solid could be isolated.

Yield: 1.25 g, 6.90 mmol, 65%.
^{1}H NMR: (400 MHz, D_2O): δ = 3.61 (s, 3 H), 3.60-3.55 (m, 2 H), 3.50-3.44 (m, 2 H) ppm.
m.p.: 109-110 °C.

Isocyanate 10

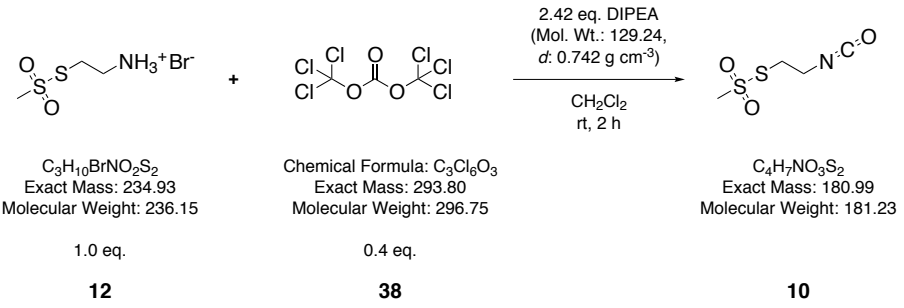

The hydrobromide **12** (43.2 mg, 183 μmol, 1.0 eq.) was stirred in 4 mL CH_2Cl_2. As 4.4 mL (443 μmol, 2.42 eq.) of a freshly prepared 0.1 M solution of *N*,*N*-diisopropylethylamine (DIPEA) in CH_2Cl_2 were added, the colourless solid dissolved. In a round-bottomed flask, triphosgene **(38)** (21.7 mg, 73.0 μmol, 0.4 eq.) was dissolved in 4 mL CH_2Cl_2 before the flask was sealed with a septum and equipped with a cannula to release excess pressure. Via syringe the solution of **12** and DIPEA was slowly added to the triphosgene. After addition of about 0.5 mL a colourless solid started to precipitate, after the addition of about 2 mL gas formation could be observed. After completion of the addition the septum was exchanged for a bubble counter. The mixture was stirred for a total of 2 h and subsequently slowly transferred into a separating funnel filled with 20 mL H_2O and 0.64 mL of the 0.1 M solution of DIPEA in CH_2Cl_2. Upon washing, the organic phase turned clear and was separated from the aqueous phase, which was extracted with additional 2 x 20 mL of CH_2Cl_2. The combined organic phases were dried (Na_2SO_4) and after complete evaporation of the volatiles the isocyanate **10** was isolated as a colourless oil. Since the compound undergoes decomposition quite fast it should be prepared freshly prior to subsequent use.

Yield: 15.6 mg, 86.1 μmol, 47%.
^{1}H NMR (400 MHz, $CDCl_3$): δ = 3.72 (t, *J* = 6.4 Hz, 2 H), 3.44-3.31 (m, 5 H) ppm.
^{13}C NMR (100.6 MHz, $CDCl_3$): δ = 123.7, 51.1, 42.9, 37.4 ppm.

Enantiopure, diol-functionalised bipyridine 8

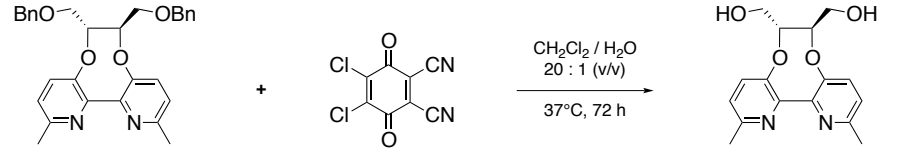

$C_{30}H_{30}N_2O_4$	$C_8Cl_2N_2O_2$		$C_{16}H_{18}N_2O_4$
Exact Mass: 482.22	Exact Mass: 225.93		Exact Mass: 302.13
Molecular Weight: 482.57	Molecular Weight: 227.00		Molecular Weight: 302.32
1.0 eq.	3 x 3.0 eq.		
7	**39**		**8**

The benzyl ether-protected bipyridine **7** (29.0 mg, 60 μmol, 1.0 eq.) was dissolved in 6 mL CH_2Cl_2. A first portion of 3.0 equivalents 2,3-dichloro-5,6-dicyano-1,4-benzoquinone **(39)** (DDQ, 40.9 mg, 180 μmol) was added and the resulting mixture was diluted with additional 4 mL CH_2Cl_2 and 0.5 mL H_2O. The mixture was heated to 37 °C bath temperature. After 24 h reaction time the second portion of 3.0 equivalents DDQ **(39)**, and after another 24 h the last portion of 3.0 equivalents DDQ **(39)** were added. After a total of 72 h reaction time the volatiles were removed *in vacuo* and the resulting red solid was dried for several hours to remove traces of H_2O. The crude product was subjected to column-chromatography (SiO_2, CH_2Cl_2/CH_3OH 15:1, UV detection). To remove remainders of DDQ the isolated substance was purified via column-chromatography a second time (Al_2O_3, CH_2Cl_2/CH_3OH 15:1, UV detection).

Yield: 8.7 mg, 28 μmol, 48%.
MS (ESI+): m/z (%) = 303.0 (6, $[M+H]^+$), 324.9 (100, $[M+Na]^+$).
^{1}H NMR (400 MHz, CD_3CN): δ = 7.49-7.43 (m, 2 H), 7.29-7.24 (m, 2 H), 3.98-3.89 (m, 2 H), 3.83-3.74 (m, 2 H), 3.68-3.58 (m, 2 H), 3.26 (br s, 2 H), 2.53 (m, 6 H) ppm. The spectrum is shown in the appendix (see page 262).
^{13}C NMR (62.9 MHz, CD_3CN): δ = 155.1, 154.2, 149.4, 131.4, 125.4, 87.2, 62.9, 23.9 ppm.
TLC: R_f = 0.65 (Al_2O_3, CH_2Cl_2/CH_3OH 15:1, UV detection).

Enantiopure bipyridine disulfide 13

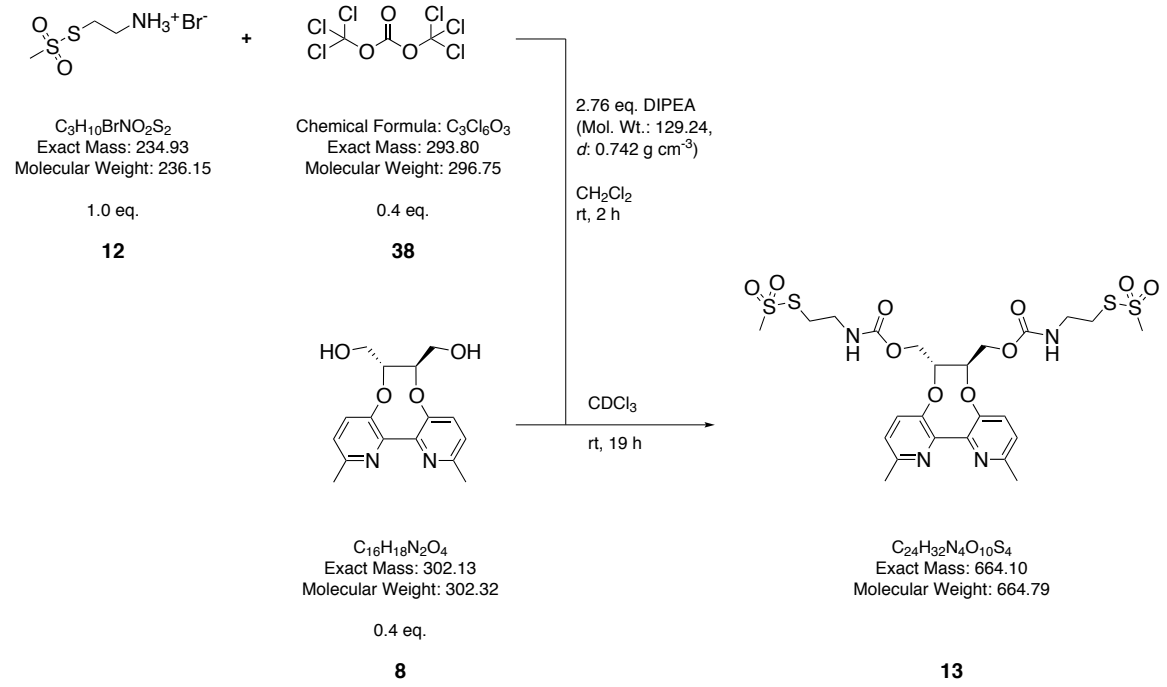

For in situ preparation of isocyanate **10**, triphosgene **(38)** (16.6 mg, 56 μmol, 1.6 eq.) was dissolved in 6 mL CH_2Cl_2 and 0.62 mL of a freshly prepared 0.1 M solution of *N*,*N*-diisopropylethylamine (DIPEA) in CH_2Cl_2 were added. The flask was sealed with a septum and equipped with a cannula to release excess pressure. In a separate flask, 33.1 mg of hydrobromide **12** (140 μmol, 4.0 eq.) were suspended in 3 mL CH_2Cl_2. Upon addition of 2.14 mL of the 0.1 M solution of DIPEA the colourless solid dissolved. Via syringe the solution of **12** was added dropwise to the solution of **38** upon which the yellow solution got turbid and a colourless solid precipitated. The mixture was stirred at room temperature for 2 h, during which it turned almost completely colourless. Subsequently it was added dropwise to a mixture of 15 mL H_2O and 0.5 mL of the 0.1 M solution of DIPEA. After separation of the phases the aqueous phase was extracted with 2 x 10 mL CH_2Cl_2. The combined organic phases were dried (Na_2SO_4) and evaporated to dryness. The resulting crude isocyanate **10** was used for the next step without additional purification: It was dissolved in 3 mL $CDCl_3$ and a solution of 10.5 mg of the diol-functionalised bipyridine **8** (35 μmol, 1.0 eq.) in 2 mL $CDCl_3$ was added dropwise. The resulting mixture was stirred at room temperature for 19 h and afterwards the solvents were removed *in vacuo*. The resulting crude product was purified via column-chromatography (SiO_2, CH_2Cl_2/CH_3OH 25:1 $\rightarrow$ CH_3OH, UV detection, staining with I_2 vapor) to yield the title compound.

Yield: Upon removal of the solvents from the fractions obtained from column-chromatography the product was contaminated with another species. Based on NMR data the yield was estimated to be 60%.
MS (ESI+): m/z (%) = 665.1 (100, $[M+H]^+$), 687.1 (35, $[M+Na]^+$).
^{1}H NMR (400 MHz, CD_2Cl_2): δ = 7.38 (d, J = 8.3 Hz, 2 H), 7.23 (d, J = 8.3 Hz, 2 H), 5.59-5.46 (m, 2 H),

4.45-4.26 (m, 4 H), 4.12 (br s, 2 H), 3.59-3.51 (m, 4 H), 3.38-3.27 (m, 10 H), 2.59 (s, 6 H) ppm. The spectrum is shown in the appendix (see page 263).

^{13}C NMR (100.6 MHz, CD_2Cl_2): δ = 155.6, 153.3, 148.7, 130.7, 127.8, 125.2, 83.4, 65.0, 51.2, 41.2, 36.8, 24.3 ppm.

TLC: R_f = 0.62 (SiO_2, CH_2Cl_2/CH_3OH 7:1, UV detection, staining with I_2 vapor).

Isothiocyanate-activated lysine derivative 15

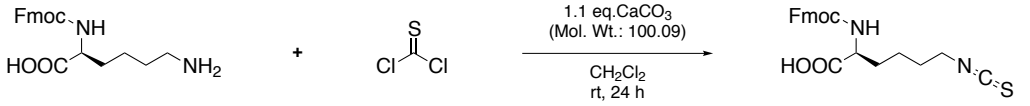

$C_{21}H_{24}N_2O_4$
Exact Mass: 368.17
Molecular Weight: 368.43

1.0 eq.

14

CCl_2S
Exact Mass: 113.91
Molecular Weight: 114.98
d: 1.50 g cm^{-3}

1.5 eq.

40

$C_{22}H_{22}N_2O_4S$
Exact Mass: 410.13
Molecular Weight: 410.49

15

In 200 mL CH_2Cl_2, 29.8 mg $CaCO_3$ (298 μmol, 1.1 eq.) were stirred vigorously for 30 minutes. 4.07 mL of a 0.1 M solution of thiophosgene **(40)** in dry CH_3CN (46.5 mg, 407 μmol, 1.5 eq.) were added, immediately followed by the Fmoc-protected lysine derivative **14** (100 mg, 271 μmol, 1.0 eq.). The flask was closed with a bubble counter, connected to two wash bottles of which the second was filled with a saturated aqueous solution of Na_2CO_3. The mixture was stirred for 24 h at room temperature, subsequently 80 mL H_2O were added, followed by 3.25 mL of a 0.1 M aqueous HCl (325 μmol, 1.2 eq.). After the mixture was stirred vigorously for 90 minutes the phases were separated and the neutral aqueous phase was extracted with additional 4 x 100 mL CH_2Cl_2, the combined organic phases were dried ($MgSO_4$) and evaporated to dryness to give a colourless glassy solid. The crude product was subjected to column-chromatography (SiO_2, CH_2Cl_2/CH_3OH 25:1 $\rightarrow$ 9:1, UV detection). TLCs of early fractions containing the product revealed a contamination with another compound which could not be detected using ^{1}H NMR or ESI-MS. The substance collected from these fractions was subjected to column-chromatography a second time (SiO_2, CH_2Cl_2/CH_3OH 50:1 $\rightarrow$ 9:1, UV detection) to give another portion of the pure product, which was dried *in vacuo* overnight to remove traces of solvents.

Note: Neither after storage in CD_2Cl_2 at room temperature nor pure in the solid state at -25°C for several weeks any decomposition could be monitored via ^{1}H NMR. Yet results of the subsequent reaction with the amino-functionalised cryptates **Ln-1** (see page 241) were found to proceed more efficiently with relatively fresh portions of **15**.

Yield: 52.3 mg, 127 μmol, 47%.
MS (ESI+): m/z (%) = 413.3 (10), 433.2 (100, $[M+Na]^+$), 449.1 (43, $[M+K]^+$).
^{1}H NMR (400 MHz, CD_2Cl_2): δ = 7.79 (d, *J* = 7.6 Hz, 2 H), 7.62 (d, *J* = 7.5 Hz, 2 H), 7.46-7.28 (m, 4 H), 4.49-4.31 (m, 3 H), 4.24 (t, *J* = 6.6 Hz, 1 H), 3.59-3.47 (m, 2 H), 2.00-1.30 (m, 6 H) ppm. The spectrum is shown in the appendix (see page 264).
^{13}C NMR (100.6 MHz, CD_2Cl_2): δ = 177.1, 157.0, 144.3, 141.8, 130.3, 128.3, 127.6, 125.6, 120.5, 67.6, 47.7, 45.4, 31.9, 30.3, 29.9, 23.1 ppm.
TLC: R_f = 0.20 (SiO_2, CH_2Cl_2/CH_3OH 15:1, UV detection).

4,4',6,6'-Tetramethyl-2,2'-bipyrimidine (23)

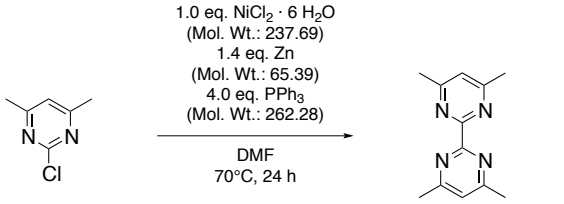

$C_6H_7ClN_2$
Exact Mass: 142.03
Molecular Weight: 142.59

1.0 eq.

41

$C_{12}H_{14}N_4$
Exact Mass: 214.12
Molecular Weight: 214.27

23

The synthesis of 4,4',6,6'-tetramethyl-2,2'-bipyrimidine (**23**) was performed slightly modified to a procedure reported earlier.[141][299][300]

Under N_2, $NiCl_2 \cdot 6\,H_2O$ (8.22 g, 35.1 mmol, 1 eq.) and PPh_3 (36.8 g, 140 mmol, 4.0 eq.) were suspended in 160 mL DMF (peptide grade). The dark blue suspension was degassed by three freeze-pump-thaw cycles. After zinc powder (3.21 g, 49.1 mmol, 1.4 eq.) was added another freeze-pump-thaw cycle was performed. The mixture was stirred at room temperature for 1 h during which it turned brown. Under N_2 in a separate flask 4,6-dimethyl-2-chloropyrimidine[298] **41** was dissolved in 30 mL DMF (peptide grade) and degassed by three freeze-pump-thaw cycles. The yellow solution was added to the brown suspension and stirred for 24 h at 70 °C bath temperature. After the resulting dark mixture was allowed to come to room temperature it was poured onto 630 mL 4 M aqueous ammonia. A dark solid precipitated and the suspension was stirred vigorously for 30 minutes before the solid was separated from the blue solution via filtration. The filtrate was extracted with 4 x 250 mL CH_2Cl_2, the combined organic phases were dried ($MgSO_4$) and evaporated to dryness. The resulting residue was taken up in 140 mL 1 M HCl and extracted with 3 x 100 mL Et_2O. The aqueous phase was brought to pH 8-9 with saturated aqueous Na_2CO_3 and extracted with 4 x 100 mL $CHCl_3$. The combined $CHCl_3$-phases were dried ($MgSO_4$) and after removal of the solvent *in vacuo* 1.73 g (8.07 mmol, 46%) of the slightly yellow product were obtained. After extraction of the dark solid obtained from filtration with 400 mL CH_2Cl_2 and twofold purification according to the procedure described above another portion of the product could be isolated (1.07 g, 4.99 mmol, 28%).

The product can also be purified via column-chromatography (SiO_2, CH_2Cl_2/CH_3OH 100:1 $\rightarrow$ 24:1, UV detection).[141]

Yield: 2.80 g, 13.06 mmol, 74%.
MS (ESI+): m/z (%) = 215.0 (26, $[M+H]^+$), 237.0 (100, $[M+Na]^+$), 253.0 (13, $[M+K]^+$), 451.1 (85, $[2\,M+Na]^+$).
^{1}H NMR (400 MHz, $CDCl_3$): δ = 7.11 (s, 2 H), 2.62 (s, 12 H) ppm.
^{13}C NMR (100.6 MHz, $CDCl_3$): δ = 167.9, 163.0, 120.5, 24.5 ppm.

Octabromide 24 and heptabromide 27 of the bipyrimidine

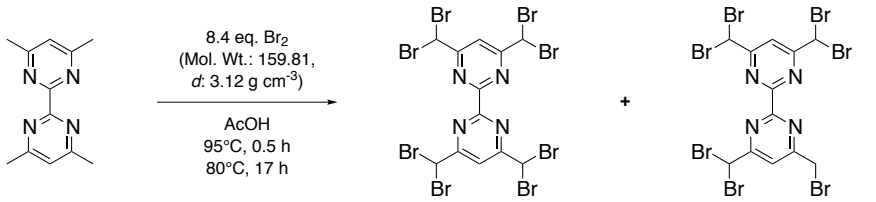

$C_{12}H_{14}N_4$
Exact Mass: 214.12
Molecular Weight: 214.27

1.0 eq.

23

$C_{12}H_6Br_8N_4$
Exact Mass: 837.41
Molecular Weight: 845.43

24

$C_{12}H_7Br_7N_4$
Exact Mass: 759.50
Molecular Weight: 766.54

27

The synthesis of octabromide **24** and heptabromide **27** was performed slightly modified to a procedure reported earlier.[141]

In a two-necked flask equipped with an internal thermometer and a reflux condenser, 4,4',6,6'-tetramethyl-2,2'-bipyrimidine **(23)** (636 mg, 2.97 mmol, 1 eq.) was dissolved under stirring in 48 mL glacial acetic acid to give an orange solution. 1.28 mL Br_2 (3.99 g, 25.0 mmol, 8.4 eq.) were added and the dark brown solution was heated quickly until the temperature of the reaction mixture reached 80 °C. A colourless solid precipitated from the mixture and the lower thirds of the cooler were filled with orange vapor. After 0.5 h reaction time the temperature of the oil bath was lowered to 80 °C and the mixture was stirred at this temperature for further 17 h during which more of the colourless solid precipitated. The light orange suspension was allowed to come to room temperature and the volatiles were condensed into an external cool trap in which a light yellow solid sublimated. After concentration to dryness 20 ml of a saturated aqueous $NaHCO_3$ solution were added to the orange solid left in the flask. The substance showed hydrophobic behaviour. 80 mL $CHCl_3$ were added and the mixture was stirred vigorously for several minutes until the solid was completely dissolved. The dark orange organic phase was separated from the aqueous phase which was extracted with 2 x 80 mL $CHCl_3$. The combined organic phases were dried ($MgSO_4$) and concentrated to give the crude product which was subsequently subjected to column-chromatography (SiO_2, $CHCl_3$, UV detection, staining with I_2 vapor). The octabromide **24** (which was eluted from the column prior to the heptabromide **27**) was obtained with significant contaminations which could easily be removed by recrystallisation from warm $CHCl_3$. To do so the impure octabromide **24** was suspended in $CHCl_3$ and treated in an ultra-sonic bath until the suspended solid was very fine and could be brought into solution completely with a water bath of 40 °C. The clear solution was stored at 4 °C for 48 h during which the product precipitated as colourless needles.

Octabromide 24:[141]
Yield: 349 mg, 0.41 mmol, 15%.
^{1}H NMR (400 MHz, $CDCl_3$): δ = 8.51 (s, 2 H), 6.72 (s, 4 H) ppm.

^{13}C NMR (100.6 MHz, $CDCl_3$): δ = 170.2, 120.2, 118.1, 37.5 ppm.
TLC: R_f = 0.83 (SiO_2, $CHCl_3$, UV detection, staining with I_2 vapor).

Heptabromide 27:
Yield: 1.124 g, 1.47 mmol, 53%.
MS (ESI+): m/z (%) = 788.4 (100, $[M+Na]^+$, Br_7-isotope pattern), 804.4 (19, $[M+K]^+$, Br_7-isotope pattern).
^{1}H NMR (400 MHz, $CDCl_3$): δ = 8.49 (s, 1 H), 8.17 (s, 1 H), 6.73 (s, 2 H), 6.69 (s, 1 H), 4.67 (s, 2 H) ppm.
^{13}C NMR (100.6 MHz, $CDCl_3$): δ = 170.1, 169.2, 168.7, 160.7, 160.3, 119.1, 117.9, 38.8, 38.6, 31.4 ppm.
TLC: R_f = 0.59 (SiO_2, $CHCl_3$/CH, UV detection, staining with I_2 vapor).

Tetrabromide 25 of the bipyrimidine

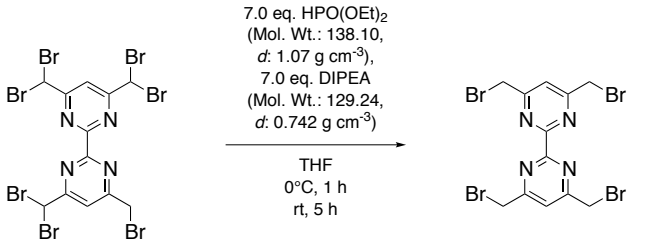

$C_{12}H_7Br_7N_4$
Exact Mass: 759.50
Molecular Weight: 766.54

1.0 eq.

27

$C_{12}H_{10}Br_4N_4$
Exact Mass: 525.76
Molecular Weight: 529.85

25

The synthesis of tetrabromide **25** from heptabromide **27** was performed slightly modified to a procedure reported for the preparation of **25** from octabromide **24**.[141]

The *N*,*N*-diisopropylethylamine (DIPEA) used in the experiment was stirred overnight with KOH to remove H_2O.

Under N_2, 596 mg (0.78 mmol, 1 eq.) of heptabromide **27** were dissolved in 22 mL dry THF. The slightly yellow solution was cooled in an ice-bath before 0.70 mL diethyl phosphite (752 mg, 5.45 mmol, 7.0 eq.), were added via syringe, followed by the addition of 0.95 mL of *N*,*N*-diisopropylethylamine (DIPEA, 704 mg, 5.45 mmol, 7.0 eq.), via syringe. The slightly brown solution was stirred at 0 °C for 1 h before the ice-bath was removed and the mixture was stirred at room temperature for further 5 h upon which it turned increasingly dark and a colourless solid precipitated. The suspension was poured onto 50 g ice and the resulting turbid orange mixture was stirred at room temperature until the ice was completely molten. 50 mL of $CHCl_3$ were added, after separation of the organic phase the aqueous phase was extracted with 3 x 50 mL $CHCl_3$ and the combined organic phases were dried ($MgSO_4$). The solvent was evaporated and the resulting oily residue was dried *in vacuo* for several hours. Upon addition of 5 mL CH_3OH it turned into a suspension of an orange solution and a fine colourless solid. It was stirred at room temperature for 60 h before the solid was separated from the solution by filtration. The solid was dissolved in $CHCl_3$, evaporated to dryness and extracted by stirring another time (5 mL CH_3OH, 12 h). After filtration the title compound could be isolated as a beige solid.

The crude mixture can also be purified via column-chromatography (SiO_2, CH_2Cl_2/CH_3OH 100:1 $\rightarrow$ 25:1, UV detection, staining with I_2 vapor).

Yield: 285 mg, 0.54 mmol, 69%.
MS (ESI+): m/z (%) = 530.8 (100, $[M+H]^+$, Br_4-isotope pattern), 552.7 (12, $[M+Na]^+$), 568.1 (9, $[M+K]^+$).

^{1}H NMR (400 MHz, $CDCl_3$): δ = 7.84 (s, 2 H), 4.62 (s, 8 H) ppm.

^{13}C NMR (100.6 MHz, $CDCl_3$): δ = 167.6, 162.2, 120.1, 31.6 ppm.

Elemental Analysis: Anal. Calcd. for $C_{12}H_{10}Br_4N_4$ (M_r = 529.85): C, 27.20; H, 1.90; N, 10.57. Found: C, 27.62; H, 1.88; N, 10.75.

TLC: R_f = 0.40 (SiO_2, CH_2Cl_2/CH_3OH 25:1, UV detection, staining with I_2 vapor).

Tetra-(*tert*-butyl)iminodiacetate bipyrimidine 32

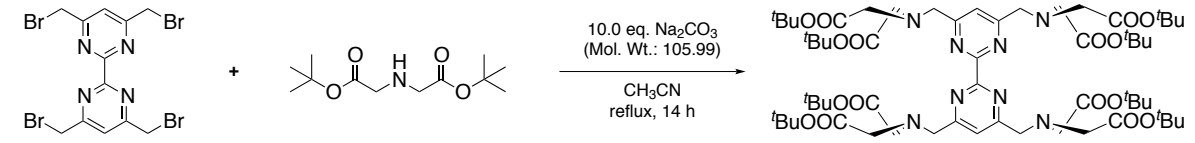

$C_{12}H_{10}Br_4N_4$
Exact Mass: 525.76
Molecular Weight: 529.85

1.0 eq.

25

$C_{12}H_{23}NO_4$
Exact Mass: 245.16
Molecular Weight: 245.31

4.4 eq.

33

$C_{60}H_{98}N_8O_{16}$
Exact Mass: 1186.71
Molecular Weight: 1187.46

32

In 25 mL CH_3CN (HPLC-grade), tetrabromide **25** (38.9 mg, 73.4μmol, 1 eq.), di-(*tert*-butyl)iminodiacetate **(33)** (79.2 mg, 323 μmol, 4.4 eq.) and Na_2CO_3 (77.8 mg, 734 μmol, 10 eq.) were suspended, upon which a slight emission of gas could be observed. The suspension was brought to reflux temperature and stirred for 14 h. Afterwards the yellow mixture was concentrated to dryness and subjected to column-chromatography (SiO_2, CH_2Cl_2/CH_3OH 25:1, UV detection). The signals in the ^{1}H NMR spectrum of the isolated substance (38.4 mg) pointed towards the successful preparation of the target compound, but also showed a significant contamination with starting material **33**. The substance was taken up in 5 mL $CHCl_3$ and poured onto a mixture of 0.2 mL 1 M aqueous Na_2CO_3 and 2 mL H_2O. Both phases turned turbid and did not become clear upon addition of 2 mL H_2O and 5 mL $CHCl_3$. The phases were mixed vigorously before the organic phase was separated and the aqueous was extracted with 4 x 10 mL $CHCl_3$. After the combined organic phases were dried ($MgSO_4$) and evaporated to dryness via ^{1}H NMR spectroscopy only a slight improvement of the purity of the compound (now 26.5 mg) could be ascertained. Finally a second purification via column-chromatography (basic Al_2O_3, CH_2Cl_2/CH_3OH 100:1 $\rightarrow$ 9:1, UV detection, staining with I_2 vapor) allowed for the isolation of the sufficiently pure title compound.

Note: Presumably the column-chromatography with basic Al_2O_3 is the relevant step for purification. If the previous steps which were undertaken for purification are not performed a higher yield might be possible.

Yield: 6.9 mg, 5.8 μmol, 8%.
MS (ESI+): m/z (%) = 1209.7 (100, $[M+Na]^+$).
^{1}H NMR (400 MHz, $CDCl_3$): δ = 8.12 (s, 2 H), 4.21 (s, 8 H), 3.52 (s, 16 H), 1.44 (br s, 72 H) ppm.
^{13}C NMR (100.6 MHz, $CDCl_3$): δ = 170.6, 170.3, 162.9, 117.6, 81.2, 59.6, 56.1, 28.3 ppm.
TLC: R_f = 0.45 (Al_2O_3, CH_2Cl_2/CH_3OH 15:1, UV detection, staining with I_2 vapor).

8.3 Sodium Cryptates

Enantiopure, diol-functionalised sodium cryptate Na-5

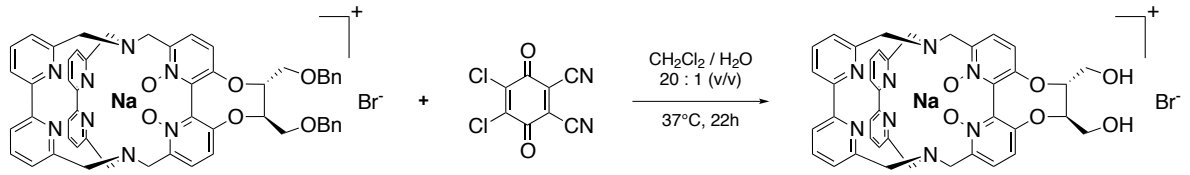

$C_{54}H_{48}BrN_8NaO_6$
Exact Mass: 1006.28
Molecular Weight: 1007.90

1.0 eq.

Na-6

$C_8Cl_2N_2O_2$
Exact Mass: 225.93
Molecular Weight: 227.00

9.0 eq.

39

$C_{40}H_{36}BrN_8NaO_6$
Exact Mass: 826.18
Molecular Weight: 827.66

Na-5

The benzyl-protected sodium cryptate **Na-6** (12.8 mg, 12.6 μmol, 1.0 eq.) was dissolved in 6 mL CH_2Cl_2 to give a slightly yellow solution. 2,3-Dichloro-5,6-dicyano-1,4-benzoquinone **(39)** (DDQ, 25.9 mg, 114 μmol, 9.0 eq.) was added in portions, upon which the mixture turned red. It was diluted with additional 4 mL CH_2Cl_2 and 0.5 mL H_2O, and heated to 37 °C bath temperature. After 22 h the mixture was allowed to come to room temperature and the volatiles were removed *in vacuo*. The resulting red solid was taken up in 7 mL CH_3CN (HPLC-grade), poured onto 7 mL of a saturated aqueous solution of $NaHCO_3$ and extracted with 3 x 15 mL $CHCl_3$. The combined organic phases were dried (Na_2SO_4), evaporated to dryness and the resulting crude product was purified by column-chromatography (Al_2O_3, CH_2Cl_2/CH_3OH 25:1 $\rightarrow$ CH_3OH, UV detection).

Yield: 4.8 mg, 5.8 μmol, 45%.
MS (ESI+): m/z (%) = 715.4 (7, $[M\text{-}2O\text{-}Br]^+$), 731.4 (11, $[M\text{-}O\text{-}Br]^+$), 747.4 (100, $[M\text{-}Br]^+$).
^{1}H NMR (400 MHz, CD_3OD): δ = 8.02-7.80 (m, 10 H), 7.56-7.44 (m, 6 H), 4.26 (d, J = 12.0 Hz, 2 H), 4.15-4.08 (m, 2 H), 3.95-3.82 (m, 6 H), 3.75-3.66 (m, 2 H), 3.58 (d, J = 12.9 Hz, 2 H), 3.50-3.39 (m, 4 H) ppm. The spectrum is shown in the appendix (see page 265).
^{1}H-^{1}H COSY NMR (400 MHz, CD_3OD): The spectrum is shown in the appendix (see page 266).
TLC: R_f = 0.12 (SiO_2, CH_2Cl_2/CH_3OH 1:1, UV detection).

Enantiopure, twofold disulfide-functionalised sodium cryptate Na-9

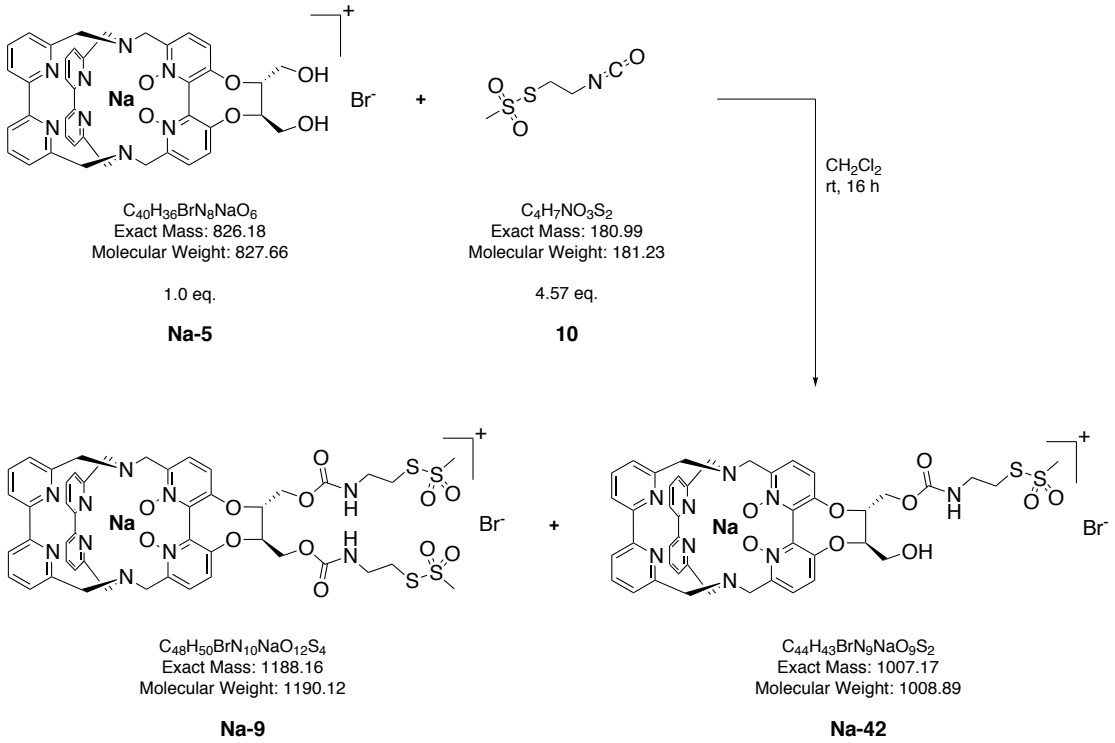

Isocyanate **10** (4.8 mg, 26.5 μmol, 4.57 eq.) and the diol-functionalised sodium cryptate **Na-5** (4.8 mg, 5.8 μmol, 1.0 eq.) were dissolved in 2 mL CH_2Cl_2 each. The latter solution was added dropwise to the solution of isocyanate **10** and the mixture was stirred at room temperature overnight. Subsequently the volatiles were completely removed *in vacuo*. The resulting residue was purified by column-chromatography (SiO_2, CH_2Cl_2/CH_3OH 50:1 $\rightarrow$ 15:1, UV detection) to yield separately the disulfide-functionalised sodium cryptate **Na-9** and the only mono-functionalised sodium cryptate **Na-42** as byproduct.

Note: Due to the small amounts isolated no yield could be determined.
MS (ESI+): m/z (%) = 913.3 (7), 983.1 (20), 1061.1 (6, $[M\text{-}3O\text{-}Br]^+$) 1109.0 (100, $[M\text{-}Br]^+$).
^{1}H NMR (400 MHz, CD_2Cl_2): The spectrum is shown in the appendix (see page 267).
TLC: R_f = 0.49 (SiO_2, CH_2Cl_2/CH_3OH 7:1, UV detection, staining with I_2 vapor).

Byproduct: Enantiopure disulfide-functionalised sodium cryptate Na-42:
MS (ESI+): m/z (%) = 928.1 (100, $[M\text{-}Br]^+$).
^{1}H NMR (400 MHz, CD_2Cl_2): The spectrum is shown in the appendix (see page 268).

TLC: R_f = 0.44 (SiO_2, CH_2Cl_2/CH_3OH 7:1, UV detection, staining with I_2 vapor).

Azide-functionalised sodium cryptate Na-2

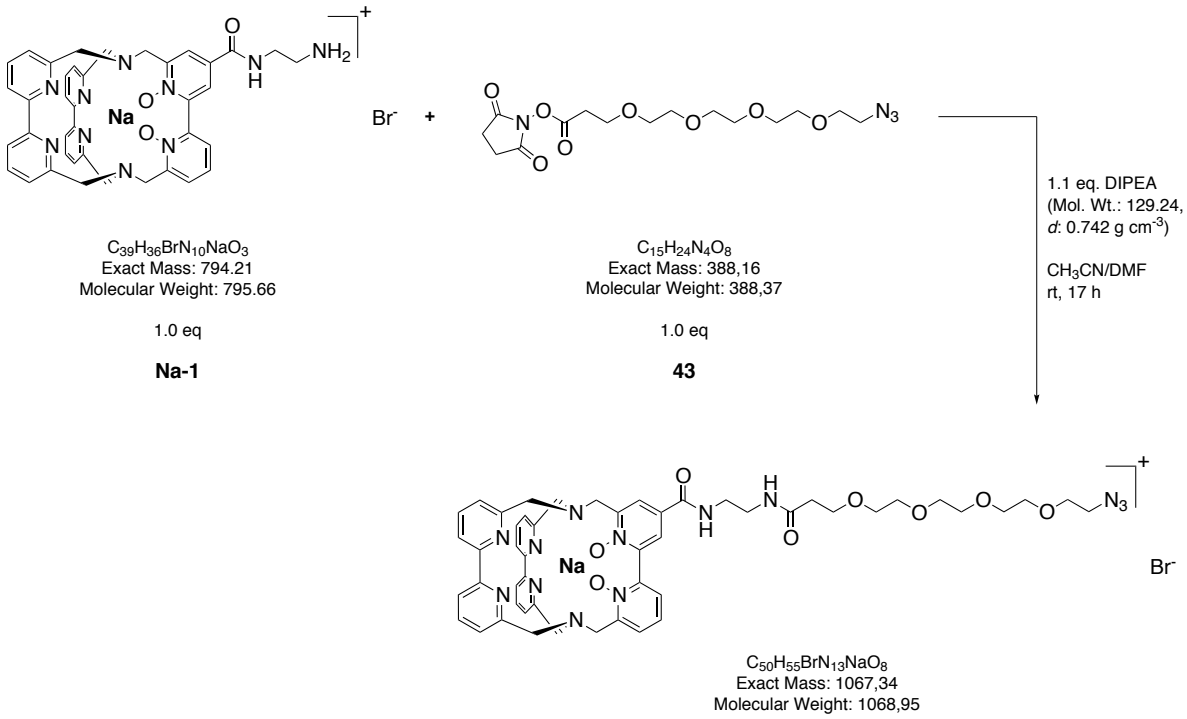

The amino-functionalised sodium cryptate **Na-1** (16.7 mg, 21.0 μmol, 1.0 eq.) was suspended in 5 mL CH_3CN (HPLC-grade), the resulting slightly yellow mixture was stirred several minutes. As also upon addition of 1.2 eq. *N*,*N*-diisopropylethylamine (DIPEA, 2.97 mg, 23.1 μmol, 4.0 μL) the starting material was not completely dissolved, 2 mL DMF (peptide grade) were added. The resulting clear solution was stirred a few more minutes before the NHS-ester **43** (8.16 mg, 21.0 μmol, 1.0 eq., dissolved in 0.5 mL CH_3CN (HPLC-grade)) was added. The mixture was diluted with 1 mL CH_3CN (HPLC-grade) and stirred at room temperature for 17 h. Afterwards the solvents were removed *in vacuo* and the resulting yellow to orange oil was dried thoroughly. The crude product was purified by column-chromatography (SiO_2, CH_2Cl_2/CH_3OH 25:1 $\rightarrow$ 7:1, UV detection) to give the azide-functionalised sodium cryptate **Na-2**.

Yield: 9.1 mg, 8.5 μmol, 40%.
MS (ESI+): m/z (%) = 988.6 (100, $[M\text{-}Br]^+$).
^{1}H NMR (400 MHz, CD_3OD): δ = 9.09 (br, 1 H), 8.72 (d, *J* = 2.6 Hz, 1 H), 8.50 (d, *J* = 2.5 Hz, 1 H), 8.07 (br, 1 H), 7.91 (dd, *J* = 7.8, 2.1 Hz, 1 H), 7.87-7.73 (m, 8 H), 7.54 (dd, *J* = 7.8, 2.1 Hz, 1 H), 7.44-7.34 (m, 5 H), 4.40-4.25 (m, 2 H), 4.01-3.88 (m, 4 H), 3.77-3.33 (m, 25 H), 3.27-3.19 (m, 1 H), 2.67 (s, H), 2.54 (t, *J* = 6.2 Hz, 2 H) ppm. The spectrum is shown in the appendix (see page 264).
TLC: R_f = 0.42 (SiO_2, CH_2Cl_2/CH_3OH 7:1, UV detection).

Lysine-functionalised sodium cryptate Na-16

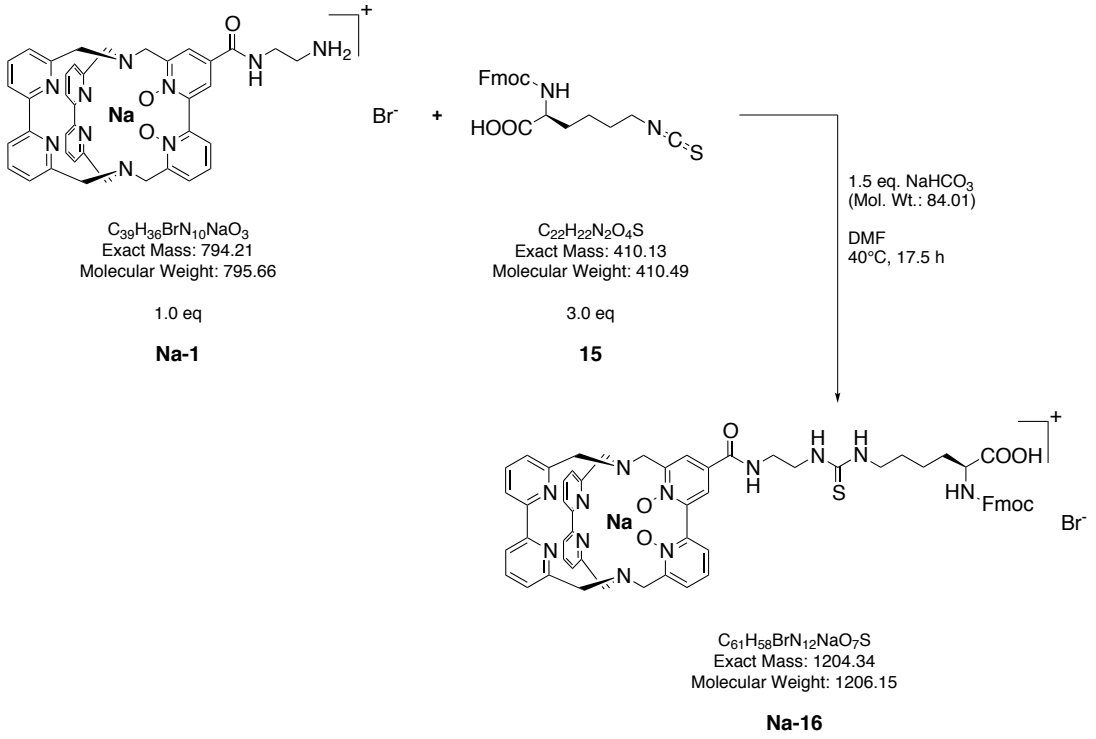

$C_{39}H_{36}BrN_{10}NaO_3$
Exact Mass: 794.21
Molecular Weight: 795.66

1.0 eq

Na-1

$C_{22}H_{22}N_2O_4S$
Exact Mass: 410.13
Molecular Weight: 410.49

3.0 eq

15

$C_{61}H_{58}BrN_{12}NaO_7S$
Exact Mass: 1204.34
Molecular Weight: 1206.15

Na-16

In 3 mL dry DMF the sodium cryptate **Na-1** (15.1 mg, 19 μmol, 1.0 eq.) was dissolved and $NaHCO_3$ (2.4 mg, 29 μmol, 1.5 eq.) was added. The slightly yellow solution was warmed to 30 °C bath temperature. After addition of the isothiocyanate-functionalised lysine derivative **15** (23.0 mg, 56 μmol, 3.0 eq.) in 2 mL dry DMF, the mixture was heated to 40 °C and stirred for 17.5 h before the solvent was removed *in vacuo* and the remaining solid was dried thoroughly. The crude product was subjected to column-chromatography (SiO_2, CH_2Cl_2/CH_3OH 7:1, UV detection) to yield the title compound as an off-white solid.

Yield: 11.6 mg, 9.6 μmol, 51%.
MS (ESI+): m/z (%) = 741.3 (8), 927.3 (9), 1125.3 (100, $[M\text{-}Br]^+$), 1141.2 (13, $[M\text{-}Na+K\text{-}Br]^+$), 1147.2.(12), 1173.2 (16).
^{1}H NMR (500 MHz, $CD_3OD + CD_2Cl_2$): The spectrum is shown in the appendix (see page 269).
^{1}H-^{1}H COSY NMR (500 MHz, $CD_3OD + CD_2Cl_2$): The spectrum is shown in the appendix (see page 270).
TLC: R_f = 0.09 (SiO_2, CH_2Cl_2/CH_3OH 7:1, UV detection).

Bromide-functionalised sodium cryptate Na-28

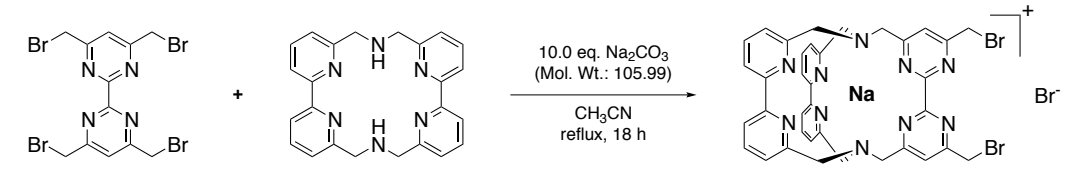

$C_{12}H_{10}Br_4N_4$
Exact Mass: 525.76
Molecular Weight: 529.85

1.0 eq.

25

$C_{24}H_{22}N_6$
Exact Mass: 394.19
Molecular Weight: 394.47

1.0 eq.

44

$C_{36}H_{30}Br_3N_{10}Na$
Exact Mass: 862.01
Molecular Weight: 865.39

Na-28

In a two-necked flask, tetrabromide **25** (123 mg, 233 μmol, 1.0 eq.) and Na_2CO_3 (247 mg, 2.33 mmol, 10.0 eq.) were given into 130 mL CH_3CN (HPLC-grade) and the resulting mixture was brought to reflux temperature. A total of 91.8 mg (233 μmol, 1.0 eq.) of the macrocyclus **44**[311] was added in portions over a period of 3.5 h. Afterwards the mixture was refluxed for further 14.5 h, then it was filtered hot. The solid residue was washed with CH_3CN (HPLC-grade) and the organic phases were evaporated to dryness before the crude product was purified by column-chromatography (SiO_2, CH_2Cl_2/CH_3OH 25:1 $\rightarrow$ 4:1, UV detection). Prior to the title compound remainders of the starting material **25** (39.7 mg, 74.9 μmol, 32%) and subsequently the byproduct, sodium dicryptate **Na-Na-26** (20.4 mg, 17.0 μmol, 7%), were eluted from the column.

Yield: 54.7 mg, 63.2 μmol, 51%.
MS (ESI+): m/z (%) = 741.1 (56, [M-Br+Cl-Br]$^+$, BrCl-isotope pattern), 785.0 (100, [M-Br]$^+$, Br_2-isotope pattern), 825.0 (14, Br_2-pattern), 870.9 (26, BrCl-isotope pattern).
^{1}H NMR (400 MHz, CD_3OD): δ = 8.08 (m, 4 H), 7.90 (t, *J* = 7.8 Hz, 4 H), 7.74 (s, 2 H), 7.40 (m, 4 H), 4.70-4.66 (m, 4 H), 3.96-3.82 (m, 12 H) ppm. The spectrum is shown in the appendix (see page 271).
^{1}H-^{1}H COSY NMR (400 MHz, CD_3OD): The spectrum is shown in the appendix (see page 271).
^{13}C NMR (100.6 MHz, CD_3OD + $CDCl_3$): δ = 171.4, 168.9, 162.6, 159.7, 156.7, 139.6, 125.3, 122.1, 121.8, 60.3, 59.4, 31.5 ppm.
TLC: R_f = 0.36 (SiO_2, CH_2Cl_2/CH_3OH 9:1, UV detection).

Di-(*tert*-butyl)iminodiacetate-functionalised sodium cryptate Na-31

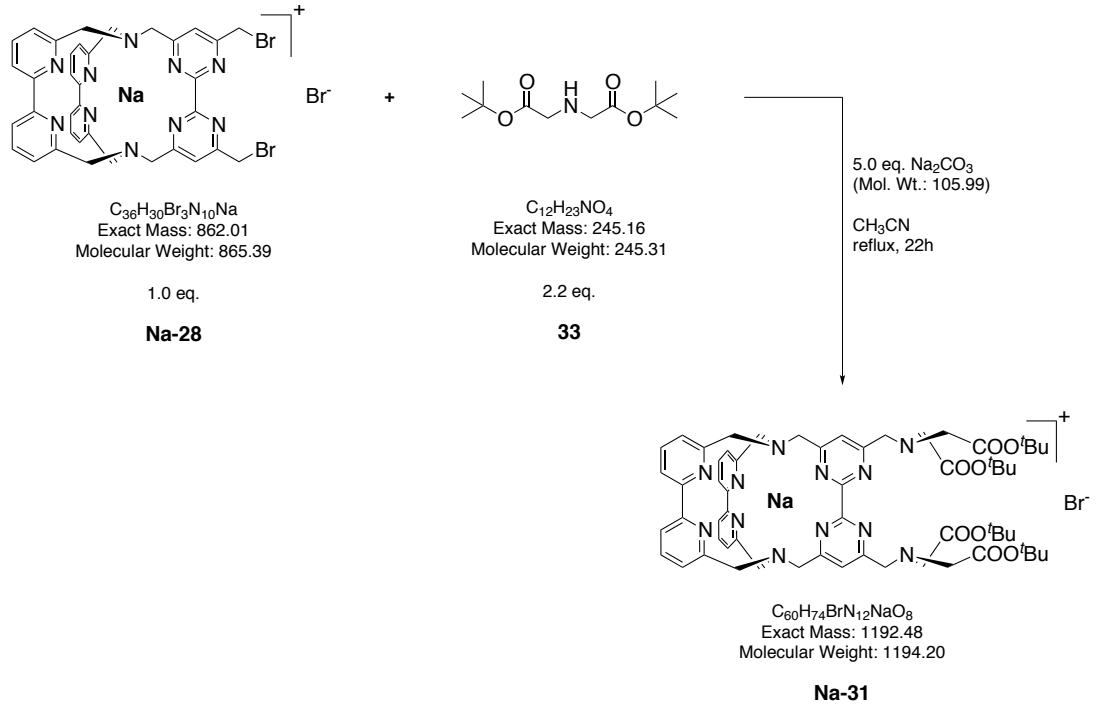

$C_{36}H_{30}Br_3N_{10}Na$
Exact Mass: 862.01
Molecular Weight: 865.39

1.0 eq.

Na-28

$C_{12}H_{23}NO_4$
Exact Mass: 245.16
Molecular Weight: 245.31

2.2 eq.

33

$C_{60}H_{74}BrN_{12}NaO_8$
Exact Mass: 1192.48
Molecular Weight: 1194.20

Na-31

In 15 mL CH_3CN (HPLC-grade), 17.1 mg (19.8 μmol, 1.0 eq.) of the bromide-functionalised sodium cryptate **Na-28**, 10.7 mg (43.6 μmol, 2.2 eq.) di-(*tert*-butyl)iminodiacetate **33** and 10.5 mg (99.0 μmol, 5.0 eq.) Na_2CO_3 were brought to reflux temperature. The suspension which at first was slightly yellow gradually turned dark and finally a solid started to precipitate. After 22 h reaction time the suspension was concentrated to dryness and the resulting crude product was subjected to column-chromatography (basic Al_2O_3, CH_2Cl_2/CH_3OH 100:1 $\rightarrow$ 9:1, UV detection). The product was obtained as a slightly yellow solid.

Yield: 3.8 mg, 3.2 μmol, 16%.
MS (ESI+): m/z (%) = 1113.6 (12, $[M\text{-}Br]^+$).
^{1}H NMR (400 MHz, CD_3OD): δ = 8.11-8.06 (m, 4 H), 7.93-7.87 (m, 6 H), 7.43-7.38 (m, 4 H), 4.16 (s, 4 H), 3.95-3.81 (m, 12 H), 3.52 (s, 8 H), 1.38 (s, 36 H) ppm. The spectrum is shown in the appendix (see page 273).
TLC: R_f = 0.16 (SiO_2, CH_2Cl_2/CH_3OH 9:1, UV detection).

Methoxy-functionalised sodium cryptate Na-34

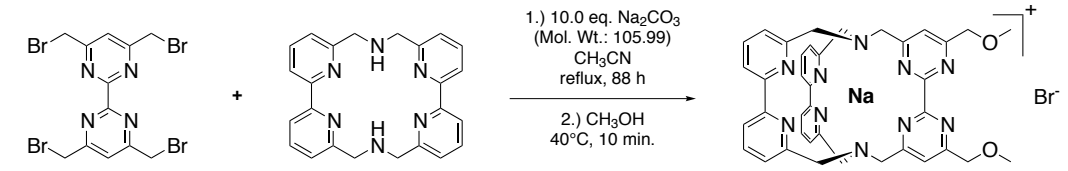

$C_{12}H_{10}Br_4N_4$
Exact Mass: 525.76
Molecular Weight: 529.85

1.0 eq.

25

$C_{24}H_{22}N_6$
Exact Mass: 394.19
Molecular Weight: 394.47

1.0 eq.

44

$C_{38}H_{36}BrN_{10}NaO_2$
Exact Mass: 766.21
Molecular Weight: 767.65

Na-34

In a 1 L Schlenk flask 98.0 mg of tetrabromide **25** (185 μmol, 1.0 eq.), 72.9 mg of macrocyclus **44**[311] (185 μmol, 1.0 eq.) and 196 mg of Na_2CO_3 (0.185 μmol, 10 eq.) were dried *in vacuo* (membrane pump), for several hours. Afterwards the solids were set under Ar and 550 mL CH_3CN (HPLC-grade) were added. The suspension was brought to reflux and stirred for 88 h after which the solvent was removed *in vacuo* and the resulting solid was dried. 100 mL CH_3OH were added, the mixture was stirred for 10 minutes before the volatiles were evaporated. During this the mixture turned dark green, but the colouring disappeared upon column-chromatography (SiO_2, CH_2Cl_2/CH_3OH 25:1 $\rightarrow$ 9:1, UV detection) from which the product was isolated as a solid of a rather dark yellow colour, compared to other sodium cryptates. After the product the byproduct, sodium dicryptate **Na-Na-26** (11.3 , 9.41 μmol, 5%) was eluted.

Yield: 23.7 mg, 30.9 μmol, 17%.
MS (ESI+): m/z (%) = 657.1 (12, $[M\text{-}2CH_3\text{-}Br]^+$), 687.2 (100, $[M\text{-}Br]^+$).
^{1}H NMR (400 MHz, CD_3OD): δ = 8.10-8.05 (m, 4 H), 7.93-7.86 (m, 4 H), 7.65 (s, 2 H), 7.42-7.37 (m, 4 H), 4.70-4.66 (m, 4 H), 3.93-3.81 (m, 12 H), 3.56-3.49 (m, 6 H) ppm. The spectrum is shown in the appendix (see page 272).
^{13}C NMR (100.6 MHz, CD_3OD): δ = 171.1, 170.6, 162.4, 159.9, 156.7, 139.6, 125.3, 121.8, 119.3, 74.7, 60.3, 59.6, 59.5 ppm.
TLC: R_f = 0.26 (SiO_2, CH_2Cl_2/CH_3OH 9:1, UV detection).

8.4 Lanthanoid Cryptates

Amino-functionalised lanthanoid cryptates Ln-1: general procedure[160]

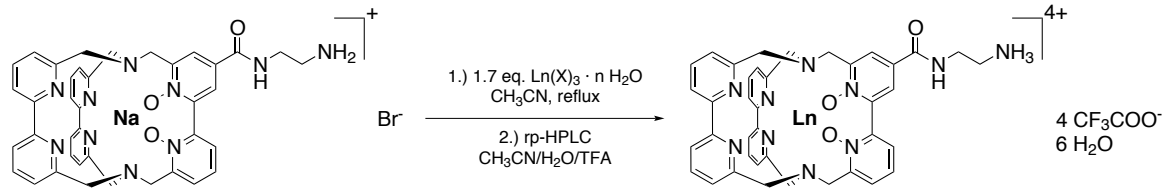

$C_{39}H_{36}BrN_{10}NaO_3$
Exact Mass: 794.21
Molecular Weight: 795.66

1.0 eq

Na-1

$C_{47}H_{49}F_{12}N_{10}O_{17}Ln$

Ln = Sm, Eu, Tb, Yb, Lu

Ln-1

Sodium cryptate **Na-1**[161][160] (1.0 eq.) and lanthanoid salt $Ln(X)_3 \cdot n\,H_2O$ (1.7 eq.) were suspended in CH_3CN (HPLC-grade) and heated to reflux for at least 40 h. Volatile components of the mixture were removed *in vacuo* and the resulting residue was subjected to semi-preparative reversed-phase HPLC (Lichrospher RP-18e (Merck), 250x10 mm - 10 μm, flow rate: 3 mL min^{-1}, UV detection: 300 nm) and program **A**. The product was isolated from the pure fractions as off-white or faintly yellow solid after evaporation to dryness *in vacuo* at room temperature.

Note: The exact nature and number of bound anions and solvent molecules could not be determined unambiguously. ^{19}F NMR data strongly indicate that at least one CF_3COO^- is bound and from general experience the assumption of several water molecules being attached after HPLC purification is reasonable.

Amino-functionalised samarium cryptate Sm-1

10.0 mg of sodium cryptate **Na-1** (13.0 μmol, 1.0 eq.) and 8.1 mg $SmCl_3 \cdot 6\,H_2O$ (Mol. Wt.: 364.81 g/mol, 22 μmol, 1.7 eq.) in 15 mL CH_3CN (HPLC-grade), 65 h reflux.

$C_{47}H_{49}F_{12}N_{10}O_{17}Sm$
Molecular Weight: 1404.29

Yield: 7.6 mg, 5.4 μmol, 42%.
^1H NMR (400 MHz, CD_3OD): δ = 9.47 (d, *J* = 7.9 Hz, 1 H), 9.36 (d, *J* = 8.1 Hz, 1 H), 9.03 (d, *J* = 8.0 Hz, 1 H), 8.98-8.88 (m, 2 H), 8.84 (t, *J* = 8.0 Hz, 1 H), 8.46 (d, *J* = 2.4 Hz, 1 H), 8.24-7.95 (m, 6 H), 7.92 (d, *J* = 7.8 Hz, 1 H), 9.47 (d, *J* = 7.9 Hz, 1 H), 7.75 (dd, *J* = 7.8, 2.0 Hz, 1 H), 7.01 (d, *J* = 12.6 Hz, 1 H), 6.73 (d, *J* = 12.6 Hz, 1 H), 6.66-6.58 (m, 2 H), 3.66 (t, *J* = 5.9 Hz, 2 H), 3.15 (t, *J* = 6.0 Hz, 2 H), 3.01-2.89 (m, 2 H), 2.60-2.50 (m, 2 H), 1.49-1.35 (m, 2 H), 0.95-0.77 (m, 2 H), 0.61 (d, *J* = 15.1 Hz, 1 H), 0.50 (d, *J* = 15.3 Hz, 1 H) ppm. The spectrum is shown in the main text (see page 39).
^{19}F NMR (376 MHz, CD_3OD): δ = -77.4 (s) ppm.
MALDI-MS (2,5-dihydroxybenzoic acid (DHB), RP mode, pos. mode): m/z (%) = 992.64 (26, [M - O +

$[DHB\text{-}H]^-$ + e^- + 11 (from reaction with COH_2)]$^+$, Sm-isotope pattern), 1118.21 (100, [M - 2 O + 2 [DHB-H]$^-$]$^+$, Sm-isotope pattern).
HR ESI-MS (pos. mode): $[SmC_{39}H_{36}N_{10}O_3{+}HCOO^-]^{2+}$: calculated: m/z = 444.60674,
found: m/z = 444.60658.
HPLC: R_f = 11.8 min (analytical reversed-phase HPLC, program **A**).

Amino-functionalised europium cryptate Eu-1
35.0 mg of sodium cryptate **Na-1** (44.0 μmol, 1.0 eq.) and 27.4 mg $EuCl_3 \cdot 6\,H_2O$ (Mol. Wt.: 366.41 g/mol, 74.8 μmol 1.7 eq.) in 17 mL CH_3CN (HPLC-grade), 70 h reflux.

$C_{47}H_{49}F_{12}N_{10}O_{17}Eu$
Molecular Weight: 1405.89

Yield: 14.3 mg, 10.2 μmol, 23%.
^{1}H NMR (400 MHz, CD_3OD): δ = 27.04 (br s, 1 H), 26.15 (br s, 1 H), 23.92 (br s, 2 H), 13.31 (s, 2 H), 10.39-10.04 (m, 2 H), 9.98-9.88 (m, 1 H), 9.88-9.77 (m, 2 H), 9.29 (t, *J* = 7.8 Hz, 1 H), 9.12 (d, *J* = 7.8 Hz, 1 H), 7.15 (s, 1 H), 7.05-6.75 (m, 3 H), 5.48-5.40 (m, 1 H), 5.10-5.02 (m, 1 H), 4.28-4.19 (m, 1 H), 4.18-4.09 (m, 1 H), 3.93-3.76 (m, 3 H), 3.69-3.61 (m, 1 H), 3.39 (t, *J* = 6.0 Hz, 2 H), 1.76-1.66 (m, 1 H), 1.17-1.10 (m, 1 H), -8.79-(-8.99) (m, 1 H), -9.51-(-9.70) (m, 1 H), -11.19 (br s, 1 H), -12.82 (br s, 1 H) ppm. The spectrum is shown in the main text (see page 39).
^{19}F NMR (376 MHz, CD_3OD): δ = -77.5 (s) ppm.
MALDI-MS (2,5-dihydroxybenzoic acid (DHB), RP mode, pos. mode): m/z (%) = 966.15 (100, [M - 2 O - H^+ + CF_3OO^- + CH_3CN]$^+$, Eu-isotope pattern), 1119.16 (6, [M - 2 O + CF_3OO^- + [ox. DHB] + CH_3CN + e^-]$^+$).
HR ESI-MS (pos. mode): $[EuC_{39}H_{36}N_{10}O_3{+}HCOO^-]^{2+}$: calculated: m/z = 445.10749,
found: m/z = 445.10750.
HPLC: R_f = 11.7 min (analytical reversed-phase HPLC, program **A**).

Amino-functionalised terbium cryptate Tb-1
Synthesis and analytical data of **Tb-1** have already been reported elsewhere.[162]
30.0 mg of sodium cryptate **Na-1** (37.7 μmol, 1.0 eq.) and 23.9 mg $TbCl_3 \cdot 6\,H_2O$ (Mol. Wt.: 373.38 g/mol, 64.1 μmol 1.7 eq.) in 17 mL CH_3CN (HPLC-grade), 40 h reflux.

$C_{47}H_{49}F_{12}N_{10}O_{17}Tb$
Molecular Weight: 1412.85

Yield: 14.6 mg, 10.3 μmol, 27%.
^{1}H NMR (500 MHz, CD_3OD): δ = 228.45, 186.01, 86.05, 70.51, 63.09, 51.93, 43.10, 37.51, 33.04, 24.90, 9.13, -14.38, -19.22, -21.77, -22.44, -59.14, -72.76, -95.46, -95.83, -102.88, -110.60, -211.95, -212.47, -273.68, -277.62, -307.42, -328.51 ppm. In the middle region of the spectrum not all signals could be identified unambiguously. The spectrum is shown in the main text (see page 40).

^{19}F NMR (376 MHz, CD_3OD): δ = -77.0 (s) ppm.
MALDI-MS (2,5-dihydroxybenzoic acid (DHB), RP mode, pos. mode): m/z (%) = 999.68 (15, [M - O + [DHB-H]$^-$ + e$^-$ + 11 (from reaction with COH_2)]$^+$), 1125.23 (100, [M - 2 O + 2 [DHB-H]$^-$]$^+$), 1141.24 (4, [M - O + 2 [DHB-H]$^-$]$^+$).
HR ESI-MS (pos. mode): [$TbC_{39}H_{36}N_{10}O_3$+$HCOO^-$]$^{2+}$: calculated: m/z = 448.10954,
found: m/z = 448.10949.
HPLC: R_f = 11.4 min (analytical reversed-phase HPLC, program **A**).

Amino-functionalised ytterbium cryptate Yb-1
Synthesis and analytical data of **Yb-1** have already been reported elsewhere.[160]
30.0 mg of sodium cryptate **Na-1** (37.7 μmol, 1.0 eq.) and 25.2 mg $YbCl_3 \cdot 6\,H_2O$ (Mol. Wt.: 387.49 g/mol, 64.1 μmol 1.7 eq.) in 15 mL CH_3CN (HPLC-grade), 186 h reflux.

$C_{47}H_{49}F_{12}N_{10}O_{17}Yb$
Molecular Weight: 1426.97

Yield: 14.0 mg, 9.81 μmol, 26%.
^{1}H NMR (400 MHz, CD_3CN): δ = 153.5 (2 H), 135.3-134.0 (2 H), 113.2 (2 H), 69.1/69.0 (2 H), 61.8/61.4 (2 H), 34.1/33.9 (2 H), 22.6/21.6 (2 H), 12.8/10.9 (2 H), 12.04/11.97 (2 H), 0.02 (1 H), -3.2/-4.1 (2 H), -12.8/-13.7 (2 H), -13.2/14.6 (2 H), -15.6/-15.9 (2 H), -66.0/-69.4 (2 H) ppm. The signals representing the four protons of the ethylene group could not be identified unambiguously, as in the corresponding region of the spectrum there are several solvent signals. The assignment of the signals is discussed in the main text (see chapter 3.3.4).
^{19}F NMR (376 MHz, CD_3OD): δ = -77.0 (s, 9 F), -114.4 (s, 3 F) ppm.
MS (ESI+): m/z (%) = 489.7 (100, [M + CF_3OO^- + e$^-$]$^{2+}$), 560.8 (58).
MALDI-MS (2,5-dihydroxybenzoic acid (DHB), RP mode, pos. mode): m/z (%) = 987.24 (55, [M - 2 O - H$^+$ + CF_3OO^- + CH_3CN]$^+$, Yb-isotope pattern), 1002.24 (8, [M - O - H$^+$ + [DHB-H]$^-$]$^+$, 1014.71 (8), 1140.27 (100, [M - 2 O + CF_3OO^- + [ox. DHB] + CH_3CN + e$^-$]$^+$, Yb-isotope pattern).
HPLC: R_f = 11.4 min (analytical reversed-phase HPLC, program **A**, setup **A**), 12.7 min (analytical reversed-phase HPLC, program **A**, setup **B**).

Amino-functionalised lutetium cryptate Lu-1
Synthesis and analytical data of **Lu-1** have already been reported elsewhere.[160]
20.0 mg of sodium cryptate **Na-1** (25.0 μmol, 1.0 eq.) and 27.0 mg $Lu(OTf)_3$ (Mol. Wt.: 622.17 g/mol, 43 μmol 1.7 eq.) in 15 mL CH_3CN (HPLC-grade), 168 h reflux.

$C_{47}H_{49}F_{12}N_{10}O_{17}Lu$
Molecular Weight: 1428.89

Yield: 18.3 mg, 12.8 μmol, 51%.

^{1}H NMR (400 MHz, CD_3OD): δ = 10.0 (t, *J* = 4.6 Hz, 1 H), 8.90 (d, *J* = 2.3 Hz, 1 H), 8.70 (d, *J* = 2.4 Hz, 1 H), 8.48 (dd, *J* = 1,7, 7.8 Hz, 1 H), 8.33-8.28 (m, 2 H), 8.23-8.05 (m, 8 H), 7.62-7.55 (m, 4 H), 4.79-4.71 (m, 4 H), 4.13-3.93 (m, 6 H), 3.84 (d, *J* = 13.1 Hz, 1 H), 3.80-3.64 (m, 5 H), 3.23 (t, *J* = 5.3 Hz, 1 H) ppm.
MS (ESI+): m/z (%) = 360.4 (87), 478.3 (79), 561.3 (84), 697.3 (100).
MALDI-MS (2,5-dihydroxybenzoic acid (DHB), RP mode, pos. mode): m/z (%) = 988.24 (44, $[M - H^+ - 2\,O + CF_3OO^- + CH_3CN]^+$), 1003.23 (6, $[M - O - H^+ + [DHB\text{-}H]^-]^+$), 1101.24 (7, $[M - 2\,O + CF_3OO^- + [DHB\text{-}H]^-]^+$), 1015.74 (28), 1141.28 (100, $[M - 2\,O + CF_3OO^- + [ox.\ DHB] + CH_3CN + e^-]^+$).
HPLC: R_f = 12.6 min (analytical reversed-phase HPLC, program **A**, setup **B**).

Azide-functionalised europium cryptate Eu-2

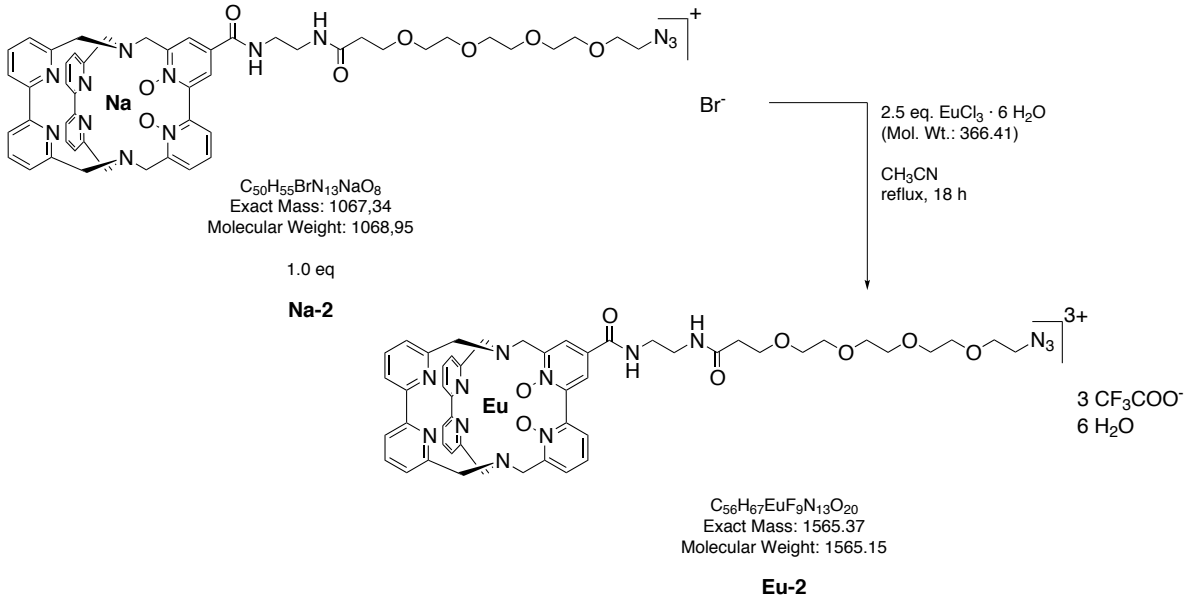

Caution: Organic azides are potentially explosive, appropriate measures should be undertaken when the reaction is performed.

3.3 mg of the azide-functionalised sodium cryptate **Na-2** (3.1 μmol, 1.0 eq.) and 2.8 mg $EuCl_3 \cdot 6\,H_2O$ (7.8 μmol, 2.5 eq.) were suspended in 3 mL CH_3CN (HPLC-grade) and brought to reflux temperature. Upon heating the mixture became turbid and a pale solid started to precipitate. After 18 h the mixture was allowed to cool to room temperature and subsequently the solvent was removed *in vacuo*. The crude product was purified by semi-preparative reversed-phase HPLC (Lichrospher RP-18e (Merck), 250x10 mm - 10 μm, flow rate: 3 mL min^{-1}, UV detection: 300 nm) and program **A**. The product was isolated from the pure fractions *in vacuo* at room temperature.

Note: The exact nature and number of bound anions and solvent molecules could not be determined unambiguously. ^{19}F NMR data strongly indicate that at least one CF_3COO^- is bound and from general experience the assumption of several water molecules being attached after HPLC purification is reasonable.

Yield: 3.2 mg, 2.0 μmol, 65%.
^1H NMR (400 MHz, CD_3OD): δ = 27.19 (br s, 1 H), 26.31 (br s, 1 H), 23.93 (br s, 2 H), 13.32 (d, *J* = 8.1 Hz, 2 H), 10.43-10.05 (m, 2 H), 10.03-9.66 (m, 3 H), 9.33 (t, *J* = 7.7 Hz, 1 H), 9.16 (d, *J* = 8.0 Hz, 1 H), 7.22-6.73 (m, 5 H), 5.47-5.33 (m, 1 H), 5.12-5.03 (m, 1 H), 4.28-4.07 (m, 2 H), 3.97-3.57 (m, 8 H), 3.55-3.44 (m, 1 H), 2.99 (t, *J* = 4.9 Hz, 2 H), 2.68-2.50 (m, 2 H), 1.65 (d, *J* = 7.7 Hz, 1 H), 1.15 (d, *J* = 7.6 Hz, 1 H), -8.76-(-8.90) (m, 1 H), -9.42-(-9.62) (m, 1 H), -11.16 (br s, 1 H), -12.64 (br, 1 H) ppm. Not all signals representing the protons of the PEG-linker could be identified unambiguously as in the corresponding region of the spec-

trum there are several solvent signals. The spectrum is shown in the main text (see page 49).
^{19}F NMR (376 MHz, CD_3OD): δ = -77.4 (s) ppm.
MALDI-MS (sinapinic acid (SA), RP mode, pos. mode): m/z = 1101.72 (9, [M - O + 2 e^-]$^+$, Eu-isotope pattern), 1309.74 (100, [M - 2 O + [SA-H]$^-$ + e^-]$^+$, Eu-isotope pattern), 1533.51 (17, [M - 2 O + [SA-H]$^+$ + SA + e^-]$^+$).
MALDI-MS (2,5-dihydroxybenzoic acid (DHB), RP mode, pos. mode): m/z = 1238.42 (100, [M - 2 O + [DHB-H]$^+$ + e^-]$^+$, Eu-isotope pattern).
R_f = 13.9 min (analytical reversed-phase HPLC, program **A**).

NHS-functionalised europium cryptate Eu-3

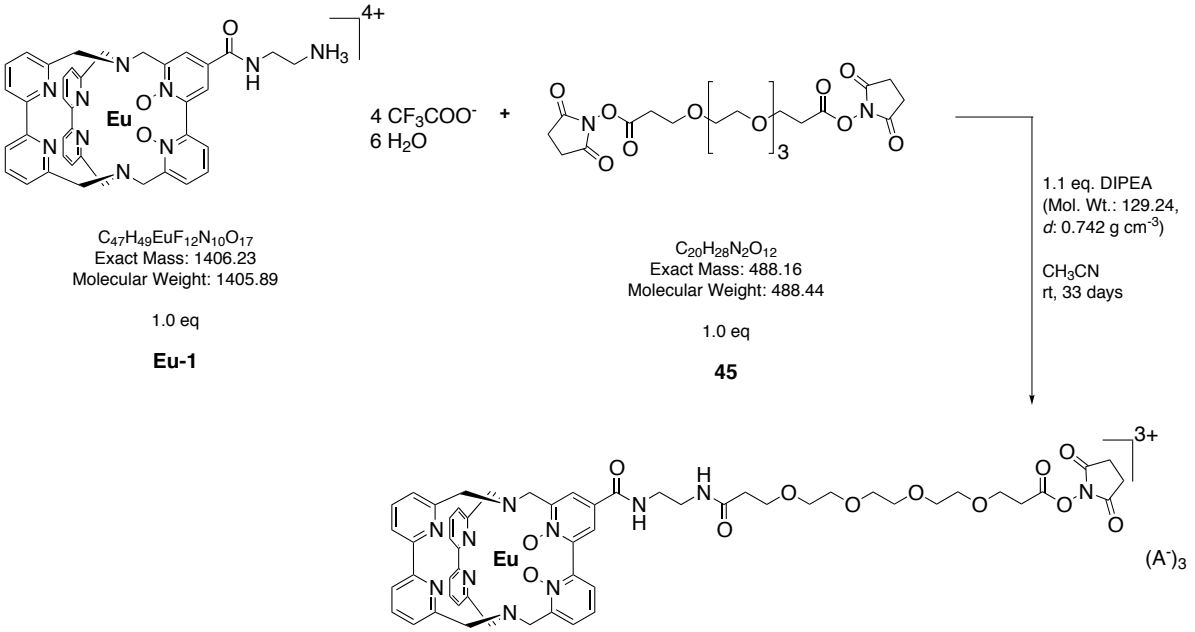

$C_{47}H_{49}EuF_{12}N_{10}O_{17}$
Exact Mass: 1406.23
Molecular Weight: 1405.89

1.0 eq

Eu-1

$C_{20}H_{28}N_2O_{12}$
Exact Mass: 488.16
Molecular Weight: 488.44

1.0 eq

45

$C_{55}H_{59}EuN_{11}O_{12}(A)_3$

Eu-3

With 10 mL CH_3CN (HPLC-grade) the bis-NHS-functionalised PEG-linker **45** (1.6 mg, 3.3 μmol, 1.0 eq.) was transferred into a 1000 mL three-necked flask equipped with a magnetic stirrer. The solution was diluted with additional 400 mL of solvent. The europium cryptate **Eu-1** (4.7 mg, 3.3 μmol, 1.0 eq.) was transferred into a 500 mL three-necked flask and dissolved in a total of 265 ml CH_3CN (HPLC-grade). 100 μL of a freshly prepared 6.33 mM solution of *N*,*N*-diisopropylethylamine (DIPEA) in CH_3CN (HPLC-grade) (0.47 mg, 3.67 μmol, 0.633 μL, 1.1 eq.) were added to the latter solution. Via a thin Teflon tube the diluted europium cryptate **Eu-1** was added with a low drop rate to the stirred solution of **45**. After 19 days the solution had been completely transferred and additional 100 mL CH_3CN (HPLC-grade) were filled in the empty flask to transfer the remainders of the cryptate, which was done in the course of one more day. Subsequently the mixture was stirred for 13 days at room temperature before the solvent was removed *in vacuo* and the remaining orange residue was dried thoroughly.

^{1}H NMR: The spectrum is shown in the main text (see page 51).
^{19}F NMR (376 MHz, CD_3CN): δ = -75.8 (s) ppm.
MS (ESI+): m/z (%) = 552.2 (17, $[M - O - [C_4NO_2H_4]]^{2+}$), 560.2 (60, $[M - [C_4NO_2H_4]]^{2+}$), 1201.4 (13, $[M - O - H^+ + e^-]^+$), 1217.4 (100, $[M - H^+ + e^-]^+$). The spectrum is shown in the appendix (see page 276).

BCN-functionalised europium cryptate Eu-4

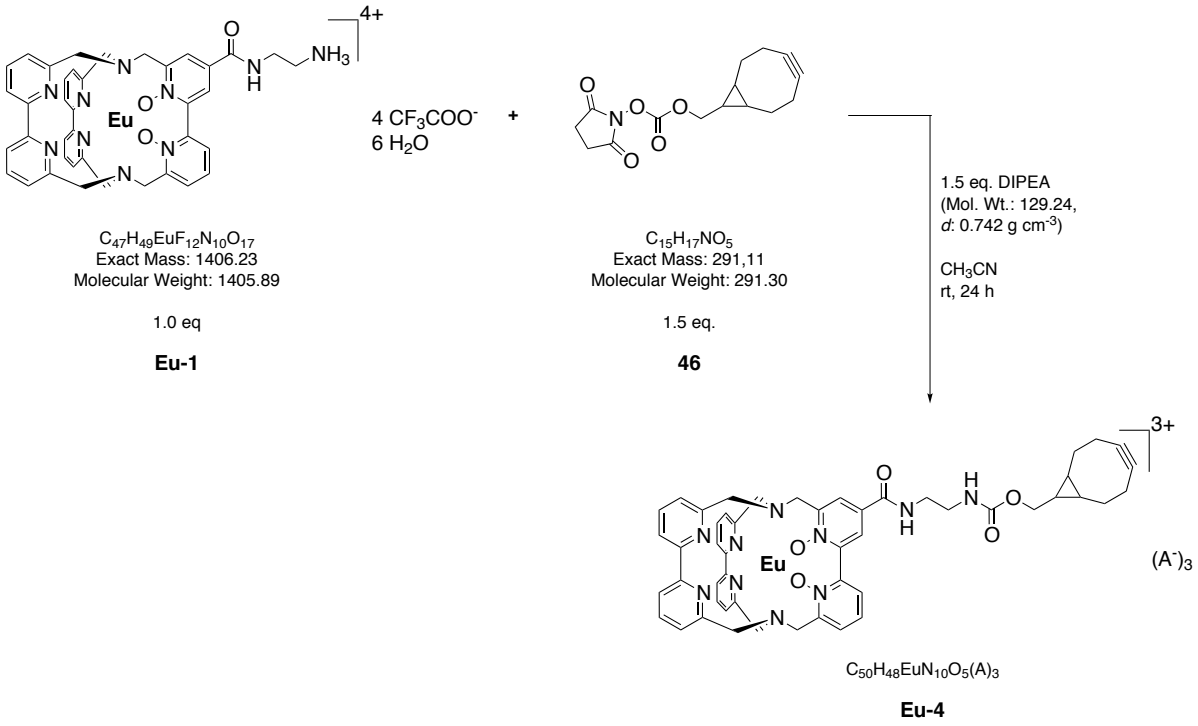

$C_{47}H_{49}EuF_{12}N_{10}O_{17}$
Exact Mass: 1406.23
Molecular Weight: 1405.89

1.0 eq

Eu-1

$C_{15}H_{17}NO_5$
Exact Mass: 291,11
Molecular Weight: 291.30

1.5 eq.

46

$C_{50}H_{48}EuN_{10}O_5(A)_3$

Eu-4

The HPLC-purified europium cryptate **Eu-1** (5.2 mg, 3.7 μmol, 1.0 eq) was dissolved in 0.2 mL CH_3CN (HPLC-grade). A solution of 1.61 mg (5.5 μmol, 1.5 eq) (1R,8S,9S)-bicyclo[6.1.0]non-4-yn-9-ylmethyl *N*-succinimidyl carbonate **46** in 0.1 mL CH_3CN (HPLC-grade) was added dropwise and the mixture was diluted with additional 0.3 mL of solvent. 100 μL of a freshly prepared 9.6 mM solution of *N*,*N*-diisopropylethylamine (DIPEA) in CH_3CN (HPLC-grade) (0.7 mg, 5.5 μmol, 0.96 μL, 1.5 eq.) were added and the resulting mixture was stirred at room temperature for 24 h. Afterwards the solvents were removed in a stream of air and the resulting product was dried *in vacuo* to remove residual solvents and excess DIPEA.

Note: The exact nature and number of bound anions and solvent molecules could not be determined unambiguously. The observation of additional strongly shifted signals in the ^{1}H NMR spectrum which do not belong to the europium cryptate itself suggest that a small organic molecule is bound directly to the Eu^{III}.

^{1}H NMR: The spectrum is shown in the main text (see page 54).
MALDI-MS (2,5-dihydroxybenzoic acid (DHB), RP mode, pos. mode): m/z = 1016.72 (14), 1142.46 (100, $[M - 2\,O + [DHB\text{-}H]^- + e^-]^+$), 1158.49 (27, $[M - O + [DHB\text{-}H]^- + e^-]^+$), 1304.50 (20, $[M + DHB + DIPEA + 2\,e^-]^+$).
HPLC: R_f = 16.0 min (see main text page 53, analytical reversed-phase HPLC, program **A**).

Enantiopure, diol-functionalised terbium cryptate Tb-5

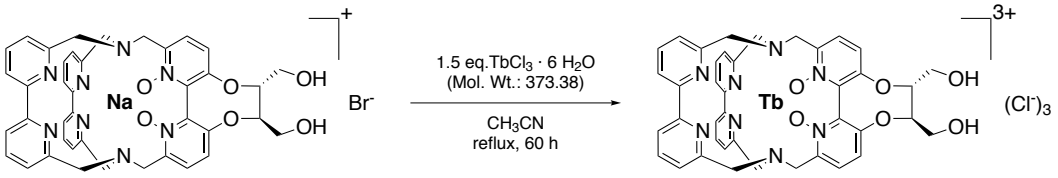

$C_{40}H_{36}BrN_8NaO_6$
Exact Mass: 826.18
Molecular Weight: 827.66

1.0 eq.

Na-5

$C_{40}H_{36}Cl_3N_8O_6Tb$
Exact Mass: 988.11
Molecular Weight: 990.05

Tb-5

The sodium cryptate **Na-5** (15.3 mg, 18.5. μmol, 1.0 eq.) and $TbCl_3 \cdot 6\,H_2O$ (10.4 mg, 27.8 μmol, 1.5 eq.) were suspended in 8 mL CH_3CN (HPLC-grade) and brought to reflux temperature. After 60 h the mixture was allowed to come to room temperature and subsequently the volatiles were removed *in vacuo* and the resulting pale yellow solid was dried thoroughly. The crude product was dissolved in a minimum amount of CH_3OH, filtered over cotton and overlayered with Et_2O. Upon storage at 4 °C overnight a pale yellow solid precipitated which was collected via filtration (0.45 μm nylon membrane filter (GE Healthcare Life Sciences)), washed with cold Et_2O and dried.

Yield: 18.2 mg, 18.4 μmol, 99%.
^{1}H NMR: The middle region of the spectrum is shown in the main text (see page 78).
MALDI-MS (2,5-dihydroxybenzoic acid (DHB), RP mode, pos. mode): m/z (%) = 1065.37 (72, [M - O + [DHB-H]$^-$ + $CH_3CH_2O^-$]$^+$), 1157.27 (100, [M - 2 O - H^+ + 2 [DHB-H]$^-$]$^+$), 1173.29 (9, [M - O - H^+ + 2 [DHB-H]$^-$]$^+$).
HR ESI-MS (pos. mode): $[TbC_{40}H_{36}N_8O_6{+}HCOO^-]^{2+}$: calculated: m/z = 464.09884, found: m/z = 464.09876.
HPLC: R_f = 11.4 min (analytical reversed-phase HPLC, program **A**).

Lysine-functionalised lanthanoid cryptates Ln-16

Method A: From the HPLC-purified amino-functionalised lanthanoid cryptates **Ln-1**

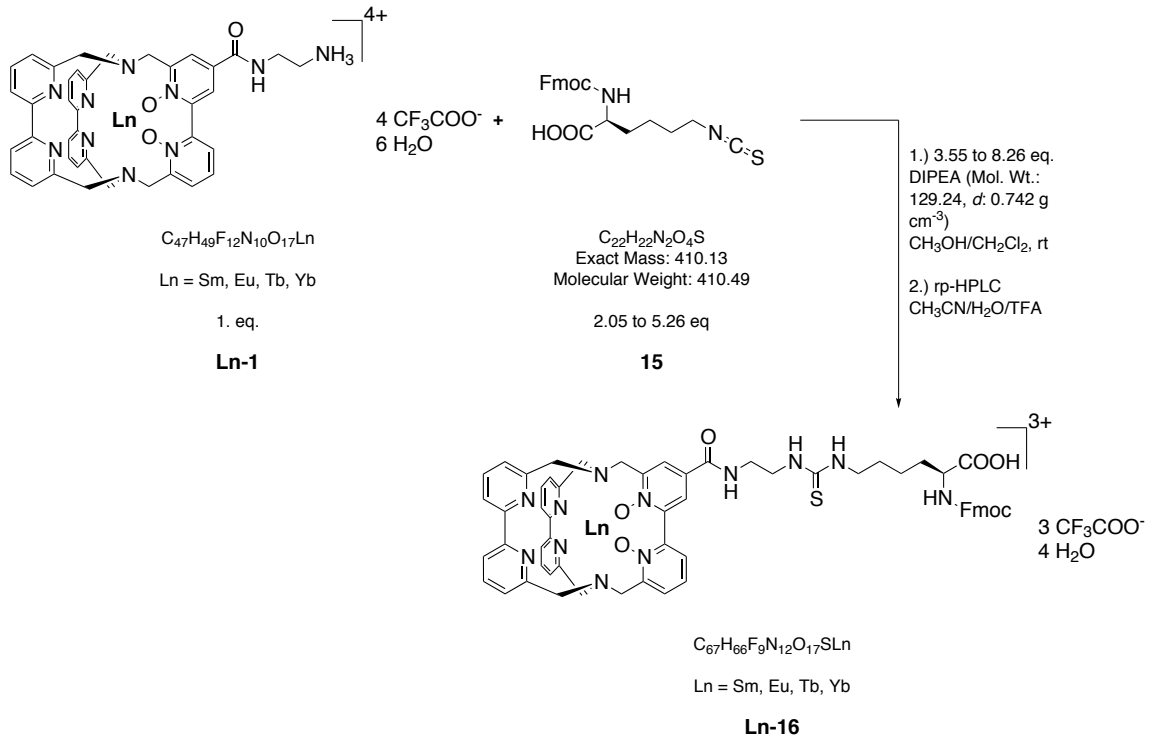

Representative experiments performed for the preparation of **Ln-16** (Ln = Sm, Eu, Tb, Yb) are described below. DIPEA was used as a 0.1 M solution in CH_3OH. For purification the material was dissolved in CH_3CN/1 vol.-%TFA in H_2O (1:1, v/v), filtered and subjected to semi-preparative reversed-phase HPLC (Lichrospher RP-18e (Merck), 250x10 mm - 10 μm, flow rate: 3 mL min^{-1}, UV detection: 300 nm). If program **A** was used, usually the product obtained from any run after the first one was contaminated with a not identified compound, and needed to be subjected to HPLC another time. This problem could be circumvented by the use of the elongated program **B**. The product was isolated as off-white or faintly yellow solid after evaporation of the pure fractions to dryness *in vacuo* at room temperature. In many cases unreacted **Ln-1** could be isolated after HPLC.

Lysine-functionalised samarium cryptate Sm-16

2.9 mg of **Sm-1** (2.1 μmol, 1.0 eq.) were dissolved in 0.5 mL CH_3OH. 62.2 μL of the 0.1 M solution of DIPEA (6.22 μmol, 1.5 + 1.5 eq.) were added and the mixture was stirred for several minutes before 1.3 mg (3.1 μmol, 1.5 eq.) of **15** were added dropwise in a total of 0.3 mL of CH_3OH/CH_2Cl_2 (1:1, v/v). After 30 minutes, 31.1 μL of the 0.1 M solution of DIPEA (3.11 μmol, 1.5 eq.) were added, followed by another portion of **15** (1.3 mg, 3.1 μmol, 1.5 eq.), added dropwise in a total of 0.3 mL of CH_3OH/CH_2Cl_2 (1:1, v/v). 19 h after the first addition of **15** the volatiles were removed in a stream of air and the resulting residue was dried thoroughly *in vacuo*. For purification a reversed-phase HPLC as described above with program **A** was performed.

$C_{67}H_{66}F_9N_{12}O_{17}Sm$
Molecular Weight: 1664.72

Yield: 0.9 mg, 0.5 μmol, 24%.
^{1}H NMR: The spectrum is shown in the main text (see page 105).
^{19}F NMR (376 MHz, CD_3OD): δ = -77.4 (s) ppm.
MALDI-MS (2,5-dihydroxybenzoic acid (DHB), RP mode, pos. mode): m/z (%) = 1376.27 (100, [M - 2 O - H^+ + [DHB-H]$^-$]$^+$, Sm-isotope pattern).
HR ESI-MS (pos. mode): [$SmC_{61}H_{57}N_{12}O_7S$-H^++$HCOO^-$]$^+$: calculated: m/z = 1298.33623,
found: m/z = 1298.33181.
HPLC: R_f = 17.1 min (analytical reversed-phase HPLC, program **A**).

Lysine-functionalised europium cryptate Eu-16
In this experiment a solution of reagent **15** was continuously added to the starting material with the aid of a dropping funnel:
In a 50 mL three-necked flask 2.1 mg of **Eu-1** (1.5 μmol, 1.0 eq.) were dissolved in 5 mL CH_3OH. 53.3 μL of the 0.1 M solution of DIPEA (5.33 μmol, 1.5 + 2.1 eq.) were added. 1.28 mL of a 1 mg/mL solution of **15** in dry CH_2Cl_2 (3.11 μmol, 2.1 eq.) were transferred into a dropping funnel and diluted with 1 mL CH_2Cl_2 and 2 mL HPLC-grade CH_3OH. The resulting mixture was added to the solution of **Eu-1** over the course of 20 minutes. 15 h after the start of the addition of **15** the volatiles were removed in a stream of air and the resulting residue was dried thoroughly *in vacuo*. For purification a reversed-phase HPLC as described above with program **A** was performed.

$C_{67}H_{66}F_9N_{12}O_{17}Eu$
Molecular Weight: 1666.32

Yield: 0.5 mg, 0.3 μmol, 20%.
^{1}H NMR: The spectrum is shown in the main text (see page 105).
^{19}F NMR (376 MHz, CD_3OD): δ = -77.3 (s) ppm.
MALDI-MS (2,5-dihydroxybenzoic acid (DHB), RP mode, pos. mode): m/z (%) = 1190.38 (23, [M - 4 O - H^+ + e^-]$^+$, Eu-isotope pattern), 1206.36 (26, [M - 3 O - H^+ + e^-]$^+$, Eu-isotope pattern), 1222.35 (100, [M - 2 O - H^+ + e^-]$^+$, Eu-isotope pattern), 1375.40 (9, [M - 2 O - H^+ + [DHB-H]$^-$]$^+$, Eu-isotope pattern).
HR ESI-MS (pos. mode): [$EuC_{61}H_{57}N_{12}O_6S$-H^++$HCOO^-$]$^+$: calculated: m/z = 1283.34281,
found: m/z = 1283.3398.
HPLC: R_f = 17.1 min (analytical reversed-phase HPLC, program **A**).

Lysine-functionalised terbium cryptate Tb-16
3.6 mg of **Tb-1** (2.5 μmol, 1.0 eq.) were dissolved in 0.5 mL CH_3OH. 76.0 μL of the 0.1 M solution of DIPEA (7.60 μmol, 1.5 + 1.5 eq.) were added and the mixture was stirred for several minutes before 1.6 mg (3.8 μmol, 1.5 eq.) of **15** were added dropwise in a total of 0.3 mL of CH_3OH/CH_2Cl_2 (1:1, v/v). After

30 minutes, 38.0 μL of the 0.1 M solution of DIPEA (3.80 μmol, 1.5 eq.) were added, followed by another portion of **15** (1.6 mg, 3.8 μmol, 1.5 eq.), added dropwise in a total of 0.3 mL of CH_3OH/CH_2Cl_2 (1:1, v/v). 14 h after the first addition of **15** the volatiles were removed in a stream of air and the resulting residue was dried thoroughly *in vacuo*. For purification a reversed-phase HPLC as described above with program **A** was performed.

$C_{67}H_{66}F_9N_{12}O_{17}Tb$
Molecular Weight: 1673.28

Yield: 1.7 mg, 1.0 μmol, 40%.
^{1}H NMR: The spectrum is shown in the main text (see page 106).
^{19}F NMR (376 MHz, CD_3OD): δ = -77.2 (s) ppm.
MALDI-MS (2,5-dihydroxybenzoic acid (DHB), RP mode, pos. mode): m/z (%) = 1349.33 (45, [M - 4 O - H^+ + [DHB-H]$^-$]$^+$), 1365.32 (30, [M - 3 O - H^+ + [DHB-H]$^-$]$^+$, 1381.31 (100, [M - 2 O - H^+ + [DHB-H]$^-$]$^+$).
HR ESI-MS (pos. mode): $[TbC_{61}H_{58}N_{12}O_7S+HCOO^-]^{2+}$: calculated: m/z = 653.17456,
found: m/z = 653.17430.
HPLC: R_f = 17.1 min (analytical reversed-phase HPLC, program **A**).

Lysine-functionalised ytterbium cryptate Yb-16
4.4 mg of **Yb-1** (3.1 μmol, 1.0 eq.) were dissolved in 0.5 mL CH_3OH. 87.5 μL of the 0.1 M solution of DIPEA (8.75 μmol, 1.5 + 1.34 eq.) were added and the mixture was stirred for several minutes before 1.7 mg (4.1 μmol, 1.34 eq.) of **15** were added dropwise with a total of 0.6 mL of CH_3OH/CH_2Cl_2 (1:1, v/v). After 30 minutes, 21.9 μL of the 0.1 M solution of DIPEA (2.2 μmol, 0.71 eq.) were added, followed by another portion of **15** (0.9 mg, 2.2 μmol, 0.71 eq.), added dropwise in a total of 0.3 mL of CH_3OH/CH_2Cl_2 (1:1, v/v). 17 h after the first addition of **15** the volatiles were removed in a stream of air and the resulting residue was dried thoroughly *in vacuo*. For purification a reversed-phase HPLC as described above with program **A** was performed.

$C_{67}H_{66}F_9N_{12}O_{17}Yb$
Molecular Weight: 1687.40

Yield: 3.1 mg, 1.8 μmol, 58%.
^{1}H NMR: The spectrum is shown in the main text (see page 106).
^{19}F NMR (376 MHz, CD_3OD): δ = -77.2 (s) ppm.
MALDI-MS (2,5-dihydroxybenzoic acid (DHB), RP mode, pos. mode): m/z (%) = 1243.34 (500, [M - 2 O - H^+ + e^-]$^+$, Yb-isotope pattern), 1363.37 (32, [M - 4 O - H - H^+ + [DHB-H]$^-$]$^+$, Yb-isotope pattern), 1380.38 (13, [M - 3 O - H^+ + [DHB-H]$^-$]$^+$, Yb-isotope pattern), 1396.37 (100, [M - 2 O - H^+ + [DHB-H]$^-$]$^+$, Yb-isotope pattern).
HPLC: R_f = 16.9 min (analytical reversed-phase HPLC, program **A**).

Note: The lysine-functionalised lanthanoid cryptates **Ln-16** can also be prepared from the crude complexes **Ln-1**. In this case, after the synthesis of **Ln-1** the material obtained after evaporation of the solvents is subjected to the next reaction step without any purification. The content of the actual lanthanoid cryptate in these crude materials can only be estimated (for stoichiometry the material was assumed to be the pure chloride of **Ln-1**), consequently the equivalents of the reagents employed can not be controlled completely and it is not reasonable to determine yields from these reactions. But as the reaction also proceeds properly with the crude starting material and the reduction of HPLC purifications safes a significant amount of time this variation is reasonable when bigger amounts of lysine-functionalised lanthanoid cryptates **Ln-16** are to be prepared.

Method B: From the crude amino-functionalised lanthanoid cryptates **Ln-1**

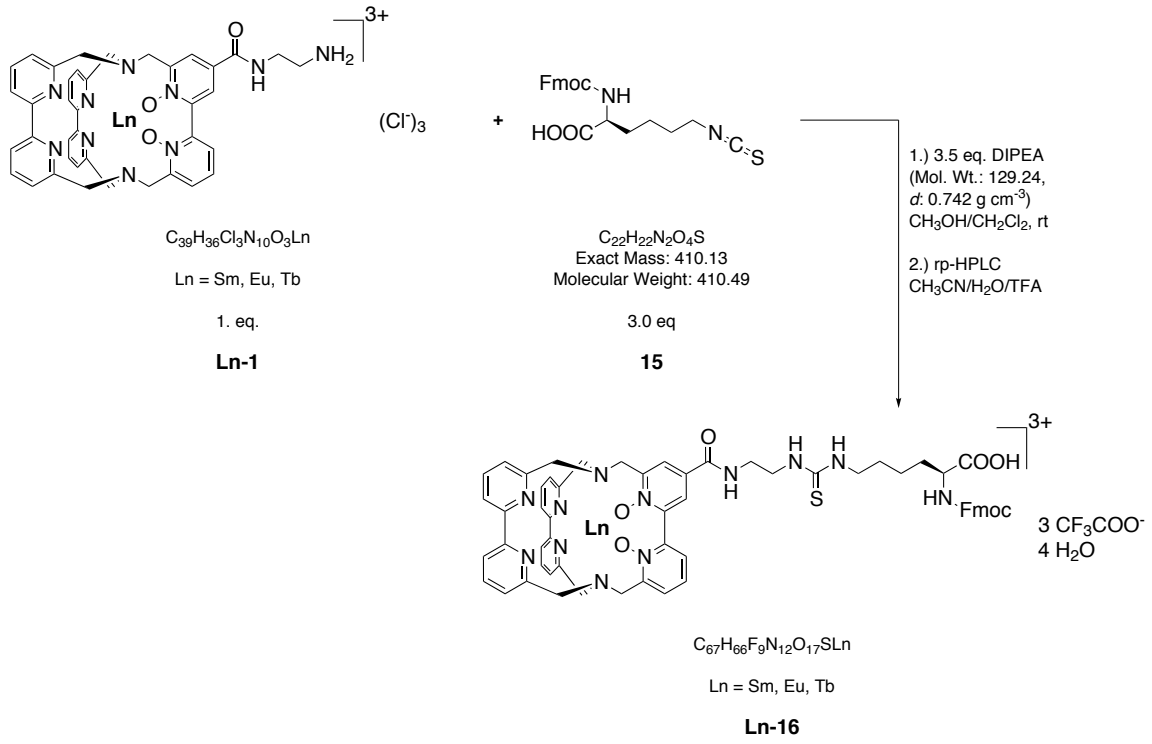

The crude amino-functionalised lanthanoid cryptate **Ln-1** (1.0 eq.) was dissolved in CH_3OH (about 0.1 mL per mg starting material) and stirred for a few minutes. 2 eq. of a 0.1 M solution of *N*,*N*-diisopropylethylamine (DIPEA) in CH_3OH were added and the resulting slightly yellow solution was stirred for a few minutes. The first portion of **15** (1.5 eq) was taken up in 3.5 eq. of the 0.1 M solution of DIPEA and the resulting solution was added to the starting material dropwise, upon which a yellow solid precipitated. The mixture was diluted with a freshly prepared mixture of CH_3OH and CH_2Cl_2 (1:1, v/v) (about 0.02 mL per mg starting material). After 30 minutes the second portion of **15** (1.5 eq.) was added to the reaction mixture with a total of 0.6 mL CH_3OH/CH_2Cl_2 (1:1, v/v) per mg starting material. After at least 13.5 h the volatiles were removed in a stream of air and for purification the crude product was treated as described above (program **A** or **B**).

Using this method the complexes **Ln-16** with Ln = Sm^{III}, Eu^{III} and Tb^{III} were prepared. Their properties were found to be identical to the ones of the complexes prepared following the method starting from the HPLC-purified amino-functionalised lanthanoid cryptates **Ln-1**.

Enantiopure lanthanoid cryptates Ln-22: General procedure[267]

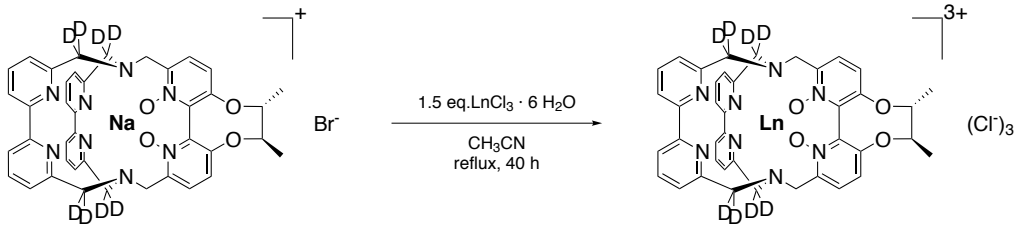

$C_{40}H_{28}D_8BrN_8NaO_4$

Ln = Sm, Eu

1.0 eq.

Na-22

$C_{40}H_{28}D_8Cl_3N_8O_4Ln$

Ln = Sm, Eu

Ln-22

The general procedure for the synthesis of the respective lanthanoid cryptates from the corresponding sodium cryptates **Na-22** was already described earlier.[134]

1.0 eq. of the enantiopure sodium cryptate **Na-22**[134] and 1.5 eq. of the lanthanoid salt $LnCl_3 \cdot 6\,H_2O$ were suspended in CH_3CN (HPLC-grade) and brought to reflux temperature whereby the mixture got turbid. After 40 h the solvent was removed *in vacuo* and the resulting residue was dried thoroughly before it was taken up in a minimum amount of CH_3OH. The yellow solution was filtered over cotton, overlayered with Et_2O and stored overnight at 4 °C. The product was isolated as faintly yellow precipitate which was collected on a 0.45 μm nylon membrane filter (GE Healthcare Life Sciences), washed with cold Et_2O and dried.

Enantiopure samarium cryptate Sm-22

Synthesis and analytical data of **Sm-22** have already been reported elsewhere.[267]

5.0 mg of sodium cryptate **Na-22** (6.3 μmol, 1.0 eq.) and 3.4 mg $SmCl_3 \cdot 6\,H_2O$ (Mol. Wt.: 364.81 g/mol, 9.4 μmol 1.5 eq.) in 7 mL CH_3CN (HPLC-grade), 40 h reflux.

$C_{40}H_{28}D_8Cl_3N_8O_4Sm$
Molecular Weight: 957.54

Yield: 3.61 mg, 3.80 μmol, 61%.
^{1}H NMR (400 MHz, CD_3OD): δ = 9.54 (d, J = 8.1 Hz, 2 H), 9.11-9.00 (m, 2 H), 8.95 (d, J = 7.3 Hz, 2 H), 8.26-8.14 (m, 2 H), 7.93-7.65 (m, 8 H), 6.21 (br s, 2 H), 4.17 (br s, 2 H), 2.62-2.43 (m, 2 H), 1.52-1.39 (m, 6 H) ppm. The spectrum is shown in the appendix (see page 323).
HR ESI-MS (pos. mode): $[SmC_{40}H_{28}D_8N_8O_4{+}HCOO^-]^{2+}$: calculated: m/z = 448.62623,
found: m/z = 448.62667
HPLC: R_f = 14.0 min (analytical reversed-phase HPLC, program **A**).

Enantiopure europium cryptate Eu-22

Synthesis and analytical data of **Eu-22** have already been reported elsewhere.[267]

5.0 mg of sodium cryptate **Na-22** (6.3 μmol, 1.0 eq.) and 3.4 mg $EuCl_3 \cdot 6\,H_2O$ (Mol. Wt.: 366.41 g/mol, 9.4 μmol 1.5 eq.) in 7 mL CH_3CN (HPLC-grade), 40 h reflux.

$C_{40}H_{28}D_8Cl_3N_8O_4Eu$
Molecular Weight: 959.14

Yield: 3.62 mg, 3.81 μmol, 61%.
^{1}H NMR (400 MHz, CD_3OD): δ = 16.49 (s, 2 H), 11.54 (s, 2 H), 9.25 (s, 2 H), 9.03 (s, 2 H), 6.19 (s, 2 H), 3.09-2.43 (m, 6 H), 1.00-0.66 (m, 8 H), -10.40 (s, 2 H), -17.53 (s, 2 H) ppm. The spectrum is shown in the appendix (see page 323).
HR ESI-MS (pos. mode): $[EuC_{40}H_{28}D_8N_8O_4{+}HCOO^-]^{2+}$: calculated: m/z = 449.12698,
found: m/z = 449.12706
HPLC: R_f = 13.7 min (analytical reversed-phase HPLC, program **A**).

Dicryptate coordinating two erbium-ions Er-Er-26

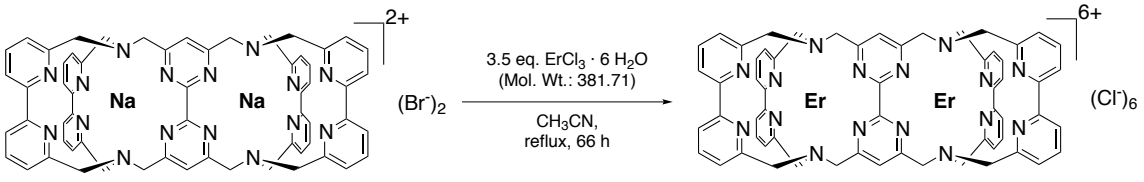

$C_{60}H_{50}Br_2N_{16}Na_2$
Exact Mass: 1198.26
Molecular Weight: 1200.93

1.0 eq.

Na-Na-26

$C_{60}H_{50}Cl_6N_{16}Er_2$
Exact Mass: 1536.11
Molecular Weight: 1542.38

Er-Er-26

7.9 mg of sodium dicryptate **Na-Na-26**[141] (6.6 μmol, 1.0 eq) and 10.1 mg $ErCl_3 \cdot 6\,H_2O$ (26.3 μmol, 4.0 eq) were suspended in 10 mL CH_3CN (HPLC-grade) and brought to reflux temperature. Soon a light solid started to precipitate. The mixture was heated for a total of 42 h before the volatiles were removed *in vacuo*. The crude product was dried thoroughly before it was dissolved in a minimum amount of MeOH, filtered over cotton and overlayered with Et_2O. After storage at 4 °C for several days the product which precipitated from the solution was collected on a 0.45 μm nylon membrane filter (GE Healthcare Life Sciences), washed with cold Et_2O and dried under air.

Yield: 4.4 mg, 2.9 μmol, 44%.

Note: The characterisation of the isolated material is discussed in the main text.

Dicryptate coordinating two lanthanoid ions in a statistical mixture Ln^1/Ln^2-26: General procedure

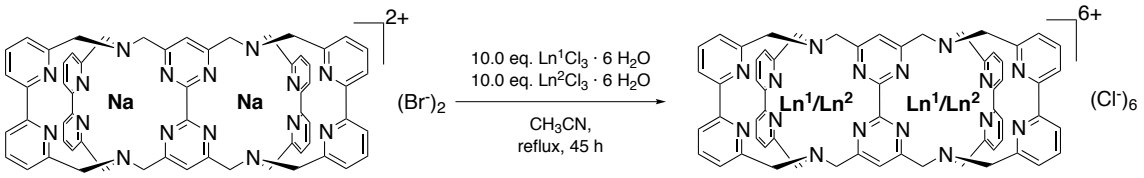

$C_{60}H_{50}Br_2N_{16}Na_2$
Exact Mass: 1198.26
Molecular Weight: 1200.93

1.0 eq.

Na-Na-26

$C_{60}H_{50}Cl_6N_{16}Ln^1Ln^2$

Ln^1/Ln^2 = Eu/Tb or
Ln^1/Ln^2 = Eu/Y

Ln^1/Ln^2-26

1.0 eq. of the sodium dicryptate **Na-Na-26**[141] and 10.0 eq. of both lanthanoid salts $Ln^1Cl_3 \cdot 6\,H_2O$ and $Ln^2Cl_3 \cdot 6\,H_2O$ each were suspended in CH_3CN (HPLC-grade, about 1.25 ml per 1 mg sodium dicryptate **Na-Na-26**). The suspension was brought to reflux temperature and stirred for 45 h during which a light solid precipitated. The mixture was evaporated to dryness and the remaining solid was dried *in vacuo*.

Dicryptate coordinating europium and terbium in a statistical mixture Eu/Tb-26

8.4 mg sodium dicryptate **47** (7.0 μmol, 1.0 eq), 25.7 mg (70.0 μmol, 10.0 eq) $EuCl_3 \cdot 6\,H_2O$ and 25.1 mg (70.0 μmol, 10.0 eq) $TbCl_3 \cdot 6\,H_2O$ in 10 mL CH_3CN (HPLC-grade).

After synthesis the crude product **Eu/Tb-26** was used for initial studies on its photophysical properties but no attempts for a further purification were undertaken.

Dicryptate coordinating yttrium and europium in a statistical mixture Y/Eu-26

8.4 mg sodium dicryptate **Na-Na-26** (7.0 μmol, 1.0 eq), 21.1 mg (70.0 μmol, 10.0 eq) $YCl_3 \cdot 6\,H_2O$ and 25.5 mg (70.0 μmol, 10.0 eq) $EuCl_3 \cdot 6\,H_2O$ in 10 mL CH_3CN (HPLC-grade). The crude mixture was taken up in 5 mL CH_3CN/H_2O (1:1, v/v) with a few drops of H_2O + 1 vol.-% CF_3COOH, filtered and subjected to semi-preparative reversed-phase HPLC (Lichrospher RP-18e (Merck), 250x10 mm - 10 μm, flow rate: 3 mL min^{-1}, UV detection: 300 nm, program **A**) The fractions containing the product were evaporated to dryness *in vacuo* at room temperature.

Yield: 4.4 mg, 2.9 μmol, 44%.
^{1}H NMR: The spectrum is shown in the appendix (see page 274).
HPLC: a representative HPLC trace of the isolated material is shown in the appendix (see page 182).

Methoxy-functionalised ytterbium cryptate Yb-34

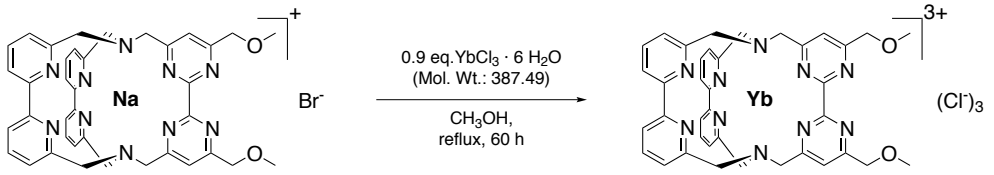

$C_{38}H_{36}BrN_{10}NaO_2$
Exact Mass: 766.21
Molecular Weight: 767.65

1.0 eq.

Na-34

$C_{38}H_{36}Cl_3N_{10}O_2Yb$
Exact Mass: 943.15
Molecular Weight: 944.16

Yb-34

16.6 mg of the methoxy-functionalised sodium cryptate **Na-34** (22 μmol, 1.0 eq) and 7.8 mg $YbCl_3 \cdot 6\,H_2O$ (20 μmol, 0.9 eq) were dissolved in 25 mL CH_3OH. The resulting clear, yellow solution was brought to reflux temperature and stirred for 60 h during which no solid precipitated. After complete removal of the solvent the dried orange to brown solid was taken up in a minimum amount of CH_3OH, filtered over cotton and overlayered with Et_2O. Stored at 4 °C overnight a orange solid precipitated. It was separated from the solution but found to contain mainly the starting material **Na-34**. The solution obtained from filtration was evaporated to dryness and CH_2Cl_2 was added, upon which the solid partially dissolved. The suspension was stirred for a few minutes before it was filtered over cotton. The solid was washed with a few millilitres of CH_2Cl_2 and washed with CH_3OH from the filter material to isolate the product.

Yield: 6.5 mg, 6.9 μmol, 31%.
^{1}H NMR (500 MHz, CD_3OD): The spectrum is shown in the main text (see page 195).

8.5 Peptides

Peptide H_2N-Cys-Gly-Gly-Gly-Cys-Gly-COOH 17

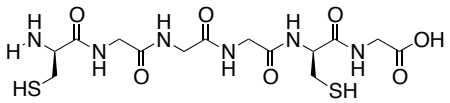

H-Cys-Gly-Gly-Gly-Cys-Gly-OH

$C_{14}H_{24}N_6O_7S_2$
Exact Mass: 452.11
Molecular Weight: 452.51

Method A: standard procedure for commercially available amino acids
168 mg of the Fmoc-Gly-Tentagel® PHB resin (equals 33.6 μmol of the bound Fmoc-Gly, 1.0 eq.) were swelled in in a plastic syringe equipped with a PE frit. After an initial deprotection step 5.0 eq. Fmoc-Cys(Trt)-OH (98.4 mg, 168 μmol), 4.9 HATU (62.6 mg, 165 μmol) and 10.0 eq. DIPEA (43.4 mg, 336 μmol, 58.5 μL) were added for the first coupling step. After 30 minutes reaction time the solution was drained, the resin was washed and deprotected. The next coupling step was performed with 5.0 eq. Fmoc-Gly-OH (49.9 mg, 168 μmol), after deprotection two more coupling/deprotection procedures with 5.0 eq. Fmoc-Gly-OH and a final coupling/deprotection procedure with 5.0 eq. Fmoc-Cys(Trt)-OH was performed. After the resin with the attached deprotected peptide was shrinked, 5 mL TFA with 5 vol.-% H_2O were added and the suspension was shaken for 2 h for cleavage. The solution was drained into a round-bottomed flask and evaporated to dryness to give the title compound.

MS (ESI+): m/z (%) = 165.5 (4), 243.7 (11), 423.9 (3), 454.1 (9), 460.1 (5), 475.5 (100, $[M + Na]^+$), 679.5 (2).
HPLC: a HPLC trace of the isolated material is shown in the appendix (see page 275).

Method B: modified procedure for amino acids with limited availability
The synthesis was performed analogously to method A with 168 mg of the Fmoc-Gly-Tentagel® PHB resin in a plastic syringe equipped with a PE frit, but in all coupling steps the equivalents were reduced to 1.1 eq. of the Fmoc-protected amino acid (21.7 mg of Fmoc-Cys(Trt)-OH or 11.0 mg of Fmoc-Gly-OH, 37.0 μmol), 1.05 eq. HATU (13.4 mg, 35.3 μmol) and 2.2 eq. DIPEA (9.6 mg, 73.9 μmol, 12.9 μL) and the reaction times were elongated to at least 24 h.

MS (ESI+): m/z (%) = 165.5 (3), 243.7 (11), 423.9 (3), 454.1 (8), 460.1 (4), 475.5 (100, $[M + Na]^+$), 679.5 (2).
HPLC: a HPLC trace of the isolated material is shown in the appendix (see page 275).

Peptide Fmoc-Lys(Eu)-Gly-COOH 18

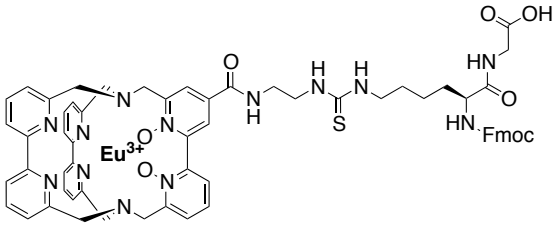

Fmoc-Lys(Eu)-Gly-OH

$C_{63}H_{61}EuN_{13}O_8S^{3+}$
Exact Mass: 1312.37
Molecular Weight: 1312.27

In a plastic syringe equipped with a PE frit, 0.52 mg of the Fmoc-Gly-Tentagel® PHB resin (equals 0.10 μmol of the bound Fmoc-Gly, 1.0 eq.) were swelled and the first amino acid bound to the resin was deprotected. For the subsequent coupling step 1.1 eq. of the lysine-functionalised europium cryptate **Eu-16** (0.19 mg, 0.11 μmol), 1.05 eq. HATU (0.04 mg, 0.11 μmol) and 2.2 eq. DIPEA (0.03 mg, 0.23 μmol, $3.9 \cdot 10^{-2}$ μmL, 10 μL of a mixture of 3.9 μL DIPEA and 996.1 μL DMF) were added to the resin and the resulting suspension was shaken for 24 h. Subsequently the solution was drained, the resin was washed and shrinked. The product was cleaved from the resin with 2 mL TFA with 5 vol.-% H_2O (70 minutes reaction time) and the volatiles were removed *in vacuo*.

Note: Due to the very small scale of this reaction no attempts for purification of the isolated substance were undertaken. Since the amount of substance isolated was very small a thorough analysis was not possible. Results from the study of the substance are presented in the main text.

Peptide H_2N-Gly-Lys(Eu)-Gly-COOH 19

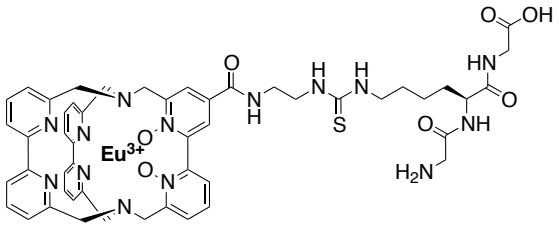

H-Gly-Lys(Eu)-Gly-OH

$C_{50}H_{54}EuN_{14}O_7S^{3+}$
Exact Mass: 1147.32
Molecular Weight: 1147.08

In the custom-build glass-vessel 0.52 mg of the Fmoc-Gly-Tentagel® PHB resin (equals 0.10 μmol of the bound Fmoc-Gly, 1.0 eq.) were swelled. After an initial deprotection step, 1.1 eq. of the lysine-functionalised europium cryptate **Eu-16** (0.19 mg, 0.11 μmol), 1.05 eq. HATU (0.04 mg, 0.11 μmol) and 2.2 eq. DIPEA (0.03 mg, 0.23 μmol, $3.9 \cdot 10^{-2}$ μmL, 10 μL of a mixture of 3.9 μL DIPEA and 996.1 μL DMF) were added for the first coupling step (24 h reaction time). Afterwards a capping step was performed (0.1 mL Ac_2O and 0.1 mL DIPEA in 1 mL DMF), followed by deprotection and a second coupling step with 5.0 eq. Fmoc-Gly-OH (0.15 mg, 0.52 μmol), 4.9 eq. HATU (0.19 mg, 0.51 μmol) and 2.2 eq. DIPEA (0.13 mg, 1.04 μmol, $17.5 \cdot 10^{-2}$ μmL, 10 μL of a mixture of 17.5 μL DIPEA and 992.5 μL DMF). The resulting suspension was shaken overnight. After this step no capping was performed but it was deprotected before shrinkage. The product was cleaved from the resin with TFA with 5 vol.-% H_2O (60 minutes reaction time). To ensure completeness of the reaction the resin was treated with another two portions of TFA with 5 vol.-% H_2O (30 minutes). From the combined TFA-solutions the product was obtained after complete evaporation of the volatiles.

Note: Due to the very small scale of this reaction no attempts for purification of the isolated substance were undertaken. Since the amount of substance isolated was very small a thorough analysis was not possible. Results from the study of the substance are presented in the main text.

Peptide H_2N-Lys(Sm)-Gly-Lys(Eu)-Gly-COOH 20

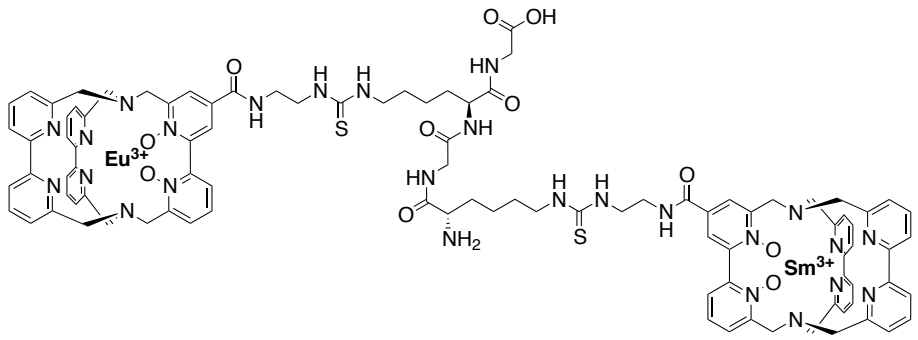

H·Lys(Sm)-Gly-Lys(Eu)-Gly-OH

$C_{96}H_{100}EuN_{26}O_{11}S_2Sm^{6+}$
Exact Mass: 2161.59
Molecular Weight: 2160.44

In the custom-build glass-vessel 0.52 mg of the Fmoc-Gly-Tentagel® PHB resin (equals 0.10 μmol of the bound Fmoc-Gly, 1.0 eq.) were swelled. After deprotection, the first coupling step was performed with 1.1 eq. of the lysine-functionalised europium cryptate **Eu-16** (0.19 mg, 0.11 μmol), 1.05 eq. HATU (0.04 mg, 0.11 μmol) and 2.2 eq. DIPEA (0.03 mg, 0.23 μmol, $3.9{\cdot}10^{-2}$ μmL, 10 μL of a mixture of 3.9 μL DIPEA and 996.1 μL DMF) and 24 h reaction time. After capping (0.1 mL Ac_2O and 0.1 mL DIPEA in 1 mL DMF) it was deprotected and 5.0 eq. Fmoc-Gly-OH (0.15 mg, 0.52 μmol), 4.9 eq. HATU (0.19 mg, 0.51 μmol) and 2.2 eq. DIPEA (0.13 mg, 1.04 μmol, $17.5{\cdot}10^{-2}$ μmL, 10 μL of a mixture of 17.5 μL DIPEA and 992.5 μL DMF) were added to perform the second coupling step for which the suspension was shaken overnight. Afterwards no capping step was performed prior to deprotection and addition of the third amino acid: 1.1 eq. of the lysine-functionalised samarium cryptate **Sm-16** (0.19 mg, 0.11 μmol), 1.05 eq. HATU (0.04 mg, 0.11 μmol) and 2.2 eq. DIPEA (0.03 mg, 0.23 μmol, $3.9{\cdot}10^{-2}$ μmL, 10 μL of a mixture of 3.9 μL DIPEA and 996.1 μL DMF), 24 h reaction time. After a final deprotection step the resin was shrinked and the peptide was cleaved with TFA with 5 vol.-% H_2O (60 minutes reaction time). To ensure completeness of the reaction the resin was treated with another two portions of TFA with 5 vol.-% H_2O (30 minutes) before the product was obtained from the combined solutions via complete evaporation of the volatiles.

Note: Due to the very small scale of this reaction no attempts for purification of the isolated substance were undertaken. Since the amount of substance isolated was very small a thorough analysis was not possible. Results from the study of the substance are presented in the main text.

Peptide H_2N-Lys(Eu)-Gly(^{13}C)-Lys(Tb)-Gly(^{15}N)-Lys(Sm)-Gly-COOH 21

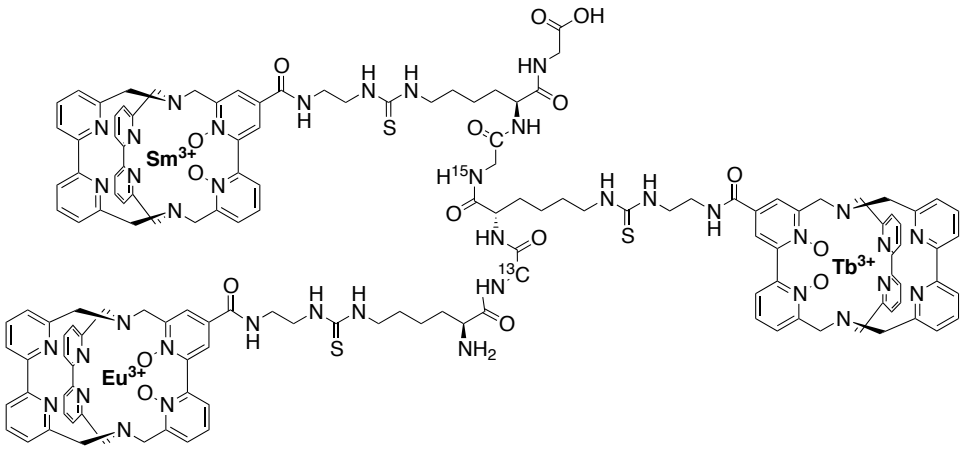

H·Lys(Eu)-Gly(^{13}C)-Lys(Tb)-Gly(^{15}N)-Lys(Sm)-Gly-OH

$C_{143}{}^{13}CH_{147}EuN_{38}{}^{15}NO_{16}S_3SmTb^{9+}$
Exact Mass: 3239.87
Molecular Weight: 3239.41

For this synthesis freshly distilled DIPEA was used. DMF (Acros Organics, 99.8%, for peptide synthesis), piperidine (Roth, $\geq$ 99.5%, for peptide synthesis) and Ac_2O (Merck, EMSURE®, for analysis) were taken from fresh bottles and all mixtures were freshly prepared shortly before usage.

6.01 mg of the Fmoc-Gly-Tentagel® PHB resin (equals 1.20 μmol of the bound Fmoc-Gly, 1.0 eq.) were swelled in the custom-build glass-vessel. After initial deprotection the following steps were performed:

1.) Coupling of the lysine-functionalised samarium cryptate **Sm-16**

1.5 eq. of **Sm-16** (3.00 mg, 1.80 μmol), 1.45 eq. HATU (0.66 mg, 1.74 μmol), and 3 eq. DIPEA (0.47 mg, 3.60 μmol, 0.63 μL, 10 μL of a mixture of 6.3 μL DIPEA and 93.7 μL DMF). Total volume of 2 mL of DMF, reaction time of 16 h. After this coupling step a capping step and a subsequent deprotection step were performed.

2.) Coupling of the ^{15}N-labeled Glycine Fmoc-Gly(^{15}N)-OH

5 eq. of Fmoc-Gly(^{15}N)-OH (1.79 mg, 6.01 μmol), 4.9 eq. HATU (2.24 mg, 5.89 μmol), and 10 eq. DIPEA (1.55 mg, 12.01 μmol, 2.09 μL, 10 μL of a mixture of 20.9 μL DIPEA and 79.1 μL DMF). Total volume of 2 mL of DMF, reaction time of 11 h. After the solution was drained, the resin was washed and a freshly prepared equivalent coupling mixture was added. Total volume of 2 mL of DMF, reaction time of 0.5 h. The coupling procedure was followed by a capping and a deprotection step.

3.) Coupling of the lysine-functionalised terbium cryptate **Tb-16**

1.5 eq. of **Tb-16** (3.02 mg, 1.80 μmol), 1.45 eq. HATU (0.66 mg, 1.74 μmol), and 3 eq. DIPEA (0.47 mg, 3.60 μmol, 0.63 μL, 10 μL of a mixture of 6.3 μL DIPEA and 93.7 μL DMF). Total volume of 2 mL of DMF, reaction time of 12 h. After this coupling step a capping step and a subsequent deprotection step were performed.

4.) Coupling of the 2-^{13}C-labeled Glycine Fmoc-Gly(^{13}C)-OH

5 eq. of Fmoc-Gly(^{13}C)-OH (1.79 mg, 6.01 μmol), 4.9 eq. HATU (2.24 mg, 5.89 μmol), and 10 eq. DIPEA (1.55 mg, 12.01 μmol, 2.09 μmL, 10 μL of a mixture of 20.9 μL DIPEA and 79.1 μL DMF). Total volume of 2 mL of DMF, reaction time of 9 h. After the solution was drained, the resin was washed and a freshly prepared equivalent coupling mixture was added. Total volume of 2 mL of DMF, reaction time of 30 minutes. The coupling procedure was followed by a capping and a deprotection step.

5.) Coupling of the lysine-functionalised europium cryptate **Eu-16**

1.5 eq. of **Eu-16** (3.00 mg, 1.80 μmol), 1.45 eq. HATU (0.66 mg, 1.74 μmol), and 3 eq. DIPEA (0.47 mg, 3.60 μmol, 0.63 μL, 10 μL of a mixture of 6.3 μL DIPEA and 93.7 μL DMF). Total volume of 2 mL of DMF, reaction time of 12 h. After this coupling step a capping step and a subsequent deprotection step were performed.

Afterwards the resin was shrinked and treated with three portions of TFA with 5 vol.-% H_2O (3 x 60 minutes reaction time). The TFA-solutions were drained into a round-bottomed flask and evaporated to dryness. Subsequently 1 ml of CH_3OH was added to the resin. The suspension was shaken for 1 h, afterwards the solution was drained and it was washed with two more portions of 1 ml of CH_3OH. The combined methanolic solutions were given to the substance obtained from the TFA solution, the volatiles were removed *in vacuo* and the obtained product was dried thoroughly.

Note: Due to the very small scale of this reaction no attempts for purification of the isolated substance were undertaken. Since the amount of substance isolated was very small a thorough analysis was not possible. Results from the study of the substance are presented in the main text.

8.6 Further procedures and experiments

Purification of the macrocyclus 44 consisting of two bipyridines

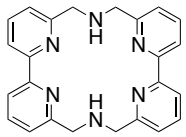

$C_{24}H_{22}N_6$
Exact Mass: 394.19
Molecular Weight: 394.47

44

Typically the macrocyclus **44** is prepared from two equivalents 6,6'-bis(bromomethyl)-2,2'-bipyridine and *p*-toluenesulfonamide monosodium salt.[127] As the compound has only a very limited solubility purification is typically difficult and often impurities of *p*-toluenesulfonic acid remain in the material, which results in further problems when the stoichiometry of a macrobicyclisation shall be controlled. In some cases even a separation of *p*-toluenesulfonic acid from the following products of the sequence of synthesis did not succeed.
To circumvent these problems the following procedure for the separation of *p*-toluenesulfonic acid from macrocyclus **44** was developed:

3.0 g of the crude material were pestled and suspended in 200 mL H_2O. The mixture containing the hydrophobic solid was stirred vigorously overnight before the solid was collected on a Büchner funnel, washed with further 100 mL H_2O and dried under air. With 200 mL $CHCl_3$ most of the solid could be dissolved and was collected in a separate flask. The solution was dried ($MgSO_4$), evaporated to dryness and dried *in vacuo* to give 1.8 g of the purified macrocyclus **44** as colourless solid.

The ^{1}H NMR spectrum of the isolated compound revealed the successful removal of *p*-toluenesulfonic acid.

Mn(II) complex of the bipyridine cryptate bpy_3O_2 Mn^{II}-48

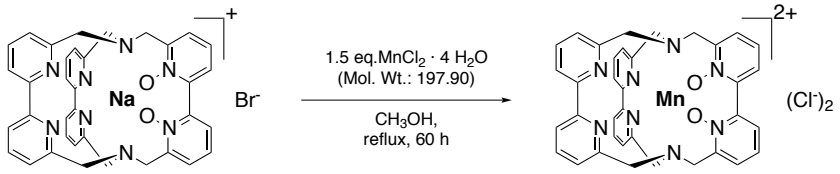

$C_{36}H_{30}BrN_8NaO_2$
Exact Mass: 708.16
Molecular Weight: 709.57

1.0 eq.

Na-48

$C_{36}H_{30}Cl_2MnN_8O_2$
Exact Mass: 731.12
Molecular Weight: 732.52

Mn^{II}-48

The sodium cryptate **Na-48** (2.1 mg, 3.0 μmol, 1.0 eq.) and $MnCl_2 \cdot 4\ H_2O$ were dissolved in 4 mL CH_3OH. The clear yellow solution was brought to reflux temperature and stirred for 60 h and afterwards evaporated to dryness. The ^1H NMR spectrum of the crude mixture did not show any of the typical signals of **Na-48** and an ESI-MS experiment performed with this material strongly indicated the successful formation of the desired compound (MS (ESI+): m/z (%) = 330.6 (100, $[M\text{-}2Cl]^{2+}$)). First experiments towards a purification of the material indicate that a column-chromatography using silanised SiO_2 and for example CH_2Cl_2/CH_3OH 9:1 as mobile phase might be possible. For TLC reversed-phase SiO_2 and CH_2Cl_2/CH_3OH 9:1 + 0.1 vol.-% TFA in H_2O as mobile phase yielded the most promising results so far.

The compound **Mn^{II}-48** appears to have only a limited stability under ambient conditions.

Note: The exact nature of the counteranions as indicated in the sum formula above was not established experimentally but derived in analogy to the related lanthanoid complexes.

The UV/Vis spectrum of the crude **Mn^{II}-48** in CD_3OD is shown on page 259.

9 Appendix

9.1 UV/Vis spectra

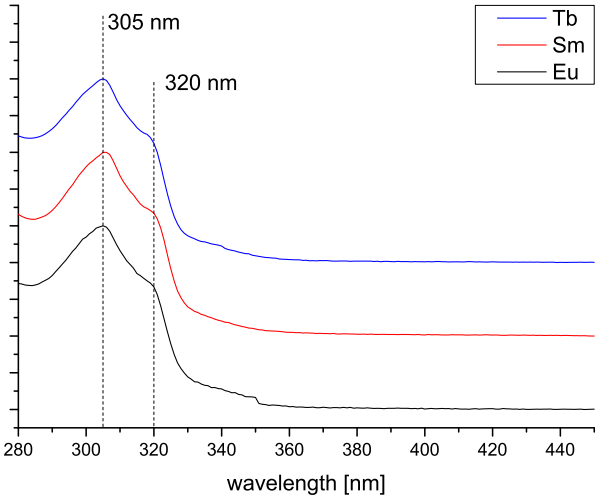

Figure 9.1: Normalised UV/Vis spectra of different **Ln-1** in CD_3OD.

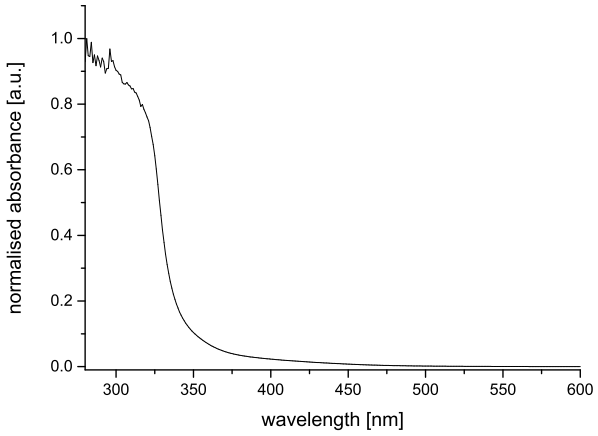

Figure 9.2: Normalised UV/Vis spectrum of (crude) **Mn^{II}-48** in CD_3OD.

9.2 Luminescence decay profiles

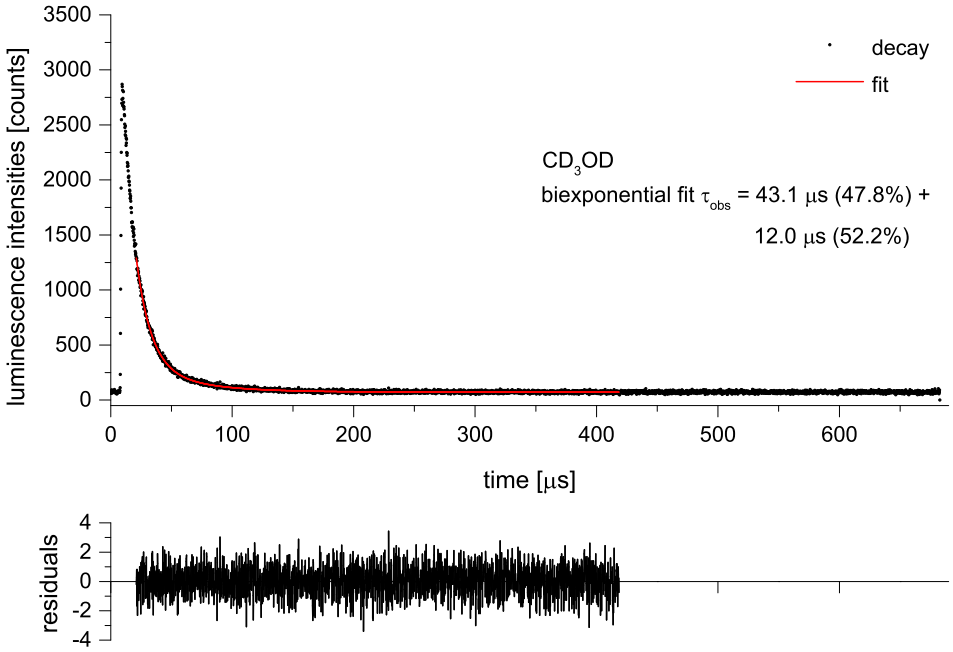

Figure 9.3: Luminescence decay profile of **Sm-1** (black) and biexponential fit in red (CD_3OD, $\lambda_{em} = 597$ nm, $\lambda_{exc} = 320$ nm).

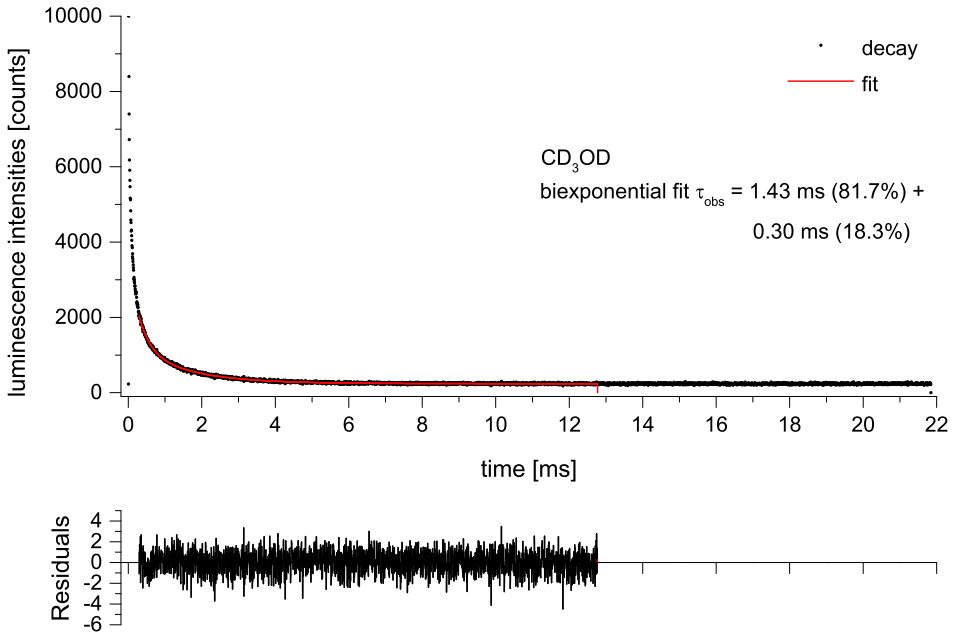

Figure 9.4: Luminescence decay profile of **Tb-1** (black) and biexponential fit in red (CD_3OD, $\lambda_{em} = 540$ nm, $\lambda_{exc} = 305$ nm).

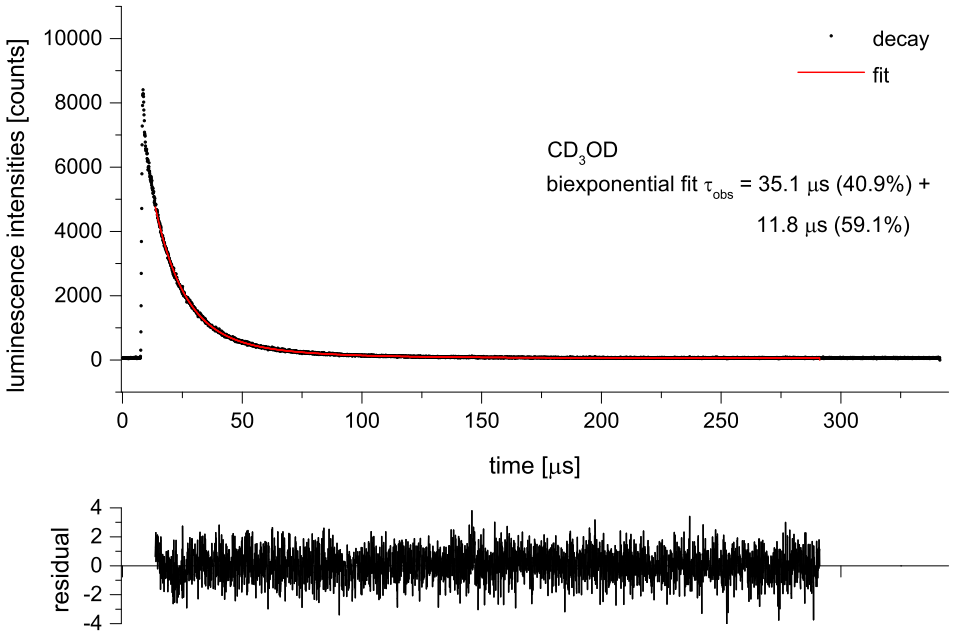

Figure 9.5: Luminescence decay profile of **Sm-16** (black) and biexponential fit in red (CD_3OD, $\lambda_{em} = 597$ nm, $\lambda_{exc} = 310$ nm).

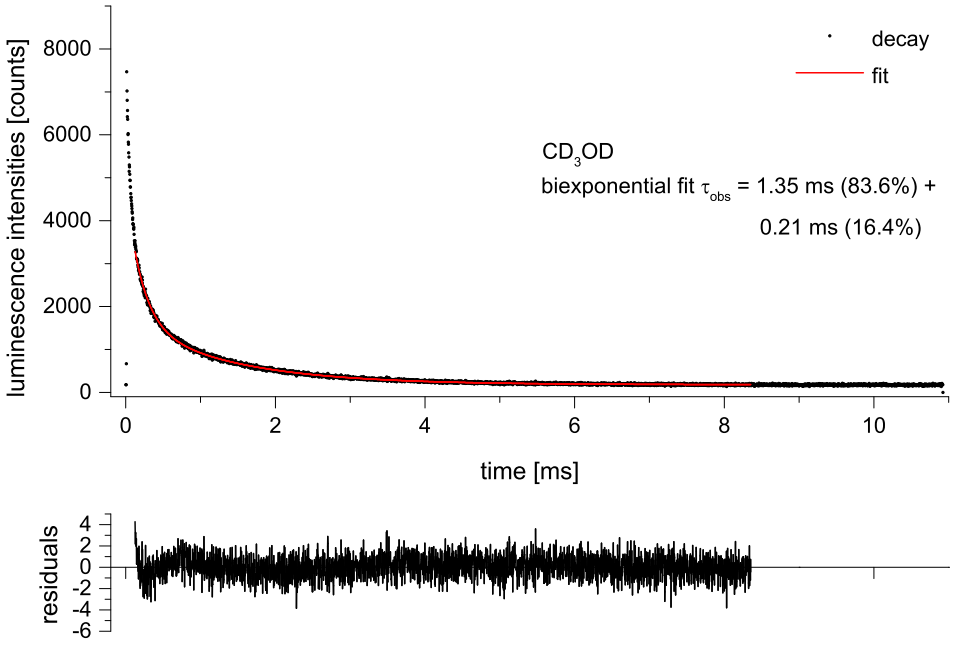

Figure 9.6: Luminescence decay profile of **Tb-16** (black) and biexponential fit in red (CD_3OD, $\lambda_{em} = 541$ nm, $\lambda_{exc} = 305$ nm).

9.3 NMR spectra

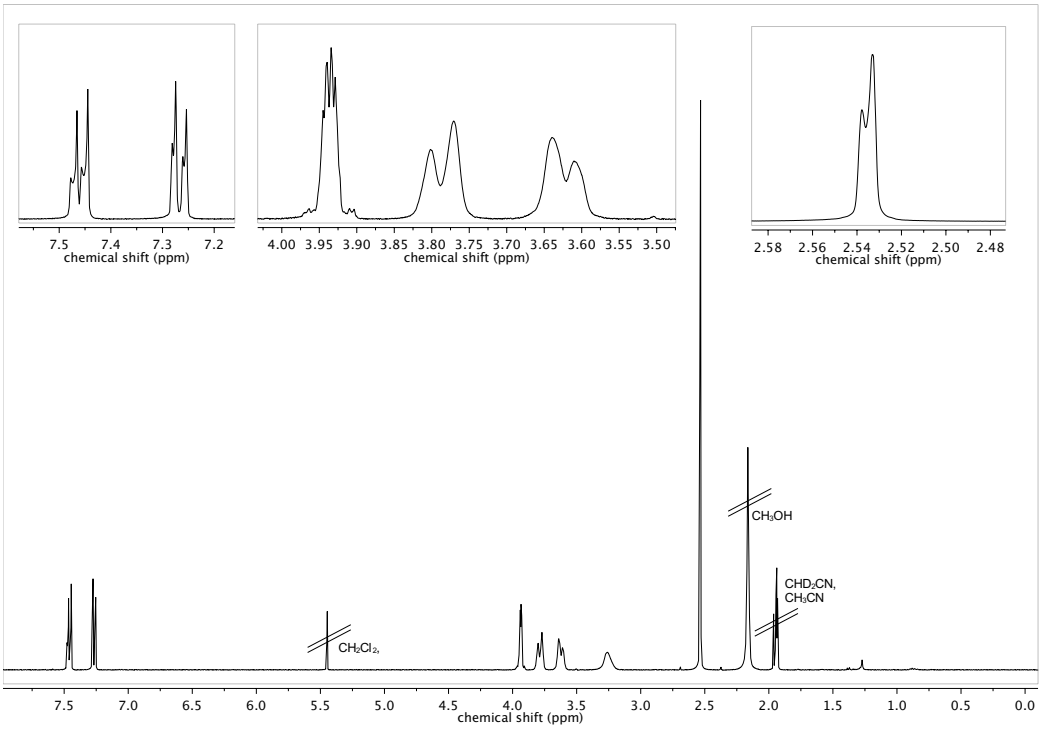

Figure 9.7: ^{1}H NMR spectrum (400 MHz, CD_3CN) of the enantiopure, diol-functionalised bipyridine **8**.

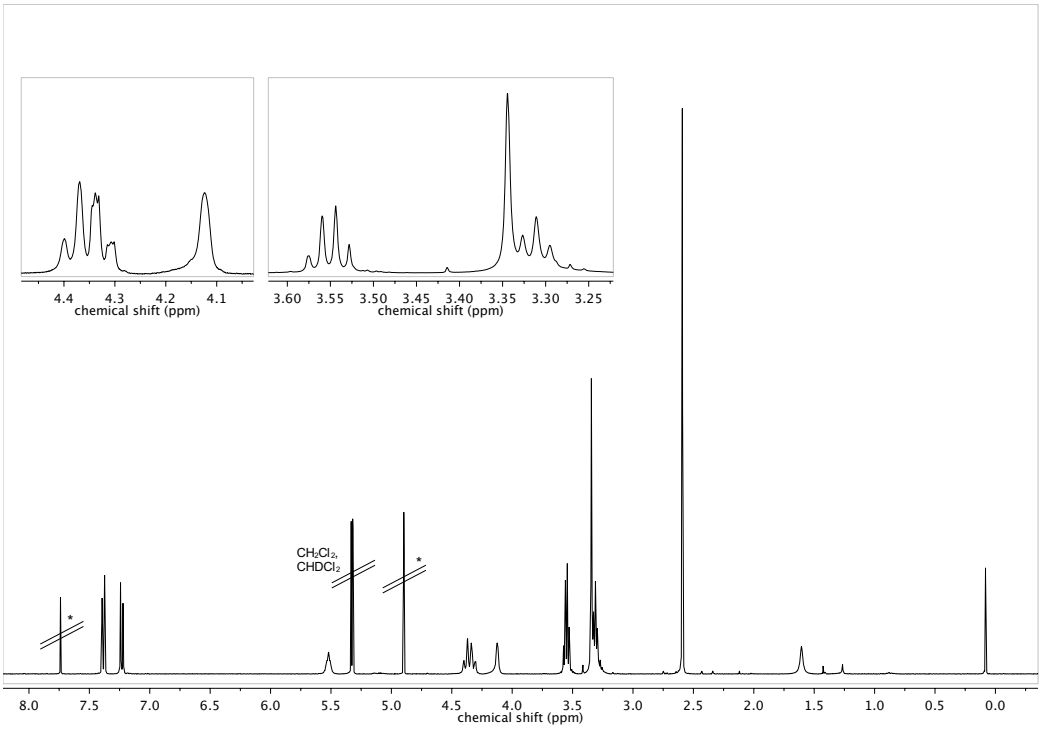

Figure 9.8: ^{1}H NMR spectrum (400 MHz, CD_2Cl_2) of the enantiopure, disulfide-functionalised bipyridine **13**. The signals marked with an asterisk originate from adventitious contamination after column-chromatography (3,6-bis(chloromethyl)pyridazine).

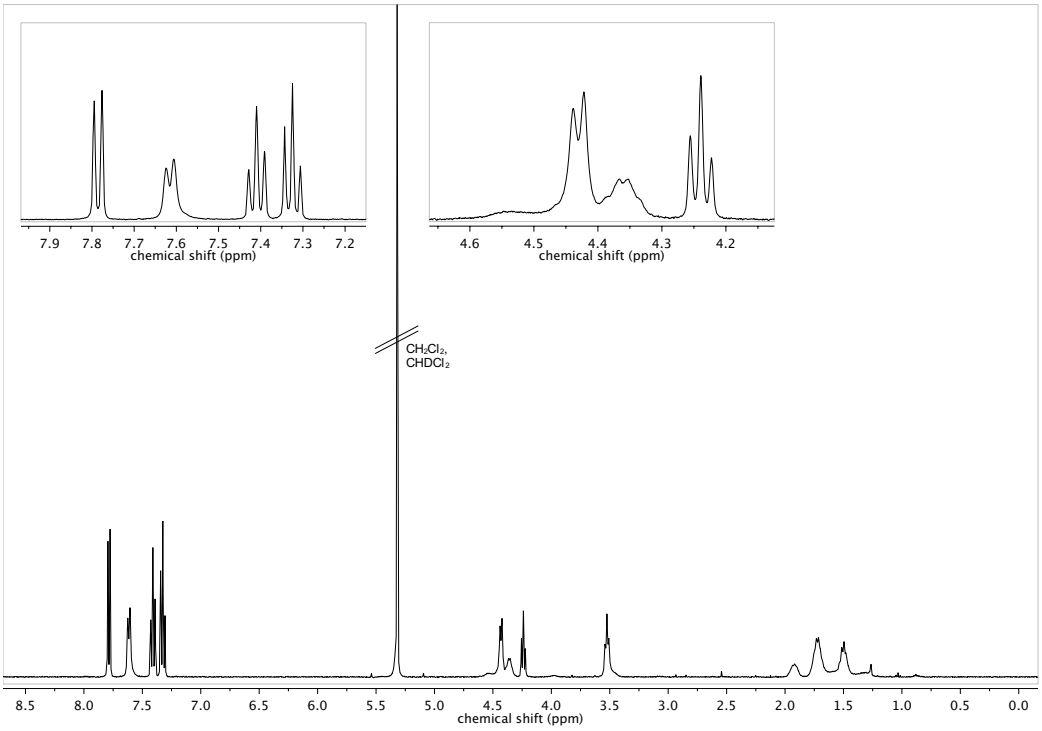

Figure 9.9: ^{1}H NMR spectrum (400 MHz, CD_2Cl_2) of the isothiocyanate-activated lysine derivative **15**.

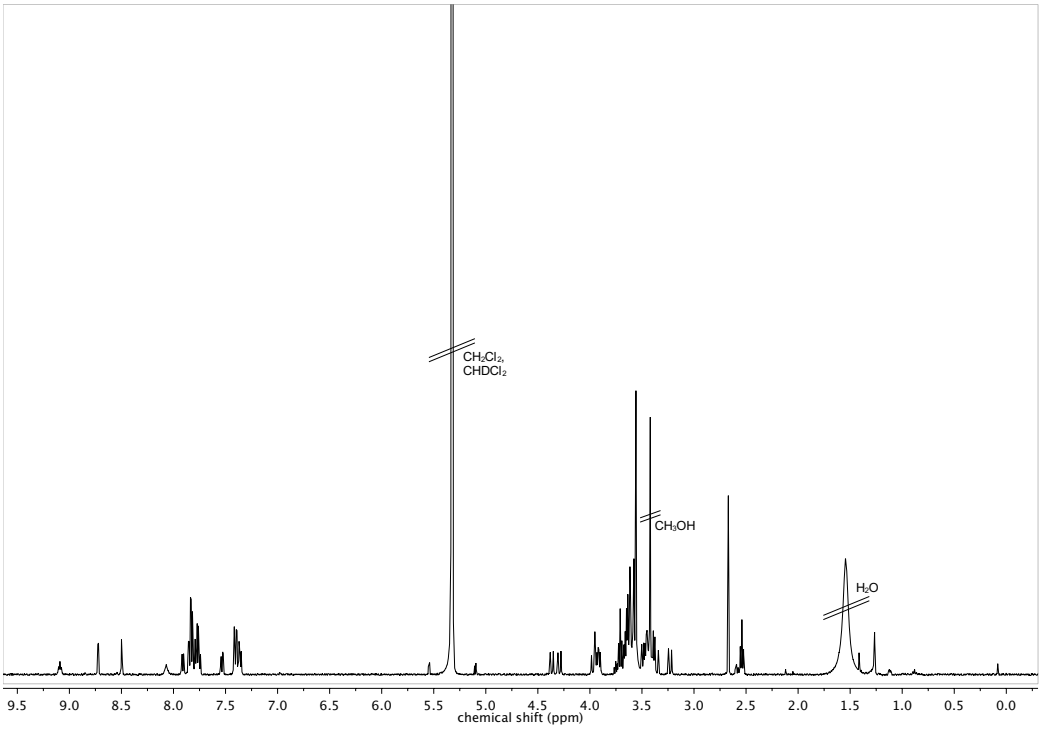

Figure 9.10: ^{1}H NMR spectrum (400 MHz, CD_2Cl_2) of the azide-functionalised sodium cryptate **Na-2**.

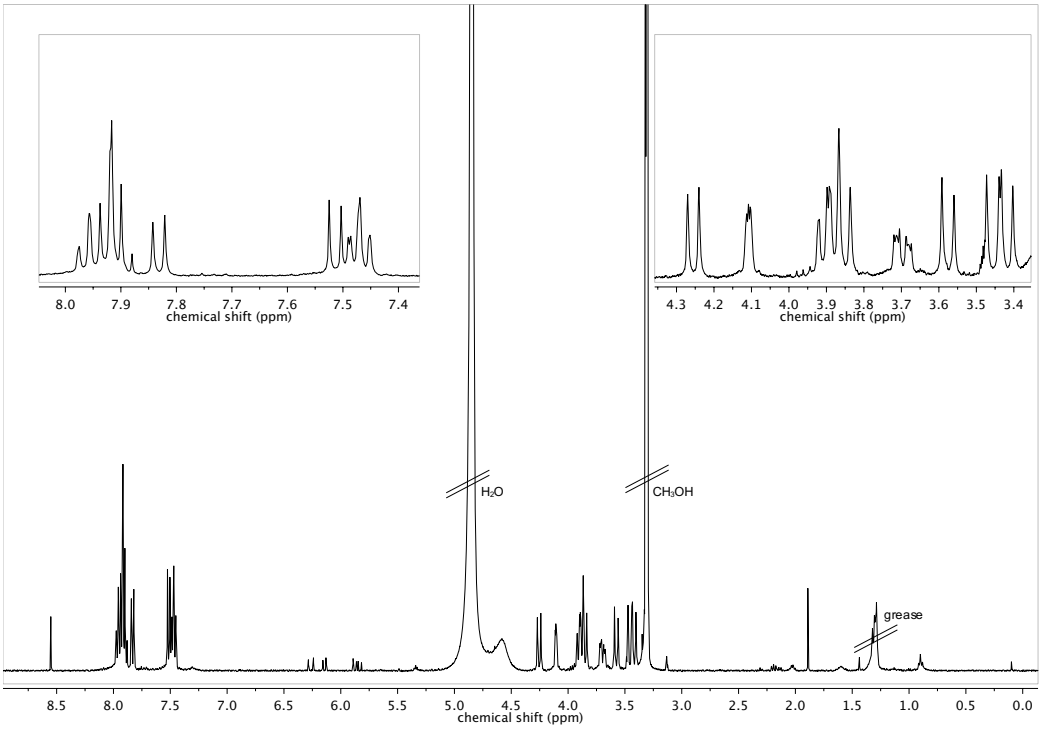

Figure 9.11: ^{1}H NMR spectrum (400 MHz, CD_3OD) of the enantiopure, diol-functionalised sodium cryptate **Na-5**.

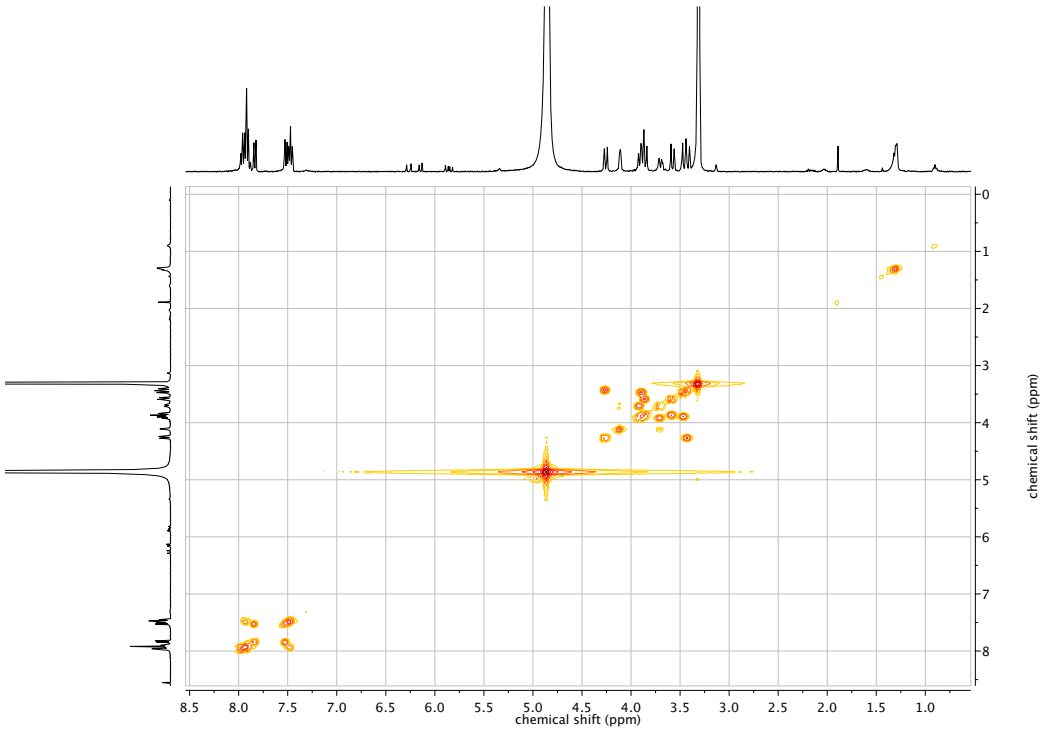

Figure 9.12: ^{1}H-^{1}H COSY NMR spectrum (400 MHz, CD_3OD) of the enantiopure, diol-functionalised sodium cryptate **Na-5**.

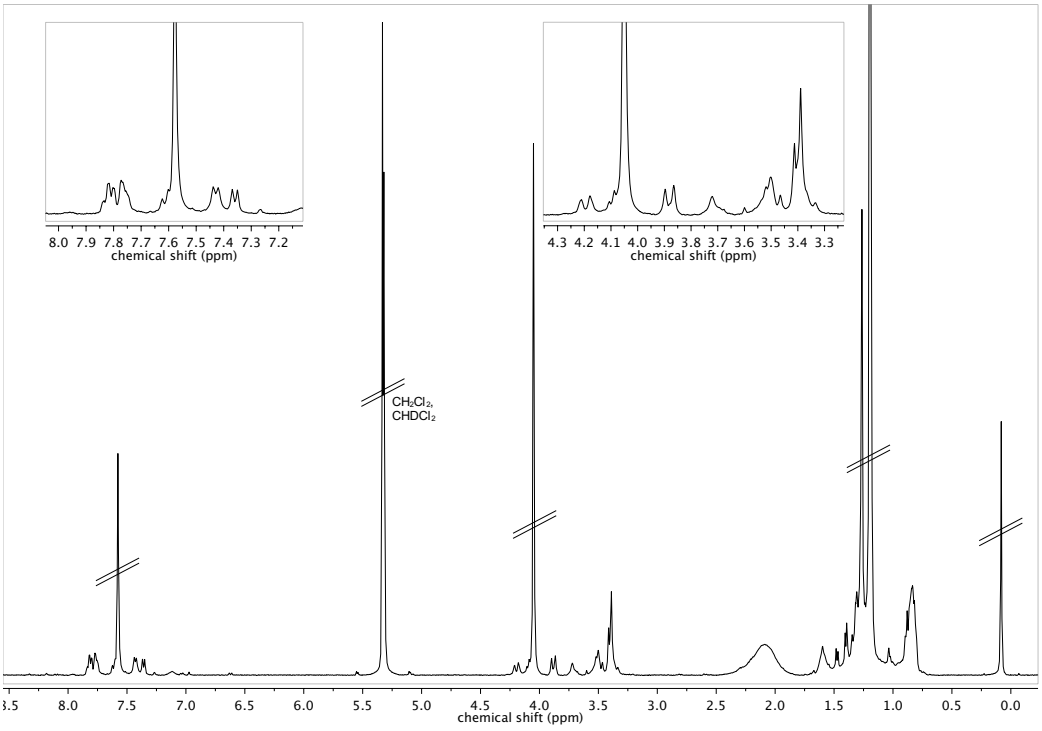

Figure 9.13: ^{1}H NMR spectrum (400 MHz, CD_2Cl_2) of the enantiopure, disulfide-functionalised sodium cryptate **Na-9**.

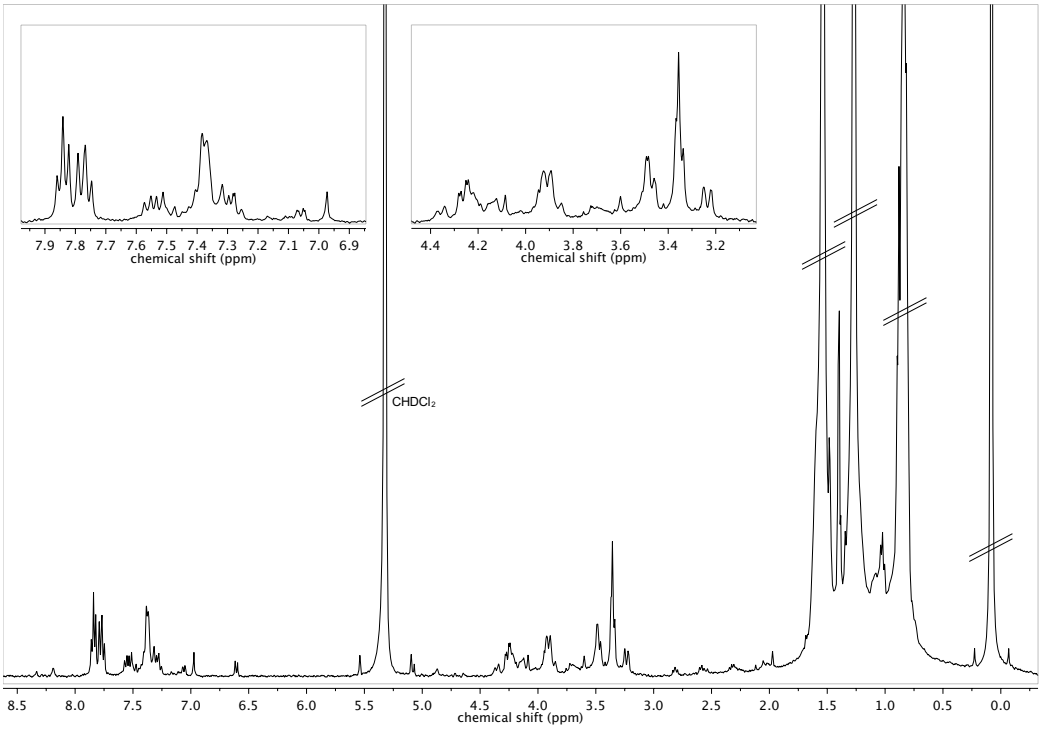

Figure 9.14: ^{1}H NMR spectrum (400 MHz, CD_2Cl_2) of the enantiopure, mono disulfide-functionalised sodium cryptate **Na-42**.

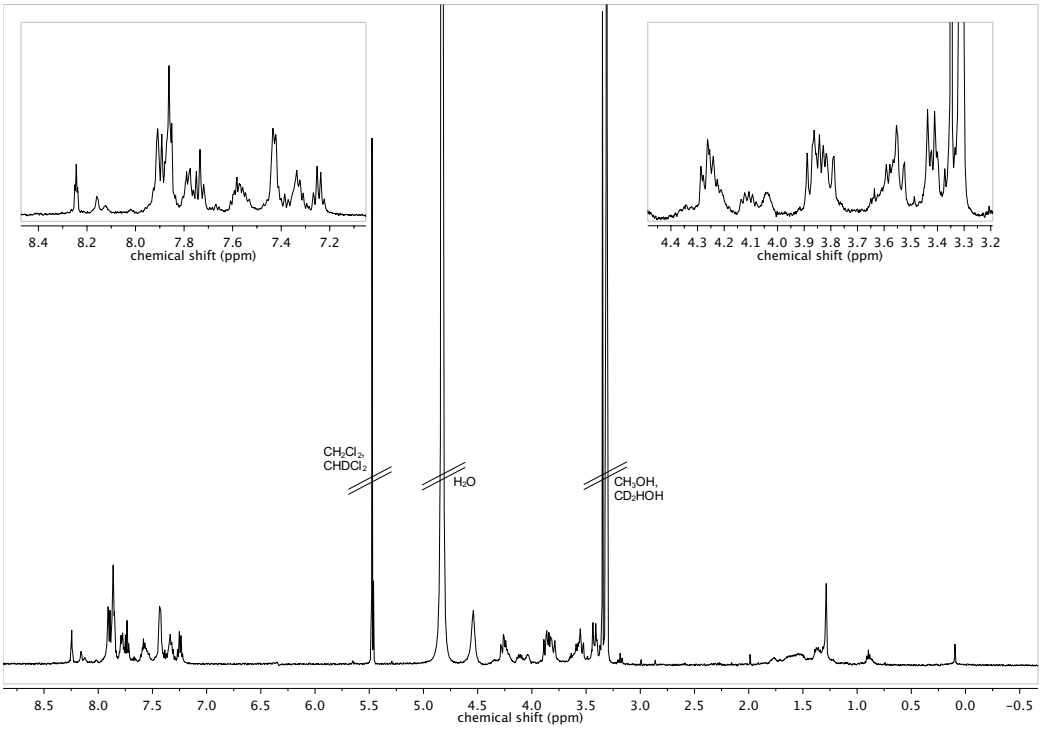

Figure 9.15: ^{1}H NMR spectrum (500 MHz, $CD_3OD + CD_2Cl_2$) of the lysine-functionalised sodium cryptate **Na-16**.

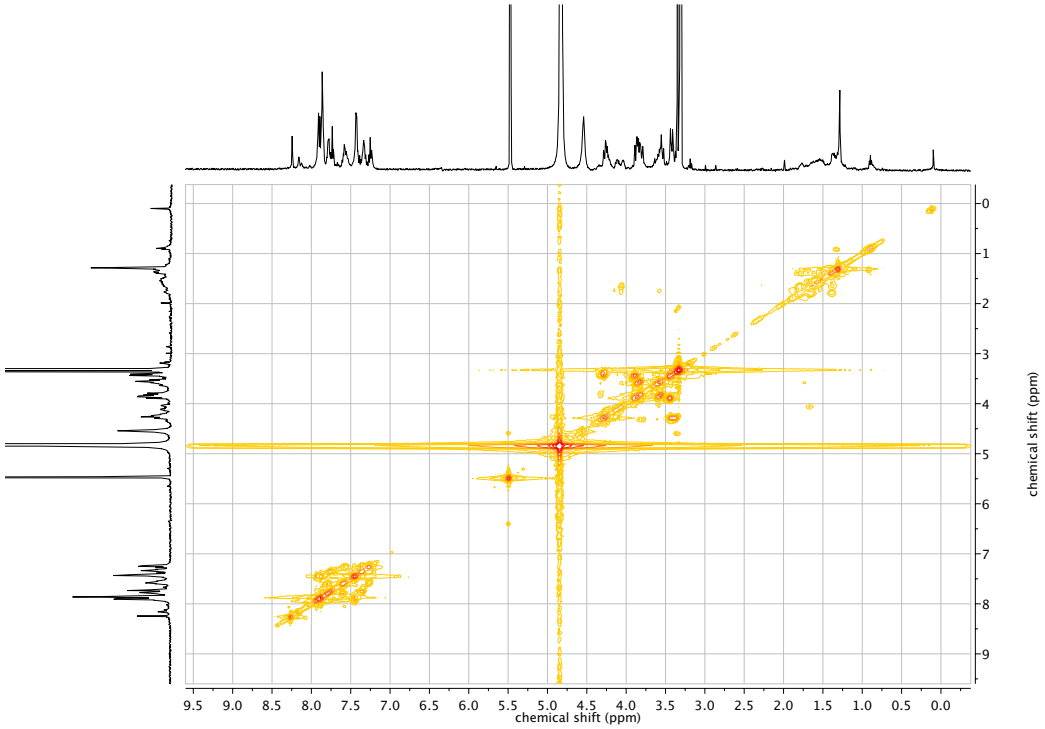

Figure 9.16: ^{1}H-^{1}H COSY NMR spectrum (500 MHz, $CD_3OD + CD_2Cl_2$) of the lysine-functionalised sodium cryptate **Na-16**.

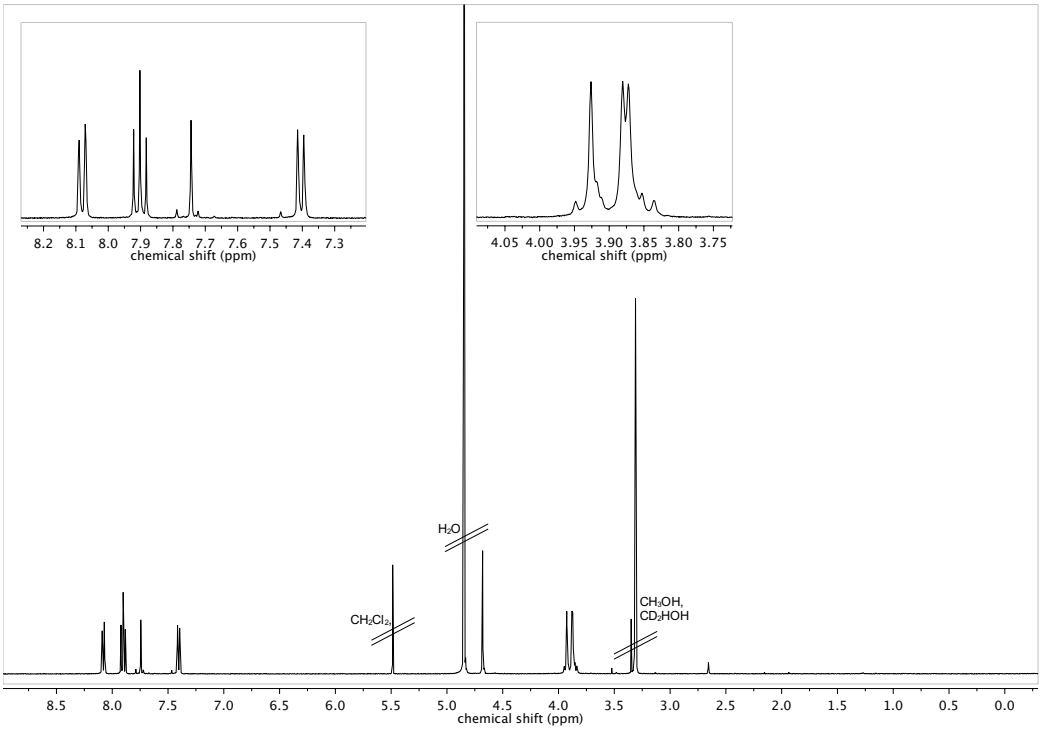

Figure 9.17: ^{1}H NMR spectrum (400 MHz, CD_3OD) of the bromide-functionalised sodium cryptate **Na-28**.

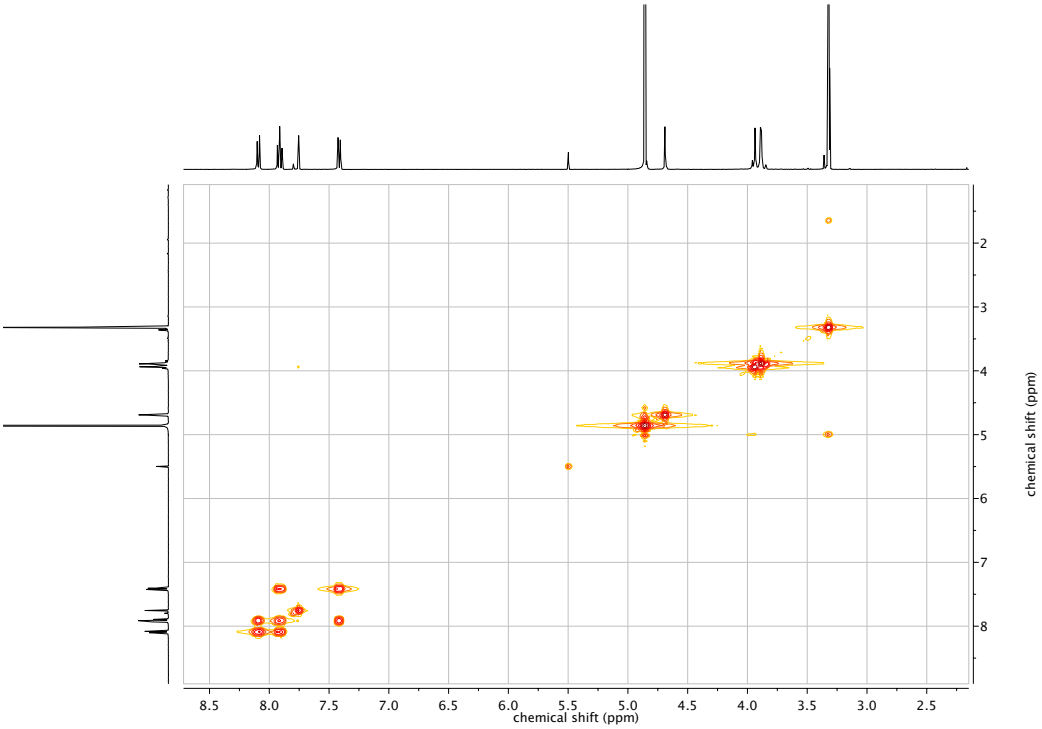

Figure 9.18: ^{1}H-^{1}H COSY NMR spectrum (400 MHz, CD_3OD) of the bromide-functionalised sodium cryptate **Na-28**.

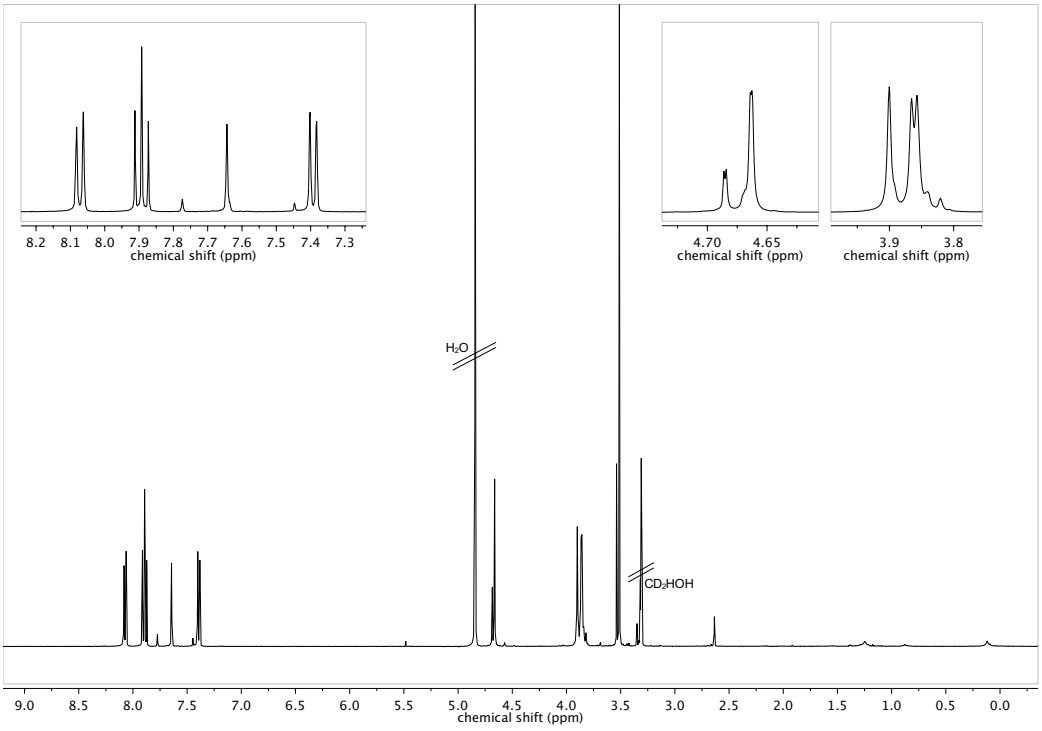

Figure 9.19: ^{1}H NMR spectrum (400 MHz, CD_3OD) of the methoxy-functionalised sodium cryptate Na-**34**.

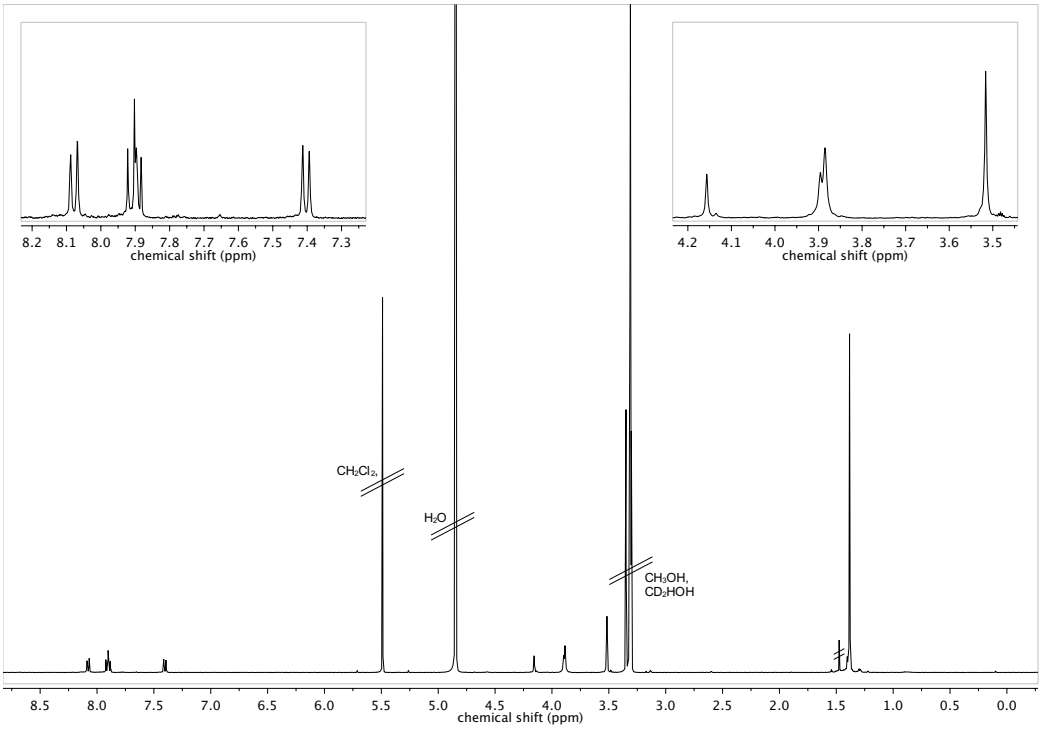

Figure 9.20: ^{1}H NMR spectrum (400 MHz, CD_3OD) of the di-(*tert*-butyl)iminodiacetate-functionalised sodium cryptate **Na-31**.

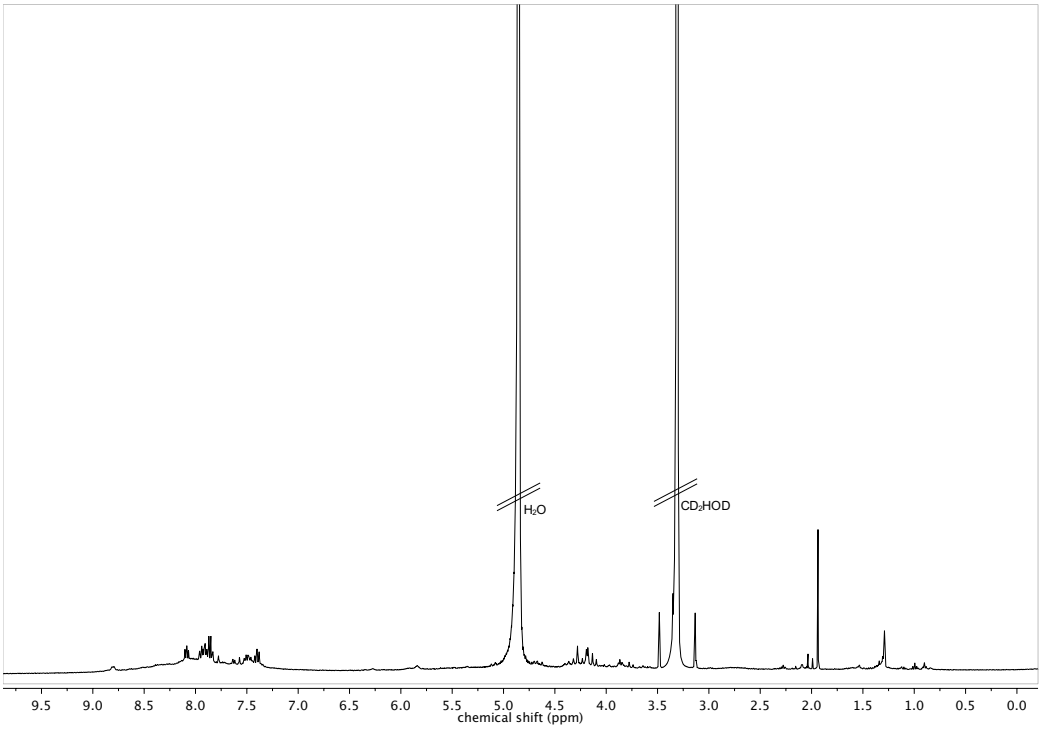

Figure 9.21: ^{1}H NMR spectrum (400 MHz, CD_3OD) of the dicryptate coordinating yttrium and europium in a statistical mixture **Y**/**Eu-26**.

9.4 HPLC traces

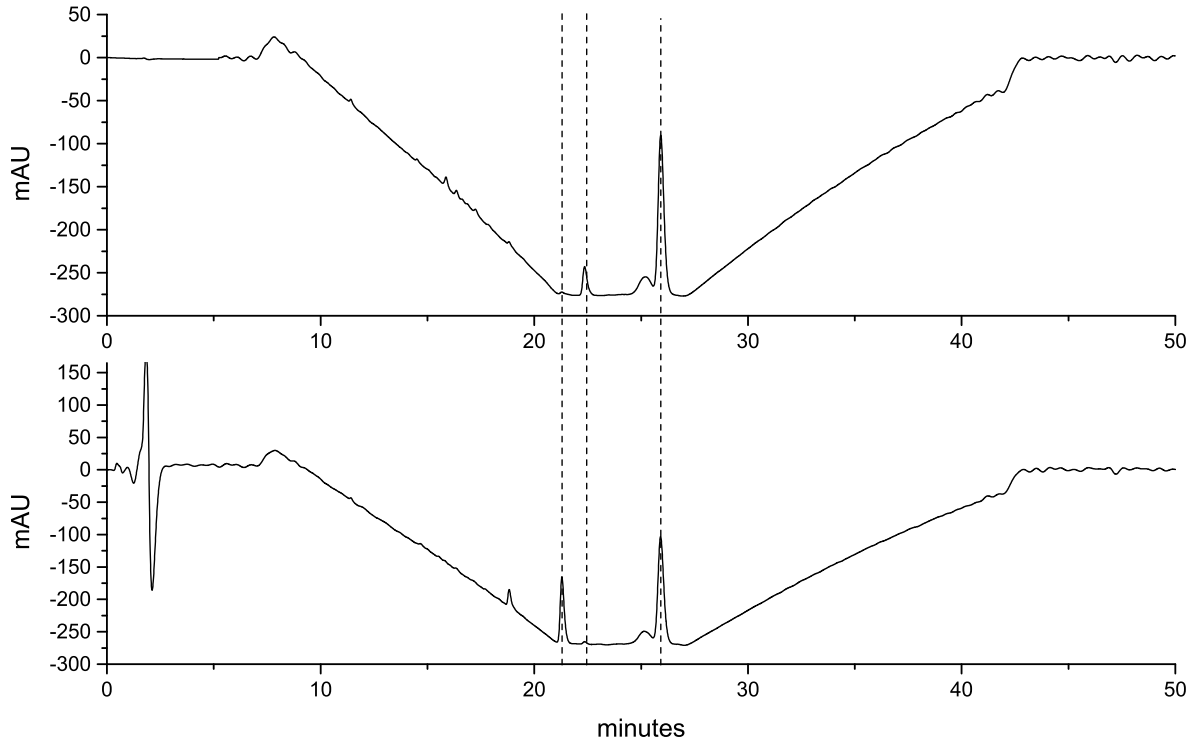

Figure 9.22: Chromatograms from the analytical HPLC (program **A**, setup **A**) of the material obtained from synthesis of peptide **17** with regular (top) and decreased (bottom) equivalents of amino acids.

9.5 ESI mass spectra

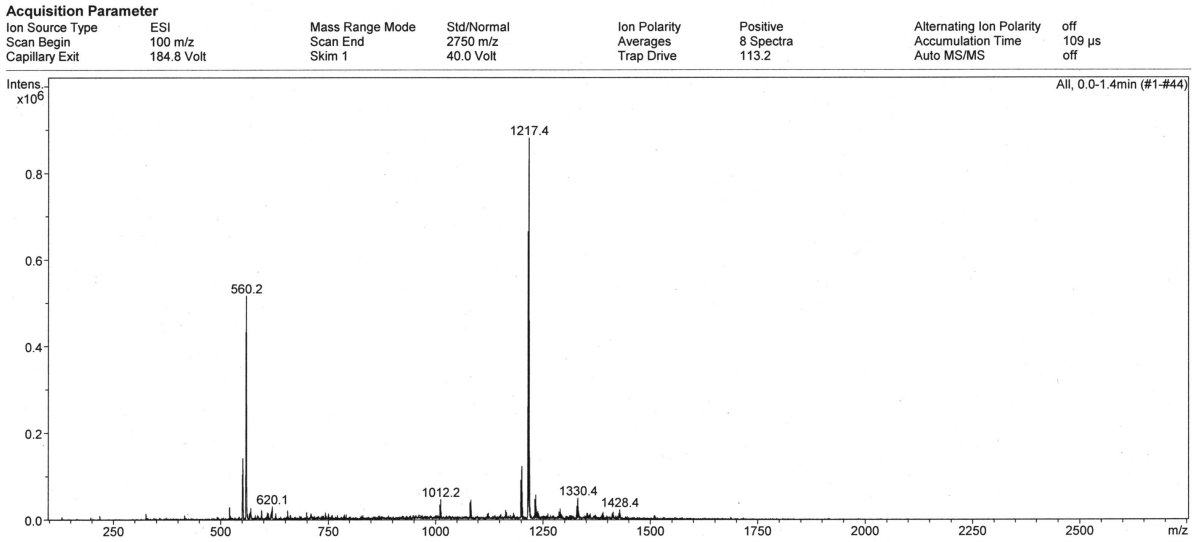

Figure 9.23: ESI mass spectrum of **Eu-3**.

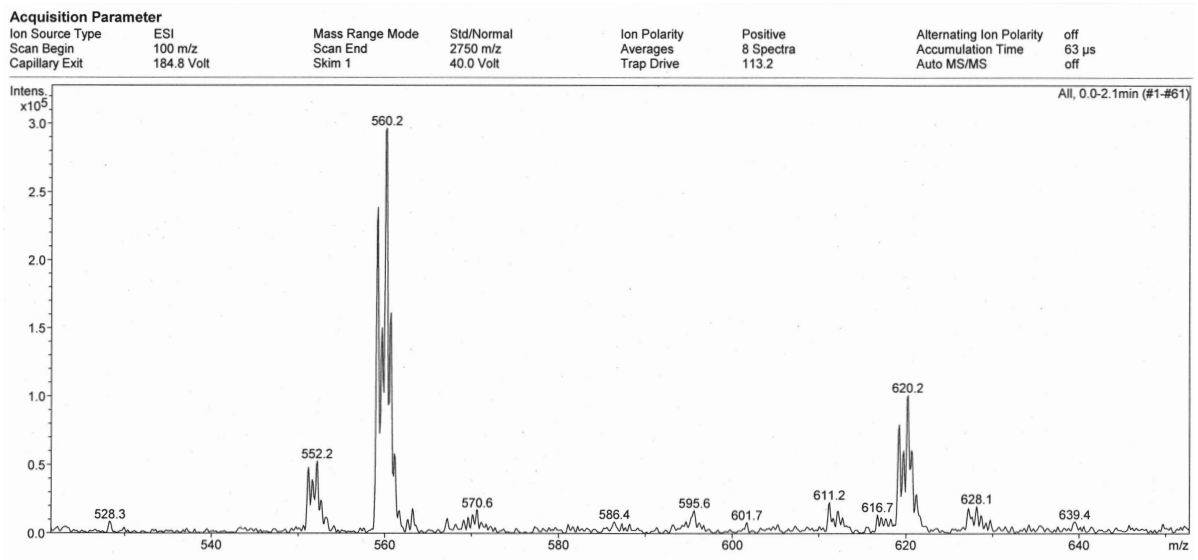

Figure 9.24: ESI mass spectrum of **Eu-3** (magnification).

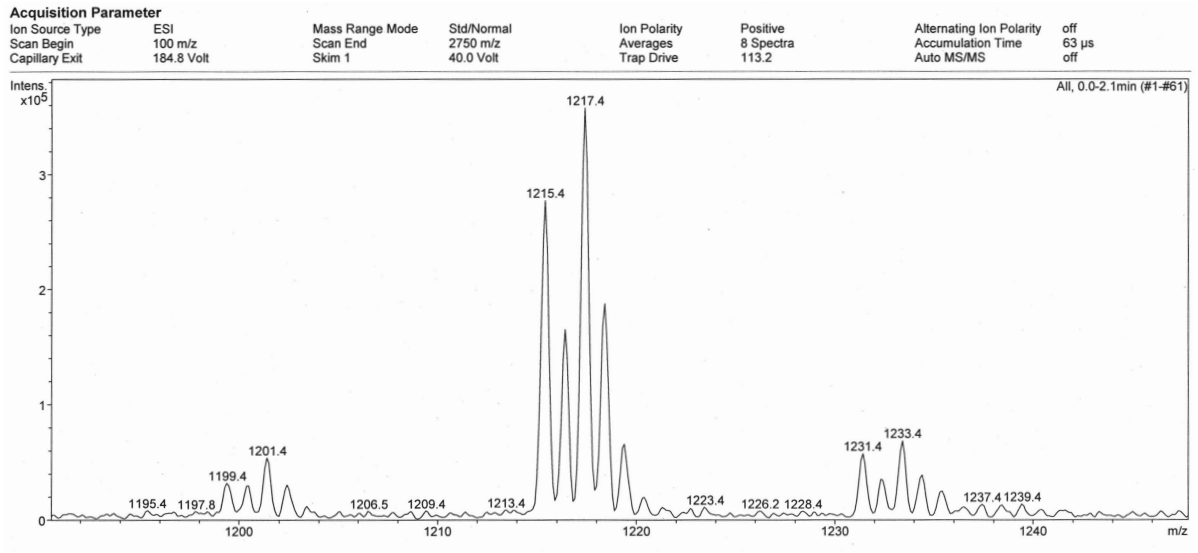

Figure 9.25: ESI mass spectrum of **Eu-3** (magnification).

9.6 mayavi2/python script for the graphical representation of the anisotropy of the magnetic susceptibility χ

```
# -*- coding: utf-8 -*-

import numpy as np
from mayavi import mlab

# define tensor
def V(x, y, z):
  return 2740*((3*z**2-((x**2+y**2+z**2)**0.5)**2)/
  (((x**2+y**2+z**2)**0.5)**5))-8601*((x**2-y**2)/
  ((((x**2+y**2+z**2)**0.5)**5)))

X, Y, Z = np.mgrid[-10:10:150j, -10:10:150j, -10:10:150j]

mlab.figure(1, bgcolor=(1, 1, 1), fgcolor=(0.8, 0.5, 0.1))

ten1=V(X, Y, Z)

# draw isosurfaces
conten1 = mlab.contour3d(X, Y, Z, V,
                contours=[12],
                opacity=0.3,
                colormap='PuBuGn',
                vmax=12,
                vmin=-12,
                transparent=True
                )

conten1 = mlab.contour3d(X, Y, Z, V,
                contours=[-12],
                opacity=0.3,
                colormap='PiYG',
                transparent=True
                )

# define molecule
abc = np.array([[0.0000, 0.0000, 0.0000],
```

```
# nitrogen atoms N35 to N43, N93
    [−0.1867, 2.3097, 1.0899],
    [5.1202, −3.2896, −10.0095],[3.0889, −1.4058, −7.4335],
    [−0.7560, 1.2276, −2.9043],
    [−2.2415, 1.3458, −0.4052],[2.2809, −1.3738, −0.4140],
    [0.7637, −1.2334, −2.9140],
    [0.2250, −2.3292, 1.0741],[−2.1796, −1.3245, 0.3718],
    [2.2022, 1.3216, 0.3544],
# carbon atoms C44 to C82
    [4.6098, 2.6613, 0.9007],
    [3.3923, 3.1932, 1.3144],[0.7617, 4.1949, 2.2352],[−0.5104, 4.6451, 2.5776],
    [4.6119, 1.4428, 0.2324],[2.2102, 2.4902, 1.0598],[0.8950, 3.0225, 1.4795],
    [−1.6238, 3.9223, 2.1543],[3.3933, 0.8007, −0.0047],
    [−1.4166, 2.7558, 1.4185],
    [3.3813, −0.4677, −0.8153],[3.9975, −1.5786, −8.5572],
    [−2.1253, 2.4944, −1.3684],
    [−1.8890, 1.9736, −2.7482],[3.5058, −1.6816, −6.1700],
    [−2.7641, 2.1220, −3.8191],
    [−2.5603, 1.9064, 0.9363],[1.4233, −0.5975, −5.1217],
    [4.1003, −3.0672, −8.9179],
    [2.5128, −1.4684, −5.0593],[−2.5211, 1.4679, −5.02676],
    [−0.5672, 0.4616, −4.0258],
    [0.5672, −0.4616, −4.0307],[−1.4361, 0.5994, −5.1071],
    [2.6140, −1.9723, 0.9072],
    [2.7715, −2.1071, −3.8420],[1.9077, −1.9690, −2.7673],
    [2.1603, −2.5029, −1.3966],
    [−3.3484, 0.4541, −0.8228],[1.4501, −2.7853, 1.4080],
    [1.6459, −3.9420, 2.1633],
    [−3.3658, −0.8257, −0.0325],[−0.8626, −3.0398, 1.4597],
    [−2.1775, −2.5185, 1.0214],
    [−4.5829, −1.4727, 0.1972],[0.5281, −4.6506, 2.5953],
    [−0.7391, −4.2013, 2.2338],
    [−3.3574, −3.2314, 1.2611],[−4.5759, −2.7005, 0.8481],
# oxygen atoms O83 to O84, O86
    [0.1711, 1.2652, −1.9554],
    [4.6431, −2.0905, −5.9170],[−0.1501, −1.2799, −1.9619]])

# correct for origin
p0 = np.array([[0.0000, 0.0000, 0.0000]])
A = abc − p0
```

```
# axis
symline = np.array([[0.0000, 0.0000, 0.0000],[0.0000, 0.0000, -4.028]])
mlab.plot3d(symline[:,0], symline[:,1], symline[:,2],
extent=[0, 0, 0, 0, -11, 11], line_width=10.0,
color=(0.3, 0.7, 0.1), tube_radius=0.1)

# connection of atoms
# rings
# ring R1 = N41, C70, C69, C63, C61, C66, close ring, to N41, to N-oxid (O86)
R1 = np.array([[0.7637, -1.2334, -2.9140],[1.9077, -1.9690, -2.7673],
[2.7715, -2.1071, -3.8420],[2.5128, -1.4684, -5.0593],
[1.4233, -0.5975, -5.1217],[0.5672, -0.4616, -4.0307],
[0.7637, -1.2334, -2.9140],[-0.1501, -1.2799, -1.9619]])
mlab.plot3d(R1[:,0], R1[:,1], R1[:,2], tube_radius=0.15)

# ring R2 = N38, C65, C67, C64, C59, C57, close ring, to N38, to N-oxid (O83)
R2 = np.array([[-0.7560, 1.2276, -2.9043],[-0.5672, 0.4616, -4.0258],
[-1.4361, 0.5994, -5.1071],[-2.5211, 1.4679, -5.02676],
[-2.7641, 2.1220, -3.8191],[-1.8890, 1.9736, -2.7482],
[-0.7560, 1.2276, -2.9043],[0.1711, 1.2652, -1.9554]])
mlab.plot3d(R2[:,0], R2[:,1], R2[:,2], tube_radius=0.15)

# ring R3 = N43, C75, C78, C82, C81, C77, close ring, to N43
R3 = np.array([[-2.1796, -1.3245, 0.3718],[-3.3658, -0.8257, -0.0325],
[-4.5829, -1.4727, 0.1972],[-4.5759, -2.7005, 0.8481],
[-3.3574, -3.2314, 1.2611],[-2.1775, -2.5185, 1.0214],
[-2.1796, -1.3245, 0.3718]])
mlab.plot3d(R3[:,0], R3[:,1], R3[:,2], tube_radius=0.15)

# ring R4 = N42, C76, C80, C79, C74, C73, close ring, to N42
R4 = np.array([[0.2250, -2.3292, 1.0741],[-0.8626, -3.0398, 1.4597],
[-0.7391, -4.2013, 2.2338],[0.5281, -4.6506, 2.5953],
[1.6459, -3.9420, 2.1633],[1.4501, -2.7853, 1.4080],[0.2250, -2.3292, 1.0741]])
mlab.plot3d(R4[:,0], R4[:,1], R4[:,2], tube_radius=0.15)

# ring R5 = N35, C53, C51, C47, C46, C50, close ring, to N35
R5 = np.array([[-0.1867, 2.3097, 1.0899],[-1.4166, 2.7558, 1.4185],
[-1.6238, 3.9223, 2.1543],[-0.5104, 4.6451, 2.5776],
```

```
[0.7617, 4.1949, 2.2352],[0.8950, 3.0225, 1.4795],[−0.1867, 2.3097, 1.0899]])
mlab.plot3d(R5[:,0], R5[:,1], R5[:,2], tube_radius=0.15)

# ring R6 = N93, C49, C45, C44, C48, C52, close ring, to N93
R6 = np.array([[2.2022, 1.3216, 0.3544],[2.2102, 2.4902, 1.0598],
[3.3923, 3.1932, 1.3144],[4.6098, 2.6613, 0.9007],
[4.6119, 1.4428, 0.2324],[3.3933, 0.8007, −0.0047],[2.2022, 1.3216, 0.3544]])
mlab.plot3d(R6[:,0], R6[:,1], R6[:,2], tube_radius=0.15)


# connection of rings
# ring R1 und R2: C66 and C65
R1R2 = np.array([[0.5672, −0.4616, −4.0307],[−0.5672, 0.4616, −4.0258]])
mlab.plot3d(R1R2[:,0], R1R2[:,1], R1R2[:,2], tube_radius=0.15)

# ring R2 and R3: C57, C56, N39, C72, C75
R2R3 = np.array([[−1.8890, 1.9736, −2.7482],[−2.1253, 2.4944, −1.3684],
[−2.2415, 1.3458, −0.4052],[−3.3484, 0.4541, −0.8228],
[−3.3658, −0.8257, −0.0325]])
mlab.plot3d(R2R3[:,0], R2R3[:,1], R2R3[:,2], tube_radius=0.15)

# ring R3 and R4: C77 and C76
R3R4 = np.array([[−2.1775, −2.5185, 1.0214],[−0.8626, −3.0398, 1.4597]])
mlab.plot3d(R3R4[:,0], R3R4[:,1], R3R4[:,2], tube_radius=0.15)

# ring R4 and R1: C73, C68, N40, C71, C70
R4R1 = np.array([[1.4501, −2.7853, 1.4080],[2.6140, −1.9723, 0.9072],
[2.2809, −1.3738, −0.4140],[2.1603, −2.5029, −1.3966],
[1.9077, −1.9690, −2.7673]])
mlab.plot3d(R4R1[:,0], R4R1[:,1], R4R1[:,2], tube_radius=0.15)

# ring R5 and R6: C50, C49
R5R6 = np.array([[0.8950, 3.0225, 1.4795],[2.2102, 2.4902, 1.0598]])
mlab.plot3d(R5R6[:,0], R5R6[:,1], R5R6[:,2], tube_radius=0.15)

# attachment R5: N39, C60, C53
zuR5 = np.array([[−2.2415, 1.3458, −0.4052],[−2.5603, 1.9064, 0.9363],
[−1.4166, 2.7558, 1.4185]])
mlab.plot3d(zuR5[:,0], zuR5[:,1], zuR5[:,2], tube_radius=0.15)
```

```
# attachment R6: N40, C54, C52
zuR6 = np.array([[2.2809, −1.3738, −0.4140],[3.3813, −0.4677, −0.8153],
[3.3933, 0.8007, −0.0047]])
mlab.plot3d(zuR6[:,0], zuR6[:,1], zuR6[:,2], tube_radius=0.15)


# diaminelinker: C63, C58, O84, C58, N37, C55, C62, N36
en = np.array([[2.5128, −1.4684, −5.0593],[3.5058, −1.6816, −6.1700],
[4.6431, −2.0905, −5.9170],[3.5058, −1.6816, −6.1700],
[3.0889, −1.4058, −7.4335],[3.9975, −1.5786, −8.5572],
[4.1003, −3.0672, −8.9179],[5.1202, −3.2896, −10.0095]])
mlab.plot3d(en[:,0], en[:,1], en[:,2], tube_radius=0.15)



mlab.points3d(A[:,0], A[:,1], A[:,2], color=(1,1,1), scale_factor=.5)
```

9.7 Sequences and structures of peptides studied via ^{1}H DOSY NMR

Kemptide

H–Leu–Arg–Arg–Ala–Ser–Leu–Gly–OH

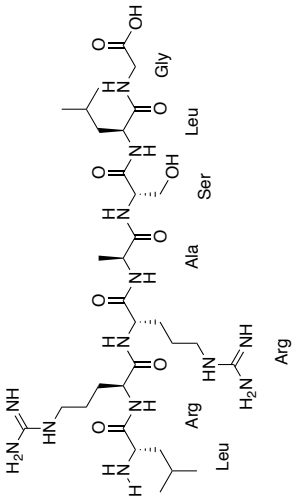

Angiotensin II

H–Asp–Arg–Val–Tyr–Ile–His–Pro–Phe–OH

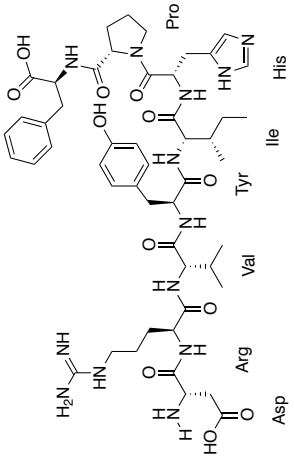

Magainin I

H–Gly–Ile–Gly–Lys–Phe–Leu–His–Ser–Ala–Gly–Lys–Phe–Gly–Lys–Ala–Phe–Val–Gly–Glu–Ile–Met–Lys–Ser–OH

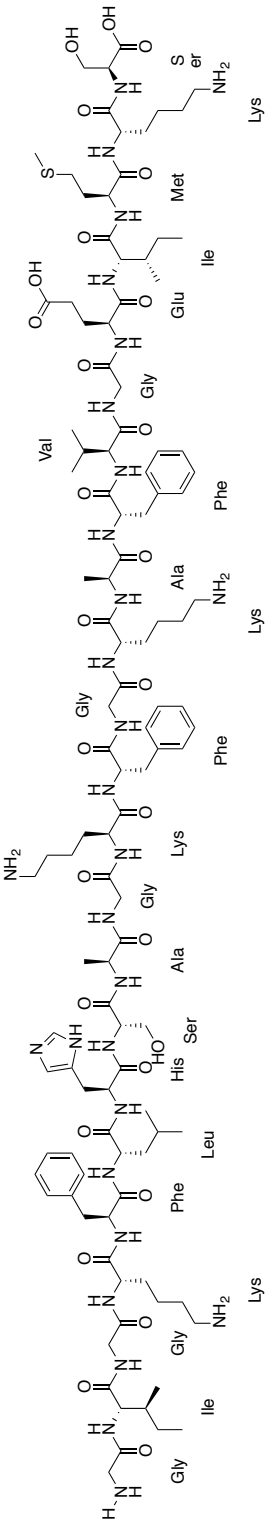

9.8 Examples for upconversion processes between different lanthanoids in nanoparticles

On the following pages some selected examples for upconversion processes as observed in nanoparticles are summarised, together with the rationalisation of the underlying processes as presented in the original publication. Aim of the selection was to reflect the special suitability of Yb^{III} for the preparation of such materials, apart from that, the selection is arbitrary.

Table 9.1: Examples for upconversion processes between different lanthanoids in nanoparticles.

lanthanoid	**hostmaterial**	**excited transition**	**upconverted transition**	**mechanism, remarks**	
Pr^{III}/Yb^{III} [312]	KPb_2Cl_5	$Pr(^3H_4 \rightarrow {}^1G_4)$, 1018 nm	$Pr(^1D_2 \rightarrow {}^3H_4)$, 601 nm	2 photon process, most intense	
			$Pr(^3P_0 \rightarrow {}^3H_4)$, 489 nm	3 photon process	
			$Pr(^3P_1 \rightarrow {}^3H_5)$		
			$(Pr(^3P_0 \rightarrow {}^3H_6))$	overlapping bands	
			$Pr(^3P_0 \rightarrow {}^3F_2)$		
		$Yb(^2F_{7/2} \rightarrow {}^2F_{5/2})$, 980 nm	$Pr(^1D_2 \rightarrow {}^3H_4)$, 601 nm		
			$Pr(^3P_0 \rightarrow {}^3H_4)$, 489 nm		more intense than emission from $^1D_2$
			$Pr(^3P_1 \rightarrow {}^3H_5)$		
			$(Pr(^3P_0 \rightarrow {}^3H_6))$	overlapping bands	
			$Pr(^3P_0 \rightarrow {}^3F_2)$		
		$Yb(^2F_{7/2} \rightarrow {}^2F_{5/2})$, 937.5 nm “high-energy wing”	$Pr(^3P_0 \rightarrow {}^3H_4)$, 489 nm		no emission from $^1D_2$!
			$Pr(^3P_1 \rightarrow {}^3H_5)$		
			$(Pr(^3P_0 \rightarrow {}^3H_6))$	overlapping bands	
			$Pr(^3P_0 \rightarrow {}^3F_2)$		
Pr^{III} [313]	KPb_2Cl_5	$Pr(^3H_4 \rightarrow {}^1G_4)$, 1018 nm	$Pr(^1D_2 \rightarrow {}^3H_4)$, 601 nm	2 photon process	
			$Pr(^3P_0 \rightarrow {}^3H_4)$, 489 nm	3 photon process	
			$Pr(^3P_1 \rightarrow {}^3H_5)$		

			($Pr(^3P_0 \rightarrow ^3H_6)$)	overlapping bands
			($Pr(^3P_1 \rightarrow ^3F_2)$)	overlapping bands
			$Pr(^3P_0 \rightarrow ^3F_2)$	
Nd^{III} [314]	Pb-Te glasses $(80\text{-}x)TeO_2$ + $20PbF_2$+ xNd_2O_3	$Nd(^4I_{3/2} \rightarrow ^4G_{7/2})$, 532 nm	$Nd(^4D_{3/2} \rightarrow ^4I_{9/2})$, 359 nm	2 photon processes. Above 0.8mol% Nd^{III}: quenching. For small concentrations the relative intensities change. Assumed mechanism: $^4I_{9/2}$ + hν $\rightarrow$ $^4G_{7/2}$ $\rightarrow$ $^4F_{3/2}$ + phonon emission; $^4F_{3/2}$ + hν $\rightarrow$ $^4D_{7/2}$ $\rightarrow$ $^4D_{3/2}$ + phonon emission; $^4D_{3/2}$ $\rightarrow$ $^4I_{ij}$ + hν.
			$Nd(^4D_{3/2} \rightarrow ^4I_{11/2})$, 383 nm	
			$Nd(^4D_{3/2} \rightarrow ^4I_{13/2})$, 415 nm	
			$Nd(^4D_{3/2} \rightarrow ^4I_{15/2})$, 451 nm	
		$Nd(^4I_{3/2} \rightarrow ^4F_{5/2}+^2H_{9/2})$, 797 nm	$Nd(^2P_{1/2} \rightarrow ^4I_{9/2})$, 430 nm	Emission can also be observed at 814 and 874 nm, $Nd(^4F_{3/2} \rightarrow ^4I_{9/2})$ und $Nd(^4F_{5/2} \rightarrow ^4I_{9/2})$. For c(Nd) < 0.5mol% an ESA mechanism dominates: $^4I_{9/2}$ + hν $\rightarrow$ $^4F_{5/2}$ $\rightarrow$ $^4F_{3/2}$ + phonon emission; $^4F_{3/2}$ + hν $\rightarrow$ $^2P_{1/2}$. For 0.5mol% < c(Nd) < 1.0mol% ETU becomes more likely: $Nd(^4F_{3/2})$ + $Nd(^4F_{3/2})$ $\rightarrow$ $Nd(^4I_{13/2})$ + $Nd(^4G_{7/2} + ^2G_{9/2})$
			$Nd(^2P_{1/2} \rightarrow ^4I_{11/2})$, 482 nm	
			$Nd(^2P_{1/2} \rightarrow ^4I_{13/2})$, 525 nm	
			$Nd(^4G_{7/2} \rightarrow ^4I_{9/2})$, 535 nm	
			$Nd(^2P_{1/2} \rightarrow ^4I_{15/2})$, 580 nm	
			$Nd(^4G_{7/2} \rightarrow ^4I_{11/2})$, 600 nm	
			$Nd(^4G_{5/2} + ^2G_{7/2} \rightarrow ^4I_{9/2})$	
			$Nd(^4G_{7/2} \rightarrow ^4I_{13/2})$, 664 nm	
			$Nd(^4G_{7/2} \rightarrow ^4I_{15/2})$, 766 nm	
Sm^{III}/Yb^{III} [315]	β-$NaYbF_4$	$Yb(^2F_{7/2} \rightarrow ^2F_{5/2})$, 980 nm	$Sm(^6F_{11/2} \rightarrow ^6H_{5/2})$, 873 nm	broad. Increases with c(Sm). Presumably phonon-assisted

	β-$NaYb_{1-x}Sm_xF_4$		Sm($^4G_{7/2}\rightarrow{}^6H_{5/2}$), 520 nm	weak	For c(Sm) < 0.4mol% a CET-mechanism seems to be predominant: 2Yb($^2F_{5/2}$) + Sm($^6H_{5/2}$) $\rightarrow$ 2Yb($^2F_{7/2}$) + Sm($^4I_{9/2}$). For higher c(Sm): ETU-mechanism.
			Sm($^4F_{3/2}\rightarrow{}^6H_{5/2}$), 541 nm		
			Sm($^4G_{7/2}\rightarrow{}^6H_{9/2}$), 657 nm		
			2xYb($^2F_{5/2}\rightarrow{}^2F_{7/2}$), 475 nm	Cooperative upconversion Yb-Yb. Almost disappearing for high c(Sm).	
Eu^{III}/Yb^{III} [316]	GGG oder YAG mit 2%Eu und 5%Yb	Yb($^2F_{7/2}\rightarrow{}^2F_{5/2}$), 980 nm	Eu($^5D_0\rightarrow{}^7F_j$)	CET: 2 Yb($^2F_{5/2}$) + Eu($^7F_0$) $\rightarrow$ 2 Yb($^2F_{7/2}$) + Eu($^5D_2$).	
Tb^{III}/Yb^{III} [316]	GGG oder YAG mit 2%Tb und 5%Yb	Yb($^2F_{7/2}\rightarrow{}^2F_{5/2}$), 980 nm	Tb($^5D_4\rightarrow{}^7F_j$)		
			Tb($^5D_3\rightarrow{}^7F_j$)	Populated from d-states, after threefold energy transfer	
Gd^{III}/Tm^{III} $/Yb^{III}$ [317]	$NaY_{1-x-y-z}Gd_xYb_yTm_zF_4$	Yb($^2F_{7/2}\rightarrow{}^2F_{5/2}$), 980 nm	Gd($^6I_j\rightarrow{}^8S_{7/2}$), 270-281 nm		Tm($^3P_{2,1}\rightarrow{}^3H_6$) and Gd($^8S_{7/2}\rightarrow{}^6I_j$) are almost resonant. Subsequent nonradiative deactivation populates Gd($^6P_{5/2}$) and Gd($^6P_{7/2}$).
			Gd($^6P_{5/2}\rightarrow{}^8S_{7/2}$), 305 nm		
			Gd($^6P_{7/2}\rightarrow{}^8S_{7/2}$), 315 nm	very intense	
			Tm($^3P_0\rightarrow{}^3H_6$), 291 nm		
			Tm($^3P_0\rightarrow{}^3F_4$), 353 nm		
			Tm($^1D_2\rightarrow{}^3H_6$), 361 nm		
			Tm($^1D_2\rightarrow{}^3F_4$), 451 nm		

			$Tm(^1G_4 \rightarrow {}^3H_6)$, 478 nm		Optimal composition: c(Gd) = 0.2 - 0.3, c(Yb) = 0.2 - 0.4, c(Tm) = 0.004 - 0.0075.
			$Tm(^3H_4 \rightarrow {}^3H_6)$, 800 nm		
			$Tm(^3F_2/{}^3F_3 \rightarrow {}^3H_6)$ or $Tm(^1G_4 \rightarrow {}^3F_4/{}^3F_5)$, 650/690 nm	strongly dependent on pump intensity	
Dy^{III}/Yb^{III} [318]	Ba-Fluoro-borate glass	$Yb(^2F_{7/2} \rightarrow {}^2F_{5/2})$, 976 nm	$2xYb(^2F_{5/2} \rightarrow {}^2F_{7/2})$, 490 nm	intense	not efficient
			$Dy(^4G_{11/2} \rightarrow {}^6H_{13/2})$, 487 nm	most intense of the Dy-transitions	
			$Dy(^4G_{11/2} \rightarrow {}^6H_{11/2})$, 569 nm	very weak	
			$Dy(^4G_{11/2} \rightarrow {}^6H_{9/2})$, 610 nm		
			$Dy(^4G_{11/2} \rightarrow {}^6H_{7/2})$, 655 nm		
Ho^{III}/Yb^{III} [319]	Y_2O_3	$Yb(^2F_{7/2} \rightarrow {}^2F_{5/2})$, 980 nm	$Ho(^5F_4, {}^5S_2 \rightarrow {}^5I_8)$, ~550 nm	ratio depends on particle size.	
			$Ho(^5F_5 \rightarrow {}^5I_8)$, 667 nm		
Er^{III}/Yb^{III} [320]	$NaYF_4$	$Yb(^2F_{7/2} \rightarrow {}^2F_{5/2})$, 980 nm	$Er(^2H_{11/2} \rightarrow {}^4I_{15/2})$		
			$Er(^4S_{3/2} \rightarrow {}^4I_{15/2})$		
			$Er(^4F_{9/2} \rightarrow {}^4I_{15/2})$		
Tm^{III}/Yb^{III} [321]	β-$NaYF_4$	$Yb(^2F_{7/2} \rightarrow {}^2F_{5/2})$, 980 nm	$Tm(^1D_2 \rightarrow {}^3H_6)$, 360 nm	4 photon process	Output-colour depends on particle size and ratio of Ln.
			$Tm(^1D_2 \rightarrow {}^3H_4)$, 450 nm	4 photon process	
			$Tm(^1G_4 \rightarrow {}^3H_6)$, 475 nm	3 photon process	

			$Tm(^1G_4 \rightarrow {}^3H_4)$, 650 nm	3 photon process	typical doping: 0.2%Tm, 40%Yb. Blue total emission. For higher c(Tm) $Tm(^1D_2)$ and $Tm(^1G_4)$ are not populated efficiently.
			$Tm(^3F_2 \rightarrow {}^3H_6)$, 695 nm	2 photon process	
			$Tm(^3F_4 \rightarrow {}^3H_6)$, 800 nm	2 photon process	
Yb^{III}/Yb^{III} [322]	$YbPO_4$	$Yb(^2F_{7/2} \rightarrow {}^2F_{5/2})$, 998 nm	2 $Yb(^2F_{5/2} \rightarrow {}^2F_{7/2})$, 497 nm	Cooperative Emission: $Yb(^2F_{5/2})$ + $Yb(^2F_{5/2})$ $\rightarrow$ $Yb(^2F_{7/2})$ + $Yb(^2F_{7/2})$ + $h\nu$.	

9.9 Research paper

For a facilitated overview, on the following pages the original research papers already published based on this work are reprinted:

“Magnetic Anisotropy in Functionalised Bipyridyl Cryptates”:
Main text: pages 291 to 299.
Supporting information: pages 300 to 312.

“Chiral Resolution of Lanthanoid Cryptates with Extreme Configurational Stability”:
Main text: pages 313 to 315.
Supporting information: pages 316 to 319.

“Circularly Polarised Luminescence in Enantiopure Samarium and Europium Cryptates”:
Main text: pages 320 to 328.
Supporting information: pages 329 to 334.

“Nonradiative Deactivation of Lanthanoid Luminescence by Multiphonon Relaxation in Molecular Complexes”:
Main text: pages 335 to 379.

Inorganic Chemistry

Article

pubs.acs.org/IC

Magnetic Anisotropy in Functionalized Bipyridyl Cryptates

Elisabeth Kreidt,[†] Caroline Bischof,[‡] Carlos Platas-Iglesias,*[,§] and Michael Seitz*[,†]

[†]Institute of Inorganic Chemistry, University of Tübingen, Auf der Morgenstelle 18, 72076 Tübingen, Germany

[‡]Inorganic Chemistry I, Ruhr-University Bochum, 44780 Bochum, Germany

[§]Departamento de Química Fundamental, Universidade da Coruña, Campus da Zapateira-Rúa da Fraga 10, 15008 A Coruña, Spain

Supporting Information

ABSTRACT: The magnetic properties of molecular lanthanoid complexes are very important for a variety of scientific and technological applications, with the unique magnetic anisotropy being one of the most important features. In this context, a very rigid tris(bipyridine) cryptand was synthesized with a primary amine functionality for future bioconjugation. The magnetic anisotropy was investigated for the corresponding paramagnetic ytterbium cryptate. With the use of a combination of density functional theory calculations and lanthanoid-induced NMR shift analysis, the magnetic susceptibility tensor was determined and compared to the unfunctionalized cryptate analogue. The size and orientation of the axial and rhombic tensor components show remarkably great resilience toward the decrease of local symmetry around the metal and anion exchange in the inner coordination sphere. In addition, the functionalized ytterbium cryptate also exhibits efficient near-IR luminescence.

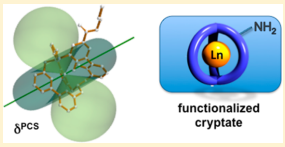

INTRODUCTION

The highly interesting physical properties of trivalent lanthanoids have made them crucial components in innovative scientific and technological applications.[1] One of the most prominent features in this respect is their unique magnetism, which has been used in many different areas such as NMR shift reagents,[2] magnetic resonance imaging contrast agents,[3] single-molecule magnets,[4] or paramagnetic tags in the structural biology of proteins.[5] One of the centrally important aspects of lanthanoid magnetism is its often very pronounced and well-defined anisotropy in the case of nonspherical f-electron distributions, that is, for all paramagnetic Ln^{3+} except Gd^{3+}. In general, the magnitude and the spatial dependence of the effects in molecular complexes are often very sensitive to the composition and the symmetry of the inner coordination sphere around the lanthanoid and the corresponding ligand field splitting of the f-orbitals. Consequently, ligand architectures that are able to provide a well-defined, unchanging coordination environment would be the best choice if time-invariant and predictable magnetic anisotropy is required. By far the most prevalent ligand class for lanthanoid complexation is based on 1,4,7,10-tetraazacyclododecane-1,4,7,10-tetraacetic acid (DOTA) and related systems.[6] Despite the great success of DOTA in fields related to lanthanoid magnetism, many DOTA-derived lanthanoid complexes often exhibit typical exchange processes that inherently affect magnetic anisotropy, for example, configurational exchange between Δ and Λ stereoisomers through rotation of the pendant arms and conformational flexibility associated with the inversion of the macrocyclic unit, which leads to interconversion between the square-antiprismatic and twisted square-antiprismatic geometries.[7] Some of these problems have been overcome with special ligand modifications[8] but remain a ubiquitous detrimental phenomenon overall. In addition, recent studies point to somewhat unpredictable magnetic behavior even in DOTA complexes with supposedly high symmetry[9] and the extreme sensitivity of the anisotropy toward exchange of additional, axially coordinated ligands such as H_2O or fluoride.[10] One of the alternatives to DOTA-derived ligand systems for lanthanoid chelation are tris(2,2′-bpy)-based cryptands (2,2′-bpy = 2,2′-bipyrdine) that have proven to be very valuable tools for bioanalytical luminescence applications.[11] Originally, they were introduced by Lehn et al. in the form of the flexible cryptates **1-Ln** (Figure 1).[12] Later development has shown the *N*,*N*′-dioxide analogues **2-Ln** to be conformationally and configurationally very stable on the NMR time scale, without any signs of the detrimental exchange processes typically observed for DOTA derivatives.[13]

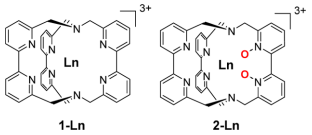

Figure 1. 2,2′-Bipyridine-based cryptate scaffolds. Flexible **1-Ln**[12] vs extremely rigid **2-Ln**.[13]

Despite the great potential that cryptates of the type **2-Ln** have in this area, this class of ligands is virtually absent from the field of lanthanoid magnetism. One of the major reasons for this phenomenon is the somewhat underdeveloped and sometimes cumbersome synthethic chemistry of cryptands, in

Received: March 8, 2016
Published: May 23, 2016

DOI: 10.1021/acs.inorgchem.6b00591
Inorg. Chem. 2016, 55, 5549−5557

contrast to the very mature synthetic methodology for the preparation of tailor-made DOTA-derivatives. Especially detrimental in this regard is the lack of cryptands with well-behaved and stable magnetic anisotropy that also have the possibility for covalent attachment via suitable, peripheral functional groups to other chemical entities such as proteins. In the past, there have been reports of a few monofunctionalized lanthanoid cryptates such as cryptates **3-Ln**[14] with a peripheral ester group or **4-Ln**[15] with a primary amine functionality for bioconjugation (Figure 2, top row). Unfortunately, these species are rather flexible and undergo the same unwanted exchange processes as seen in DOTA.

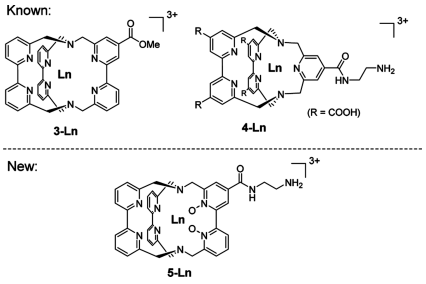

Figure 2. (top) Monofunctionalized lanthanoid cryptates **3-Ln**[14] and **4-Ln**.[15] (bottom) Rigid, monofuntionalized lanthanoid cryptate **5-Ln** developed for this study.

In this study, we alleviate this problem with the introduction of a new, monofunctionalized cryptate **5-Ln** (Figure 2, bottom) that is synthetically accessible on larger scales. For the corresponding ytterbium cryptate **5-Yb**, we investigate the influence that the functionalization and the concomitant reduction from C_2 to C_1 symmetry has on the magnetic anisotropy and the photoluminescence properties.

RESULTS AND DISCUSSION

Cryptate Design−Functionalization Strategy. The specific placement and the nature of the peripheral functional group onto the parent cryptate scaffold **2-Ln** is of crucial importance for achieving well-defined and stable complexes. First, functionalization in the 4-position on a pyridine unit is generally the most accessible from a synthetic perspective and points away from the metal binding site, therefore avoiding steric interferences with the nature of the core cryptate geometry (Figure 3). Second, our choice for the functional group fell on carboxylic acid derivatives (X in Figure 3) because of literature precedence (cf. **3-Ln** in Figure 2) and because of the great synthetic versatility of this motif for further modification/conjugation. Third and most importantly, the functionalization must be located on the 2,2′-bpy-*N*,*N*′-dioxide moiety (Figure 3, path B) and not on any of the pyridines of the 2,2′-bpy units (Figure 3, path A) to avoid the potential formation of diastereomeric cryptate species. Unfunctionalized cryptates like **2-Ln** already possess one stereogenic element in the form of the fixed helical arrangement of the biaryl moieties. Cryptates **6-Ln** (Figure 3) with the peripheral group on the bipyridines would feature a new and rather unusual stereogenic element due to the special topology of the macrobicyclic cryptand framework (Figure 4), which in turn would lead to the

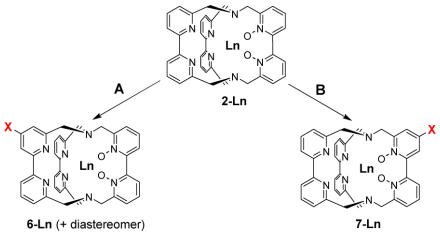

Figure 3. Possibilities for the introduction of the peripheral group X in the cryptate **2-Ln**. Path A: Functionalization at the 2,2′-bpy unit; Path B: Functionalization on the 2,2′-bpy-*N*,*N*′-dioxide moiety.

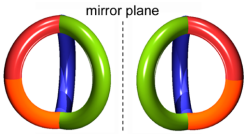

Figure 4. Unusual stereogenic element in cryptates **6-Ln** due to the topology of the macrobicyclic cryptand framework (the colors indicate the fact that all three cryptate arms are different and one is unsymmetric).

potential formation of diastereomeric cryptands. The diastereomers of the corresponding paramagnetic lanthanoid complexes would certainly have very different magnetic anisotropies which would, of course, completely defeat the purpose outlined in the introduction. The cryptates **7-Ln** do not suffer from this problem and are therefore ideal candidates for this study.

Cryptate Synthesis. The key building block for the synthesis of the cryptates **5-Ln** is the funtionalized 2,2′-bipyridine derivative **10** (Scheme 1), which is known to be

Scheme 1. Synthesis of Sodium Cryptate 15

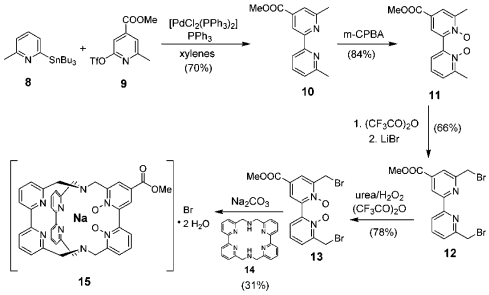

accessible by either Stille[16] or Negishi[14] cross coupling. Both reported procedures rely on chromatographic purification of **10**, which makes its preparation rather cumbersome on larger scales. We were therefore interested in developing an improved purification protocol that avoids chromatography. Our optimized approach utilizes the known Stille coupling[16] of tin precursor **8** and triflate **9** (Scheme 1). After the reaction, product **10** can conveniently be isolated in analytically pure form by a continuous liquid−liquid extraction using *n*-heptane and CH_3CN as the two liquid phases. So far, we successfully validated this protocol on scales of up to 80 mmol of starting

DOI: 10.1021/acs.inorgchem.6b00591
Inorg. Chem. 2016, 55, 5549−5557

materials (**8** and **9**) giving product **10** in rather large amounts (>13 g). The subsequent reactions to sodium cryptate **15** are straightforward and start with the oxidation of **10** to the corresponding *N*,*N*′-dioxide **11** using 3-chloroperbenzoic acid (*m*-CPBA). This is followed by a one-pot Boekelheide rearrangement/nucleophilic substitution sequence to benzylic dibromide **12**.[17] After conversion of **12** to the *N*,*N*′-dioxide **13** using improved conditions (trifluoroacetic anhydride/urea hydrogen peroxide) for the oxidation of electron-poor pyridine derivatives,[18] cryptate **15** can be obtained under standard conditions (sodium template, high dilution) by macrocyclization reaction with aza-crown ether **14**.[19]

In our first approach to transform the methyl ester in **15** into a more suitable functional group for conjugation chemistry, we were able to saponify the ester using NaOH to the corresponding carboxylate in cryptate **16** (Scheme 2) in good

Scheme 2. Synthesis of Cryptates 16 and 5-Ln

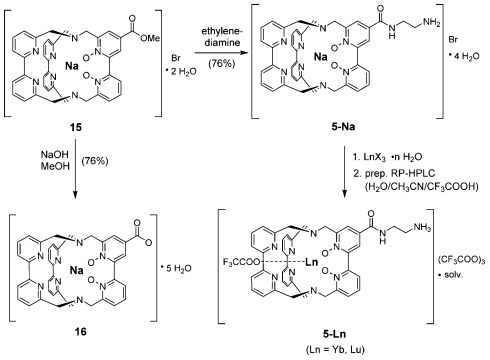

yield. Unfortunately, the carboxylate group proved to be a very sluggish reactant in peptide coupling reactions with primary amines under a variety of standard conditions (e.g., DCC/HOBt, HATU, PyBOP, etc). Because of these unexpected difficulties, we turned our attention to alternative transformations of the ester group of **15**. After a number of unsuccessful trials, we identified the reaction of **15** with an excess neat ethylene diamine to the corresponding amide **5-Na** as a very efficient way to generate a universally useful primary amine functionality for further conjugation chemistry (see analogy to cryptate **4-Ln** in Figure 2). Purification of this highly polar compound on a preparative scale is possible by column chromatography using silanized silica gel.

For the final complexation step, ytterbium was chosen as the paramagnetic center for a number of reasons: First, the analysis of its magnetic anisotropy is straightforward because of the known fact that ytterbium-induced NMR shifts in molecular complexes are overwhelmingly due to the dipolar, pseudocontact shift mechanism with only minor interference from corresponding contact shift contributions. This circumstance makes the magnetic analysis of **5-Yb** very convenient and the obtained results highly reliable. Second, we have already performed similar analyses of the magnetic anisotropies in the unfunctionalized cryptate **2-Yb** and similar species.[13d,e] Third and finally, ytterbium is not only relevant for its magnetic properties but it is also of considerable current interest in the emerging field of near-IR bioimaging because of its efficient luminescence in this spectral region.[20] In addition to the ytterbium cryptate **5-Yb**, the analogue **5-Lu** was also synthesized as a diamagnetic and photoinactive reference system. The metal exchange reaction of Ln^{3+} for Na^+ was performed similarly to the previously reported unfunctionalized cryptates **2-Ln** (Figure 1) but with the requirement for extended reaction times (t > 40 h). The crude lanthanoid cryptates with anions X^- (X = Cl, Br, or OTf) were purified by reversed-phase, preparative HPLC (H_2O+1 vol % CF_3COOH/CH_3CN). Under these harsh conditions, no decomposition of the cryptates was observed, which is an indication of the extremely high kinetic inertness of the complexes as has been seen before for similar cryptates.[11,13,15] The cryptate cations of **5-Ln** have most likely the inner-sphere composition shown in Figure 5. Because of the low pH (~1) and the great excess of

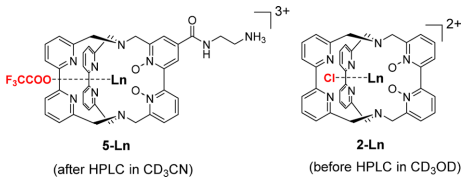

Figure 5. Composition of the inner coordination sphere of **2-Ln**[13d] and **5-Ln**.

trifluoroacetate anions in the HPLC eluent mixture, the obtained cryptates **5-Ln** are protonated at the primary amine and feature exclusively trifluoroacetate as the counteranions. From our previous studies on the corresponding unfunctionalized cryptates **2-Ln**, we know that there is exactly one available binding site in the inner coordination sphere of the lanthanoids. For example, if **2-Ln** is synthesized from $LnCl_3 \cdot 6H_2O$ and is not purified by HPLC, it features a chloride anion directly bound to the lanthanoid in methanolic solution (Figure 5, right).[13d] In the case of **5-Yb**, ^{19}F NMR in CD_3CN after HPLC purification shows two singlet resonances, one at −76.4 ppm and another at −116.5 ppm in an integrated ratio of 3:1. While the former signal is in the typical range for free trifluoroacetate anions,[21] we interpret the latter as originating from a paramagnetically shifted inner-sphere trifluoroacetate.

Chemical Structure in Solution—Nuclear Magnetic Resonance/Density Functional Theory. The investigations into the effects that structural variations of the core cryptate scaffold **2-Yb** have on the nature and spatial orientation of the corresponding magnetic anisotropy were performed by analyzing the lanthanoid-induced, paramagnetic ^1H NMR shifts. To assess these changes, we used the differences outlined in Figure 5, that is, the introduction of the peripheral functionalization in **5-Yb** resulting in the reduction of overall symmetry (from C_2 in **2-Yb** to C_1) and the exchange of a trifluoroacetate anion in **5-Yb** for the inner-sphere chlorido ligand in **2-Yb**. Both effects could potentially have an enormous impact on magnetic anisotropy as it has been documented recently in DOTA-derived systems.[9,10]

The ^1H NMR spectrum of **5-Yb** in CD_3CN (Figure 6b) shows a set of 29 paramagnetically shifted but very well-defined resonances corresponding to the immediate cryptate core structure (i.e., aromatic and benzylic hydrogen atoms in **5-Yb**). The signals for the C−H moieties in the peripheral ethylene diamine unit could not be identified unambiguously because of

DOI: 10.1021/acs.inorgchem.6b00591
Inorg. Chem. 2016, 55, 5549−5557

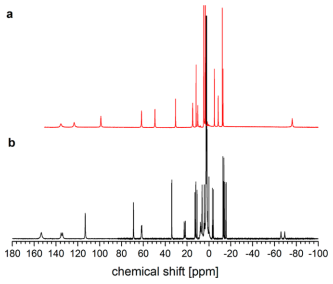

Figure 6. ^{1}H NMR spectra of (a) unfunctionalized **2-Yb** (CD_3OD, 400 MHz)[13d] with chloride in the inner coordination sphere and (b) functionalized **5-Yb** (CD_3CN, 500 MHz) with trifluoroacetate bound to the lanthanoid.

overlap with strong residual solvent signals. Overall, the spectral features are similar to the ones observed for **2-Yb** in CD_3OD (Figure 6a).[13d] Typically, signals that could be observed as singlets with an integral of two protons, in the case of **2-Yb**, split into two singlets for **5-Yb** with an integral of one proton each (see, e.g., the signals between −60 and −80 ppm in Figure 6). The shifts of the signals of the formerly equivalent protons show small separations, but the differences do not exceed 3.5 ppm. As in the case of the parent compound **2-Yb**, no exchange processes on the NMR time scale are observable for **5-Yb**.

Density functional theory (DFT) calculations in CH_3CN were performed on the cryptate cation of **5-Yb** to get a deeper understanding of the spatial structure of the cryptate. To keep the sizable computational demands as low as possible, we used a simplified model system with a water molecule bound to ytterbium instead of the actually present inner-sphere trifluoroacetate (cf. Figure 5). The obtained structure (Figure 7) shows great similarity to the calculated structure for **2-Yb**[13d]

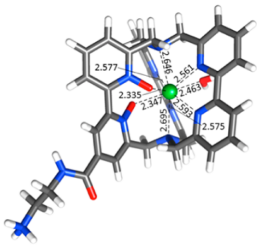

Figure 7. Calculated structure of **5-Yb** optimized in CH_3CN solution at the TPSSh/LCRECP/6-31G(d,p) level and bond distances of the metal coordination environment (Å).

(DFT) and the crystallographically determined one previously reported for the structurally related cryptate **2-Lu**.[13b] The optimized geometry for **5-Yb** retains a nearly undistorted, local C_2 symmetry in the immediate coordination sphere around the metal, where the symmetry axis contains the oxygen atoms of the coordinated water molecule and the Yb(III) ion. The general arrangement of the biaryl units remains virtually unaffected by the functionalization of the ligand.

Lanthanoid-Induced NMR Shift Analysis. The paramagnetic ^{1}H NMR shifts of the cryptate **5-Yb** were analyzed following the previously reported methodology,[13d,22] assuming that they are dominated by the pseudocontact contribution (δ^{pc}), which can be expressed as a linear combination of the five components of the magnetic susceptibility tensor χ:[23]

$$\delta^{pc} = \left(\chi_{zz} - \frac{1}{3}\mathrm{Tr}\chi\right)\left(\frac{3z^2 - r^2}{r^5}\right) + (\chi_{xx} - \chi_{yy})\left(\frac{x^2 - y^2}{r^5}\right) + \chi_{xy}\left(\frac{4E}{r^5}\right) + \chi_{xz}\left(\frac{4xz}{r^5}\right) + \chi_{yz}\left(\frac{4yz}{r^5}\right) \text{ with } r = \sqrt{x^2 + y^2 + z^2}$$

Here, x, y and z represent the Cartesian coordinates of the observed nuclei with the paramagnetic ion placed at the origin. In the principal magnetic axis system, the tensor is diagonalized, so that $\chi_{xy} = \chi_{xz} = \chi_{yz} = 0$. Thus, the pseudocontact shifts were analyzed by using a five-parameter least-squares search that minimizes the difference between the experimental and calculated pseudocontact shifts. These five parameters are $(\chi_{zz} - 1/3\mathrm{Tr}\chi)$, $(\chi_{zz} - \chi_{yy})$, and a set of Euler angles that relate the principal magnetic axis system to the molecular coordinate system. Given the small chemical shift differences introduced by the absence of C_2-symmetry in **5-Yb**, we carried out this analysis using averaged chemical shifts (Table 1). The ^{1}H NMR

Table 1. Comparison of Experimental and Calculated ^{1}H NMR Shifts[a] for 5-Yb in Acetonitrile

proton	δ_i^{exp}	δ_i^{avg} [b]	$\delta_i^{avg,cald}$ [c]
H1o	−69.35/−65.97	−67.66	−68.46
H2o	21.63/22.55	22.09	25.89
H3o	12.79/10.88	11.84	12.73
H4o	0.02	0.02	2.11
H5o	−13.19/−14.55	−13.87	−13.96
H1b	153.49[d]	153.49	148.05
H2b	61.82/61.35	61.59	63.50
H3b	−3.18/-4.07	−3.63	−2.65
H4b	−12.82/-13.72	−13.27	−11.88
H5b	−15.59/-15.85	−15.72	−15.06
H6b	12.04/11.97	12.01	10.63
H7b	34.09/33.97	34.01	33.32
H8b	69.10/68.99	69.05	68.81
H9b	113.22[d]	113.22	114.63
H10b	135.27/133.96	134.62	137.96
AF_j [e]		0.0321	
$\chi_{zz} - \frac{1}{3}Tr\chi$		2740 ± 62	ppm Å^3
$\chi_{xx} - \chi_{yy}$		−8601 ± 138	ppm Å^3

[a]See Figure 8 for numbering scheme. [b]Averaged chemical shifts. [c]Values obtained from the analysis of the paramagnetic shifts assuming that the paramagnetic shifts are purely pseudocontact in origin. [d]Only one signal is observed. [e]$AF_j = [\sum_i (\delta_i^{exp} - \delta_i^{cal})^2 / \sum_i (\delta_i^{exp})^2]^{1/2}$, where δ_i^{exp} and δ_i^{exp} represent the experimental and calculated values of a nucleus i, respectively.

chemical shifts of the unfunctionalized lutetium cryptate **2-Lu**[13d] were used to estimate the diamagnetic contributions. The DFT structure of **5-Yb** (Figure 7) optimized in acetonitrile solution provides very good agreement between the experimental and calculated Yb-induced shifts, with an agreement factor AF_j = 0.032 (Figure 8, Table 1). The excellent match between experiment and theory unambiguously proves that our DFT calculations provide a very accurate description of the

DOI: 10.1021/acs.inorgchem.6b00591
Inorg. Chem. 2016, 55, 5549−5557

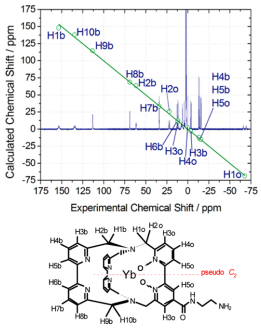

Figure 8. Experimental ^{1}H NMR spectrum (CD_3CN, 500 MHz) of **5-Yb**, plot of experimental versus calculated shifts, and numbering scheme for the hydrogen atoms in **5-Yb** (protons that would be related by the pseudo C_2 symmetry in the unfunctionalized cryptate have the same name). The solid line represents a perfect fit between experimental and calculated values.

structure of this complex, as much higher agreement factors $AF_i \approx 0.06-0.09$ have been considered to be acceptable for different nonaxial Yb(III) complexes.[24]

Magnetic Anisotropy. Multiple studies in the past have shown that magnetic anisotropy and hence the induced pseudocontact NMR shifts of Yb(III) complexes can be profoundly different upon subtle changes in the lanthanoid coordination environment.[9,10] For the purpose of this study, we can compare two factors governing the magnetic anisotropy in the related cryptates **2-Yb** and functionalized **5-Yb**, the reduction in symmetry from C_2 to C_1 and the exchange of inner-sphere monodentate ligands (Figure 5: chloride vs trifluoroacetate). As expected given the similarity of the measured chemical shifts of **2-Yb** and **5-Yb** (see Figure 6), the calculated axial ($\chi_{zz} - 1/3\mathrm{Tr}\chi$ = 2740 ppm Å^3) and rhombic ($\chi_{xx} - \chi_{yy}$ = −8601 ppm Å^3) components of the magnetic susceptibility tensor in **5-Yb** (Table 1) are very similar to those obtained previously for the unfunctionalized cryptate **2-Yb** ($\chi_{zz} - 1/3\mathrm{Tr}\chi$ = 2197 ppm Å^3; $\chi_{xx} - \chi_{yy}$ = −7916 ppm Å^3).[13d] Figure 9 shows a schematic representation of the core cryptate **5-Yb** surrounded by an isosurface of the induced pseudocontact shifts.

In addition to the size of the tensor components being similar in **2-Yb** and **5-Yb**, the relative spatial orientation of the two different tensors are also remarkably similar. Figure 10 clearly shows that the pseudocontact isosurfaces as a manifestation of the underlying tensors are almost indistinguishable apart from very small differences in size and virtually none in terms of orientation. This result underscores the very robust nature of the tensors in these cryptates with a remarkable degree of tolerance for functionalization and inner-sphere substitution of monodentate ligands.

Luminescence Properties. The unfunctionalized parent compound **2-Yb** has very favorable photoluminescence properties, especially after perdeuteration of the cryptand scaffold,[13b,d,e] which could be very interesting for bioanalytical applications using the new functionalized cryptates.[20] Therefore, we also measured the luminescence of **5-Yb** to see whether we could find any detrimental effect of functionalization on the photophysical properties. In the case of the indirect lanthanide sensitization via the surrounding organic ligand

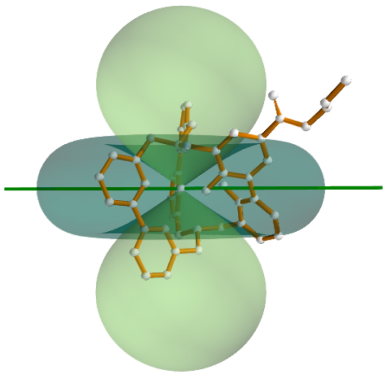

Figure 9. Graphical representation of **5-Yb** (without the bound water molecule) and the pseudocontact shift isosurface (light green: +12 ppm, dark green: −12 ppm; negative shifts correspond to shifts to lower field) corresponding to the magnetic susceptibility tensor χ. The green line illustrates the effective C_2 symmetry axis.[25]

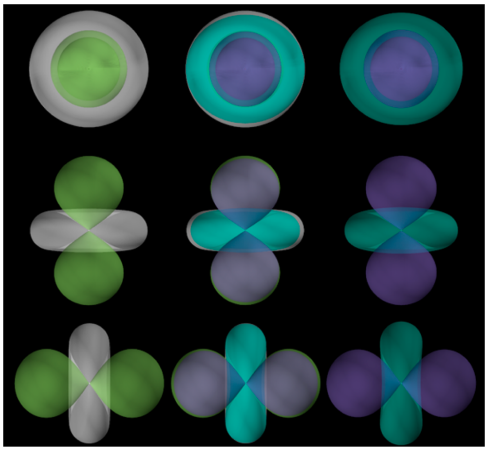

Figure 10. Graphical representation of the size and orientations of the pseudocontact shift isosurfaces of the functionalized and unfunctionalized cryptate along the three different Cartesian coordinate axes (rows) − Right column: **2-Yb**;[13d]Left column: **5-Yb**; Middle column: Overlay of **2-Yb** and **5-Yb**.

(antenna effect), the energy is usually transferred to the lanthanoid from the ligand-centered excited triplet level. From the low-temperature (77 K) steady-state emission spectrum of the photoinactive lutetium cryptate **5-Lu** (Figure 11), we could obtain an estimate for the zero-phonon $T_1 \rightarrow S_0$ transition energy $E(T_1) \approx 20\,400$ cm^{-1}, which is virtually identical to the values previously found for **2-Lu**[13b] and **2-Gd**.[26] Like **2-Yb**, functionalized **5-Yb** shows rather strong steady-state photoluminescence after excitation at λ_{ex} = 305 nm in CD_3OD (Figure 12) with an almost identical band shape of the transition $^2F_{5/2} \rightarrow {}^2F_{7/2}$ compared to the spectrum for **2-Yb**.[13c] In addition, the observed monoexponential luminescence decay (Figure 13) with a lifetime of τ_{obs} = 10.8 μs is also very similar

DOI: 10.1021/acs.inorgchem.6b00591
Inorg. Chem. 2016, 55, 5549−5557

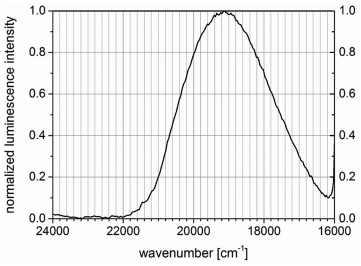

Figure 11. Low-temperature steady-state emission spectra (λ_{exc} = 315 nm, T = 77 K) for **5-Lu** in a glassy CH_3OH/EtOH matrix (1:1, v/v).

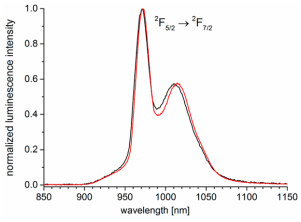

Figure 12. Normalized steady-state emission spectra for **5-Yb** (black) and for **2-Yb** (red)[13c] in solution (CD_3OD, λ_{exc} = 305 nm, emission path: long pass filter RG780).

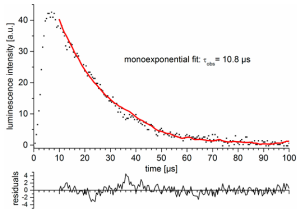

Figure 13. Luminescence decay profile of **5-Yb** (black) and monoexponential fit in red (CD_3OD, λ_{exc} = 305 nm, λ_{em} = 970 nm).

to the behavior observed for **2-Yb** (τ_{obs} = 12.3 μs) under identical conditions. Taken together, the excellent photoluminescence properties documented previously for the unfunctionalized cryptate **2-Yb** are completely retained in the functionalized cryptates **5-Yb**.

CONCLUSION

In summary, we have developed a practical synthetic route to rigid lanthanoid cryptates **5-Ln** (Ln = Yb, Lu) with a peripheral primary amino group for future conjugation chemistry to biomolecules. These species are highly stable in solution and can even be purified by reversed-phase HPLC. In addition, the functionalized ytterbium cryptate retains all excellent physical properties found in the unfunctionalized parent cryptate **2-Yb**, such as well-defined, time-invariant magnetic anisotropy and efficient photoluminescence in solution. Particularly remarkable is the great apparent resilience of its magnetic anisotropy toward changes in symmetry and anion exchange in the inner-coordination sphere. These findings show that this type of lanthanoid cryptate will be a very good candidate in future applications where stable magnetic properties are key and where DOTA-derived systems still suffer from fluxional magnetic behavior due to conformational and configurational exchange processes in the ligand backbone.

EXPERIMENTAL SECTION

General. Solvents were dried by standard procedures (tetrahydrofuran (THF), xylenes: Na; CH_2Cl_2; CaH_2), dry dimethylformamide (DMF) was used as purchased. Air-sensitive reactions were performed under a dry, dioxygen-free atmosphere of N_2 using Schlenk technique. Column chromatography was performed with silica gel 60 (Merck KGaA, 0.063−0.200 mm) or for cryptate **5-Na** with silanized silica gel 60 (Merck KGaA, 0.063−0.200 mm). Analytical thin layer chromatography (TLC) was done on silica gel 60 F_{254} plates (Merck, coated on aluminum sheets). Electrospray ionization (ESI) mass spectrometry was measured using Bruker Daltonics Esquire 3000plus or Bruker Daltonics APEX II FT-ICR (FAB). NMR spectra were measured on a Bruker AVII+500 (^{1}H: 500 MHz), AVII+400 (^{1}H: 400 MHz), DPX-250 (^{1}H: 250 MHz, ^{13}C: 62.9 MHz), and DPX-200 (^{1}H: 200 MHz, ^{13}C: 50 MHz).

Density Functional Theory Calculations. All calculations were performed employing DFT within the hybrid meta generalized gradient approximation, with the TPSSh exchange-correlation functional,[27] and the Gaussian 09 package (Revision D.01).[28] Full geometry optimizations of **5-Yb** were performed in acetonitrile solution by using the large-core relativistic effective core potential (LCRECP) of Dolg et al. and the related [5s4p3d]-GTO valence basis set for Yb,[29] and the standard 6-31G(d,p) basis set for C, H, N, and O atoms. No symmetry constraints were imposed during the optimizations. The default values for the integration grid ("fine") and the self-consistent field energy convergence criteria (1×10^{-8}) were used. The stationary points found on the potential energy surfaces as a result of the geometry optimizations were tested to represent energy minima rather than saddle points via frequency analysis. Solvent effects (acetonitrile) were taken into account by using the integral equation formalism variant of the polarizable continuum model as implemented in Gaussian 09.[30]

Luminescence Spectroscopy. Steady-state emission spectra were acquired on a PTI Quantamaster QM4 spectrofluorimeter using 1.0 cm quartz cuvettes. The excitation light source was a 75 W continuous xenon short arc lamp. Emission was monitored at 90° using a PTI P1.7R detector module (Hamamatsu PMT R5509−72 with a Hamamatsu C9525 power supply operated at −1500 V and a Hamamatsu liquid N_2 cooling unit C9940 set to −80 °C). For the near-IR steady-state emission measurements, a long-pass filter RG-780 (Schott, 3.0 mm thickness, transmission >83% between 800 and 850 nm and >99% between 850 and 1700 nm) was used in the emission channel to avoid higher-order excitation light. Low-temperature spectra were recorded on frozen glasses of solutions of **5-Lu** (MeOH/EtOH 1:1, v/v) using a dewar cuvette filled with liquid N_2 (T = 77 K). Spectral selection was achieved by single grating monochromators (excitation: 1200 grooves/mm, blazed at 300 nm; near-IR emission: 600 grooves/mm, blazed at 1200 nm). Luminescence lifetimes were determined with the same instrumental setup without the use of the long-pass filter. The light source for these measurements was a xenon flash lamp (Hamamatsu L4633; 10 Hz repetition rate, pulse width ca. 1.5 μs full width at half-maximum). Lifetime data analysis (deconvolution, statistical parameters, etc.) was performed using the software package FeliX32 from PTI. Lifetimes were determined by deconvolution fitting of the decay profiles with the instrument response function, which was determined using a dilute aqueous dispersion of colloidal silica (Ludox AM-30). The estimated uncertainties in τ are ±10%.

Synthesis. *6,6′-Dimethyl-2,2′-bipyridine-4-carboxylic Acid Methyl Ester (**10**).* Under N_2, a two-neck Schlenk flask equipped with a reflux condenser was charged with 2-methyl-6-(trifluoromethylsulfonyloxy)-isonicotinic acid methyl ester (**9**)[16] (11.97 g, 40.00 mmol, 1.0 equiv), 2-methyl-6-(tributylstannyl)pyridin (**8**)[16] (15.29 g, 40.00 mmol, 1.0 equiv), and PPh_3 (1.05 g, 4.00 mmol, 0.1 equiv) in dry

DOI: 10.1021/acs.inorgchem.6b00591
Inorg. Chem. 2016, 55, 5549−5557

xylene (300 mL, isomeric mixture). The solution was degassed by one freeze−pump−thaw cycle before solid $[PdCl_2(PPh_3)_2]$ (1.40 g, 2.00 mmol, 0.05 equiv) was added. After two additional freeze−pump−thaw cycles, the yellow suspension was heated to reflux for 24 h. The reaction mixture was allowed to come to ambient temperature and was poured into a saturated, aqueous solution of Na_2H_2EDTA (300 mL). The aqueous phase was extracted with CH_2Cl_2 (3 × 300 mL), and the combined organic phases were dried ($MgSO_4$) and concentrated under reduced pressure. The remaining residue was dissolved in CH_3CN, and the solution was extracted continuously in a liquid−liquid extractor with *n*-heptane for 24 h. The pale yellow product, which crystallized from the extract after standing overnight at room temperature, was collected, washed with *n*-heptane, and dried in vacuo (6.78 g, 70%). The analytical data were in complete agreement with the literature.[14,16]

^{1}H NMR (200 MHz, $CDCl_3$): δ = 8.72 (s, 1 H), 8.20 (d, J = 7.8 Hz, 1 H), 7.71 (s, 1 H), 7.68 (d, J = 7.8 Hz, 1 H), 7.18 (d, J = 7.8 Hz, 1 H), 3.98 (s, 3 H), 2.72 (s, 3 H), 2.69 (s, 3 H) ppm.

*6,6′-Dimethyl-4-methyloxycarbonyl-2,2′-bipyridine N,N′-dioxide (**11**).* With cooling in an ice bath, a solution of *m*-chloroperoxybenzoic acid (32.35 g of 77 wt %, 24.90 g of pure, 144 mmol, 2.4 equiv) in CH_2Cl_2 (750 mL) was added dropwise to a solution of 6,6′-dimethyl-2,2′-bipyridine-4-carboxylic acid methyl ester (**10**) (14.57 g, 60.1 mmol, 1.0 equiv) in CH_2Cl_2 (600 mL) over the course of 1.5 h. The pale yellow solution was allowed to reach room temperature over ca. 3 h and was stirred overnight. After extraction of the reaction mixture with aq. $NaHCO_3$ solution (pH 8, 2 × 300 mL) and water (300 mL), the organic layer was dried over $MgSO_4$, and the solvent was removed under reduced pressure (bath temperature <35 °C). The crude product was purified by column chromatography (SiO_2, CH_2Cl_2/MeOH 100:1 → 24:1) to afford the title compound as an off-white solid (13.85 g, 84%).

^{1}H NMR (250 MHz, $CDCl_3$): δ = 8.01 (br s, 2 H), 7.49−7.30 (m, 3 H), 3.94 (s, 3 H), 2.64 (s, 3 H), 2.61 (s, 3 H) ppm. ^{13}C NMR (62.9 MHz, $CDCl_3$): δ = 164.1, 150.2, 150.0, 143.7, 143.2, 127.3, 126.8, 125.7, 125.5, 125.3, 124.9, 52.7, 17.97, 17.94. MS (FAB, pos. mode): m/z (%) = 275.1 (100, $[M + H]^+$), 259.1 (13). TLC: R_f = 0.08 (SiO_2, CH_2Cl_2/MeOH 24:1, detection: UV). mp:190−192 °C (decomp).

*6,6′-Bis(bromomethyl)-2,2′-bipyridine-4-carboxylic Acid Methyl Ester (**12**).*[17] Under N_2, $(CF_3CO)_2O$ (44.1 mL, 66.6 g, 317 mmol, 12 equiv) was added dropwise via syringe to a yellow solution of **11** (7.25 g, 26.4 mmol, 1.0 equiv) in dry CH_2Cl_2 (80 mL). The brown reaction mixture was heated under reflux for 1.5 h before the volatiles were removed in vacuo. Under N_2, the obtained orange residue was dissolved in a mixture of dry DMF/THF (40 mL, 1:1, v/v). Under N_2 and with ice-cooling, anhydrous LiBr (18.4 g, 211 mmol, 8.0 equiv) was dissolved in dry THF (50 mL), and the cold solution was added dropwise to the reaction mixture. After it was stirred at room temperature for 12 h, the solvents were removed under reduced pressure (bath temperature 40 °C). The brown residue was dissolved in CH_2Cl_2/water (400 mL, 1:1, v/v), and the aqueous phase was adjusted to pH ≈ 6 with saturated aqueous Na_2CO_3. The organic layer was washed with additional water (2 × 150 mL), dried ($MgSO_4$), and concentrated to dryness. The crude product was purified by column chromatography (SiO_2, CH_2Cl_2/MeOH 100:1, preloading onto SiO_2) to give the product as a yellow solid (7.00 g, 66%).

^{1}H NMR (200 MHz, $CDCl_3$): δ = 8.97−8.84 (m, 1 H), 8.47−8.33 (m, 1 H), 8.08−7.96 (m, 1 H), 7.90 (t, J = 7.8 Hz, 1 H), 7.59−7.47 (m, 1 H), 4.73 (s, 2 H), 4.69 (s, 2 H), 4.02 (s, 4 H) ppm. ^{13}C NMR (50 MHz, $CDCl_3$): δ = 165.4, 157.6, 156.6, 156.4, 154.4, 139.9, 138.5, 124.4, 123.1, 121.0, 120.2, 53.0, 33.6, 33.4 ppm. MS (ESI, pos. mode): m/z (%) 258.99 (42), 336.88 (46), 400.74 (100, $[M + H]^+$), 422.69 (100, $[M + K]^+$). TLC: R_f = 0.64 (SiO_2, CH_2Cl_2/MeOH 100:1, detection UV).

*6,6′-Bis(bromomethyl)-4-methyloxycarbonyl-2,2′-bipyri-dine N,N′-dioxide (**13**).*[18] Under N_2 and with cooling in an ice bath, urea/H_2O_2 adduct (3.77 g, 40.1 mmol, 2.3 equiv) was added in portions to a suspension of **3** (6.97 g, 17.4 mmol, 1.0 equiv) in dry CH_2Cl_2 (300 mL). Then, $(CF_3CO)_2O$ (5.6 mL, 8.42 g, 40.1 mmol, 2.3 equiv) was added slowly; the mixture was allowed to warm to room temperature and stirred overnight (15 h). A saturated solution of sodium thiosulfate pentahydrate (10 mL) and water (200 mL) was added, and the mixture was stirred for 30 min. The phases were separated, and the aqueous phase was extracted with CH_2Cl_2 (2 × 75 mL). The combined organic layers were dried ($MgSO_4$) and concentrated. The isolated crude product was purified by column chromatography (SiO_2, CH_2Cl_2/MeOH 100:1 → 25:1, preloading onto SiO_2) to give the title compound as a colorless solid (5.85 g, 78%).

^{1}H NMR (200 MHz, $CDCl_3$): δ = 8.23 (d, J = 2.5 Hz, 1 H), 8.14 (d, J = 2.4 Hz, 1 H), 7.67 (dd, J = 2.0, 7.5 Hz, 1 H), 7.59−7.50 (m, 1 H), 7.34 (t, J = 7.9 Hz, 1 H), 4.73 (s, 2 H), 4.70 (s, 2 H), 3.96 (s, 3 H) ppm. ^{13}C NMR (126 MHz, $CDCl_3$): δ = 163.7, 148.4, 148.2, 143.6, 142.7, 128.0, 127.9, 127.8, 127.5, 125.3, 124.7, 53.1, 25.4, 25.1 ppm. MS (ESI$^+$): m/z (%) = 454.73 (100, $[M + Na]^+$, Br_2-pattern). TLC: R_f = 0.22 (SiO_2, CH_2Cl_2/MeOH 25:1, detection: UV).

*Sodium Cryptate **15**.* Under N_2, macrocycle **14**[19] (0.48 g, 1.22 mmol, 1.0 equiv) and the dibromide **13** (0.53 g, 1.22 mmol, 1.0 equiv) were dissolved in CH_3CN (500 mL, HPLC grade), and Na_2CO_3 (1.29 g, 12.2 mmol, 10 equiv) was added. The mixture was heated under reflux for 40 h, cooled to ambient temperature, and filtered. The filtrate was concentrated under reduced pressure, and the resulting residue was subjected to column chromatography (SiO_2, gradient: CH_2Cl_2/MeOH 15:1 → 9:1) to yield the title compound as a light-yellow solid (0.30 g, 31%).

^{1}H NMR (200 MHz, $CDCl_3$): δ = 8.26−8.18 (m, 1 H), 8.10−8.02 (m, 1 H), 8.01−7.92 (m, 1 H), 7.88−7.60 (m, 8 H), 7.58−7.33 (m, 4 H), 4.32 (d, J = 12.0 Hz, 1 H), 4.29 (d, J = 11.7 Hz, 1 H), 4.08−3.31 (m, 13 H) ppm. ^{13}C NMR (50.3 MHz, $CDCl_3$): δ = 163.6, 158.8, 158.4 157.8, 157.6, 157.1, 157.0, 156.4, 156.2, 148.6, 148.5, 145.5, 144.0, 138.32, 138.30, 130.2, 128.6, 126.9, 126.8, 125.4, 125.3, 124.74, 124.68, 122.2, 122.1, 121.3, 121.2, 60.9, 60.70, 60.66, 60.62, 54.6, 54.3, 53.1 ppm. MS (ESI, pos. mode): m/z (%) = 687.20 (100, $[M]^+$).TLC: R_f = 0.45 (SiO_2, CH_2Cl_2/MeOH 9:1, detection UV + I_2 vapor). Anal. Calcd (Found) for $C_{38}H_{32}BrN_8NaO_4{\cdot}2\,H_2O$ (M_r = 803.64): C, 56.79 (56.61); H, 4.52 (4.28); N, 13.94 (13.73).

*Sodium Cryptate **16**.* Compound **15** (71.0 mg, 88.3 μmol, 1.0 equiv) was dissolved in MeOH (8 mL), and a solution of NaOH (18.5 mg, 462 μmol, 5.2 equiv) in water (2 mL) was added dropwise. The solution was stirred at 40 °C (bath temperature) for 3 h. The solvents were removed, and the residue was subjected to column chromatography (SiO_2, CH_2Cl_2/MeOH 2:1, detection: UV). The product was obtained as a colorless solid (51 mg, 76%).

^{1}H NMR (200 MHz, CD_3OD): δ = 8.22 (d, J = 2.3 Hz, 1 H), 8.14 (d, J = 2.3 Hz, 1 H), 7.99−7.73 (m, 10 H), 7.66−7.36 (m, 5 H), 4.30 (d, J = 11.8 Hz, 2 H), 3.95−3.75 (m, 4 H), 3.64−3.34 (m, 6 H) ppm. ^{13}C NMR (50.3 MHz, CD_3OD): δ = 169.5, 160.1, 159.3, 159.2, 157.91, 157.88, 150.2, 149.5, 146.6, 145.9, 139.5, 139.3, 131.0, 130.6, 128.5, 128.4, 128.1, 125.61, 125.56, 125.51, 123.13. 123.11, 122.34, 122.31, 61.81, 61.73, 61.69, 55.63, 55.55 ppm. MS (ESI, pos. mode): m/z (%) = 673.21 (66, $[M + H]^+$), 695.17 (100, $[M + Na]^+$). R_f = 0.17 (SiO_2, CH_2Cl_2/MeOH 2:1, detection: UV). Anal. Calcd (Found) for $C_{37}H_{29}N_8NaO_4{\cdot}5H_2O$ (M_r = 762.74): C, 58.26 (57.96); H, 5.15 (4.94); N, 14.69 (14.72).

*Sodium Cryptate **5-Na**.* Under N_2 and with ice-cooling, **15** (250.7 mg, 0.327 mmol, 1.0 equiv) was added as a solid to freshly dried and distilled ethylenediamine (3.5 mL, 3.15 g, 52.4 mmol, 150 equiv). The slightly red suspension was allowed to warm to room temperature and stirred for 2 d before the volatiles were removed in vacuo. The crude product was subjected to column chromatography (silanized SiO_2, CH_2Cl_2/MeOH 24:1, preloading onto silanized SiO_2) to give pure **5-Na** as an off-white solid (197 mg, 76%).

^{1}H NMR (250 MHz, CD_3OD): δ = 8.48 (d, J = 2.3 Hz, 1 H), 8.35 (d, J = 2.6 Hz, 1 H), 7.96−7.82 (m, 9 H), 7.79 (dd, J = 2.0, 7.8 Hz, 1 H), 7.62−7.53 (m, 1 H), 7.51−7.42 (m, 4 H), 4.43−4.30 (m, 2 H), 4.02−3.85 (m, 4 H), 3.83−3.60 (m, 4 H), 3.59−3.39 (m, 4 H), 3.30−3.20 (m, 2 H) ppm. ^{13}C NMR (62.9 MHz, CD_3OD): δ = 166.3, 160.1, 159.3, 159.2, 158.3, 157.8, 150.25, 150.23, 146.2, 146.0, 139.6, 139.4, 131.9, 131.4, 128.71, 128.69, 126.8, 125.7, 123.2, 122.4, 61.9, 61.82, 61.75, 61.6, 55.5, 55.4, 41.0, 39.4 ppm. MS (ESI, pos. mode): m/z (%) 357.99 (34), 715.10 (100, $[M]^+$). Anal. Calcd (Found) for

DOI: 10.1021/acs.inorgchem.6b00591
Inorg. Chem. 2016, 55, 5549−5557

$C_{39}H_{36}BrN_{10}NaO_3 \cdot 4\ H_2O$ (M_r = 867.72): C, 53.98 (53.85); H, 5.11 (4.92); N, 16.14 (16.00). TLC: R_f = 0.48 (SiO_2, CH_2Cl_2/MeOH 4:1, detection UV + ninhydrin).

Synthesis of Ln Complexes ***5-Ln****—General Procedure.* The sodium cryptate **5-Na** (1.0 equiv) and $Ln(X)_3 \cdot nH_2O$ (1.7 equiv) were suspendend in CH_3CN (HPLC grade), and the mixture was heated under reflux for at least 40 h. The solvent was removed in vacuo, and the remaining residue was taken up in a minimum of CH_3CN/H_2O (1:1, v/v) and subjected to preparative reversed-phase HPLC (Lichrospher RP-18e, 250× 10 mm-10 μm, flow rate: 3.0 mL min^{-1}, UV detection: 300 nm) with H_2O (+1% TFA, v/v) as mobile Phase A, CH_3CN (HPLC grade) as mobile Phase B, and the following gradient: 0 min: 85%A/15%B; 5 min 85%A/15%B; 19 min: 45%A/55%B; 25 min: 45%A/55%B; 40 min: 85%A/15%B; 50 min: 85%A/15%B.

The composition of the collected fractions was checked by analytical, reversed-phase HPLC (Lichrospher RP-18e, 125 × 4 mm-5 μm, flow rate: 1 mL min^{-1}, UV detection: 300 nm), using the same mobile phase mixture and gradient (see Supporting Information for HPLC traces). Fractions containing pure lanthanoid complexes **5-Ln** were combined (retention times $t_r \approx$ 12.6−12.7 min) and evaporated to dryness at room temperature. The complexes were isolated as off-white or faintly yellow solids.

Ytterbium Cryptate ***5-Yb****.* **5-Na** (30 mg, 38 μmol, 1.0 equiv) and $YbCl_3 \cdot 6\ H_2O$ (25 mg, 63 μmol, 1.7 equiv) in 15 mL of CH_3CN (HPLC grade). Yield: 14 mg.

^{1}H NMR (500 MHz, CD_3CN): δ = 153.5 (H1b, 2 H), 135.3/134.0 (H10b, 2 H), 113.2 (H9b, 2 H), 69.1/69.0 (H8b, 2 H), 61.8/61.4 (H2b, 2 H), 34.1/33.9 (H7b, 2H), 22.6/21.6 (H2o, 2H), 12.8/10.9 (H3o, 2 H), 12.04/11.97 (H6b, 2 H), 0.02 (H4o, 1 H), −3.2/−4.1 (H3b, 2 H), −12.8/−13.7 (H4b, 2 H), −13.2/−14.6 (H5o, 2 H), −15.6/−15.9 (H5b, 2 H), −66.0/−69.4 (H1o, 2H) ppm. Remarks: (a) The signals representing the four protons of the ethylene group could not be identified unambigiously, as in the respective region of the spectrum there are several solvent signals; (b) The numbering scheme uses the same name for protons that would be symmetry-related in the unfunctionalized cryptate, see Figure 8. ^{19}F NMR (376 MHz, CD_3CN): δ = −76.4 (s, 9 F), −116.5 (s, 3 F) ppm. ^{19}F NMR (376 MHz, CD_3OD): δ = −77.0 (s, 9 F), −114.4 (s, 3 F) ppm. MS (ESI, pos. mode): *m*/*z* (%) = 489.7 (100, $\{[Yb(II)(L)] + CF_3COO\}^{2+}$), 560.8 (58). Analytical HPLC: t_r = 12.7 min (see Figure S13 in the Supporting Information).

Lutetium Cryptate ***5-Lu****.* **5-Na** (20 mg, 25 μmol, 1.0 equiv) and $Lu(OTf)_3$ (27 mg, 43 μmol, 1.7 equiv) in 15 mL of CH_3CN (HPLC grade). Yield: 18 mg.

^{1}H NMR (400 MHz, CD_3CN): δ = 10.0 (t, *J* = 4.6 Hz, 1 H), 8.90 (d, *J* = 2.3 Hz, 1 H), 8.70 (d, *J* = 2.4 Hz, 1 H), 8.48 (dd, *J* = 1.7, 7.8 Hz, 1 H), 8.33−8.28 (m, 2 H), 8.23−8.05 (m, 8 H), 7.62−7.55 (m, 4 H), 4.79−4.71 (m, 4 H), 4.13−3.93 (m, 6 H), 3.84 (d, *J* = 13.1 Hz, 1 H), 3.80−3.64 (m, 5 H), 3.23 (t, *J* = 5.3 Hz, 2 H) ppm. MS (ESI, pos. mode.): *m*/*z* (%) = 360. (87), 478.3 (79), 561.3 (84), 697.3 (100). Analytical HPLC: t_r = 12.6 min (see Figure S14 in the Supporting Information).

■ ASSOCIATED CONTENT

Supporting Information

The Supporting Information is available free of charge on the ACS Publications website at DOI: 10.1021/acs.inorgchem.6b00591.

NMR spectra of the compounds **10**, **11**, **12**, **13**, **15**, **16**, **5-Na**, and **5-Lu**. HPLC traces for **5-Ln**. Cartesian coordinates for the structure of **5-Yb** as obtained by DFT calculations. (PDF)

■ AUTHOR INFORMATION

Corresponding Authors

*E-mail: michael.seitz@uni-tuebingen.de. (M.S.)

*E-mail: carlos.platas.iglesias@udc.es. (C.P.-I.)

Notes

The authors declare no competing financial interest.

■ ACKNOWLEDGMENTS

Financial support is gratefully acknowledged from DFG (Emmy Noether and Heisenberg Fellowships for M.S., Research Grant SE 1448/6-1), German National Academic Foundation (predoctoral fellowship for E.K.), and Int. Max Planck Research School in Chemical Biology (predoctoral fellowship for C.B.). C.P.-I. thanks Centro de Supercomputación de Galicia (CESGA) for providing the computer facilities.

■ REFERENCES

(1) *The Rare Earth Elements - Fundamentals and Applications;* Atwood, D. A., Ed.; Wiley: Chichester, U.K., 2012.

(2) Geraldes, C. F. G. C. Lanthanide Shift Reagents. In *The Rare Earth Elements - Fundamentals and Applications;* Atwood, D. A., Ed.; Wiley: Chichester, U.K., 2012; p 501.

(3) *The Chemistry of Contrast Agents in Medical Magnetic Resonance Imaging,* 2nd ed.; Merbach, A. S., Helm, L., Toth, E., Eds.; Wiley: Chichester, U.K., 2013.

(4) (a) Habib, F.; Murugesu, M. *Chem. Soc. Rev.* **2013**, *42*, 3278. (b) Woodruff, D. N.; Winpenny, R. E. P.; Layfield, R. A. *Chem. Rev.* **2013**, *113*, 5110. (c) Liddle, S. T.; van Slageren, J. *Chem. Soc. Rev.* **2015**, *44*, 6655.

(5) (a) Su, X.-C.; Otting, G. *J. Biomol. NMR* **2010**, *46*, 101. (b) Otting, G. *Annu. Rev. Biophys.* **2010**, *39*, 387. (c) Liu, W.-M.; Overhand, M.; Ubbink, M. *Coord. Chem. Rev.* **2014**, *273*−*274*, 2.

(6) Selected review: Stasiuk, G. J.; Long, N. J. *Chem. Commun.* **2013**, *49*, 2732 and references cited therein..

(7) Selected reviews: (a) Parker, D.; Dickins, R. S.; Puschmann, H.; Crossland, C.; Howard, J. A. K. *Chem. Rev.* **2002**, *102*, 1977. (b) Platas-Iglesias, C. *Eur. J. Inorg. Chem.* **2012**, *2012*, 2023.

(8) Selected examples: (a) Martins, A. F.; Eliseeva, S. V.; Carvalho, H. F.; Teixeira, J. M. C.; Paula, C. T. B.; Hermann, P.; Platas-Iglesias, C.; Petoud, S.; Toth, E.; Geraldes, C. F. G. C. *Chem. - Eur. J.* **2014**, *20*, 14834. (b) Polasek, M.; Rudovsky, J.; Hermann, P.; Lukes, I.; Vander Elst, L.; Muller, R. N. *Chem. Commun.* **2004**, 2602. (c) Keizers, P. H. J.; Desreux, J. F.; Overhand, M.; Ubbink, M. *J. Am. Chem. Soc.* **2007**, *129*, 9292.

(9) (a) Boulon, M.-E.; Cucinotta, G.; Luzon, J.; Degl'Innocenti, C.; Perfetti, M.; Bernot, K.; Calvez, G.; Caneschi, A.; Sessoli, R. *Angew. Chem., Int. Ed.* **2013**, *52*, 350. (b) Cucinotta, G.; Perfetti, M.; Luzon, J.; Etienne, M.; Car, P. E.; Caneschi, A.; Calvez, G.; Bernot, K.; Sessoli, R. *Angew. Chem., Int. Ed.* **2012**, *51*, 1606.

(10) (a) Blackburn, O. A.; Chilton, N. F.; Keller, K.; Tait, C. E.; Myers, W. K.; McInnes, E. J. L.; Kenwright, A. M.; Beer, P. D.; Timmel, C. R.; Faulkner, S. *Angew. Chem., Int. Ed.* **2015**, *54*, 10783. (b) Liu, T.; Nonat, A.; Beyler, M.; Regueiro-Figueroa, M.; Nchimi Nono, K.; Jeannin; Camerel, O. F.; Debaene, F.; Cianférani-Sanglier, S.; Tripier, R.; Platas-Iglesias, C.; Charbonnière, L. J. *Angew. Chem., Int. Ed.* **2014**, *53*, 7259. (c) Blackburn, O. A.; Edkins, R. M.; Faulkner, S.; Kenwright, A. M.; Parker, D.; Rogers, N. J.; Shuvaev, S. *Dalton Trans.* **2016**, *45*, 6782.

(11) Review: Zwier, J. M.; Bazin, H.; Lamarque, L.; Mathis, G. *Inorg. Chem.* **2014**, *53*, 1854.

(12) Alpha, B.; Lehn, J.-M.; Mathis, G. *Angew. Chem., Int. Ed. Engl.* **1987**, *26*, 266.

(13) (a) Lehn, J.-M.; Roth, C. O. *Helv. Chim. Acta* **1991**, *74*, 572. (b) Doffek, C.; Alzakhem, N.; Molon, M.; Seitz, M. *Inorg. Chem.* **2012**, *51*, 4539. (c) Doffek, C.; Seitz, M. *Angew. Chem., Int. Ed.* **2015**, *54*, 9719. (d) Doffek, C.; Alzakhem, N.; Bischof, C.; Wahsner, J.; Güden-Silber, T.; Lügger, J.; Platas-Iglesias, C.; Seitz, M. *J. Am. Chem. Soc.* **2012**, *134*, 16413. (e) Güden-Silber, T.; Doffek, C.; Platas-Iglesias, C.; Seitz, M. *Dalton Trans.* **2014**, *43*, 4238.

DOI: 10.1021/acs.inorgchem.6b00591
Inorg. Chem. 2016, 55, 5549−5557

(14) (a) Havas, F.; Danel, M.; Galaup, C.; Tisnes, P.; Picard, C. *Tetrahedron Lett.* **2007**, *48*, 999. (b) Havas, F.; Leygue, N.; Mestre, B.; Galaup, C.; Picard, C. *Tetrahedron* **2009**, *65*, 7673.
(15) (a) Lamarque, L.; Bazin, H.; Blanche, E. (Cisbio International). Patent WO 2010/070232, June 24, 2010. (b) Ansanay, H.; Fink, M.; Mathis, G.; Maurel, D.; Trinquet, E.; Pin, J.-P. (Cisbio International). Patent WO 2006/085040, August 17, 2006.
(16) Mathieu, J.; Marsura, A. *Synth. Commun.* **2003**, *33*, 409.
(17) In analogy to: Psychogios, N.; Regnouf-de-Vains, J.-B.; Stoeckli-Evans, H. M. *Eur. J. Inorg. Chem.* **2004**, *2004*, 2514.
(18) In analogy to: Caron, S.; Do, N. M.; Sieser, J. E. *Tetrahedron Lett.* **2000**, *41*, 2299.
(19) Newkome, G. R.; Pappalardo, S.; Gupta, V. K.; Fronczek, F. R. *J. Org. Chem.* **1983**, *48*, 4848.
(20) Selected reviews: (a) Bünzli, J.-C. G. *J. Lumin.* **2016**, *170*, 866. (b) Bünzli, J.-C. G.; Eliseeva, S. V. *J. Rare Earths* **2010**, *28*, 824. (c) Comby, S.; Bünzli, J.-C. G. In *Handbook on the Physics and Chemistry of Rare Earths;* Gschneidner, K. A., Jr., Bünzli, J.-C. G., Pecharsky, V. K., Eds.; Elsevier: Amsterdam, 2007; Vol. *37*, pp 217.
(21) Emsley, J. W.; Phillips, L. *Prog. Nucl. Magn. Reson. Spectrosc.* **1971**, *7*, 1.
(22) Rodríguez-Rodríguez, A.; Esteban-Gómez, D.; de Blas, A.; Rodríguez-Blas, T.; Fekete, M.; Botta, M.; Tripier, R.; Platas-Iglesias, C. *Inorg. Chem.* **2012**, *51*, 2509.
(23) Forsberg, J. H.; Delaney, R. M.; Zhao, Q.; Harakas, G.; Chandran, R. *Inorg. Chem.* **1995**, *34*, 3705.
(24) Lisowski, J.; Sessler, J. L.; Lynch, V.; Mody, T. D. *J. Am. Chem. Soc.* **1995**, *117*, 2273. (b) Lima, L. M. P.; Lecointre, A.; Morfin, J.-F.; de Blas, A.; Visvikis, D.; Charbonnière, L. J.; Platas-Iglesias, C.; Tripier, R. *Inorg. Chem.* **2011**, *50*, 12508. (c) del C. Fernández-Fernández, M.; Bastida, R.; Macías, A.; Pérez-Lourido, P.; Platas-Iglesias, C.; Valencia, L. *Inorg. Chem.* **2006**, *45*, 4484.
(25) Graphical representation calculated using the program Mayavi 2: Ramachandran, P.; Varoquaux, G. *Comput. Sci. Eng.* **2011**, *13*, 40.
(26) Prodi, L.; Maestri, M.; Balzani, V.; Lehn, J.-M.; Roth, C. *Chem. Phys. Lett.* **1991**, *180*, 45.
(27) Tao, J. M.; Perdew, J. P.; Staroverov, V. N.; Scuseria, G. E. *Phys. Rev. Lett.* **2003**, *91*, 146401.
(28) Frisch, M. J. et al. *Gaussian 09,* Revision D.01; Gaussian, Inc: Wallingford, CT, 2009.
(29) Dolg, M.; Stoll, H.; Savin, A.; Preuss, H. *Theor. Chim. Acta* **1989**, *75*, 173.
(30) Tomasi, J.; Mennucci, B.; Cammi, R. *Chem. Rev.* **2005**, *105*, 2999.

DOI: 10.1021/acs.inorgchem.6b00591
Inorg. Chem. 2016, 55, 5549−5557

Magnetic Anisotropy in Functionalized Bipyridyl Cryptates

Elisabeth Kreidt,[a] Caroline Bischof,[b] Carlos Platas-Iglesias,*[c] and Michael Seitz*[a]

[a] Institute of Inorganic Chemistry, University of Tübingen, Auf der Morgenstelle 18, 72076 Tübingen, Germany.

[b] Inorganic Chemistry I, Ruhr-University Bochum, 44780 Bochum, Germany.

[c] Departamento de Química Fundamental, Universidade da Coruña, Campus da Zapateira-Rúa da Fraga 10, 15008 A Coruña, Spain

Email: michael.seitz@uni-tuebingen.de, carlos.platas.iglesias@udc.es

Supporting Information

Table of Contents Page

1. NMR Spectra

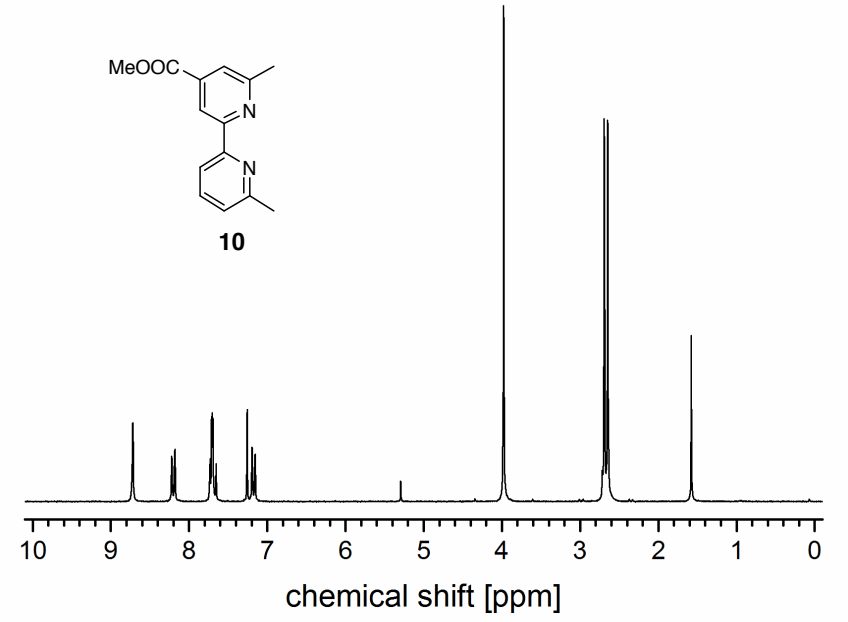

Figure S1. ^{1}H NMR (200 MHz, $CDCl_3$) of **10**.

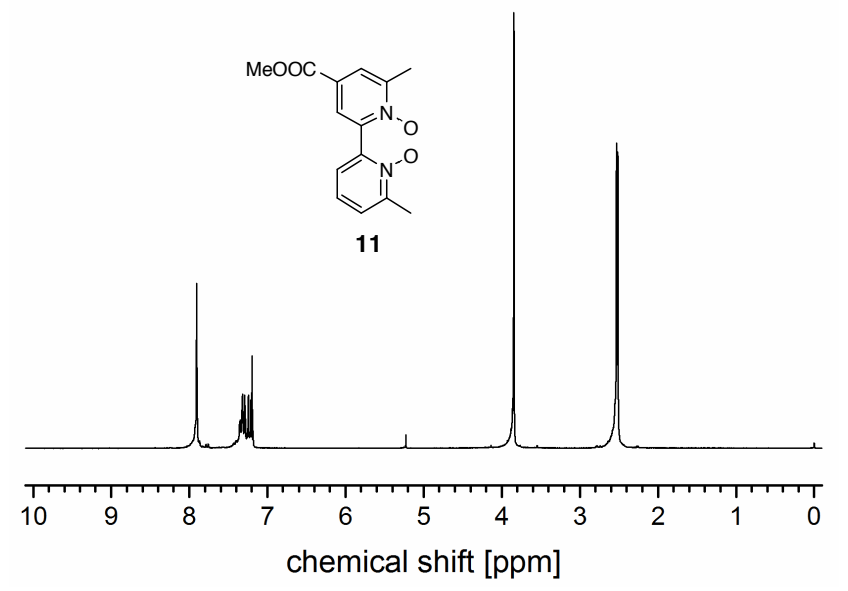

Figure S2. ^{1}H NMR (250 MHz, $CDCl_3$) of **11**.

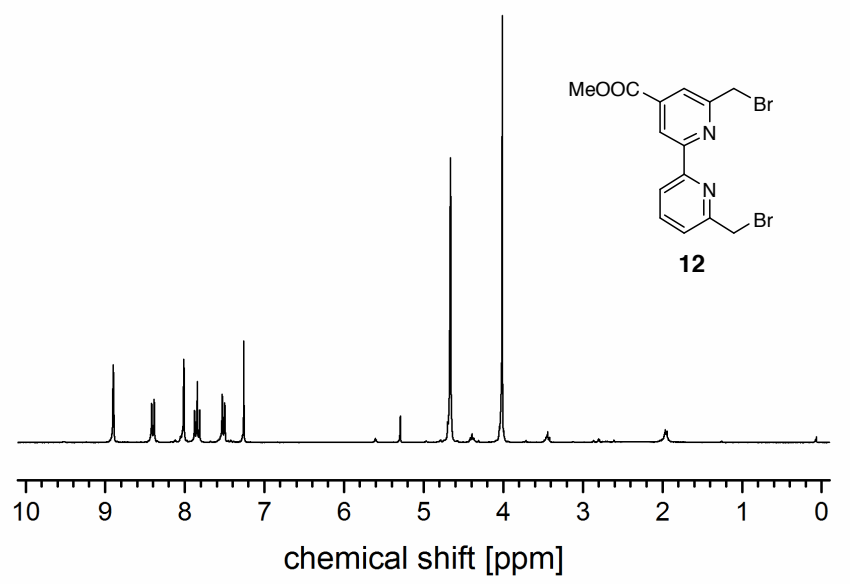

Figure S3. ^{1}H NMR (200 MHz, $CDCl_3$) of **12**.

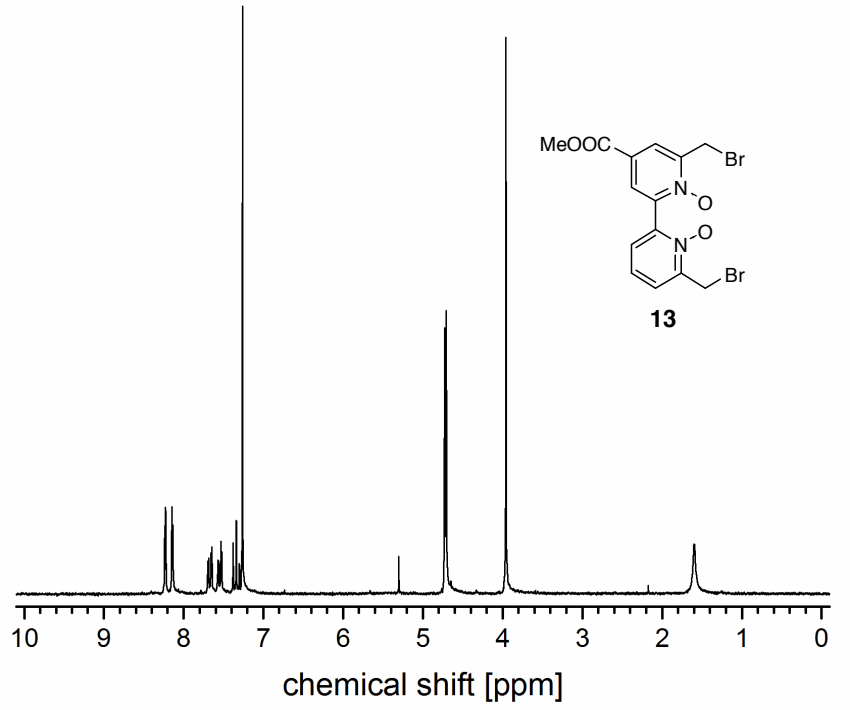

Figure S4. ^{1}H NMR (200 MHz, $CDCl_3$) of **13**.

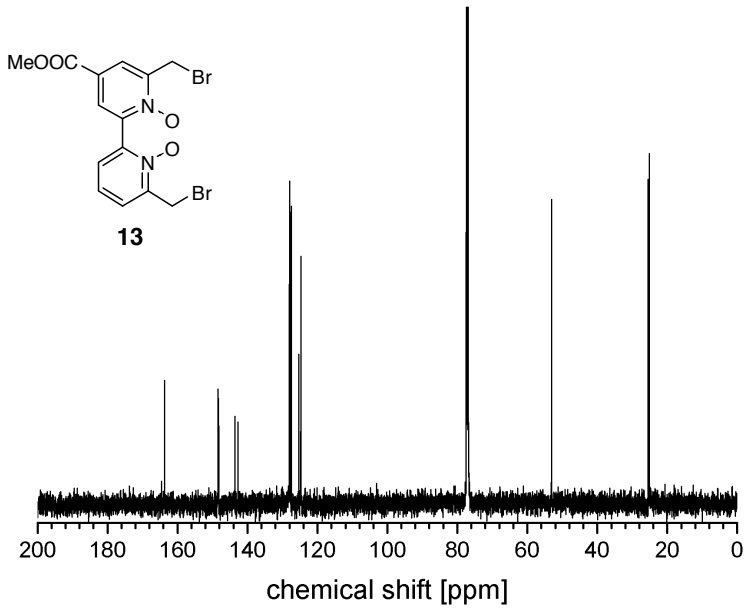

Figure S5. ^{13}C NMR (126 MHz, $CDCl_3$) of **13**.

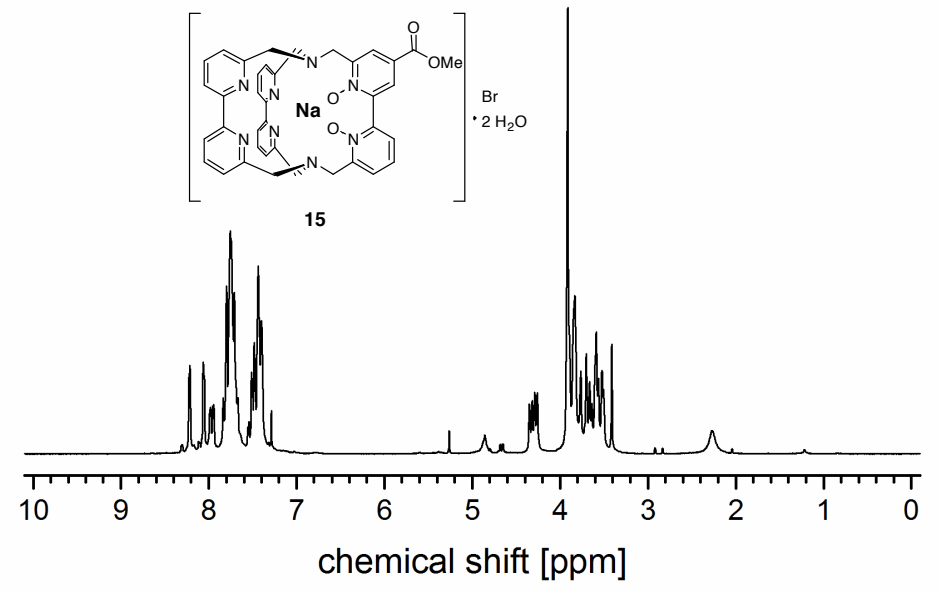

Figure S6. ^{1}H NMR (200 MHz, $CDCl_3$) of **15**.

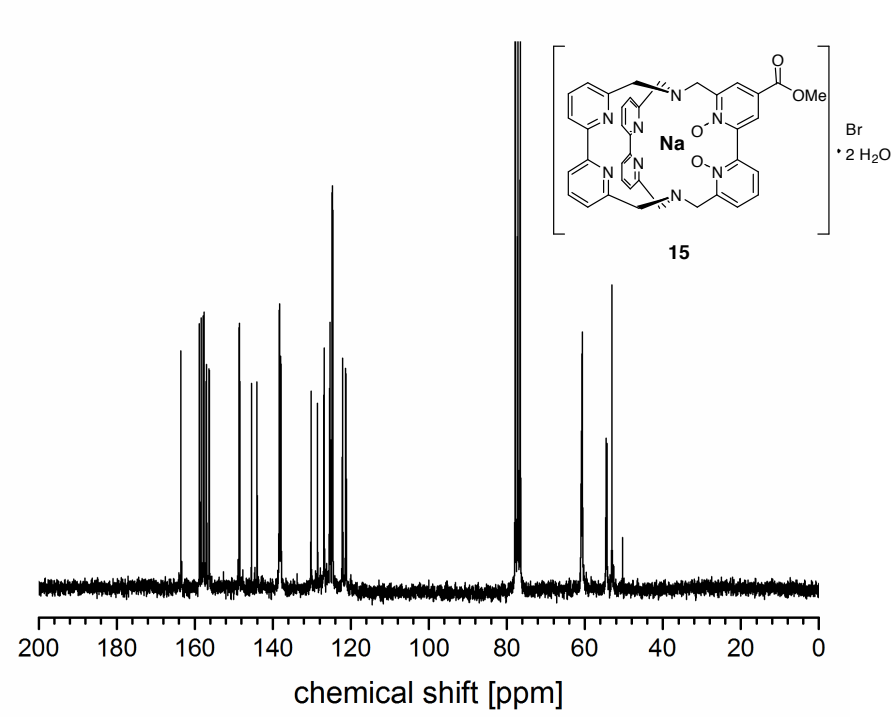

Figure S7. ^{13}C NMR (50.3 MHz, $CDCl_3$) of **15**.

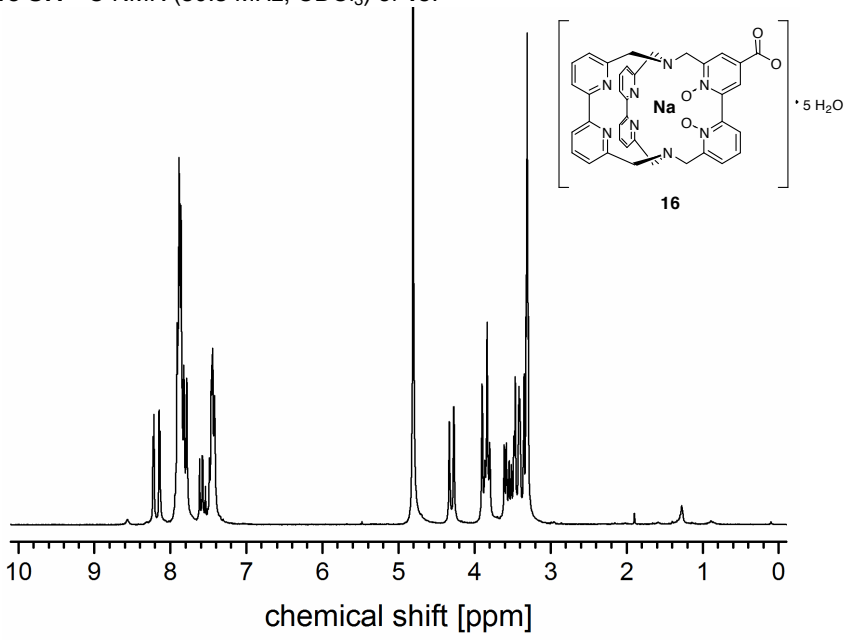

Figure S8. ^{1}H NMR (200 MHz, CD_3OD) of **16**.

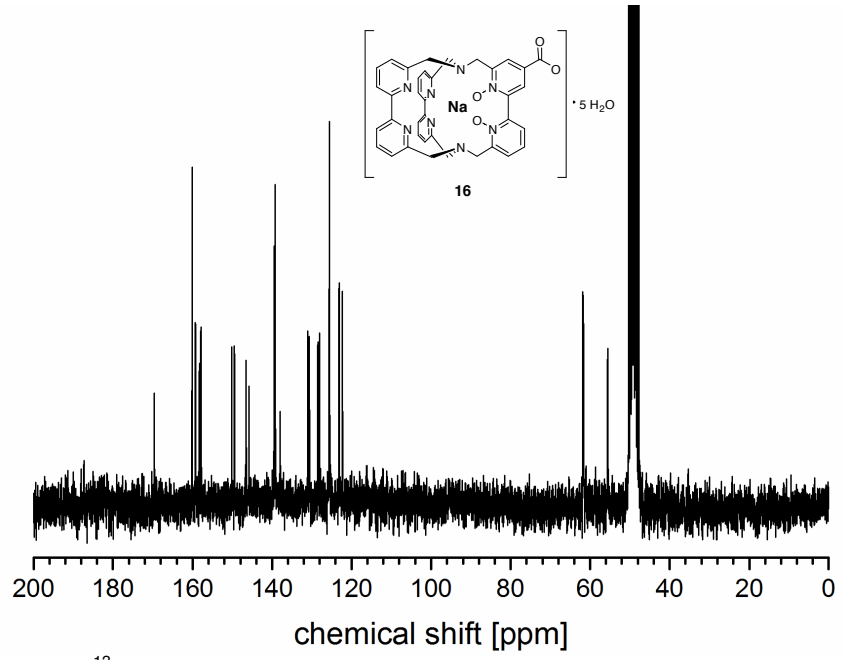

Figure S9. ^{13}C NMR (50.3 MHz, CD_3OD) of **16**.

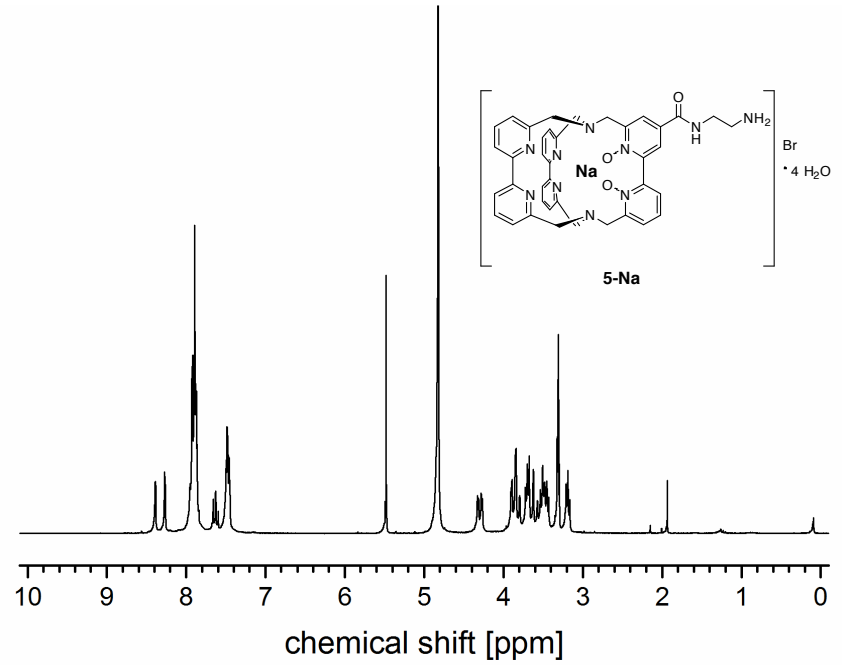

Figure S10. ^{1}H NMR (250 MHz, CD_3OD) of **5-Na**.

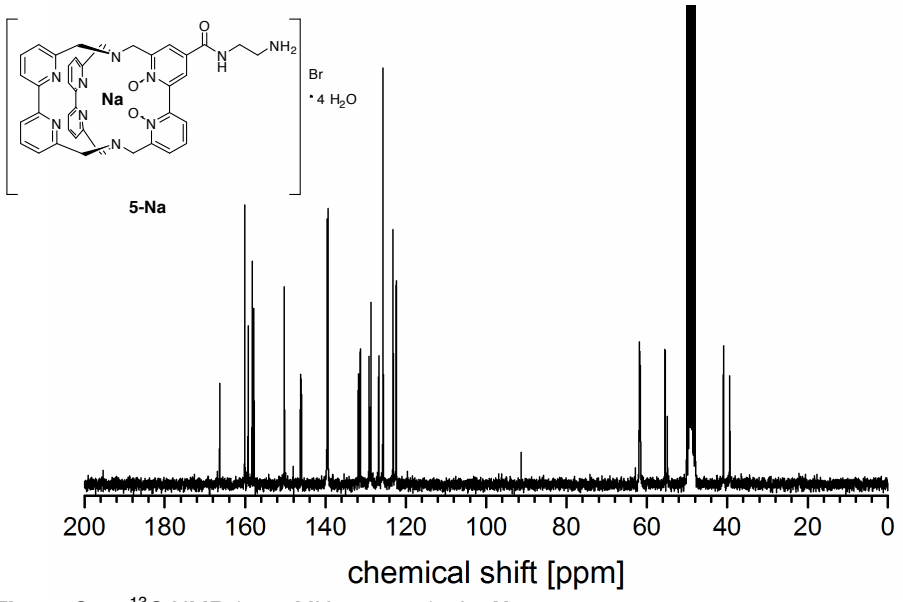

Figure S11. ^{13}C NMR (62.9 MHz, CD_3OD) of **5-Na**.

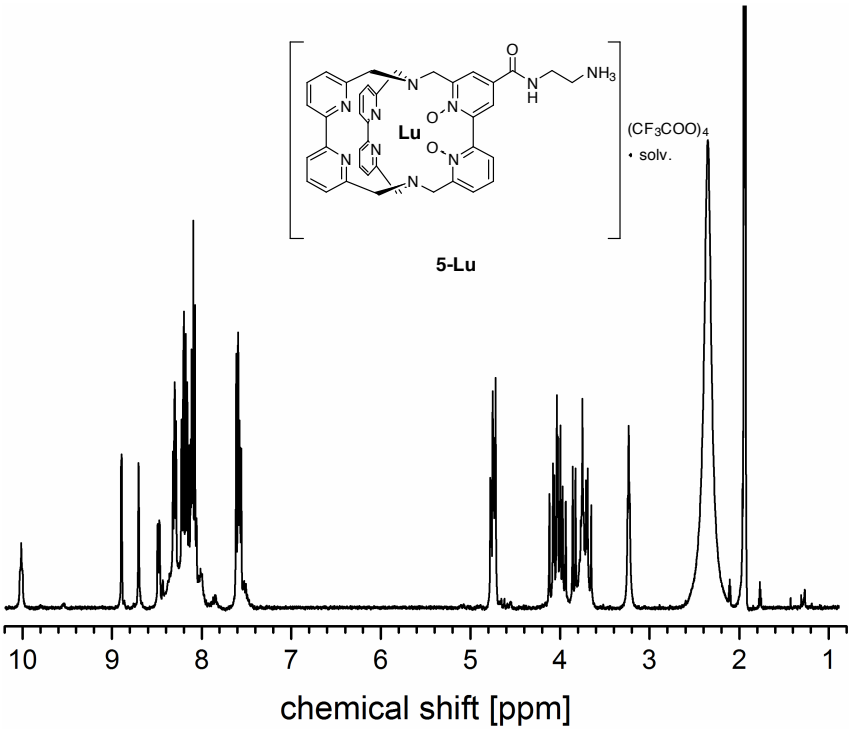

Figure S12. ^{1}H NMR (400 MHz, CD_3CN) of **5-Lu**.

2. HPLC traces of 5-Ln

For the detailed HPLC conditions see the main article.

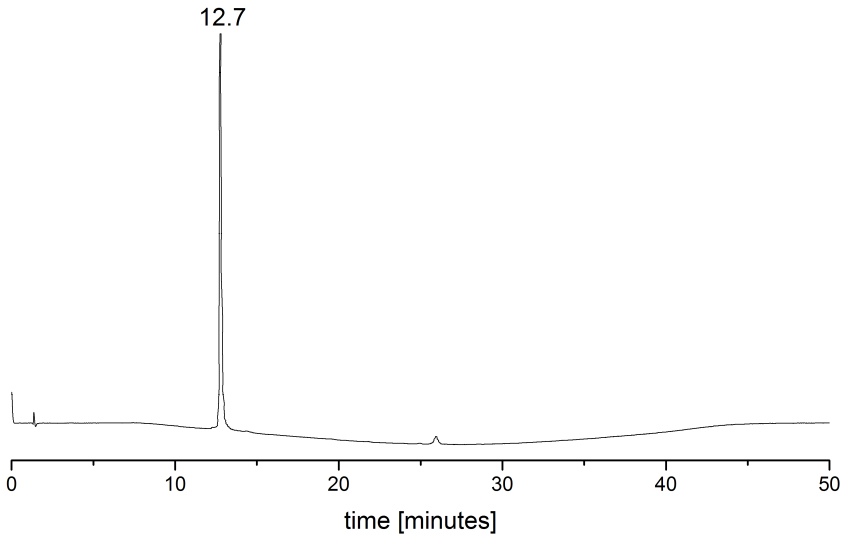

Figure S13. Analytical HPLC trace of **5-Yb** (after preparative HPLC purification).

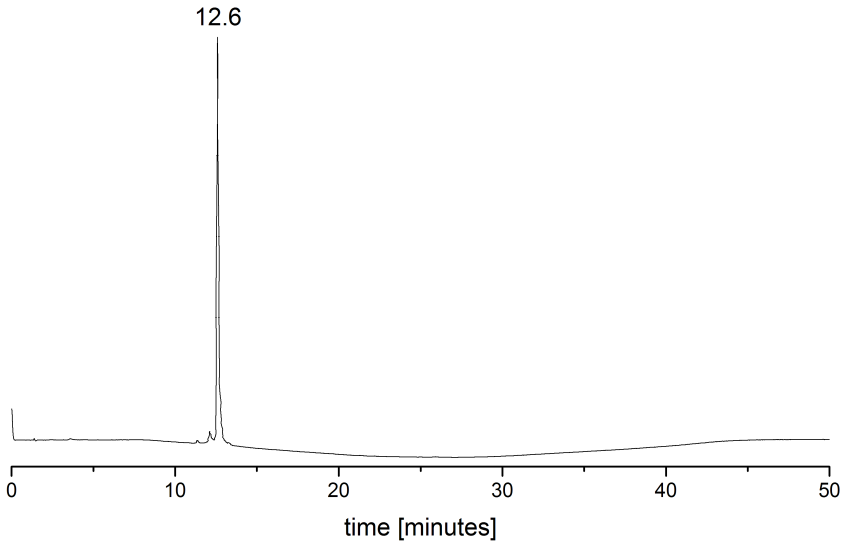

Figure S14. Analytical HPLC trace of **5-Lu** (after preparative HPLC purification).

3. DFT Calculations

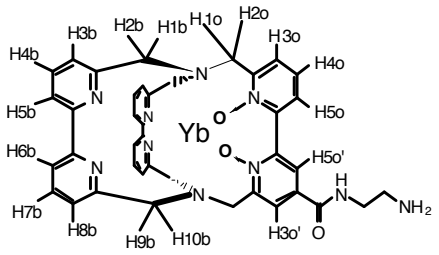

Figure S15. Numbering scheme for the hydrogen atoms in **5-Yb**.

Cartesian coordinates for the calculated structure of 5-Yb in acetonitrile:

```
# FAWYbLehnNox2F3_TPSSh
# Created by GaussView 5.0.8
#

#
#

@<TRIPOS>MOLECULE
Molecule Name
93 101
SMALL
NO_CHARGES


@<TRIPOS>ATOM
1 Yb1     0.0000     0.0000     0.0000 Yb
2 H2     -1.2913     3.1217    -1.0487 H
3 H3      1.3329    -3.1404    -1.0784 H
4 H4     -3.0447     3.0902    -1.3609 H
5 H5      3.0824    -3.0948    -1.4112 H
6 H6     -3.6455     2.7370    -3.6818 H
7 H7      3.6720    -2.6996    -3.7317 H
8 H8     -3.1949     1.5865    -5.8662 H
9 H9      1.2429     0.0339    -5.9834 H
10 H10    -1.2659    -0.0050    -5.9897 H
11 H11     4.9767    -1.1943    -8.2605 H
12 H12     3.6222    -0.9892    -9.3956 H
13 H13     4.4360    -3.6436    -8.0568 H
14 H14     3.1545    -3.4623    -9.2871 H
15 H15     2.8279    -1.1554     1.6059 H
16 H16    -2.7150     1.0679     1.6241 H
17 H17    -3.4882     2.4916     0.9054 H
18 H18     3.5156    -2.5946     0.8410 H
```

19	H19	-2.6314	4.2492	2.3834 H
20	H20	2.6509	-4.2730	2.3984 H
21	H21	-0.6290	5.5529	3.1587 H
22	H22	0.6385	-5.5484	3.1929 H
23	H23	1.6298	4.7539	2.5571 H
24	H24	-1.6124	-4.7513	2.5569 H
25	H25	3.3709	4.1450	1.8270 H
26	H26	-3.3346	-4.1900	1.7610 H
27	H27	5.5357	3.1897	1.0984 H
28	H28	-5.4995	-3.2366	1.0354 H
29	H29	5.5350	0.9884	-0.1086 H
30	H30	-5.5074	-1.0162	-0.1368 H
31	H31	4.3553	-0.9691	-0.7432 H
32	H32	-4.3181	0.9626	-0.7412 H
33	H33	-3.2072	0.1963	-1.8769 H
34	H34	3.2395	-0.1924	-1.8648 H
35	N35	-0.1867	2.3097	1.0899 N
36	N36	5.1202	-3.2896	-10.0095 N
37	N37	3.0889	-1.4058	-7.4335 N
38	N38	-0.7560	1.2276	-2.9043 N
39	N39	-2.2415	1.3458	-0.4052 N
40	N40	2.2809	-1.3738	-0.4140 N
41	N41	0.7637	-1.2334	-2.9140 N
42	N42	0.2250	-2.3292	1.0741 N
43	N43	-2.1796	-1.3245	0.3718 N
44	C44	4.6098	2.6613	0.9007 C
45	C45	3.3923	3.1932	1.3144 C
46	C46	0.7617	4.1949	2.2352 C
47	C47	-0.5104	4.6451	2.5776 C
48	C48	4.6119	1.4428	0.2324 C
49	C49	2.2102	2.4902	1.0598 C
50	C50	0.8950	3.0225	1.4795 C
51	C51	-1.6238	3.9223	2.1543 C
52	C52	3.3933	0.8007	-0.0047 C
53	C53	-1.4166	2.7558	1.4185 C
54	C54	3.3813	-0.4677	-0.8153 C
55	C55	3.9975	-1.5786	-8.5572 C
56	C56	-2.1253	2.4944	-1.3684 C
57	C57	-1.8890	1.9736	-2.7482 C
58	C58	3.5058	-1.6816	-6.1700 C
59	C59	-2.7641	2.1220	-3.8191 C
60	C60	-2.5603	1.9064	0.9363 C
61	C61	1.4233	-0.5975	-5.1217 C
62	C62	4.1003	-3.0672	-8.9179 C
63	C63	2.5128	-1.4684	-5.0593 C
64	C64	-2.5211	1.4679	-5.0267 C
65	C65	-0.5672	0.4616	-4.0258 C

```
66 C66      0.5672    -0.4616    -4.0307 C
67 C67     -1.4361     0.5994    -5.1071 C
68 C68      2.6140    -1.9723     0.9072 C
69 C69      2.7715    -2.1071    -3.8420 C
70 C70      1.9077    -1.9690    -2.7673 C
71 C71      2.1603    -2.5029    -1.3966 C
72 C72     -3.3484     0.4541    -0.8228 C
73 C73      1.4501    -2.7853     1.4080 C
74 C74      1.6459    -3.9420     2.1633 C
75 C75     -3.3658    -0.8257    -0.0325 C
76 C76     -0.8626    -3.0398     1.4597 C
77 C77     -2.1775    -2.5185     1.0214 C
78 C78     -4.5829    -1.4727     0.1972 C
79 C79      0.5281    -4.6506     2.5953 C
80 C80     -0.7391    -4.2013     2.2338 C
81 C81     -3.3574    -3.2314     1.2611 C
82 C82     -4.5759    -2.7005     0.8481 C
83 O83      0.1711     1.2652    -1.9554 O
84 O84      4.6431    -2.0905    -5.9170 O
85 O85     -0.3713     0.0025     2.4346 O
86 O86     -0.1501    -1.2799    -1.9619 O
87 H87      6.0509    -2.9593    -9.7348 H
88 H88      4.8646    -2.8106   -10.8786 H
89 H89     -0.1613     0.7483     3.0168 H
90 H90      2.1140    -1.2206    -7.6286 H
91 H91      5.2068    -4.2870   -10.2289 H
92 H92     -0.3459    -0.7907     2.9909 H
93 N93      2.2022     1.3216     0.3544 N
@<TRIPOS>BOND
1 1 83 1
2 1 85 1
3 1 86 1
4 2 56 1
5 3 71 1
6 4 56 1
7 5 71 1
8 6 59 1
9 7 69 1
10 8 64 1
11 9 61 1
12 10 67 1
13 11 55 1
14 12 55 1
15 13 62 1
16 14 62 1
17 15 68 1
18 16 60 1
```

```
19 17 60 1
20 18 68 1
21 19 51 1
22 20 74 1
23 21 47 1
24 22 79 1
25 23 46 1
26 24 80 1
27 25 45 1
28 26 81 1
29 27 44 1
30 28 82 1
31 29 48 1
32 30 78 1
33 31 54 1
34 32 72 1
35 33 72 1
36 34 54 1
37 35 50 Ar
38 35 53 Ar
39 36 62 1
40 36 87 1
41 36 88 1
42 36 91 1
43 37 55 1
44 37 58 Ar
45 37 90 1
46 38 57 Ar
47 38 65 Ar
48 38 83 1
49 39 56 1
50 39 60 1
51 39 72 1
52 40 54 1
53 40 68 1
54 40 71 1
55 41 66 Ar
56 41 70 Ar
57 41 86 1
58 42 73 Ar
59 42 76 Ar
60 43 75 Ar
61 43 77 Ar
62 44 45 Ar
63 44 48 Ar
64 45 49 Ar
65 46 47 Ar
```

```
66 46 50 Ar
67 47 51 Ar
68 48 52 Ar
69 49 50 1
70 49 93 Ar
71 51 53 Ar
72 52 54 1
73 52 93 Ar
74 53 60 1
75 55 62 1
76 56 57 1
77 57 59 Ar
78 58 63 1
79 58 84 2
80 59 64 Ar
81 61 63 Ar
82 61 66 Ar
83 63 69 Ar
84 64 67 Ar
85 65 66 1
86 65 67 Ar
87 68 73 1
88 69 70 2
89 70 71 1
90 72 75 1
91 73 74 Ar
92 74 79 Ar
93 75 78 Ar
94 76 77 1
95 76 80 Ar
96 77 81 Ar
97 78 82 Ar
98 79 80 Ar
99 81 82 Ar
100 85 89 1
101 85 92 1
```

Inorganic Chemistry

Communication

pubs.acs.org/IC

Chiral Resolution of Lanthanoid Cryptates with Extreme Configurational Stability

Elisabeth Kreidt,[†] Carolin Dee,[†] and Michael Seitz*[,†]

[†]Institute of Inorganic Chemistry, University of Tübingen, Auf der Morgenstelle 18, 72076 Tübingen, Germany

Supporting Information

ABSTRACT: Chiral resolution is achieved for racemic tris(2,2′-bipyridine)-based lanthanoid cryptates by chiral HPLC. The resolved complexes exhibit very rare configurational stability under extreme conditions.

Chirality is one of the most fundamental aspects of chemistry. In this context, enantiopure metal complexes have long been recognized to play a crucial role in a wide variety of areas, most prominently in the recent past as catalysts in asymmetric catalysis. The archetypes of this class of compounds are octahedral tris(bidentate) complexes such as $[Ru(bpy)_3]^{n+}$, which in many instances can be chirally resolved and often show remarkable configurational stability in enantiopure form.[1] In contrast, lanthanoid complexes, due to their inherent kinetic lability and generally rather fluxional coordination sphere, rarely show similarly advantageous properties and usually only form configurationally stable complexes with enantiopure ligands.[2] For example, the chiral europium complex anion $[Eu(dpa)_3]^{3-}$ (with dpa ≡ dipicolinate) shows very fast exchange between its Δ and Λ enantiomers with a half-life on the order of a few tens of milliseconds in aqueous solution at ambient temperature.[3] Despite the great potential that enantiopure lanthanoid complexes have for unique applications such as paramagnetic NMR shift reagents[4] or circularly polarized luminescence (CPL) probes,[5] there is currently only one practically useful ligand platform based on 1,4,7-triazacyclononane that provides lanthanoid complexes which can be chirally resolved and which show sufficient configurational stability after resolution.[6] It has so far proven very difficult to develop other ligands for lanthanoid chelation with the same advantageous properties. Here, we report the chiral resolution of tris(2,2′-bipyridine)-based lanthanoid cryptates as a different class of universally applicable rare earth chelators and their remarkable chemical and configurational stability under rather harsh conditions.

Rigidified bipyridine cryptands such as (±)-**1**-Ln (Scheme 1, left) have proven to be excellent ligands for lanthanoids, providing kinetically inert complexes with outstanding photophysical and interesting magnetic properties.[7] Due to the helical arrangement of the overall cryptate architecture and the axial chirality of the 2,2′-bipyridine-*N*,*N*′-dioxide units, these cryptates are chiral but have so far almost exclusively been synthesized and used as racemates.

Cryptates of this type are also accessible as single enantiomers using enantiomerically pure cryptands,[8] but the much more desirable and practically straightforward chiral resolution to obtain both enantiomers of the corresponding cryptates with racemic or achiral cryptands has not been achieved so far. In order to test the latter possibility, we subjected a series of previously realized cryptates (±)-**1**-Ln (with Ln = Pr, Nd, Sm, Er, Lu)[7c,d] to chiral HPLC. Under optimized HPLC conditions (stationary phase, CHIRALPAK IE; eluent, isocratic CH_3OH + 0.5 vol % CF_3COOH), the racemates could be sufficiently resolved for all lanthanoids investigated along the series. As a representative example, Figure 1 shows the HPLC traces for the racemate (±)-**1**-Lu, as well as the isolated enantiomers **1**-Lu-ent1 (first fraction) and **1**-Lu-ent2 (second fraction) after the preparative resolution (see Figure S1 in the Supporting Information for the HPLC traces for all other lanthanoids). The HPLC trace of the racemate shows the two peaks assigned to the enantiomers in the expected 50:50 ratio. The recovery of the pure enantiomers from the racemate was quite good with 72% for **1**-Lu-ent1 and 88% for **1**-Lu-ent2 (see the Supporting Information for details). Both of these resolved fractions showed no sign of the other enantiomer in the HPLC traces, identical ^1H NMR spectra (Figure S1 in the Supporting Information) in CD_3OD, and perfect mirror-image CD spectra in CH_3OH (Figure 2). Taken together, this constitutes conclusive evidence that the two fractions contain the corresponding enantiomers and that the enantiopurity of each form is very high. At the moment, we cannot assign the absolute configurations of the two enantiomers, but efforts in this direction are underway.

In order to test the configurational stability of the resolved enantiomers, **1**-Lu-ent1 was subjected to two rather harsh environments, and the progress over time was monitored by chiral HPLC (Figure 3). On the one hand, we evaluated

Scheme 1. Chiral Resolution of the Racemic Cryptates 1-Ln

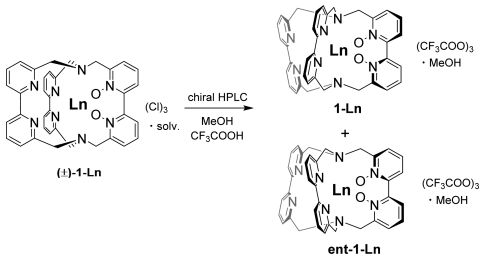

Received: June 7, 2017

DOI: 10.1021/acs.inorgchem.7b01407
Inorg. Chem. XXXX, XXX, XXX−XXX

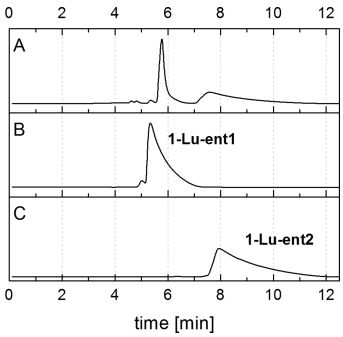

Figure 1. HPLC traces (CHIRALPAK IE, CH_3OH + 0.5 vol % CF_3COOH, UV detection: 300 nm). (A) Preparative separation of racemic (±)-**1**-Lu. (B and C) Analytical HPLC of the purified enantiomers **1**-Lu-ent1 (B) and **1**-Lu-ent2 (C) from the preparative run in A.

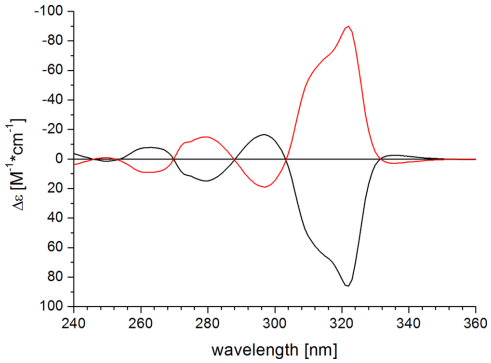

Figure 2. CD spectra of both enantiomers: **1**-Lu-ent1 (black) and **1**-Lu-ent2 (red) in CH_3OH ($c \approx 0.4$ mM).

potential racemization reactions in solutions of this enantiomer in neat CF_3COOH at room temperature, conditions which usually favor rapid decomplexation and/or configurational instability in most other lanthanoid chelates. Second, we also heated **1**-Lu-ent1 in CH_3CN under reflux with 10 equiv of externally added $LuCl_3{\cdot}6H_2O$ and monitored the potential self-exchange of the lutetium cations which would lead to the appearance of the second enantiomer **1**-Lu-ent2. In neither of these experiments could we detect any chemical instability or any sign of the other enantiomer after 5 days.

In conclusion, we could show that the lanthanoid cryptates (±)-**1**-Ln can be separated into pure enantiomers by chiral HPLC and that the resolved, enantiopure complexes show very high configurational stability. This extraordinary and very rare ability to preserve the absolute stereochemical information under extremely challenging conditions makes these enantiopure cryptates very interesting lanthanoid chelates. We expect that this will open up entirely new prospects for applications where enantiopurity is a key requirement, for example for the development of new CPL probes in the near-IR wavelength range, a spectral region where we have already shown the great worth of these cryptates.[7b−d]

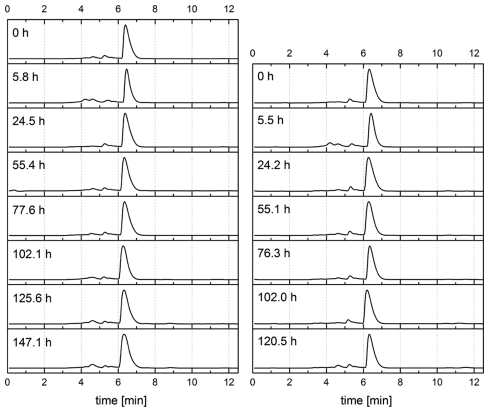

Figure 3. Configurational stability tests by chiral HPLC of **1**-Lu-ent1 under the following conditions: Left, neat CF_3COOH, room temperature; Right, 10 equiv $LuCl_3{\cdot}6H_2O$ in CH_3CN, reflux.

■ ASSOCIATED CONTENT

Supporting Information

The Supporting Information is available free of charge on the ACS Publications website at DOI: 10.1021/acs.inorgchem.7b01407.

Experimental details for chiral HPLC measurements, the configurational stability studies, and CD spectroscopy; chiral HPLC traces of the racemates (±)-**1**-Ln (Ln = Pr, Nd, Sm, Er); and NMR spectra of **1**-Lu-ent1 and **1**-Lu-ent2 (PDF)

■ AUTHOR INFORMATION

Corresponding Author

*E-mail: michael.seitz@uni-tuebingen.de.

ORCID

Michael Seitz: 0000-0002-9313-2779

Notes

The authors declare no competing financial interest.

■ ACKNOWLEDGMENTS

We gratefully acknowledge financial support from the German Research Foundation (DFG, research grant SE 1448/6-1) and the German National Academic Foundation (predoctoral fellowship for E.K.). We thank Mrs. Joana Tavares Macedo (Interfaculty Institute for Biochemistry, University of Tübingen) for help with the CD measurements.

■ REFERENCES

(1) *Stereochemistry of Coordination Compounds*; von Zelewsky, A., Ed.; John Wiley & Sons Ltd.: Chichester, 1996.

(2) Reviews: (a) Aspinall, H. C. Chiral Lanthanide Complexes: Coordination Chemistry and Applications. *Chem. Rev.* **2002**, *102*, 1807−1850. (b) Di Bari, L.; Salvadori, P. Solution structure of chiral lanthanide complexes. *Coord. Chem. Rev.* **2005**, *249*, 2854−2879. Selected examples: (c) Ranganathan, S. R.; Raju, N.; Fan, H.; Zhang, X.; Tweedle, M. F.; Desreux, J. F.; Jacques, V. Polymethylated DOTA Ligands. 2. Synthesis of Rigidified Lanthanide Chelates and Studies on the Effect of Alkyl Substitution on Conformational Mobility and Relaxivity. *Inorg. Chem.* **2002**, *41*, 6856−6866. (d) Mamula, O.; Lama,

DOI: 10.1021/acs.inorgchem.7b01407
Inorg. Chem. XXXX, XXX, XXX−XXX

M.; Telfer, S. G.; Nakamura, A.; Kuroda, R.; Stoeckli-Evans, H.; Scopelitti, R. A Trinuclear Eu^{III} Array within a Diastereoselectively Self-Assembled Helix Formed by Chiral Bipyridine-Carboxylate Ligands. *Angew. Chem.* **2005**, *117*, 2583−2587. (e) Seitz, M.; Moore, E. G.; Ingram, A. J.; Muller, G.; Raymond, K. N. Enantiopure, Octadentate Ligands as Sensitizers for Europium and Terbium Circularly Polarized Luminescence in Aqueous Solution. *J. Am. Chem. Soc.* **2007**, *129*, 15468−15470. (f) Lama, M.; Mamula, O.; Kottas, G. S.; Rizzo, F.; De Cola, L.; Nakamura, A.; Kuroda, R.; Stoeckli-Evans, H. Lanthanide Class of a Trinuclear Enantiopure Helical Architecture Containing Chiral Ligands: Synthesis, Structure, and Properties. *Chem. - Eur. J.* **2007**, *13*, 7358−7373. (g) Montgomery, C. P.; Murray, B. S.; New, E. J.; Pal, R.; Parker, D. Cell-Penetrating Metal Complex Optical Probes: Targeted and Responsive Systems Based on Lanthanide Luminescence. *Acc. Chem. Res.* **2009**, *42*, 925−937. (h) Harada, T.; Nakano, Y.; Fujiki, M.; Naito, M.; Kawai, T.; Hasegawa, Y. Circularly Polarized Luminescence of Eu(III) Complexes with Point- and Axis-Chiral Ligands Dependent on Coordination Structures. *Inorg. Chem.* **2009**, *48*, 11242−11250.

(3) Metcalf, D. H.; Snyder, S. W.; Demas, J. N.; Richardson, F. S. Excited-state racemization kinetics and chiroptical activity of a labile metal complex in aqueous solution. Time-resolved circularly polarized luminescence study of $Eu(dpa)_3^{3-}$ in H_2O and D_2O. *J. Am. Chem. Soc.* **1990**, *112*, 469−479.

(4) Wenzel, T. J.; Wilcox, J. D. Chiral Reagents for the Determination of Enantiomeric Excess and Absolute Configuration Using NMR Spectroscopy. *Chirality* **2003**, *15*, 256−270.

(5) (a) Muller, G. Luminescent chiral lanthanide(III) complexes as potential molecular probes. *Dalton Trans.* **2009**, 9692−6707. (b) Zinna, F.; Di Bari, L. Lanthanide Circularly Polarized Luminescence: Bases and Applications. *Chirality* **2015**, *27*, 1−13.

(6) (a) Frawley, A. T.; Pal, R.; Parker, D. Very bright, enantiopure europium(III) complexes allow time-gated chiral contrast imaging. *Chem. Commun.* **2016**, *52*, 13349−13352. (b) Evans, N. H.; Carr, R.; Delbianco, M.; Pal, R.; Yufit, D. S.; Parker, D. Complete stereocontrol in the synthesis of macrocyclic lanthanide complexes: direct formation of enantiopure systems for circularly polarised luminescence applications. *Dalton Trans.* **2013**, *42*, 15610−15616. (c) Walton, J. W.; Di Bari, L.; Parker, D.; Pescitelli, G.; Puschmann, H.; Yufit, D. S. Structure, resolution and chiroptical analysis of stable lanthanide complexes of a pyridylphenylphosphinate triazacyclononane ligand. *Chem. Commun.* **2011**, *47*, 12289−12291.

(7) (a) Lehn, J.-M.; Roth, C. O. 56. Synthesis and Properties of Sodium and Europium(III) Cryptates Incorporating the 2,2′-Bipyridine 1,1′-Dioxide and 3,3′-Biisoquinoline 2,2′-Dioxide Units. *Helv. Chim. Acta* **1991**, *74*, 572−578. (b) Doffek, C.; Alzakhem, N.; Molon, M.; Seitz, M. Rigid, Perdeuterated Lanthanoid Cryptates: Extraordinarily Bright Near-IR Luminophores. *Inorg. Chem.* **2012**, *51*, 4539−4545. (c) Doffek, C.; Wahsner, J.; Kreidt, E.; Seitz, M. Breakdown of the Energy Gap Law in Molecular Lanthanoid Luminescence: The Smallest Energy Gap Is Not Universally Relevant for Nonradiative Deactivation. *Inorg. Chem.* **2014**, *53*, 3263−3265. (d) Doffek, C.; Alzakhem, N.; Bischof, C.; Wahsner, J.; Güden-Silber, T.; Lügger, J.; Platas-Iglesias, C.; Seitz, M. Understanding the Quenching Effects of Aromatic C−H- and C−D-Oscillators in Near-IR Lanthanoid Luminescence. *J. Am. Chem. Soc.* **2012**, *134*, 16413−16423.

(8) Güden-Silber, T.; Doffek, C.; Platas-Iglesias, C.; Seitz, M. The first enantiopure lanthanoid cryptate. *Dalton Trans.* **2014**, *43*, 4238−4241.

DOI: 10.1021/acs.inorgchem.7b01407
Inorg. Chem. XXXX, XXX, XXX−XXX

Chiral Resolution of Lanthanoid Cryptates with Extreme Configurational Stability

Elisabeth Kreidt[a], Carolin Dee[a] and Michael Seitz[*a]

[a] Institute of Inorganic Chemistry, University of Tübingen, Auf der Morgenstelle 18, 72076 Tübingen, Germany.

Email: michael.seitz@uni-tuebingen.de

Supporting Information

Table of Contents Page

1. Materials and Methods

NMR spectra were recorded on a Bruker AVII+400 spectrometer (^{1}H: 400 MHz) using CD_3OD (≥ 99.8% D) as the solvent. The racemic lanthanoid cryptates were synthesized as described previously from the corresponding sodium cryptates using $LnCl_3 \cdot x\ H_2O$ (x = 7 for Ln = Pr, x = 6 for Ln = Nd, Sm, Er, or Lu).[1]

2. Chiral HPLC

All chiral HPLC runs of **(±)-1-Ln** (with Ln = Pr, Nd, Sm, Er, Lu) were performed on a Knauer Azura HPLC system (UV detection at λ = 300 nm), equipped with a CHIRALPAK IE column (Daicel, particle size: 5 μm, internal diameter: 4.6 mm, column length: 150 mm) using MeOH with additional 0.5 vol.-% CF_3COOH as mobile phase with a flow of 1.0 mL/min. All samples were prepared using HPLC-grade MeOH and filtered with a membrane filter (nylon, 0.45 μm pore size, 13 mm diameter) in a stainless steel filter holder prior to injection. The obtained HPLC traces for **(±)-1-Ln** with Ln = Pr, Nd, Sm, Er are shown in Figure S1 and for **(±)-1-Lu** in Figure 1 in the manuscript.

Notes: The separation efficiency and the relative and absolute retention of the two enantiomers is dependent on the concentration of the analyte. Special care has to be taken that only freshly prepared MeOH/CF_3COOH mobile phases are used.

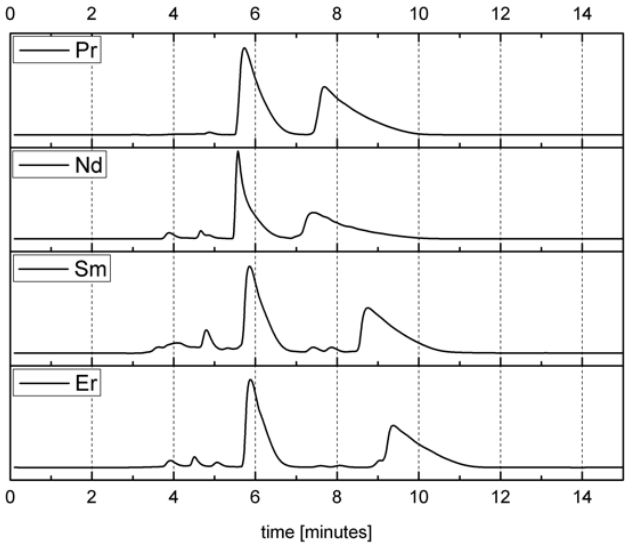

Figure S1. Normalized chiral HPLC traces of the racemates **(±)-1-Ln** (Ln = Pr, Nd, Sm, Er).

Preparative chiral resolution of 1-Lu:
Racemic **1-Lu**[1a] (8.0 mg, 6.4 μmol, 2.0 equivs.) was dissolved in MeOH (2.7 mL, HPLC-grade) and filtered through a membrane filter (vide infra). The filter was washed with additional 0.5 mL of MeOH (HPLC-grade), to yield a total volume of 3.2 mL and a concentration of 2.5 mg/mL, which was found to be the optimal compromise between separation and time efficiency. The solution was subjected to chiral HPLC in portions of 100 μL. The collected fractions of the respective enantiomers were combined and the solvents were removed in vacuo at room temperature. After drying, samples of the enantiomers were redissolved in MeOH (HPLC-grade), filtered and injected to verify the enantiopurity (see main article). After this HPLC purification with MeOH/CF_3COOH (0.5 vol.-%) as mobile phase, a molecular composition of $[C_{36}H_{30}N_8O_2Ln]$ $(O_2C_2F_3)_3 \cdot CH_3OH$ was assumed, resulting in a molar mass of M = 1152.74 g/mol in the case of Lu.

1-Lu-ent1: 2.7 mg (2.3 μmol, 72% yield) of a colorless solid
^{1}H NMR (400 MHz, CD_3OD): δ = 8.48 (d, *J* = 7.9 Hz, 2 H), 8.42-8.36 (m, 4 H), 8.28-8.14 (m, 8 H), 7.70 (d, *J* = 7.7 Hz, 2 H), 7.66 (d, *J* = 7.8 Hz, 2 H), 4.82 (d, *J* = 12.7 Hz, 2 H), 4.81 (d, *J* = 15.8 Hz, 2 H), 4.14 (d, *J* = 15.3 Hz, 2 H), 4.10 (d, *J* = 15.2 Hz, 2 H), 3.95 (d, *J* = 12.9 Hz, 2 H), 3.70 (d, *J* = 15.7 Hz, 2 H) ppm.

1-Lu-ent2: 3.2 mg (2.8 μmol, 88% yield) of a colorless solid
^{1}H NMR (400 MHz, CD_3OD): δ = 8.48 (d, *J* = 8.1 Hz, 2 H), 8.42-8.35 (m, 4 H), 8.27-8.14 (m, 8 H), 7.70 (d, *J* = 7.8 Hz, 2 H), 7.66 (d, *J* = 7.8 Hz, 2 H), 4.82 (d, *J* = 12.9 Hz, 2 H), 4.81 (d, *J* = 15.9 Hz, 2 H), 4.14 (d, *J* = 15.1 Hz, 2 H), 4.10 (d, *J* = 15.1 Hz, 2 H), 3.95 (d, *J* = 12.8 Hz, 2 H), 3.70 (d, *J* = 15.8 Hz, 2 H) ppm.

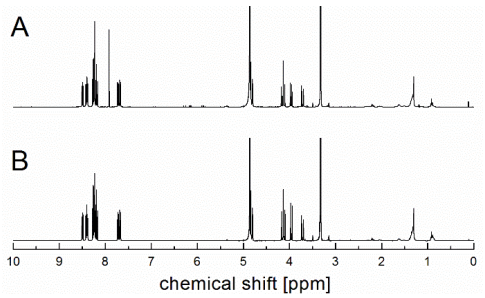

Figure S2. ^{1}H NMR spectra (400 MHz, CD_3OD) of **1-Lu-ent1** (A) and **1-Lu-ent2** (B).

Configurational stability studies:
A) Neat CF_3COOH, room temperature
1-Lu-ent1 (0.25 mg) was dissolved in CF_3COOH (3.3 mL) and the solution was stirred at room temperature for seven days. In total eight samples of 200 μL were taken at different times (see Figure 4 in the manuscript).

B) 10 eq. $LuCl_3 \cdot 6\ H_2O$, reflux
1-Lu-ent1 (0.25 mg, 0.22 μmol, 1.0 equiv.) and $LuCl_3 \cdot 6\ H_2O$ (0.84 mg, 2.2 μmol, 10 equivs.) were dissolved in CH_3CN (3.3 mL, HPLC-grade) and heated under reflux for six days. In total seven samples of 200 μL were taken at different times (see Figure 4 in the manuscript). To prevent the mixture from running dry, several additional portions of CH_3CN were added at

different times (24.2 h: 0.4 mL; 51.3 h: 2.5 mL; 57.8 h: 1.5 mL; 76.3: 0.8 mL; 102 h: 1.8 mL; 120 h, 1.9 mL).

For both studies (A and B), the samples were treated as follows:
The solvents were concentrated under a stream of air and the residues were taken up in MeOH (100 μL). The solutions were filtered through a membrane filter (nylon, 0.45 μm pore size), the filter was washed with additional MeOH (0.3 mL) and the combined methanolic filtrates were concentrated. For chiral HPLC analysis, the dry samples were redissolved in MeOH (100 μL) directly before the HPLC run.

3. Circular Dichroism Spectroscopy

CD spectra were collected on a Jasco J-720 spectropolarimeter, using a bandwidth of 1.0 nm, a response time of 2 seconds and a scan speed of 50 mm/min. Samples of the enantiomers (**1-Lu-ent1**: 0.21 mg, **1-Lu-ent2**: 0.19 mg) were dissolved in MeOH (400 μL each), yielding solutions with concentrations of c = 0.46 mmol/L (**1-Lu-ent1**) and c = 0.41 mmol/L (**1-Lu-ent2**), respectively. The solutions were measured in rectangular quartz cuvettes (Suprasil, d = 1 mm path length).

4. References

[1] a) Pr, Nd, and Er, Lu: Doffek, C.; Alzakhem, N.; Bischof, C.; Wahsner, J.; Güden-Silber, T.; Lügger, J.; Platas-Iglesias, C.; Seitz, M.; *J. Am. Chem. Soc.*, **2012**, *134*, 16413; b) Sm: Doffek, C.; Wahsner, J.; Kreidt, E.; Seitz, M.; *Inorg. Chem.*, **2014**, *53*, 3263; c) Doffek, C.; Seitz, M.; *Angew. Chem. Int Ed.* **2015**, *54*, 9719

ChemPubSoc Europe

DOI: 10.1002/chem.201802196

CHEMISTRY A European Journal Full Paper

Lanthanoid Compounds

Circularly Polarised Luminescence in Enantiopure Samarium and Europium Cryptates

Elisabeth Kreidt,*[a] Lorenzo Arrico,[b] Francesco Zinna,[c] Lorenzo Di Bari,*[b] and Michael Seitz[a]

Abstract: Circularly polarised luminescence (CPL) is a chiroptical phenomenon gaining more and more attention, as the availability of the necessary spectrometers is getting better and first applications in bioimaging or for the preparation of OLEDs (organic light emitting diodes) are coming within range. Until now most examples of distinctly CPL-active compounds were europium and terbium complexes though theoretically the electronic structure of samarium should be as suitable as the one of terbium. This discrepancy can be accounted for by the high susceptibility of samarium to non-radiative deactivation processes. The aim of this study was to strategically circumvent this difficulty by the use of a ligand scaffold which has already proven to efficiently suppress these processes, namely the cryptates. The prepared partly deuterated samarium and europium complexes exhibit distinct circularly polarised luminescence with dissymmetry factors up to $g_{lum} = +0.13$ (Sm^{III}) or $g_{lum} = -0.19$ (Eu^{III}).

Introduction

Chirality is a ubiquitous concept in science and technology and of special importance in chemistry and related fields. The handedness of molecules is crucial for various phenomena. Many of these phenomena depend on the interplay of chiral matter with (polarised) light, for example, optical rotation, circular dichroism (CD) or circularly polarised luminescence (CPL). Especially the latter is of special interest for various applications. A compound which exhibits CPL emits different intensities of left and right circularly polarised light at specific wavelengths after excitation with unpolarised light.[1] This property is usually quantified by means of the luminescence dissymmetry factor g_{lum}, which is defined as quotient of the difference of the intensities of left and right polarised light ($I_L - I_R$) and the half of the total intensity ($I_L + I_R$) [Eq. (1)]:

$$g_{lum} = \frac{I_L - I_R}{1/2(I_L + I_R)} = \frac{\Delta I}{I} \quad (1)$$

[a] E. Kreidt, Prof. M. Seitz
Institute of Inorganic Chemistry, University of Tübingen
Auf der Morgenstelle 18, 72076 Tübingen (Germany)
E-mail: elisabeth.kreidt@uni-tuebingen.de

[b] L. Arrico, Prof. L. Di Bari
Dipartimento di Chimica e Chimica Industriale, Università di Pisa
Via Moruzzi 13, 56124 Pisa (Italy)
E-mail: lorenzo.dibari@unipi.it

[c] Dr. F. Zinna
Department of Organic Chemistry, University of Geneva
30 quai Ernest Ansermet, 1211 Geneva 4 (Switzerland)

Supporting information and the ORCID identification numbers for the authors of this article can be found under: https://doi.org/10.1002/chem.201802196.

The luminescence dissymmetry factor of a given transition a→b depends on the ratio of the transition's rotatory strength R_{ab} and the oscillator strength D_{ab}. The rotatory strength is determined by the magnitudes and the relative orientation of the magnetic and electric dipole transition moments ($R_{ab} = |M_{ba}||P_{ab}|\cos\tau_{ab}$), whereas the oscillator strength can be approximated as the square of the electric dipole moment ($D_{ab} = |P_{ab}|^2$), giving [Eq. (2)]:[1b]

$$g_{lum} = \frac{4\,R_{ab}}{|D_{ab}|} = \frac{4\,|M_{ba}|\cos\tau_{ab}}{|P_{ab}|} \quad (2)$$

The dependence on the angle τ_{ab} between the magnetic and electric dipole transition moments points towards the high sensitivity of CPL towards subtle changes in the coordination geometry. This makes it a useful tool in the study of biomolecules.[2] Also, the circularly polarised nature of the emitted light offers great potential for applications, for example, in bioimaging, as it enables a substantial improvement of the signal to noise ratio.[3] Another field which will greatly benefit from circularly polarised luminescence are innovative organic light emitting diodes (OLEDs).[4] In the past few years CPL has evolved from a quite exotic speciality measured on custom-built devices to a more established technique. Subsequently, attempts to realise applications in the fields mentioned above are getting more concrete.

For all kinds of applications, substances with high g_{lum} values are desired. While for purely organic molecules usually values in the range of 10^{-4} to 10^{-2} are reported,[1f] a special class of coordination compounds, namely lanthanoid complexes, may reach g_{lum} values between 0.1 and 1.38 (or up to 1.45 in the solid state).[1,5] This is not the only exceptionality of lanthanoid complexes, other peculiarities like long luminescence lifetimes,

ChemPubSoc Europe

CHEMISTRY A European Journal Full Paper

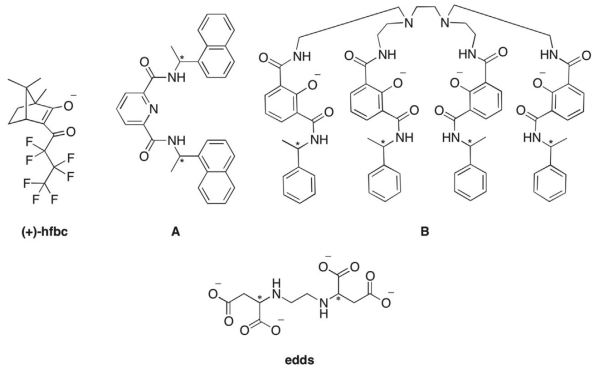

Figure 1. Ligands used for the preparation of CPL-active samarium complexes. (+)-hfbc = (+)-3-heptafluorobutyrylcamphorate,[5b] A = pyridine-2,6-dicarboxylic acid bis-[(1-naphthalen-1-yl-ethyl)-amide],[11e] B = 1-phenylethylamine substituted 2-hydroxyisophthalamide,[11d] edds = ethylenediamine-*N*,*N*′-disuccinate.[11f]

very sharp emission spectra or very high magnetic anisotropies have led to flourishing research on these compounds in the past years.[6]

Both the general electronic structure of the lanthanoid and the influence of the crystal field control the CPL properties of a lanthanoid complex. From Equation (2) it becomes evident that the highest luminescence dissymmetry factors can be expected for transitions which are magnetic dipole allowed and electric dipole forbidden and satisfy the magnetic dipole selection rule ($\Delta J = 0, \pm 1$; except $J' = J'' = 0$). Already in 1980 Richardson identified the transitions of the lanthanoids for which the highest dissymmetry factors can be expected.[7] The $^5D_0 \rightarrow {}^7F_1$ transition of Eu^{III} with its purely magnetic dipole character offers by far the best prerequisites for observing large dissymmetry factors. But also the electronic structures of for example, Tb^{III} and Sm^{III} allow for sizeable g_{lum} values. Although Richardson's classification of the transitions has proven to be very reliable and successful, the influence of the coordination situation around the lanthanoid is only poorly understood until now. Also against the background of the lanthanoid's intrinsic kinetic lability it is very difficult to establish correlations of structural features of a complex and its CPL properties such as the magnitude of the luminescence dissymmetry factor or the shape of the CPL spectrum, however there have been some efforts.[8]

A wealth of europium complexes exhibiting CPL has been reported until now, in line with this metal's exceptional suitability for observing CPL.[9] Though the electronic nature of the $^5D_4 \rightarrow {}^7F_5$ transition of terbium is less favourable for the observation of CPL, the generally high luminescence of this lanthanoid is beneficial for the detection of CPL and many examples have been reported.[8e,10] Following Richardson's classification of the transitions of lanthanoids, the suitability for the observation of CPL of the $^4G_{5/2} \rightarrow {}^6H_{5/2}$ transition of samarium should be comparable to the one of the $^5D_4 \rightarrow {}^7F_5$ transition of terbium. But in contrast to terbium, samarium complexes are usually only weakly luminescent, which is due to this lanthanoid's high susceptibility to multiphonon quenching. Consequently, the study of CPL has to a certain degree been limited to complexes of europium and terbium so far. To the best of our knowledge, until now four molecular samarium complexes were known to exhibit CPL in solution.[5b,11] For these compounds which were studied as enantiopure samples also dissymmetry factors were reported. The ligands used for the preparation of these compounds are shown in Figure 1. The most intense samarium-centred CPL was found for $Cs[Sm((+)\text{-hfbc})_4]$ with maximum g_{lum} values of -1.15 ($^4G_{5/2} \rightarrow {}^6H_{5/2}$) and $+1.15$ ($^4G_{5/2} \rightarrow {}^6H_{7/2}$). The respective europium complex $Cs[Eu((+)\text{-hfbc})_4]$[5] exhibits the highest g_{lum} value ($+1.38$ in $CHCl_3$) reported so far, which points towards an exceptional suitability for CPL of the coordination geometry and electronic structure of the ligand found in these complexes. The fact that the g_{lum} value of the samarium compound reaches the same order of magnitude as the europium compound gives evidence of the high potential of samarium-centred CPL. Remarkably high g_{lum} values were also found for the complexes of Sm^{III} and the pyridyldiamide **A** (up to 0.50 for $^4G_{5/2} \rightarrow {}^6H_{5/2}$ and up to 0.28 for $^4G_{5/2} \rightarrow {}^6H_{7/2}$).[11e] The complex of Sm^{III} and the 2-hydroxyisophthalamide **B** is the third example of a samarium complex for which g_{lum} values were reported (-0.027 for $^4G_{5/2} \rightarrow {}^6H_{5/2}$ and -0.028 for $^4G_{5/2} \rightarrow {}^6H_{7/2}$).[11d] In the case of the complex consisting of the disuccinate **edds** and Sm^{III} only for the $^4G_{5/2} \rightarrow {}^6H_{7/2}$ transition (which is typically more luminescent) a g_{lum} value ($+0.066$) could be reported.[11f] Interestingly, in two of these four examples, for the $^4G_{5/2} \rightarrow {}^6H_{5/2}$ and the $^4G_{5/2} \rightarrow {}^6H_{7/2}$ transitions identical g_{lum} values were reported, though according to Richardson's classification one would expect the dissymmetry factor to be considerably higher in the case of the $^4G_{5/2} \rightarrow {}^6H_{5/2}$ transition.

Rigidified bipyridine cryptands (Figure 2) are C_2-symmetric and offer an extremely high conformational and configurational stability. The propeller-like arrangement of the three bipyri-

ChemPubSoc Europe

CHEMISTRY A European Journal Full Paper

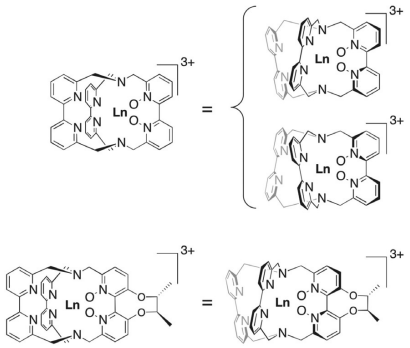

Figure 2. Rigidified lanthanoid cryptates are usually isolated as racemic mixture (top). By attachment of a stereogenic element to one of the bipyridine units a preorganisation of the building blocks and enantiopure synthesis can be achieved (bottom).[12]

dine-units results in helical (M/P) or axial chirality (R_a/S_a). Usually, lanthanoid cryptates are synthesised as racemic mixture of two enantiomers, but it has been shown that it is also possible to prepare these complexes selectively in an enantiopure fashion.[12]

The luminescence properties of the racemic lanthanoid cryptates have already been studied in detail.[13] The three bipyridine units around the lanthanoid ion cause both an efficient shielding from surrounding solvent molecules and an efficient indirect population of the excited state of the lanthanoid via the so-called antenna effect,[6a–e] affording lanthanoid complexes with long luminescence lifetimes and good quantum yields.[14]

Lanthanoids for which the energetic difference between the electronic states is typically small (e.g. Sm^{III} or Yb^{III}) are especially sensitive towards nonradiative deactivation processes caused by multiphonon quenching. Past studies have shown that deuterated derivatives of the cryptates have a special ability to protect this group of lanthanoids against nonradiative deactivation processes, leading to extraordinarily long luminescence lifetimes of the corresponding Yb^{III} and Sm^{III} complexes in deuterated solvents.[13d,e] In the case of Sm^{III} this also leads to very promising conditions for the observance of CPL. The aim of this work was to realise an enantiopure samarium cryptate and study whether such a compound is indeed suitable to enlarge the repertory of samarium complexes exhibiting CPL.

Results and Discussion

Complex design

As shown before, it is possible to prepare lanthanoid cryptates in an enantiopure form (Figure 2).[12] For this purpose a tether derived from (*S*,*S*)-2,3-butanediol is attached to the *N*-*N*′-dioxide modified bipyridine unit of the ligand scaffold. ^{1}H NMR experiments on samples of corresponding lanthanoid cryptates in enantiopure solvents (methyl-L-lactate and methyl-D-lactate) already gave evidence of the enantiopurity of the samples. Due to the presence of transitions with small energetic differences ΔE between the electronic states, samarium complexes are especially sensitive towards non-radiative deactivation processes and some additional efforts are necessary to prepare luminescent samarium complexes. Generally, deuteration of the ligand scaffold can suppress multiphonon quenching processes efficiently, most efficiently in the case of the benzylic positions.[13c,d,14,15] Furthermore the deuteration of only the benzylic positions of the non-oxidised bipyridine units offers an acceptable trade-off between efficient ligand synthesis and the improvement of the luminescence properties. The synthesis of the resulting enantiopure and partly deuterated ligand core has already been reported.[12] This ligand offers optimal preconditions for the preparation of a CPL-active samarium compound (Figure 3). Additionally, the respective europium complex was prepared. The special electronic structure of Eu^{III} is not only suitable for observing CPL but it also offers the extraction of additional information from the study of the photophysical properties like for example the radiative luminescence lifetime τ_{rad}, which is not always easily accessible in the case of the other lanthanoids.

Synthesis

The synthesis of the ligand and the corresponding samarium and europium complexes was performed analogously to procedures already described (Scheme 1).[12] Experimental details for the preparation of the lanthanoid complexes **1-Sm** and **1-Eu** from the sodium complex are given in the experimental

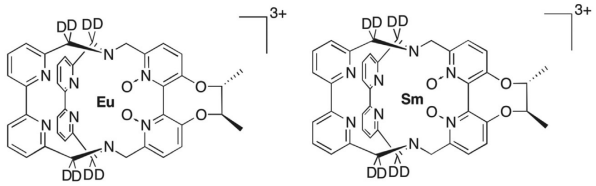

1-Eu **1-Sm**

Figure 3. Enantiopure, luminescent lanthanoid cryptates prepared for this study.

ChemPubSoc Europe

CHEMISTRY A European Journal Full Paper

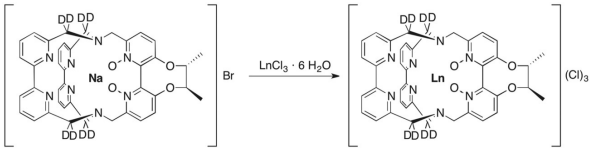

Scheme 1. Preparation of the enantiopure, partly deuterated lanthanoid cryptates from the corresponding sodium cryptates.

section. After complex synthesis, the obtained crude products were purified via recrystallisation. Analytical HPLC (high performance liquid chromatography) runs were performed to check the purity of the isolated compounds, whereby no remains of the sodium cryptate were detected (see Experimental Section and Supporting Information).

Chemical structure in solution: nuclear magnetic resonance

The spectra of **1-Sm** and **1-Eu** consist of relatively sharp signals, giving evidence of the expected rigid structure, the presence of only one species in solution and the C_2-symmetry of the complexes.

The pronounced magnetic susceptibility anisotropy of **1-Eu** leads to considerable shifts of the signals in the ^{1}H NMR spectrum (CD_3OD) of the compound (Figure 4). The signals are distributed over about 35 ppm, and most of them are well separated from each other. Only in the range between 2.5 to 3.0 ppm and 1.0 to 0.7 ppm signals are overlapping, so that an individual integration is not possible. In total ten signals with an integral of two protons and one multiplet of two overlapping signals with a total integral of eight protons can be identified, perfectly mirroring the expected C_2-symmetry of the molecule. Usually the pseudo-contact component of the paramagnetic shift that a signal experiences will be more pronounced when the corresponding nucleus is spatially close to the paramagnetic centre. In compliance with that, in previous detailed NMR studies on paramagnetic lanthanoid cryptates the most shifted signals could always be assigned to the benzylic protons.[12,13c] Accordingly, the strongly shifted signals at about −10 and −17.5 ppm most likely correspond to the protons in the benzylic position, which is also in agreement with the NMR data reported for the unfunctionalised europium cryptate and a study on a modified europium cryptate, in which for the respective protons very similar lanthanoid induced shifts were found.[13b,16] Because of their long distance from the lanthanoid, the signal of the methyl groups (0.85 ppm, overlaid with another signal of two protons) is experiencing only a slight shift compared to the diamagnetic analogue.[12]

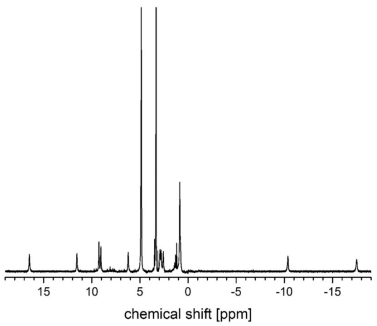

Figure 4. ^{1}H NMR (CD_3OD, 400 MHz) of **1-Eu**.

As for **1-Eu**, the spectrum of **1-Sm** (in CD_3OD) gives evidence of the C_2-symmetry of the complex (Figure 5). The eight partly overlapping signals between 7.5 ppm and 9.8 ppm with integrals of two protons each correspond to the aromatic protons of the ligand and the signal at 1.45 ppm with an integral of six protons can be assigned to the methyl groups. Sm^{III} is only slightly paramagnetic, yet some signals experience a considerable shift. Whereas in the diamagnetic **1-Lu**[12] no signals could be detected in the ranges between 1.5 ppm to 3.0 ppm and between 5.0 ppm to 7.5 ppm, in the spectrum of **1-Sm** two signals can be detected in these ranges. As these signals experience the strongest paramagnetic shifts they most likely correspond to the protons which are closest to the lanthanoid, namely the benzylic protons. In contrast, the two remaining protons of the tether are relatively apart from the paramagnetic centre. Their ^{1}H NMR signal will not experience a consider-

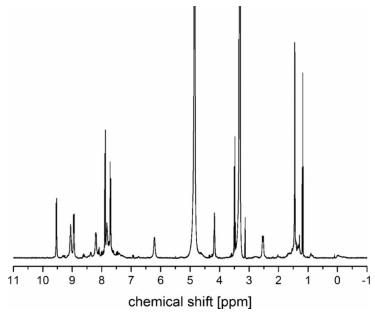

Figure 5. ^{1}H NMR (CD_3OD, 400 MHz) of **1-Sm**.

ChemPubSoc Europe

CHEMISTRY A European Journal Full Paper

able paramagnetic shift and can be detected at about 4.2 ppm.

In conclusion, the ^{1}H NMR spectra of both compounds under study give evidence of the presence of one C_2-symmetric species in solution. As expected the structure of the complexes is well defined and no exchange or rearrangement processes are observable.

Steady-state emission spectra

In accordance to the findings from the analysis of the ^{1}H NMR spectra, the high resolution luminescence spectrum of **1-Eu** (Figure 6) is completely consistent with one C_2-symmetric Eu^{III}-species, exhibiting one $^5D_0 \rightarrow {}^7F_0$ transition and three sublevels of the $^5D_0 \rightarrow {}^7F_1$ transition.[17] As **1-Sm** is highly luminescent, a partial resolution of the transition's fine structure was possible, by the use of a narrow emission monochromator slit width (1 nm) (Figure 7). In addition, the transitions in the near-infrared could also be detected (Figure 8).

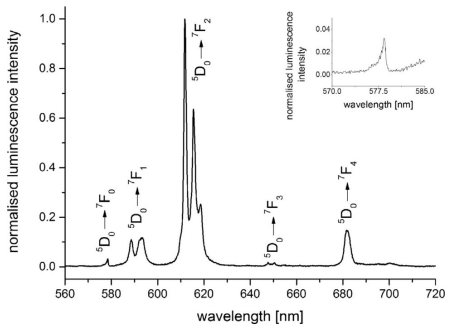

Figure 6. Emission spectrum of **1-Eu** in CD_3OD at room temperature. $\lambda_{exc} = 305$ nm, $A_{305\,nm} = 0.22$. Insert: Magnification of the $^5D_0 \rightarrow {}^7F_0$ transition.

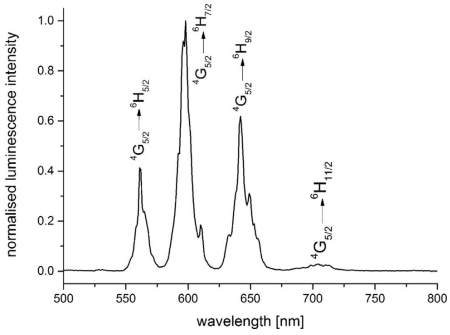

Figure 7. Emission spectrum of **1-Sm** in CD_3OD at room temperature. $\lambda_{exc} = 320$ nm, $A_{320\,nm} = 0.26$.

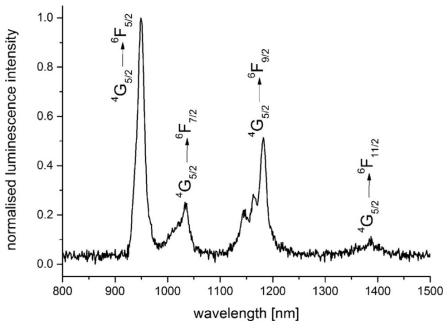

Figure 8. Near-infrared emission spectrum of **1-Sm** in CD_3OD at room temperature. $\lambda_{exc} = 320$ nm, $A_{320\,nm} = 0.26$.

Luminescence lifetimes and quantum yields

For both complexes **1-Sm** and **1-Eu** the luminescence lifetimes τ_{obs} and absolute quantum yields φ^L_{Ln} were determined (see Table 1). Both complexes exhibit a monoexponential decay (see supporting information), which is another evidence of the stable and well-defined structure of **1-Sm** and **1-Eu** in solution.

Table 1. Luminescence lifetimes τ_{obs}, radiative lifetimes τ_{rad}, intrinsic quantum yields φ^{Ln}_{Ln}, overall quantum yields φ^L_{Ln} and sensitisation efficiencies η_{sens} of **1-Eu** and **1-Sm** in CD_3OD.

Compound	τ_{obs}	τ_{rad}	$\varphi^{L\,[a]}_{Ln}$	$\varphi^{Ln[b]}_{Ln}$	$\eta_{sens}{}^{[c]}$
1-Eu	1.6 ms[d]	4.2 ms	5.9%	38%	15%
1-Sm	90 µs[e]	–	0.26%	–	–

[a] Determined using quinine in 0.5 M H_2SO_4 as reference compound, see supporting information and reference [20]. [b] $\varphi^{Ln}_{Ln} = \tau_{obs}/\tau_{rad}$. [c] $\eta_{sens} = \varphi^L_{Ln}/\varphi^{Ln}_{Ln}$. [d] $\lambda_{exc} = 320$ nm, $\lambda_{em} = 610$ nm ($^5D_0 \rightarrow {}^7F_2$). [e] $\lambda_{exc} = 320$ nm, $\lambda_{em} = 597$ nm ($^4G_{5/2} \rightarrow {}^6H_{7/2}$).

As expected, τ_{obs} and φ^L_{Ln} are significantly higher in the case of **1-Eu**. In a rough approximation, due to the absence of C/H- and O/H-oscillators, CD_3OD, CD_3CN and D_2O can be assumed to be solvents which do not cause nonradiative deactivation of the excited lanthanoid. Indeed at least the O/D-oscillators will cause some nonradiative deactivation and analogously to general experiences shorter lifetimes can be expected for measurements in D_2O and longer lifetimes for measurements in CD_3CN.[18] Keeping this in mind, a rough comparison of lifetime data measured in these solvents is possible.

The determined luminescence lifetime τ_{obs} of **1-Eu** in CD_3OD is about one third higher than the previously reported value for the unfunctionalised europium cryptate in D_2O ($\tau_{obs} = 1.15$ ms).[13a] This increase of the lifetime can be accounted for by the partial deuteration of the ligand scaffold by which eight of the quite efficient C/H-oscillators are replaced by less efficient C/D-oscillators. Interestingly the overall quantum yield φ^L_{Ln} of **1-Eu** is almost one order of magnitude smaller than the

ChemPubSoc Europe

CHEMISTRY A European Journal Full Paper

value for the previously reported unfunctionalised compound (φ^{L}_{Ln} = 30%, in D_2O).[13a]

Due to the purely magnetic dipole character of the $^5D_0 \rightarrow {}^7F_1$ transition of Eu^{III} the intrinsic luminescence lifetime τ_{rad} of the corresponding complexes is proportional to the ratio of integrated total emission intensity I_{tot} and the integrated emission intensity of the $^5D_0 \rightarrow {}^7F_1$ transition (I_{MD}).[19] Consequently, it can be obtained directly from the corrected steady state emission spectrum [Eq. (3)]:

$$\frac{1}{\tau_{rad}} = A_{MD,0} \times n^3 \left(\frac{I_{tot}}{I_{MD}}\right) \quad (3)$$

in which $A_{MD,0}$ corresponds to the probability of spontaneous emission of the $^5D_0 \rightarrow {}^7F_1$ transition in vacuo (14.65 s^{-1}) and n is the refractive index of the surrounding medium (1.326 for CD_3OD). The intrinsic quantum yield φ^{L}_{Ln} of **1-Eu** can be determined as the quotient of the observed luminescence lifetime τ_{obs} and the intrinsic luminescence lifetime τ_{rad}.

The sensitisation efficiency η_{sens} ($=\varphi^{L}_{Ln}/\varphi^{Ln}_{Ln}$) determined for **1-Eu** is somewhat lower than expected, which indicates some kind of energetic mismatch between the ligand and the trivalent europium ion. A less efficient energy transfer from the ligand to the lanthanoid would also explain the relatively low overall quantum yield. Indeed, the introduction of the tether at the oxidised bipyridine unit is likely to alter the electronic structure at the ligand. Nevertheless, the UV/Vis spectra of the complexes (see supporting information) correspond to the spectra typically obtained for tris(2,2′-bipyridine)-*N*,*N*-dioxide cryptates.

As expected, the luminescence lifetime of the partly deuterated **1-Sm** in CD_3OD lies between the luminescence lifetimes determined for the undeuterated and the perdeuterated unfunctionalised analogues in CD_3CN (31 and 394 μs, respectively).[13d] The threefold increase compared to the undeuterated compound, despite the more pronounced non-radiative deactivation in CD_3OD, points towards the high impact of the oscillators in the benzylic positions of the ligand scaffold.

Chiroptical properties: circular dichroism and circularly polarised luminescence

The normalised CD spectra of **1-Eu** and **1-Sm** (Figure 9) are quite similar to the previously reported CD spectra of enantiopure, unfunctionalised Lu^{III}-cryptates.[21] This indicates that the geometry of the ligand around the lanthanoid and the helicity is comparable to the one found in unfunctionalised lanthanoid cryptates.

After the complexes were found to meet the photophysical and structural expectations, finally circularly polarised luminescence was studied. The spectra of both complexes feature transitions with distinct rotatory strengths. Figures 10 and 11 show the normalised CPL (with the luminescence dissymmetry factors g_{lum}) and total emission spectra of **1-Eu** and **1-Sm**. In the case of **1-Sm** the $^4G_{5/2} \rightarrow {}^6H_{5/2}$ and the $^4G_{5/2} \rightarrow {}^6H_{7/2}$ transition exhibit distinct rotatory strengths, leading to g_{lum} values of up to +0.13 ($^4G_{5/2} \rightarrow {}^6H_{5/2}$) (Figure 10). In the case of the

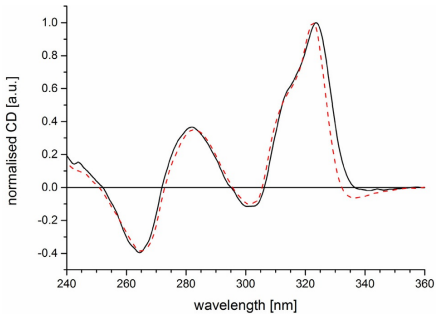

Figure 9. CD spectra of **1-Eu** (black, solid line) and **1-Sm** (red, dashed line) in CD_3OD (3 mM) at room temperature. Both spectra were independently normalised on a scale of 0 to 1.

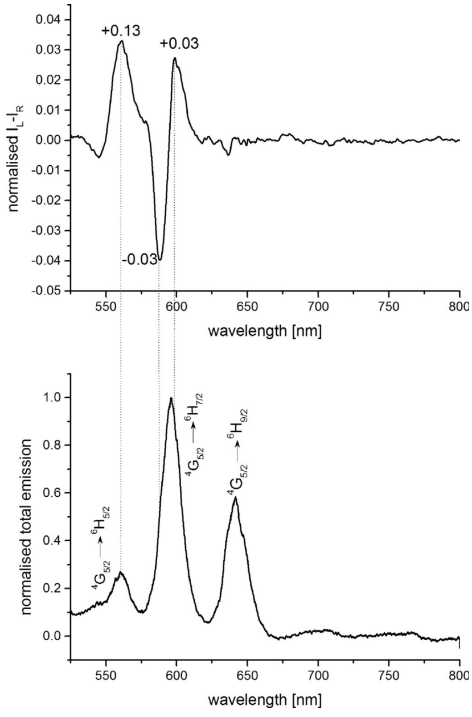

Figure 10. Normalised CPL spectrum (top) with the luminescence dissymmetry factors g_{lum} and total emission spectrum (bottom) of **1-Sm** (λ_{exc} = 254 nm, c = 3 mM in CD_3OD).

$^4G_{5/2} \rightarrow {}^6H_{7/2}$ transition the opposite signs of the components of the transition give additional information about the fine struc-

ChemPubSoc Europe

CHEMISTRY A European Journal Full Paper

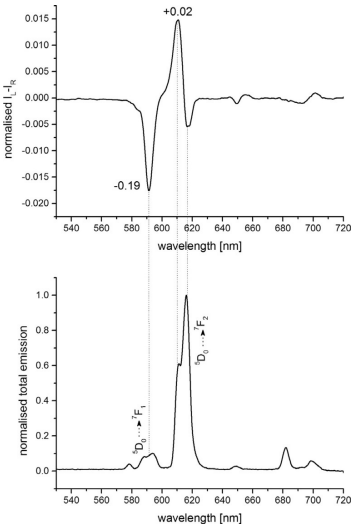

Figure 11. Normalised CPL spectrum (top) with the luminescence dissymmetry factors g_{lum} and total emission spectrum (bottom) of **1-Eu** ($\lambda_{exc}=254$ nm, $c=3$ mM in CD_3OD).

ture of the band, which could not be resolved in the total luminescence spectrum, not even in the high-resolution spectrum (Figure 7). For this transition g_{lum} values of -0.03 and $+0.03$ were determined. Consequently, in the case of **1-Sm** Richardson's prediction of the $^4G_{5/2} \rightarrow {}^6H_{5/2}$ transition exhibiting more intense CPL than the $^4G_{5/2} \rightarrow {}^6H_{7/2}$ transition was experimentally confirmed. In the CPL spectrum of **1-Eu**, the $^5D_0 \rightarrow {}^7F_2$ transition is split into two components with opposite signs (Figure 11). On the other hand the $^5D_0 \rightarrow {}^7F_1$ transition exhibits opposite sign with respect to the major CPL component associated with the hypersensitive transition and quite similar rotatory strengths, as it can often be observed in CPL spectra of Eu-complexes. Resulting from the lower total luminescence intensity of the $^5D_0 \rightarrow {}^7F_1$ transition (and in congruence with Richardson's classification), the corresponding luminescence dissymmetry factor g_{lum} is about one order of magnitude higher than the one allied to the $^5D_0 \rightarrow {}^7F_2$ transition. Interestingly the maximum g_{lum} values determined for **1-Sm** and **1-Eu** are in the same order of magnitude, as it had already been reported for Cs[Ln((+)-hfbc)$_4$].[5b] Consequently the results reported herein give another evidence for the high potential of samarium-centred CPL.

Conclusions

In summary we could show that enantiopure cryptates are indeed a well-suited scaffold for the observation of circularly polarised luminescence. In the partly deuterated ligand scaffold under study the lanthanoid ion is efficiently protected against nonradiative deactivation processes, which is especially helpful in the case of the less luminescent lanthanoids such as samarium. As already observed for other ligand scaffolds in which samarium and europium exhibit distinct CPL-activity, in our study g_{lum} values in the same order of magnitude were determined for the europium ($g_{lum}=-0.19$) and the samarium complex ($g_{lum}=+0.13$). This points to the high potential of samarium CPL which is accessible when the non-radiative deactivation can be controlled, as it is possible in lanthanoid cryptates. The well-defined structure in solution of these complexes may be of help for a more detailed understanding of the origin of CPL and the extraordinarily high stability of these complexes under various conditions makes the lanthanoid cryptates promising candidates for upcoming applications of CPL.

Experimental Section

General

The synthesis of the ligand and respective Yb^{III} and Lu^{III} complexes has already been reported elsewhere.[12] Chemicals were purchased from commercial suppliers and used as received unless stated otherwise. CH_3CN for the synthesis of the cryptates was HPLC grade. NMR spectra were measured at 26 °C on a Bruker AVII+400 (^{1}H: 400 MHz) and analysed using MestReNova 7 (Mestrelab Research) and Origin 9.0 (OriginLab). Deuterated solvents had deuterium contents >99.8%D and were used as commercially available without additional purification or drying procedures. To confirm the purity of the complexes, samples were taken up in a minimum of CH_3CN/H_2O (1:1, v/v), filtered (0.45 μm nylon membrane filters) and subjected to analytical reversed-phase HPLC (RP-18e, 125×4 mm–5 μm, flow rate: 1 mL min^{-1}, UV detection: 300 nm) with H_2O (degassed, +1% TFA, v/v) as mobile phase A, CH_3CN (degassed, HPLC grade) as mobile phase B, and the following gradient: 0 min: 85%A/15%B; 5 min 85%A/15%B; 19 min: 45%A/ 55%B; 25 min: 45%A/55%B; 40 min: 85%A/15%B; 50 min: 85%A/ 15%B. The identity of the complexes was confirmed via high resolution ESI mass spectrometry experiments in which the formate adducts $[LnC_{40}H_{28}D_8N_8O_4+HCOO^-]^{2+}$ of the respective complexes could be identified unambiguously. The formate adducts result from the in situ oxidation of methanol during the mass spectrometry experiments.

Photophysical measurements

Steady state emission spectra were acquired on a Horiba Fluorolog-3 DF spectrofluorimeter using quartz cuvettes (suprasil, 1 cm pathlength) at room temperature. The excitation light source was a 450 W xenon lamp. Emission was monitored at 90° using a Hamamatsu R2658P PMT (UV/vis/NIR, 200 nm$<\lambda_{em}<$1010 nm) or a Hamamatsu H10330-75 PMT (NIR, 950 nm$<\lambda_{em}<$1700 nm). Spectral selection was achieved by single grating monochromators (excitation: 1200 grooves nm^{-1}, blazed at 300 nm, visible emission: 1200 grooves/nm, blazed at 500 nm, NIR emission: 600 grooves/nm, blazed at 1000 nm). Luminescence decay profiles were determined with the same instrumental setup as described above for the steady state experiments. The light source for the recording of the decay profiles was a 70 W xenon lamp (pulse width ca. 1.5 μs FWHM). Lifetime data analysis (deconvolution, statistical parameters, etc.) was performed using the software package DAS from Horiba. Lifetimes were determined by fitting the middle and tail

ChemPubSoc Europe

CHEMISTRY A European Journal Full Paper

portions of the decays. The absolute quantum yields φ^{L}_{Ln} of **1-Eu** and **1-Sm** were determined with two independent sets of samples each, using quinine sulfate in 0.5 M H_2SO_4 as quantum yield standard ($\Phi = 54.6\%$).[20] For analysis the optically dilute method was employed [Eq. (4)]:[20]

$$\Phi_X = \Phi_s \times \left(\frac{Grad_x}{Grad_s}\right) \times \left(\frac{n_x}{n_s}\right)^2 \quad (4)$$

where Φ_X/Φ_s are the quantum yields of the sample (x) or the standard (s), $Grad_x/Grad_s$ are the linearly fitted slopes from the plot of the integrated luminescence intensity of the sample (x) or the standard (s) versus the absorbance at the excitation wavelength and n_x/n_s are the refractive indices of the medium or the sample (here: CD_3OD, $n_x = 1.326$) or the standard (here: $n_s = 1.33$). For the determination of φ^{L}_{Eu} an excitation wavelength of 317 nm was chosen, for the determination of φ^{L}_{Sm} an excitation wavelength of 310 nm was chosen. All spectra were corrected and the integrated intensity of the second order peaks in the spectra of the lanthanoid complexes were subtracted from the integrated luminescence intensity. The estimated uncertainties in φ^{L}_{Ln} are $\pm 15\%$.

Chiroptical measurements

ECD (electronic circular dichroism) spectra were recorded using a Jasco J-715 spectropolarimeter, in 3 mM CD_3OD solution in a 0.1 mm optical path cell (4 accumulations). CPL spectra were measured using the home-built spectrofluoropolarimeter described in reference [8h]. The samples were irradiated by a 90° geometry employing as the source an UVC high pressure mercury lamp ($\lambda_{max} =$ 254 nm), the following acquisition parameters were used: accumulations = 2, integration time = 8 sec, scan-speed = 0.5 nm sec^{-1}.

Synthesis

Europium complex 1-Eu: The sodium cryptate 1-Na (5.02 mg, 6.25 μmol, 1.0 equiv) and $EuCl_3 \cdot 6H_2O$ (3.44 mg, 9.38 μmol, 1.5 equiv) were suspended in 7 mL dry CH_3CN (HPLC grade) and heated to reflux temperature, whereby the mixture got turbid. After 40 h the volatiles were removed. The remaining solid was dried in vacuo, afterwards taken up in a minimum amount of CH_3OH and filtered over cotton. The yellow solution was overlaid with Et_2O and stored at 4°C overnight. Afterwards the precipitate was collected on a membrane filter, washed with cold Et_2O and dried to give a faintly yellow solid (3.62 mg, 3.81 μmol, 61%). ^{1}H NMR (400 MHz, CD_3OD): $\delta = 16.49$ (s, 2H), 11.54 (s, 2H), 9.25 (s, 2H), 9.03 (s, 2H), 6.19 (s, 2H), 3.09–2.43 (m, 6H), 1.00–0.66 (m, 8H), −10.40 (s, 2H), −17.53 ppm (s, 2H). Analytical HPLC: $t_r = 13.7$ min (see Figure S1 in the Supporting Information). HR ESI-MS (pos. mode), $[EuC_{40}H_{28}D_8N_8O_4 + HCOO^-]^{2+}$: calculated: $m/z = 449.12698$, found: $m/z = 449.12706$.

Samarium complex 1-Sm: 5.02 mg (6.25 μmol, 1.0 equiv) of the sodium cryptate 1-Na together with $SmCl_3 \cdot 6H_2O$ (3.42 mg, 9.38 μmol, 1.5 equiv) were suspended in 7 mL dry CH_3CN (HPLC grade) and heated to reflux temperature. After 40 h the volatiles were removed and the crude product was treated as described for **1-Eu** to yield 3.61 mg (3.80 μmol, 61%) of a faintly yellow solid. ^{1}H NMR (400 MHz, CD_3OD): $\delta = 9.54$ (d, $J = 8.13$ Hz, 2H), 9.11–9.00 (m, 2H), 8.95 (d, $J = 7.30$ Hz, 2H), 8.26–8.14 (m, 2H), 7.93–7.65 (m, 8H), 6.21 (br s, 2H), 4.17 (br s, 2H) 2.62–2.43 (m, 2H), 1.52–1.39 (m, 6H) ppm. Analytical HPLC: $t_r = 14.0$ min (see Figure S2 in the supporting information). HR ESI-MS (pos. mode), $[SmC_{40}H_{28}D_8N_8O_4 + HCOO^-]^{2+}$: calculated: $m/z = 448.62623$, found: $m/z = 448.62667$.

Acknowledgements

Financial support is gratefully acknowledged from the German National Academic Foundation (predoctoral fellowship for E.K.) and the German Research Foundation (grant SE 1448/6-1).

Conflict of interest

The authors declare no conflict of interest.

Keywords: chirality · circularly polarized luminescence · coordination compounds · europium · samarium · lanthanoids

[1] a) J. P. Riehl, G. Muller, in *Comprehensive Chiroptical Spectroscopy, Vol. 1* (Eds.: N. Berova, P. L. Polavarapu, K. Nakanishi, R. W. Woody), Wiley, Hoboken, **2012**, pp. 65–90; b) R. Carr, N. H. Evans, D. Parker, *Chem. Soc. Rev.* **2012**, *41*, 7673–7686; c) F. Zinna, L. Di Bari, *Chirality* **2015**, *26*, 553–562; d) G. Muller, in *Luminescence of Lanthanide Ions in Coordination Compounds and Nanomaterials* (Ed.: A. de Bettencourt-Dias), Wiley, Hoboken, **2014**, pp. 77–124; e) G. Longhi, E. Castiglioni, J. Koshoubu, G. Mazzeo, S. Abbate, *Chirality* **2016**, *28*, 696–707; f) E. M. Sánchez-Carnerero, A. R. Agarrabeitia, F. Moreno, B. L. Maroto, G. Muller, M. J. Ortiz, S. de la Moya, *Chem. Eur. J.* **2015**, *21*, 13488–13500.

[2] Selected examples: a) N. Çoruh, J. P. Riehl, *Biochemistry* **1992**, *31*, 7970–7976; b) S. Abdollahi, W. R. Harris, J. P. Riehl, *J. Phys. Chem.* **1996**, *100*, 1950–1956; c) J. Yuasa, T. Ohno, H. Tsumatori, R. Shiba, H. Kamikubo, M. Kataoka, Y. Hasegawa, T. Kawai, *Chem. Commun.* **2013**, *49*, 4604–4606.

[3] A. T. Frawley, R. Pal, D. Parker, *Chem. Commun.* **2016**, *52*, 13349–13352.

[4] Selected examples: a) Y. Geng, A. Trajkovska, S. W. Culligan, J. J. Ou, H. M. P. Chen, D. Katsis, S. H. Chen, *J. Am. Chem. Soc.* **2003**, *125*, 14032–14038; b) Y. Yang, R. C. da Costa, D.-M. Smilgies, A. J. Campbell, M. J. Fuchter, *Adv. Mater.* **2013**, *25*, 2624–2628; c) F. Zinna, M. Pasini, F. Galeotti, C. Botta, L. Di Bari, U. Giovanella, *Adv. Funct. Mater.* **2017**, *27*, 1603719.

[5] a) J. L. Lunkley, D. Shirotani, K. Yamanari, S. Kaizaki, G. Muller, *J. Am. Chem. Soc.* **2008**, *130*, 13814–13815; b) J. L. Lunkley, D. Shirotani, K. Yamanari, S. Kaizaki, G. Muller, *Inorg. Chem.* **2011**, *50*, 12724–12732; c) S. Di Pietro, L. Di Bari, *Inorg. Chem.* **2012**, *51*, 12007–12014; d) J. Kumar, B. Marydasan, T. Nakashima, T. Kawai, J. Yuasa, *Chem. Commun.* **2016**, *52*, 9885–9888.

[6] Luminescence properties, selected reviews: a) J.-C. G. Bünzli, C. Piguet, *Chem. Soc. Rev.* **2005**, *34*, 1048–1077; b) J. Andres, A.-S. Chauvin, in *The Rare Earth Elements: Fundamentals and Application* (Ed.: D. A. Atwood), Wiley, Hoboken, **2012**, pp. 111–134; c) J. Andres, A.-S. Chauvin, in *The Rare Earth Elements Fundamentals and Application* (Ed.: D. A. Atwood), Wiley, Hoboken, **2012**, pp. 135–152; d) S. Shuvaev, M. Starck, D. Parker, *Chem. Eur. J.* **2017**, *23*, 9974–9989; e) J.-C. G. Bünzli, *Eur. J. Inorg. Chem.* **2017**, 5058–5063; f) magnetic properties, selected reviews: D. N. Woodruff, R. E. P. Winpenny, R. A. Layfield, *Chem. Rev.* **2013**, *113*, 5110–5148; g) S. T. Liddle, J. van Slageren, *Chem. Soc. Rev.* **2015**, *44*, 6655–6669; h) O. A. Blackburn, R. M. Edkins, S. Faulkner, A. M. Kenwright, D. Parker, N. J. Rogers, S. Shuvaev, *Dalton Trans.* **2016**, *45*, 6782–6800.

[7] F. S. Richardson, *Inorg. Chem.* **1980**, *19*, 2806–2812.

[8] Selected examples: a) J. P. Morley, J. D. Saxe, F. S. Richardson, *Mol. Phys.* **1982**, *47*, 379–406; b) J. I. Bruce, D. Parker, S. Lopinski, R. D. Peacock, *Chirality* **2002**, *14*, 562–567; c) P. Gawryszewska, J. Legendziewicz, Z. Ciunik, N. Esfandiari, G. Muller, C. Piguet, M. Cantuel, J. P. Riehl, *Chirality* **2006**, *18*, 406–412; d) T. Harada, Y. Nakano, M. Fujiki, M. Naito, T. Kawai, Y. Hasegawa, *Inorg. Chem.* **2009**, *48*, 11242–11250; e) J. Yuasa, T. Ohno, K. Miyata, H. Tsumatori, Y. Hasegawa, T. Kawai, *J. Am. Chem. Soc.* **2011**, *133*, 9892–9902; f) T. Harada, H. Tsumatori, K. Nishiyama, J. Yuasa, Y. Hasegawa, *Inorg. Chem.* **2012**, *51*, 6476–6485; g) E. R. Neil, M. A. Fox, R. Pal, L.-O. Pålsson, B. A. O'Sullivan, D. Parker, *Dalton Trans.* **2015**, *44*, 14937–14951; h) F. Zinna, T. Bruhn, C. A. Guido, J. Ahrens, M. Bröring, L. Di Bari, G. Pescitelli, *Chem. Eur. J.* **2016**, *22*, 16089–16098; i) L. Dai, W.-S. Lo, I. D. Coates, R. Pal, G.-L. Law, *Inorg. Chem.* **2016**, *55*, 9065–9070.

ChemPubSoc Europe

CHEMISTRY
A European Journal
Full Paper

[9] Selected examples for europium complexes exhibiting CPL (in solution): a) S. D. Bonsall, M. Houcheime, D. A. Straus, G. Muller, *Chem. Commun.* **2007**, 3676 – 3678; b) M. Lama, O. Mamula, G. S. Kottas, F. Rizzo, L. De Cola, A. Nakamura, R. Kuroda, H. Stoeckli-Evans, *Chem. Eur. J.* **2007**, *13*, 7358 – 7373; c) M. Seitz, E. G. Moore, A. J. Ingram, G. Muller, K. M. Raymond, *J. Am. Chem. Soc.* **2007**, *129*, 15468 – 15470; d) M. Seitz, K. Do, A. J. Ingram, E. G. Moore, G. Muller, K. N. Raymond, *Inorg. Chem.* **2009**, *48*, 8469 – 8479; e) N. H. Evans, R. Carr, M. Delbianco, R. Pal, D. S. Yufit, D. Parker, *Dalton Trans.* **2013**, *42*, 15610 – 15616; f) F. Zinna, C. Resta, S. Abbate, E. Castiglioni, G. Longhi, P. Mineo, L. Di Bari, *Chem. Commun.* **2015**, *51*, 11903 – 11906; g) B. Zercher, T. A. Hopkins, *Inorg. Chem.* **2016**, *55*, 10899 – 10906; h) T. Wu, J. Kessler, P. Bouř, *Phys. Chem. Chem. Phys.* **2016**, *18*, 23803 – 23811; i) A. Galanti, O. Kotova, S. Blasco, C. J. Johnson, R. D. Peacock, S. Mills, J. J. Boland, M. Albrecht, T. Gunnlaugsson, *Chem. Eur. J.* **2016**, *22*, 9709 – 9723; j) E. R. Neil, M. A. Fox, R. Pal, D. Parker, *Dalton Trans.* **2016**, *45*, 8355 – 8366; k) Y. Kono, K. Nakabayashi, S. Kitamura, M. Shizuma, M. Fujiki, Y. Imai, *RSC Adv.* **2016**, *6*, 40219 – 40224; l) Y. Okayasu, J. Yuasa, *Mol. Syst. Des. Eng.* **2018**, *3*, 66 – 72; m) L. Armelao, D. B. Dell'amico, L. Bellucci, G. Bottaro, L. Di Bari, L. Labella, F. Marchetti, S. Samaritani, F. Zinna, *Inorg. Chem.* **2017**, *56*, 7010 – 7018; n) B. Casanovas, F. Zinna, L. Di Bari, M. S. El Fallah, M. Font-Bardía, R. Vicente, *Dalton Trans.* **2017**, *46*, 6349 – 6357; o) N. Shi, J. Tan, X. Wan, Y. Guan, J. Zhang, *Chem. Commun.* **2017**, *53*, 4390 – 4393; p) Y. Kono, N. Hara, M. Shizuma, M. Fujiki, Y. Imai, *Dalton Trans.* **2017**, *46*, 5170 – 5174; q) E. R. Neil, D. Parker, *RSC Adv.* **2017**, *7*, 4531 – 4540.

[10] a) R. S. Dickins, J. A. K. Howard, C. L. Maupin, J. M. Moloney, D. Parker, J. P. Riehl, G. Siligardi, J. A. G. Wiliams, *Chem. Eur. J.* **1999**, *5*, 1095 – 1105; b) J. Gregoliński, P. Starynowicz, K. T. Hua, J. L. Lunkley, G. Muller, J. Lisowski, *J. Am. Chem. Soc.* **2008**, *130*, 17761 – 17773; c) A. P. S. Samuel, J. L. Lunkley, G. Muller, K. N. Raymond, *Eur. J. Inorg. Chem.* **2010**, 3343 – 3347; d) M. Leonzio, A. Melchior, G. Faura, M. Tolazzi, F. Zinna, L. Di Bari, F. Piccinelli, *Inorg. Chem.* **2017**, *56*, 4413 – 4421.

[11] a) G. L. Hilmes, J. P. Riehl, *Inorg. Chem.* **1986**, *25*, 2617 – 2622; b) R. C. Carter, C. E. Miller, R. A. Palmer, P. S. May, D. H. Metcalf, F. S. Richardson, *Chem. Phys. Lett.* **1986**, *131*, 37 – 43; c) P. S. May, D. H. Metcalf, F. S. Richardson, R. C. Carter, C. E. Miller, R. A. Palmer, *J. Lumin.* **1992**, *51*, 249 – 268; d) S. Petoud, G. Muller, E. G. Moore, J. Xu, J. Sokolnicki, J. P. Riehl, U. N. Le, S. M. Cohen, K. N. Raymond, *J. Am. Chem. Soc.* **2007**, *129*, 77 – 83; e) J. P. Leonard, P. Jensen, T. McCabe, J. E. O'Brien, R. D. Peacock, P. E. Kruger, T. Gunnlaugsson, *J. Am. Chem. Soc.* **2007**, *129*, 10986 – 10987; f) K. Murata, M. Morita, K. Eguchi, *J. Lumin.* **1988**, *42*, 227 – 234.

[12] T. Güden-Silber, C. Doffek, C. Platas-Iglesias, M. Seitz, *Dalton Trans.* **2014**, *43*, 4238 – 4241.

[13] a) L. Prodi, M. Maestri, V. Balzani, J.-M. Lehn, C. Roth, *Chem. Phys. Lett.* **1991**, *180*, 45 – 50; b) J.-M. Lehn, C. O. Roth, *Helv. Chim. Acta* **1991**, *74*, 572 – 578; c) C. Doffek, N. Alzakhem, C. Bischof, J. Wahsner, T. Güden-Silber, J. Lügger, C. Platas-Iglesias, M. Seitz, *J. Am. Chem. Soc.* **2012**, *134*, 16413 – 16423; d) C. Doffek, J. Wahsner, E. Kreidt, M. Seitz, *Inorg. Chem.* **2014**, *53*, 3263 – 3265; e) C. Doffek, M. Seitz, *Angew. Chem. Int. Ed.* **2015**, *54*, 9719 – 9721; *Angew. Chem.* **2015**, *127*, 9856 – 9858.

[14] C. Doffek, N. Alzakhem, M. Molon, M. Seitz, *Inorg. Chem.* **2012**, *51*, 4539 – 4545.

[15] C. Bischof, J. Wahsner, J. Scholten, S. Trosien, M. Seitz, *J. Am. Chem. Soc.* **2010**, *132*, 14334 – 14335.

[16] C. Dee, Master Thesis **2016**, Eberhard-Karls Universität Tübingen.

[17] K. Binnemans, *Coord. Chem. Rev.* **2015**, *295*, 1 – 45.

[18] E. Kreidt, C. Kruck, M. Seitz, in *Handbook on the Physics and Chemistry of Rare Earths, Vol. 53* (Eds.: J.-C. G. Bünzli, V. K. Pecharsky), Elsevier, Amsterdam, **2018**, pp. 35 – 79.

[19] a) M. H. V. Werts, R. T. F. Jukes, J. W. Verhoeven, *Phys. Chem. Chem. Phys.* **2002**, *4*, 1542 – 1548; b) A. Aebischer, F. Gumy, J.-C. Bünzli, *Phys. Chem. Chem. Phys.* **2009**, *11*, 1346 – 1353.

[20] W. H. Melhuish, *J. Phys. Chem.* **1961**, *65*, 229 – 235.

[21] E. Kreidt, C. Dee, M. Seitz, *Inorg. Chem.* **2017**, *56*, 8752 – 8754.

Manuscript received: May 2, 2018
Revised manuscript received: June 15, 2018
Accepted manuscript online: June 21, 2018
Version of record online: August 20, 2018

CHEMISTRY
A European Journal

Supporting Information

Circularly Polarised Luminescence in Enantiopure Samarium and Europium Cryptates

Elisabeth Kreidt,*[a] Lorenzo Arrico,[b] Francesco Zinna,[c] Lorenzo Di Bari,*[b] and Michael Seitz[a]

chem_201802196_sm_miscellaneous_information.pdf

Supporting Information

Table of Contents Page

1. HPLC traces

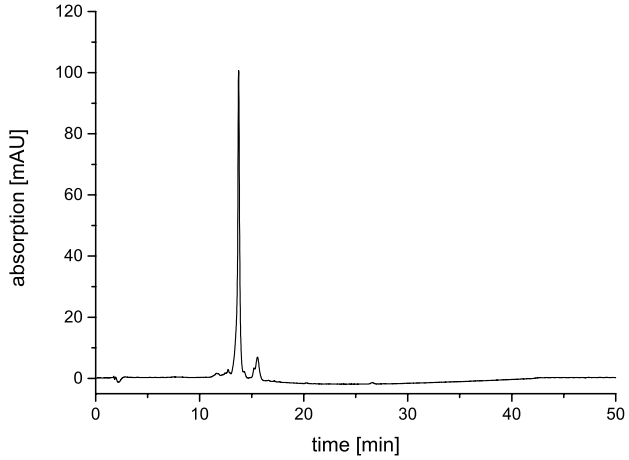

Figure S1: analytical HPLC trace of **1-Eu**.

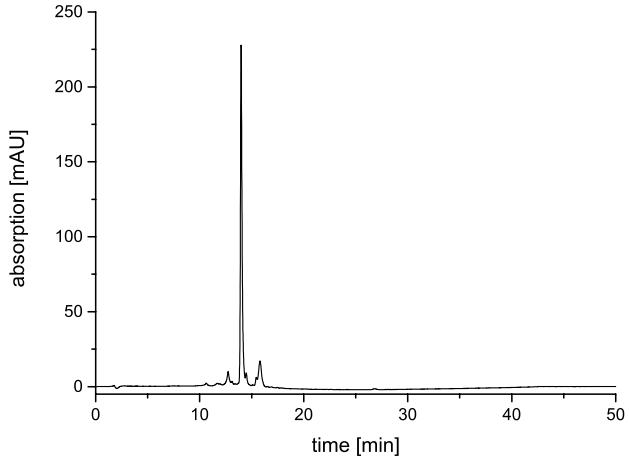

Figure S2: analytical HPLC trace of **1-Sm**.

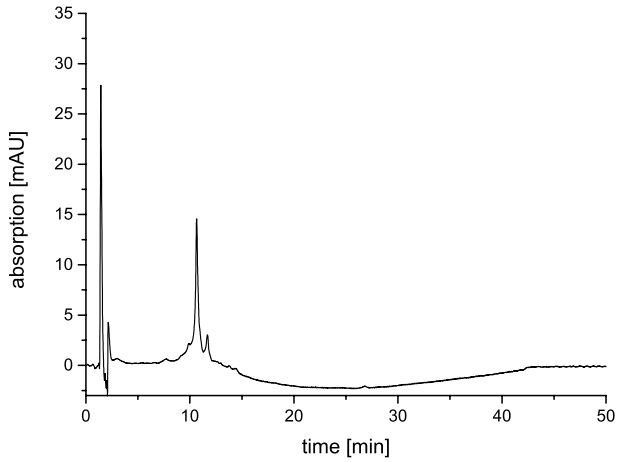

Figure S3: analytical HPLC trace of **1-Na**.

2. Absorption spectra

Absorption spectra were measured in quartz cuvettes (suprasil, 1 cm pathlength) on a Jasco-V770 spectrophotometer.

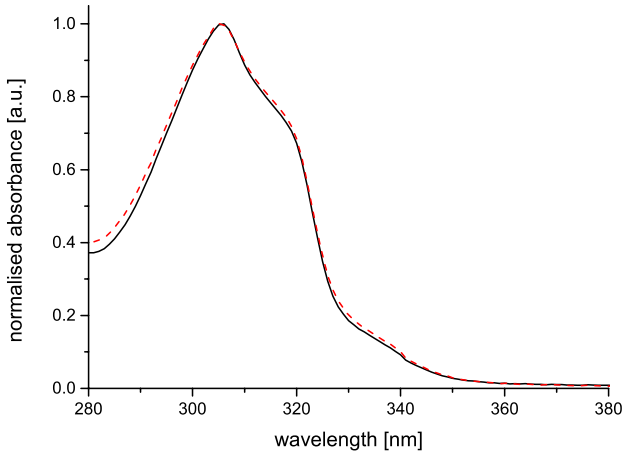

Figure S3: normalised UV/Vis spectra of **1-Eu** (red, dotted) and **1-Sm** (black, solid) in CD_3OD at room temperature.

3. Luminescence Decay Profiles

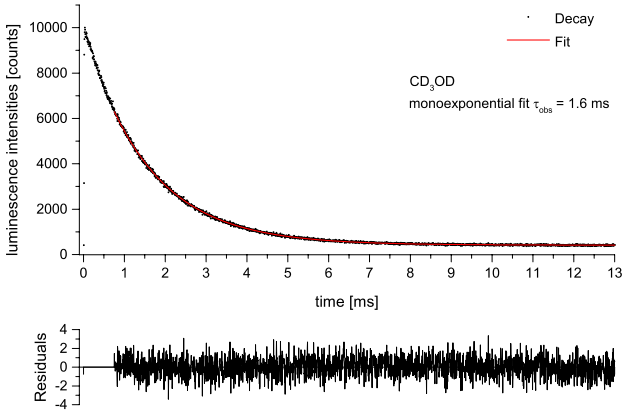

Figure S4: Luminescence decay profile of the transition $^5D_0 \rightarrow {}^7F_2$ (λ_{em} = 610 nm) in **1-Eu** (CD_3OD, λ_{exc} = 320 nm, monoexponential fit in red).

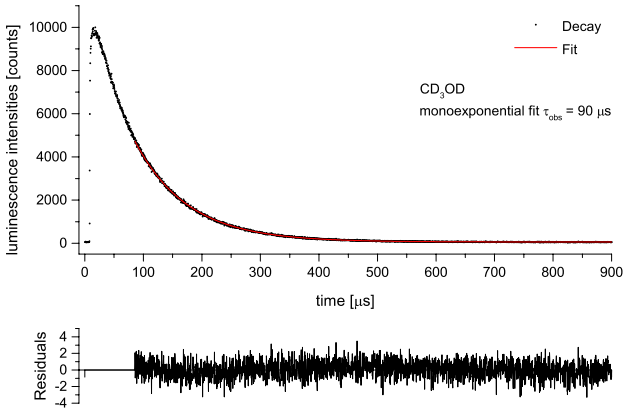

Figure S5: Luminescence decay profile of the transition $^4G_{5/2} \rightarrow {}^6H_{7/2}$ (λ_{em} = 597 nm) in **1-Sm** (CD_3OD, λ_{exc} = 320 nm, monoexponential fit in red).

4. Compilation of photophysical parameters reported for CPL-active Sm Complexes

Ref[a]	g_{lum} $^4G_{5/2}\rightarrow{}^6H_{5/2}$	g_{lum} $^4G_{5/2}\rightarrow{}^6H_{7/2}$	τ_{obs} [μs]	Φ [%]	solvent
11d	-0.027	-0.028	17 ± 2	0.3	CH_3OH
11e	0.50	0.28	-[c]	-[c]	H_2O
11f	-	0.066	~ 21	$0.67 \cdot 10^{-3}$ ($^4G_{5/2}\rightarrow{}^6H_{5/2}$), $0.98 \cdot 10^{-3}$ ($^4G_{5/2}\rightarrow{}^6H_{7/2}$), $0.33 \cdot 10^{-3}$ ($^4G_{5/2}\rightarrow{}^6H_{9/2}$)	H_2O
5b	-1.15 (553)[b], -0.35 (561), 0.96 (575)	-0.45 (588), 1.15 (598), -0.76 (605), 0.24 (611), 0.15 (617)	-[c]	-[c]	$CHCl_3$
This work	+0.13	±0.03	90	0.26	CD_3OD

a) In ref 11a CPL is observed in racemic complexes after circularly polarized excitation; in refs 11b and 11c g_{lum} values are not reported. b) Wavelengths (nm). c) values are not reported.

Chapter 300

Nonradiative Deactivation of Lanthanoid Luminescence by Multiphonon Relaxation in Molecular Complexes

Elisabeth Kreidt[2], **Christian Kruck**[2] **and Michael Seitz**[1]
University of Tübingen, Institute of Inorganic Chemistry, Tübingen, Germany
[1]*Corresponding author: e-mail: michael.seitz@uni-tuebingen.de*

Chapter Outline

1 INTRODUCTION

1.1 Outline and Scope

Lanthanoid luminescence in molecular complexes with trivalent lanthanoid ions has matured into a well-developed and thoroughly investigated field of research with a plethora of interesting photonic applications in various and diverse fields,

2. Both authors contributed equally.

Handbook on the Physics and Chemistry of Rare Earths, Vol. 53. https://doi.org/10.1016/bs.hpcre.2018.04.001

ranging from time-resolved luminescence immunoassays, biomedical imaging, lasers, to optical telecommunications [1]. For most purposes, of course, high luminescence efficiencies are desirable and many of the phenomena governing the photoluminescence of trivalent lanthanoids are well understood. The typical case of molecular lanthanoid luminophores in this context involves sensitization of luminescent f–f transitions with an appropriate antenna ligand. Fig. 1 shows the prototypical, photophysical processes, from singlet–singlet absorption, intersystem crossing (ISC) to an excited triplet state, energy transfer onto an excited lanthanoid state, and subsequent luminescence to the lanthanoid ground-state manifold. Particularly important for the design of highly luminescent lanthanoid complexes is an intricate knowledge of the processes that can lead to unwanted dissipation of the excitation energy and hence reduced lanthanoid emission intensity. Much research has been devoted over the years to studying this sensitization approach and many strategies have been identified and successfully implemented to make emission as efficient as possible (e.g., ISC and Förster or Dexter energy transfer) or to avoid detrimental processes leading to diminished luminescence (e.g., deactivation by $^3O_2$ or by low-lying CT states).

One important mechanism for deactivation once the energy has reached a lanthanoid excited state is the energy transfer to overtones of molecular vibrations in the vicinity of the metal center, either in the ligands bound or in the surrounding medium (see Fig. 1). In solid-state lanthanoid materials, this has long been known as "multiphonon relaxation" (MR), and for the sake of simplicity, we will use the same term for the analogous processes in molecular complexes. This phenomenon, which is much more opaque to our understanding and harder to control chemically than other design factors in molecular lanthanoid complexes, is one of the major drivers of nonradiative deactivation

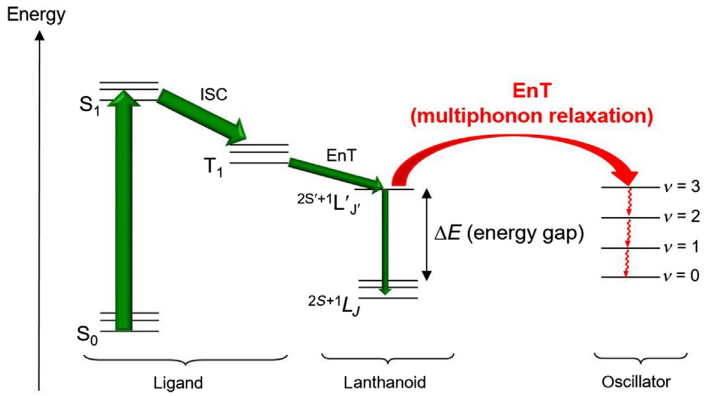

FIG. 1 Schematic representation of the typical sensitization process using the antenna effect and the energy transfer leading to multiphonon relaxation (*EnT*: energy transfer; *ISC*: intersystem crossing; S_0/S_1: ground/excited singlet states; T_1: excited triplet state; *v*: vibrational quantum number).

and crucial for the understanding of luminescence in the majority of lanthanoids, especially for the ones exhibiting near-IR emission. This review, which aims to emphasize primarily molecular Ln^{3+} complexes in solution, will cover the theoretical approaches for the qualitative and quantitative description of MR, highlight some of the special implications of MR for molecular complexes, explain strategies to minimize nonradiative deactivation by MR, and document some of the recent results for different lanthanoids.

1.2 f–f Transitions in Trivalent Lanthanoid Ions

Trivalent lanthanoid ions have the electronic ground-state configuration [Xe] $4f^x$ = [Kr] $4d^{10}$ $5s^2$ $5p^6$ $4f^x$ (with $x = 0$–14) which gives rise to unique properties compared to all other elements in the periodic table. The fundamental difference is that the 4f valence orbitals are closer to the atomic nucleus than the filled 5s and 5p orbitals, essentially shielding the 4f electrons from the surrounding chemical environment. This phenomenon has well-known chemical (e.g., the lanthanoid contraction, the flexible coordination geometry, the predominance of ionic instead of covalent bonding to the metal center, etc.) and physical (e.g., the very narrow emission spectra, very small ligand field splitting, etc.) consequences [1]. This particular electronic situation also has implications for the nature of the processes involved in MR of lanthanoid excited states.

In general, two limiting cases for MR can be distinguished, depending on the nature of the coupling between emitting and accepting states [2]. A good illustration of these two prototypical cases is the photophysics of octahedral chromium(III) complexes with d^3 electronic configurations, where both the excited states ^2E_g and $^4T_{2g}$ can be affected by MR to the $^4A_{2g}$ ground state (Fig. 2) [3].

For example, the spin-allowed transition between the excited-state $^4T_{2g}$ and the ground-state $^4A_{2g}$ involves the change of the electronic configuration from $(t_{2g})^2(e_g)^1$ to $(t_{2g})^3$ and considerable redistribution of electron density around the chromium center (Fig. 2, right side). This usually leads to large displacement of the nuclear coordinates (Fig. 2: d_{M-L}) of the equilibrium geometries in the two states (Fig. 2: shift of the energy surface to the right for $^4T_{2g}$). This phenomenon makes it much more likely that the two energy surfaces intersect at some point close to the equilibrium geometry of the excited-state $^4T_{2g}$. This so-called strong coupling case provides for a straightforward nonradiative deactivation pathway via the surface crossing point. For the initial step of surface crossing, only a rather small amount of energy has to be disposed of via vibrational energy transfer. For this situation, in principle all vibrations (including low-frequency oscillators) are suitable for accepting the excited-state energy and therefore isotopic substitution is not expected to make a large difference. Contrary to this, the $^4A_{2g}$ ground state and the excited ^2E_g state both have the electronic configuration $(t_{2g})^3$ and only differ

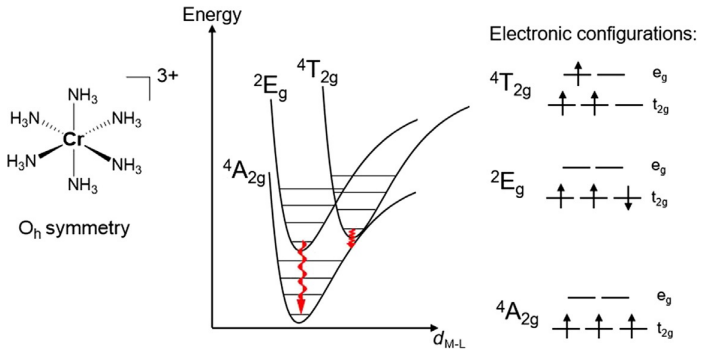

FIG. 2 Electronic configurations of the ground and excited states in octahedral chromium(III) complexes (e.g., the hexammine complex shown)—schematic potential energy surfaces of the corresponding ligand field states: weak coupling between ^2E_g and $^4A_{2g}$/strong coupling between $^4T_{2g}$ and $^4A_{2g}$.

in the orientations of their respective spins involved (Fig. 2, right side). Consequently, the electron distributions around the metal and the bonding situation to the ligands are very similar resulting in only minor geometric distortions upon spin-forbidden transitions from $^4A_{2g}$ to ^2E_g or vice versa. As a consequence, the two potential energy surfaces are offset in energy but have a very similar position with respect to their respective nuclear coordinates (d_{M-L}). This situation is called "weak-coupling" limit and it does not provide for easy access to surface crossing points between the two nested states. For this case, where a rather large amount of energy has to be dissipated in any nonradiative process, the best candidates for MR are high-energy and highly anharmonic oscillators such as local-mode X–H (X = O, N, C, etc.) or C═O stretching vibrations. Isotopic substitution in the form of replacing X–H with X–D (i.e., deuteration) often has a considerable effect due to the concomitant considerable decrease in vibrational energy (vide infra).

For Ln^{3+}, redistribution of electrons within the shielded f-orbitals does not alter the ionic bonding to ligands and therefore almost no geometric changes occur after f–f transitions. Consequently, the states involved in lanthanoid luminescence usually are only weakly coupled and therefore MR of lanthanoid excited states is mostly induced by anharmonic, high-energy oscillators. The susceptibility of lanthanoid excited states to nonradiative deactivation due to MR depends qualitatively on the amount of excess energy that needs to be dissipated via transfer to vibrational overtones, with smaller energies leading to larger MR rates and therefore lower emission intensities. Conventionally, the measure for this assessment is the energy gap ΔE between the emitting level and its neighboring state immediately below. The situation in this respect is unique to each individual luminescent lanthanoid and this phenomenon can

affect different emitting states in one single lanthanoid differently, of course. Fig. 3 shows a comprehensive energy-level diagram for the relevant trivalent lanthanoids, indicating often encountered emitting states and their corresponding values for ΔE [4,5]. The lanthanoids fall roughly into three, somewhat arbitrarily chosen, categories depending on the largest energy gap present in their respective energy-level scheme. First, the ones with large gaps $\Delta E >$ ca. 12,000 cm^{-1} are represented by the visible emitters Eu^{3+} ($^5D_0$: $\Delta E = 12{,}400\,cm^{-1}$) and Tb^{3+} ($^5D_4$: $\Delta E = 14{,}800\,cm^{-1}$). These ions are rather resistant to MR compared to the other lanthanoids and many highly efficient emitters with excellent quantum yields even in aqueous solution have been developed over the last decades [1,6,7]. The second category of Ln^{3+} exhibits intermediate values for the largest gaps with ΔE between ca. 6800 and 12,000 cm^{-1} and comprises the visible/near-IR emitters Pr^{3+} ($^1D_2$: $\Delta E = 6960\,cm^{-1}$), Sm^{3+} ($^4G_{5/2}$: $\Delta E = 7410\,cm^{-1}$), Dy^{3+} ($^4F_{9/2}$: $\Delta E = 7380\,cm^{-1}$), and Yb^{3+} ($^2F_{5/2}$: $\Delta E = 10{,}250\,cm^{-1}$). These ions are much more susceptible to MR than Eu^{3+} and Tb^{3+}, but their luminescence efficiency can often benefit greatly from removing high-energy oscillators from the immediate vicinity of the lanthanoid [6]. The third category are the mostly near-IR emitting lanthanoids with very small energetic gaps $\Delta E <$ ca. 6800 cm^{-1}, namely Nd^{3+} ($^4F_{3/2}$: $\Delta E = 5450\,cm^{-1}$), Ho^{3+} ($^5S_2$: $\Delta E = 2840\,cm^{-1}$), Er^{3+} ($^4I_{13/2}$: $\Delta E = 6500\,cm^{-1}$), and Tm^{3+} ($^1G_4$: $\Delta E = 6260\,cm^{-1}$). The luminescence from these ions is usually extremely sensitive to vibrational deactivation by oscillators in surrounding ligands or solvent molecules, and even careful avoidance of high-energy vibrations often only has a rather limited beneficial effect. Generally, emission in molecular complexes of these lanthanoids in solution is exceedingly small with quantum yields commonly below 1%.

1.3 Vibrational Overtones

For the analysis of MR of excited lanthanoid states to molecular oscillator overtones in the vicinity, the characteristics of the vibrational modes play a crucial role. For an illustration of the aspects involved, Fig. 4 shows as a typical MR case of the excited state $^2F_{5/2}$ of Yb^{3+} by C–H stretching vibrations (ν_{C-H}).

Besides general symmetry considerations relevant to vibrational transitions (cf. selection rules for infrared spectroscopy), there are three important factors that determine the effectiveness of MR:

- Order of the vibrational overtone: In general, the energetic gaps ΔE in lanthanoids are several multiples of the energies of the fundamental vibrations involved (e.g., in Fig. 4: $\Delta E = 10{,}250\,cm^{-1}$ vs $\tilde{\nu}(C–H) \approx 3000\,cm^{-1}$). The higher the order of the overtone required, the less likely MR becomes. This fact is mainly connected to the probability for the transition from the vibrational ground state to the overtone required. These circumstances favor MR for anharmonic, high-energy oscillators which only require a

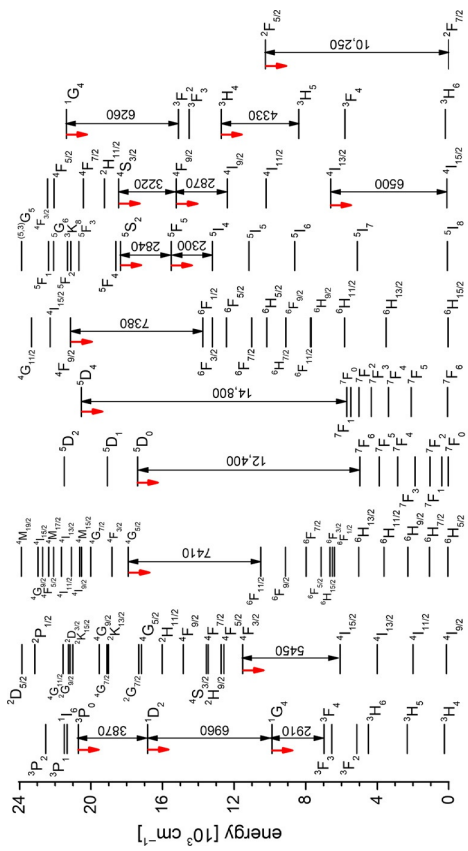

FIG. 3 Partial energy-level diagram for selected trivalent lanthanoid ions (calculated energies for Ln^{3+} (aq); exception: Yb^{3+} in LaF_3 [4])—*downward arrows*: prominent emitting levels; *double-headed arrows*: energy gap ΔE between emitting level and next lower level (in cm^{-1}). Term symbols $^{2S+1}L_J$ on the left of the lanthanoid manifolds are aligned in height with the quantum number J, the ones on the right with their multiplicities $2S+1$.

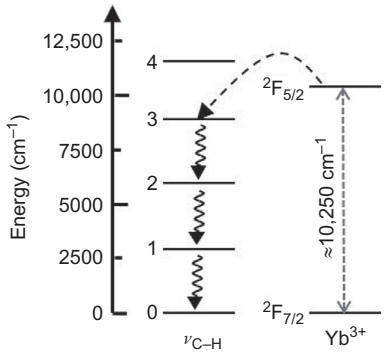

FIG. 4 Schematic representation of the C–H vibrational overtone levels and the electronic levels in Yb^{3+}.

few vibrational quanta to bridge the energetic gap and which exhibit much larger oscillator strengths for the population of their overtones.

- Energy matching: MR is more effective, the closer the energy gap in the lanthanoid matches the energy of the accepting vibrational overtones. This aspect can be understood in terms of Franck–Condon factors or spectral overlap (vide infra).

In the context of lanthanoid MR, historically the relevant vibrations have overwhelmingly been treated as idealized harmonic oscillators. This is a very good approximation when the vibrational processes in question involve the motion of many atoms simultaneously or the localized vibrations of diatomic oscillators of comparable mass, e.g., for lattice vibrations in lanthanoid-doped, extended solids, or for aromatic ring breathing motions in ligands. This approach makes the theoretical description of vibrational overtones and MR relatively easy and is therefore the basis for most variants of the energy gap law (EGL, vide infra). One of the most obvious and straightforward implications of the harmonic model is that the spacing of vibrational energy levels E_n depending on the vibrational quantum number n_{harm} is equidistant (Fig. 5).

There is, however, one serious conceptual problem for this approach in the context of lanthanoid MR in molecular complexes where the weak coupling between the emitting and accepting state necessitates the dissipation of a large amounts of energy transfer (see Fig. 3: ΔE up to 14,800 cm^{-1}) to high-energy vibrational overtones. Since the selection rule for vibrational transitions in the harmonic model only permits $\Delta n = \pm 1$, the excitation of vibrational overtones in the MR process directly from the vibrational ground state ($n = 0$) would be strongly forbidden. Therefore, only relatively small energies could be transferred (typically on the order of 800–3500 cm^{-1} for the fundamental vibrations in molecular complexes) in a single transition. This notion is not in agreement with the experimental observations which show that MR is often

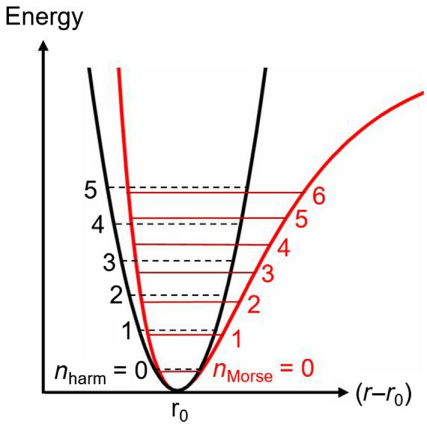

FIG. 5 Comparison of the vibrational states and energies of harmonic oscillators (quantum number n_{harm}) and anharmonic, Morse-type oscillators (quantum number n_{Morse}).

very efficient, even for energetic gaps which are several multiples of typical vibrational energies for transitions from the ground to the first excited state. It is therefore important to realize that vibrational overtones generally only gain oscillator strength and hence the ability to accept larger amounts of energy from lanthanoid states if the oscillators involved display a large degree of anharmonicity. A much more appropriate description for oscillators in molecular lanthanoid systems in solution is a local-mode Morse oscillator model which explicitly incorporates the anharmonicity of the vibrations [8]. This approach has proved to be a very successful model for the quantitative description of the energetic positions of vibrational overtones in molecular systems [9]. Most relevant for the discussion of MR in molecular lanthanoid complexes is the nonequidistant spacing of the vibrational overtone energies. Instead, the energetic differences become increasingly smaller with an increase in vibrational quantum number n (Fig. 5). In this model, the energy $\tilde{\nu}_n$ (in the wavenumber scale) for the transition from the ground state to the state with vibrational quantum number n depends on the frequency $\tilde{\nu}_0$ of the local-mode fundamental vibration and the anharmonicity parameter x according to Eq. (1) [9]

$$\tilde{\nu}_n = n \cdot \tilde{\nu}_0 - n(n+1) \cdot x \tag{1}$$

In Eq. (1), the parameter x is a very convenient measure of the degree of anharmonicity of the vibration with larger values of x indicating increasing anharmonic behavior (and ideal harmonic behavior for $x = 0$). Table 1 shows representative values for the Morse parameters in diatomic stretching vibrations relevant in typical ligand motifs for lanthanoid chelates in solution. From these data, it is clear that the most anharmonic vibrations are the ones

TABLE 1 Typical Parameters for Anharmonic Morse Oscillators—Fundamental Vibration $\tilde{\nu}_0$, Anharmonicity Parameter x, and Anharmonicity Ratio k for Various Stretching Vibrations

Oscillator	$\tilde{\nu}_0$ (cm^{-1})	x (cm^{-1})	$k = \tilde{\nu}_0/x$ (cm^{-1})	Compound	References
O–H	3515	90	39	CH_3OH (neat)	[10]
O–D	2600	50	52	CD_3OD (neat)	[11]
C–H (arom.)	3161	58	55	Pyridine (H3, H4, H5)	[12]
C–D (arom.)	2325	28	83	Pyridine (D3, D4, D5)	[12]
C=O	1860	12	155	PP-PDB (perfluorinated ester)	[13]
C–F	1255	5.0	251	Methyl perfluoropropionate	[13a]
C–Cl	775	4.5	172	CCl_4 (neat)	[13a]

involving high-energy X–H stretches such as ν_{O-H} ($x = 90\,cm^{-1}$) and ν_{C-H} ($x = 58\,cm^{-1}$), whereas less energetic vibrations such as C–F ($x = 5\,cm^{-1}$) are also much more harmonic. In addition, the respective values for isotopologic oscillators such as C–H/C–D show the typical reduction of vibrational frequencies with the increase in reduced mass for the diatomic vibrations according to Eq. (2):

$$\frac{\tilde{\nu}_{C-H}}{\tilde{\nu}_{C-D}} = \sqrt{\frac{\mu_{C-D}}{\mu_{C-H}}} = \sqrt{\frac{(m_C \cdot m_D)/(m_C + m_D)}{(m_C \cdot m_H)/(m_C + m_H)}} = 1.36 \tag{2}$$

Equally or even more relevant, however, is the reduction of vibrational anharmonicity upon deuteration. As a rule of thumb, the anharmonicity parameter x decreases to roughly half the value found for the protiated oscillators (e.g., Table 1: $x_{O-H} = 90\,cm^{-1}$ vs $x_{O-D} = 50\,cm^{-1}/x_{C-H} = 56\,cm^{-1}$ vs $x_{C-D} = 28\,cm^{-1}$).

Crucially, anharmonicity does not only determine the energetic positions of the vibrational overtones but also significantly influences the oscillator strength of the vibrational transition to higher overtones during MR energy transfer from the lanthanoid. Within the local-mode Morse model, the integrated absorption band intensities (e.g., expressed by the molar extinction coefficients ε) for the transition to the overtone with vibrational quantum number n are determined by the anharmonicity ratio $k = \tilde{\nu}_0/x$ as shown in Eq. (3) [9]:

$$I_n = \int \varepsilon(\tilde{\nu}) d\tilde{\nu} \propto \frac{n!}{n^2} \cdot k^{1-n} \tag{3}$$

Eq. (3) makes two things clear. First, with increasing n the intensities I_n rapidly decrease ($n > 0$ and $k > 0$), and second, the intensities go down more slowly for anharmonic vibrations because of smaller values for k and because $1 - n < 0$. Or to put it the other way around, the overtone oscillator strengths are much higher for strongly anharmonic oscillators compared to more harmonic ones. While every vibration has unique features determining its vibrational overtone intensities, as a very crude approximation, the oscillator strength goes down by one order of magnitude with each overtone order n. Experimentally, these effects are often not easy to measure, but this aspect has long been known in fiber optical telecommunications which operates in the same energy regime as the one relevant to lanthanoid MR [13]. Over the years, many studies for the development of low-loss optical fibers and of the effects that anharmonic oscillators such as O–H or C–H in plastic optical fibers have on the attenuation of the near-infrared signals to be transmitted have yielded a wealth of empirical data on overtone positions and oscillator strengths. Fig. 6 shows a graphical compilation of different oscillators and their relative intensities. It gives a very good impression of the strong effects that anharmonicity has on the oscillator strength of successive overtones (e.g., compare the slopes for C–H vs C–F vibrations). In particular, it illustrates that

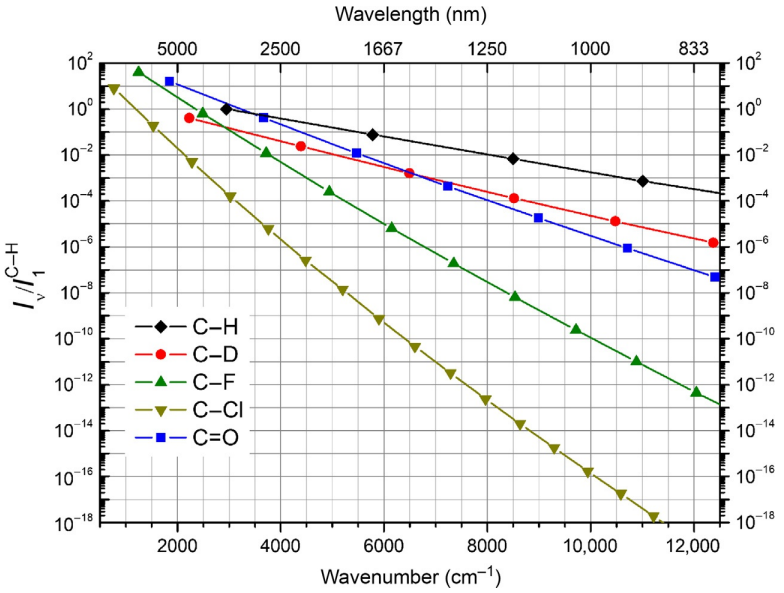

FIG. 6 Experimentally determined vibrational overtone positions and typical integrated absorption band strength relative to the band strength of the fundamental C–H stretching vibrations $I_1^{C-H} \equiv 1$. *Data from W. Groh, Overtone absorption in macromolecules for polymer optical fibers, Makromol. Chem. 189 (1988) 2861–2874.*

the effects for different moieties are not small but involve absorption intensity differences of several orders of magnitudes for a given energy gap. For example, at the vibrational overtone energy of 8400 cm^{-1} the ratio $I^{C-H}/I^{C-F} \approx 10^{-6}$, i.e., the oscillator strength for a the C–H overtone is 1 million times higher than for a C–F overtone of the same energy.

As a special case, the intensity ratios of the same overtones for isotopic oscillators can be analyzed theoretically from Eq. (4) with the use of the anharmonicity ratios k:

$$\frac{I_n^H}{I_n^D} \propto \left(\frac{k^D}{k^H}\right)^{n-1} \tag{4}$$

Since for this exponential expression, both the basis ($k_D/k_H > 1$) and the exponent ($n - 1 \geq 1$) are greater than 1 for transitions to higher overtones ($n > 2$), the intensity ratio becomes increasingly larger with n, i.e., the intensities of the X–H overtones are greater than the corresponding X–D overtones.

Another very important aspect is the nature of the vibrations that one should consider for the analysis of MR processes. So far, we have only taken into account diatomic, localized stretching vibrations despite the fact that

many vibrations show coupling to other vibrations, maybe most prominently illustrated by symmetric and asymmetric stretching vibrations in chemical motifs XH_2 found in water molecules H_2O or in methylene groups $–CH_2–$. For example, in liquid water, the rather strong near-IR absorption band around 1940 nm (5140 cm^{-1}) is a combination of the asymmetric stretching and a bending vibration [14]. This complication potentially makes the analysis of vibrational overtones immensely complex and a lot of effort has been devoted to the assignment of the identity of vibrational signatures in a myriad of molecules. Fortunately, however, the situation is alleviated by a few circumstances that greatly simplify the discussion of vibrational overtones [9b]. First, the oscillator strengths of overtone combination bands involving high- or low-frequency vibrations are usually considerably smaller than isolated, local-mode overtones of diatomic high-energy oscillators. Second, the higher the order of the overtone, the more the overtones become decoupled and the more local-mode character is gained. In practice, it is often a reasonable, albeit crude approximation that the first overtones are already local mode in nature. For example, it has been shown that for the four visible lanthanoid emitters Sm^{3+}, Eu^{3+}, Tb^{3+}, and Dy^{3+} with relatively large energy gaps ($\Delta E > 7380\,cm^{-1}$, see Fig. 3) the two O–H moieties of H_2O can be considered as two diatomic, decoupled O–H overtone oscillators [15]. In addition, another implication of the local-mode model is, of course, that as a first approximation, similar oscillators in different molecules, which are not involved in strong intra- or intermolecular noncovalent bonds, should have similar Morse parameters, regardless of the individual chemical environment. For example, aromatic C–H/C–D oscillators in pyridines show very similar anharmonicity, no matter if observed in pyridine [16], in pyridine-based lanthanoid cryptates [12], or even in benzene [17] or toluene [18]. The situation for O–H or N–H oscillators is complicated by the fact that their vibrational properties are strongly affected by hydrogen bonding. For example, it is known that hydrogen bonding increases the anharmonicity of O–H oscillators considerably, for example, in alcohol dimer motifs [19] or upon absorption of alcohols on silica surfaces featuring Si–OH motifs [20]. It is very plausible that similar effects are operative for inner- and second-sphere water molecules in molecular lanthanoid complexes, but reliable studies on this subject are yet to be reported.

2 THE QUANTITATIVE DESCRIPTION OF MR IN MOLECULAR COMPLEXES

2.1 The EGL in Molecular Complexes

The quantitative description of nonradiative deactivation of lanthanoid excited states by MR has traditionally been based on the EGL which correlates the energy gap ΔE (see Fig. 3) between emitting and next-lower state with the

induced quenching rate contribution k_{nr} of a certain deactivating oscillator. Over the years, many versions of the EGL have been developed [21] which in its simplest manifestation has the form shown in Eq. (5):

$$k_{nr} = C_1 \cdot e^{-\left(C_2 \cdot \frac{\Delta E}{\hbar\omega_M}\right)} \tag{5}$$

with C_1 and C_2 being constants characteristic for a particular system, which are fitted to experimental data, and $\hbar\omega_M$ being the energy of the deactivating vibrational mode. The various forms of the EGL all suppose MR being induced by harmonic oscillators and are based on assumptions regarding the relative energies relevant for the system, for example, that the energy gap is much larger than the energy of the deactivating mode ($\Delta E \gg \hbar\omega_M$) or that the available thermal energy is negligible compared to the vibrational energy ($\hbar\omega_M \gg k_B T$). The EGL, although initially developed for the description of luminescence in aromatic hydrocarbons, has proved its great utility also in other fields such as inorganic photophysics, e.g., in solid-state materials doped with trivalent lanthanoid ions [22] or certain molecular transition metal complexes [23]. The application of the EGL to molecular lanthanoid complexes in a quantitative way has also been reported many times, mostly with qualitatively plausible results [24]. One has to recognize, however, that this can necessarily only be a very crude approximation. Eq. (5) makes this fact quite obvious since it does not treat different oscillators differently but lumps all distance and structure dependencies of the vibrational properties into the two constants C_1 and C_2. In addition, the main deactivating oscillators for lanthanoids in low-phonon host matrices or for most molecular transition metal complexes mentioned earlier are usually very different from the ones involving molecular lanthanoid complexes involving high-energy oscillators in the ligands or the surrounding solvent. For example, in yttrium aluminum garnet (YAG) hosts the phonon energy with $\hbar\omega_M \approx 700\,\mathrm{cm}^{-1}$ corresponds to harmonic lattice vibrations. Even in the case of molecular complexes with very similar ligand architectures, the moieties mainly responsible for MR can be very different, as depicted in the two 2,2′-bipyridine-based complexes shown in Fig. 7. For the osmium complex (Fig. 7A), harmonic pyridine ring-breathing mode overtones are the major contributors to MR [23a], whereas for the superficially similar ytterbium cryptate (Fig. 7B), the main quenching overtones are high-energy, highly anharmonic, local-mode C–H stretching vibrations [12].

As a consequence of the nature of the deactivating overtone modes (high energy and anharmonicity) in molecular lanthanoid complexes and the fact that the energy gap ΔE is often only within one to three multiples of the energy of the accepting oscillator energies, the fundamental assertions underlying the derivation of the EGL are not completely valid (cf. the assumption

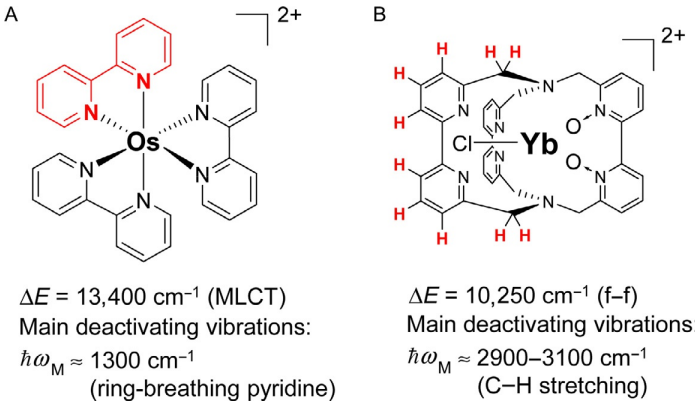

FIG. 7 Comparison of the main deactivating oscillators in molecular metal complex luminophores with very similar 2,2′-bipyridine motifs in solution. (A) Harmonic ring-breathing modes in osmium(II) complexes showing MLCT emission [23a]; (B) anharmonic C–H stretching modes in f–f-luminescent ytterbium(III) complexes [12].

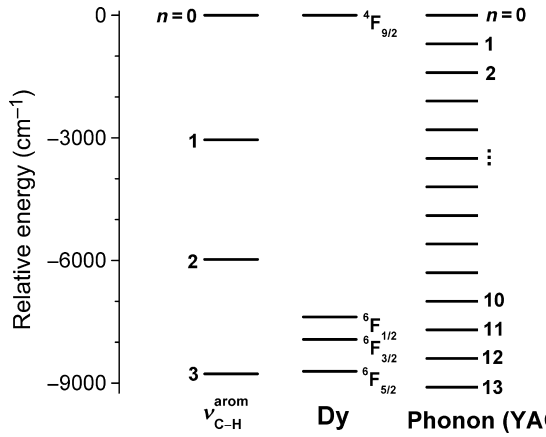

FIG. 8 Partial energy-level diagram for the Dy^{3+} levels (emitting $^4F_{9/2}$ and lower ^6F_J) compared to the vibrational overtones of local-mode, aromatic C–H oscillators [12,25] and lattice phonons in yttrium aluminum garnet (YAG, $\hbar\omega_M \approx 700\ cm^{-1}$) [22c].

($\Delta E \gg \hbar\omega_M$) for the EGL above). Fig. 8 shows typical situations for dysprosium ions ($\Delta E = 7380\,cm^{-1}$ for the gap between the emitting state $^4F_{9/2}$ and the next lower state $^6F_{1/2}$) in different cases involving on the one hand low-phonon host matrices such as YAG (Fig. 8, right) and on the other molecular lanthanoid complexes having aromatic C–H oscillators (Fig. 8, left).

There are several fundamental aspects that are crucial for the understanding of the differences between the two cases:

- ΔE vs $\hbar\omega_M$: For molecular complexes, the overtone energy of deactivating C–H oscillators is only two to three multiples of the energy gap $\Delta E = 7380\,cm^{-1}$, whereas for the much lower-phonon YAG modes at least 10 vibrational quanta are needed to bridge the gap. The latter situation is well suited for the application of the EGL, the former is clearly not.
- Anharmonicity: As already discussed in Section 1.3, the high anharmonicity of the C–H stretching vibration is not included in the descriptions using the EGL. Probably the smaller problem associated with this fact is that the anharmonic overtone energies are at slightly different positions compared to a model assuming harmonic vibrations. The much more serious issue is that the overtone intensities for anharmonic oscillators can be several orders of magnitude higher compared to harmonic vibrational descriptions as used by the EGL (see Fig. 6).
- Energy matching (Franck–Condon factors): The EGL implicitly assumes that the smallest energy gap ΔE from the emitting state (in this case $^4F_{9/2} \rightarrow {}^6F_{1/2}$) is responsible for the determination which overtone order is required for MR to take place. In the case of small vibrational quanta (here $\hbar\omega_M \approx 700\ cm^{-1}$ in YAG) the gap ΔE always matches a suitable overtone close in energy, e.g., with $n = 10$ or $n = 11$ for $^6F_{1/2}$ in Fig. 8. Since the lower matching overtone ($n = 10$) always has an oscillator strength more than an order of magnitude higher than the next overtone ($n = 11$), the former will always dominate MR even if the energy of a higher overtone would have a perfect energetic match with a lower-lying state at the metal. In this case, the energy gap ΔE is a very good measure for the quantitative analysis of MR and hence the EGL is a very suitable model. Often, the situation for molecular lanthanoid complexes will be similar and the EGL will make reasonable predictions. On the other hand, the situation for MR with the high-energy C–H oscillators in molecular complexes can be very different as shown in Fig. 8 on the left side. There, the energy gap ΔE does not match the energy of the first ($n = 2$) or second ($n = 3$) C–H overtone and the energetic difference to the gap energy is in both cases more than $1000\,cm^{-1}$, a situation which can only happen for high-energy oscillators found in molecular complexes. This prevents efficient energy transfer from the emitting state to the oscillator via the transition from $^4F_{9/2}$ to $^6F_{1/2}$ corresponding to the conventionally defined energy gap ΔE. Instead, the second overtone ($n = 3$) perfectly matches the energy of the larger gap $^4F_{9/2}$–$^6F_{5/2} \approx 8700\,cm^{-1}$ and even though the oscillator strength associated with this overtone is much smaller than for the first overtone, the MR process is highly likely to proceed via the transition $^4F_{9/2}$–$^6F_{5/2}$ [25]. The EGL is ill equipped to deal with situations like these because the relevant energy gap ΔE for high-energy oscillators is not predetermined a priori and can be very different from the traditionally defined smallest one, depending on the circumstances. Similar breakdowns of the EGL have also been observed for MR involving C–H and C–D oscillators in Sm^{3+} and Pr^{3+} complexes (vide infra) [25,26]. It should

be pointed out, however, that these abnormal cases are only likely for situations where one has to compare MR from overtones that are close in quantum number (e.g., $n = 2$ and $n = 3$ in Fig. 8 on the left side). If the overtone orders are further apart, it is unlikely that better energy matching can overcome the much lower overtone oscillator strengths associated with higher vibrational quantum numbers (e.g., the oscillator strength for a third overtone C–H is roughly 100 times smaller than for the corresponding first overtone C–H).

In summary, the application of the EGL for the quantitative analysis of MR in molecular lanthanoid complexes is not without problems. While most of the time, it will give the right qualitative picture, it cannot account for the potentially severe influence of strong Franck–Condon overlap with lower-lying states. In addition, vibrational anharmonicity needs to be accounted for because of the differences in overtone energies and especially in oscillator strengths that anharmonic overtones exhibit compared to the harmonic model.

2.2 The Inductive-Resonant Mechanism of Nonradiative Transitions

In light of the shortcomings of the EGL for molecular complexes, a different approach, proposed by Ermolaev and Sveshnikova, is more suitable, the so-called inductive-resonant mechanism of nonradiative transitions (IRM) [27]. In this model, the MR energy transfer from the lanthanoid to the anharmonic oscillators is effected mainly through electric dipole–dipole interactions under inductive-resonant conditions. As such, the principle underlying this approach is the same as for the better-known Förster resonance energy transfer (FRET) for the nonradiative energy transfer between different electronic states, maybe most prominently exemplified for FRET between organic and inorganic luminophores [28]. The IRM expresses the rate k_{nr} of nonradiative deactivation due to MR from the lanthanoid excited state to a particular oscillator in the vicinity of the lanthanoid by Eq. (6) [27]:

$$k_{nr} = \frac{9000 \cdot \ln(10) \cdot \kappa^2}{128 \cdot \pi^5 \cdot N_A} \cdot \frac{k_r}{n^4 \cdot r^6} \cdot \mathrm{SOI} = 5.857 \times 10^{-25} \frac{k_r}{n^4 \cdot r^6} \cdot \mathrm{SOI} \qquad (6)$$

with the following constants and parameters: k_r is the rate of the radiative transition, κ^2 is a factor depending on the relative orientations of the transition dipole moments of the donor (the lanthanoid) and the vibrational acceptor moiety which amounts to $\kappa^2 = 2/3$ in the dynamic isotropic limit, n is the refractive index of the medium, N_A is Avogadro's number, and r is the distance between the lanthanoid and the oscillator with the usual inverse sixth-power dependence characteristic for dipole–dipole interactions. The spectral overlap integral (SOI) is a Förster-type expression in the wavenumber scale $\tilde{\nu}$ shown in Eq. (7):

$$\mathrm{SOI} = \int I_{norm}(\tilde{\nu}) \cdot \varepsilon_{vib}(\tilde{\nu}) \cdot \tilde{\nu}^{-4} d\tilde{\nu} \qquad (7)$$

Within the integral expression in Eq. (7), $\varepsilon_{\mathrm{vib}}(\tilde{\nu})$ is the decimal molar vibrational absorption spectrum (with the usual units $\mathrm{M}^{-1}\,\mathrm{cm}^{-1}$) which implicitly takes into account the accurate energetic position of all vibrational overtones and the actual oscillator strengths for each individual overtone. Furthermore, $I_{\mathrm{norm}}(\tilde{\nu})$ is the (dimensionless) emission spectrum normalized to unit area defined by Eq. (8):

$$I_{\mathrm{norm}}(\tilde{\nu}) = \frac{I_{\mathrm{em}}(\tilde{\nu})}{\int I_{\mathrm{em}}(\tilde{\nu})\, d\tilde{\nu}} \;\Rightarrow \int I_{\mathrm{norm}}(\tilde{\nu})\, d\tilde{\nu} = 1 \tag{8}$$

Eqs. (6)–(8) only take into account one single oscillator at a certain distance r from the lanthanoid. In order to obtain the overall MR rate Σk_{nr}, the contributions from every relevant oscillator must be summed up over all oscillators according to Eq. (9):

$$\sum k_{\mathrm{nr}} = 5.857 \times 10^{-25} \cdot n^{-4} \cdot k_r \cdot \left(\sum_i \left(r_i^{-6} \cdot \mathrm{SOI}_i \right) \right) \tag{9}$$

The IRM model defined by Eqs. (6)–(9) alleviates a number of the limitations of the EGL discussed earlier. In particular, contrary to the EGL, it implicitly treats vibrational anharmonicity by incorporating experimentally accessible vibrational absorption spectra $\varepsilon_{\mathrm{vib}}(\tilde{\nu})$ which reflect the actual vibrational properties quite well and conceptually in an unbiased manner. In addition, it treats different oscillators as different localized entities with individual distances and vibrational properties, which are much more intuitive from the perspective of a molecular chemist and also more consistent with the description of molecular vibrations by a local-mode Morse oscillator approach (see Section 1.3). On the other hand, the IRM loses the conceptual simplicity of the EGL as a necessary trade-off for the much more comprehensive approach for the description of MR. For its quantitative use, it requires very specific information that is not always easy to obtain. For example, the crucial parameters k_{r}, r, and $\varepsilon_{\mathrm{vib}}(\tilde{\nu})$ in solution are often rather inaccessible experimentally or subject to dynamic changes on the experimental timescale. The most crucial and tedious to obtain at the same time is quantitative information regarding the vibrational overtone absorption signatures $\varepsilon_{\mathrm{vib}}(\tilde{\nu})$ of the high-energy oscillators X–H, which in turn is essential for the calculation of SOIs. This is often difficult because the exact geometric relationship between oscillator and lanthanoid is often not known and is also subject to structural changes, e.g., through dynamic changes in the coordination sphere. In addition, solvent molecules in the first, second, and outer solvation spheres, which are often the most important drivers of MR in solution (e.g., in H_2O), are often especially difficult or even impossible to measure from a vibrational standpoint because the absorption spectrum of the bulk solvent (which is often easily accessible) may not reflect the vibrational properties of oscillators

most relevant for quenching, e.g., inner-sphere water molecules at the metal center. While there is only a very small body of work for the quantitative analysis of $\varepsilon_{vib}(\tilde{\nu})$ and its impact on MR in molecular coordination compounds [12,25–27,29–31], a lot of high-quality data on vibrational overtone spectra of simple organic and inorganic molecules have been compiled in the literature [9,14] by a variety of experimental methods such as conventional near-IR absorption spectrophotometry, ICL-PAS (intracavity laser photoacoustic spectroscopy) [16b], or CRDS (cavity ring-down spectroscopy) [32]. In a lot of cases where the vibrational properties should not be affected by the chemical environment, these data can give a very good starting point for the analysis of coordination compounds that possess similar structural motifs. For example, nonexchangeable, aromatic local-mode C–H oscillators are very good candidates for this purpose. Fig. 9 shows a very good example where the aromatic C–H overtones in the bidentate chelator motif 2,2′-bipyridine could be measured quantitatively in solution [12]. The obtained overtone bands are in very good agreement with data for the corresponding tris(bipyridine) lanthanoid cryptates (Ln = Lu) [12]. For oscillators like these, it seems even possible to determine the properties of the higher overtone bands (i.e., energies, widths, molar absorption coefficients) by fitting the measured overtones (Fig. 9; $n = 2$–4) as simple Gaussian band shapes $\varepsilon^n_{vib}(\tilde{\nu})$ and extrapolating the parameters for higher overtones (Table 2, $n = 5$) [33]:

$$\varepsilon^n_{vib}(\tilde{\nu}) = A^n \cdot e^{-\frac{1}{2}\cdot\left(\frac{\tilde{\nu}-\tilde{\nu}^n_{max}}{\sigma^n}\right)^2} \tag{10}$$

In this way, the overall vibrational function $\varepsilon_{vib}(\tilde{\nu})$ can be generated in analytical form as the sum of individual, local mode overtone signatures $\varepsilon^n_{vib}(\tilde{\nu})$ according to Eq. (11):

$$\varepsilon_{vib}(\tilde{\nu}) = \sum_n \varepsilon^n_{vib}(\tilde{\nu}) \tag{11}$$

This approach will likely not be possible for more complicated oscillators involved in strong hydrogen bonding or similarly complicating circumstances but provides a promising prospect for the simplification of the analysis using the IRM.

Based on the fundamental IRM framework defined by Eqs. (6) and (7), a few conceptual modifications have been made by introducing rather crude approximations in order to simplify the analysis. For example, Galanin and Frank [34] have developed a model where two approximations are made: (1) no quenching oscillators are present In a sphere of radius r_{min} around the lanthanoid; (2) for distances from the lanthanoid greater than r_{min}, oscillators are homogeneously distributed (instead of the discrete distribution in real molecular species) over the entire space with a constant linear absorption

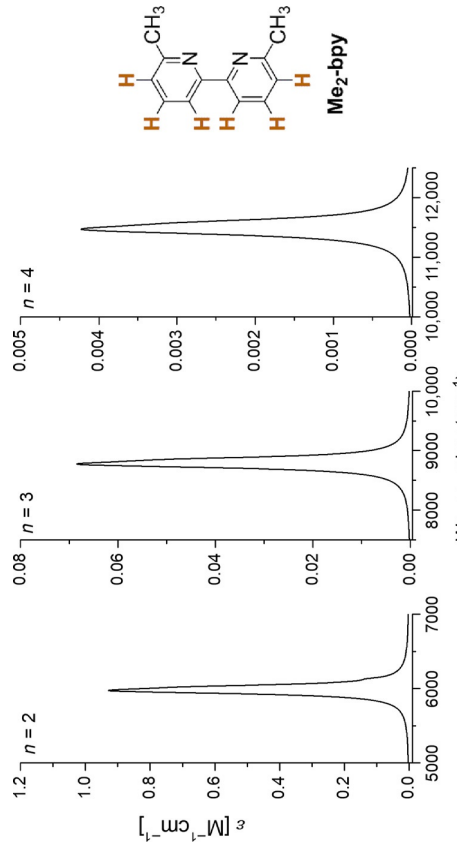

FIG. 9 Measured and spectrally extracted vibrational signatures for the spectral regions of the first, second, and third overtones ($n = 2$–4) of the three aromatic C–H oscillators (with indistinguishable vibrational signatures) in **Me_2-bpy** in $CDCl_3$ solution. *Redrawn from C. Doffek, N. Alzakhem, C. Bischof, J. Wahsner, T. Güden-Silber, J. Lügger, C. Platas-Iglesias, M. Seitz, Understanding the quenching effects of aromatic C-H- and C-D-oscillators in near-IR lanthanoid luminescence, J. Am. Chem. Soc. 134 (2012) 16413–16423 with permission—copyright 2012 American Chemical Society.*

TABLE 2 Parameters of the Gaussians ($\tilde{\nu}^n_{max}$:Center Wavenumber; σ^n: Gaussian Width; A^n: Amplitude) Describing the Different Overtone Signatures $\varepsilon^n_{vib}(\tilde{\nu})$ of the Aromatic C–H Oscillators in Me_2-bpy [33]

Quantum Number n	Maximum $\tilde{\nu}^n_{max}$ (cm^{-1})	σ^n (cm^{-1})	A^n ($M^{-1}\,cm^{-1}$)
2 (measured data)	5984.4	61.13	8.639×10^{-1}
3 (measured data)	8792.0	90.21	6.399×10^{-2}
4 (measured data)	11,493	129.1	3.910×10^{-3}
5 (calculated data)	14,065[a]	161.5[b]	2.716×10^{-4}[c]

[a] *Calculated using* $\tilde{\nu}^n_{max} = \nu \times 3170\,cm^{-1} - n \cdot (n+1) \cdot 59\,cm^{-1}$.
[b] *Calculated using* $\sigma^n = n \cdot 34.0\,cm^{-1} - 8.53\,cm^{-1}$.
[c] *Calculated using* $\log(A^n) = 2.295 - \nu \cdot 1.172$.

coefficient $a_{vib}(\tilde{\nu})$ that incorporates the contributions from all oscillators. In this scenario, k_{nr} can be calculated by Eq. (12):

$$k_{nr} = \frac{1}{(2\pi)^4} \cdot \frac{k_r}{n^4 \cdot (r_{min})^3} \cdot SOI^* \tag{12}$$

$$SOI^* = \int I_{norm}(\tilde{\nu}) \cdot a_{vib}(\tilde{\nu}) \cdot \tilde{\nu}^{-4} d\tilde{\nu} \tag{13}$$

where all parameters have the indicated meaning and $a_{vib}(\tilde{\nu})$ are in units of cm^{-1}. This model has been used particularly in the context of near-IR luminescence in erbium complexes [29,31] where Eq. (12) was further simplified to Eq. (14) [29]:

$$k^{Er}_{nr} \approx \frac{(\lambda_{em})^4}{(2\pi)^4} \cdot \frac{k_r \cdot \langle a_A \rangle_{Er}}{n^4 \cdot (r_{min})^3} \tag{14}$$

with $\langle a_A \rangle_{Er}$ being the vibrational absorption coefficient (on the wavelength scale) averaged over the erbium emission band centered around $\lambda_{em} = 1530\,nm$ and with all other parameters having the meaning defined earlier.

3 STRATEGIES FOR THE REDUCTION OF MR

The reduction of MR in molecular lanthanoid complexes is conceptually straightforward but practically a formidable task. The foremost priority, of course, is to avoid high-energy oscillators X–H (X = O, N, C) in the ligand environment around the lanthanoid. Two strategies have been developed to achieve this goal, deuteration [35] and perhalogenation [36]. Perhalogenation via fluorination or chlorination provides very efficient suppression of

vibrational quenching compared to perdeuteration due to the lower energy of the C–F/Cl stretching vibration and its smaller anharmonicity. It cannot, however, be used for every ligand system (e.g., amino carboxylates, DOTA derivatives, cryptates) because of the chemical instability of the perhalogenated species. Therefore, this strategy can only be used for a limited number of ligands, usually only with low denticities (e.g., acetylacetonates, imidodiphosphinates). The substitution of hydrogen for deuterium, on the other hand, does not change the basic chemistry of the ligand architectures and therefore allows the adaptation of virtually any ligand systems for perdeuteration, usually also without substantially altering the fundamental photophysical properties (except the MR properties). This topic has been covered extensively in a number of recent excellent reviews [6,36,37]. Fig. 10 and Table 3 show selected examples of highly efficient molecular lanthanoid luminophores (except for Eu and Tb) designed using the two strategies of halogenation and deuteration and recently reported.

4 MR ISOTOPE EFFECTS IN DEUTERATED COMPLEXES

One of the most powerful tools for the investigation of MR in molecular lanthanoid complexes is the analysis of selectively deuterated complex architectures compared to the nondeuterated parent compounds. Isotopic substitution of deuterium for hydrogen can have a strong effect on MR but usually does not change the structural parameters (e.g., distance Ln-H/D, orientation factor κ^2) in molecular complexes significantly and presumably also not the basic photophysics during the sensitization process (e.g., k_r). Under identical experimental conditions, the measured differences in luminescence lifetimes τ_{obs} can directly be correlated to the differences in MR rates Δk_{nr} for the oscillator in question (Eq. 15):

$$\Delta k_{nr} = \frac{1}{\tau_{obs}^{H}} - \frac{1}{\tau_{obs}^{D}} \tag{15}$$

In addition, for the analysis within the IRM framework [27], the ratio of MR rates of two isotopologic oscillators simplifies from Eq. (6) to Eq. (16), where only the two different spectral overlap integrals SOI^H and SOI^D are required:

$$\frac{k_{nr}^{H}}{k_{nr}^{D}} = \frac{\int I_{norm}(\tilde{\nu}) \cdot \varepsilon_{vib}^{H}(\tilde{\nu}) \cdot \tilde{\nu}^{-4} d\tilde{\nu}}{\int I_{norm}(\tilde{\nu}) \cdot \varepsilon_{vib}^{D}(\tilde{\nu}) \cdot \tilde{\nu}^{-4} d\tilde{\nu}} = \frac{SOI^{H}}{SOI^{D}} \tag{16}$$

The differences in k_{nr} due to isotopic substitution in solvents, and in particular due to O–H/D oscillators, have already been recognized and analyzed early on by the pioneering work of (among others) Kropp and Windsor [47], Heller [15a], Gallagher [15b], and Haas, Stein, and Würzberg [24b–d].

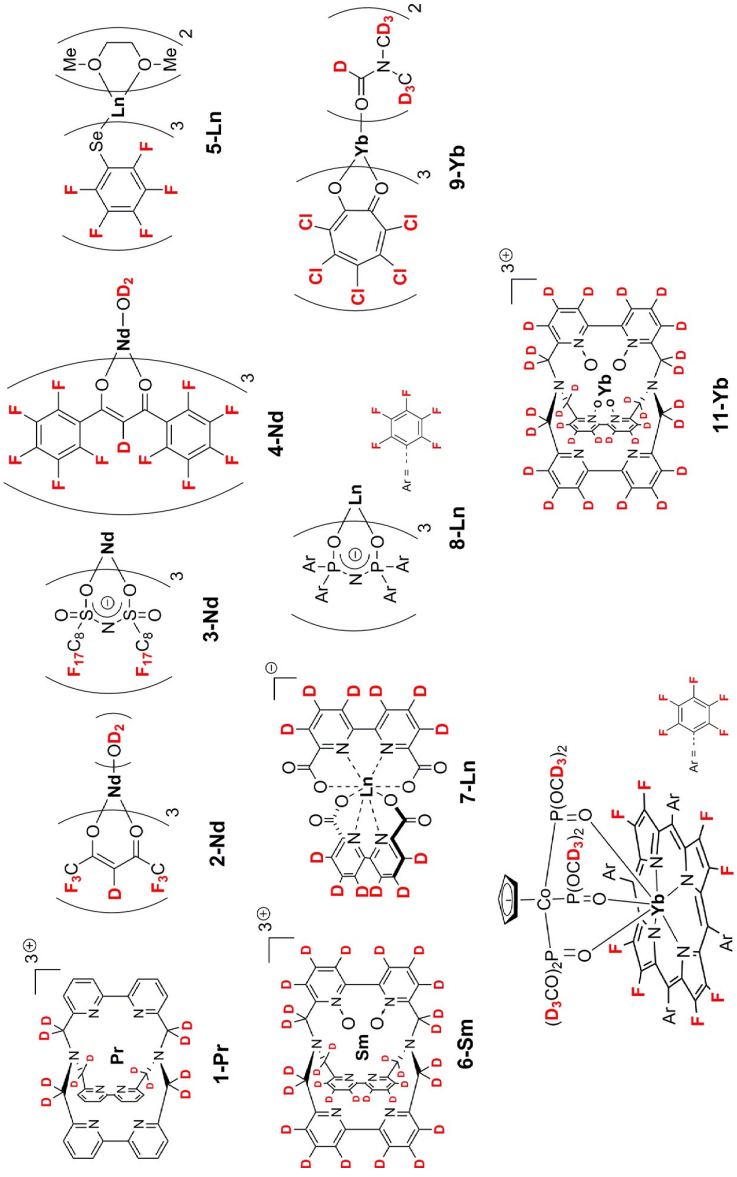

FIG. 10 Selected examples of highly luminescent lanthanoid complexes (except Eu and Tb) with reduced MR due to halogenation and deuteration (see Table 3 for references).

TABLE 3 Luminescence Data at Room Temperature for Selected Lanthanoid Complexes Showing Reduced MR Due to Halogenation and Deuteration (See Fig. 10 for Structures)

Complex	Sample Form	Lifetime τ_{obs} (μs) (Emitting Level)	Quantum Yield Φ_{Ln}^{L} (%)	References
1-Pr	$[D_6]$-DMSO	0.595 ($^1D_2$)	n.d.	[26]
2-Nd	$[D_6]$-DMSO	6.3 ($^4F_{3/2}$)	1.1	[38]
3-Nd	$[D_6]$-acetone	13 ($^4F_{3/2}$)	3.2	[39]
4-Nd[a]	$[D_8]$-THF	2.8 ($^4F_{3/2}$)	1.4	[40]
5-Nd	solid	92 ($^4F_{3/2}$)	n.d.	[41]
8-Nd	CD_3CN	44 ($^4F_{3/2}$)	n.d.	[42a]
6-Sm	CD_3CN	394 ($^4G_{5/2}$)	n.d.	[25]
7-Dy	CD_3OD	194 ($^4F_{9/2}$)	n.d.	[25]
8-Dy	CD_3CN	300 ($^4F_{9/2}$)	n.d.	[42a]
5-Er	solid	850 ($^4I_{13/2}$)	n.d.	[41]
8-Er	CD_3CN	741 ($^4I_{13/2}$)	n.d.	[42]
5-Tm	solid	89 ($^3H_4$)	n.d.	[41]
7-Tm	$[D_6]$-DMSO	4.6 ($^1G_4$)	0.12[b]	[43]
8-Yb	CD_3CN	1111 ($^2F_{5/2}$)	n.d.	[42a]
9-Yb	solid	180 ($^2F_{5/2}$)	n.d.	[44]
10-Yb	CD_2Cl_2	714 ($^2F_{5/2}$)	63	[45]
11-Yb	CD_3OD	172 ($^2F_{5/2}$)	12	[46]

[a] *Direct Nd excitation at* $\lambda_{exc} = 585$ *nm.*
[b] *Partial QY for the transition* $^1G_4 \rightarrow {}^3H_6$ *only.*

More recently, careful structure–property correlations on the basis of measured Δk_{nr} values have allowed the development of empirical equations for the reliable determination of inner-sphere water molecules for europium (Horrocks [48], Parker [49]), terbium (Parker [49]), and ytterbium (Parker [49]). In addition, an analogous relation has been reported for the analysis in MeOH for ytterbium (Beeby, Faulkner, and Ward [50]). The situation has also been analyzed for neodymium [50–52], samarium [53], and dysprosium [54] but with less success. Apart from these more empirical studies, extensive qualitative and quantitative analysis using the IRM model has been done by Sveshnikova and Ermolaev [27]. In general, the topic of solvent isotope

effects has often been reviewed over the years and further details can be found in a number of excellent summaries in the literature [1,35,37]. Unfortunately, the usually very fluxional nature of lanthanoid–solvent interactions in the inner- and second-sphere and the concomitant rapid (and often unknown) changes in critically important parameters (e.g., distances Ln oscillator, $\varepsilon_{vib}(\tilde{\nu})$, etc.) make the rigorous quantitative analysis of isotope effects in MR extremely challenging. This section will therefore highlight selected examples for MR rate differences Δk_{nr} due to deuteration of well-defined oscillators. In general, the description will focus on rigidly attached C–H/D or well-defined N–H/D oscillators, where the number and nature of deuterated oscillators as well as their approximate geometries relative to the metal center are known or can be estimated with a high degree of confidence. In addition, some of the observed phenomena specific to a particular lanthanoid will be discussed.

4.1 Europium and Terbium Complexes

Trivalent europium ($^5D_0$: $\Delta E = 12{,}400\,cm^{-1}$) and terbium ($^5D_4$: $\Delta E = 14{,}800\,cm^{-1}$) have relatively large energy gaps and are therefore only affected moderately by MR of high-energy oscillators. Apart from the well-known, empirically documented effect that O–H and N–H oscillators (especially water) have on the two lanthanoids [48,49], the extent of C–H-induced MR detrimental to luminescence efficiencies is very limited (Tables 4 and 5). Interestingly, the deuterated C–D oscillators of aliphatic moieties in DOTA complexes (Fig. 11: H_4L^1 [49]) are reported to sometimes even have a slightly higher MR efficiency than the isotopologic C–H analogues (see Table 5, first entry).

4.2 Samarium and Dysprosium Complexes

For samarium and dysprosium complexes, despite their relative importance as visible lanthanoids emitters, only a very limited number of examples are reported for the determination of MR rate differences in isotopologic C–H/D oscillators (Table 6). For both lanthanoids, Δk_{nr} values for the main emitting levels (Sm^{3+}: $^4G_{5/2}$ and Dy^{3+}: $^4F_{9/2}$) are on the order of roughly 0.1–1 ms^{-1} per oscillator.

In the case of aromatic C–H/D oscillator overtones, it could be shown (Fig. 12) that the relevant energy gaps for both lanthanoids are not the usually assumed smallest gaps (Sm^{3+}: $^4G_{5/2}$–$^6F_{11/2}$ and Dy^{3+}: $^4F_{9/2}$–$^6F_{1/2}$) but larger ones that are in much better resonance with the second C–H overtone ($n = 3$) or with the third C–D overtone ($n = 4$) [25].

4.3 Praseodymium, Holmium, and Thulium Complexes

For molecular complexes of Pr, Ho, and Tm in solution, only a handful of reports of lanthanoid-centered luminescence are known. Even less is known about the effect that molecular vibrations in the ligands have on the MR

TABLE 4 Selected Nonradiative Deactivation Rate Differences Δk_{nr} Between Nondeuterated and Deuterated Systems Containing Molecular Eu Complexes (See Fig. 11 for Structures of the Deuterated Ligands)

Ligand	Emitting State	Isotopologic Oscillators	Approximate Distance Ln-(H/D) (Å)	Δk_{nr} (H–D) (s^{-1})	References
H_4L^1	$^5D_0$	CH_2/CD_2 (acetate)	3.7–4.4	45 (2 H)	[49]
H_4L^1	$^5D_0$	CH_2/CD_2 (cyclen)	3.7–4.5	28 (2 H)	[49]
H_3L^2	$^5D_0$	NH/ND (amide)	5.1–5.2	75 (1 H)	[49]
H_3L^2	$^5D_0$	NH/ND (amine)	2.7–3.0	1200 (1 H)	[49]
H_3L^3	$^5D_0$	CH_2/CD_2 (ethylene/acetate)	3.5–4.4	1300 (14 H)	[54]
HL^4	$^5D_0$	CH/CD (diketonate)	4.6–4.7	86–112 (1 H)	[55]
H_4L^5	$^5D_0$	CH_2/CD_2 (benzylic/acetate)	3.5–4.4	35 (6 H)	[56]
HL^6	$^5D_0$	CH/CD (diketonate)	4.7–4.9	52 (1 H)	[57]
HL^6	$^5D_0$	$C(CH_3)_3/C(CD_3)_3$ (*tert*-butyl)	4.4–6.5	29 (9 H)	[57]
L^7	$^5D_0$	CH/CD (phen)	3.3–6.8	67 (8 H)	[58]

TABLE 5 Selected Nonradiative Deactivation Rate Differences Δk_{nr} Between Nondeuterated and Deuterated Systems Containing Molecular Tb Complexes (See Fig. 11 for Structures of the Deuterated Ligands)

Ligand	Emitting State	Isotopologic Oscillators	Approximate Distance Ln-(H/D) (Å)	Δk_{nr} (H–D) (s^{-1})	References
H_4L^1	$^5D_4$	CH_2/CD_2 (cyclen)	3.7–4.5	−6 (2 H)	[49]
H_3L^2	$^5D_4$	NH/ND (amine)	2.7–3.0	90 (1 H)	[49]
H_3L^3	$^5D_4$	CH_2/CD_2 (acetate/ethylene)	3.6–4.8	1050 (14 H)	[59]
H_4L^5	$^5D_4$	CH_2/CD_2 (benzylic/acetate)	3.5–4.4	0 (6 H)	[56]

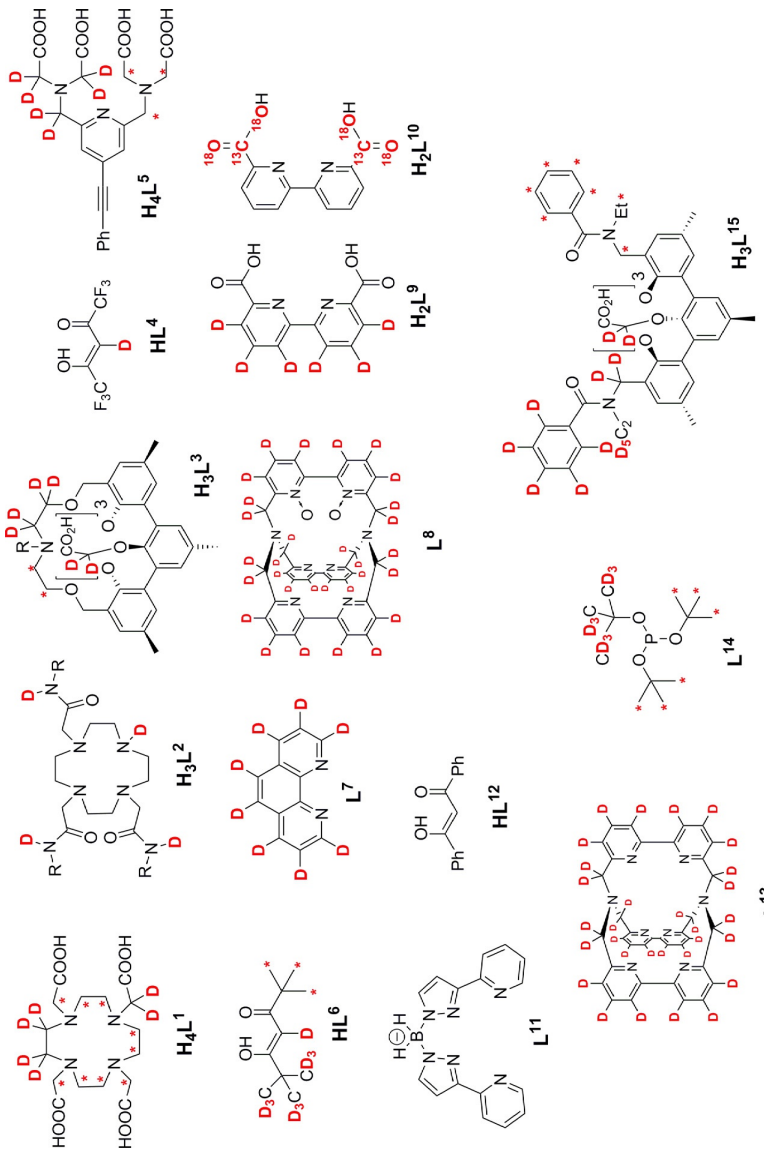

FIG. 11 Ligands used for the investigation of Δk_m with highlighted oscillator groups (equivalent positions that can also be deuterated are marked with *.

TABLE 6 Selected Nonradiative Deactivation Rate Differences Δk_{nr} Between Nondeuterated and Deuterated Systems Containing Molecular Sm and Dy Complexes (See Fig. 11 for Structures of the Deuterated Ligands)

Complex	Emitting State	Isotopologic Oscillators	Approximate Distance Ln-(H/D) (Å)	Δk_{nr} (H–D) (ms^{-1})	References
H_3L^3 (Sm)	$^4G_{5/2}$	CH_2/CD_2 (ethylene/acetate)	3.5–4.4	6.0 (14 H)	[59]
L^8 (Sm)	$^4G_{5/2}$	CH_2/CD_2, CH/CD (benzylic/aromatic)	3.4–6.3	30 (30 H)	[25]
H_2L^9 (Dy)	$^4F_{9/2}$	Pyridine (3-H,4-H,5-H)	5.5–6.3	1.1 (3 H)	[25]

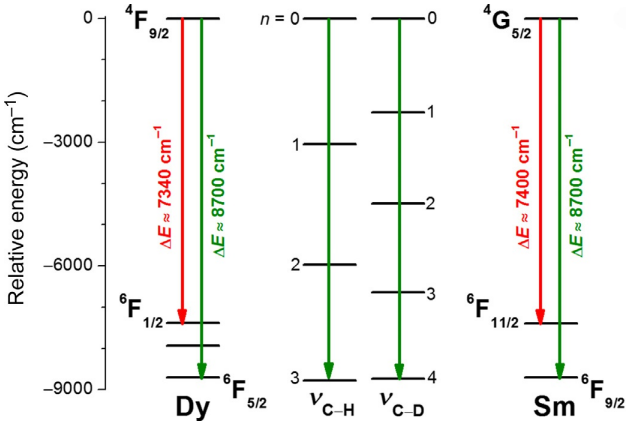

FIG. 12 Partial energy level diagram for Dy(III) and Sm(III) showing the energy gaps ΔE according to the energy gap law (smaller ΔE) and the ones actually relevant for MR of aromatic C–H/D oscillators (larger ΔE). *Reprinted with permission from C. Doffek, J. Wahsner, E. Kreidt, M. Seitz, Breakdown of the energy gap law in molecular lanthanoid luminescence: the smallest energy gap is not universally relevant for nonradiative deactivation, Inorg. Chem. 53 (2014) 3263–3265—copyright 2015 American Chemical Society.*

efficiencies (Table 7). Holmium, with its many and closely spaced energy levels (Fig. 3: $\Delta E < 3000\,\mathrm{cm}^{-1}$), is especially prone to vibrational deactivation, even by fundamentals of high-energy oscillators. It is therefore not entirely surprising but still a rare observation that even minor vibrational isotope effects can have an observable impact on the luminescence intensities. For instance, a surprisingly large effect could be shown for a near-IR emission band of holmium around 974 nm ($^3K_8 \rightarrow {}^5I_5$) which increases its intensity by approximately 45% (Fig. 13) upon isotopic labeling of the four inner-sphere carboxylates of complexes with ligand H_2L^{10} (Fig. 11) labeled with ^{13}C and ^{18}O [62]. This only changes the vibrational C═O stretching frequency of the carboxylates by roughly 5% from $\tilde{\nu}_{^{12}C=^{16}O} = 1624\,\mathrm{cm}^{-1}$ to $\tilde{\nu}_{^{13}C=^{18}O} = 1549\,\mathrm{cm}^{-1}$ and should also have no significant effect on anharmonicity. Unfortunately, the observed luminescence intensities were too small to allow for detailed measurements of the lifetime differences between the isotopologues. As expected, the luminescence of other lanthanoids such as Eu^{3+} or Sm^{3+} is entirely unaffected by isotopic substitution in the carboxylates due to their much larger energy gaps so that small changes in $\tilde{\nu}_{C=O}$ do not play any role [62].

For thulium, which also rarely shows luminescence in molecular systems in solution, one report by Faulkner et al. [61] shows the large isotope effect that deuteration of solvent CH_3 groups has on the luminescence of thulium(III) triflate in MeOH and DMSO (Table 7). In both cases, Δk_{nr} on the order of $10^3\,\mathrm{ms}^{-1}$ are found. Presumably, the CH_3/CD_3 groups are (at least in part) in the inner sphere

TABLE 7 Selected Nonradiative Deactivation Rate Differences Δk_{nr} Between Nondeuterated and Deuterated Systems Containing Molecular Pr and Tm Complexes (See Fig. 11 for Structures of the Deuterated Ligands)

Ligand/ Complex	Emitting State	Isotopologic Oscillators	Approximate Distance LN-(H/D) (Å)	Δk_{nr} (H–D) (ms^{-1})	References
$[Pr(L^{11})(L^{12})_2]$	$^1D_2$	CH_3OH (solv.) CD_3OD (solv.)	Unknown	67,800 (3 H)	[60]
L^{13} (Pr)	$^1D_2$	Benzylic CH_2/CD_2	3.4–4.4	788 (2 H)	[26]
L^{13} (Pr)	$^1D_2$	Pyridine (3-H,4-H,5-H)	5.5–6.3	−45 (3 H)	[26]
$[Tm(OTf)_3]$	$^1G_4$	CH_3OD (solv.) CD_3OD (solv.)	Unknown	3700 (3 H)	[61]
$[Tm(OTf)_3]$	$^1G_4$	DMSO (solv.) $[D_6]$-DMSO (solv.)	Unknown	2500 (6 H)	[61]
$[Tm(OTf)_3]$	$^1D_2$	CH_3OD (solv.) CD_3OD (solv.)	Unknown	2900 (3 H)	[61]
$[Tm(OTf)_3]$	$^1D_2$	DMSO (solv.) $[D_6]$-DMSO (solv.)	Unknown	2100 (6 H)	[61]
H_2L^9 (Tm)	$^1G_4$	Pyridine (3-H,4-H,5-H)	5.5–6.3	112 (3 H)	[43]

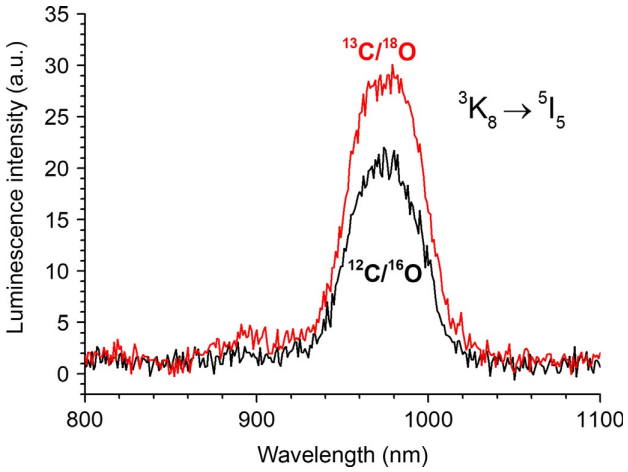

FIG. 13 Partial steady-state emission spectra for $^{13}C/^{18}O$-labeled complex $[Ho(L^{10})_2](HNEt_3)$ and its nonlabeled analogue in $[D_6]$-DMSO ($c = 10\,\mu M$, $\lambda_{exc} = 306\,nm$). *Redrawn from J. Wahsner, M. Seitz, Non-radiative deactivation of lanthanoid excited states by inner-sphere carboxylates, Inorg. Chem. 54 (2015) 10841–10848 with permission—copyright 2015 American Chemical Society.*

of the lanthanoid with relatively short distances Tm–H (ca. 3.5–4.2 Å) albeit without any detailed knowledge of the number of oscillators close to the thulium ion or the precise geometrical arrangements for the solvent oscillator groups. Aromatic C–H oscillators relatively far away from the metal center with well-defined geometries (distances ≈ 5.5–6.3 Å) in complexes with ligand H_2L^9 (Fig. 11 and Table 7) show large $\Delta k_{nr} = 112\,ms^{-1}$ (3 H) [43], which is two orders of magnitude greater than for the less sensitive Dy complex [25] of the same ligand (Table 6: $\Delta k_{nr} = 1.1\,ms^{-1}$, 3 H).

As for Ho and Tm, luminescence from molecular praseodymium luminophores is very rare in solution, in part due to its strong susceptibility to deactivation by MR. This is exemplified by the huge quenching rate difference of $\Delta k_{nr} = 67{,}800\,ms^{-1}$ (Table 7) for the combined effect of O–H and C–H deuteration of methanol solvent molecules for the complex $[Pr(L^{11})(L^{12})_2]$. Praseodymium also shows a very peculiar isotope effect for vibrational deactivation of the emitting $^1D_2$ state with benzylic and aromatic C–H/D oscillators in cryptates with the tris(bipyridine)-based cryptand L^{13} (Fig. 11) [26]. While the benzylic methylene groups induce a normal decrease in MR rates upon deuteration (Table 7: $\Delta k_{nr} = 788\,ms^{-1}$), the aromatic C–H moieties of the pyridines anomalously lead to slightly smaller quenching compared to corresponding C–D modes (Table 7: $\Delta k_{nr} = -45\ ms^{-1}$). This phenomenon has been rationalized with the much better spectral overlap of the second aromatic C–D overtones with the energy gap of $\Delta E \approx 7000\,cm^{-1}$ compared to the first aromatic overtone C–H (Fig. 14A). In the case of benzylic oscillators,

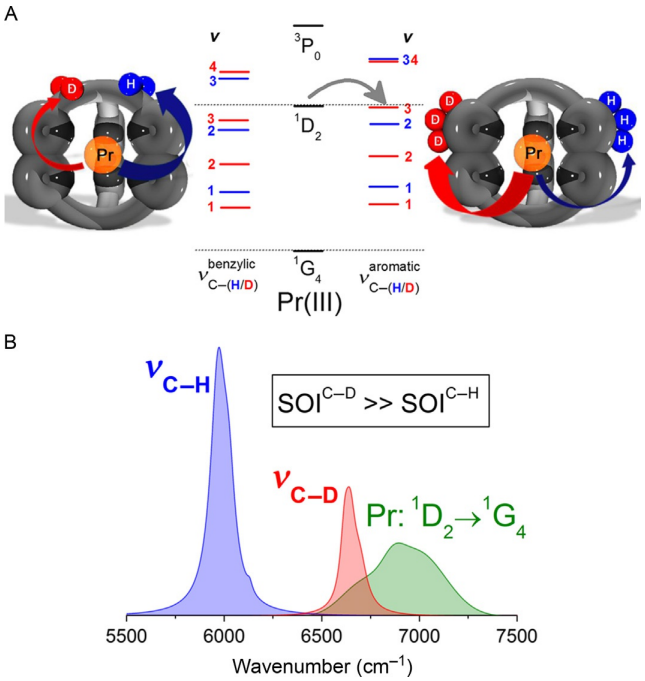

FIG. 14 (A) Partial energy level diagram for Pr(III) and the position of the overtones of C–H/D oscillators in tris(bipyridine)-based cryptates relative to the emitting $^1D_2$ and the lower $^1G_4$ level; (B) schematic representation of the spectral overlap of the praseodymium emission $^1D_2 \rightarrow {}^1G_4$ and the different aromatic overtones C–H and C–D (band intensities not to scale). *Reprinted with permission from C. Doffek, N. Alzakhem, C. Bischof, J. Wahsner, T. Güden-Silber, J. Lügger, C. Platas-Iglesias, M. Seitz, Understanding the quenching effects of aromatic C-H- and C-D-oscillators in near-IR lanthanoid luminescence, J. Am. Chem. Soc. 134 (2012) 16413–16423; J. Scholten, G. A. Rosser, J. Wahsner, N. Alzakhem, C. Bischof, F. Stog, A. Beeby, M. Seitz, Anomalous reversal of C−H and C−D quenching efficiencies in luminescent praseodymium cryptates, J. Am. Chem. Soc. 134 (2012) 13915–13917—copyright 2012 American Chemical Society.*

both isotopologues with lower vibrational frequencies than their aromatic counterparts seem to be out of resonance with ΔE, and consequently, the higher oscillator strength of C–H leads to considerably faster MR and consequently the normally expected behavior upon deuteration. This explanation could later be confirmed by quantitative calculations of the SOI for the two different aromatic oscillators C–H/D using Eq. (16) [12]. Fig. 14B shows a schematic depiction of the energetic positions of the relevant overtone absorption/lanthanoid emission bands. A similar effect had qualitatively already been described for the emission from the $^3P_0$ state in Pr complexes with a deuterated *m*-terphenyl-based ligand [59].

4.4 Neodymium Complexes

Neodymium luminescence has been an intense subject of research over the years and many quite successful molecular Nd complexes have been developed [63]. Nevertheless, the main emitting level $^4F_{3/2}$ has a very small energy gap of $\Delta E = 5450\,cm^{-1}$ (Fig. 3) and is therefore very prone to nonradiative deactivation by MR. Relatively numerous studies have determined values for Δk_{nr} upon deuteration of C–H groups in well-defined systems (Table 8). The observed differences vary considerably with the structural conditions but are generally on the order of $\Delta k_{nr} \approx 1\text{–}100\,ms^{-1}$ per C–H/D oscillator.

4.5 Erbium Complexes

Luminescent erbium complexes are of particular interest because of their near-IR luminescence bands around 1550 nm ($^4I_{13/2} \rightarrow {}^4I_{15/2}$) which are in the most useful wavelength range for fiber-optical telecommunication [68]. Much effort has been invested in the reduction of MR in molecular complexes, which is most effectively achieved by halogenation strategies [29,36,41,42]. Deuteration has been realized for quite some time now to be rather ineffective for emission efficiency improvements [30,31]. The main reason for this is the good resonance of the second vibrational overtones in C–D oscillators (e.g., aromatic $\tilde{\nu}^3_{C-D} \approx 6600\,cm^{-1}$, [12]) with the relevant energy gap $\Delta E = 6500\,cm^{-1}$ for erbium, which makes C–D oscillators also very efficient vibrational quenchers. Table 9 shows isotopologic rate differences $\Delta k_{nr} \approx 1\text{–}100\,ms^{-1}$ per C–H/D oscillator, which is very similar to other lanthanoids sensitive to MR such as Nd, Pr, or Tm.

4.6 Ytterbium Complexes

For a number of reasons, ytterbium luminescence around 1000 nm is one of the most interesting among all other near-IR-emitting lanthanoids. For one, Yb with its relatively large energy gap $\Delta E = 10{,}250\,cm^{-1}$ is not as sensitive as other near-IR emitters and can be expected to achieve high quantum efficiencies if properly protected from detrimental MR effects. The progress in this area has been spectacular with the recent development of a number of highly luminescent luminophores with absolute quantum yields of 12% [46] or even 63% [45] in solution due to decreased vibrational quenching enabled by deuteration and/or halogenation (see Section 3). In addition to the efficiency gains during the last years, a number of quantitative studies of Δk_{nr} in well-defined isotopologues have been reported (Table 10), which will undoubtedly facilitate further improvement in the field by advancing a much better quantitative understanding of MR. As a crude rule of thumb, the deuteration of individual C–H oscillators can be expected to yield Δk_{nr} of ca. $1\text{–}10\,ms^{-1}$.

Particularly noteworthy is a very recent study by Zhang et al. [71] which investigated the MR differences well-defined O–H/D in porpholactol-based Yb complexes with ligand H_2L^{21} (Fig. 15). Fig. 16 shows the two

TABLE 8 Selected Nonradiative Deactivation Rate Differences Δk_{nr} Between Nondeuterated and Deuterated Systems Containing Molecular Nd Complexes (See Fig. 11 for Structures of the Deuterated Ligands)

Complex	Emitting State	Isotopologic Oscillators	Approximate Distance Ln-(H/D) (Å)	Δk_{nr} (H–D) (ms^{-1})	References
HL^4	$^4F_{3/2}$	CH/CD (diketonate)	4.7–4.8	92 (1 H)	[31a]
L^{14}	$^4F_{3/2}$	$C(CH_3)_3/C(CD_3)_3$ (*tert*-butyl)	ca. 6.5	22 (9 H)	[64]
L^{13}	$^4F_{3/2}$	CH_2/CD_2 (benzylic)	3.5–4.4	94 (2 H)	[65]
L^{13}	$^4F_{3/2}$	Pyridine (3-H,4-H,5-H)	5.5–6.4	9.4 (3 H)	[65]
L^8	$^4F_{3/2}$	CH_2/CD_2 (benzylic)	3.4–4.6	309 (4 H)	[12,66]
L^8	$^4F_{3/2}$	Pyridine (3-H,4-H,5-H)	5.7–6.9	55 (6 H)	[12,66]
L^8	$^4F_{3/2}$	CH_2/CD_2 (benzylic, *N*-oxide)	3.7–4.7	253 (4 H)	[12,66]
L^8	$^4F_{3/2}$	Pyridine-*N*-oxide (3-H,4-H,5-H)	5.9–6.9	14 (6 H)	[12,66]
H_3L^3	$^4F_{3/2}$	CH_2/CD_2 (ethylene/acetate)	3.5–4.4	142 (14 H)	[59]
H_3L^{15}	$^4F_{3/2}$	Various types of CH_x/CD_x	3.8–8.0	218 (30 H)	[67]

TABLE 9 Selected Nonradiative Deactivation Rate Differences Δk_{nr} Between Nondeuterated and Deuterated Systems Containing Molecular Er Complexes (See Fig. 11 for Structures of the Deuterated Ligands)

Complex	Emitting State	Isotopologic Oscillators	Approximate Distance Ln-(H/D) (Å)	Δk_{nr} (H–D) (ms^{-1})	References
HL^4	$^4I_{13/2}$	CH/CD (diketonate)	4.7	116 (1 H)	[31]
L^8	$^4I_{13/2}$	CH_2/CD_2 (benzylic)	3.6–4.6	89 (4 H)	[12,66]
L^8	$^4I_{13/2}$	Pyridine (3-H,4-H,5-H)	5.5–6.9	29 (6 H)	[12,66]
L^8	$^4I_{13/2}$	CH_2/CD_2 (benzylic, *N*-oxide)	3.3–4.5	59 (4 H)	[12,66]
L^8	$^4I_{13/2}$	Pyridine-*N*-oxide (3-H,4-H,5-H)	5.9–6.9	25 (6 H)	[12,66]
H_3L^{15}	$^4I_{13/2}$	Various types of CH_x/CD_x	3.8–8.0	118 (30 H)	[67]

TABLE 10 Selected Nonradiative Deactivation Rate Differences Δk_{nr} Between Nondeuterated and Deuterated Systems Containing Molecular Yb Complexes (See Figs. 11 and 15 for Structures of the Deuterated Ligands)

Complex	Emitting State	Isotopologic Oscillators	Approximate Distance Ln-(H/D) (Å)	Δk_{nr} (H–D) (ms^{-1})	References
H_4L^1	$^2F_{5/2}$	CH_2/CD_2 (acetate)	3.6–4.2	13 (2 H)	[49]
H_4L^1	$^2F_{5/2}$	CH_2/CD_2 (cyclen)	3.6–4.3	11 (2 H)	[49]
HL^4	$^2F_{5/2}$	CH/CD (diketonate)	4.6–4.7	10.7 (1 H)	[31a]
HL^{12}	$^2F_{5/2}$	CH/CD (diketonate)	4.6–4.7	4.8 (1 H)	[69]
HL^{16}	$^2F_{5/2}$	CH/CD (diketonate)	4.6–4.7	3.2 (1 H)	[69]
L^{13}	$^2F_{5/2}$	CH_2/CD_2 (benzylic)	3.5–4.2	7.7 (2 H)	[65]
L^{13}	$^2F_{5/2}$	Pyridine (3-H,4-H,5-H)	5.4–6.2	2.2 (3 H)	[65]
L^8	$^2F_{352}$	CH_2/CD_2 (benzylic)	3.6–4.6	23.6 (4 H)	[12,66]
L^8	$^2F_{5/2}$	Pyridine (3-H,4-H,5-H)	5.5–6.9	2.8 (6 H)	[12,66]
L^8	$^2F_{5/2}$	CH_2/CD_2 (benzylic, *N*-oxide)	3.3–4.5	20.5 (4 H)	[12,66]
L^8	$^2F_{5/2}$	Pyridine-*N*-oxide (3-H,4-H,5-H)	5.9–6.9	3.1 (6 H)	[12,66]
L^{17}	$^4F_{3/2}$	CH_2/CD_2, CH/CD (benzylic/aromatic)	3.3–6.9	32.5 (30 H)	[46]
H_3L^3	$^2F_{5/2}$	CH_2/CD_2 (ethylene/acetate)	3.5–4.4	21 (14 H)	[59]
H_3L^{15}	$^2F_{5/2}$	Various types of CH_x/CD_x	3.8–8.0	33.5 (30 H)	[67]
H_8L^{18}	$^2F_{5/2}$	CH_2/CD_2 (benzylic, aliphatic)	3.6–4.3	13.2 (12 H)	[70]
L^{19}	$^2F_{5/2}$	CH_3/CD_3 (methoxy)	4.3–5.7	2.9 (3 H)	[45]
H_2L^{20}	$^2F_{5/2}$	CH/CD (porphyrin, β)	5.2–5.4	3.2 (2 H)	[45]
H_2L^{21}	$^2F_{5/2}$	OH/OD (porpholactol, up)	ca. 4.3–5.5	18.5 (1 H)	[71]
H_2L^{21}	$^2F_{5/2}$	OH/OD (porpholactol, down)	ca. 5.9–6.4	9.2 (1 H)	[71]

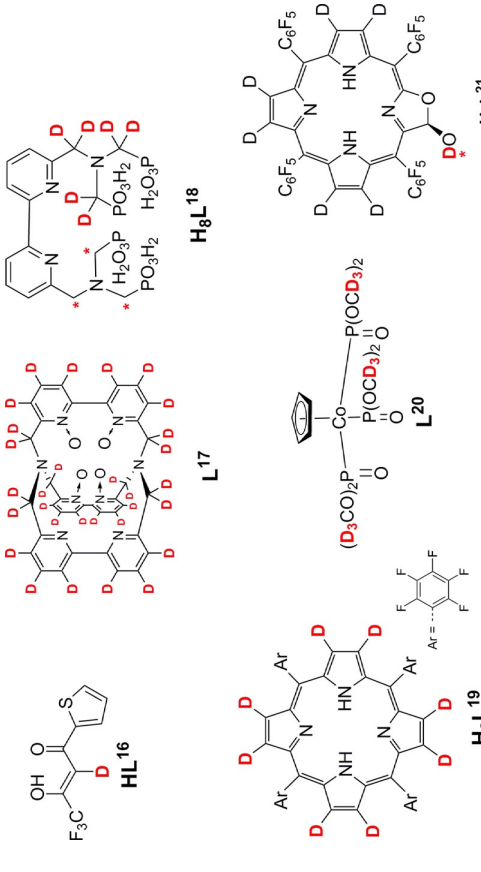

FIG. 15 Ligands used for the investigation of Δk_{nr} in Yb complexes with highlighted oscillator groups (equivalent positions that can also be deuterated are marked with *.

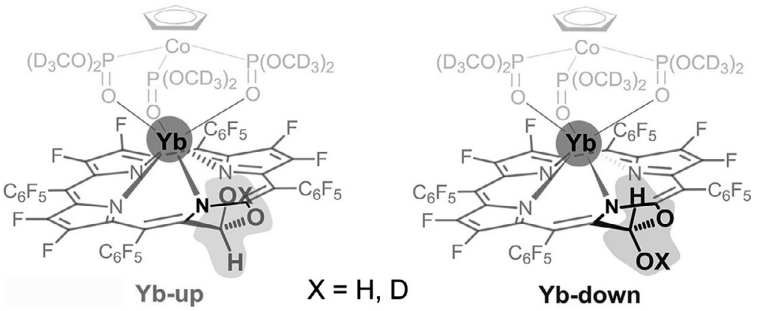

FIG. 16 Diastereomeric ytterbium complexes Yb-up and Yb-down with geometrically well-defined O–H/D oscillators for the determination of Δk_{nr} (OH–OD). *Adapted from Y. Ning, Y.-W. Liu, Y.-S. Meng, J.-L. Zhang, Design of near-infrared luminescent lanthanide complexes sensitive to environmental stimulus through rationally tuning the secondary coordination sphere, Inorg. Chem. 57 (2018) 1332–1341 with permission—copyright 2018 American Chemical Society.*

diastereomeric complexes Yb-up and Yb-down used for this purpose, which represent very rare examples where the relative spatial orientation of the O–H oscillators is reasonably well established and can be analyzed. The authors showed that the observed nonradiative rate differences between the OH- and OD-containing species in either complex are solely induced by isotopologic hydroxyl overtones with no measurable effect of the concomitant change in orientation of the geminal C–H oscillators at the lactol motif (Table 10). It remains unclear, if the observed values for Δk_{nr} are mainly due to differences in the Ln-oscillator distances or if the potentially different vibrational signatures also play a role, e.g., via strong hydrogen-bonding interactions.

5 CONCLUSION AND OUTLOOK

The chemical development of highly luminescent, molecular lanthanoid complexes has made enormous strides over the last decades. Despite these great advances, the understanding of the role that MR induced by molecular vibrations plays for the associated photophysical processes is still qualitative in nature rather than rigorously quantitative. Detailed studies of this important phenomenon in well-defined molecular systems are still only few in number but already provide tantalizing glimpses into the unique aspects that MR in molecular complexes exhibits compared to other areas of inorganic photophysics. Especially important will be the recognition of the exact role that vibrational anharmonicity plays for the crucial overtone energies and oscillator strengths. Work in this area would not only enable even more efficient lanthanoid luminophores to be designed but would more importantly also further a much deeper understanding of the role that molecular vibrations play for other fundamental photophysical aspects such as internal conversion between different lanthanoid states. It stands to reason that with the recent emergence

of highly efficient near-IR luminophores, more elaborate studies into MR will be within reach that were previously unthinkable. This in turn will undoubtedly enable the realization of even more sophisticated and fascinating aspects such as molecular upconversion.

ACKNOWLEDGMENTS

The authors gratefully acknowledge the financial support from the German Research Foundation (DFG, research Grants SE1448/5-1 and SE1448/6-1) and the German Academic Scholarship Foundation (Studienstiftung des deutsches Volkes, predoctoral fellowship for E.K.).

ABBREVIATIONS

DMSO	dimethyl sulfoxide
EGL	energy gap law
EnT	energy transfer
Φ_{Ln}^{L}	absolute quantum yield
FRET	Förster resonance energy transfer
IRM	inductive-resonant mechanism of nonradiative transitions
ISC	intersystem crossing
MR	multiphonon relaxation
n.d.	not determined
rt.	room temperature
THF	tetrahydrofurane
τ_{obs}	observed luminescence lifetime

REFERENCES

[1] (a) J.-C.G. Bünzli, C.V. Eliseeva, Photophysics of lanthanoid coordination compounds, in: J. -Reedijk, K. Poeppelmeier (Eds.), Comprehensive Inorganic Chemistry II, vol. 8, Elsevier, Oxford, 2013, pp. 339–398. (b) P. Hänninen, H. Härma (Eds.), Lanthanide Luminescence, Springer, Heidelberg, 2011. (c) J.-C.G. Bünzli, Lanthanide luminescence: from a mystery to rationalization, understanding, and applications, in: J.-C.G. Bünzli, V.K. Pecharsky (Eds.), Handbook on the Physics and Chemistry of Rare Earths, vol. 50, Elsevier, Amsterdam, 2016, pp. 141–176.

[2] (a) R. Englman, J. Jortner, The energy gap law for radiationless transitions in large molecules, Mol. Phys. 18 (1970) 145–164. (b) K.F. Freed, J. Jortner, Multiphonon processes in the nonradiative decay of large molecules, J. Chem. Phys. 52 (1970) 6272–6291.

[3] (a) P.S. Wagenknecht, P.C. Ford, Metal centered ligand field excited states: their roles in the design and performance of transition metal based photochemical molecular devices, Coord. Chem. Rev. 255 (2011) 591–616. (b) A.D. Kirk, Photochemistry and photophysics of chromium(III) complexes, Chem. Rev. 99 (1999) 1607–1640. (c) L.S. Forster, The photophysics of chromium(III) complexes, Chem. Rev. 90 (1990) 331–353. (d) S. Otto, M. Dorn, C. Förster, M. Bauer, M. Seitz, K. Heinze, Understanding and exploiting long-lived near-infrared emission of a molecular ruby, Coord. Chem. Rev. 359 (2018) 102–111.

[4] (a) W.T. Carnall, P.R. Fields, K. Rajnak, Electronic energy levels in the trivalent lanthanide aquo ions. I. Pr^{3+}, Nd^{3+}, Pm^{3+}, Sm^{3+}, Dy^{3+}, Ho^{3+}, Er^{3+}, and Tm^{3+}, J. Chem. Phys. 49 (1968) 4424–4442. (b) W.T. Carnall, P.R. Fields, K. Rajnak, Electronic energy levels of the trivalent lanthanide aquo ions. III. Tb^{3+}, J. Chem. Phys. 49 (1968) 4447–4449. (c) W.T. Carnall, P.R. Fields, K. Rajnak, Electronic energy levels of the trivalent lanthanide aquo ions. IV. Eu^{3+}, J. Chem. Phys. 49 (1968) 4450–4455. (d) W.T. Carnall, G.L. Goodman, K. Rajnak, R.S. Rana, A systematic analysis of the spectra of the lanthanides doped into single crystal LaF_3, J. Chem. Phys. 90 (1989) 3443–3457.

[5] The values for ΔE also depend on the extent of ligand-field splitting of the corresponding levels which can amount to a few hundred cm^{-1}.

[6] J.-C.G. Bünzli, On the design of highly luminescent lanthanide complexes, Coord. Chem. Rev. 293–294 (2015) 19–47.

[7] Selected examples: (a) S. Petoud, S. M. Cohen, J.-C. G. Bünzli, K. N. Raymond, Stable lanthanide luminescence agents highly emissive in aqueous solution: multidentate 2-hydroxyisophthalamide complexes of Sm^{3+}, Eu^{3+}, Tb^{3+}, Dy^{3+}, J. Am. Chem. Soc. 125 (2003) 13324–13325.
(b) J.W. Walton, A. Bourdolle, S.J. Butler, M. Soulie, M. Delbianco, B.K. McMahon, R. Pal, H. Puschmann, J.M. Zwier, L. Lamarque, O. Maury, C. Andraud, D. Parker, Very bright europium complexes that stain cellular mitochondria, Chem. Commun. 49 (2013) 1600–1602.

[8] P.M. Morse, Diatomic molecules according to the wave mechanics. II. Vibrational levels, Phys. Rev. 34 (1929) 57–64.

[9] (a) M.S. Child, L. Halonen, Overtone frequencies and intensities in the local mode picture, Adv. Chem. Phys. 57 (1984) 1–58. (b) B.R. Henry, Use of local modes in the description of highly vibrationally excited molecules, Acc. Chem. Res. 10 (1977) 207–213. (c) B.R. Henry, The local mode model and overtone spectra: a probe of molecular structure and conformation, Acc. Chem. Res. 20 (1987) 429–435. (d) C. Sandorfy, R. Buchet, G. Lachenal, Principles of molecular vibrations for near-infrared spectroscopy, in: Y. Ozaki, W.F. McClure, A.A. Christy (Eds.), Near-Infrared Spectroscopy in Food Science and Technology, John Wiley & Sons, Hoboken, 2007, pp. 11–46.

[10] R.L. Swofford, M.E. Long, M.S. Burberry, A.C. Albrecht, "Free" O-H overtone absorption of methanols in the visible region by thermal lensing spectroscopy, J. Chem. Phys. 66 (1977) 664–668.

[11] H. Morita, S. Nagakura, Hydrogen-bonded O-H and O-D overtone bands and potential energy curve of methanol, J. Mol. Spectrosc. 49 (1974) 401–413.

[12] C. Doffek, N. Alzakhem, C. Bischof, J. Wahsner, T. Güden-Silber, J. Lügger, C. Platas-Iglesias, M. Seitz, Understanding the quenching effects of aromatic C-H- and C-D-oscillators in near-IR lanthanoid luminescence, J. Am. Chem. Soc. 134 (2012) 16413–16423.

[13] (a) W. Groh, Overtone absorption in macromolecules for polymer optical fibers, Makromol. Chem. 189 (1988) 2861–2874. (b) Y. Koike, K. Koike, Progress in low-loss and high-bandwidth plastic optical fibers, J. Polym. Sci. B 49 (2011) 2–17. (c) K. Kuriki, Y. Koike, Y. Okamoto, Plastic optical fiber lasers and amplifiers containing lanthanide complexes, Chem. Rev. 102 (2002) 2347–2356. (d) S. Tanabe, Rare-earth-doped glasses for fiber amplifiers in broadband telecommunication, C. R. Chim. 5 (2002) 815–824.

[14] (a) L.G. Weyer, S.-C. Lo, P.R. Griffiths, Spectra-structure correlations in the near-infrared, in: J.M. Chalmers, P.R. Griffiths (Eds.), Handbook of Vibrational Spectroscopy, Wiley, London, 2006, pp. 1817–1837. (b) J. Workman Jr., L. Weyer, Practical Guide and Spectral Atlas for Interpretive Near-Infrared Spectroscopy, second ed., CRC Press, Boca Raton, 2012.

[15] (a) A. Heller, Formation of hot OH bonds in the radiationless relaxations of excited rare earth ions in aqueous solutions, J. Am. Chem. Soc. 88 (1966) 2058–2059. (b) P.K. Gallagher, Fluorescence of trivalent europium in D_2O–H_2O mixtures, J. Chem. Phys. 43 (1965) 1742–1744.

[16] (a) R. Bini, P. Foggi, R.G. Della Valle, Vibrational analysis of C-H stretching overtones in pyridine and 2,6-lutidine, J. Phys. Chem. 95 (1991) 3027–3031. (b) H.G. Kjaergaard, R.J. Proos, D.M. Turnbull, B.R. Henry, CH stretching overtone investigation of relative CH bond lengths in pyridine, J. Phys. Chem. 100 (1996) 19273–19279. (c) D.L. Snavely, J.A. Overly, V.A. Walters, Vibrational overtone spectroscopy of pyridine and related compounds, Chem. Phys. 201 (1995) 567–574.

[17] R.H. Page, R.Y. Shen, Y.T. Lee, Local modes of benzene and benzene dimer, studied by infrared-ultraviolet double resonance in a supersonic beam, J. Chem. Phys. 88 (1988) 4621–4636.

[18] H.G. Kjaergaard, D.M. Turnbull, B.R. Henry, Methyl versus aryl CH and CD stretching overtone intensities in the vapor phase spectra of toluenes, J. Phys. Chem. A 101 (1997) 2589–2596.

[19] (a) C. Sándorfy, Hydrogen bonding: how much anharmonicity? J. Mol. Struct. 790 (2006) 50–54. (b) F. Kollipost, K. Papendorf, Y.-F. Lee, Y.-P. Lee, M.A. Suhm, Alcohol dimers—how much diagonal OH anharmonicity? Phys. Chem. Chem. Phys. 16 (2014) 15948–15956.

[20] C. Carteret, Mid- and near-infrared study of hydroxyl groups at a silica surface: H-bond effect, J. Phys. Chem. C 113 (2009) 13300–13308.

[21] (a) G.W. Robinson, R.P. Frosch, Electronic excitation transfer and relaxation, J. Chem. Phys. 38 (1963) 1187–1203. (b) B.R. Henry, W. Siebrand, Radiationless transitions, in: J.B. Birks (Ed.), Organic Molecular Photophysics, vol. I, Wiley, London, 1973, pp. 153–237.

[22] (a) T.T. Basiev, Y.V. Orlovskii, K.K. Pukhov, F. Auzel, Multiphonon relaxation of the energy of electronic excitation in optical crystals doped with rare-earth ions, Laser Phys. 7 (1997) 1139–1152. (b) B.Z. Malkin, Ion-phonon interactions, in: G. Liu, B. Jacquier (Eds.), Spectroscopic Properties of Rare Earths in Optical Materials (Springer Series in Material Science), vol. 83, Springer, Berlin, 2005, pp. 130–190. (c) J.M.F. van Dijk, M.F.H. Schuurmans, On the nonradiative and radiative decay rates and a modified exponential energy gap law for 4f–4f transitions in rare-earth ions, J. Chem. Phys. 78 (1983) 5317–5323. (d) K.K. Pukhov, F. Pelle, J. Heber, Multiphonon relaxation of excited rare-earth ions in ionic matrices, Mol. Phys. 101 (2003) 1001–1006. (e) H.W. Moos, Spectroscopic relaxation processes of rare earth ions in crystals, J. Lumin. 1–2 (1970) 106–121.

[23] Selected examples: (a) J. V. Caspar, E. M. Kober, B. P. Sullivan, T. J. Meyer, Application of the energy gap law to the decay of charge-transfer excited states, J. Am. Chem. Soc. 104 (1982) 630–632.
(b) E.M. Kober, J.V. Caspar, R.S. Lumpkin, T.J. Meyer, Application of the energy gap law to excited-state decay of osmium(II)-polypyridine complexes: calculation of relative nonradiative decay rates from emission spectral profiles, J. Phys. Chem. 90 (1986) 3722–3734. (c) J.S. Wilson, N. Chawdhury, M.R.A. Al-Mandhary, M. Younus, M.S. Khan, P.R. Raithby, A. Köhler, R.H. Friend, The energy gap law for triplet states in Pt-containing conjugated polymers and monomers, J. Am. Chem. Soc. 123 (2001) 9412–9417. (d) C.E. Whittle, J.A. Weinstein, M.W. George, K.S. Schanze, Photophysics of diimine platinum(II) bis-acetylide complexes, Inorg. Chem. 40 (2001) 4053–4062.

[24] (a) C. Reinhard, H.U. Güdel, High-resolution optical spectroscopy of $Na_3[Ln(dpa)_3]\cdot 13\ H_2O$ with Ln = Er^{3+}, Tm^{3+}, Yb^{3+}, Inorg. Chem. 41 (2002) 1048–1055. (b) Y. Haas, G. Stein,

E. Würzberg, Radiationless transitions in solutions: isotope and proximity effects on Dy^{3+} by C-H and C-N bonds, J. Chem. Phys. 60 (1974) 258–263. (c) G. Stein, E. Würzberg, Energy gap law in the solvent isotope effect on radiationless transitions of rare earth ions, J. Chem. Phys. 62 (1975) 208–213. (d) G. Stein, E. Würzberg, Radiative and radiationless transitions in solutions: isotope and proximity effects on Sm^{3+} by C-H, C≡N and O-H bonds, Z. Phys. Chem. 101 (1976) 163–170. (e) A. Brandner, T. Kitahara, N. Beare, C. Lin, M.T. Berry, P.S. May, Luminescence properties and quenching mechanisms of $Ln(Tf_2N)_3$ complexes in the ionic liquid bmpyr Tf_2N, Inorg. Chem. 50 (2011) 6509–6520.

[25] C. Doffek, J. Wahsner, E. Kreidt, M. Seitz, Breakdown of the energy gap law in molecular lanthanoid luminescence: the smallest energy gap is not universally relevant for nonradiative deactivation, Inorg. Chem. 53 (2014) 3263–3265.

[26] J. Scholten, G.A. Rosser, J. Wahsner, N. Alzakhem, C. Bischof, F. Stog, A. Beeby, M. Seitz, Anomalous reversal of C-H and C-D quenching efficiencies in luminescent praseodymium cryptates, J. Am. Chem. Soc. 134 (2012) 13915–13917.

[27] (a) E.B. Sveshnikova, V.L. Ermolaev, Inductive resonant theory of nonradiative transitions in lanthanide and transition metal ions, Opt. Spectrosc. 111 (2011) 34–50. (b) V.L. Ermolaev, E.B. Sveshnikova, E.N. Bodunov, Inductive-resonant mechanism of nonradiative transitions in ions and molecules in condensed phase, Phys. Usp. 39 (1996) 261–282. (c) V.L. Ermolaev, E.B. Sveshnikova, The application of luminescence-kinetic methods in the study of the formation of lanthanide ion complexes in solution, Russ. Chem. Rev. 63 (1994) 905–922.

[28] T. Förster, Zwischenmolekulare Energiewanderung und Fluoreszenz, Ann. Phys. 437 (1948) 55–75.

[29] (a) F. Quochi, R. Orrù, F. Cordella, A. Mura, G. Bongiovanni, F. Artizzu, P. Deplano, M.L. Mercuri, L. Pilia, A. Serpe, Near infrared light emission quenching in organolanthanide complexes, J. Appl. Phys. 99 (2006) 053520. (b) F. Artizzu, M.L. Mercuri, A. Serpe, P. Deplano, NIR-emissive erbium–quinolinolate complexes, Coord. Chem. Rev. 255 (2011) 2514–2529.

[30] (a) A. Monguzzi, A. Milani, L. Lodi, M.I. Trioni, R. Tubino, C. Castiglioni, Vibrational overtones quenching of near infrared emission in Er^{3+} complexes, New J. Chem. 33 (2009) 1542–1548. (b) A. Monguzzi, M.I. Trioni, R. Tubino, A. Milani, L. Brambila, C. Castiglioni, Anharmonic overtones quenching in Er^{3+} complexes, Synth. Met. 159 (2009) 2410–2412. (c) A. Monguzzi, A. Milani, A. Mech, L. Brambilla, R. Tubino, C. Castellano, F. Demartin, F. Meinardi, C. Castiglioni, Predictive modeling of the vibrational quenching in emitting lanthanides complexes, Synth. Met. 161 (2012) 2693–2699.

[31] (a) R.H.C. Tan, M. Motevalli, I. Abrahams, P.B. Wyatt, W.P. Gillin, Quenching of IR luminescence of erbium, neodymium, and ytterbium β-diketonate complexes by ligand C-H and C-D bonds, J. Phys. Chem. B 110 (2006) 24476–24479. (b) L. Winkless, R.H.C. Tan, Y. Zheng, M. Motevalli, P.B. Wyatt, W.P. Gillin, Quenching of Er(III) luminescence by ligand C–H vibrations: implications for the use of erbium complexes in telecommunications, Appl. Phys. Lett. 89 (2006) 111115.

[32] S. DeMille, R. H. deLaat, R. M. Tanner, R. L. Brooks, N. P. C. Westwood, Comparison of CRDS to ICL-PAS and phase-shift CRDS spectroscopies for the absolute intensities of C-H ($\Delta v_{CH} = 6$) overtone absorptions, Chem. Phys. Lett. 366 (2002) 383–389.

[33] C. Wang, S. Otto, M. Dorn, E. Kreidt, J. Lebon, L. Sršan, P. Di Martino-Fumo, M. Gerhards, U. Resch-Genger, M. Seitz, K. Heinze, Deuterated molecular ruby with record luminescence quantum yield, Angew. Chem. Int. Ed. 57 (2018) 1112–1116.

[34] M.D. Galanin, I.M. Frank, Quenching of fluorescence by a light-absorbing medium, Zh. Eksp. Teor. Fiz. 21 (1951) 114–120.

[35] W.R. Browne, J.G. Vos, The effect of deuteriation on the emission lifetime of inorganic compounds, Coord. Chem. Rev. 219–221 (2001) 761–787.
[36] I. Hernández, W.P. Gillin, Organic chromophores-based sensitization of NIR-emitting lanthanides: toward highly efficient halogenated environments, in: J.-C.G. Bünzli, V.K. Pecharsky (Eds.), Handbook on the Physics and Chemistry of Rare Earths, vol. 47, Elsevier, Amsterdam, 2015, pp. 1–100.
[37] (a) S. Comby, J.-C.G. Bünzli, Lanthanide near-infrared luminescence in molecular probes and devices, in: K.A. Gschneidner Jr., J.-C.G. Bünzli, V.K. Pecharsky (Eds.), Handbook on the Physics and Chemistry of Rare Earths, vol. 37, Elsevier, Amsterdam, 2007, pp. 217–470. (b) J.-C.G. Bünzli, S.V. Eliseeva, Lanthanide NIR luminescence for telecommunications, bioanalyses and solar energy conversion, J. Rare Earths 28 (2010) 824–842.
[38] Y. Hasegawa, Y. Kimura, K. Murakoshi, Y. Wada, J.-H. Kim, N. Nakashima, T. Yamanaka, S. Yanagida, Enhanced emission of deuterated Tris(hexafluoroacetylacetonato)neodymium (III) complex in solution by suppression of radiationless transition via vibrational excitation, J. Phys. Chem. 100 (1996) 10201–10205.
[39] Y. Hasegawa, T. Ohkubo, K. Sogabe, Y. Kawamura, Y. Wada, N. Nakashima, S. Yanagida, Luminescence of novel neodymium sulfonylaminate complexes in organic media, Angew. Chem. Int. Ed. 39 (2000) 357–360.
[40] M. Iwamuro, Y. Wada, T. Kitamura, N. Nakashima, S. Yanagida, Photosensitized luminescence of novel β-diketonato Nd(III) complexes in solution, Phys. Chem. Chem. Phys. 2 (2000) 2291–2296.
[41] W. Wu, X. Zhang, A.Y. Kornienko, G.A. Kumar, D. Yu, T.J. Emge, R.E. Riman, J.G. Brennan, Efficient NIR emission from Nd, Er, and Tm complexes with fluorinated selenolate ligands, Inorg. Chem. 57 (2018) 1912–1918.
[42] (a) P.B. Glover, A.P. Bassett, P. Nockemann, B.M. Kariuki, R. Van Deun, Z. Pikramenou, Fully fluorinated imidodiphosphinate shells for visible- and NIR-emitting lanthanides: hitherto unexpected effects of sensitizer fluorination on lanthanide emission properties, Chemistry 13 (2007) 6308–6320. (b) G. Mancino, A.J. Ferguson, A. Beeby, N.J. Long, T.S. Jones, Dramatic increases in the lifetime of the Er^{3+} ion in a molecular complex using a perfluorinated imidodiphosphinate sensitizing ligand, J. Am. Chem. Soc. 127 (2005) 524–525.
[43] J. Wahsner, M. Seitz, Perdeuterated 2,2'-bipyridine-6,6′-dicarboxylate: an extremely efficient sensitizer for thulium luminescence in solution, Inorg. Chem. 52 (2013) 13301–13303.
[44] I. Hernández, Y.-X. Zheng, M. Motevalli, R.H.C. Tan, W.P. Gillin, P.B. Wyatt, Efficient sensitized emission in Yb(III) pentachlorotropolonate complexes, Chem. Commun. 49 (2013) 1933–1935.
[45] J.-Y. Hu, Y. Ning, Y.-S. Meng, J. Zhang, Z.-Y. Wu, S. Gao, J.-L. Zhang, Highly near-IR emissive ytterbium(III) complexes with unprecedented quantum yields, Chem. Sci. 8 (2017) 2702–2709.
[46] C. Doffek, M. Seitz, The radiative lifetime in near-IR luminescent ytterbium cryptates: the key to extremely high quantum yields, Angew. Chem. Int. Ed. 54 (2015) 9719–9721.
[47] (a) J.L. Kropp, M.W. Windsor, Enhancement of fluorescence yield of rare-earth ions by heavy water, J. Chem. Phys. 39 (1963) 2769–2770. (b) J.L. Kropp, M.W. Windsor, Luminescence and energy transfer in solutions of rare-earth complexes. I. Enhancement of fluorescence by deuterium substitution, J. Chem. Phys. 42 (1965) 1599–1608.
[48] (a) R.M. Supkowski, W.D.W. Horrocks Jr., On the determination of the number of water molecules, q, coordinated to europium(III) ions in solution from luminescence decay lifetimes, Inorg. Chim. Acta 340 (2002) 44–48. (b) R.M. Supkowski, W.D.W. Horrocks Jr.,

Displacement of inner-sphere water molecules from Eu^{3+} analogues of Gd^{3+} MRI contrast agents by carbonate and phosphate anions: dissociation constants from luminescence data in the rapid-exchange limit, Inorg. Chem. 38 (1999) 5616–5619.

[49] (a) A. Beeby, I.M. Clarkson, R.S. Dickins, S. Faulkner, D. Parker, L. Royle, A.S. de Sousa, J.A.G. Williams, M. Woods, Non-radiative deactivation of the excited states of europium, terbium and ytterbium complexes by proximate energy-matched OH, NH and CH oscillators: an improved luminescence method for establishing solution hydration states, J. Chem. Soc., Perkin Trans. 2 (1999) 493–503. (b) R.S. Dickins, D. Parker, A.S. de Sousa, J.A.G. Williams, Closely diffusing O-H, amide N-H and methylene C-H oscillators quench the excited state of europium complexes in solution, Chem. Commun. (1996) 697–698.

[50] A. Beeby, B.P. Burton-Pye, S. Faulkner, G.R. Motson, J.C. Jeffery, J.A. McCleverty, M.D. Ward, Synthesis and near-IR luminescence properties of neodymium(III) and ytterbium(III) complexes with poly(pyrazolyl)borate ligands, J. Chem. Soc. Dalton Trans. (2002) 1923–1928.

[51] T. Kimura, Y. Kato, Luminescence study on determination of the inner-sphere hydration number of Am(III) and Nd(III), J. Alloys Compd. 271–273 (1998) 867–871.

[52] S. Faulkner, A. Beeby, M.-C. Carrié, A. Dadabhoy, A.M. Kenwright, P.G. Sammes, Time-resolved near-IR luminescence from ytterbium and neodymium complexes of the Lehn cryptand, Inorg. Chem. Commun. 4 (2001) 187–190.

[53] T. Kimura, Y. Kato, Luminescence study on hydration states of lanthanide(III) polyaminocarboxylate complexes in aqueous solution, J. Alloys Compd. 275–277 (1998) 806–810.

[54] M.P. Oude Wolbers, F.C.J.M. van Veggel, B.H.M. Snellink-Ruël, J.W. Hofstraat, F.A.J. Geurts, D.N. Reinhoudt, Novel preorganized hemispherands to encapsulate rare earth ions: shielding and ligand deuteration for prolonged lifetimes of excited Eu^{3+} ions, J. Am. Chem. Soc. 119 (1997) 138–144.

[55] K. Nakamura, Y. Hasegawa, H. Kawai, N. Yasuda, Y. Tsukahara, Y. Wada, Improvement of lasing properties of europium (III) complexes by increase of emission quantum yield, Thin Solid Films 516 (2008) 2376–2381.

[56] I. Hemmilä, V.-M. Mukkala, H. Takalo, Effect of C-H bonds on the quenching of luminescent lanthanide chelates, J. Fluoresc. 5 (1995) 159–163.

[57] T.C. Schwendemann, P.S. May, M.T. Berry, Y. Hou, C.Y. Meyers, Effect of ligand deuteration on the decay of $Eu^{3+}(^5D_0)$ in Tris(2,2,6,6-tetramethyl-3,5-heptanedionato)europium(III), J. Phys. Chem. A 102 (1998) 8690–8694.

[58] S. Ogata, A. Ishii, C.L. Lu, T. Kondo, N. Yajima, M. Hasegawa, Polymorphism-based luminescence of lanthanide complexes with a deuterated 1,10-phenanthroline, J. Photochem. Photobiol. A 334 (2017) 55–60.

[59] M.P. Oude Wolbers, F.C.J.M. van Veggel, B.H.M. Snellink-Ruël, J.W. Hofstraat, F.A.J. Geurts, D.N. Reinhoudt, Photophysical studies of *m*-terphenyl-sensitized visible and near-infrared emission from organic 1:1 lanthanide ion complexes in methanol solutions, J. Chem. Soc., Perkin Trans. 2 (1998) 2141–2150.

[60] G.M. Davies, R.J. Aarons, G.R. Motson, J.C. Jeffery, H. Adams, S. Faulkner, M.D. Ward, Structural and near-IR photophysical studies on ternary lanthanide complexes containing poly(pyrazolyl)borate and 1,3-diketonate ligands, Dalton Trans. (2004) 1136–1144.

[61] O.A. Blackburn, M. Tropiano, T.J. Sørensen, J. Thom, A. Beeby, L.M. Bushby, D. Parker, L.S. Natrajan, S. Faulkner, Luminescence and upconversion from thulium(III) species in solution, Phys. Chem. Chem. Phys. 14 (2012) 13378–13384.

[62] J. Wahsner, M. Seitz, Non-radiative deactivation of lanthanoid excited states by inner-sphere carboxylates, Inorg. Chem. 54 (2015) 10841–10848.

[63] S. Yanagida, Y. Hasegawa, K. Murakoshi, Y. Wada, N. Nakashima, T. Yamanaka, Strategies for enhancing photoluminescence of Nd^{3+} in liquid media, Coord. Chem. Rev. 171 (1998) 461–480.

[64] E.M. Goryaeva, A.V. Shablya, A.P. Serov, Luminescence and stimulated emission for solutions of complexes of neodymium nitrate with perdeuterotributyl phosphate, J. Appl. Spectrosc. 28 (1978) 55–59.

[65] C. Bischof, J. Wahsner, J. Scholten, S. Trosien, M. Seitz, Quantification of C-H quenching in near-IR luminescent ytterbium and neodymium cryptates, J. Am. Chem. Soc. 132 (2010) 14334–14335.

[66] C. Doffek, N. Alzakhem, M. Molon, M. Seitz, Rigid, perdeuterated lanthanoid cryptates: extraordinarily bright near-IR luminophores, Inorg. Chem. 51 (2012) 4539–4545.

[67] G.A. Hebbink, D.N. Reinhoudt, F.C.J.M. van Veggel, Increased luminescent lifetimes of Ln^{3+} complexes emitting in the near-infrared as a result of deuteration, Eur. J. Org. Chem. (2001) 4101–4106.

[68] H.Q. Ye, Z. Li, Y. Peng, C.C. Wang, T.Y. Li, Y.X. Zheng, A. Sapelkin, G. Adamopoulos, I. Hernández, P.B. Wyatt, W.P. Gillin, Organo-erbium systems for optical amplification at telecommunications wavelengths, Nat. Mater. 13 (2014) 382–386 and references cited therein.

[69] M.P. Tsvirko, S.B. Meshkova, V.Y. Venchikov, Z.M. Topilova, D.V. Bol'shoi, Determination of contributions of various molecular groups to nonradiative deactivation of electronic excitation energy in β-diketonate complexes of ytterbium(III), Opt. Spectrosc. 90 (2001) 669–673.

[70] N. Souri, P. Tian, C. Platas-Iglesias, K.-L. Wong, A. Nonat, L.J. Charbonnière, Upconverted photosensitization of Tb visible emission by NIR Yb excitation in discrete supramolecular heteropolynuclear complexes, J. Am. Chem. Soc. 139 (2017) 1456–1459.

[71] Y. Ning, Y.-W. Liu, Y.-S. Meng, J.-L. Zhang, Design of near-infrared luminescent lanthanide complexes sensitive to environmental stimulus through rationally tuning the secondary coordination sphere, Inorg. Chem. 57 (2018) 1332–1341.

10 Bibliography

[1] R. E. Connick, *J. Chem. Soc.* **1949**, 235–241.

[2] A. de Bettencourt-Dias in *The Rare Earth Elements: Fundamentals and Applications* (Ed.: D. A. Atwood), John Wiley & Sons, Ltd, Chichester, **2012**, pp. 27–34.

[3] L. Sorace, D. Gatteschi in *Lanthanides and Actinides in Molecular Magnetism*, Wiley-VCH Verlag GmbH & Co. KGaA, Weinheim, **2015**, pp. 1–26.

[4] B. G. Wybourne, *Spectroscopic Properties of Rare Earths*, John Wiley & Sons, New York, **1965**.

[5] J. Andres, A.-S. Chauvin in *The Rare Earth Elements: Fundamentals and Applications* (Ed.: D. Atwood), John Wiley & Sons, Chichester, **2013**, pp. 111–134.

[6] W. T. Carnall, P. R. Fields, K. Rajnak, *J. Chem. Phys.* **1968**, *49*, 4450–4455.

[7] W. T. Carnall, P. R. Fields, K. Rajnak, *J. Chem. Phys.* **1968**, *49*, 4447–4449.

[8] W. T. Carnall, P. R. Fields, K. Rajnak, *J. Chem. Phys.* **1968**, *49*, 4443–4446.

[9] W. T. Carnall, P. R. Fields, K. Rajnak, *J. Chem. Phys.* **1968**, *49*, 4424–4442.

[10] W. T. Carnall, G. L. Goodman, K. Rajnak, R. S. Rana, *J. Chem. Phys.* **1989**, *90*, 3443–3457.

[11] E. Kreidt, C. Kruck, M. Seitz in *Handbook on the Physics and Chemistry of Rare Earths*, Elsevier B.V., Amsterdam, 1st ed., **2018**, pp. 35–79.

[12] J.-C. G. Bünzli, C. Piguet, *Chem. Soc. Rev.* **2005**, *34*, 1048–1077.

[13] J.-C. G. Bünzli, *Chem. Lett.* **2009**, *38*, 104–109.

[14] O. A. Blackburn, A. M. Kenwright, P. D. Beer, S. Faulkner, *Dalton Trans.* **2015**, *44*, 19509–19517.

[15] O. A. Blackburn, J. D. Routledge, L. B. Jennings, N. H. Rees, A. M. Kenwright, P. D. Beer, S. Faulkner, *Dalton Trans.* **2016**, *45*, 3070–3077.

[16] O. A. Blackburn, A. M. Kenwright, A. R. Jupp, J. M. Goicoechea, P. D. Beer, S. Faulkner, *Chem. Eur. J.* **2016**, *22*, 8929–8936.

[17] J.-C. G. Bünzli, *Chem. Rev.* **2010**, *110*, 2729–2755.

[18] J. C. G. Bünzli, *J. Lumin.* **2016**, *170*, 866–878.

[19] J.-C. G. Bünzli, A.-S. Chauvin, H. K. Kim, E. Deiters, S. V. Eliseeva, *Coord. Chem. Rev.* **2010**, *254*, 2623–2633.

[20] J. C. G. Bünzli, *Coord. Chem. Rev.* **2015**, *293-294*, 19–47.

[21] E. B. Sveshnikova, V. L. Ermolaev, *Opt. Spectrosc.* **2011**, *111*, 34–50.

[22] J. L. Kropp, M. W. Windsor, *J. Chem. Phys.* **1963**, *39*, 2769–2770.

[23] J. L. Kropp, M. W. Windsor, *J. Chem. Phys.* **1965**, *42*, 1599–1608.

[24] W. D. W. Horrocks, D. R. Sudnick, *J. Am. Chem. Soc.* **1979**, *101*, 334–340.

[25] R. M. Supkowski, W. D. Horrocks, *Inorg. Chim. Acta* **2002**, *340*, 44–48.

[26] A. Beeby, B. P. Burton-Pye, S. Faulkner, G. R. Motson, J. C. Jeffery, J. A. McCleverty, M. D. Ward, *J. Chem. Soc. Dalton Trans.* **2002**, 1923–1928.

[27] A. Beeby, I. M. Clarkson, R. S. Dickins, S. Faulkner, D. Parker, L. Royle, A. S. de Sousa, J. A. G. Williams, M. Woods, *J. Chem. Soc. Perkin Trans. 2* **1999**, *2*, 493–504.

[28] A. Nonat, C. F. Chan, T. Liu, C. Platas-Iglesias, Z. Liu, W.-T. Wong, W.-K. Wong, K.-L. Wong, L. J. Charbonnière, *Nat. Commun.* **2016**, *7*, 11978–11985.

[29] L. Aboshyan-Sorgho, C. Besnard, P. Pattison, K. R. Kittilstved, A. Aebischer, J.-C. G. Bünzli, A. Hauser, C. Piguet, *Angew. Chem. Int. Ed.* **2011**, *50*, 4108–4112.

[30] Y. Suffren, B. Golesorkhi, D. Zare, L. Guénée, H. Nozary, S. V. Eliseeva, S. Petoud, A. Hauser, C. Piguet, *Inorg. Chem.* **2016**, *55*, 9964–9972.

[31] B.-W. Wang, S. Gao in *The Rare Earth Elements: Fundamentals and Applications* (Ed.: D. Atwood), John Wiley & Sons, Chichester, **2013**, pp. 153–160.

[32] S. T. Liddle, J. van Slageren, *Chem. Soc. Rev.* **2015**, *44*, 6655–69.

[33] C. Doffek, PhD thesis, Ruhr-Universität Bochum, **2015**.

[34] K. Poeppelmeier, I. Chemistry, V. Oxford, C. Sciences, R. Korea in *Comprehensive Inorganic Chemistry II*, *Vol. 8*, Elsevier Ltd., Amsterdam, **2013**, pp. 339–398.

[35] P. Caravan, J. J. Ellison, T. J. McMurry, R. B. Lauffer, *Chem. Rev.* **1999**, *99*, 2293–2352.

[36] M. Bottrill, L. Kwok, N. J. Long, *Chem. Soc. Rev.* **2006**, *35*, 557–571.

[37] R. Sessoli, A. K. Powell, *Coord. Chem. Rev.* **2009**, *253*, 2328–2341.

[38] D. N. Woodruff, R. E. P. Winpenny, R. A. Layfield, *Chem. Rev.* **2013**, *113*, 5110–5148.

[39] G. Otting, *Annu. Rev. Biophys.* **2010**, *39*, 387–405.

[40] K. N. Allen, B. Imperiali, *Curr. Opin. Chem. Biol.* **2010**, *14*, 247–254.

[41] I. Bertini, C. Luchinat, G. Parigi, R. Pierattelli, *ChemBioChem* **2005**, *6*, 1536–1549.

[42] W.-M. Liu, M. Overhand, M. Ubbink, *Coord. Chem. Rev.* **2014**, *273-274*, 2–12.

[43] K. C. Pilla, G. Otting, T. Humber in *Bioinformatics: Volume II. Structure, Function, and Applications* (Ed.: J. M. Keith), Humana Press, New York, **2017**, pp. 3–22.

[44] J. Olsen, *Int. J. Quantum Chem.* **2011**, *111*, 3267–3272.

[45] K. Bernot, J. Luzon, L. Bogani, M. Etienne, C. Sangregorio, M. Shanmugam, A. Caneschi, R. Sessoli, D. Gatteschi, *J. Am. Chem. Soc.* **2009**, *131*, 5573–5579.

[46] L. Ungur, L. F. Chibotaru in *Lanthanides and Actinides in Molecular Magnetism*, Wiley-VCH Verlag GmbH & Co. KGaA, Weinheim, **2015**, pp. 153–184.

[47] J. Rinehart, J. Long, *Chem. Sci.* **2011**, *2*, 2078–2085.

[48] C. A. P. Goodwin, F. Ortu, D. Reta, N. F. Chilton, D. P. Mills, *Nature* **2017**, *548*, 439–442.

[49] N. F. Chilton, D. Collison, E. J. McInnes, R. E. Winpenny, A. Soncini, *Nat. Commun.* **2013**, *4*, 1–7.

[50] P. H. J. Keizers, M. Ubbink, *Prog. Nucl. Magn. Reson. Spectrosc.* **2011**, *58*, 88–96.

[51] K. Chen, N. Tjandra, *NMR Proteins Small Biomol.* **2012**, 47–68.

[52] X.-C. Su, G. Otting, *J. Biomol. NMR* **2010**, *46*, 101–12.

[53] C. C. Hinckley, *J. Am. Chem. Soc.* **1969**, *91*, 5160–5162.

[54] H. Friebolin, *Basic One- and Two-Dimensional Spectroscopy*, Wiley-VCH Verlag GmbH & Co. KGaA, Weinheim, 5th ed., **2011**.

[55] H. M. McConnell, *J. Chem. Phys.* **1957**, *27*, 226–229.

[56] I. Bertini, C. Luchinat, G. Parigi, *Prog. Nucl. Magn. Reson. Spectrosc.* **2002**, *40*, 249–273.

[57] B. Bleaney, *J. Magn. Reson.* **1972**, *8*, 91–100.

[58] A. M. Funk, K.-L. N. A Finney, P. Harvey, A. M. Kenwright, E. R. Neil, N. J. Rogers, P. Kanthi Senanayake, D. Parker, *Chem. Sci.* **2015**, *6*, 1655–1662.

[59] O. A. Blackburn, R. M. Edkins, S. Faulkner, A. M. Kenwright, D. Parker, N. J. Rogers, S. Shuvaev, *Dalton Trans.* **2016**, *45*, 6782–6800.

[60] E. A. Suturina, K. Mason, C. F. G. C. Geraldes, I. Kuprov, D. Parker, *Angew. Chem. Int. Ed.* **2017**, *56*, 12215–12218.

[61] V. S. Mironov, Y. G. Galyametdinov, A. Ceulemans, C. Görller-Walrand, K. Binnemans, *J. Chem. Phys.* **2002**, *116*, 4673–4685.

[62] V. S. Mironov, Y. G. Galyametdinov, A. Ceulemans, C. Görller-Walrand, K. Binnemans, *Chem. Phys. Lett.* **2001**, *345*, 132–140.

[63] L. Lee, B. D. Sykes, *Biochemistry* **1983**, *22*, 4366–4373.

[64] G. Pintacuda, M. John, X.-C. Su, G. Otting, *Acc. Chem. Res.* **2007**, *40*, 206–212.

[65] M. C. Mahawaththa, B. J. Pearce, M. Szabo, B. Graham, C. D. Klein, C. Nitsche, G. Otting, *Antiviral Res.* **2017**, *142*, 141–147.

[66] N. Ishikawa, T. Iino, Y. Kaizu, *J. Phys. Chem. A* **2002**, *106*, 9543–9550.

[67] N. Ishikawa, M. Sugita, T. Okubo, N. Tanaka, T. Iino, Y. Kaizu, *Inorg. Chem.* **2003**, *42*, 2440–2446.

[68] M. Damjanovic, K. Katoh, M. Yamashita, M. Enders, *J. Am. Chem. Soc.* **2013**, *135*, 14349–14358.

[69] M. Hiller, S. Krieg, N. Ishikawa, M. Enders, *Inorg. Chem.* **2017**, *56*, 15285–15294.

[70] J. C. G. Bünzli, *J. Coord. Chem.* **2014**, *67*, 3706–3733.

[71] N. Sabbatini, M. T. Indelli, M. T. Gandolfi, V. Balzani, *J. Phys. Chem.* **1982**, *86*, 3585–3591.

[72] A. K. R. Junker, L. R. Hill, A. L. Thompson, S. Faulkner, T. J. Sørensen, *Dalton Trans.* **2018**, *47*, 4794–4803.

[73] D. L. Dexter, *J. Chem. Phys.* **1953**, *21*, 836–850.

[74] T. Forster, *Naturwissenschaften* **1946**, *33*, 166–175.

[75] J. C. G. Bünzli, S. V. Eliseeva, *J. Rare Earths* **2010**, *28*, 824–842.

[76] A. Monguzzi, A. Milani, A. Mech, L. Brambilla, R. Tubino, C. Castellano, F. Demartin, F. Meinardi, C. Castiglioni, *Synth. Met.* **2012**, *161*, 2693–2699.

[77] L. Winkless, R. H. C. Tan, Y. Zheng, M. Motevalli, P. B. Wyatt, W. P. Gillin, *Appl. Phys. Lett.* **2006**, *89*, 87–90.

[78] N. Sakagami, Y. Yamada, T. Konno, K.-i. Okamoto, *Inorg. Chim. Acta* **1999**, *288*, 7–16.

[79] C. Platas-Iglesias, D. M. Corsi, V. Elst, R. N. Muller, D. Imbert, J.-C. G. Bünzli, É. Tóth, J. A. Peters, *Dalton Trans.* **2003**, 727–737.

[80] R. J. Holmberg, I. Korobkov, M. Murugesu, *RSC Adv.* **2016**, *6*, 72510–72518.

[81] S. Aime, M. Botta, *Inorg. Chim. Acta* **1990**, *177*, 101–105.

[82] A. P. Samuel, E. G. Moore, M. Melchior, J. Xu, K. N. Raymond, *Inorg. Chem.* **2008**, *47*, 7535–7544.

[83] M. Seitz, K. Do, A. J. Ingram, E. G. Moore, G. Muller, K. N. Raymond, *Inorg. Chem.* **2009**, *48*, 8469–8479.

[84] E. G. Moore, A. P. Samuel, K. N. Raymond, *Acc. Chem. Res.* **2009**, *42*, 542–552.

[85] E. G. Moore, C. J. Jocher, J. Xu, E. J. Werner, K. N. Raymond, *Inorg. Chem.* **2007**, *46*, 5468–5470.

[86] K. Binnemans in *Handbook on the Physics and Chemistry of Rare Earths*, *Vol. 35*, Elsevier, Amsterdam, **2005**, pp. 107–272.

[87] K. Wang, *Rare Earth Coord. Chem. Fundam. Appl.* **2010**, 41–89.

[88] M. L. Bhaumik, *J. Inorg. Nucl. Chem.* **1965**, *27*, 243–244.

[89] P. A. Brayshaw, J. C. Bünzli, P. Froidevaux, J. M. Harrowfield, Y. Kim, A. N. Sobolev, *Inorg. Chem.* **1995**, *34*, 2068–2076.

[90] N. Ouali, B. Bocquet, S. Rigault, P. Y. Morgantini, J. Weber, C. Piguet, *Inorg. Chem.* **2002**, *41*, 1436–1445.

[91] X. C. Su, H. Liang, K. V. Loscha, G. Otting, *J. Am. Chem. Soc.* **2009**, *131*, 10352–10353.

[92] A. Chauvin, F. Gumy, D. Imbert, J. G. Bünzli, *Spectrosc. Lett.* **2004**, *37*, 517–532.

[93] V.-M. Mukkala, C. Sund, M. Kwiatkowski, P. Pasanen, M. Högberg, J. Kankare, H. Takalo, *Helv. Chim. Acta* **1992**, *75*, 1621–1632.

[94] H.-R. Mürner, E. Chassat, R. P. Thummel, J.-C. G. Bünzli, *J. Chem. Soc. Dalton Trans.* **2000**, 2809–2816.

[95] C. Galaup, J. M. Couchet, S. Bedel, P. Tisnès, C. Picard, *J. Org. Chem.* **2005**, *70*, 2274–2284.

[96] H. Hakala, P. Liitti, J. Peuralahti, J. Karvinen, V. M. Mukkala, J. Hovinen, *J. Lumin.* **2005**, *113*, 17–26.

[97] M. J. Remuiñán, H. Román, M. T. Alonso, J. C. Rodríguez-Ubis, *J. Chem. Soc. Perkin Trans. 2* **1993**, 1099–1102.

[98] E. Brunet, O. Juanes, R. Sedano, J.-C. Rodríguez-Ubis, *Photochem. Photobiol. Sci.* **2002**, *1*, 613–618.

[99] S. Comby, J. G. Bünzli in *Handbook on the Physics and Chemistry of Rare Earths, Vol. 37* (Eds.: K. A. Gschneidner, J. G. Bünzli, V. K. Pecharsky), Elsevier B.V., **2007**, pp. 217–470.

[100] V.-M. Mukkala, M. Kwiatkowski, J. Kankare, H. Takalo, *Helv. Chim. Acta* **1993**, *76*, 893–899.

[101] L. N. Puntus, K. A. Lyssenko, I. S. Pekareva, J. C. G. Bünzli, *J. Phys. Chem. B* **2009**, *113*, 9265–9277.

[102] J.-C. G. Bünzli, L. J. Charbonnière, R. F. Ziessel, *J. Chem. Soc. Dalton Trans.* **2000**, 1917–1923.

[103] J. Wahsner, M. Seitz, *Inorg. Chem.* **2013**, *52*, 13301–13303.

[104] N. Weibel, L. J. Charbonnière, M. Guardigli, A. Roda, R. Ziessel, *J. Am. Chem. Soc.* **2004**, *126*, 4888–4896.

[105] F. A. Hart, F. P. Laming, *J. Inorg. Nucl. Chem.* **1964**, *26*, 579–585.

[106] L. N. Puntus, K. A. Lyssenko, M. Y. Antipin, J.-C. G. Bünzli, *Inorg. Chem.* **2008**, *47*, 11095–11107.

[107] L. R. Melby, N. J. Rose, E. Abramson, J. C. Caris, *J. Am. Chem. Soc.* **1964**, *86*, 5117–5125.

[108] T. Uchida, K. Nozaki, M. Iwamura, *Chem. Asian J.* **2016**, *11*, 2415–2422.

[109] R. Ziessel, N. Weibel, L. Charbonnière, *Synthesis* **2006**, *2006*, 3127–3133.

[110] C. W. Tang, S. A. Vanslyke, *Appl. Phys. Lett.* **1987**, *51*, 913–915.

[111] H. Xu, R. Chen, Q. Sun, W. Lai, Q. Su, W. Huang, X. Liu, *Chem. Soc. Rev.* **2014**, *43*, 3259–3302.

[112] R. Van Deun, P. Fias, K. Driesen, K. Binnemans, C. Görller-Walrand, *Phys. Chem. Chem. Phys.* **2003**, *5*, 2754–2757.

[113] D. Imbert, S. Comby, A.-S. Chauvin, J.-C. G. Bünzli, *Chem. Commun.* **2005**, 1432–1434.

[114] M. Albrecht, O. Osetska, R. Fröhlich, J.-C. G. Bünzli, A. Aebischer, F. Gumy, J. Hamacek, *J. Am. Chem. Soc.* **2007**, *129*, 14178–14179.

[115] M. Albrecht, O. Osetska, J. Klankermayer, R. Fröhlich, F. Gumy, J.-C. G. Bünzli, *Chem. Commun.* **2007**, 1834–1836.

[116] M. F. Loncin, J. F. Desreux, E. Merciny, *Inorg. Chem.* **1986**, *25*, 2646–2648.

[117] W. P. Cacheris, S. K. Nickle, A. D. Sherry, *Inorg. Chem.* **1987**, *26*, 958–960.

[118] X. Wang, T. Jin, V. Comblin, A. Lopez-Mut, E. Merciny, J. F. Desreux, *Inorg. Chem.* **1992**, *31*, 1095–1099.

[119] A. C. L. Opina, M. Strickland, Y.-S. Lee, N. Tjandra, R. A. Byrd, R. E. Swenson, O. Vasalatiy, *Dalton Trans.* **2016**, *45*, 4673–4687.

[120] M. Meyer, V. Dahaoui-Gindrey, C. Lecomte, R. Guilard, H. Poincare, I. Nancy, *Coord. Chem. Rev.* **1998**, *180*, 1313–1405.

[121] U. Cosentino, A. Villa, D. Pitea, G. Moro, V. Barone, A. Maiocchi, *J. Am. Chem. Soc.* **2002**, *124*, 4901–4909.

[122] B. Alpha, J.-M. Lehn, G. Mathis, *Angew. Chemie* **1987**, *99*, 259–261.

[123] B. Dietrich, J.-M. Lehn, J. Sauvage, *Tetrahedron Lett.* **1969**, *10*, 2889–2892.

[124] J.-M. Lehn, *Acc. Chem. Res.* **1978**, *11*, 49–57.

[125] O. A. Gansow, A. R. Kausar, K. M. Triplett, M. J. Weaver, E. L. Yee, *J. Am. Chem. Soc.* **1977**, *99*, 7087–7089.

[126] N. Sabbatini, S. Dellonte, M. Ciano, A. Bonazzi, V. Balzani, *Chem. Phys. Lett.* **1984**, *107*, 212–216.

[127] J.-C. Rodriguz-Ubis, B. Alpha, D. Plancherel, J.-M. Lehn, *Helv. Chim. Acta* **1984**, *67*, 2264–2269.

[128] B. Alpha, R. Ballardini, V. Balzani, J.-M. Lehn, S. Perathoner, N. Sabbatini, *Photochem. Photobiol.* **1990**, *52*, 299–306.

[129] N. Sabbatini, M. Guardigli, J.-M. Lehn, *Coord. Chem. Rev.* **1993**, *123*, 201–228.

[130] I. Bkouche-Waksman, J. Guilhem, C. Pascard, B. Alpha, R. Deschenaux, J.-M. Lehn, *Helv. Chim. Acta* **1991**, *74*, 1163–1170.

[131] J.-M. Lehn, C. O. Roth, *Helv. Chim. Acta* **1991**, *74*, 572–578.

[132] L. Prodi, M. Maestri, V. Balzani, J.-M. Lehn, C. Roth, *Chem. Phys. Lett.* **1991**, *180*, 45–50.

[133] C. Doffek, N. Alzakhem, M. Molon, M. Seitz, *Inorg. Chem.* **2012**, *51*, 4539–4545.

[134] T. Güden-Silber, C. Doffek, C. Platas-Iglesias, M. Seitz, *Dalton Trans.* **2014**, *43*, 4238–4241.

[135] C. Doffek, N. Alzakhem, C. Bischof, J. Wahsner, T. Güden-Silber, J. Lügger, C. Platas-iglesias, M. Seitz, *J. Am. Chem. Soc.* **2012**, *134*, 16413–16423.

[136] R. Englman, J. Jortner, *Mol. Phys.* **1970**, *18*, 145–164.

[137] T. Basiev, V. O. Yu, K. K. Pukhov, F. Auzel, *Laser Phys.* **1997**, *7*, 1139–1152.

[138] A. Brandner, T. Kitahara, N. Beare, C. Lin, M. T. Berry, P. S. May, *Inorg. Chem.* **2011**, *50*, 6509–6520.

[139] C. Doffek, J. Wahsner, E. Kreidt, M. Seitz, *Inorg. Chem.* **2014**, *53*, 3263–3265.

[140] C. Doffek, M. Seitz, *Angew. Chem. Int. Ed.* **2015**, *54*, 9719–9721.

[141] J. Wahsner, M. Seitz, *Inorg. Chem.* **2015**, *54*, 9681–9683.

[142] B. Mollwitz, E. Brunk, S. Schmitt, F. Pojer, M. Bannwarth, M. Schiltz, U. Rothlisberger, K. Johnsson, *Biochemistry* **2012**, *51*, 986–994.

[143] R. A. Evangelista, A. Pollak, B. Allore, A. F. Templeton, R. C. Morton, E. P. Diamandis, *Clin. Biochem.* **1988**, *21*, 173–178.

[144] T. Nishioka, K. Fukui, K. Matsumoto in *Handbook on the Physics and Chemistry of Rare Earths, Vol. 37* (Eds.: K. A. Gschneidner, J. G. Bünzli, V. K. Pecharsky), Elsevier B.V, Amsterdam, **2007**, pp. 171–216.

[145] F. Sellrie, M. Beck, N. Hildebrandt, B. Micheel, *Anal. Methods* **2010**, *2*, 1298–1301.

[146] Y. Kitamura, T. Ihara, Y. Tsujimura, Y. Osawa, A. Jyo, *Nucleic Acids Symp. Ser.* **2006**, *50*, 105–106.

[147] A. Thibon, V. C. Pierre, *Anal. Bioanal. Chem.* **2009**, *394*, 107–120.

[148] S. Mohandessi, M. Rajendran, D. Magda, L. W. Miller, *Chem. Eur. J.* **2012**, *18*, 10825–10829.

[149] J. Xu, T. M. Corneillie, E. G. Moore, G. L. Law, N. G. Butlin, K. N. Raymond, *J. Am. Chem. Soc.* **2011**, *133*, 19900–19910.

[150] X. Zou, M. Rajendran, D. Magda, L. W. Miller, *Bioconjug. Chem.* **2015**, *26*, 460–465.

[151] K. Hanaoka, K. Kikuchi, H. Kojima, Y. Urano, T. Nagano, *J. Am. Chem. Soc.* **2004**, *126*, 12470–12476.

[152] R. Ahrends, S. Pieper, A. Kühn, H. Weisshoff, M. Hamester, T. Lindemann, C. Scheler, K. Lehmann, K. Taubner, M. W. Linscheid, *Mol. Cell. Proteomics* **2007**, *6*, 1907–1916.

[153] K. Brückner, K. Schwarz, S. Beck, M. W. Linscheid, *Anal. Chem.* **2014**, *86*, 585–591.

[154] P. H. J. Keizers, A. Saragliadis, Y. Hiruma, M. Overhand, M. Ubbink, *J. Am. Chem. Soc.* **2008**, *130*, 14802–14812.

[155] G. Otting, *J. Biomol. NMR* **2008**, *42*, 1–9.

[156] I. Bertini, C. Luchinat, G. Parigi, *Concepts Magn. Reson.* **2002**, *14*, 259–286.

[157] C. Dee, D. Esteban-Gómez, C. Platas-Iglesias, M. Seitz, *Inorg. Chem.* **2018**, *57*, 7390–7401.

[158] J. Mathieu, A. Marsura, *Synth. Commun.* **2003**, *33*, 409–414.

[159] S. Caron, N. M. Do, J. E. Sieser, *Tetrahedron Lett.* **2000**, *41*, 2299–2302.

[160] E. Kreidt, C. Bischof, C. Platas-Iglesias, M. Seitz, *Inorg. Chem.* **2016**, *55*, 5549–5557.

[161] C. Bischof, PhD thesis, Ruhr-Universität Bochum, **2013**.

[162] E. Kreidt, Master thesis, Ruhr-University Bochum, **2014**.

[163] K. Binnemans, *Coord. Chem. Rev.* **2015**, *295*, 1–45.

[164] J. P. Cross, A. Dadabhoy, P. G. Sammes, *J. Lumin.* **2004**, *110*, 113–124.

[165] C. Doffek, M. Seitz, *Angew. Chem. Int. Ed.* **2015**, *54*, 9719–9721.

[166] J. M. Baskin, J. A. Prescher, S. T. Laughlin, N. J. Agard, P. V. Chang, I. A. Miller, A. Lo, J. A. Codelli, C. R. Bertozzi, *Proc. Natl. Acad. Sci.* **2007**, *104*, 16793–16797.

[167] P. V. Chang, J. A. Prescher, E. M. Sletten, J. M. Baskin, I. A. Miller, N. J. Agard, A. Lo, C. R. Bertozzi, *Proc. Natl. Acad. Sci.* **2010**, *107*, 1821–1826.

[168] J. A. Peters, J. Huskens, D. J. Raber, *Prog. Nucl. Magn. Reson. Spectrosc.* **1996**, *28*, 283–350.

[169] A. Rodríguez-Rodríguez, D. Esteban-Gómez, A. de Blas, T. Rodríguez-Blas, M. Botta, R. Tripier, C. Platas-Iglesias, *Inorg. Chem.* **2012**, *51*, 13419–13429.

[170] J. Reuben, *J. Magn. Reson.* **1973**, *11*, 103–104.

[171] J. H. Forsberg, R. M. Delaney, Q. Zhao, G. Harakas, R. Chandran, *Inorg. Chem.* **1995**, *34*, 3705–3715.

[172] P. Ramachandran, G. Varoquaux, *Comput. Sci. Eng.* **2011**, *13*, 40–51.

[173] P. J. Kocienski, *Protecting Groups*, Georg Thieme Verlag, Stuttgart, 2nd ed., **2005**.

[174] P. G. M. Wuts, T. W. Greene, *Greene's Protective Groups in Organic Synthesis*, John Wiley & Sons, Inc., Hoboken, **2006**.

[175] E. M. Mash, K. A. Nelson, S. Van Deusen, S. B. Hemperley, *Org. Synth.* **1990**, *68*, 92–99.

[176] M. Seitz, *unpublished results.*

[177] G. Stavrakov, M. Keller, B. Breit, *Eur. J. Org. Chem.* **2007**, *2007*, 5726–5733.

[178] A. Klemer, M. Bieber, H. Wilbers, *Liebigs Ann. Chemie* **1983**, *1983*, 1416–1421.

[179] R. Binkley, D. Hehemann, *J. Org. Chem.* **1990**, *55*, 378–380.

[180] R. Giuliano, F. Villani, *J. Org. Chem.* **1995**, *60*, 202–211.

[181] M. H. Park, R. Takeda, K. Nakanishi, *Tetrahedron Lett.* **1987**, *28*, 3823–3824.

[182] F. J. Ablenas, *Can. J. Chem.* **1989**, *67*, 699–702.

[183] Y. Oikawa, T. Yoshioka, O. Yonemitsu, *Tetrahedron Lett.* **1982**, *23*, 885–888.

[184] N. Nakajima, T. Hamada, T. Tanaka, Y. Oikuwa, O. Yonemitsu, *J. Am. Chem. Soc.* **1986**, *108*, 4645–4647.

[185] M. A. Rahim, S. Matsumura, K. Toshima, *Tetrahedron Lett.* **2005**, *46*, 7307–7309.

[186] P. H. J. Keizers, J. F. Desreux, M. Overhand, M. Ubbink, *J. Am. Chem. Soc.* **2007**, *129*, 9292–9293.

[187] N. L. Fawzi, M. R. Fleissner, N. J. Anthis, T. Kálai, K. Hideg, W. L. Hubbell, G. M. Clore, *J. Biomol. NMR* **2011**, *51*, 105–114.

[188] G. L. Kenyon, T. W. Bruice, *Methods Enzymol.* **1976**, *47*, 407–430.

[189] T. P. Johnston, *J. Org. Chem.* **1990**, *26*, 3780–3783.

[190] T. D. Ladd, F. Jelezko, R. Laflamme, Y. Nakamura, C. Monroe, J. L. O'Brien, *Nature* **2010**, *464*, 45–53.

[191] E. Katz, V. Bocharova in *Mol. Supramol. Inf. Process.*, Wiley-VCH Verlag GmbH & Co. KGaA, Weinheim, **2013**, pp. 1–9.

[192] U. Pischel, J. Andréasson, D. Gust, V. F. Pais, *ChemPhysChem* **2013**, *14*, 28–46.

[193] T. Tamaki, T. Ogawa, *Top. Curr. Chem.* **2017**, *375*, 1–29.

[194] A. Extance, *Nature* **2016**, *537*, 22–24.

[195] S. Clancy, W. Brown, *Nat. Educ.* **2008**, *1*, 101.

[196] S. M. H. Tabatabaei Yazdi, Y. Yuan, J. Ma, H. Zhao, O. Milenkovic, *Sci. Rep.* **2015**, *5*, 1–10.

[197] J. Bornholt, L. Ceze, R. Lopez, G. Seelig, D. M. Carmean, K. Strauss, *ASPLOS 2016 (International Conference on Architectural Support for Programming Languages and Operating Systems)*, **2016**.

[198] L. Organick, S. D. Ang, Y.-J. Chen, R. Lopez, S. Yekhanin, K. Makarychev, M. Z. Racz, G. Kamath, P. Gopalan, B. Nguyen, C. Takahashi, S. Newman, H.-Y. Parker, C. Rashtchian, K. Stewart, G. Gupta, R. Carlson, J. Mulligan, D. Carmean, G. Seelig, L. Ceze, K. Strauss, *bioRxiv* **2017**, 114553–114567.

[199] S. M. H. Tabatabaei Yazdi, R. Gabrys, O. Milenkovic, *Sci. Rep.* **2017**, *7*, 1–6.

[200] Y. Zhao, Y. Cheng, L. Shang, J. Wang, Z. Xie, Z. Gu, *Small* **2015**, *11*, 151–174.

[201] A. Czarnik, *Curr. Opin. Chem. Biol.* **1997**, *1*, 60–66.

[202] K. Braeckmans, S. C. de Smedt, M. Leblans, C. Roelant, R. Pauwels, J. Demeester, *Mod. Drug Discov.* **2003**, 28–31.

[203] H. M. Geysen, C. D. Wagner, W. M. Bodnar, C. J. Markworth, G. J. Parke, F. J. Schoenen, D. S. Wagner, D. S. Kinder, *Chem. Biol.* **1996**, *3*, 679–688.

[204] M. He, B. Hu, Y. Zeng, Z. Jiang, *J. Alloys Compd.* **2005**, *390*, 168–174.

[205] K. Inagaki, H. Haraguchi, *Analyst* **1999**, *125*, 191–196.

[206] F. Zhang, R. C. Haushalter, R. W. Haushalter, Y. Shi, Y. Zhang, K. Ding, D. Zhao, G. D. Stucky, *Small* **2011**, *7*, 1972–1976.

[207] X. Zhang, Y. Ren, M. Chen, L. Wu, *J. Colloid Interface Sci.* **2011**, *358*, 347–353.

[208] J. Lee, P. W. Bisso, R. L. Srinivas, J. J. Kim, A. J. Swiston, P. S. Doyle, *Nat. Mater.* **2014**, *13*, 524–529.

[209] Y. Zhang, L. Zhang, R. Deng, J. Tian, Y. Zong, D. Jin, X. Liu, *J. Am. Chem. Soc.* **2014**, *136*, 4893–4896.

[210] A. Al Ouahabi, J.-A. Amalian, L. Charles, J.-f. Lutz, *Nat. Commun.* **2017**, *8*, 967–975.

[211] G. Cavallo, S. Poyer, J.-A. Amalian, F. Dufour, A. Burel, C. Carapito, L. Charles, J.-F. Lutz, *Angew. Chem. Int. Ed.* **2018**, *57*, 1–5.

[212] R. B. Merrifield, *J. Am. Chem. Soc.* **1963**, *85*, 2149–2154.

[213] C. W. Tornøe, C. Christensen, M. Meldal, *J. Org. Chem.* **2002**, *67*, 3057–64.

[214] S. Lee, J. Xie, X. Chen, *Biochemistry* **2010**, *49*, 1364–1376.

[215] A. V. Schally, A. Nagy, *Eur. J. Endocrinol.* **1999**, *141*, 1–14.

[216] K. Fosgerau, T. Hoffmann, *Drug Discov. Today* **2015**, *20*, 122–128.

[217] E. Gazit, *Chem. Soc. Rev.* **2007**, *36*, 1263–1269.

[218] K. Sajna, A. M. Fracaroli, O. M. Yaghi, K. Tashiro, *Inorg. Chem.* **2015**, *54*, 1197–9.

[219] P. Vairaprakash, H. Ueki, K. Tashiro, O. M. Yaghi, *J. Am. Chem. Soc.* **2011**, 759–761.

[220] P. K. Sukul, P. Bose, T. Takei, O. Yaghi, Y. He, M. Lee, K. Tashiro, *Chem. Commun.* **2015**, *52*, 5–7.

[221] P. Bose, P. K. Sukul, O. M. Yaghi, *J. Vis. Exp.* **2016**, 5–11.

[222] *Fmoc Solid Phase Peptide Synthesis*, (Eds.: W. C. Chan, P. D. White), Oxford University Press, **2000**.

[223] E. Valeur, M. Bradley, *Chem. Soc. Rev.* **2009**, *38*, 606–631.

[224] G. T. Hermanson in *Bioconjugate Techniques*, Elsevier, Amsterdam, **2013**, pp. 395–463.

[225] S. Sharma, *Synthesis* **1978**, *11*, 803–820.

[226] T. Houben, Heinrich J., Weyl, *Methods of Organic Chemistry, Vol. IX, 4th Edition: Sulfur, Selenium, Tellurium Compounds*, Thieme, Stuttgart, **1955**, p. 875 ff.

[227] X. Lou, B. F. De Waal, J. L. Van Dongen, J. A. Vekemans, E. W. Meijer, *J. Mass Spectrom.* **2010**, *45*, 1195–1202.

[228] M. Hesse, H. Meier, B. Zeeh, *Spektroskopische Methoden in der organischen Chemie*, Georg Thieme Verlag, Stuttgart, **2012**.

[229] C. Johnson, *Prog. Nucl. Magn. Reson. Spectrosc.* **1999**, *34*, 203–256.

[230] A. Macchioni, G. Ciancaleoni, C. Zuccaccia, D. Zuccaccia, *Chem. Soc. Rev.* **2008**, *37*, 479–489.

[231] R. Evans, Z. Deng, A. K. Rogerson, A. S. McLachlan, J. J. Richards, M. Nilsson, G. A. Morris, *Angew. Chem. Int. Ed.* **2013**, *52*, 3199–3202.

[232] J. C. Chambron, C. Dietrich-Buchecker, J. P. Sauvage in *Supramolecular Chemistry I - Directed Synthesis and Molecular Recognition*, Springer, Berlin, **1993**, pp. 131–162.

[233] K.-H. Hellwich, *Stereochemie - Grundbegriffe*, Springer, Heidelberg, **2007**.

[234] M. Górecki, L. Carpita, L. Arrico, F. Zinna, L. Di Bari, *Dalton Trans.* **2018**, *47*, 7166–7177.

[235] R. Carr, N. H. Evans, D. Parker, *Chem. Soc. Rev.* **2012**, *41*, 7673.

[236] J. P. Riehl, G. Muller, *Comprehensive Chiroptical Spectroscopy*, John Wiley & Sons, Inc., Hoboken, **2011**, pp. 65–91.

[237] G. Muller in *Lumin. Lanthan. Ions Coord. Compd. Nanomater.* (Ed.: A. de Bettencourt-Dias), John Wiley & Sons, Hoboken, **2014**, pp. 77–123.

[238] F. Zinna, L. Di Bari, *Chirality* **2015**, *27*, 1–13.

[239] E. M. Sánchez-Carnerero, A. R. Agarrabeitia, F. Moreno, B. L. Maroto, G. Muller, M. J. Ortiz, S. De La Moya, *Chem. Eur. J.* **2015**, *21*, 13488–13500.

[240] G. Longhi, *Chirality* **2016**, *28*, 696–707.

[241] S. Abdollahi, W. R. Harris, J. P. Riehl, *J. Phys. Chem.* **1996**, *100*, 1950–1956.

[242] N. Çoruh, J. P. Riehl, *Biochemistry* **1992**, *31*, 7970–7976.

[243] J. Yuasa, T. Ohno, H. Tsumatori, R. Shiba, H. Kamikubo, M. Kataoka, Y. Hasegawa, T. Kawai, *Chem. Commun.* **2013**, *49*, 4604–4606.

[244] F. Zinna, U. Giovanella, L. D. Bari, *Adv. Mater.* **2015**, *27*, 1791–1795.

[245] F. Zinna, M. Pasini, F. Galeotti, C. Botta, L. Di Bari, U. Giovanella, *Adv. Funct. Mater.* **2017**, *27*, 1603719–1603719–8.

[246] A. T. Frawley, R. Pal, D. Parker, *Chem. Commun.* **2016**, *52*, 13349–13352.

[247] L. Di Bari, P. Salvadori in *Comprehensive Chiroptical Spectroscopy, Volume 1: Instrumentation, Methodologies, and Theoretical Simulations* (Eds.: N. Berova, P. L. Polavarapu, K. Nakanishi, R. W. Woody), John Wiley & Sons, Inc., Hoboken, **2012**, pp. 221–246.

[248] F. S. Richardson, *Inorg. Chem.* **1980**, *19*, 2806–2812.

[249] R. S. Dickins, J. A. Howard, C. L. Maupin, J. M. Moloney, D. Parker, J. P. Riehl, G. Siligardi, J. A. Williams, *Chem. Eur. J.* **1999**, *5*, 1095–1105.

[250] A. P. S. Samuel, J. L. Lunkley, G. Muller, K. N. Raymond, *Eur. J. Inorg. Chem.* **2010**, *2010*, 3343–3347.

[251] J. Gregolinski, P. Starynowicz, *J. Am. Chem. Soc.* **2008**, *130*, 17761–17773.

[252] J. Yuasa, T. Ohno, K. Miyata, H. Tsumatori, Y. Hasegawa, T. Kawai, *J. Am. Chem. Soc.* **2011**, *133*, 9892–9902.

[253] M. Leonzio, A. Melchior, G. Faura, M. Tolazzi, F. Zinna, L. Di Bari, F. Piccinelli, *Inorg. Chem.* **2017**, *56*, 4413–4421.

[254] G. L. Hilmes, J. P. Riehl, *Inorg. Chem.* **1986**, *25*, 2617–2622.

[255] R. C. Carter, C. E. Miller, R. A. Palmer, P. S. May, D. H. Metcalf, F. S. Richardson, *Chem. Phys. Lett.* **1986**, *131*, 37–43.

[256] P. S. May, D. H. Metcalf, F. S. Richardson, R. C. Carter, C. E. Miller, R. A. Palmer, *J. Lumin.* **1992**, *51*, 249–268.

[257] S. Petoud, G. Muller, E. G. Moore, J. Xu, J. Sokolnicki, J. P. Riehl, U. N. Le, S. M. Cohen, K. N. Raymond, *J. Am. Chem. Soc.* **2007**, *129*, 77–83.

[258] J. P. Leonard, P. Jensen, T. McCabe, J. E. O'Brien, R. D. Peacock, P. E. Kruger, T. Gunnlaugsson, *J. Am. Chem. Soc.* **2007**, *129*, 10986–10987.

[259] K. Murata, M. Morita, K. Eguchi, *J. Lumin.* **1988**, *42*, 227–234.

[260] T. Wu, P. Bour, *Chem. Commun.* **2018**, *54*, 1790–1792.

[261] J. I. Bruce, D. Parker, S. Lopinski, R. D. Peacock, *Chirality* **2002**, *14*, 562–567.

[262] J. L. Lunkley, D. Shirotani, K. Yamanari, S. Kaizaki, G. Muller, *J. Am. Chem. Soc.* **2008**, *130*, 13814–13815.

[263] J. Kumar, B. Marydasan, T. Nakashima, T. Kawai, J. Yuasa, *Chem. Commun.* **2016**, *52*, 9885–9888.

[264] J. L. Lunkley, D. Shirotani, K. Yamanari, S. Kaizaki, G. Muller, *Inorg. Chem.* **2011**, *50*, 12724–12732.

[265] S. Di Pietro, L. Di Bari, *Inorg. Chem.* **2012**, *51*, 12007–12014.

[266] C. L. Maupin, R. S. Dickins, L. G. Govenlock, C. E. Mathieu, D. Parker, J. A. Gareth Williams, J. P. Riehl, *J. Phys. Chem. A* **2000**, *104*, 6709–6717.

[267] E. Kreidt, L. Arrico, F. Zinna, L. Di Bari, M. Seitz, *Chem. Eur. J.* **2018**, *24*, 13556–13564.

[268] C. Bischof, J. Wahsner, J. Scholten, S. Trosien, M. Seitz, *J. Am. Chem. Soc.* **2010**, *132*, 14334–14335.

[269] W. H. Melhuish, *J. Phys. Chem.* **1961**, *65*, 229–235.

[270] M. H. V. Werts, R. T. F. Jukes, J. W. Verhoeven, *Phys. Chem. Chem. Phys.* **2002**, *4*, 1542–1548.

[271] A. Aebischer, F. Gumy, J.-C. G. Bünzli, *Phys. Chem. Chem. Phys.* **2009**, *11*, 1346.

[272] E. Kreidt, C. Dee, M. Seitz, *Inorg. Chem.* **2017**, *56*, 8752–8754.

[273] C. Andraud, O. Maury, *Eur. J. Inorg. Chem.* **2009**, 4357–4371.

[274] A. Bagheri, H. Arandiyan, C. Boyer, M. Lim, *Adv. Sci.* **2016**, *3*, 1–25.

[275] H. Dong, L.-D. Sun, C.-H. Yan, *Chem. Soc. Rev.* **2015**, *44*, 1608–1634.

[276] M.-F. Joubert, *Opt. Mater.* **1999**, *11*, 181–203.

[277] O. a. Blackburn, M. Tropiano, T. J. Sørensen, J. Thom, A. Beeby, L. M. Bushby, D. Parker, L. S. Natrajan, S. Faulkner, *Phys. Chem. Chem. Phys.* **2012**, *14*, 13378–13384.

[278] L. J. Charbonnière, *Dalton Trans.* **2018**, *47*, 8566–8570.

[279] X. Xiao, J. P. Haushalter, G. W. Faris, *Opt. Lett.* **2005**, *30*, 1674–1676.

[280] C. Reinhard, H. U. Güdel, *Inorg. Chem.* **2002**, *41*, 1048–1055.

[281] D. Atwood, *The Rare Earth Elements: Fundamentals and Application*, John Wiley & Sons, Hoboken, **2013**.

[282] F. Wang, L. X., *J. Am. Chem. Soc.* **2008**, *130*, 5642.

[283] T. J. Sørensen, O. A. Blackburn, M. Tropiano, S. Faulkner, *Chem. Phys. Lett.* **2012**, *541*, 16–20.

[284] A. Zaïm, S. V. Eliseeva, L. Guénée, H. Nozary, S. Petoud, C. Piguet, *Chemistry* **2014**, *20*, 12172–12182.

[285] S. Faulkner, S. J. A. Pope, *J. Am. Chem. Soc.* **2003**, *125*, 10526–10527.

[286] C. Gao, A. M. Kirillov, W. Dou, X. Tang, L. Liu, X. Yan, Y. Xie, P. Zang, W. Liu, Y. Tang, *Inorg. Chem.* **2014**, *53*, 935–942.

[287] C. M. Andolina, J. R. Morrow, *Eur. J. Inorg. Chem.* **2011**, 154–164.

[288] K. E. Knope, D. T. De Lill, C. E. Rowland, P. M. Cantos, A. De Bettencourt-Dias, C. L. Cahill, *Inorg. Chem.* **2012**, *51*, 201–206.

[289] P. Harvey, A. Nonat, C. Platas-Iglesias, L. S. Natrajan, L. J. Charbonnière, *Angew. Chem. Int. Ed.* **2018**, *57*, 9921–9924.

[290] M. Albin, W. D. Horrocks, *Inorg. Chem.* **1985**, *24*, 895–900.

[291] S. T. Frey, W. D. W. Horrocks, *Inorg. Chim. Acta* **1995**, *229*, 383–390.

[292] G. R. Choppin, Z. M. Wang, *Inorg. Chem.* **1997**, *36*, 249–252.

[293] A. Nonat, M. Regueiro-Figueroa, D. Esteban-Gõmez, A. De Blas, T. Rodríguez-Blas, C. Platas-Iglesias, L. J. Charbonnière, *Chem. Eur. J.* **2012**, *18*, 8163–8173.

[294] N. Souri, P. Tian, C. Platas-Iglesias, K.-L. Wong, A. Nonat, L. J. Charbonnière, *J. Am. Chem. Soc.* **2017**, *139*, 1456–1459.

[295] N. Souri, P. Tian, A. Lecointre, Z. Lemaire, S. Chafaa, J.-M. Strub, S. Cianférani, M. Elhabiri, C. Platas-Iglesias, L. J. Charbonnière, *Inorg. Chem.* **2016**, *55*, 12962–12974.

[296] B. S. K. Chong, E. G. Moore, *Dalton Trans.* **2016**, *45*, 12200–12205.

[297] I. Hyppänen, S. Lahtinen, T. Ääritalo, J. Mäkelä, J. Kankare, T. Soukka, *ACS Photonics* **2014**, *1*, 394–397.

[298] G. Vlád, I. T. Horváth, *J. Org. Chem.* **2002**, *67*, 6550–6552.

[299] Q.-D. Liu, R. Wang, S. Wang, *Dalton Trans.* **2004**, *35*, 2073–2079.

[300] A. Inagaki, S. Yatsuda, S. Edure, A. Suzuki, T. Takahashi, M. Akita, *Inorg. Chem.* **2007**, *46*, 2432–2445.

[301] F. Havas, N. Leygue, M. Danel, B. Mestre, C. Galaup, C. Picard, *Tetrahedron* **2009**, *65*, 7673–7686.

[302] F. Vögtle, R. Hochberg, F. Kochendörfer, P.-M. Windscheif, M. Volkmann, M. Jansen, *Chem. Ber.* **1990**, *123*, 2181–2185.

[303] Q. D. Zhong, Y. Z. Xue, H. Yan, X. Q. Song, R. G. Zhong, *Bioorganic Med. Chem. Lett.* **2010**, *20*, 5532–5535.

[304] J. J. P. Stewart, *MOPAC2016*, **2016**.

[305] J. J. P. Stewart, *J. Mol. Model.* **2013**, *19*, 1–32.

[306] J. D. L. Dutra, M. A. M. Filho, G. B. Rocha, R. O. Freire, A. M. Simas, J. J. P. Stewart, *J. Chem. Theory Comput.* **2013**, *9*, 3333–3341.

[307] L. J. Farrugia, *J. Appl. Crystallogr.* **1999**, *32*, 837–838.

[308] A. Altomare, G. Cascarano, C. Giacovazzo, A. Guagliardi, *J. Appl. Crystallogr.* **1993**, *26*, 343–350.

[309] G. M. Sheldrick, *SHELX97-Programs for Chrystal Structure Analysis*, **1998**.

[310] F. Zinna, T. Bruhn, C. A. Guido, J. Ahrens, M. Bröring, L. Di Bari, G. Pescitelli, *Chem. Eur. J.* **2016**, *22*, 16089–16098.

[311] G. R. Newkome, S. Pappalardo, V. K. Gupta, F. R. Fronczek, *J. Org. Chem.* **1983**, *48*, 4848–4851.

[312] R. Balda, J. Fernandez, A. Mendioroz, M. Voda, M. Al-Saleh, *Phys. Rev. B* **2003**, *68*, 165101–165101–7.

[313] R. Balda, J. Fernandez, A. Mendioroz, M. Voda, M. Al-Saleh, *Opt. Mater.* **2003**, *24*, 91–95.

[314] P. V. Ramakrishna, S. V. N. Pammi, K. Samatha, *Solid State Commun.* **2013**, *155*, 21–24.

[315] X. Wang, X. Yan, C. Kan, *J. Lumin.* **2011**, *131*, 2325–2329.

[316] R. Martin-Rodriguez, R. Valiente, S. Polizzi, M. Bettinelli, A. Speghini, F. Piccinelli, *J. Phys. Chem. C* **2009**, *113*, 12195–12200.

[317] Y. Y. Zhang, L. W. Yang, C. F. Xu, J. X. Zhong, C. Q. Sun, *Appl. Phys. B Lasers Opt.* **2010**, *98*, 243–247.

[318] C.-R. Li, S.-F. Li, B. Dong, J.-C. Sun, X.-F. Bo, X.-N. Fan, *Chin. Phys. B* **2012**, *21*, 097803–097803–4.

[319] M. Xing, W. Cao, H. Zhong, Y. Zhang, X. Luo, Y. Fu, W. Feng, T. Pang, X. Yang, *J. Alloys Compd.* **2011**, *509*, 5725–5730.

[320] M. Wang, Y. Zhu, C. Mao, *Langmuir* **2015**, *31*, 7084–7090.

[321] A. X. Yin, Y. W. Zhang, L. D. Sun, C. H. Yan, *Nanoscale* **2010**, *2*, 953–959.

[322] E. Nakazawa, S. Shionoya, *Phys. Rev. Lett.* **1970**, *25*, 1710–1712.